Theory and Design of High-Index-Contrast Microphotonic Circuits

by

Miloš Popović

B.Sc.E. (Electrical and Computer Engineering)
Queen's University, Canada (1999)

S.M. (Electrical Engineering and Computer Science)
Massachusetts Institute of Technology (2002)

Submitted to the Department of Electrical Engineering and Computer Science
in partial fulfillment of the requirements for the degree of

Doctor of Philosophy in Electrical Engineering

at the

MASSACHUSETTS INSTITUTE OF TECHNOLOGY

February 2008

Author .....
Department of Electrical Engineering and Computer Science
September 15, 2007

Certified by .....
Erich P. Ippen
Elihu Thomson Professor of Electrical Engineering
Professor of Physics
Thesis Supervisor

Certified by .....
Franz X. Kärtner
Professor of Electrical Engineering
Thesis Supervisor

Accepted by .....
Terry P. Orlando
Chairman, Department Committee on Graduate Students

Theory and Design of High-Index-Contrast Microphotonic Circuits

by

Miloš Popović

Submitted to the Department of Electrical Engineering and Computer Science
on September 15, 2007, in partial fulfillment of the
requirements for the degree of
Doctor of Philosophy in Electrical Engineering

Abstract

Advanced microphotonic device designs in strongly confining silicon and silicon nitride waveguides, novel photonic device concepts, and the first experimental demonstrations of these structures are described. They show a progression of new optical signal processing capabilities that enable chip-scale microphotonic routers for high bandwidth and fine granularity optical wavelength routing networks. Rigorous theoretical models are developed that enable the design of efficient high-index-contrast (HIC) microphotonic components and set theoretical bounds for their capabilities. They take into account new, coupling induced resonance-frequency shifting and parasitic loss effects.

Based on microring resonators and HIC silicon and silicon nitride waveguides, the first telecom-grade microphotonic channel add-drop filters are demonstrated, including novel, dispersion-free switchable and widely tunable designs. Several new classes of optical devices are proposed. The first, universally balanced interferometers, enable filters capable of "fully transparent" tuning and increased accessible wavelength range, facilitate a novel proposed photonic-circuit "hot-swapping" functionality, and approximate an optical near-inverse operator in a general way. The second, loop-coupled resonators, enable optimally sharp filters and flat-top, dispersionless light-slowing structures that are not limited by the Kramers-Kronig amplitude-dispersion tradeoff. A third class provides a general approach to disabling both the amplitude and phase response of resonant systems to achieve a full-transparency off state. They allow a robust integrated solution to hitless, errorless filter tuning and wavelength-reach expansion in filters, topical problems of considerable technological importance.

Taken together these developments permit a complete tunable/reconfigurable optical add-drop multiplexer (T/R-OADM) to be constructed on a silicon chip, with performance well beyond that of current technology. Such a demonstration device was designed and fabricated. This work also provides new general building blocks for microphotonic circuits, and design guidelines for strong confinement photonics.

Thesis Supervisor: Erich P. Ippen
Title: Elihu Thomson Professor of Electrical Engineering
Professor of Physics

Thesis Supervisor: Franz X. Kärtner
Title: Professor of Electrical Engineering

Massachusetts Institute of Technology
Department of Electrical Engineering and Computer Science
Research Laboratory of Electronics

Doctor of Philosophy Dissertation

Theory and Design of High-Index-Contrast Microphotonic Circuits

by

Miloš Popović

Supervisors: Erich P. Ippen and Franz X. Kärtner

Cambridge, Massachusetts, 2007

To my Katherine,

to my sister, parents and grandparents,

and

to Prof. Hermann Haus.

In gratitude.

Contents

Acknowledgments

This thesis documents aspects of my work over the past seven years. I am grateful to Professor Hermann Haus, who was my Ph.D. advisor from 2000 until his death in 2003. I found a great affinity with his ways of thinking in general terms, and his positive energy with respect to both work and personal relationships left a great impression on me. His vision for high-index-contrast photonic circuits, cultivated from the early 90's, led to the MIT-Pirelli R-OADM project (2001–2006) that this work was mainly done under. I owe a great debt to my subsequent advisors over, as it turned out, the course of most of my Ph.D., Professors Erich P. Ippen and Franz X. Kärtner who, after Prof. Haus' death, without hesitation continued to support me in my work to its completion. Prof. Ippen is also responsible for my first having joined this research group in 2000. His thoughtful but discreet support and genuine professional feedback throughout the years have been very important to me and helped give focus to my research. Franz Kärtner's tremendous support, positive thinking, dedication to our project and our shared conceptual interests and affinities have likewise contributed a great deal to sustaining my efforts.

Regarding the work presented in this thesis, I would like foremost to acknowledge Tymon Barwicz, Peter Rakich and Mike Watts, my colleagues and closest collaborators on the MIT-Pirelli project that marked our time at MIT. Their exceptional work is equally responsible for the experimental results reported in this thesis. Tymon developed the processes and fabrication techniques, and fabricated all of the SiN and Si devices in this work. Tymon and I later jointly led the silicon device effort. Mike Watts and I jointly worked on simulation of silicon nitride filters, besides his other creative and important contributions in polarization handling. Peter characterized and experimentally studied the properties of all of the silicon nitride devices, and at the same time taught me many things about experimental work.

In the work on silicon structures, from 2005 onward, Tymon and I were joined by Fuwan Gan, Charles Holzwarth (Trey) and Marcus Dahlem, all of whom made essential contributions to this work. Fuwan, with our guidance, did all of the thermal modeling and microheater design, in addition to contributing a great fun-loving personality to keep us all up-beat. Trey completed the microheater fabrication after Tymon's departure, mounted, wire-bonded and passivated the silicon chips, and has in general been a great, reliable and generous colleague. Marcus, with our input, designed the thermal-sink Si chip holder and circuit boards, and characterized most of the silicon structures; his eye for esthetics leaves its mark even in our scientific results.

I also thank Prof. Hank Smith who, through his presence on the entire project and gen-

uine input, has been an unofficial advisor. All devices demonstrated here were fabricated under his guidance at the MIT Nanostructures Lab. I would like to thank our colleagues from Pirelli Labs: first, Luciano Socci, for a great two years of working together at MIT, and for managing our constant dialogue with Pirelli. Luciano and Marco Romagnoli gave us many challenges, including the problem of hitless tuning in 2003. I also thank Maurizio Tormen, Matteo Cherchi and Fabrizio Giacometti. My first officemates, Christina Manolatou and Jalal Khan, introduced me to integrated optics. Christina's FDTD codes, that we inherited, made it possible for me to focus my on the physics (and on developing other tools). I thank all of my many colleagues and friends in the OQE group that made life at the office fun – you know who you are.

I thank Prof. Rajeev Ram for serving on my thesis committee, and in general for his open, positive and friendly attitude. Prof. Lionel Kimerling, Dr. Kazumi Wada, Dr. Jurgen Michel and many of their students played an important role in my early graduate work, and also worked in tandem with us on the MIT-Pirelli project. Mark Beals, thanks for working hard to manage the Pirelli program.

Another important thanks goes to Anatoly Khilo, who is continuing the design-oriented research effort. In him, I have found not only a great colleague, but most closely similar interests in theoretical matters, which gives me confidence that this line of investigation will not be lost in our group. When one is in a place of such collegial support as MIT it is impossible to write a complete acknowledgment in two pages and not leave someone out – to everyone in this category, thanks.

Lastly, I owe the greatest debt to my family. My sister and my parents have been pillars of support all my life. Every step of the way, they understood me and encouraged me in the best possible way. Their confidence in me allowed me to complete such a long journey. They have even managed to understand my neglect of them during the last couple of years of intense focus on this thesis work. My grandparents – their pride and support – gave me strength to bring this work to completion.

The last thanks is to my wife and partner of seven years, Katherine. Her companionship brought to me an internal joy I'm only beginning to understand the depths of. Her love made the time in graduate school the happiest and strongest I have been despite the heavy workload, and way beyond the limitations of happiness that the discovery of a new concept or idea can bring. Her sacrifices for me during this time were ones few people can bear. She deserves more than anyone my gratitude for helping me see through such an arduous journey.

Miloš Popović
Berlin, Germany
September 18, 2007

Support

In addition to Pirelli Labs, aspects of my work in the first two years were supported by an MIT Presidential Fellowship and a National Science and Engineering Research Council (NSERC) of Canada Scholarship, and in the last year by DARPA.

Chapter 1

Introduction

Over the 50 years since the invention of the laser as a source of bright monochromatic light [1–3], optical technology has developed at a rapid rate in new directions, spawning numerous new fields of study and technologies. Bright, coherent light made novel applications possible including globe-spanning optical communication networks, high-density data storage from compact discs to holographic data storage and volume holograms, high-resolution and depth resolving imaging (optical coherence tomography), and fine-resolution, large-area photolithography which makes possible the fabrication of today's microprocessors with billions of transistors on a 1 cm^2 die. Hence, optical technology already occupies an important place in recent technological progress.

Spectrally pure coherent light also opens the door to fundamentally new functionality that can be obtained in chip-scale photonic circuits by the use of resonators. Resonant systems can tailor the amplitude and shape of optical transmission and route frequency components of light for wavelength-routing communication network applications; assemble them into optical phased arrays that can generate arbitrary optical-antenna-type radiation patterns emanating from a chip; slow down light resonantly for the purposes of nonlinear all-optical logic using the high optical fields accumulated when light is slowed down, as well as for optical buffers in all-optical telecom network routing switches (so-called slow-light applications); and enable fundamentally new ways to harness substantial optical forces at small optical powers due to large resonant enhancements of coherent light [4–6].

To everyday experience, these coherent light effects are new and counter-intuitive not only because they occur in structures on the micron scale (the scale of the wavelength of visible light), where they are generally inaccessible to human experience, but also because in nature everyday experience gives us access only to incoherent light – scrambled in phase – that does not display the additional unique

and useful interference properties of coherent light. Yet, these coherent properties are exploited in all of the photonic circuits described in this thesis, and in much of the growing field of microphotonic circuits. The opportunity to discover new ways that these unique properties of light can be used, and building a new form of intuition for light on the small scale that can be harnessed to develop novel technologies and new micron-scale machines is what makes the field of photonics both promising and exciting.

Photonic microchips

The coherent properties of light (and associated quantum properties of matter) have been exploited in macro-scale systems, for example to demonstrate slowing light to bicycle speed in atomic vapours [7]. However, just as bulk-component electonic circuits do not lend themselves to the construction of a modern billion-transistor, GHz-rate microprocessor using resistors, diodes and a soldering iron, so bulk experiments in new optical effects cannot be easily scaled to technologically relevant complexities. Microphotonic circuits, which confine light on the micron scale on a chip, promise not only the opportunity to create complex, densely integrated photonic circuits on a chip, but simultaneously make use of the size scaling to operate on the wavelength scale of light, enabling the robust exploitation of coherent effects.

For microphotonic circuits to develop into an everyday, pervasive technology, means are needed to efficiently confine, guide and route light around a chip on the micron scale. Much research has been invested into this goal over the last 10–15 years.

Coherent light and optical resonators

The resonator concept is at the heart of technology for manipulating coherent light. An electromagnetic resonator in the most general sense is an energy storage element for the excitations of a wave system. Coherence means that interference only allows energy to accumulate at certain frequencies that have wavelengths compatible with the size of the cavity in order to constructively build up an energy amplitude inside. The correspondence of energy and frequency means that resonators, by virtue of being energy storage elements, also select light based on photon energy. Furthermore, since wavelength changes with frequency, larger resonant cavities can accommodate a larger number of resonant modes in a particular frequency range. These observations lead to the consideration of the concept of strong confinement and micron-scale photonic structures.

Strong confinement

Wavelength-scale resonators were the central technology in microwave circuits before being replaced in the 1970's by monolithic microwave integrated circuits (MMICs) that confine the electromagnetic waves on a sub-wavelength scale by supporting terminating surface charges for the modal field in so-called transverse electric-magnetic (TEM, or plane-wave), metallic structures. At optical frequencies, size reduction below the wavelength scale for the majority of applications is less promising. This is because good conductors are not available at optical frequencies, and therefore low-loss TEM transmission lines cannot be constructed [8].

Therefore, optics is likely to be confined to refractive index confinement and wavelength-scale circuits for high-fidelity signal processing applications. Confinement of light in resonant cavities by step index discontinuities with low radiation loss is enabled by high index contrast between the core and cladding material. On the other hand, the number of high-Q resonant modes in the cavity, i.e. their number density per unit of frequency range in the resonant frequency spectrum, is sparser in smaller cavities. In cavities with quasi-linear propagation, such as Fabry-Perot or microring resonators, the cavity length (and group index) determine the frequency spacing of longitudinal resonances – the free spectral range (FSR).

For efficient control and manipulation of light by resonant photonic circuits it is typically desirable to use one resonant mode per cavity. When this is done, manipulation of the dimensions and properties of each cavity directly maps to design of the behaviour of one mode. When single-mode cavities are not possible, the best approach is to maximize the FSR, so that a single resonance can access the largest possible frequency spectrum of interest, that may be up to one FSR. This strategy leads to small microcavities, which in turn require strong optical confinement of the mode to simultaneously support low radiation losses (high quality factor, Q). This is the impetus for strong confinement photonics.

Strong confinement is a term used in this thesis to indicate support for small, wavelength-scale confined mode dimensions, high intrinsic cavity mode Q's, and large FSRs (multiple THz). Strong confinement implies a high index contrast, of the order of 2:1 (e.g. that needed for a complete photonic bandgap), in all directions, such that the optical mode can support tight bend radii in an optically single-mode structure. The term "strong confinement" (SC) is used because high index contrast (HIC) and high$-\Delta$ and ultra-high$-\Delta$) have previously been used to refer to index contrasts of the order of 1-2% in silica integrated optics [9], which support very weak confinement by the standards of this work, and insufficiently small microring bend radii for telecom applications, for example. Secondly, the term "high index contrast" may be used to refer to silicon ridge waveguides, for example, which may have very weak lateral confinement depending on etch depth, but which indeed have a large index contrast between the silicon core and overhead air "top

cladding"[10].

The beginnings of strong-confinement photonics can be found in the late 1980's and early 1990's in the work on photonic crystals [11, 12], and in early proposals for high index contrast conventional waveguides, microring resonators and microwave-like classical wavelength-scale devices [13, 14]. While a number of theoretical investigations have been carried out [15, 16], and early experimental demonstrations validated the concept of strong confinement [17, 18], progress to the acceptance of strong confinement photonic circuits has been slow and few if any high fidelity photonic devices were demonstrated when the present work was begun in 2002.

This slow acceptance of SC photonics is not without reason. Strongly confined, high-index-contrast structures have extreme sensitivity to dimensional variations, refractive index variations, surface roughness and polarization, and their behaviour in coupling and scattering differs from silica integrated optics in that SC photonic circuits have hybrid-polarized modes and highly dispersive waveguide propagation. Therefore a systematic and rigorous approach to addressing all of these issues is necessary on the way to realization of high-fidelity signal processing devices in SC photonics.

This thesis work, along with complementary work by my colleagues [19–21], is concerned with addressing these fundamental challenges for strong confinement photonic circuits, and demonstrating the first high fidelity optical signal processing devices based on strong-confinement microphotonic circuits using the discovered and proposed solutions.

1.1 Microphotonic circuits for wavelength-routing networks

In densely wavelength-division multiplexed (DWDM) optical networks, there is an opportunity for microphotonic technology to enable reaching the limits of bandwidth efficiency and total aggregate bandwidth by providing sophisticated filtering capabilities (such as dispersion-free filters, proposed in this thesis) which escape other approaches or whose bulk-optical analogues are difficult or impractical to realize (such as is the case with truly hitless tunable filtering). A central component for reconfigurable (agile) wavelength routing networks, in which microphotonic technology based on strong confinement can play an important role, is the tunable/reconfigurable optical add-drop multiplexer (T-OADM/R-OADM).

An optical ring network is shown in Fig. 1.1(a), illustrating the role of OADMs. Multiple wavelength channels traverse each optical fiber strand, passing nodes of the ring network one at a time. At any one node, most channels will continue on, while a small number will have reached their destination and will need to be dropped from the spectrum and routed to an output port. With the spectral slot of the dropped wavelength channel freed, an outgoing data stream at that node can

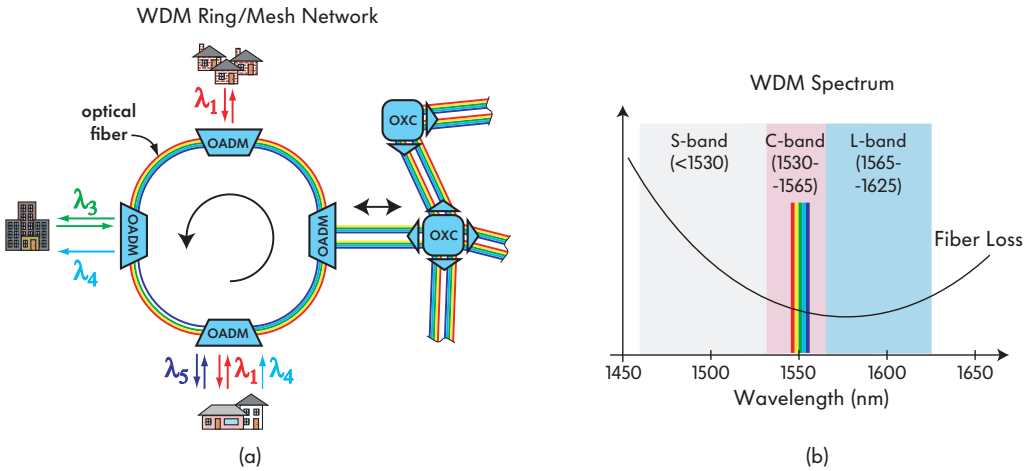

Figure 1.1: (a) Wavelength routing optical networks require tunable, reconfigurable optical add-drop multiplexer (OADM) nodes, ideally suited for chip-scale implementation in strong-confinement microphotonic circuit technology (illustration based on drawing by T. E. Murphy [22]); (b) the S-, C- and L-band telecommunication windows cover 20 THz of bandwidth with low optical propagation loss in optical fibers ("all wave" fibers with the water absorption peak eliminated); see [23].

be modulated onto the same wavelength and inserted into the vacated channel to access the network.

Fig. 1.1(b) illustrates the wavelength range of low optical loss in standard optical fibers (in particular "all-wave" fibers with the water absoption peak removed). The S-, C- and L-band cover about 20 THz of optical bandwidth, allowing an upper limit aggregate data rate of the order of 20 Tbps per strand of fiber (for binary signaling).

Selecting a set of wavelengths, dropping/adding the signal at these wavelengths to and from local ports, and passing the through-passing (express) channels together with the newly added channels onto an output port with minimal loss is the function of an optical add-drop multiplexer (OADM). The OADM may comprise a set of channel add-drop filters, as shown in Fig. 1.2(a), each of which drops and adds a selected wavelength channel.

The operation of a channel add-drop filter (CADF) on a spectrum of densely packed wavelength channels is illustrated in Fig. 1.2(b). A selected wavelength channel (cyan colored) is dropped from the spectrum into a drop port. The vacated spectral slot can be filled by a new data stream, added in from the add port (red colored). Small signal levels underneath the added channel in the through port and the dropped channel in the drop port show any residual signal remaining from the input and add ports, respectively. Such residual signal must be suppressed to low enough levels to avoid corrupting the main signal.

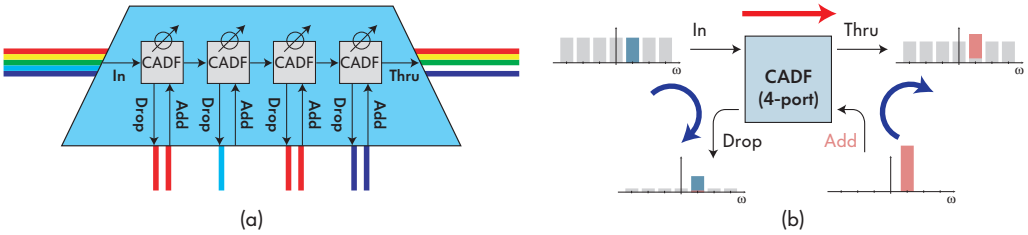

Figure 1.2: (a) Tunable, reconfigurable optical add-drop multiplexer (OADM) with four channel add-drop elements; (b) illustrating the function of a single channel add-drop filter.

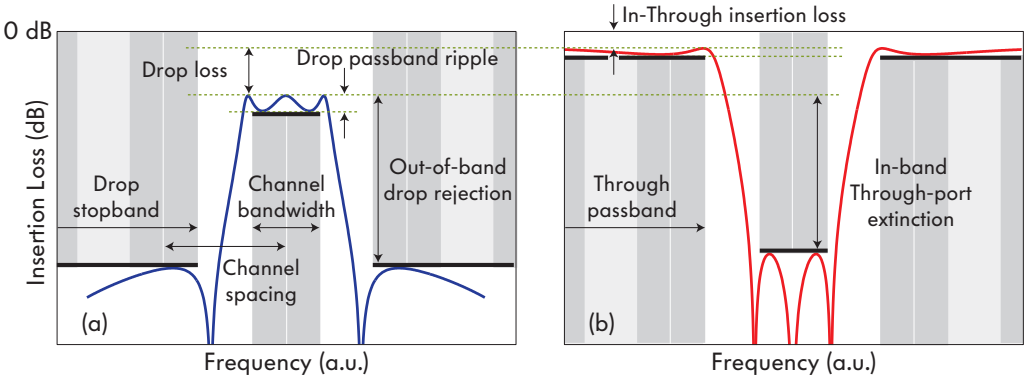

Figure 1.3: Typical spectral response specifications for WDM channel add-drop filters for (a) the drop-port response and (b) the through-port response.

Telecom-grade channel add-drop filter requirements

In order to perform the channel add-drop filtering operation without introducing significant distortion into the amplitude or phase spectrum of either the filtered channel or the bypassing channels, a set of rigorous performance requirements is imposed on telecom-grade channel add-drop filters. Some specifications of interest in the amplitude response are illustrated in Fig. 1.3. To avoid amplitude distortion, the channel dropping filter must have a flat-top response in the channel window, but roll off quickly to reject the adjacent channel by >30 dB. The specifications required for a channel add-drop filter for a wavelength channel ITU* grid of 100 GHz channel spacing are shown in Table 1.1†

The specifications in the table are challenging to meet by any means. However, in particular when narrow passbands are required (40 GHz, 20 GHz, 10 GHz), bulk technologies such as thin-film filters (TFFs) become less economical. Furthermore, the introduction of more complex and sophisticated functionality – including fully hitless, errorless tuning and switching, wide tuning and multiple channel drops

*International Telecommunications Union.

†These particular specifications were provided to the author by colleague Luciano Socci at Pirelli Labs, S.p.A., Milan, Italy. The majority of the research in this thesis was done in support of an effort to demonstrate technology for a tunable OADM based on strong confinement photonic structures, supported by Pirelli Labs through an MIT-Pirelli collaboration, Nov. 2001–Sep. 2006.

Table 1.1: Typical WDM channel add-drop filter specs for 100 GHz ITU grid

Parameter	Requirement	units
Operating wavelength range	>30	nm
Channel spacing	100	GHz
Pass-through loss (non-dropped channels)	<3	dB
Pass-through loss uniformity	<1	dB
Pass-through rejection (dropped channels)	>30	dB
Drop/add loss	<3	dB
Drop/add rejection (adjacent channels)	>30	dB
Drop/add rejection (non-adjacent channels)	>40	dB
Passband width (-1 dB point)	>40	GHz
Passband ripple	<0.5	dB
Center wavelength accuracy	$< \pm 2.5$	GHz
Tunable wavelength range	30	nm
Tuning time	<10	ms
Return loss (reflection)	>45	dB
Directivity	>45	dB
Polarization dependent loss	<0.2	dB
Chromatic dispersion	$< \pm 20$	ps/nm

– makes realization in bulk technologies more and more challenging. Complexity, interferometric structures and complex device topologies, and low power and dense integration afforded by chip-scale miniaturization are all advantages available in microphotonic implementations.

Several architectures exist for OADMs, the most common being ones similar to Fig. 1.4(a). This approach does not scale very well to high wavelength channel count and granularity because all channels are split up and recombined at each network node, leading to substantial signal distortion and loss with continued cascading. Since few channels are typically dropped at any node, a more profitable approach is the architecture in Fig. 1.4(b), which relies on the design of a tunable wavelength selecting add-drop filter, that can be turned off while tuning from one wavelength to another. This is referred to as hitless (errorless) tuning. s

Hitless tuning and reconfiguration of add-drop filters

Hitless tuning is an important and topical problem in channel routing and multiplexing devices for wavelength routing networks, and is also addressed in this work for SC microphotonic structures.

Dynamic reconfigurability is increasingly important in wavelength-routing, transparent optical networks [23]. As a result, *hitless* tuning has become a pre-

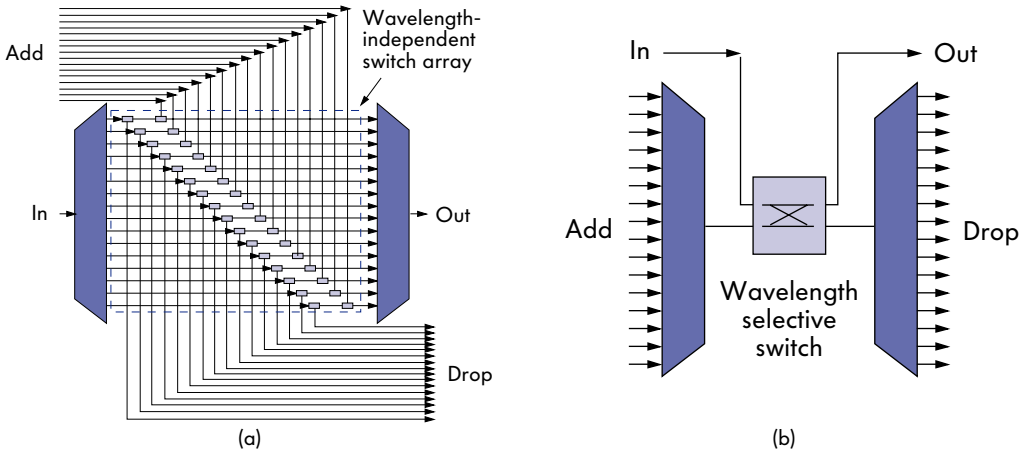

Figure 1.4: Previous approaches to reconfigurable wavelength routing and R-OADMs: (a) demultiplex all channels, route by a broadband switch on each channel, re-multiplex express channels; (b) a wavelength-selective switch may extract a subset of wavelengths without demultiplexing the entire channel spectrum. (illustration adapted from [24].)

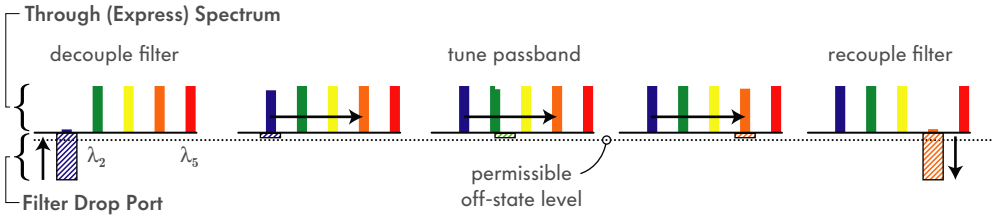

Figure 1.5: Basic approach required for hitless wavelength tuning of a tunable optical add-drop multiplexer (T-OADM): disable all resonant modes associated with a channel-dropping filter passband, tune the disabled resonant cavities to the new wavelength of interest, and re-enable the filter.

requisite for prospective designs of tunable and reconfigurable optical add-drop multiplexers (T/R-OADMs). It requires that other wavelength channels be undisturbed (on the granularity of single bits) during the reconfiguration of an add-drop filter to a target wavelength or an off-state [25, 26]. Yet efficient means of hitless tuning for emerging microphotonic filter implementations are few [25–29], and a general approach is lacking. This is evidenced by the relatively commonplace adoption of the fundamentally lossy wavelength-blocker (WB) R-OADM designs [30].

The expected channel changing operation of a hitless tunable filter is illustrated in Fig. 1.5. The add-drop filter must be turned off so that it is transparent to all channels, and the wavelength channel being dropped ceases to be dropped from the spectrum. Then the filter passband position is tuned to a new wavelength channel, so that the operation of tuning does not introduce loss, substantial dispersion or bit errors into intermediate channels. Finally, at the target channel, the filter can be re-enabled.

Resonator-based microphotonic approaches proposed for hitless tuning have a transparent amplitude transmission in the off state of the filter, but have a remaining dispersive response in the through port. This dispersive response may both introduce bit errors and add a sensitivity to waveguide loss into the spectrum. In this thesis, several approaches are proposed and demonstrated that allow "fully transparent" tuning in the off state, i.e. disable both the amplitude and phase response of a resonant system during tuning.

1.2 Challenges in strong confinement microphotonics

There is a number of challenges to realizing high-fidelity signal processing devices based on strongly confined microphotonic circuits. All are related to the ultrasensitivity of high-index-contrast micron-scale waveguides and resonators to dimensional errors, and the lithographic resolvability of the fine sub-micron features (resonator coupling gaps) required in such devices.

Sub-micron silicon microresonators have a resonance frequency sensitivity to waveguide width error in excess of 100 GHz/nm (see Chap. 5). This makes it very challenging to realize multiple-resonator structures with tolerances acceptable for industrial manufacture. They also have proportionately high propagation-loss sensitivity to waveguide surface roughness.

Furthermore, the TE and TM polarization modes have very different resonance sensitivities, which leads to the conclusion that polarization independent operation cannot be obtained except by exerting sub-atomic absolute dimensional control in fabrication (see Chap. 5). This has led to the demonstration, associated with this work, of symmetry-based approaches to polarization transparent operation of strongly confined photonic circuits [31–33].

Sub-micron SC microphotonic structures also have very small critical dimensions that place demanding requirements on fabrication.

Other applications

Developing the photonic technology based on strong confinement waveguides and resonators has important applications beyond telecommunication networks. First, opportunities for the integration of microphotonic circuits and CMOS electronics have recently given rise to new potential applications such as photonics-assisted high-bandwidth and high-resolution sampling systems illustrated in Fig. 1.6. Secondly, the high-fidelity optical signal processing structures developed for telecom applications give an impetus for research on SC microphotonic devices that will enable reaching the ultimate limits in WDM network aggregate bandwidth and spectral efficiency. Such work is motivated by recent investigations into the construction of photonic networks on a microprocessor die to lower the power require-

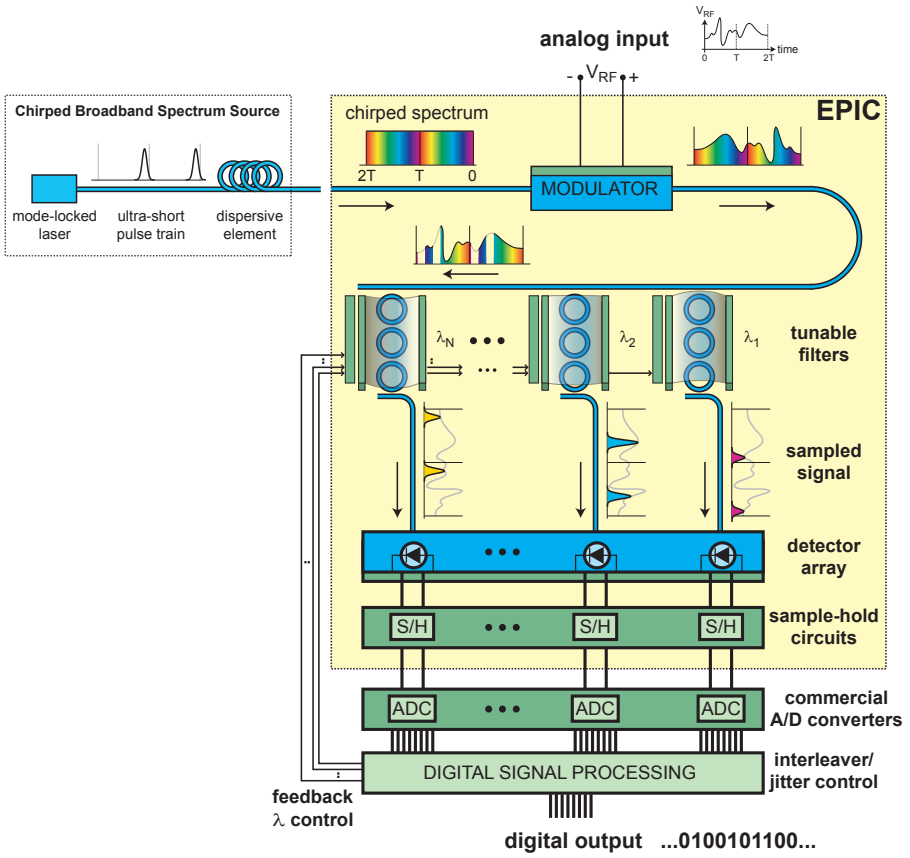

Figure 1.6: Illustration of strong-confinement photonic circuits integrated with CMOS electronics for high-speed, high-resolution photonic sampling and analog-to-digital (A/D) converters [34, 35].

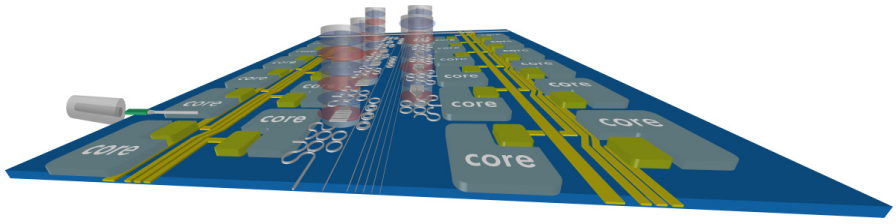

Figure 1.7: Illustration of strong-confinement photonic circuits enabling entire microphotonic communication networks on a microprocessor chip for power reduction and scaling of multiple core processors for supercomputers.

ments and eliminate the memory bottleneck in multicore CPUs. Such an intrachip photonic network is illustrated in Fig. 1.7.

1.3 Outline of the thesis

In this thesis, several dominant problems in strong confinement microphotonics are addressed, theoretical solutions proposed and in some cases experimental demonstrations provided.

In Chapter 2, canonical representations are developed for optical 2-ports and reflectionless 4-ports such as microring resonator circuits. Their general symmetry properties are deduced, and general representations are found that provide a physical insight into the various degrees of freedom in lossless and lossy 4-ports, and provide physically meaningful parameter templates for the extraction of models from numerical simulations. For general passive 4-ports, a characteristic phase is defined, and a new constraint on it is derived that restricts the degrees of freedom of the device when it is closer to lossless.

In Chapter 3, the electromagnetic relationships are derived that are relevant for strong confinement waveguides and resonators, including for wavelength tunability, free-spectral range and perturbations in dispersive structures.

In Chapter 4, rigorous design of SC microresonator filters is addressed. Coupling-induced resonance frequency shifts (CIFS) are reported. CIFS are electromagnetic self-coupling perturbations in coupled resonators that require appropriate corrections before standard filter responses with high extinction can be successfully demonstrated. It is shown that CIFS can be of positive or negative sign, and the physics of the shift is discussed.

In Chapter 5, a systematic study and optimization of silicon waveguide and resonator designs for tunable filters is described. Novel waveguide and resonator designs are proposed, in equivalent TE and TM variants, that provide substantially higher tolerance to errors, lower loss, and favourable performance with respect to a dozen other criteria relevant for tunable resonant filters, in comparison to silicon waveguides of conventional cross-sections. Generic design maps are provided that may be used to find optimum designs based on other criteria than chosen in this study. Preliminary experimental results validate the designs.

In Chapter 6, the design of strong-confinement, widely tunable filters for telecom applications, based on microring resonators, is described. Resonant-frequency-independent passband shape design, and rigorous simulation of high-index-contrast microring structures is described. The widest known full-FSR tuning of 20 nm (exceeding a 16 nm FSR) is demonstrated in silicon resonators, and the first higher-order telecom-grade *tunable* filters (fourth order) are demonstrated using microring resonators in silicon.

In Chapter 7, the first telecom-grade channel add-drop filters based on microring resonators are demonstrated. Silicon nitride waveguides and resonators are used with a multiple-stage arrangement of low-order stages to demonstrate 40 GHz-wide add-drop filters for 100 GHz spaced channels, having 50 dB in-band extinction ratio. This was the first demonstration of high through-port extinction in

high-order microphotonic filters. These static filters demonstrated the feasibility of tunable filters later demonstrated in Chap. 6.

In Chapter 8, a new family of optical interferometers – universally balanced interferometers – is proposed, which act, to within a phase (spectrum), as the cascade of an arbitrary optical operator and its inverse. These structures are shown to be usable as bypass interferometers for dispersion-free FSR multiplication of resonant passbands to extend the wavelength reach of resonant filters and permit scaling to larger spectral utilization without scaling of index contrast; for hitless tuning of resonator based add-drop filters without introducing dispersion; and for "hot-swapping" of photonic circuits in live optical networks.

In Chapter 9, a general approach is proposed for switching resonant passbands to a "fully transparent" off state – having no amplitude attenuation or phase distortion. A new family of microphotonic devices is proposed that is capable of suppressing resonant passbands in a fully transparent way for hitless tuning and FSR doubling for telecom applications. This approach and that in Chap. 8 are complementary and are used in combination in more complex designs realizing hitless, FSR doubled filters.

Furthermore, several important results of this work could not be included in greater detail and are summarized in Appendices.

In Appendix A, a simple approach to accurately evaluate intracavity propagation losses is described, which relies on weakly coupled resonators. Sensitivity requirements of the known Fabry-Perot loss measurement method are derived and discussed.

In Appendix C, a new class of optical resonant structures is proposed based on the loop coupling of cavities. A geometrical invariant quantity, called the *loop coupling phase*, is defined and determines the physical properties of the structures. Based on this topology, optimally sharp and linear-phase microring and microcavity filters are proposed that are not subject to the usual Kramers-Kronig amplitude-dispersion tradeoff. As a result, flat-top filters are possible with linear phase over more than 80% of the filter bandwidth, with a smaller number of resonators than required by a conventional filter followed by an allpass dispersion compensator. In addition, high-order structures for optical delay line purposes are described. These structures have analogues in microwave design, but are more general in the microphotonic implementation because of their hybrid form in the case of microring resonators – allowing more general responses. These structures are likely to have important applications in both optical telecom and chip-scale photonic network applications, and in microwave photonics.

In Appendix D, a complex-frequency/complex-β mode solver in cylindrical and Cartesian is described that makes use of complex-coordinate stretching to provide efficient absorbing boundary conditions for leaky modes. It has been used to numerically simulate in three dimensions all of the resonant structures presented

in this thesis, and for the simulation study of optimal Si waveguide designs in Chap. 5.

In Appendix E, the rigorous design and experimental demonstration of the first channel add-drop filters is described, using the Si-rich SiN waveguide core platform. The first low-loss and wide FSR, high-order microring resonator filters were demonstrated in this work. In order to achieve high through-port extinction levels, CIFS and lithographically induced frequency mismatch were compensated in fabrication to demonstrate experimentally the first frequency matched filters – the first higher-order filters in strongly confined waveguides to show a high through-port extinction ratio (14 dB). Furthermore, rigorous simulations were used for the first time for the complete design of the filter, addressing new loss mechanisms due to mode reconfinement effects in strongly bent ring waveguides and small-gap directional couplers. This work was followed by the multistage SiN filter demonstration in Sec. 7.1, and by the tunable filter work in Chap. 6.

In Appendix F, a novel structure is proposed for compact, efficient waveguide crossings that is inspired by periodically focused beam waveguides from the 1960's. The silicon microphotonic structure matches its periodicity to a low-loss Bloch wave that focuses across waveguide crossings to provide simulated losses lower than 0.04 dB, a factor of 5 improvement over comparable previous work. The loss is further lowered when multiple crossings are traversed at once. The concepts used in these structures also have interesting potential applications to similar active devices, such as carrier-injection modulators. In such devices, focusing may be used to minimize optical absorption loss at periodic electrical contacts placed in proximity to the optical field.

Part I

Analytic and numerical modeling

Chapter 2

Abstract photonic circuits

In this chapter, abstractions and representations of photonic circuits are developed that facilitate the simpler treatment of new electromagnetic coupling effects and novel device designs in strongly confined (SC) photonic structures, in forthcoming chapters, in a physically transparent manner. A new phase constraint valid for arbitrary passive 4-ports is derived and numerically verified; besides being of theoretical interest, it provides useful guidelines for the design of phase sensitive devices in the presence of loss.

Analysis of photonic circuits by transfer and scattering matrices is straightforward and already well known. However, a careful development of the general properties of optical multi-ports reveals a number of important observations regarding their capabilities and limitations, and facilitates the consideration of effects previously unaccounted in strong-confinement photonic structures (e.g. CIFS in Sec. 4.1). It also reveals new practical device geometries, as well as useful guidelines for the number of independent degrees of freedom in device models for the purposes of extracting device parameters from rigorous numerical simulations that are necessary for the design of SC photonic structures.

The first part of this chapter defines lossless and lossy 2-ports and reflectionless 4-ports (*"hybrids"*), and describes the constraints upon the pole-zero pattern of the reflection- and transmission-mode response functions of each of these types of devices imposed by energy conservation and by reciprocity, and their relationship. The results are used, for example, in the section proposing loop-coupled resonant structures (Appendix C).

The second part of the chapter develops general "abstract photonic circuit" representations of lossless and lossy 2-ports and reflectionless 4-ports. The factors of an eigendecomposition and singular value decomposition of the response matrix of the device are interpreted in physical terms, and the number of degrees of

freedom related to the physical symmetries of the device. This section provides a general framework in which arbitrary photonic circuits can be described by disassembling them into abstract elements – including "ideal" 4-port directional couplers, phase-shifters and delay lines. These elements may be used as the smallest scale (fundamental) building blocks on the one hand, or to envelope entire subcircuits on the other (to make use of their known global properties in terms of symmetry). The latter is used, for example, extensively in the chapter on universally balanced interferometers (Chap. 8).

The abstract elements may be wavelength and/or time dependent*. Abstract directional couplers, phase shifters and delay lines, which provide a photonic "equivalent circuit", should not be confused with the concrete photonic device they each represent. For example, a (concrete) combination of a microring-resonator all-pass filter in series with a directional coupler may be described by a single abstract directional coupler, with wavelength-dependent phase factors. We adopt the terminology "abstract" and "concrete" from their analogous use for electronic circuits by Belevitch [36].

Representation by decomposition into abstract elements permits a structured discussion of several contributions in this thesis including: coupling induced resonance-frequency shifts in coupled resonators (CIFS, see Sec. 4.1); lossy couplers in microring filters including the characteristic-phase constraint impact on filter response, and low-loss design; UBIs and folded UBIs (Chap. 8), and loop-coupled resonators and their transmission zeros (Appendix C). In circuit theory, equivalent circuits, abstract elements and standard forms (e.g. Cauer canonical form, Foster canonical form) are used to provide for systems abstract physical representations that are well-matched to theoretical techniques, so that the design or understanding of structures by using and combining such forms is straightforward. In this chapter, such canonical representations are developed for photonic circuits, including lossless and lossy 4-port hybrids, as a basis for analysis and design of structures in further chapters.

2.1 Energy-conservation constraints on the pole-zero distribution of transmission functions

2.1.1 Reflectionless multiports, biconjugate networks and optical hybrids; and reciprocity

In this section, we define the class of *reflectionless* $2N$-port photonic devices and describe their scattering-matrix properties and relationship to generic N-ports.

*Frequency- and time-dependence are *not* the same in this context: frequency-dependence refers to the time dependence of the impulse response of a time-invariant system; time dependence refers to a time-variant system (i.e. a time-dependent frequency response, when the two time scales are different enough).

These properties are important for later discussions of CIFS and coupler loss in microring filters in Section 4.1 and Appendix E, of universally balanced interferometers (UBIs) in Chap. 8, and of loop-coupled resonators in Appendix C.

Reflectionless optical multiports (later abbreviated as "R multiports") as discussed here are characterized by having an even number, $2N$, of ports of interest, that can be divided into two groups of N ports each in the following particular way. A reflectionless $2N$-port, when excited by a signal at a particular port, has intrinsically little or no reflection to all N ports in the same group as the excited port, including the excited port. We may refer to the first group (I) of ports as the input ports, and the second group (II) as the output ports (the roles may be reversed).

The scattering matrix of the $2N$-port may be represented as

$$\begin{bmatrix} \vec{b^I} \\ \hline \vec{b^{II}} \end{bmatrix} = \overline{\overline{\mathbf{S}}} \begin{bmatrix} \vec{a^I} \\ \hline \vec{a^{II}} \end{bmatrix} \tag{2.1}$$

where

$$\overline{\overline{\mathbf{S}}} = \left[\begin{array}{c|c} \overline{\overline{\mathbf{R^{I,I}}}} & \overline{\overline{\mathbf{T^{I,II}}}} \\ \hline \overline{\overline{\mathbf{T^{II,I}}}} & \overline{\overline{\mathbf{R^{II,II}}}} \end{array}\right]. \tag{2.2}$$

If the $2N$-port is reflectionless as defined, then $\overline{\overline{\mathbf{R^{I,I}}}} = \overline{\overline{\mathbf{R^{II,II}}}} = 0$. Furthermore, if it is reciprocal, $\overline{\overline{\mathbf{S}}} = \overline{\overline{\mathbf{S}}}^T$ so that $\overline{\overline{\mathbf{T^{II,I}}}} = \overline{\overline{\mathbf{T^{I,II}}}}^T$.

For any 2-port, one can find an equivalent reflectionless 4-port hybrid (and vice versa), since each has four non-zero transfer functions between a chosen two input and two output ports. That there is no constraint placed by reciprocity on the symmetry of the transmission matrix $\overline{\overline{\mathbf{T^{II,I}}}}$ itself means that a reciprocal, reflectionless $2N$-port can mimic the properties of a general (reciprocal or non-reciprocal) N-port. This property is used in Appendix C to argue that traveling-wave optical filters can realize response functions of non-reciprocal electrical circuit prototypes, with implications for group delay properties.

Dielectric-waveguide photonic circuits are naturally well-suited to construct reflectionless $2N$-ports. Examples include 4-port directional couplers based on evanescent coupling [37], and channel add-drop filters based on microring, and more generally traveling-wave, resonators [38] which lead to inherent impedance matching (no reflection) at all ports, over a substantial frequency range. Such reflectionless devices naturally lead to separation of ports between input and output signals, which is useful in practice (e.g. for add-drop filters) and avoids the use of circulators.

Inherently reflectionless designs are not the norm in electrical circuits and microwave structures, where explicit attention must be paid to design to achieve all-port impedance matching, usually over a limited frequency range [39]. In those fields, N-ports that are impedance matched at every port are referred to as

hybrids, and 4-ports that are lossless and that have the more specific port-group reflectionless property as described with reference to Eq. (2.2) are referred to as *biconjugate networks* [36, p. 202].

Hence, we may also refer to reflectionless photonic devices as *optical hybrids*, by analogy with electronic circuits such as telephone hybrids† [39, p. 375].

Conversion of N-ports to equivalent $2N$-port hybrids

In this section, we briefly describe several ways in which an optical N-port can be converted into an equivalent $2N$-port hybrid. They include well-known use of circulators, balanced embedding interferometers and standing-to-traveling-wave (or equivalent dual-mode) structure conversion.

Conceptually, the simplest way to convert a 2-port [Fig. 2.1(a)] into an equivalent 4-port hybrid [Fig. 2.1(b)] is to attach an ideal 3-port circulator to each of the two ports [Fig. 2.1(c)]. A bulk circulator is often added to fiber and integrated Bragg grating filters [40–42]. Then, for a suitable choice of input ports, the transmission matrix of the equivalent 4-port hybrid, $\overline{\overline{\mathbf{T}^{\mathbf{II},\mathbf{I}}}}$, is equal to the S-matrix of the 2-port (to within a few trivial phase factors representing propagation). With interchanged input and output ports, the other transmission matrix, $\overline{\overline{\mathbf{T}^{\mathbf{I},\mathbf{II}}}}$, is relevant and is equal to the identity matrix, representing a trivial, perfect-reflector 2-port. For an equivalent 4-port hybrid that corresponds to the 2-port "in both directions", an identical pair of the 2-ports may be placed between two 4-port ideal circulators [Fig. 2.1(e)]‡

It is preferable, where possible, to avoid use of circulators, and in general non-reciprocal elements that require use of magnetooptic materials and magnetic bias fields, because the available magnetooptic materials are lossy and difficult to integrate.

In general, the 4-port in Fig. 2.1(e) may represent a different 2-port in each of the two directions (represented by the two embedded 2-ports). However, when it is permissible that the embedded 2-ports be identical, as is usually the case, the structure may be simplified to one without circulators, that makes use instead only of (passive, reciprocal) 3 dB couplers, as shown in Fig. 2.1(f). Such schemes are commonly in use for separating the input and through ports of fiber and integrated-waveguide Bragg grating filters [22, 42],[8, Ch. 1, Fig. 12(b)]. They were also, less frequently, used previously in microwave circuits [44, 45]. Because a lossless 3 dB coupler has an inherent 90° relative phase shift between ports in each direction, the reflected signals from the two 2-ports destructively interfere into the input port

†Telephone hybrid circuits have been used since the 1920s to transfer signals from a 2-wire transmission line with a bidirectional signal to a pair of 2-wire transmission lines each with a unidirectional signal propagation (serving a similar function as a circulator). The name comes from hybrid coils, comprising both inductive and resistive impedance, which form part of the circuit [36].

‡The topological representation of a 4-port circulator – see Fig. 2.1(d) – in this figure is that of a directional coupler, which is common to known microphotonic circulator implementations [43].

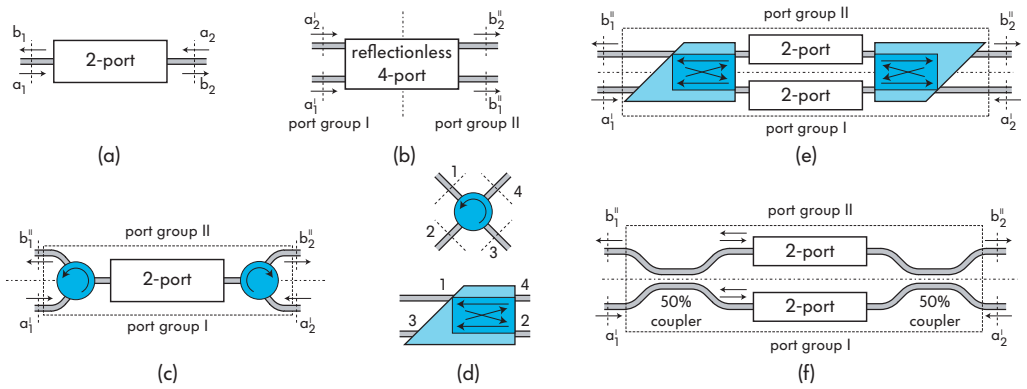

Figure 2.1: N-ports and equivalent reflectionless (ER) $2N$-ports: (a) a 2-port, (b) a reflectionless 4-port showing port groups, (c) ER 4-port using circulators in one direction; (d) abstract 4-port circulator and typical microphotonic 4-port circulator port arrangement [43]; (e) reflectionless 4-port comprising pairs of 2-ports and 4-port circulators permits equivalence to the same or a different 2-port for each of the two possible choices of port groups; (f) for identical 2-ports for both port group choices, ER 4-port constructed using 3dB couplers only and no non-reciprocal elements.

and constructively into a separate output port. This scheme works for arbitrary 2-ports.

More generally, we can conclude that both the circulator and 3 dB splitter schemes may be applied to convert arbitrary N-ports to equivalent $2N$-port hybrids, by allocating one circulator or coupler, respectively, per port of the N-port. Each 3 dB coupler terminates in two ports of the $2N$-port, of which one belongs to each of the input and output port groups. Furthermore, introducing a π-radian phase shift between the 3 dB coupler and one of the embedded N-ports exchanges the two terminating ports associated with that coupler between the two port groups. More generally, since the two ports at each coupler are separated and can be made degenerate (in propagation constant), an arbitrary phase shift may be used to project arbitrarily chosen, orthogonal superpositions of the ports into the input and output port groups. Analogously, in the case where 4-port circulators are used, reversing the sense (direction) of the circulator exchanges the two terminal ports attached to it.

In the scheme employing 3 dB couplers, it is important to design broadband and fabrication-error-tolerant couplers, to guarantee high transmission efficiency and low crosstalk. While symmetry can be employed, the symmetry geometries are different in reflection and in transmission [46, 47], posing a substantial design challenge. Design of broadband 3 dB couplers suitable for precisely such geometries was discussed by Tormen and Cherchi [47].

A third scheme for converting an N-port to a $2N$-port is available for resonators, and may be illustrated by considering direct-coupled-cavity filters [38, 48, 49]. Illustrating this scheme, notably optical microring-resonator add-drop filters [38] are, in usual (e.g. series-coupled) configurations, intrinsically 4-port hybrids

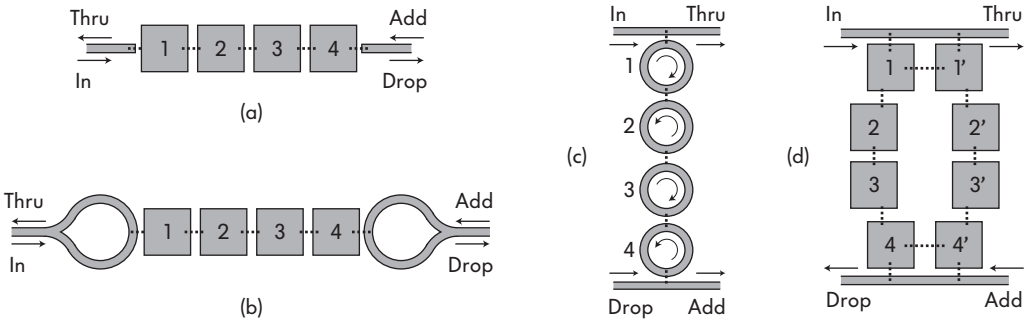

Figure 2.2: N-port and equivalent reflectionless (ER) $2N$-port resonators: (a) 2-port direct-coupled-cavity filter topology suitable for microwave circuits [48] and photonic crystal circuits, (b) loop-mirror based 2-port topology suitable for dielectric optical standing-wave resonators. The third approach to form ER 4-ports is illustrated by (c) a 4-port series-coupled microring-resonator filter [38], and (d) a 4-port circuit that simulates a ring filter by exciting two degenerate sets of standing-wave resonators [14, 52–54].

[Fig. 2.2(c)], while their electronic and microwave counterparts [48, 50], as well as standing-wave optical-resonator filters (including photonic crystal cavities and integrated Bragg resonators [42]) are regular 2-ports, with the through-port response obtained in reflection at the input [Fig. 2.2(a)]. Since each port waveguide needs to support ∼100% reflection when the cavities are unexcited, the topology in Fig. 2.2(a) is suitable for microwave metallic-cavity and photonic crystal circuits, but dielectric waveguides will radiate substantially when terminated. For dielectric-waveguide standing-wave-resonator systems, the topology in Fig. 2.2(b) is proposed utilizing waveguide loop mirrors to excite the standing wave cavities evanescently.[§]

Returning to conversion to a 4-port hybrid, a more explicit approach illustrating this scheme, which mimics the operation of a ring resonator and thereby illustrates the basic physical principle at work in it, is the use of a pair of identical resonant structures, suitably coupled [52, 53, 55] [Fig. 2.2(d)]. Each port of the N-port is represented in this $2N$-port realization by a 2-port waveguide, and each of the two structures is coupled to each of the waveguides in a symmetric way. Furthermore, the corresponding cavities in the two structures that are coupled to a waveguide are also potentially coupled to each other to restore degeneracy broken by coupling via the waveguide.

All schemes enabling N-port to equivalent-$2N$-port-hybrid conversion that are reciprocal (do not involve circulators) require twice the number of resonant modes in the hybrid. This is true also in the standard microring-resonator optical circuits insofar as each microring (or traveling-wave) resonator has two degenerate resonant modes at each resonant frequency corresponding to each one resonant mode in the

[§]Such geometries are present (with microring resonators) in an early patent by Marcatili [51] transplanting various microwave concepts to optics, but are in general absent in the optics literature and have been neglected in favour of the more useful and intuitive hybrid forms.

corresponding standing-wave structure, though the number of cavities is typically the same.

The various $2N$-port hybrid realizations form an equivalence class for a given N-port. All of the reciprocal realizations [Figs. 2.1(f) and 2.2(d)] rely on symmetry. These will be of use in the development of various new device geometries and designs in other sections. From here on, the port superscripts I and II will be dropped and are understood in the context of hybrids; and the S-matrix of a 2-port and the (corresponding) off-diagonal transmission matrix of a reflectionless 4-port will both be represented by $\overline{\overline{\mathbf{S}}}$ (or in some sections by $\overline{\overline{\mathbf{T}}}$ or $\overline{\overline{\mathbf{U}}}$).

2.1.2 Para-unitarity: "energy conservation" at complex frequencies

In this section, we show the constraints imposed by energy conservation, and a more stringent requirement called para-unitarity, on the spectral response properties of 2-ports and their reflectionless 4-port equivalents. In particular, the reflection zeros at the two ports of a 2-port are shown to be complex conjugates of each other, and the *transmission* zeros of reciprocal 2-ports are shown to occur in complex-conjugate pairs. Reciprocal 4-port optical hybrids are shown to support fundamentally more general response functions in transmission than their 2-port equivalents, thereby enabling new optical filter types that do not have practical equivalents in the electronic and microwave circuit domains.

The CMT-in-time model of a multiport Mth-order resonator leads to a representation of the S-matrix entries as M-pole and M-zero rational functions of two polynomials in frequency (where some of the poles and zeros may be trivial, i.e. at infinite detuning). Transmission nulls enable advanced spectral response design including phase engineering (non-Kramers-Kronig-limited, non-minimum-phase and in particular all-pass filters) and sharp amplitude responses (elliptic and sharp linear-phase filters) [56]. We consider the general constraints placed on the transmission-zero positions by energy conservation and para-unitarity.

Providing sharp 2-port passbands requires transmission (drop port) response zeros at real frequencies, while dispersion flattening calls for complex zeros (like in an all-pass filter). What responses are permitted?

Energy conservation and reciprocity place constraints on the allowed zeros of the transmission (off-diagonal) and reflection (diagonal) S-matrix elements, $s_{ij}(\omega)$, these being the response functions of a 2-port. If the 2-port is lossless, $\overline{\overline{\mathbf{S}}}^{\dagger}\overline{\overline{\mathbf{S}}} = \overline{\overline{\mathbf{S}}}\overline{\overline{\mathbf{S}}}^{\dagger} = \bar{\bar{\mathbf{I}}}$, so that $|s_{11}|^2 + |s_{21}|^2 = 1$, $|s_{11}| = |s_{22}|$, $|s_{12}| = |s_{21}|$, and

$$\frac{s_{11}^*}{s_{22}} = -\frac{s_{21}^*}{s_{12}}. \tag{2.3}$$

Eq. (2.3) *also* holds if we replace all conjugated functions s_{ij}^* with *para-conjugates* defined as $s_{*ij}(\omega) \equiv [s_{ij}(\omega^*)]^*$ [36, p. 72], i.e. the frequency ω is not conjugated. In this case, Eq. (2.3) holds in the entire complex-ω plane by analytic continuation,

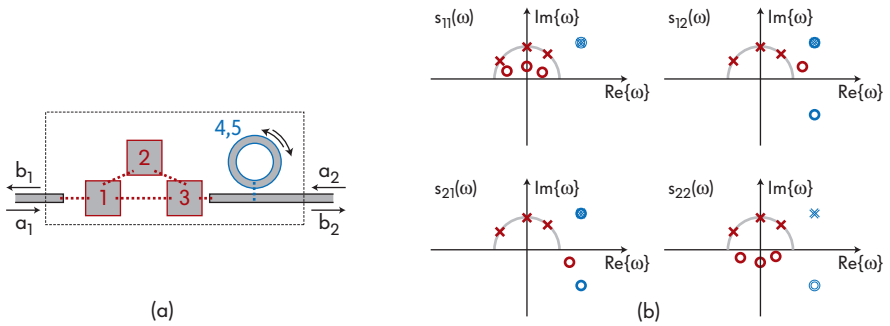

Figure 2.3: Illustration of constraints of para-unitarity on pole-zero pattern of S-matrix transfer functions: (a) notional 2-port to illustrate pole-zero symmetries, constraints and cancellation; (b) its four response functions showing that all four formally share all poles, s_{11} and s_{22} always have mutually complex-conjugate zeros, s_{12} and s_{21} have conjugate zeros (which are on the real-ω axis or in conjugate pairs for a reciprocal 2-port), and pole-zero cancellation results from an embedded all-pass filter.

except at the poles, since ω is unconjugated in $\overline{\overline{\mathbf{S}}}_\dagger \overline{\overline{\mathbf{S}}} = \overline{\overline{\mathbf{I}}}$ (a property referred to as *para-unitarity* in circuit theory [36, p. 161]).

As the modified expression holds in the entire complex-ω plane, we may now consider its consequences for the poles and zeros. Since all four response functions have the same (system) poles[¶], $\omega_{p,n}$, the frequency-dependent phase due to poles cancels in Eq. (2.3). The remaining frequency-dependent phase is due to zeros $\omega_{z,n(i,j)}$ in the response functions, so there must be pairs of corresponding zeros to balance Eq. (2.3). Furthermore, energy conservation requires that s_{11} cannot have coincident zeros with s_{21} since $|s_{11}|^2 + |s_{21}|^2 = 1$ (or with s_{12}). Therefore, *all zeros of s_{11} must be complex conjugates of zeros of s_{22}, while all zeros of s_{12} must be complex conjugates of zeros of s_{21} (in the absence of pole-zero cancellation). If the 2-port is reciprocal, $s_{12} = s_{21}$, and transmission zeros are restricted to be on the real frequency axis or to occur in complex conjugate pairs in s_{12}*. These constraints have important implications constraining responses that can be realized in 2-port and hybrid 4-port photonic circuits.

These constraints are best illustrated by an example, before we consider their further implications. Fig. 2.3(a) shows a notional 2-port comprising a 3$^{\text{rd}}$-order standing-wave-cavity bandpass filter (red), followed by a single-ring all-pass filter (blue). The system formally has five poles since the standing-wave cavities have one resonant mode each and the ring cavity has two degenerate modes near the frequency of interest. All (four) response functions formally share the same poles which are the loaded resonances of the system. On the other hand, zeros resulting from feed-forward interference can be different in each response function, which also means that some of the response functions may have a reduced number of effective poles due to pole-zero cancellation. Let us first consider the three-cavity

[¶]Formally we will assign M poles to an Mth order resonant system, though in some response functions the effective number may be reduced by pole-zero cancellation.

filter, disregarding the ring. If we also disregard the cavity 1–3 coupling for the moment, then this is a well-known series-coupled-cavity (SCC) filter geometry [38]. It accounts for the three (red) poles and the three reflection zeros near the origin in Fig. 2.3(b). If the input is port 1, then the drop port is port 2 while the through-port response is at port 1 in reflection. The three coupled cavities give a set of three system supermodes distributed around a center frequency by the frequency splitting. A symmetric filter may have a high-extinction through port and zeros on the real-ω axis. Here, the input coupling to cavity 1 is made weaker (larger gap), so the system is undercoupled from port 1 and has minimum-phase (i.e. upper half-plane) zeros. From port 2, the reflection sees an over-coupled response (in the limit of zero coupling at port 1 it becomes an all-pass filter), so the zeros are in the lower half-plane, satisfying the complex-conjugate condition. That a 2-port system which is minimum-phase in reflection from one port is maximum-phase from the other port is generally well known for optical filters [57]. The SCC filter considered thus far is all-pole meaning that it contributes no finite *transmission* zeros to the off-diagonal response functions in Fig. 2.3(b). A (red) transmission zero shown in the off-diagonal responses is brought about by introducing a further cavity 1–3 coupling thus forming a coupling loop (see Appendix C) that provides a sort of feed-forward interference. Only if the 3-cavity filter has non-reciprocal elements can the zero be off the real axis, in conjugate locations in s_{12} and s_{21} [Fig. 2.3(b)], while for a reciprocal filter it must be on the real-ω axis as described.

A final variation on the pole-zero distribution is the possibility of pole-zero cancellation. This is brought out by considering the ring all-pass filter in Fig. 2.3(a), which itself is a 2-port hybrid, equivalent to a 1-port Gires-Tournois interferometer. A single-cavity all-pass filter typically has a pole and a zero that are complex conjugates. However, if we assume a single pole in the upper half-plane and zero in the lower half-plane for s_{12} of the ring all-pass, then the conditions just described require a complex-conjugate zero that cancels the pole in s_{21}, removing any all-pass response in the other direction, which is not the correct outcome. The resolution of this problem lies in the fact that the ring resonator, and any traveling-wave cavity, has two degenerate modes (clockwise and anti-clockwise), if it is reciprocal, near the frequency of interest. Therefore, there is a double pole [as shown in Fig. 2.3(b)], and a pair of complex-conjugate zeros in the off-diagonals, s_{12} and s_{21}. In each direction of excitation, one zero cancels the unexcited resonance and the other provides for the dispersive all-pass response (for example, propagating from left to right the clockwise resonance is not excited). In reflection, s_{11} has both zeros cancelling the ring resonances because the ring is never excited, while s_{22} has both zeros in the lower half-plane since the ring is excited in both directions.

Since the energy flow between the three-cavity filter and the ring all-pass is in one direction only, there is no coupling that normally leads to frequency splitting

and the response (and pole-zero distribution) of the 2-port is the superposition of the individual three-cavity filter and ring all-pass. Note that if the ring all-pass frequency and linewidth is tuned appropriately, a second pole-zero cancellation can be effected by in transmission (s_{12} and s_{21}) by overlapping one of the minimum-phase zeros with a system pole.

This example shows the most general constraints on the pole-zero distribution of a 2-port. The possibility of realizing more general, non-reciprocal 2-port response functions in reciprocal equivalent 4-port hybrids is suggested in this thesis work, and is explored in proposed designs in Appendix C. While it can be shown that energy-amplitude reference phases may be chosen for cavity modes to define all coupling coefficients as real in reciprocal standing-wave resonators, this is not the case for traveling-wave modes in a non-reciprocal structure or a hybrid. Therefore, a greater flexibility in synthesis is permitted.

2.2 Canonical representations of optical 2-ports and reflectionless 4-ports

In this section, we describe the properties of lossless and lossy reflectionless 4-ports, described as abstract directional couplers (and represented by physical analogues of the eigen and singular value decompositions of their T-matrices), and the constraints on violation of the unitary phase condition (UPC) in systems with loss.

2.2.1 Representations of lossless optical 2-ports and 4-port hybrids

Having established in Section 2.1.1 the relationship between 2-ports and their equivalent 4-port hybrids, we propose in this section general abstract representations of 4-port hybrids which are relevant to photonic circuits. In the lossless case, the matrix representation is well known, but its physical significance has not been adequately used in photonic circuits. Based on this work, CIFS and coupler loss were accounted (Chap. 4) and the first telecom-grade filters were demonstrated in SC photonics, using SiN waveguides (Appendix E, Sec. 7.1).

The purpose of this section is to propose and introduce standard abstract representations for optical 4-port hybrids, and provide an "equivalent-circuit"-like form for representation of arbitrary photonic circuits that makes it easier to manipulate the design and visualize the effect of symmetries, reciprocity, perturbations, etc. These device representations are equivalent circuits for optical elements, to serve people with an intuition for wave propagation.

The transmission matrix of a linear, reflectionless 4-port [$\overline{\overline{\mathbf{T}^{\mathbf{II,I}}}}$ in Eq. (2.2)], or the S-matrix of a 2-port [$\overline{\overline{\mathbf{S}}}$ in Eq. (2.1)] can be represented by a 2×2 matrix $\overline{\overline{\mathbf{U}}}$ as,

$$\vec{b} = \overline{\overline{\mathbf{U}}} \cdot \vec{a} = \begin{bmatrix} u_{11} & u_{12} \\ u_{21} & u_{22} \end{bmatrix} \cdot \vec{a} \tag{2.4}$$

where $u_{mn} \equiv |u_{mn}|\, e^{i\phi_{mn}}$, and where $\vec{a} = [a_1, a_2]^T$ are the input mode amplitudes at ports 1 and 2 of the input port group, while $\vec{b} = [b_1, b_2]^T$ are the output mode amplitudes at ports 1 and 2 of the output port group, normalized so that their square magnitudes represent the power. $\overline{\overline{\mathbf{U}}}$ is complex, and thus is fully specified by 8 real values which may be wavelength and time dependent.

Reflections, rotations and symmetries

The reflectionless property of a 4-port hybrid is preserved under three geometrical operations on the structure as illustrated in Fig. 2.4:

- $\mathcal{V}$ transformation: exchange of port groups (reflection about an axis dividing the input and output port groups),
- $\mathcal{H}$ transformation: exchange of ports in each group (reflection about an axis dividing the ports in each group), and
- $\mathcal{HV}$ transformation: the combination of both (rotation by 180° in the plane of the photonic circuit).

The transmission matrix of the reflectionless 4-port after any of these transformations is applied can be expressed in terms of the transmission matrix $\overline{\overline{\mathbf{U}}}$ of the original 4-port as shown in Fig. 2.4. The same result can be obtained in one of two ways: either assuming a lossless (but not necessarily reciprocal) 4-port and using time reversal; or assuming a reciprocal (but not necessarily lossless) 4-port[‖]. In the former case, $\mathcal{V}$ and $\mathcal{HV}$ operations include additionally applying a sign reversal to any bias DC magnetic field in a non-reciprocal 4-port.

To simplify notation, we introduce a *cross transpose* operation on a matrix [59], by analogy with the transpose[**]. Whereas the transpose $\overline{\overline{\mathbf{U}}}^T$ of a matrix $\overline{\overline{\mathbf{U}}}$ is the matrix obtained by reflecting $\overline{\overline{\mathbf{U}}}$ about its main diagonal, the cross transpose $\overline{\overline{\mathbf{U}}}^C$ is the matrix obtained by reflecting $\overline{\overline{\mathbf{U}}}$ about its second or cross diagonal. For a 2×2 matrix, the cross transpose $\overline{\overline{\mathbf{U}}}^C$ is defined by exchanging the diagonal elements u_{11} and u_{22} [59]:

$$\overline{\overline{\mathbf{U}}}^C \equiv \overline{\overline{\mathbf{J}}} \cdot \overline{\overline{\mathbf{U}}}^T \cdot \overline{\overline{\mathbf{J}}} = \begin{bmatrix} u_{22} & u_{12} \\ u_{21} & u_{11} \end{bmatrix} \tag{2.5}$$

where permutation matrix $\overline{\overline{\mathbf{J}}} \equiv [0, 1; 1, 0]$.

[‖] The occurrence of similar results for lossless, non-reciprocal and for lossy, reciprocal cases is common. For example, consider unconjugated and conjugated overlap integrals for lossless and lossy waveguide modes [58].

[**] In previous publications [60–62], we have also used the term *diagonal transpose* (suggested by Bartolomeo Tirloni). In this thesis, the term "cross transpose" has been adopted to stay consistent with a previous work that has made use of this operator [59].

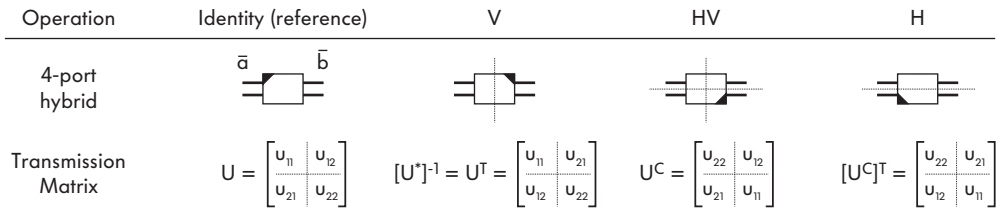

Figure 2.4: Left-to-right transmission matrix of reflectionless 4-port under geometrical reflection transformations in the plane. The third, out-of-plane dimension is unchanged in all cases.

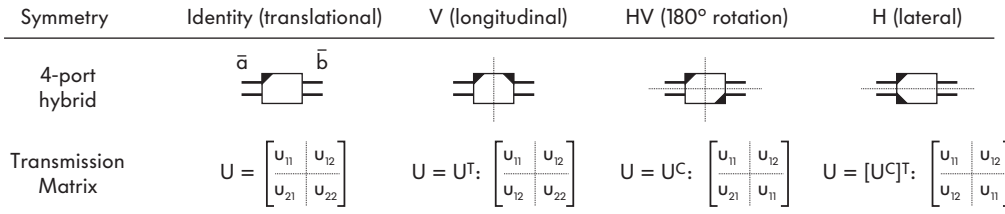

Figure 2.5: Form of transmission matrix of reflectionless 4-ports having H, V or HV geometrical symmetry.

The transmission matrices of the 4-port hybrid ($\overline{\overline{\mathbf{U}}}$) after $\mathcal{H}$, $\mathcal{V}$ and $\mathcal{HV}$ geometrical operations are $\overline{\overline{\mathbf{U}}}^{CT}$, $\overline{\overline{\mathbf{U}}}^{T}$ and $\overline{\overline{\mathbf{U}}}^{C}$, respectively (Fig. 2.4). A physical explanation of how these relationships may be derived via time reversal or reciprocity is given in Section 8.1.1 on universally balanced interferometers.

The form of the matrix $\overline{\overline{\mathbf{U}}}$ is simplified to a reduced number of degrees of freedom if the geometrical structure (dielectric $\overline{\bar{\epsilon}}$ and permeability $\overline{\bar{\mu}}$ distribution) of the 4-port has a symmetry, i.e. is invariant under one or more of these three operations, as shown in Fig. 2.5. Invariance with respect to both $\mathcal{V}$ and $\mathcal{H}$, or both $\mathcal{V}$ and $\mathcal{HV}$, gives the same form of $\overline{\overline{\mathbf{U}}}$ as $\mathcal{H}$-invariance, but bias field $\mathbb{H} = 0$.

Losslessness, physical canonical form and unitary phase condition

In a reflectionless 4-port that is lossless, power is conserved $\vec{b}^{\dagger}\vec{b} = \vec{a}^{\dagger}\overline{\overline{\mathbf{U}}}^{\dagger}\overline{\overline{\mathbf{U}}}\vec{a} = \vec{a}^{\dagger}\vec{a}$, so transmission matrix $\overline{\overline{\mathbf{U}}}$ is unitary, $\overline{\overline{\mathbf{U}}}^{\dagger}\overline{\overline{\mathbf{U}}} = \overline{\bar{\mathbf{I}}}$, i.e. its 2-norm $\|\overline{\overline{\mathbf{U}}}\|_2 = 1$. While the 2×2 T-matrix $\overline{\overline{\mathbf{U}}}$ is in general represented by 4 complex numbers or 8 real numbers (degrees of freedom) at each frequency, with (2.4) expanded as

$$\overline{\overline{\mathbf{U}}} = \begin{bmatrix} |u_{11}|e^{i\phi_{11}} & |u_{12}|e^{i\phi_{12}} \\ |u_{21}|e^{i\phi_{21}} & |u_{22}|e^{i\phi_{22}} \end{bmatrix} \tag{2.6}$$

unitarity constrains $\overline{\overline{\mathbf{U}}}$ to a form with 4 free parameters through power conservation constraints for single-input excitation $|u_{11}|^2 + |u_{21}|^2 = 1$ and $|u_{12}|^2 + |u_{22}|^2 = 1$, and a constraint on transmission-response phases [63–66]

$$\phi_{11} + \phi_{22} - \phi_{21} - \phi_{12} = \mp\pi. \tag{2.7}$$

We shall refer to this constraint as the *unitary phase condition* (UPC) and name the left-hand-side quantity as the *characteristic phase*

$$\Omega \equiv \phi_{11} + \phi_{22} - \phi_{21} - \phi_{12} \tag{2.8}$$

as this quantity will play an important role in later results. Based on these constraints, $\overline{\overline{\mathbf{U}}}$ has the most general form

$$\overline{\overline{\mathbf{U}}} = \begin{bmatrix} \sqrt{1-\kappa}e^{i\phi_{11}} & \sqrt{\kappa}e^{i\phi_{12}} \\ \sqrt{\kappa}e^{i(\phi_{11}+\phi_{22}-\phi_{12}\pm\pi)} & \sqrt{1-\kappa}e^{i\phi_{22}} \end{bmatrix}. \tag{2.9}$$

One may also use $\sqrt{1-\kappa} \equiv \cos(\theta_\kappa)$, $\sqrt{\kappa} \equiv \sin(\theta_\kappa)$, where θ_κ is analogous to the optical coupling length κL in coupled-mode theory in space [67, p. 220].

It is of interest to see how symmetries further restrict this form and how this abstract representation can be physically interpreted in the context of a physical directional coupler. A recast form of (2.9) that better maps parameters to bear out the physical symmetries of the structure is

$$\overline{\overline{\mathbf{U}}} = e^{i\theta_o} \begin{bmatrix} \sqrt{1-\kappa}e^{+i\theta_1} & i\sqrt{\kappa}e^{+i\theta_2} \\ i\sqrt{\kappa}e^{-i\theta_2} & \sqrt{1-\kappa}e^{-i\theta_1} \end{bmatrix} \tag{2.10}$$

with

$$\begin{aligned} \theta_o &\equiv \frac{\phi_{11}+\phi_{22}}{2} \\ \theta_1 &\equiv \frac{\phi_{11}-\phi_{22}}{2} \\ \theta_2 &\equiv \phi_{12} - \frac{\phi_{11}+\phi_{22}\pm\pi}{2} = \frac{\phi_{12}-\phi_{21}}{2}. \end{aligned}$$

In the various forms, there are four real-number free parameters: splitting ratio κ (or θ_k), and phases $\{\theta_o, \theta_1, \theta_2\}$ (or alternatively $\{\phi_{11}, \phi_{22}, \phi_{12}\}$).

The mapping of the theta parameters to physical symmetries is borne out by a decomposition of (2.10) into a bare coupling matrix $\overline{\overline{\mathbf{K}}}$ with one degree of freedom, and two diagonal phase matrices $\overline{\overline{\mathbf{\Theta_i}}}$, $\overline{\overline{\mathbf{\Theta_o}}}$,

$$\begin{aligned} \overline{\overline{\mathbf{U}}} &= \overline{\overline{\mathbf{\Theta_i}}} \cdot \overline{\overline{\mathbf{K}}} \cdot \overline{\overline{\mathbf{\Theta_o}}} \\ &= e^{i\theta_o} \begin{bmatrix} e^{i(\theta_1+\theta_2)/2} & \\ & e^{i(-\theta_1-\theta_2)/2} \end{bmatrix} \begin{bmatrix} \sqrt{1-\kappa} & i\sqrt{\kappa} \\ i\sqrt{\kappa} & \sqrt{1-\kappa} \end{bmatrix} \begin{bmatrix} e^{i(\theta_1-\theta_2)/2} & \\ & e^{i(-\theta_1+\theta_2)/2} \end{bmatrix}. \end{aligned} \tag{2.11}$$

This decomposition shows that an arbitrary lossless, reflectionless (LR) 4-port can be represented at each frequency as a basic abstract LR 4-port "scatterer" with one free parameter κ (middle matrix in (2.11)), augmented with pre- and post-scattering phase shifters. The phase shifts θ_o, θ_1 and θ_2 exhibit uniform (common-mode), antisymmetric and "quadrupole" phase shifter distributions – for the three possible degrees of freedom – as illustrated in Fig. 2.6.

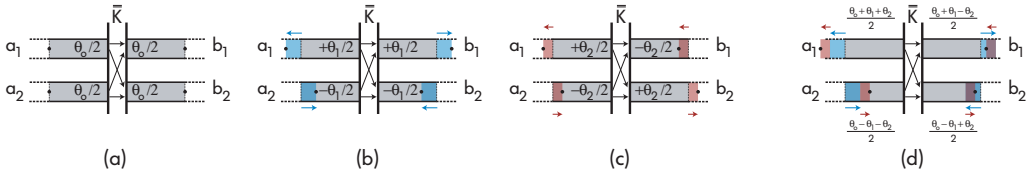

Figure 2.6: Lossless reflectionless 4-port decomposition into symmetry orders at each frequency: (a) common-mode phase θ_o, (b) antisymmetric phase θ_1 that is common-mode longitudinally across the scattering point, (c) antisymmetric-antisymmetric phase θ_2, and (d) the complete representation showing the physical contribution of the 3 phases.

According to Fig. 2.6 (or Fig. 2.5), an LR 4-port that is longitudinally symmetric ($\mathcal{V}$-invariant) has $\theta_2 = 0$; one that is invariant with respect to 180° rotation in the plane ($\mathcal{HV}$-invariant) has $\theta_1 = 0$; and one that is laterally symmetric ($\mathcal{H}$-invariant) has $\theta_1 = \theta_2 = 0$.

Therefore the number of degrees of freedom at each frequency of an arbitrary LR 4-port is dictated by the degree of its physical symmetry. This is useful in prediction of the most general responses supported by such devices, as well as in knowing the number of independent degrees of freedom that must be determined from numerical simulations of such devices, such as using FDTD[68].

We will use an *abstract directional coupler* as a representation for the matrix (2.10), as illustrated in Fig. 2.7(b), where it is understood that the parameters $\{\kappa, \theta_o, \theta_1, \theta_2\}$ are in general frequency- (and possibly time-) dependent. This is analogous to the implicit use of an *abstract mirror* representation for arbitrary 2-ports, with reflection and transmission coefficients from each side in general frequency- and/or time-dependent.

Before continuing on to lossy multiports, it is worthwhile to consider the physical content of the characteristic phase Ω. Being defined in (2.8) as the addition of two angles and subtraction of another two angles, it can also be seen as the overall phase of the transmission function $u_{11}u_{22}u_{12}^*u_{21}^*$, which describes a signal traversing the 4-port in four ways, one after another. Furthermore, as conjugation amounts to time reversal, the characteristic phase comprises traversing paths u_{11} and u_{22} forward in time, and u_{12} and u_{21} backwards. One can picture "walking" from input port 1 to output port 1 (u_{11}), then stepping backwards from output port 1 to input port 2 (u_{12}^*), then forward again to output port 2 (u_{22}), and finally backwards to the starting position at input port 1 (u_{21}^*). Therefore, Ω is the excess phase accumulated in a full-circle traversal of the ports of the 4-port without retracing the path, always "facing forward while walking".

Example: concrete directional couplers and coupling-induced phase shifts

In this section, the LR 4-port T-matrix representation of the previous section is interpreted for a physical waveguide directional coupler. Directional couplers form part of various structures including interferometers and microring-resonator

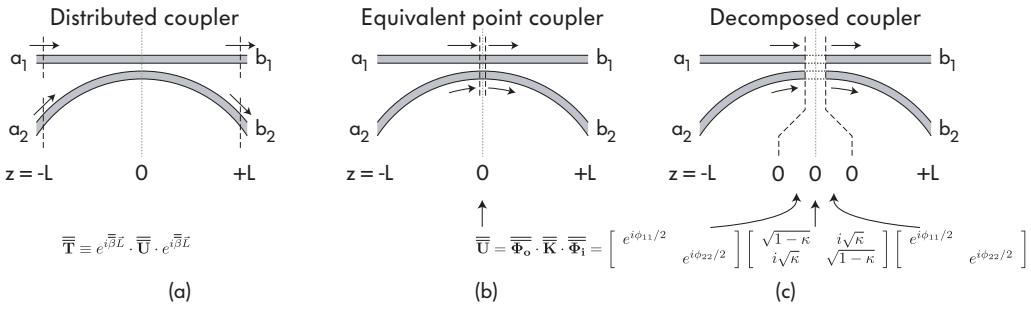

Figure 2.7: Theoretical modeling of directional couplers: (a) a distributed 4-port coupler, modeled as a reflectionless 4-port with T-matrix T, may be represented as (b) an equivalent point coupler with coincident input and output reference planes and T-matrix U, where the propagation is factored out and all remaining phase is coupling-induced and will have wavelength dependence only due to coupling. In a $\mathcal{V}$-symmetric coupler, the equivalent point coupler may be decomposed into a pair of coupling-induced phase sections and an ideal abstract coupler (that has no phase degrees of freedom).

filters described in this thesis. It should be borne in mind that until this point, the abstract directional coupler representation was used for arbitrary LR 4-ports.

A physical ring-bus waveguide directional coupler is shown in Fig. 2.7. In Fig. 2.7(a) the coupler ports are four chosen reference planes forming a box such as may be an FDTD computational window, where the gap (wall-to-wall spacing) between ring and bus determines the power fraction coupled. Even with lossless waveguides and a large gap, and with coupling approaching $\kappa \to 0$, the T-matrix of the coupler $\overline{\overline{\mathbf{T}}}$ is not the identity matrix. It is strongly wavelength dependent, even though the coupling is not, because the reference planes envelope a finite length of waveguide propagation and account for the dynamical phase ($e^{i\overline{\overline{\beta}}\cdot\vec{L}}$). A more convenient treatment, for resonator analysis, of a directional coupler results when all reference planes are collocated at $z = 0$ [Fig. 2.7(b)], by factoring out the propagation phase in the waveguides – in the uncoupled state (infinite coupling gap). Then the T-matrix $\overline{\overline{\mathbf{U}}}$ will be substantially wavelength independent – any phase and wavelength dependence of it is due to so-called coupling-induced phase shifts described in Sec. 4.1.4. For a geometrically $\mathcal{V}$-symmetic coupler as shown in Fig. 2.7, there are only two independent phases, ϕ_{11} and ϕ_{22}, the bus-side and ring-side coupling-induced phase shifts. The coupler representation can further be factored into a virtual waveguide section pair imposing $\{\phi_{11}/2, \phi_{22}/2\}$ phase shift, an abstract directional coupler κ with one degree of freedom, and the other half of the phase shifts. This form of coupler makes clear that coupling-induced phase shifts cannot alone be responsible for asymmetric spectral distortion, shown to be present in lossy resonator-based filters.

Because a reciprocal reflectionless 4-port's transfer matrix is equivalent to the scattering matrix of a non-reciprocal 2-port in general, four free parameters are needed. Several previous treatments of the T-matrix for a directional coupler [67, 69–71] are not sufficiently general to describe arbitrary structures, and include

3 rather than 4 free parameters. In some treatments, the leading phase factor [θ_o in Eq. (8.1)] is dropped. However, this factor is not trivial, and in our general treatment may be wavelength dependent – as is the case with an all-pass filter. The response of a microring-resonator all-pass filter on one waveguide is all in θ_o.

2.2.2 Representations of lossy 2-ports and 4-port hybrids

In general, 4-ports are not lossless. In this section, physically inspired canonical representations are given for reflectionless 4-ports *not* restricted to be lossless (or passive), hence having a total of 8 free parameters per 2×2 T-matrix. Similarly to the lossless case, symmetry places constraints on the degrees of freedom, while the degree of lossiness (expressed by a minimum and a maximum gain) determines a new phase inequality that must be satisfied, which is analogous to the unitary phase condition (2.7) for the lossless case.

This approach and results appear to be entirely new with respect to the present literature. The decomposition is useful in several ways: 1) to constrain the number of independent parameters (degrees of freedom) that need to be extracted from numerical simulations, 2) provide limitations on the characteristic phase in the low-loss case, 3) provide straightforward simplifications of these constraints in the low-loss case, 4) to provide a tool for design of photonic devices taking into account symmetry constraints.

2.2.3 A characteristic phase constraint in passive 4-ports

For lossy 4-ports, an inequality can be derived that their characteristic phase Ω must satisfy. For a low-loss 4-port, the inequality is more strongly constraining, and in the limit of zero loss it produces the unitary phase condition (2.7). This generalization of the UPC appears to be a new result.

The inequality is first derived, and then used to address two relevant design problems – the first concerns allowable models of scattering loss in waveguide directional couplers, and the second concerns phase tolerance of lossy UBIs.

Here, to derive the characteristic phase inequality (CPI), a general passive 4-port is considered. In the passive case, total output power does not exceed total input power so that $\vec{b}^\dagger\vec{b} \leq \vec{a}^\dagger\vec{a}$, or $\vec{a}^\dagger\overline{\overline{\mathbf{U}}}^\dagger\overline{\overline{\mathbf{U}}}\vec{a} \leq \vec{a}^\dagger\vec{a}$. Stated differently, the 2-norm is less than unity, $\|\overline{\overline{\mathbf{U}}}\|_2 < 1$. The inequality is derived starting with the fact that $\|\overline{\overline{\mathbf{U}}}\|_2 = \sqrt{\lambda_{\max}}$, where $\lambda_{\max}$ is the largest eigenvalue of $\overline{\overline{\mathbf{A}}} \equiv \overline{\overline{\mathbf{U}}}^\dagger\overline{\overline{\mathbf{U}}}$:

$$\overline{\overline{\mathbf{A}}} \equiv \overline{\overline{\mathbf{U}}}^\dagger\overline{\overline{\mathbf{U}}} = \begin{bmatrix} |u_{11}|^2 + |u_{21}|^2 & u_{12}u_{11}^* + u_{22}u_{21}^* \\ u_{12}^*u_{11} + u_{22}^*u_{21} & |u_{22}|^2 + |u_{12}|^2 \end{bmatrix} = \begin{bmatrix} a_{11} & a_{12} \\ a_{21} & a_{22} \end{bmatrix}.$$

Here,

$$\begin{aligned} 0 \le a_{11} \le 1, \qquad & a_{11} \text{ real} \\ 0 \le a_{22} \le 1, \qquad & a_{22} \text{ real} \\ a_{21}^* = a_{12}, \qquad & a_{12} \text{ complex.} \end{aligned}$$

The eigenvalues of $\overline{\overline{\mathbf{A}}}$ are all non-negative real[††],

$$\lambda = \underbrace{\frac{a_{11}+a_{22}}{2}}_{+\text{ve}} \pm \sqrt{\underbrace{\left(\frac{a_{11}-a_{22}}{2}\right)^2}_{+\text{ve}} + \underbrace{|a_{12}|^2}_{+\text{ve}}}. \tag{2.12}$$

Since each of the three terms in (2.12) is positive definite, the relevant (largest) eigenvalue takes the $+$ sign,

$$\lambda_{\max} = \frac{a_{11}+a_{22}}{2} + \sqrt{\left(\frac{a_{11}-a_{22}}{2}\right)^2 + |a_{12}|^2}.$$

Comparing this result with $\|\overline{\overline{\mathbf{U}}}\|_2 = \sqrt{\lambda_{\max}} \le 1$, i.e. $\lambda_{\max} \le 1$, yields the condition

$$0 \le |a_{12}|^2 \le 1 - a_{11} - a_{22} + a_{11}a_{22}.$$

This condition on matrix $\overline{\overline{\mathbf{A}}}$ translates to a condition in terms of parameters of the 4-port transmission matrix $\overline{\overline{\mathbf{U}}}$ of the 4-port:

$$0 \le |u_{11}^* u_{12} + u_{21}^* u_{22}|^2 \le \delta_1 \delta_2$$

where $\delta_{1,2}$ are the total fractional losses when launching power into only input 1 or 2, respectively,

$$\begin{aligned} 1 - \delta_1 &\equiv |u_{11}|^2 + |u_{21}|^2 = a_{11} \\ 1 - \delta_2 &\equiv |u_{22}|^2 + |u_{12}|^2 = a_{22}. \end{aligned} \tag{2.13}$$

Expressing the middle term of the inequality in terms of amplitudes $|u_{mn}|$ and phases ϕ_{mn}, the new phase condition is derived:

$$\begin{aligned} -\frac{|u_{11}u_{12}|^2 + |u_{21}u_{22}|^2}{2|u_{11}u_{12}u_{21}u_{22}|} &\le \cos(\phi_{12}+\phi_{21}-\phi_{11}-\phi_{22}) \le \\ &\le \frac{(1-|u_{11}|^2)(1-|u_{22}|^2) + (1-|u_{21}|^2)(1-|u_{12}|^2) - 1}{2|u_{11}u_{12}u_{21}u_{22}|} \end{aligned}$$

[††]For arbitrary, complex $\overline{\overline{\mathbf{U}}}$, matrix $\overline{\overline{\mathbf{U}}}^\dagger\overline{\overline{\mathbf{U}}}$ is Hermitian and furthermore positive semidefinite (has all non-negative eigenvalues). This is easily proven by considering the singular value decomposition $\overline{\overline{\mathbf{U}}} = \overline{\overline{\mathbf{Y}\boldsymbol{\Sigma}\mathbf{V}}}^\dagger$. Then $\overline{\overline{\mathbf{U}}}^\dagger\overline{\overline{\mathbf{U}}} = \overline{\overline{\mathbf{V}\boldsymbol{\Sigma}}}^\dagger\overline{\overline{\mathbf{Y}}}^\dagger\overline{\overline{\mathbf{Y}\boldsymbol{\Sigma}\mathbf{V}}}^\dagger = \overline{\overline{\mathbf{V}}}(\overline{\overline{\boldsymbol{\Sigma}}}^\dagger\overline{\overline{\boldsymbol{\Sigma}}})\overline{\overline{\mathbf{V}}}^\dagger$ is the eigendecomposition with $\overline{\overline{\boldsymbol{\Sigma}}}^\dagger\overline{\overline{\boldsymbol{\Sigma}}}$ a diagonal matrix of non-negative eigenvalues. In simple terms $\overline{\overline{\mathbf{U}}}^\dagger\overline{\overline{\mathbf{U}}}$ looks like the complex matrix equivalent of absolute value, analogous to $u^*u = |u|^2$ for complex numbers, which is always non-negative.

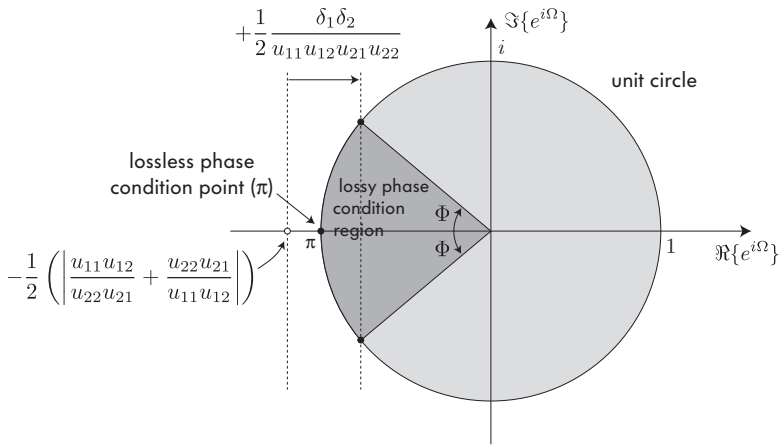

Figure 2.8: Graphical representation of the characteristic phase constraining inequality (2.14) valid for all passive reflectionless 4-ports.

alternatively expressed as

$$-\frac{1}{2}\left(\left|\frac{u_{11}u_{12}}{u_{22}u_{21}}\right|+\left|\frac{u_{22}u_{21}}{u_{11}u_{12}}\right|\right)\leq\cos(\phi_{12}+\phi_{21}-\phi_{11}-\phi_{22})\leq \tag{2.14}$$
$$\leq-\frac{1}{2}\left(\left|\frac{u_{11}u_{12}}{u_{22}u_{21}}\right|+\left|\frac{u_{22}u_{21}}{u_{11}u_{12}}\right|\right)+\frac{1}{2}\frac{\delta_1\delta_2}{|u_{11}u_{12}u_{21}u_{22}|}.$$

The leftmost term may be recognized as having the form $-(x+1/x)/2$ and therefore never exceeds -1. On the other hand, all values below -1 are not accessible for real phase angles ϕ_{mn}, simplifying the phase condition, without loss of generality, further to (replacing the phase sum with Ω, see (2.8))

$$-1\leq\cos(\Omega)\leq-\frac{1}{2}\left(\left|\frac{u_{11}u_{12}}{u_{22}u_{21}}\right|+\left|\frac{u_{22}u_{21}}{u_{11}u_{12}}\right|\right)+\frac{1}{2}\frac{\delta_1\delta_2}{|u_{11}u_{12}u_{21}u_{22}|}. \tag{2.15}$$

For a $\mathcal{V}$-symmetric 4-port where $u_{12}=u_{21}$, the condition may also be expressed in terms of the loss coefficients $\delta_{1,2}$ as

$$0\leq\sin^2(\Phi/2)\leq\frac{1}{4}\left(\frac{\delta_+-\delta_-}{1-\delta_+-|u_{21}|^2}+\frac{\delta_+\delta_-}{|u_{21}|^2(1-\delta_+-|u_{21}|^2)}\right) \tag{2.16}$$

where

$$\begin{aligned}\Phi &\equiv \Omega\pm\pi=\phi_{11}+\phi_{22}-\phi_{12}-\phi_{21}\pm\pi\\ \delta_+ &= \max(\delta_1,\delta_2)\\ \delta_- &= \min(\delta_1,\delta_2).\end{aligned}$$

The general passive reflectionless 4-port phase constraint (2.15) or (2.16) reduces to the well-known unitary phase condition (2.7) in the lossless limit. In (2.15), $|u_{11}u_{12}/u_{22}u_{21}|\to 1$ and $\delta_1=\delta_2\to 0$, so the upper limit is also -1, while in (2.16), $\delta_+=\delta_-\to 0$ setting the upper limit to 0. In each case, the result is

an equality. Furthermore, for lossy 4-ports having an $\mathcal{H}$ symmetry (see Fig. 2.5), $|u_{11}| = |u_{22}|$ so $\delta_1 = \delta_2$ and the first term on the RHS of (2.16) cancels, leaving the phase condition constrained by the "higher-order-in-δ", second term.

The general condition [using the variables in (2.14)] is illustrated on the complex-plane $e^{i\Omega}$ unit circle in Fig. 2.8. It shows the lossless operation point with the characteristic phase $\Omega = \pi$, and the range of deviation angles $\pm\Phi$ permitted by a given degree of lossiness described by δ_1 and δ_2.

The phase condition (2.15),(2.16) is relevant for addressing a phase-skew-induced spectral shape distortion in microring filters with lossy couplers, as well as in the analysis of lossy UBIs. The phase condition is demonstrated in Sec. (2.2.4) using the singular value approach that follows.

2.2.4 Physical representation by singular value decomposition

While the characteristic phase constraint was derived using restrictions on the norm, a more helpful approach to this inequality, and to analysis of R 4-ports, is through canonical representations of passive and active 4-ports by a physical analogue of singular value decomposition. This approach gives insight into the physical meaning of each of the 8 free parameters associated with a general reflectionless 4-port, and makes apparent the reduction in degrees of freedom brought about by symmetries in the physical structure.

In this section, first the singular value decomposition (SVD) is introduced and used as a basis for introducing a canonical representation of 4-ports. The properties of this representation are described. Then, the passive 4-port characteristic phase condition is examined in the context of this representation and verified by computer experiments. The phase condition is shown to be more stringent for lower levels of loss, and for splitting ratios of the 4-port closer to $50:50$.

An arbitrary reflectionless 4-port with no restriction regarding losslessness, or even passivity, is represented by a completely unconstrained 2×2 T-matrix, $\overline{\overline{\mathbf{T}}}$, and therefore 4 complex (8 real) numbers at each frequency. Every such arbitrary complex matrix may be represented by a singular value decomposition [72, p. 28],[73, p. 70],[74, p. 50]

$$\overline{\overline{\mathbf{T}}} \equiv \overline{\overline{\mathbf{U}}} \cdot \overline{\overline{\mathbf{\Sigma}}} \cdot \overline{\overline{\mathbf{V}}}^{\dagger}$$

where $\overline{\overline{\mathbf{U}}}$ and $\overline{\overline{\mathbf{V}}}$ are unitary matrices ($\overline{\overline{\mathbf{U}}}^{\dagger}\overline{\overline{\mathbf{U}}} = \overline{\overline{\mathbf{V}}}^{\dagger}\overline{\overline{\mathbf{V}}} = 1$), and $\overline{\overline{\mathbf{\Sigma}}}$ is a diagonal matrix with non-negative real coefficients on the diagonal.

This mathematical decomposition can be mapped to the (abstract) physical representation in Fig. 2.9. It employs a first lossless directional coupler $\overline{\overline{\mathbf{V}}}^{\dagger}$, a pair of zero-length propagation paths with gains Σ_{11} and Σ_{22}, and a second lossless directional coupler $\overline{\overline{\mathbf{U}}}$. This representation makes it apparent that Σ_{11} and Σ_{22} represent maximum and minimum gain coefficients for the optical field. Without loss of generality we may define $g_{\max} \equiv \Sigma_{11}$ and $g_{\min} \equiv \Sigma_{22}$. The maximum

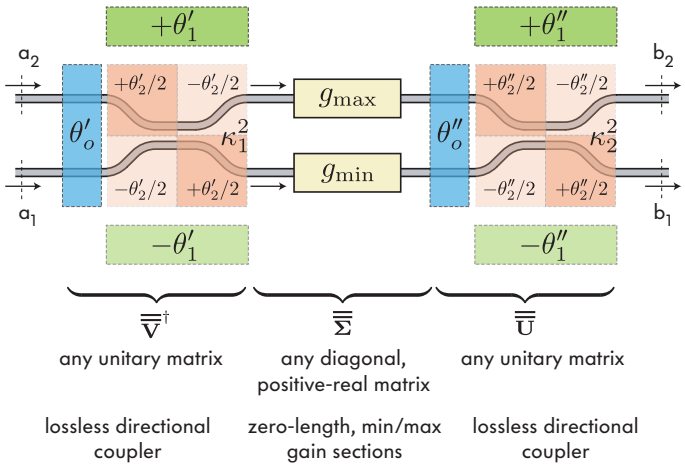

Figure 2.9: Abstract canonical representation of an arbitrary reflectionless 4-port, based on singular value decomposition of its T-matrix in Section2.2.4. It comprises a pair of lossless directional couplers and a zero-length propagation section pair, respectively having the minimum and maximum gain attainable from the 4-port.

and minimum gain are obtained only for particular relative amplitude and phase excitation of the input ports for which all power exits the first directional coupler $\overline{\overline{\mathbf{V}}}^\dagger$ in only one of the two abstract waveguides. For other excitations, various intermediate levels of effective gain are obtained. This can be justified by a simple thought experiment: consider the excitation of a Y-junction splitter in reverse, from the two output ports. Since there is only one input port, let us add a second input port terminated in an absorber to arrive at a reflectionless 4-port. If the two output ports are excited as inputs, and in phase, there is no loss and the maximum gain $g_{\max} = 1$ is seen. When excited out of phase, all power is radiated and none is guided to the inputs if those are single-mode waveguides. In this case the minimum gain $g_{\min} = 0$ is seen.

For a passive 4-port, $0 \leq g_{\min}, g_{\max} \leq 1$. For a lossless 4-port, $g_{\min} = g_{\max} = 1$ and the T-matrix, $\overline{\overline{\mathbf{T}}} = \overline{\overline{\mathbf{U}}}\overline{\overline{\mathbf{V}}}^\dagger$, is reduced to a product of two Hermitian matrices, so $\overline{\overline{\mathbf{T}}}$ is also a Hermitian matrix. Therefore, this SVD-based model reduces to the lossless 4-port model in Section 2.2.1 when loss is constrained to be zero. For cases with low but non-zero loss, which are technologically relevant, the SVD representation could be used in conjunction with first-order Taylor-series expansion to arrive at simplified representations and constraints.

Factorization of degrees of freedom as symmetry-orders expansion

A reduced canonical representation of reflectionless 4-ports may be found that makes evident the physical significance of each of the 8 degrees of freedom and their relation to physical symmetries. The SVD representation in Fig. 2.9 has 12 parameters and therefore overspecifies an arbitrary R 4-port which has 8 degrees

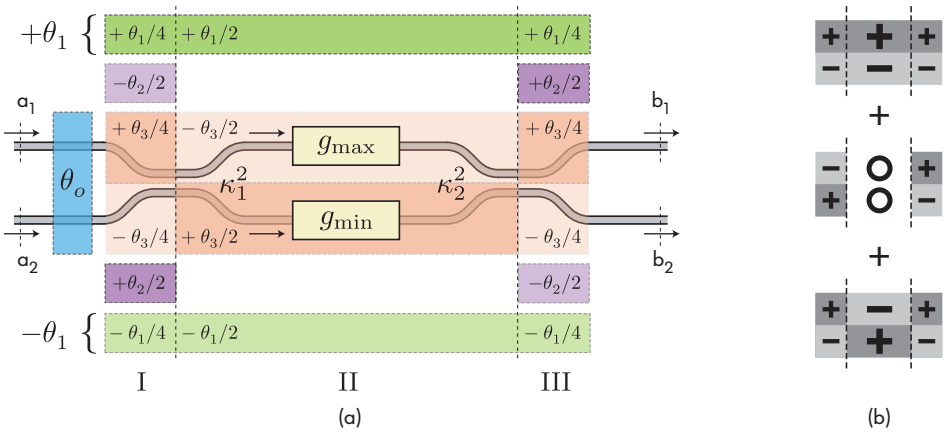

Figure 2.10: (a) Canonical representation of an arbitrary reflectionless 4-port, showing 8 degrees of freedom. It comprises two coupling ratios, a maximum and a minimum gain, one commonmode phase, and three orders of antisymmetric phases due to the two couplers. The latter three phases are illustrated in (b).

of freedom in a 2×2 T-matrix[‡‡].

Recall that the lossless form in (2.10) has three phase parameters – one phase parameter that is common-mode (symmetric) between the input ports, but two that are antisymmetric. This is because the common-mode phase θ_o "commutes" with the coupling matrix $\overline{\overline{\mathbf{K}}}$ (see 2.11), while the antisymmetric phase does not. Therefore, the latter case requires two degrees of freedom, θ_1 and θ_2.

Returning to the more general case considered here, this understanding enables us to define the required degrees of freedom. Since the present model in Fig. 2.9 has two couplers, while one common-mode phase is again sufficient, now three antisymmetric phase parameters are needed. The reduced canonical representation of an arbitrary reflectionless 4-port (for one propagation direction) is given in Fig. 2.10. The latter phase parameters are given as an expansion of symmetric and antisymmetric terms in three regions – before the first coupler κ_1, between couplers, and after the second coupler κ_2.

The transmission matrix of the arbitrary reflectionless 4-port, described by the

[‡‡]Of course, a non-reciprocal reflectionless 4-port may have a different 2×2 T-matrix in each direction, and then two copies of the model in Fig. 2.9 are needed, one for each direction, connected to the ports via ideal 3-port circulators.

canonical form in Fig. 2.10, is given by the decomposition

$$\begin{aligned}\overline{\overline{\mathbf{T}}} &\equiv \overline{\overline{\mathbf{U}}} \cdot \overline{\overline{\mathbf{\Sigma}}} \cdot \overline{\overline{\mathbf{V}}}^{\dagger} = \overline{\overline{\mathbf{\Theta_o}}} \cdot \overline{\overline{\mathbf{K_2}}} \cdot \overline{\overline{\mathbf{G}}} \cdot \overline{\overline{\mathbf{K_1}}} \cdot \overline{\overline{\mathbf{\Theta_i}}} \\ &= e^{i\theta_o} \begin{bmatrix} e^{i(\theta_1+2\theta_2+\theta_3)/4} & \\ & e^{-i(\theta_1+2\theta_2+\theta_3)/4} \end{bmatrix} \cdot \begin{bmatrix} \sqrt{1-\kappa_2} & i\sqrt{\kappa_2} \\ i\sqrt{\kappa_2} & \sqrt{1-\kappa_2} \end{bmatrix} \cdot \\ &\quad \cdot \begin{bmatrix} g_{\max} e^{i(\theta_1-\theta_3)/2} & \\ & g_{\min} e^{-i(\theta_1-\theta_3)/2} \end{bmatrix} \cdot \begin{bmatrix} \sqrt{1-\kappa_1} & i\sqrt{\kappa_1} \\ i\sqrt{\kappa_1} & \sqrt{1-\kappa_1} \end{bmatrix} \cdot \\ &\quad \cdot \begin{bmatrix} e^{i(\theta_1-2\theta_2+\theta_3)/4} & \\ & e^{-i(\theta_1-2\theta_2+\theta_3)/4} \end{bmatrix}. \end{aligned} \tag{2.17}$$

Redefining $\sqrt{\kappa_i} \equiv \sin(\theta_{\kappa,i})$, $\sqrt{1-\kappa_i} \equiv \cos(\theta_{\kappa,i})$ for $i = 1, 2$, the reduced form is

$$\overline{\overline{\mathbf{T}}} = \begin{bmatrix} T_{11} & T_{22} \\ T_{21} & T_{22} \end{bmatrix} \tag{2.18}$$

with

$$\begin{aligned} T_{11} &= e^{i\theta_1} g_{\max} \cos\theta_{\kappa 1} \cos\theta_{\kappa 2} - e^{i\theta_3} g_{\min} \sin\theta_{\kappa 1} \sin\theta_{\kappa 2} \\ T_{12} &= e^{-i(\theta_1-2\theta_2+\theta_3)/2} \left(e^{i\theta_1} g_{\max} \sin\theta_{\kappa 1} \cos\theta_{\kappa 2} + e^{i\theta_3} g_{\min} \cos\theta_{\kappa 1} \sin\theta_{\kappa 2} \right) \\ T_{21} &= e^{-i(\theta_1+2\theta_2+\theta_3)/2} \left(e^{i\theta_1} g_{\max} \cos\theta_{\kappa 1} \sin\theta_{\kappa 2} + e^{i\theta_3} g_{\min} \sin\theta_{\kappa 1} \cos\theta_{\kappa 2} \right) \\ T_{22} &= e^{-i\theta_1} g_{\min} \cos\theta_{\kappa 1} \cos\theta_{\kappa 2} - e^{-i\theta_3} g_{\max} \sin\theta_{\kappa 1} \sin\theta_{\kappa 2}. \end{aligned}$$

From the representation in Fig. 2.10 the physical meaning of each of the 8 parameters is apparent by inspection. They comprise coupling ratios κ_1 and κ_2, maximum and minimum gains $g_{\max}$ and $g_{\min}$, and the four discussed phases: one common-mode, and three antisymmetric. The "analyzing" coupler κ_1 projects the input excitation into the maximum- and minimum-gain states of the system, while the "synthesizing" coupler κ_2 provides a rotation into output states after the gain or loss is applied.

The particular choice made by the author in the expansion of the longitudinal phase into 3 degrees of freedom was made to provide terms that correspond to physical symmetries, and to simplify the form of (2.18)[§§].

Physical symmetries of a 4-port reduce the number of degrees of freedom in the canonical form, as may be determined by inspection of Fig. 2.5. In the case of $\mathcal{V}$, $\mathcal{HV}$ and $\mathcal{H}$ physical symmetries, the number of degrees of freedom is reduced from 8 respectively to 6, 6 and 4.

[§§]The expansion turns out to look like the first three eigenstates of a uniform, finite 3-point lattice potential well, or of the matrix $[0, 1, 0; 1, 0, 1; 0, 1, 0]$. But it is not unique, and any other convenient choice may be made.

Simplification of the phase inequality using SVD canonical model

In this section, a simpler form of the characteristic phase inequality (2.15) is derived, based on the parameters of the SVD canonical representation. It is shown that a tight bound can be derived with only two parameters that directly control the bound: the SVD maximum power loss of the 4-port, $\delta_{\max} \equiv 1 - g_{\max}^2$; and the maximum splitting ratio among the port combinations, $r_{\max} \equiv \max\left(|u_{21}/u_{11}|^2, |u_{12}/u_{22}|^2\right)$ (and of their inverses). The maximum loss is expected to control the bound, as the inequality was derived from the passivity property of the 4-port, and for zero loss, the lossless equality condition (2.7) is obtained as a limit. The reason why the maximum splitting ratio also plays a role is that a large splitting ratio puts little power in one arm and then a phase shift is less noticeable to the interferometer, so it is more difficult to violate the phase condition.

First, the lossy phase condition (2.15) is recast in terms of loss and splitting ratio parameters only. By defining a splitting ratio from each input port,

$$r_1 \equiv \left|\frac{u_{21}}{u_{11}}\right|^2 \qquad\qquad r_2 \equiv \left|\frac{u_{12}}{u_{22}}\right|^2 \tag{2.19}$$

we can express (2.13) as

$$\begin{aligned} 1-\delta_1 &= |u_{11}|^2(1+r_1) = |u_{21}|^2(1+1/r_1) \\ 1-\delta_2 &= |u_{22}|^2(1+r_2) = |u_{12}|^2(1+1/r_2) \end{aligned} \tag{2.20}$$

and obtain all four transfer functions in terms of loss and splitting ratio parameters:

$$|u_{11}|^2 = \frac{1-\delta_1}{1+r_1} \qquad\qquad |u_{21}|^2 = \frac{1-\delta_1}{1+1/r_1} \tag{2.21}$$

$$|u_{22}|^2 = \frac{1-\delta_2}{1+r_2} \qquad\qquad |u_{12}|^2 = \frac{1-\delta_2}{1+1/r_2} \tag{2.22}$$

Inserting these parameters into the characteristic phase condition (2.15), a more useful form is obtained,

$$\begin{aligned} \cos(\phi_{12}+\phi_{21}-\phi_{11}-\phi_{22}) \leq -\frac{1}{2}\left(\sqrt{\frac{r_2}{r_1}}+\sqrt{\frac{r_1}{r_2}}\right) + \\ + \frac{\delta_1\delta_2\sqrt{(1+r_1)(1+\frac{1}{r_1})(1+r_2)(1+\frac{1}{r_2})}}{2(1-\delta_1)(1-\delta_2)}. \end{aligned} \tag{2.23}$$

When the system is lossless, on the RHS the right-hand term goes to zero and the left-hand term goes to -1, hence the lossless phase condition (2.7) is recovered. On the other hand, with larger loss, the right-hand term is positive and the inequality is generally less constraining for larger and larger loss values. The lossier the system, the looser the bound.

It should be noted that a splitting ratio r_i or a maximum splitting ratio $r_{\max}$ may be specified either as, e.g. $100:1$ ($r = 100$) or as its reciprocal $1:100$ ($r = 0.01$)

as it will be seen that the relevant expressions, such as (2.23), are invariant with respect to an $r \to 1/r$ transformation.

Because it is the SVD-model maximum loss $\delta_{\max}$ that dictates the looseness of the bound rather than the losses from each port (as will be shown), the next step is to replace δ_1 and δ_2 with corresponding SVD-model parameters. Whereas $g_{\max}$ and $g_{\min}$ of a 4-port (referring to Fig. 2.9) are the maximum and minimum achievable field gain coefficients, respectively, for particular excitations at the input ports, we define complementary power-loss parameters, analogous to δ_1 and δ_2, named $\delta_{\max}$ and $\delta_{\min}$, which represent the maximum and minimum fractional power loss possible in transmission through the 4-port, with appropriate excitation of the inputs:

$$\delta_{\max} = 1 - g_{\min}^2 \qquad\qquad \delta_{\min} = 1 - g_{\max}^2 \tag{2.24}$$

A naive approach might assign $\delta_1 = \delta_2 = \delta_{\max}$. In such a case, the condition (2.23) remains true, but it becomes a much looser bound than necessary. This is because, although there may be cases where both single-input losses are close to $\delta_{\max}$, those cases are forced to stay far from the worst-case bounds of (2.23), and rather close to $\Omega = \pm\pi$. This "naive bound" will be shown and compared with the rigorous bound, next derived, in numerical experiments in Section 2.2.4.

Relating δ_1 and δ_2 to $\delta_{\max}$ requires a brief departure now. What we are after is a simple expression that tightly (rigorously) envelopes the region of admissable phase values. Therefore, finding an expression that delineates the boundary between the admissable region and the inadmissable region (for Ω) leads to the desired result. The boundary is described when the inequality (2.23) is made an equality, the case when the larger eigenvalue $\lambda_{\max} = \sigma_{\max}^2 = g_{\max}^2 = 1$ (compare to inequality that was used thus far, after (2.12)). Since $g_{\max} = 1$ ($\delta_{\min} = 0$) is fixed to set the system to the boundary of the bound, it is $g_{\min}$, i.e. $\delta_{\max}$ that controls the size of the bounding region. It should be noted here, and can be easily verified by following the same procedure as we did here with $\lambda_{\max}$, that $\lambda_{\min}$ (the second eigenvalue of $\overline{\overline{\mathbf{A}}}$) does not place any constraints on the phases.

The next step is to relate $g_{\max}$ and $g_{\min}$ to δ_1 and δ_2. By referring to the canonical SVD-based representation in Fig. 2.9 this is straightforward to do. Consider that $(1 - \delta_1)$ represents the sum of the output port powers when unity power is sent into input port 1 of the 4-port. This value is only determined by the first abstract lossless coupler κ_1, and the gain stages $[g_{\max}, g_{\min}]$. The output lossless coupler κ_2 can be ignored since it only redistributes power between the two output ports and we are summing the total output power in any case to get $(1 - \delta_1)$. Therefore, tracing power from each input port in Fig. 2.9 we conclude that

$$\begin{aligned}(1-\kappa_1^2)g_{\max}^2 + \kappa_1^2 g_{\min}^2 &= 1 - \delta_1 \\ \kappa_1^2 g_{\max}^2 + (1-\kappa_1^2)g_{\min}^2 &= 1 - \delta_2.\end{aligned}$$

When considering the boundary of the bounding region for which $g_{\max} = 1$ while $g_{\min} = 1 - \delta_{\max}$ is arbitrary, it follows from the previous equations that

$$\delta_{\max} = \delta_1 + \delta_2. \tag{2.25}$$

It should be stressed again that this result is only valid when $g_{\max} = 1$.

We wish to use (2.25) to replace the δ_1 and δ_2 terms in the inequality (2.23). Since there is one equation, we may only eliminate one of them at first:

$$\frac{\delta_1\delta_2}{(1-\delta_1)(1-\delta_2)} \rightarrow \frac{\delta_1(1-\delta_{\max})}{(1-\delta_1)(1-\delta_{\max}+\delta_1)} \tag{2.26}$$

However, since we wish to describe the system bound only in terms of the worst-case loss $\delta_{\max}$, we may simply take the worst-case bound over all values of δ_1. This preserves a tight bound, because one may arbitrarily choose a system with any δ_1, and the bound must hold true for it. Since $0 \leq \delta_1, \delta_2 \leq 1$, then also $0 \leq \delta_1, \delta_2 \leq \delta_{\max}$, which means that the expression (2.26) has a maximum. Differentiation with respect to δ_1 and setting the outcome equal to zero yields a maximum at

$$\delta_1\Big|_{\text{maxbound}} = \frac{\delta_{\max}}{2} \tag{2.27}$$

and using (2.25), $\delta_2 = \delta_1$. This solution provides the largest positive value for the second right-hand-side term of (2.23) and hence a valid bound for all possible δ_1. Substituting into (2.23), the characteristic phase inequality is further simplified to depend only on splitting ratios and the worst-case loss, $\delta_{\max}$:

$$\cos(\Omega) \leq -\frac{1}{2}\left(\sqrt{\frac{r_2}{r_1}} + \sqrt{\frac{r_1}{r_2}}\right) + \frac{\sqrt{(1+r_1)(1+\frac{1}{r_1})(1+r_2)(1+\frac{1}{r_2})}}{2(\frac{2}{\delta_{\max}}-1)^2}. \tag{2.28}$$

A further simplification can be made because the left-hand term is never greater than -1, and r_1 and r_2 could be replaced by a single worst-case splitting ratio, $r_{\max}$, defined as

$$r_{\max} \equiv \max\left(r_1, 1/r_1, r_2, 1/r_2\right).$$

Since $(1+r)(1+1/r)$ has a minimum at $r = 1$, setting the splitting ratio to the maximum of the various splitting ratios in the device will not violate the bound. Furthermore, since the largest gains $g_{\max}$ and the largest splitting ratios push the phase closest to the boundary of the bound, this substitution does *not* loosen the bound, as will be demonstrated. In final form, the lossy reflectionless 4-port characteristic phase condition has been derived as

$$-1 \leq \cos(\phi_{12} + \phi_{21} - \phi_{11} - \phi_{22}) \leq -1 + \frac{1}{2}\frac{(1+r_{\max})(1+\frac{1}{r_{\max}})}{(\frac{2}{\delta_{\max}}-1)^2}. \tag{2.29}$$

This straightforward expression only requires knowledge (or estimates) of two parameters of a 4-port – it's worst-case power loss, and largest splitting ratio from one

input port to the two outputs. In the limit of no loss $\delta_{\max} \to 0$, the right-hand term goes to zero, and (2.29) becomes the lossless phase condition equality (2.7). On the other hand, in the limit of large splitting ratios, $r_{\max} \to +\infty$ or 0, the RHS of the inequality goes to $+\infty$ and the phase is completely unconstrained, as expected. Therefore, to see a narrow constraint window on the phase, both the loss must be small enough and the splitting ratio close enough to 1. However, as we show next, "small enough" is in practice relatively generous, and the inequality provides useful information even for losses of the order of 70% and splitting ratios greater than $10:1$.

Demonstration of phase condition bounds by computer experiments

In this section, computer experiments are used to verify the correctness of inequality (2.29) and to demonstrate the tightness of the derived bound to generated sample data as well as its range of applicability. It is compared to the naive bound described in the previous section. In addition, a threshold loss-level $\delta_{\max}$ is derived, as a function of the splitting ratio bound, beyond which the characteristic phase Ω is completely unconstrained.

The approach taken is to generate a large, "uniformly distributed" set of random T-matrices that correspond to passive, reflectionless 4-ports; compute their characteristic phase $\Omega \equiv (\phi_{11} + \phi_{22} - \phi_{12} - \phi_{21})$, maximum loss coefficient $\delta_{\max}$ and maximum splitting ratio $r_{\max}$; and plot the characteristic phase against the maximum loss coefficient for subsets of the entire set of randomly generated 4-ports which do not exceed various values of maximum splitting ratio. This data is compared against the analytical bound (2.29).

To generate random transmission matrices, we construct them using their SVD $\overline{\overline{\mathbf{T}}} = \overline{\overline{\mathbf{U}}}\,\overline{\overline{\mathbf{\Sigma}}}\,\overline{\overline{\mathbf{V}}}^{\dagger}$ from randomly generated matrices $\overline{\overline{\mathbf{U}}}$, $\overline{\overline{\mathbf{V}}}$ and $\overline{\overline{\mathbf{\Sigma}}}$. This approach has several advantages. First, it permits direct generation of T-matrices having a chosen norm, or ones having a chosen possible range of minimum and maximum gain – by choosing $\overline{\overline{\mathbf{\Sigma}}} = \mathrm{diag}([g_{\max}, g_{\min}])$, where the gains may be fixed, or may be chosen randomly from a range $g_{\max}, g_{\min} \in [g_{\min,\mathrm{limit}}, g_{\max,\mathrm{limit}}]$. In the present case, we sample the entire range of *passive* 4-ports, so the lower and upper gain limits are, respectively, $g_{\min,\mathrm{limit}} = 0$, $g_{\max,\mathrm{limit}} = 1$, and the gains are randomly chosen from a uniform distribution over this range.

Next, two random unitary matrices, $\overline{\overline{\mathbf{U}}}$ and $\overline{\overline{\mathbf{V}}}$, need to be generated. One cannot choose arbitrarily random coefficients for the matrix because it must satisfy the unitary condition. However, it is well known that complex versions of the so-called QR matrix decomposition $\overline{\overline{\mathbf{QR}}} = \overline{\overline{\mathbf{A}}}$ (see [73]) can factorize any arbitrary complex matrix into a product of a unitary matrix $\overline{\overline{\mathbf{Q}}}$ and an upper-triangular matrix $\overline{\overline{\mathbf{R}}}$. This is useful because one does not need to worry about choosing the coefficients under the constraint of unitarity – we simply create an arbitrary matrix $\overline{\overline{\mathbf{A}}}$ by choosing 4 random real and 4 random imaginary coefficients in the ranges

$[0, 1]$ and $[0, i]$. The QR decomposition produces a random unitary matrix $\overline{\overline{\mathbf{Q}}}$ as a result.

Another advantage of using the QR decomposition is that it produces a set of random unitary matrices that is uniformly distributed with respect to the so-called Haar measure [75–77], if the matrix used as the input into the QR decomposition has uniformly distributed entry values. For matrices, this is the analogue of generating a uniformly distributed random variable. This is advantageous because it facilitates sampling the entire space of possible unitary matrices, so the distribution is truly random and we obtain a sufficient number of samples with all possible parameter combinations. If one chooses to construct a unitary matrix by choosing some entries randomly by hand and computing others to ensure unitarity, the transformations involved may skew the distribution to have few samples in some important part of the parameter space of interest.

For a set of 100,000 samples, the results are plotted in Fig. 2.11. The plots show a dot for each generated sample 4-port at the plot coordinate determined by its SVD maximum loss, $\delta_{\max}$, and its characteristic phase, Ω. Shown in the four plots is only the subset of 4-ports from the distribution having a maximum splitting ratio, $r_{\max}$, that is less than 1.5, 4, 10 and 100, respectively, as indicated in the figure titles. Accordingly, the characteristic phase bound (2.29) is different for each maximum-splitting-ratio ceiling value. The number of samples from the generated distribution of 100,000 4-ports that had an $r_{\max}$ lower than the ceiling $r_{\max}$ is indicated as N in the lower-left corner of each plot.

It can be observed clearly in each of the plots that all randomly generated passive 4-ports do obey the inequality (2.29), i.e. their Ω falls between the bound and 180°. Furthermore, the bound very tightly wraps the distribution of samples. This is because no approximations were made in the derivation of (2.29), and therefore it rigorously divides a parameter region where passive 4-ports are admissible, and a region where they are not admissible. As such the bound is very useful as it gives one the exact set of 4-ports that are excluded from existence, given a choice of constraints on $\delta_{\max}$ and $r_{\max}$. The tightness of the bound is more clearly illustrated in the plots in Fig. 2.12, which show the same result as Fig. 2.11 but with ten times as many randomly generated points (N = 1,000,000).

The bound is more restrictive on Ω for low maximum-loss levels and smaller maximum splitting ratios. Regarding the former, in the limit of zero loss, $\delta_{\max} \to 0$ and $\Omega = \pm 180^\circ$, reducing to the well-known lossless phase condition (2.7). Regarding the latter, the plots illustrate that not only is the admissable region for Ω larger for larger permitted $r_{\max}$ values, but furthermore there exists a threshold $\delta_{\max}$ beyond which the characteristic phase is completely unconstrained. The threshold occurs when the RHS of (2.29) is equal to 2. Therefore the *unconstrained*-Ω

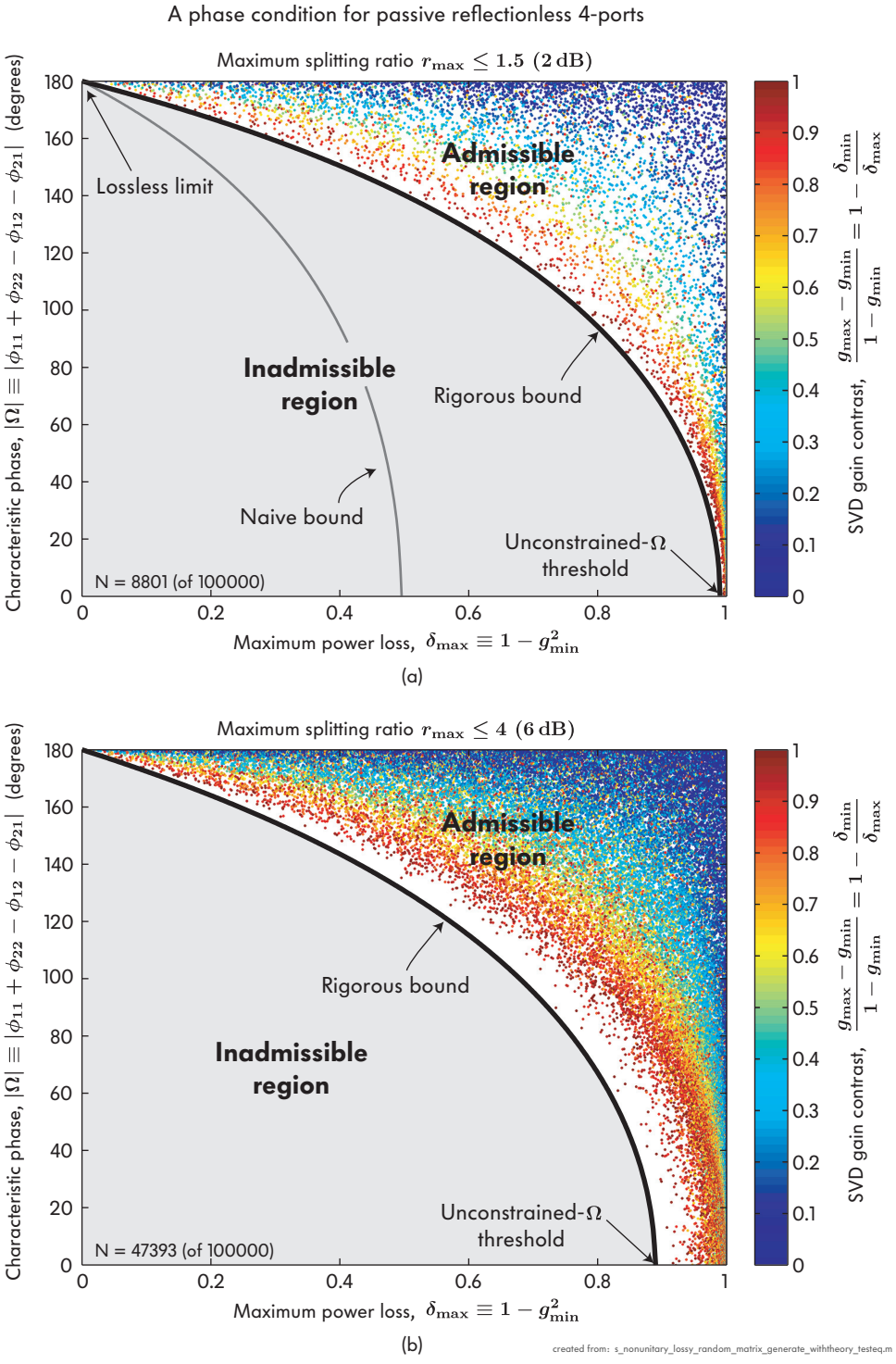

Figure 2.11: Numerical experiments verifying the characteristic phase constraint (2.29) (labeled 'rigorous bound') by generating 100,000 random passive 4-port T-matrices. Each dot represents a randomly generated 4-port, and is placed at coordinates determined by its $\delta_{\max}$ and characteristic phase Ω. The dot colour indicates its SVD gain contrast, as shown on the right axis. The experiments demonstrate that all of the random 4-ports fall within the analytically derived bound. Each plot also shows the . . . (continued on next page)

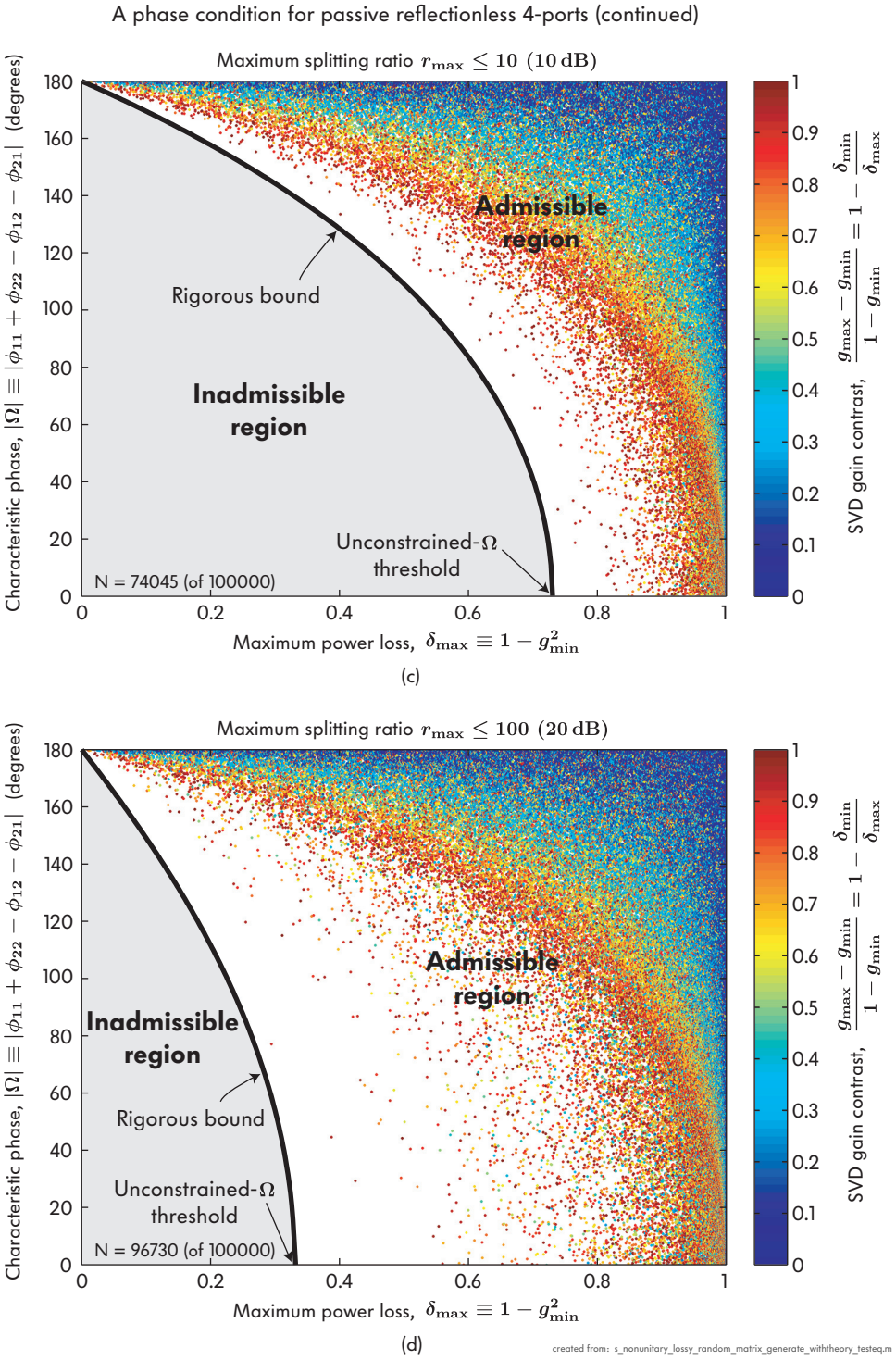

Figure 2.11 (continued) . . . unconstrained-Ω threshold (2.30). (a) Plot for 4-ports with maximum splitting ratio less than 1.5. Also shown is the lossless point corresponding to the well-known unitary phase condition (2.7), and the naive bound (see Sec. 2.2.4) which has the same shape as the rigorous bound, but is "compressed" by a factor of 2 along the horizontal axis; (b),(c),(d) plots for $r_{\max} \leq 4$ (no more than 6 dB splitting), 10 and 100, respectively.

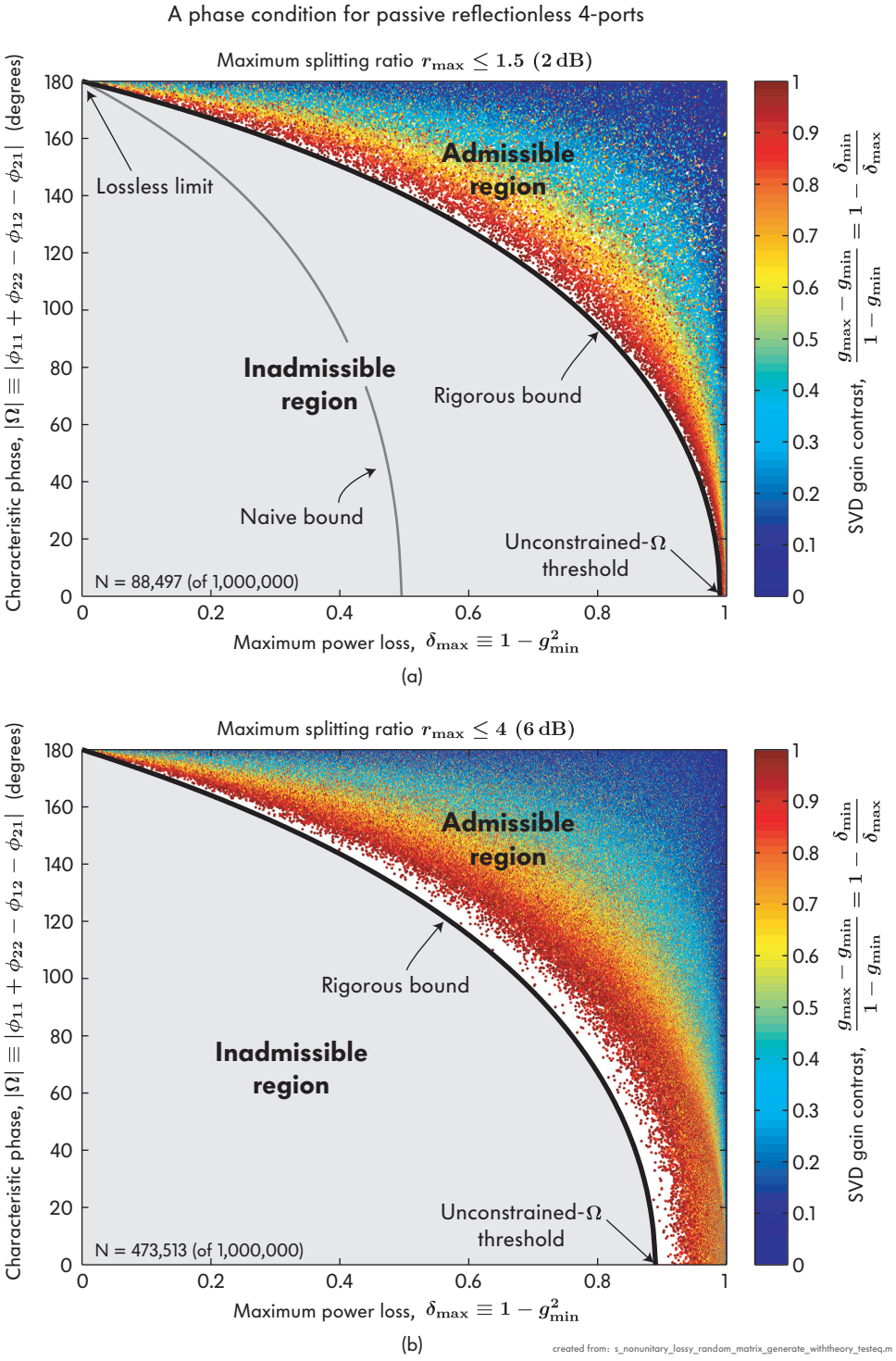

Figure 2.12: Numerical experiments verifying the characteristic phase constraint (2.29) (labeled 'rigorous bound') by generating 1,000,000 random passive 4-port T-matrices. Each dot represents a randomly generated 4-port, and is placed at coordinates determined by its $\delta_{\max}$ and characteristic phase Ω. The dot colour indicates its SVD gain contrast, as shown on the right axis. The experiments demonstrate that all of the random 4-ports fall within the analytically derived bound. Each plot also shows . . . (continued on next page)

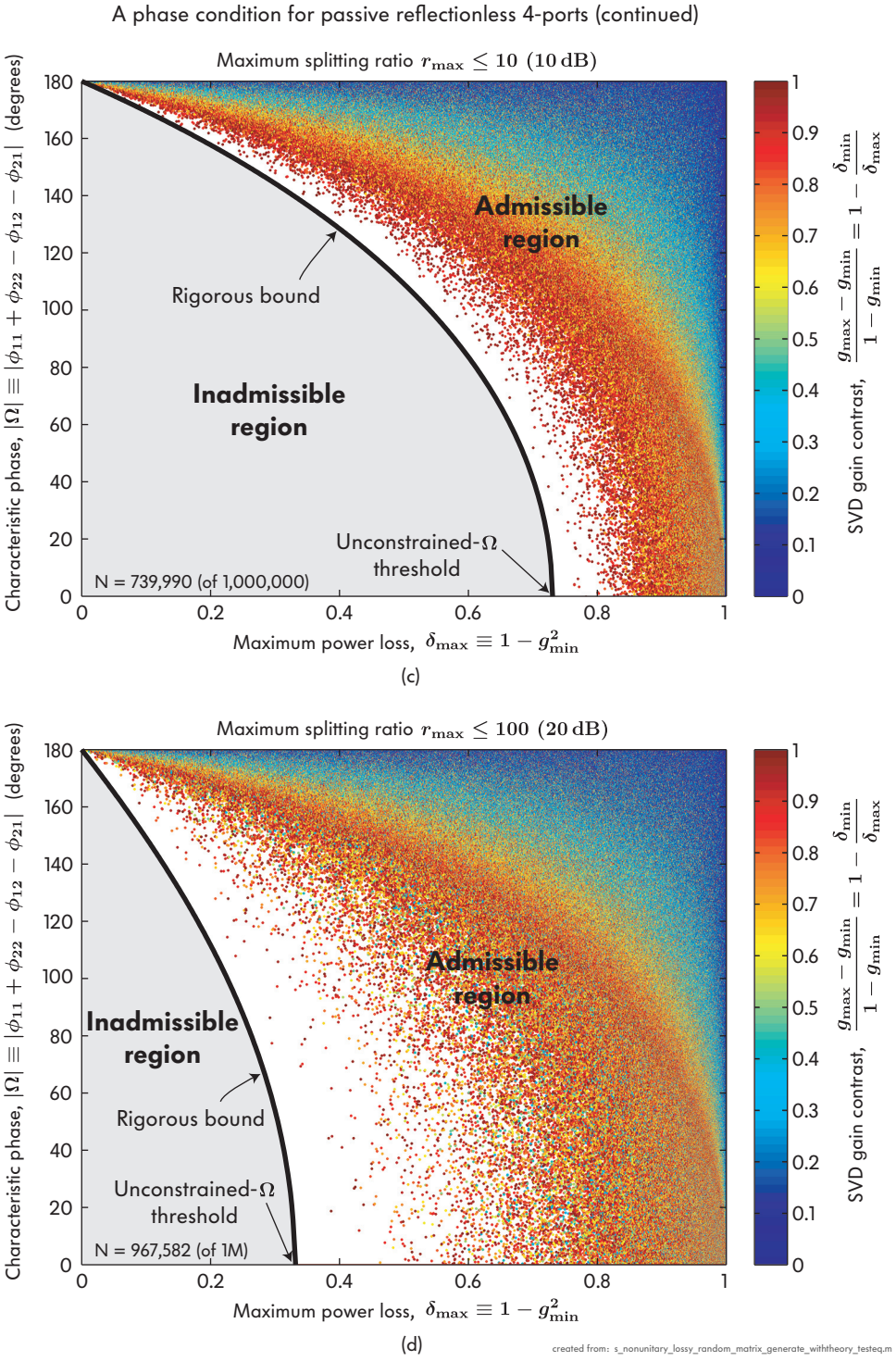

Figure 2.12 (continued) . . . the unconstrained-Ω threshold (2.30). (a) Plot for 4-ports with maximum splitting ratio less than 1.5. Also shown is the lossless point corresponding to the well-known unitary phase condition (2.7), and the naive bound (see Sec. 2.2.4) which has the same shape as the rigorous bound, but is "compressed" by a factor of 2 along the horizontal axis; (b),(c),(d) plots for $r_{\max} \leq 4$ (no more than 6 dB splitting), 10 and 100, respectively.

threshold is,

$$\delta_{\max,\text{threshold}} = \frac{1}{\frac{1}{2}+\frac{1}{2}\sqrt{\left(\frac{1+r_{\max}}{2}\right)\left(\frac{1+1/r_{\max}}{2}\right)}} \sim \frac{1}{\frac{1}{2}+\frac{1}{4}\sqrt{r_{\max}}} \tag{2.30}$$

where the asymptotic expression on the right is valid for $r_{\max} \gg 1$ (or $r_{\max} \ll 1$). For example, for $r_{\max} = 100$, $\delta_{\max,\text{threshold}} \approx 0.33$ which agrees with its position shown in Fig. 2.11(d).

It should be noted that, when there is *no* upper limit specified on the maximum splitting ratio, $r_{\max}$, the characteristic phase is unconstrained at all maximum-loss levels $\delta_{\max}$. Namely, when $r_{\max}$ increases indefinitely, the unconstrained-Ω threshold $\delta_{\max,\text{threshold}} \to 0$. This means that for completely arbitrary passive 4-ports, the characteristic phase is completely unconstrained and the inadmissable region shrinks to zero area. However, the bound still provides very useful information in practice because even for extremely large finite splitting ratios of $100:1$ it already constrains the phase considerably for technologically relevant losses of the order of 1 dB.

In the plots, only half of the angular spectrum, $[0, 180^\circ]$, is shown because the behaviour is symmetric in the range $[180, 360^\circ]$. For example, in Fig. 2.11(a), at $\delta_{\max} = 0.5$ the admissible region for Ω is from about 140 to 220 degrees.

The dot colour, corresponding to the right-axis colour code, has been used to indicate the level of $g_{\max}$ relative to $g_{\min}$ for each 4-port. We have used $g_{\max} = 1$ to derive the bound. In the plot, $g_{\min} = 1 - \delta_{\max}$ is fixed at each $\delta_{\max}$, and $g_{\max}$ can take on values between $g_{\min}$ and 1. The colour coding shows that generally a higher $g_{\max}$ brings a 4-port away from the 180° line and closer to the edge of the bound, consistent with intuition from the bound derivation. This trend is not exclusive, and the plots show a sparse population of red dots close to the 180° line, and a few blue dots closer to the bound. However, there will be no blue dots found on the edge of the bound (see next paragraph). The colour code is labeled as SVD gain contrast because it shows a normalized excursion of $g_{\max}$ above $g_{\min}$, these being the gains of the two "internal modes" of the 4-port. It could also be referred to as *internal loss-mode contrast*, corresponding to the second form shown in the axis.

A second simple case exists, besides the one that describes the boundary of the inequality (that being $g_{\max} = 1$). When $g_{\max} = g_{\min}$, then a passive 4-port satisfies the *lossless* unitary phase condition (2.7) that holds for lossless 4-ports, and $\Omega = \pm 180^\circ$, even if it is *not lossless*. This is because for $g_{\max} = g_{\min}$ the gain sections in Fig. 2.9 "commute" with the abstract couplers so that the gain section and a coupler can be interchanged without affecting the device and the T-matrix is $\overline{\overline{\mathbf{T}}} = \overline{\overline{\mathbf{U\Sigma V}}}^\dagger = \overline{\overline{\mathbf{\Sigma UV}}}^\dagger = g_{\max}\overline{\overline{\mathbf{UV}}}^\dagger$. Now, $\overline{\overline{\mathbf{UV}}}^\dagger$ is a unitary matrix, representing a lossless 4-port for which (2.7) holds. Therefore, all blue dots are on the $\Omega = \pm\pi$

line, except those where $\delta_{\max} \to 1$, i.e. $g_{\max} = g_{\min} \to 0$, where phase loses meaning and any phase is "allowed".

Finally, Fig. 2.11(a) also shows the naive bound obtained by setting the values of δ_1 and δ_2 in (2.23) to $\delta_{\max}$. This bound holds true, but is very loose and does not rigorously divide the admissible and inadmissible regions. The naive bound has the same curve shape as the rigorous bound but is shrunk in the horizontal direction by a factor of 2. This is because the rigorous bound requires (2.27).

Asymptotic forms of the characteristic phase inequality

For technologically relevant 4-ports with low maximum power loss $\delta_{\max}$, simplified forms of the characteristic phase inequality (2.29) may be found that are simple enough for use as a rule of thumb and for back-of-envelope calculations. In the low loss limit, a Taylor-series expansion about $\delta_{\max} = 0$ yields

$$-1 \leq \cos(\Omega) \leq -1 + \frac{1}{2}\frac{(1+r_{\max})(1+\frac{1}{r_{\max}})}{4}\delta_{\max}^2 \qquad \text{if } \delta_{\max} \ll 1$$

valid, in other words, for about $\delta_{\max} <\sim 1/10$. The boundary of the inequality is described by turning the RHS of the previous expression into an equality, and may be described as a linear deviation $\Phi = \pi - \Omega$ from the lossless case $\Phi = 0$ ($\Omega = \pi$). Defining $R \equiv (1+r_{\max})(1+1/r_{\max})$ and taking another Taylor expansion about $\delta_{\max} = 0$ yields

$$\begin{aligned} \pi - \Omega = \Phi &= \cos^{-1}\left[1 - R\delta_{\max}^2\right] \\ &= \sqrt{2R}\,\delta_{\max}\left(1 + \frac{A}{12}\delta_{\max}^2 + \mathcal{O}(\delta_{\max}^4)\right) \\ &\approx \sqrt{2R}\,\delta_{\max} \qquad \text{if } \frac{A}{12}\delta_{\max}^2 \ll 1 \end{aligned} \tag{2.31}$$

which, given that $\delta_{\max} < 1/10$, corresponds to $r_{\max} < 1200$ or so at least, which means this estimate is valid at low-loss levels for virtually any maximum splitting ratio of practical interest. Finally, in (2.31), $R = 2$ for near-equal splitting and $R \approx r_{\max}$ for large or small splitting ratios.

Conclusions

In this section, canonical representations for reflectionless 4-ports were described, based on abstract directional couplers, phase shifters and loss elements. These representations are useful for analysis and design of photonic devices such as UBIs (Chap. 8), microring filter directional couplers (e.g. Appendix E, Sec. 7.1 and Chap. 6). For passive and active 4-ports, an SVD-based representation offers insight into the 8 degrees of freedom of the 2×2 T-matrix.

Furthermore, for low-loss passive 4-ports, a rigorous bound was derived for the characteristic phase, which is a generalization of the well-known unitary phase

condition. It seems worthwhile to draw the reader's attention to this result, because of its potential usefulness in the design of microphotonic circuits (e.g. with regard to lossy UBIs in Chap. 8, and with regard to resonant filter spectrum distortion due to lossy waveguide-resonator coupling – Appendix E, Sec. 7.1), and because it appears to the author to be new despite there being considerable literature on the rather well studied subject of 2×2 matrices. This result may be of utility in other fields where near-unitary or non-unitary operators are of interest and used to model coherent systems, such as in quantum computation.

It should be possible to use the presented approach to arrive at other similar or further generalized bounds on the characteristic phase, such as ones for active structures. Since the randomly generated 4-ports are in all cases much more sparsely distributed near the bound than near the $\Omega = 180^\circ$ line, it would also be interesting to investigate the distribution of the 4-ports in this parameter space, and to study the properties of the few 4-ports that do land near the bound to see what unique properties characterize them, beyond those already described here.

Chapter 3

Modeling of concrete electromagnetic structures

3.1 Continuum electromagnetic fields and modes

3.1.1 Mode index and group index

The *refractive index* and *group index* at a given frequency of a transparent material determine the phase propagation constant and its first-order frequency dependence, respectively, for plane waves in the medium. They define, respectively, the phase and group velocities, $v_p \equiv c/n$ and $v_g \equiv c/n_g$. In a dispersive medium, they are not equal, but they are related (see Sec. 3.2).

In a guided-wave system, a guided mode has by analogy an *effective mode index*, β/k_o, and an *effective group index*, $\partial\beta/\partial k_o$, respectively. In strong-confinement (high-index-contrast) waveguides, there is large structural (form) dispersion, and therefore these indices are not equal and both enter into fundamental relationships relevant to design. Although in previous literature each of these has been referred to as "effective index", henceforth, the effective mode index is referred to as effective index, and the effective group index simply as group index. Where it is not obvious from the context, the distinction is made between effective group index and material group index.

3.1.2 Role of the group index in strong-confinement structures

Cavity resonant-frequency tuning

Optical cavity mode resonance frequencies can be tuned by applying perturbations to the refractive index distribution that overlaps with the mode field – for example

by thermooptic or carrier-induced index change, or using mechanically movable dielectric membranes.

Resonant-frequency tuning of an optical traveling-wave-cavity mode due to a perturbation is determined by the induced shift in effective mode index, normalized by the mode group index, of the cross-section of the waveguide that constitutes the resonator:

$$\frac{\delta\omega}{\omega_o} \simeq \frac{\delta\lambda}{\lambda_o} \simeq -\frac{\delta n_{\text{eff}}}{n_{\text{group}}} \tag{3.1}$$

The reason for the unusual combination of the effective index differential in the numerator, but the group index magnitude in the denominator, is due to a combination of effective index change and frequency change needed to effect and track a shifting resonance frequency.

This simple formula can be justified by a thought experiment that explains its derivation in a physical way. Resonance-frequency tuning due to an abstract perturbation parameter, q, can be thought of as the combination of an index change due to the perturbation, Δq, and the frequency change $\Delta\omega$ needed to return to resonance.

Consider a waveguide cross-section with a propagation constant β at the resonant frequency ω_o and in the state q (in a concrete example, q might be the temperature, T, in the case of thermooptic tuning). Since the cavity is resonant at ω_o, β has a value that gives an integer number of wavelengths over a round trip length L, i.e. $\beta L = 2\pi N$ with N integer. To determine the tuning, first, we change the state q, by a small amount dq, which changes the propagation constant. Now, β has changed by $\delta\beta_q$ and is no longer resonant at ω_o. The second step we take is to change the frequency so that β goes back to its original value in the new state q and is resonant again. Then, the new frequency is the tuned resonant frequency of the cavity. In the two-step thought experiment the propagation constant changes as

$$\beta \to \beta + \delta\beta_q \to \beta + \delta\beta_q + \delta\beta_\omega = \beta \tag{3.2}$$

which expands to

$$\begin{aligned} \delta\beta_q + \delta\beta_\omega &= 0 \\ \frac{\omega_o}{c}\frac{\partial n_{\text{eff}}}{\partial q}\bigg|_{q_o,\omega_o}\Delta q + \frac{n_{\text{group}}}{c}\bigg|_{q_o+\Delta q,\omega_o}\Delta\omega &= 0 \\ \frac{\Delta\omega}{\omega_o} &= -\frac{1}{n_{\text{group}}}\bigg|_{q_o+\Delta q,\omega_o}\cdot\frac{\partial n_{\text{eff}}}{\partial q}\bigg|_{q_o,\omega_o}\Delta q. \end{aligned} \tag{3.3}$$

For thermal tuning where $q \equiv T$, and for infinitesimal ΔT and $\Delta\omega$ ($\omega_o = \omega$), this gives the "local" tuning formula

$$\frac{\Delta\omega}{\omega} = -\frac{\Delta n_{\text{eff}}}{n_{\text{group}}} = -\frac{1}{n_{\text{group}}}\frac{\partial n_{\text{eff}}}{\partial T}\Delta T. \tag{3.4}$$

Here, $\partial n_{\text{eff}}/\partial T$ is the effective thermooptic coefficient of the waveguide mode which depends on the overlap integral of the mode with the thermal index perturbation. Since the materials constituting the waveguide may have different thermooptic coefficients, for simple geometries such as ones having a single core material and a single cladding material, this coefficient may be broken down into the two contributing parts:

$$\frac{\partial n_{\text{eff}}}{\partial T} = \frac{\partial n_{\text{eff}}}{\partial n_{\text{core}}}\frac{\partial n_{\text{core}}}{\partial T} + \frac{\partial n_{\text{eff}}}{\partial n_{\text{clad}}}\frac{\partial n_{\text{clad}}}{\partial T}. \tag{3.5}$$

The first coefficient in each term is a weighting factor related to the fraction of guided power in each material region, and the second is the thermooptic coefficient of the core or cladding material, respectively.

For large tuning over T and ω ranges over which n_{group} and $\partial n_{\text{eff}}/\partial T$ are not substantially constant, Eq. 3.4 must be integrated to arrive at the predicted tuning range due to the perturbation.

3.2 A theorem relating the phase and group velocities of dielectric waveguide modes

In this section, an exact relationship is derived for the phase and group effective index (i.e. velocity) of dielectric waveguide modes involving only the propagation constant, the mode field and the index distribution. The formula is a generalization of the $v_g v_p = c^2$ identity that holds for plane waves in plasmas and hollow metallic waveguides. It permits the determination of group index from the known propagation constant and mode profile at a single frequency, and reduces properly to the plane-wave case. Scalar and vector forms are derived.

3.2.1 Scalar case

In plasmas and hollow metallic waveguides, $v_g v_p = c^2$. In dielectric waveguides a similar trend is apparent and it is of interest to see if the phase and group velocity, i.e. phase and group effective indices, can be exactly related. Phase and group effective index (n_p,n_g) of a mode at a given frequency are defined by the Taylor-series expansion of the propagation constant in frequency ($k_o \equiv \omega/c$):

$$\beta(\omega) = \beta(\omega_o) + \left.\frac{\partial\beta}{\partial k_o}\right|_{\omega_o}\Delta k_o + \cdots = (n_p k_o)\Big|_{\omega_o} + n_g\Big|_{\omega_o}\Delta k_o + \cdots \tag{3.6}$$

To relate the indices similar to $v_g v_p = c^2$,

$$n_p n_g = \frac{\beta}{k_o}\frac{\partial\beta}{\partial k_o} = \frac{1}{2k_o}\frac{\partial}{\partial k_o}\beta^2 \tag{3.7}$$

Now β^2 is found in the defining eigenvalue equation for waveguide modes described by the scalar wave equation (e.g. TE slab modes),

$$\left[\nabla_t^2 + (k_o n(x,y;k_o))^2 - \beta(k_o)^2\right]\Phi(x,y;k_o) = 0 \tag{3.8}$$

where index distribution $n(x,y)$, propagation constant β, and mode field $\Phi(x,y)$ all may depend on frequency k_o. Multiplying by Φ^* and integrating (3.8), a stationary formula for β^2 is

$$\beta^2 \langle\Phi|\Phi\rangle = \langle\Phi|\nabla_t^2 + (k_o n)^2|\Phi\rangle \tag{3.9}$$

This formula can be differentiated with respect to k_o to seek the relationship in (3.7),

$$\frac{\partial}{\partial k_o}\left(\beta^2\langle\Phi|\Phi\rangle\right) = \frac{\partial}{\partial k_o}\langle\Phi|\nabla_t^2|\Phi\rangle + \frac{\partial}{\partial k_o}\langle\Phi|(k_o n)^2|\Phi\rangle .$$

The product rule gives

$$\begin{aligned}\langle\Phi|\Phi\rangle\frac{\partial}{\partial k_o}\beta^2 + \beta^2\left\langle\frac{\partial\Phi}{\partial k_o}\middle|\Phi\right\rangle + \beta^2\left\langle\Phi\middle|\frac{\partial\Phi}{\partial k_o}\right\rangle = \\ -\left(\left\langle\frac{\partial}{\partial k_o}\nabla_t\Phi\middle|\nabla_t\Phi\right\rangle + \left\langle\nabla_t\Phi\middle|\frac{\partial}{\partial k_o}\nabla_t\Phi\right\rangle\right) + \\ +\left(\left\langle\frac{\partial\Phi}{\partial k_o}\middle|(k_o n)^2\middle|\Phi\right\rangle + \left\langle\Phi\middle|\frac{\partial}{\partial k_o}(k_o n)^2\middle|\Phi\right\rangle + \left\langle\Phi\middle|(k_o n)^2\middle|\frac{\partial\Phi}{\partial k_o}\right\rangle\right)\end{aligned}$$

Rearranging terms,

$$\begin{aligned}\langle\Phi|\Phi\rangle\frac{\partial}{\partial k_o}\beta^2 = \left\langle\Phi\middle|\frac{\partial}{\partial k_o}(k_o n)^2\middle|\Phi\right\rangle + \left\langle\frac{\partial\Phi}{\partial k_o}\middle|\nabla_t^2\middle|\Phi\right\rangle + \left\langle\frac{\partial\Phi}{\partial k_o}\middle|(k_o n)^2\middle|\Phi\right\rangle - \beta^2\left\langle\frac{\partial\Phi}{\partial k_o}\middle|\Phi\right\rangle + \\ + \left\langle\Phi\middle|\nabla_t^2\middle|\frac{\partial\Phi}{\partial k_o}\right\rangle + \left\langle\Phi\middle|(k_o n)^2\middle|\frac{\partial\Phi}{\partial k_o}\right\rangle - \beta^2\left\langle\Phi\middle|\frac{\partial\Phi}{\partial k_o}\right\rangle\end{aligned}$$

Now, observe that terms 2-4 on the right hand side are the wave equation (3.8) operating on the ket, and are thus identically zero. Likewise, terms 5-7 on RHS are the wave equation operating leftward on the bra (or by integration by parts on the ket), and are identically zero. Thus only the first RHS term survives (and with some manipulation):

$$n_p n_g = \frac{1}{2k_o}\frac{\partial}{\partial k_o}\beta^2 = \frac{\left\langle\Phi\left|n\frac{\partial}{\partial k_o}(k_o n)\right|\Phi\right\rangle}{\langle\Phi|\Phi\rangle} \longrightarrow \frac{\langle\Phi|n^2|\Phi\rangle}{\langle\Phi|\Phi\rangle}, \text{ for non-dispersive media.} \tag{3.10}$$

This formula is an exact relationship for group and phase effective index product, and is the mode field overlap with the spatial distribution of the material group-phase index product. The relationship gives the mode group index, n_g, once the mode field and n_p are known. The formula reduces to the plane wave/hollow metallic waveguide case for uniform cross-sections $n(x,y)$. For non-dispersive media, it also reduces to the low-index-contrast effective index approximation formula if we let $n_p \approx n_g = n_{\text{eff}}$ (paraxial).

3.2.2 Vector case

A similar procedure yields a more general relationship using vector fields. From the vector curl equations that govern general dielectric waveguide modes,

$$\nabla_t \times E + j\omega\mu_o H = j\beta\hat{z} \times E$$
$$\nabla_t \times H - j\omega\epsilon \cdot E = j\beta\hat{z} \times H$$

a stationary formula for the propagation constant can be obtained as [78],

$$j\beta = \frac{\int (H^* \cdot \nabla_t \times E - E^* \cdot \nabla_t \times H + jE^* \cdot \omega\epsilon \cdot E + jH^* \cdot \omega\mu \cdot H)\,\mathrm{da}}{\int E \times H^* + E^* \times H \cdot \hat{z}\,\mathrm{da}}$$

By differentiating with respect to k_o and following a similar approach to the above, it is possible to arrive at an analogous expression using vector fields:

$$n_g = \frac{\partial\beta}{\partial k_o} = \frac{\int E^* \cdot \left(\frac{\partial}{\partial k_o}(\omega\epsilon)\right) \cdot E + H^* \cdot \left(\frac{\partial}{\partial k_o}(\omega\mu)\right) \cdot H\,\mathrm{da}}{\int E \times H^* + E^* \times H \cdot \hat{z}\,\mathrm{da}} \tag{3.11}$$

The group index may be obtained from the mode. The propagation constant (β) information is contained in the fields. This formula reduces to expression (3.10) in the scalar (slab TE) case where μ is frequency-independent. It is the vector-field generalized form of $v_g v_p = c^2$.

The previous formula may be found in previous waveguide work [58, 79, 80].

3.3 Conclusions

In this section, a rigorous relationship was established between the effective modal and group indices of strongly-confined waveguide modes in HIC photonic structures, for the simplified 2D TE case (scalar), and for 3D, arbitrary-polarization waveguides (full vector field). This result is used in Chap. 5 to obtain the group index from modesolver-computed modal field distributions and corresponding modal effective indices in a computationally efficient way (without requiring further modesolver computations).

The group index plays an important role in many important characteristics of SC waveguides and resonators. Its role was clarified in resonant-mode wavelength tuning, and in defining the FSR in presence of dispersion.

Part II

Electromagnetic design of HIC devices

Chapter 4

High-index-contrast resonator-based filters

4.1 Coupling-induced resonance frequency shifts*

Coupling-induced resonance frequency shifts (CIFS) are theoretically described, and are found to be an important fundamental source of resonance frequency mismatch between coupled optical cavities that would be degenerate in isolation. Their deleterious effect on high-order resonant filter responses and complete correction by pre-distortion are described. Analysis of the physical effects contributing to CIFS shows that a positive index perturbation may bring about a resonance shift of either sign. Higher-order CIFS effects, the scaling of CIFS-caused impairment with finesse, FSR and index contrast, and the tolerability of frequency mismatch in telecom-grade filters are addressed. The results also suggest possible designs and applications for CIFS-free coupled-resonator systems. The first full FDTD simulation of a higher-order microring-resonator filter is reported, showing a near ideal frequency response, corresponding to synthesis, only after appropriate correction of the CIFS.

4.1.1 Introduction

High-Q dielectric resonators, like microrings and photonic crystal micro-cavities, are enabling the use of microphotonic circuits for filtering, sensing, nonlinear interaction and lasers [38, 81–84]. Complex, high-order resonant structures, of importance for bandpass channel add-drop filters, dispersion elements or slow-wave structures [8, 38, 49, 53, 54, 71, 85, 86], are formed by coupling multiple

*This section is reproduced nearly verbatim from my paper on the subject [46], with some expansions and additions as allowed by the available space.

optical cavities. The spectral response is engineered by the choice of resonance frequencies of, and coupling strengths between, the constituent cavities. Therefore, command of the resonance frequencies in design is important. For example, in series-coupled-cavity filters [38, 49, 54, 86], flat-top bandpass responses call for identical uncoupled cavity resonances, where the choice of coupling strengths (set by appropriate coupling gaps) determines the particular response shape. Such examples suggest a geometry employing physically identical resonators, or in Vernier schemes, different-sized cavities with coincident uncoupled resonances.

In this section, it is shown that coupling of cavities introduces self-coupling perturbations that give rise to new *effective uncoupled resonance frequencies*, leading to severe response impairments that must be corrected in design. In [87], initial findings on coupling-induced resonance frequency shifts (CIFS) were reported[†]. Here, the first more complete treatment and discussion is given, as published in [46]. First, the effect of CIFS on filter response is demonstrated by rigorous numerical eigenmode and finite-difference time-domain (FDTD) simulations. The simulations show that accounting for CIFS is necessary and sufficient for simplified transfer-matrix and coupled-mode models, supplemented by numerically computed coefficients, to accurately match full FDTD simulation results for a third-order microring-resonator filter. Next, coupled-mode theory is called upon to qualitatively explain the effect, before addressing the physical basis and rigorous evaluation of CIFS in traveling-wave and general resonators. Counter to what may be expected for positive-index perturbations, it is shown that CIFS can be of negative or positive sign. By compensating for the predicted shift, it is verified that the ideal filter response may be recovered. Next, the scaling of the effect with index contrast, inter-cavity cross-coupling strength, bandwidth and free spectral range (FSR) is analyzed. Finally, CIFS-free coupled resonator designs are discussed and comments made regarding generic methods for the compensation of CIFS.

Resonant frequency mismatch is particularly deleterious to in-band extinction in the through port of high-order add-drop filters [88, 89]. The results show that it must be accounted for in the filter design in order to achieve the desired symmetric high-extinction responses that will enable the use of resonator-based filters in channel add-drop applications.

For the sake of clarity, it is reiterated here that CIFS is a coupling effect in linear systems and refers to a perturbation of the resonance property of the electromagnetic cavity and *not* to a shift in frequency of an input signal.

4.1.2 CIFS and its effect in multipole resonators

Before demonstrating its deleterious effect on a multipole resonator, CIFS is defined through a simple example. An idealized two-cavity system in Fig. 4.1(a),

[†]The effect was first observed by C. Manolatou in 2002, as a spectral asymmetry in FDTD simulations of the frequency response of microring structures.

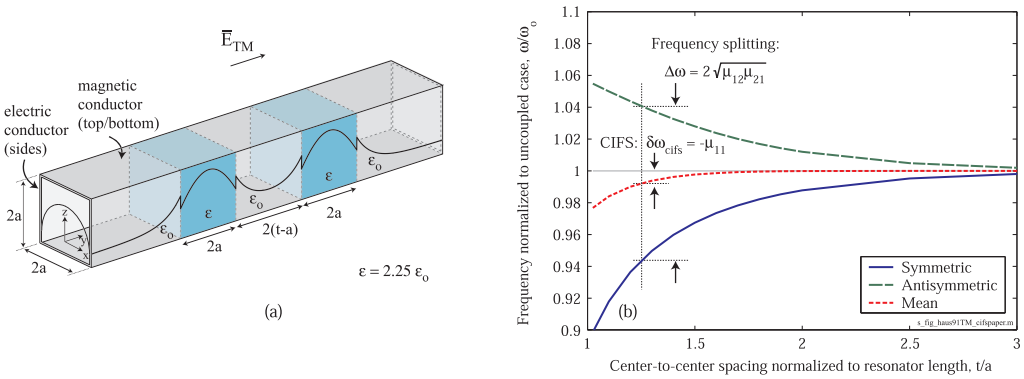

Figure 4.1: (a) Coupled-dielectric-resonator system in infinite perfect-conductor waveguide, with analytic mode solutions [78]; (b) TM_{10} supermode frequency splitting and CIFS vs. resonator spacing.

of identical dielectric blocks in an infinite conducting waveguide, has an analytic TM_{10}-mode solution (cf. [78]). Coupling results in a frequency splitting $\Delta\omega$ [Fig. 4.1(b)] of the supermodes [67, 78]. It also causes a shift $\delta\omega$ in the mean supermode frequency. The latter may be interpreted as a coupling-induced shift in *effective* uncoupled resonance frequencies, that we refer to as CIFS.

In higher-order resonators based on multiple cavities, engineering supermode poles directly is difficult. A more tractable design framework is based on individual cavity modes and uncoupled cavity resonance frequencies, with separate coupling and CIFS terms to describe the coupled configuration. Thus, the individual cavity design and the coupling design are made, to a large extent, independent. The dynamics of the system are described by coupling of modes in time (CMT) [67, 78],

$$\frac{d}{dt}\vec{a} = j\overline{\overline{\omega}}\cdot\vec{a} - j\overline{\overline{\mu}}\cdot\vec{a} \tag{4.1}$$

where the amplitudes $\vec{a}$ are associated with the resonant modes and normalized such that $|\vec{a}_n|^2$ is the energy of mode n; $\overline{\overline{\omega}}$ is a diagonal matrix of uncoupled resonance frequencies, and matrix $\overline{\overline{\mu}}$ represents mode coupling. Off-diagonal elements $\mu_{i,j}$ represent cavity-to-cavity coupling employed in engineering the supermodes. Diagonal elements $\mu_{i,i}$ represent CIFS and modify $\overline{\overline{\omega}}$ into effective cavity resonance frequencies. Solving (4.1) yields frequency splitting,

$$\omega_{s,a} = \frac{\omega_1 - \mu_{11} + \omega_2 - \mu_{22}}{2} \mp \sqrt{\left(\frac{(\omega_1 - \mu_{11}) - (\omega_2 - \mu_{22})}{2}\right)^2 + \mu_{12}\mu_{21}}. \tag{4.2}$$

CIFS ($\mu_{i,i}$) is a second-order, self-coupling effect, as compared to the direct coupling $\mu_{i,j}$ that is first-order, leads to frequency splitting [Fig. 4.1(b)] and sets the bandwidth. On the other hand, in *spectral response* models, CIFS is contained linearly, as modification of resonance frequency, while cross-coupling is squared (compare [38]). In net result, the two effects are comparable.

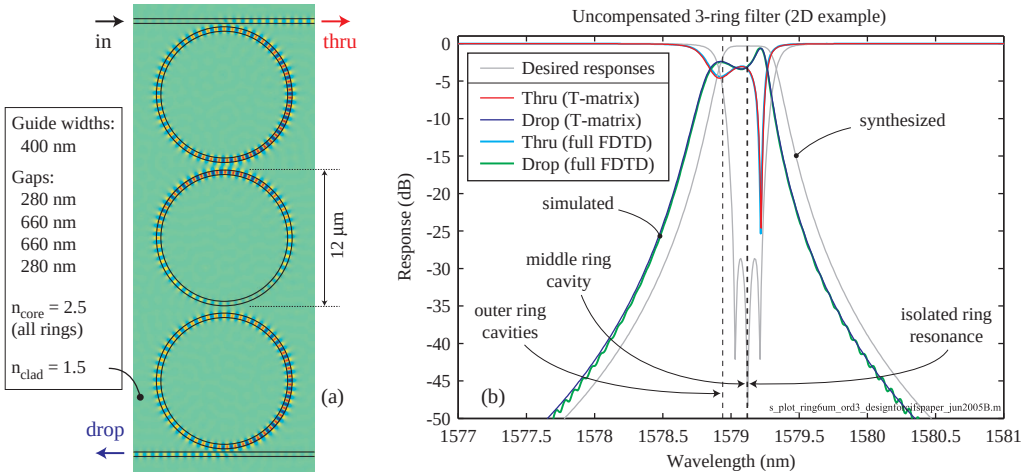

Figure 4.2: CIFS impairment of 3-cavity microring filter: (a) simulated structure using identical rings (dimensions shown); (b) ideal (synthesized) and simulated (complete-structure FDTD and model) frequency response showing apparent cavity mismatch due to CIFS.

A two-dimensional (2D) simulation demonstrates that CIFS can seriously impair a filter design. A channel add-drop filter, based on a series-coupled 3-ring resonator, was synthesized to have a 50 GHz 3 dB passband and 30 dB in-band extinction in the through port [38, 49]. The microring resonators are identical and hence degenerate in the absence of coupling, with 3200 GHz FSR near 1580 nm. The required power coupling coefficients are {0.0825, 0.00155, 0.00155, 0.0825}, corresponding to coupling gaps of {280, 660, 660, 280} nm. FDTD simulation of the complete filter was carried out to find the drop and through port spectral responses. For completeness, details of the simulations are given in Section 4.1.9. A snapshot of the field in the simulated structure is shown in Fig. 4.2(a), and the desired (synthesized) and obtained (simulated) filter responses are shown in Fig. 4.2(b). The ideal synthesized response is obtained by a transfer-matrix-method computation [71, 86] assuming matched resonators. The asymmetric simulated response is a telltale sign of resonance frequency mismatch due to CIFS [87]. To account for the observed response shape in theory, a mismatch of ∼22 GHz (on the order of the filter bandwidth) must be supposed. The response is so severely distorted that, mid-band, the signal is split evenly between the drop and through ports rather than being dropped. As shown below, this distortion is the net effect only of varying CIFS contributions in the three cavities caused by their coupling configurations. Experimentally determining CIFS is complicated by the additional fabrication-related resonance frequency offsets between cavities that can be comparable to the CIFS, and that add to the response distortion [90].

CIFS distortion and compensation is illustrated in Fig. 4.3, starting with an isolated resonant cavity, here a microring resonator [Fig. 4.3(a)]. Placing a cavity near a waveguide or near a second resonant cavity, results in coupling through the perturbation of the evanescent fields that extend outside the dielectric core region.

In addition to the coupling, the changed proximate environment that perturbs the evanescent field of a cavity causes a CIFS. For an arbitrary filter coupling coefficient distribution, the perturbation seen by the mode of each resonator will, in general, be different in accordance with the arrangement of perturbing nearby structures "seen" by its evanescent field [Fig. 4.3(b)]. When assembled in a higher-order filter, the effective resonance frequency of each cavity is shifted from its value in isolation [Fig. 4.3(c)]. Since the shifts are in general not identical, the system response is not only shifted in frequency, but also distorted. To recover the desired response, the cavities may be pre-distorted in design so that in the complete filter, the *effective uncoupled resonance frequencies* are again degenerate [Fig. 4.3(d)].

4.1.3 Physical sources and the sign of CIFS in general resonators

Next the rigorous evaluation and the physical origin of contributions to CIFS leading to shifts of either sign are considered. Then, CIFS is demonstrated in traveling and standing-wave resonators, including characteristic field patterns associated with positive and negative shifts.

Resonant modes of an isolated dielectric electromagnetic cavity [Fig. 4.3(a)], or those of the compound resonator [Fig. 4.3(c),(d)], may be computed numerically using a complex-frequency mode solver (Appendix D, [91]). Since the supermode pole distribution of a compound resonator is the result of two effects – frequency splitting and (pair-wise) mean frequency shifting (CIFS) – it is more desirable to set up the computation problem so as to separate these two effects. We partition the complete multi-cavity filter geometry into sub-structures [Fig. 4.3(b)], each selecting one resonance in the spectrum of interest associated with a cavity mode. This approach enables a series of numerical mode simulations to yield isolated CIFS and coupling parameters for each cavity.

A complex-frequency eigenmode solution [91] provides the resonance frequencies and corresponding quality factors, Q's, of the simulated (sub)structure's resonant modes. In each partitioned sub-structure, supermode splitting due to buildup of energy in a second resonance is eliminated, since only one resonance in the frequency range of interest is present. In this way the effect of CIFS on each cavity may be evaluated. One may further separate CIFS contributions due to each of the interacting objects by individual simulations. Each perturbation is small and physically isolated so the total shift is, to a good approximation, the sum of the individual isolated contributions. The Q's, on the other hand, encompass not only radiation and absorption losses, but also power coupled out of the resonator via waveguides. By properly taking guided-mode overlap integrals at access waveguide ports with the complex resonant-mode field, the total Q may be decomposed into an external coupling Q and a loss Q.

In Fig. 4.4, the CIFS due to adjacent bus waveguides is evaluated by eigenmode computation for a ring resonator identical to those in Fig. 4.2. Two symmetrically

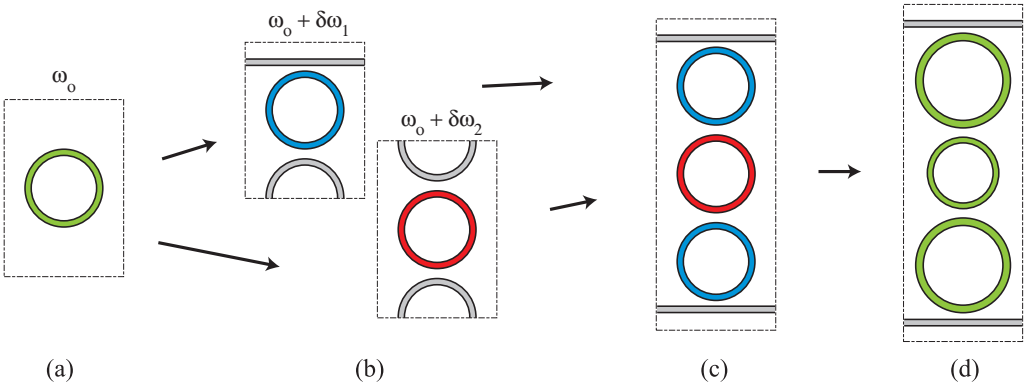

Figure 4.3: Diagram of CIFS resonance mismatch and its correction: isolated resonator (a) attains CIFS when part of a coupled structure (b); the combination of nominally degenerate resonators in a coupled-cavity filter (c) results in effectively mismatched resonators and a distorted response (Fig. 4.2), which can be (d) corrected by pre-distorting the resonators by the expected CIFS.

coupled bus waveguides are more efficiently simulated by exploiting the horizontal and vertical axis symmetry. Each waveguide contributes half of the total CIFS, found as the difference between the computed resonant frequency of the coupled, and that of the uncoupled resonator. The CIFS is plotted (in free-space wavelength units) against ring-waveguide gap spacing, and for two bus waveguide widths and polarizations for a resonance nearest 1580 nm. As expected, the magnitude of the frequency shift decreases for increasing gap width with an exponential envelope, due to the exponential tails of the interacting evanescent fields.

The sign of the frequency shift requires more attention. A small positive refractive index perturbation is typically expected to cause a negative frequency shift. The three simulated cases in Fig. 4.4 were chosen, however, to point out that the CIFS may be negative or positive, depending on geometry (here the bus waveguide width) and even on the polarization. The CIFS sign depends on contributions from effects beyond first-order index perturbation, including non-orthogonal cross-energy between the resonant mode and confined modes in nearby structures, and resonant-mode shape modification by the adjacent structures. Next, these points are briefly addressed.

The framework of coupling of modes in time (CMT), introduced phenomenologically in Eq. (4.1), is instructive for obtaining insight into the physical contributions to the net CIFS of a cavity mode in the coupled configuration. CMT can provide a rigorous treatment [78] of the interaction of a collection of modes in a coupled dielectric resonator structure of arbitrary geometry. Evolution of the mode amplitudes $\vec{a}(t)$, in a suitably formulated CMT (Section 4.1.10), may be described by a variation of the coupled-mode equations of the form of Eq. (4.1):

$$\frac{d}{dt}\vec{a} = j\overline{\overline{\omega}}\cdot\vec{a} - j\overline{\overline{\mathbf{W}}}^{-1}\cdot\overline{\overline{\mathbf{M}}}\cdot\vec{a} = j\overline{\overline{\omega}}\cdot\vec{a} - j\overline{\overline{\mu}}\cdot\vec{a} \tag{4.3}$$

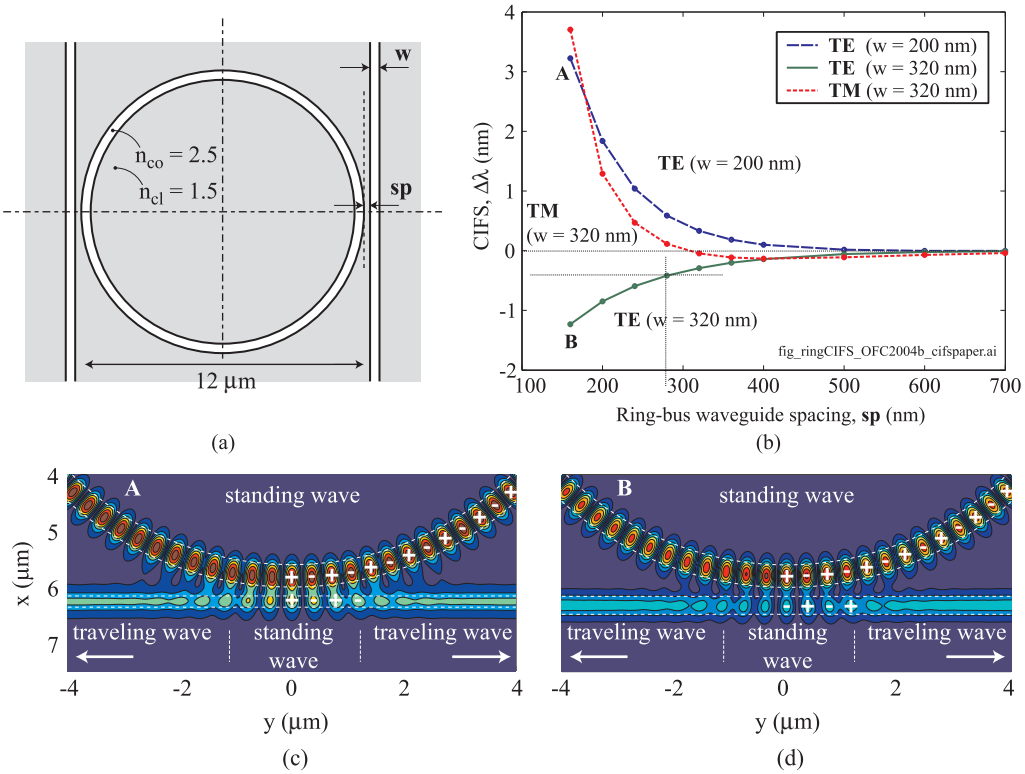

Figure 4.4: CIFS in a single-ring cavity due to side-coupled bus waveguides: (a) mode-solver-simulated structure; (b) CIFS for TE,TM resonances and for two bus widths, vs. gap spacing. Phasor-amplitude plots (c),(d) of the standing-wave-mode resonant field show a partial standing wave in the coupling region and, respectively, a symmetric-like and antisymmetric-like supermode formed with the waveguide continuum corresponding to negative- and positive-frequency CIFS.

In addition to the uncoupled resonant-frequency diagonal matrix $\overline{\overline{\omega}}$, $\overline{\overline{\mathbf{W}}}$ is the energy non-orthogonality (basis mode overlap) matrix, and $\overline{\overline{\mathbf{M}}}$ is a customary coupling overlap matrix that describes the interaction. Matrices $\overline{\overline{\mathbf{W}}}$ and $\overline{\overline{\mathbf{M}}}$ depend on the particular formulation of CMT as reduced from Maxwell's equations (c.f. [78]; another is described in Section 4.1.10). Regardless of the particular formulation of the CMT, the matrix $\overline{\overline{\mu}}$ represents a total effective coupling matrix with respect to mode amplitudes taking energy non-orthogonality into account. For example, in the case of two coupled resonators as in Fig. 4.1, the CIFS for the resonator associated with amplitude a_1 of two total modes is, according to Eq. (4.3) (Fig. 4.3):

$$\delta\omega_1 = -\mu_{11} = -\frac{M_{11} - \frac{W_{12}}{W_{22}} M_{21}}{W_{11} - \frac{W_{12}}{W_{22}} W_{21}} \tag{4.4}$$

In the absence of coupling, such as when the resonators are spaced sufficiently far apart, $\delta\omega_1 = 0$ and the resonators oscillate at their uncoupled natural frequencies in $\overline{\overline{\omega}}$. With coupling present, the CIFS is generally non-zero. We briefly consider the physical interpretation of (4.4). For a basis of orthogonal modes (e.g. a lone

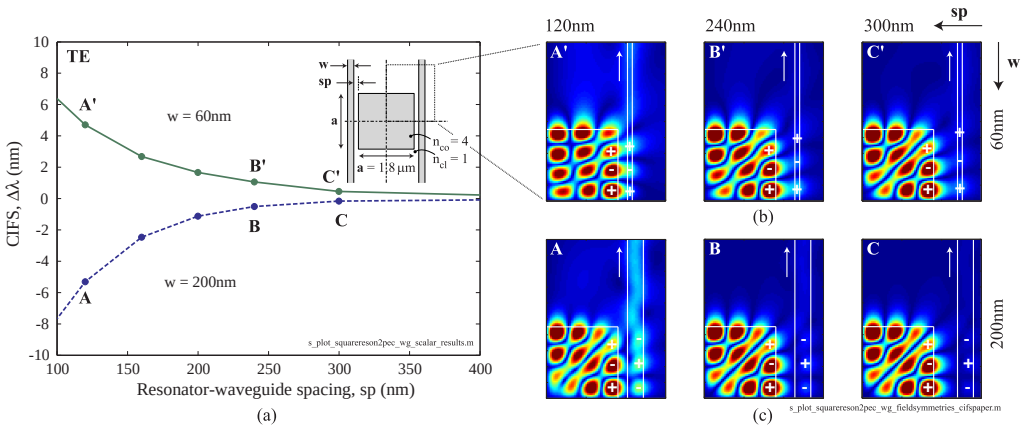

Figure 4.5: CIFS due to coupled bus waveguides in a square standing-wave cavity: (a) CIFS vs. gap spacing and waveguide width, and mode-solver simulated structure. Mode phasor magnitude plots show (b) symmetric and (c) anti-symmetric coupling, respectively, with a partial standing wave established in the waveguide, for negative- and positive-frequency CIFS. Case (b) shows significant mode shape modification caused by coupling.

resonator perturbed by a nearby dielectric object with no relevant modes of its own) $W_{12} = W_{21} = 0$, and from (4.4) the frequency shift is negative since M_{ii}/W_{ii} is positive definite in the lossless case. This is an intuitive result if one considers the wave equation, or its stationary integral for frequency (lossless case) [92]:

$$\omega^2 = \frac{\int_V \vec{E}^\dagger \cdot \nabla \times \overline{\overline{\mu}}^{-1} \cdot \nabla \times \vec{E} dv}{\int_V \vec{E}^\dagger \cdot \overline{\overline{\varepsilon}} \cdot \vec{E} dv} \tag{4.5}$$

If a positive refractive index perturbation is introduced to the isolated cavity configuration in (4.5), the frequency must decrease. In the case of adjacent evanescently-coupled resonators, the basis of uncoupled modes that are subjected to coupling is normally not orthogonal. A second, positive CIFS contribution then arises due to the cross-energy of the modes. Since cross-coupling M_{21} (source of power exchange) is a large term relative to self-coupling M_{11}, the net CIFS could be found positive. This initially unintuitive result is more easily understood in the spatial-propagation picture in Sec. 4.1.4, specific to traveling-wave resonators.

One final comment with respect to the CMT treatment is in order. In a rigorously derived CMT, meaningful estimates of the first-order coupling (supermode splitting) can be obtained from overlap integrals, with the error converging to zero with weaker coupling as expected. However, the diagonal elements representing CIFS are second-order coupling effects, and are not accurately predicted by CMT formulations, including [78, 93]. An error in the uncoupled field basis representation of the supermode field solution also translates to a second-order contribution to the CIFS, similar to the analogue in the spatial picture of directional couplers [93]. Such an error will always be present in practice, when a finite basis of modes is selected. Therefore, the relative error in the CIFS estimate by CMT does not con-

verge to zero with weaker coupling and can in general be $\mathcal{O}(1)$. This is the case because CMT is fundamentally a first-order theory. So, while valuable physical insight may be gained, CMT does not generally provide an accurate estimate of the CIFS. For design purposes, an accurate determination is obtained by using a resonator mode solver (as done in this section for the structure in Fig. 4.2) or by the FDTD method.

The general resonance treatment in time (by CMT or exact frequency eigenmode methods) is useful because it applies to all types of resonators, including standing wave resonators such as dielectric box-type resonators [55] and side-coupled, quarter-wave shifted waveguide grating resonators [42], photonic crystal cavities [53, 84], annular Bragg resonators [94], etc. For example, CIFS vs. gap width for a square resonator is shown in Fig. 4.5(a), computed by the frequency mode solver. A 2D model structure with 4:1 index contrast and 1.8 μm edge dimension supports a high-Q mode with diagonal field nulls [55] at 1559.6 nm, with a radiation Q of 203,000. Choices of bus waveguide width produce a positive or negative CIFS.

Finally, an interesting observation may be made with respect to the symmetry of characteristic field patterns for resonator interaction with the bus waveguide. It is generally appreciated that coupling of two degenerate resonators splits modes such that the symmetric supermode is of lower resonant frequency and the anti-symmetric is higher. In the case of resonator-waveguide coupling only one resonant mode is present, but it may be observed that the symmetry of the interaction of the resonator mode with a partial standing wave established over a portion of the waveguide still determines the character of the resonance frequency modification and thus the sign of the CIFS. In Figs. 4.5(b) and 4.5(c) the field phasor amplitude is plotted over a quarter of the simulated structure for two different waveguide widths. A traveling-wave (uniform-intensity) pattern is seen in the waveguide away from the interaction region, signifying leaking power associated with Q-broadening, but a more standing-wave-like pattern is seen in the immediate coupling region. In Fig. 4.5(b), the anti-symmetric standing wave pattern in the coupling region corresponds to a positive-frequency (negative-wavelength) CIFS, while in Fig. 4.5(c) the symmetric interaction pattern corresponds to a negative-frequency CIFS. This behavior is present also in the ring resonator [Fig. 4.4(c),(d)].

4.1.4 CIFS in traveling-wave-resonator structures

In this section, CIFS is treated in traveling-wave resonators, such as microring resonators; the frequency shift is related to phase perturbations in couplers; a coupler model and the constraints imposed by power conservation are investigated; and a coupling-of-modes in space look at CIFS is taken.

Traveling-wave resonators are particularly useful because they support high Q's and permit unidirectional coupling to waveguide modes. They couple to access

waveguides or other resonators via directional coupler regions. The coupling may be evaluated by considering each coupling region as a multi-port within particular reference planes [1–4 in Fig. 4.6(a)]. Reflection in these interaction regions can be neglected, so that the responses of filters using ring resonators can be obtained by a transfer matrix analysis considering only unidirectional forward wave scattering [71, 86].

CIFS may be attributed to a phase shift in propagation [from port 4 to port 3 in Fig. 4.6(a)] due to interaction in the directional coupler regions. A round-trip net phase shift of 2π (a full wavelength) would shift the resonance by one full FSR, so the CIFS is related to the phase as,

$$\frac{\Delta f_{\mathrm{CIFS}}}{\Delta f_{\mathrm{FSR}}} \approx \frac{\Delta f_{\mathrm{CIFS}} n_g L}{c} \approx -\frac{\Delta\phi}{2\pi} \tag{4.6}$$

where L is the round-trip cavity length and n_g is the group index of the traveling-wave mode. The phase perturbation $\Delta\phi$ is explicitly manifest in the transmission of T-matrix, $\overline{\overline{\mathbf{U}}}$, of a lumped, point-interaction description of the coupler in Fig. 4.6(a) (note that $\overline{\overline{\mathbf{U}}}$ is an off-diagonal 2×2 submatrix of the total 4-port scattering matrix, since reflection and backward transmission are neglected). In general, the interaction is distributed over an extended length of propagation where the fields in the traveling wave cavity and nearby coupled structure are "within reach" of each other's evanescent tails. The net effect on relevant modes may be evaluated with respect to reference planes [1–4 in Fig. 4.6(a)] that sufficiently enclose the interaction region. However, it is instructive to lump the distributed interaction into a point interaction with respect to a single reference plane, represented by a point T-matrix, $\overline{\overline{\mathbf{U}}}$. Then, propagation along the remainder of the structure in the interaction region is treated as that in the uncoupled structures. This partitioning, without loss of generality, simplifies analysis to that of isolated resonators, plus lumped point interactions. The lumped interaction matrix displays only the frequency dependence of the coupling interaction itself (and not of the propagation/dynamical phase), as seen in Fig. 4.6(b). In addition, loss due to propagation (e.g. in bent waveguides constituting the rings) and any excess loss caused by the interaction are separated. In the present simulations, the point T-matrix $\overline{\overline{\mathbf{U}}}$ is obtained by evaluating the T-matrix with respect to reference planes 1–4 of the coupled structure in Fig. 4.6(a), as well as that of the uncoupled ring and bus waveguides. The latter permit normalizing the uncoupled propagation phase and loss out of the former to obtain a point scattering S-matrix $\overline{\overline{\mathbf{U}}}$ [referenced to the red plane in Fig. 4.6(a)] which represents the perturbation due to interaction (refer to the model in Fig. 2.7).

Power conservation constraints on the point T-matrix of a lossless directional coupler permit sufficient latitude in degrees of freedom to support two independent coupling-induced phase offsets that correspond to the CIFS. A lossless coupler with two inputs, two outputs and no reflection to input ports may be represented by an

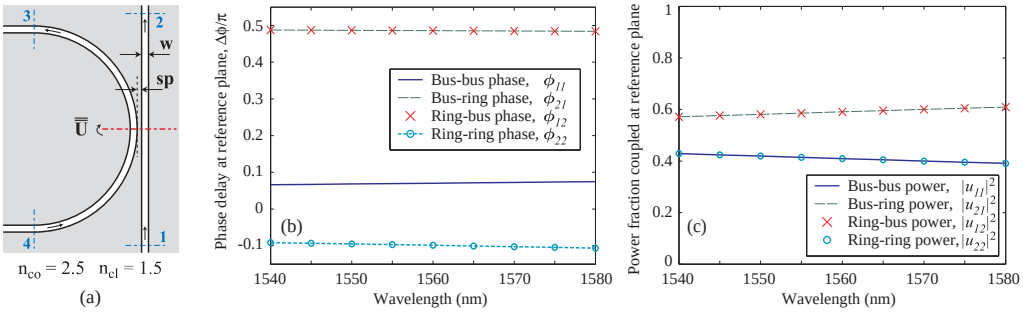

Figure 4.6: (a) Lumped point-interaction model of coupling of traveling-wave resonator and access waveguide. FDTD simulation of the coupled structure with respect to ports 1-4, and of the two waveguides individually, leads to lumped point-interaction matrix U, describing the effect of the coupling on port-to-port scattering matrix element (b) phase, and (c) power coupling.

arbitrary unitary 2×2 transfer matrix $\overline{\overline{\mathbf{U}}}$ with four degrees of freedom - a power coupling ratio κ, and three phases θ_o, θ_1, θ_2 (as described in Sec. 2.1.1):

$$\overline{\overline{\mathbf{U}}} \equiv \begin{bmatrix} u_{11}e^{i\phi_{11}} & u_{12}e^{i\phi_{12}} \\ u_{21}e^{i\phi_{21}} & u_{22}e^{i\phi_{22}} \end{bmatrix} = e^{i\theta_o} \begin{bmatrix} \sqrt{1-\kappa}e^{i\theta_1} & i\sqrt{\kappa}e^{i\theta_2} \\ i\sqrt{\kappa}e^{-i\theta_2} & \sqrt{1-\kappa}e^{-i\theta_1} \end{bmatrix} \tag{4.7}$$

where $\vec{b} = \overline{\overline{\mathbf{U}}} \cdot \vec{a}$, $\vec{b} \equiv [b_2, b_3]^T$, $\vec{a} \equiv [a_1, a_4]^T$ (Fig. 4.6(a)) and $\overline{\overline{\mathbf{U}}}$ is referenced to a single input-output reference plane. The unitary condition, $\overline{\overline{\mathbf{U}}}^{\dagger}\overline{\overline{\mathbf{U}}} = \bar{\bar{\mathbf{I}}}$, alone requires that the phases obey

$$\phi_{11} + \phi_{22} = \phi_{21} + \phi_{12} \pm \pi \tag{4.8}$$

which is explicitly satisfied by the second form in (4.7). In the absence of coupling, $\kappa \to 0$ and phases $\theta_{o,1,2} \to 0$, such that $\overline{\overline{\mathbf{U}}} \to \bar{\bar{\mathbf{I}}}$ (identity matrix) and uncoupled behavior is recovered. In the presence of coupling, κ represents power coupling and $\theta_o \pm \theta_1$ are two independent coupling-induced phase shifts (CIPhS) on either side due to interaction, which translate to resonance-frequency shifts in resonant elements. For a coupler that is symmetric about a (horizontal) axis separating the input and output ports [Fig. 4.6(a)], reciprocity combined with the geometric symmetry requires equal off-diagonal elements, i.e. $\theta_2 \to 0$, reducing the number of free parameters to three. But, the two diagonal coupling-induced phase shifts remain independently determined, permitting two different CIFS values for resonators on each side of the coupler.

Figs. 4.6(b),(c) show the FDTD computation of the elements of matrix for the ring and bus waveguide structures used in the filter example of Fig. 4.2. A narrower coupling gap of 100 nm is used in order to amplify and make clearly visible the phase shifts due to interaction. Fig. 4.6(c) shows power coupling (cross state ~60%) and its wavelength dependence due to change in mode confinement. The total output power sums to >99.9% for even smaller coupling gaps and supports this

discussion using the unitary matrix model. Fig. 4.2(b) shows the phase shifts, which by inspection can be seen to, and were verified to, obey condition (4.8). The cross-state phase shifts are equal and near 90° as expected. However, it is interesting to note that the bar-state phase shifts on the bus and ring sides are large and of opposite sign ("anomalous" and normal, respectively). This is a manifestation of the multiple contributions to the CIFS, discussed in the temporal resonance picture previously and briefly further discussed below. It implies that, for example, when coupling two resonators of different radii such as in a Vernier scheme (c.f. [38]), it is possible for the two to experience CIFS of opposite signs.

For the filter example of Fig. 4.2, using computed phase shifts for the appropriate coupling gaps, Eq. (4.6) and the cavity FSR, a CIFS of +21.75 GHz results due to each bus waveguide and a CIFS of +0.26 GHz due to each adjacent ring (note, CIFS here has the "anomalous" sign). A net mismatch results of +21.49 GHz in outer rings relative to the middle ring. These CIFS values were used in the filter model plotted in Fig. 4.2, and give a response that matches exactly the FDTD-simulated response of the complete filter, also plotted and overlapping. The "wiggles" in the wings of the FDTD-simulated drop spectrum below -30 dB are due to a slightly premature termination of the simulation. A step-function turn-off of the field leaving the drop-port while some energy remains in the computational domain causes small oscillations in the shown spectrum obtained by discrete Fourier transform (DFT) of the output field. Rigorous accounting for CIFS is thus necessary and sufficient to explain the anomalous spectrum obtained in Fig. 4.2.

Transfer-matrix-type analyses of lossless ring-resonator filter couplers (c.f. [69, 71, 86]) have generally employed the unitary scattering matrix of a two-port mirror (c.f. [67]), which is consistent also with first-order coupling-of-modes in space analysis of a directional coupler [67, p. 220]. These have one less degree of freedom than the model in eqn. (4.7) because the reference planes for input (incident) and output (reflected) waves of each port are generally coincident, unlike the 4-port reflectionless couplers considered here, where the planes may be arbitrarily chosen. Secondly, while the T-matrix phase variables may be removed by a particular choice of reference planes, in general such choices hold at a single frequency only [67], and do not provide the intuitive physical picture of the interaction obtained by collocating all four reference planes. By placing the interaction at a point and treating the remainder of the propagation as that in an uncoupled resonator, the perturbative nature of the interaction on the resonator is explicitly manifest in the forward scattering matrix $\overline{\overline{\mathbf{U}}}$ of the directional coupler, including CIFS. This is a practical approach for resonant filter design.

Coupling of modes in space picture

In view of the opposite sign of coupling-induced phase shifts on the ring and bus side of the coupler in Fig. 4.6, the physical sources of CIFS are briefly revisited in a

spatial picture. For traveling wave resonators, the CIFS may be simply understood by using a coupling of modes in space [67, 78] approach to consider the self-phase-shift accumulated in directional couplers. First, the propagation constant β_i of waveguide i is modified to $\overline{\beta_i} = \beta_i + \delta\beta_i$ by the diagonal term $\delta\beta_i$ of a coupling matrix analogous to $\overline{\overline{\mu}}$ in the temporal system of Eqns. (4.1) or (4.3), e.g.:

$$\delta\beta_1 = \frac{K_{11} - \frac{P_{12}}{P_{22}} K_{21}}{P_{11} - \frac{P_{12}}{P_{22}} P_{21}} \tag{4.9}$$

where $\delta\beta_1$ is given for mode 1 of two modes and may in general vary in value along the propagation direction, $\overline{\overline{\mathbf{K}}}$ is the coupling overlap matrix and $\overline{\overline{\mathbf{P}}}$ is the non-orthogonality matrix as in [78]. For perfectly synchronous couplers, this is the only coupling-induced phase contribution and the accumulated phase is the integral of $\delta\beta_i(z)$ along the propagation direction over the interaction region, with CIFS given by (4.6). In general, at least parts of a coupling region may be non-synchronous, and then additional phase is accumulated in each waveguide due to beating in the mismatched coupler. The total accumulated phase is obtained by considering the phase of the total integrated CMT solution [67] for bar-state propagation through a coupler. For a uniform coupler along the propagation direction, the total phase is

$$\Delta\theta_1 = \beta_1 z + \delta\beta_1 z + \left[\delta z - \arg\{\cos(\beta_o z) + j\frac{\delta}{\beta_o}\sin(\beta_o z)\}\right] \tag{4.10}$$

where $\delta \equiv (\overline{\beta}_2 - \overline{\beta}_1)/2$, $\beta_o \equiv \sqrt{\delta^2 + \overline{\kappa}^2}$ and $\overline{\kappa}^2 \equiv \overline{\kappa}_{21}\overline{\kappa}_{12}$. Non-orthogonal couplings $\overline{\kappa}_{21}$, $\overline{\kappa}_{12}$ are off-diagonal elements of $\overline{\overline{\mathbf{P}}}^{-1} \cdot \overline{\overline{\mathbf{K}}}$. In gradual couplers where synchronism, propagation constant and coupling vary with length along the propagation direction, the terms in (4.10) contain integrals with respect to distance. The three phase terms on the right-hand side of (4.10) are due to the uncoupled β, the coupling-induced β shift, and the non-synchronous slip phase. The latter two terms result from coupling and contribute a CIFS according to (4.6). The third term may be significant when asynchronous (asymmetric or bent) and interferometric couplers are employed. For synchronous ($\delta = 0$), strongly asynchronous ($|\delta| \gg |\overline{\kappa}|$), or optically short ($|\overline{\kappa}|z \ll 1$) couplers, no significant amount of power is coupled over and back with phase slip, and the second term in (4.10) is the dominant contribution.

Even without phase slip due to asynchronous coupling, this picture confirms that the CIFS can be of either sign. K_{11} is the usual positive effective index (negative CIFS) contribution due to the presence of the high index adjacent bus waveguide or resonator. The second term in (4.9) that gives a positive CIFS contribution can be understood by considering two weakly guided TE coupled slabs of half the width necessary to cut off the second guided mode. At zero wall-to-wall spacing (strong coupling regime), the two guides merge and the antisymmetric mode becomes cut off, while the symmetric mode morphs into the fundamental guided mode. In

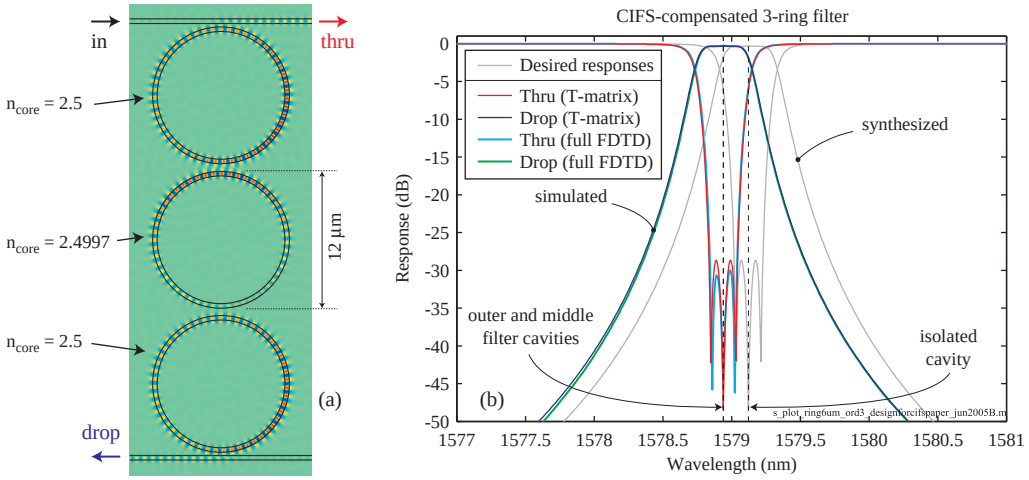

Figure 4.7: FDTD simulation of 3-cavity microring filter, with cavity resonance frequencies precompensated by design for CIFS: (a) simulated structure with lower-core-index middle ring; (b) FDTD simulation and model of the filter showing recovered ideal frequency responses.

approaching this situation, clearly the antisymmetric mode's effective index drops much faster than that of the symmetric mode rises. This example clarifies the negative contribution to the average effective index of the two supermodes, seen in Figs. 4.4 and 4.6, which for synchronous coupled waveguides corresponds to a $\delta\beta < 0$ in (4.9), or a CIFS > 0.

4.1.5 Compensation of CIFS in design

The frequency mismatch due to CIFS, observed in the filter in Fig. 4.2, can be compensated by pre-distorting the resonance frequencies of the isolated cavities in design, in anticipation of CIFS shifts. This may constitute slight cavity geometry or index modifications. In general, the pre-distorted cavity design will, in the coupled configuration, have a slightly different CIFS than the original, so that iteration would be needed to arrive at a self-consistent design. In practice, a single step is adequate. The cavity resonance frequency is sufficiently sensitive to dimensional or index changes that a small modification can produce a resonance shift equal to the CIFS without substantially affecting the mode shape, and thus the coupling and CIFS. In addition, the cavity may be modified only away from the interaction region.

Fig. 4.7 shows the simulation of a compensated filter. Recalling the example of Fig. 4.2, the outside rings had a CIFS of +21.75 GHz, and the middle ring +0.26 GHz. For the compensated filter, the core index of the middle ring was changed by -0.0003 to compensate for the net CIFS of -21.49 GHz in the middle ring by causing a frequency shift equal in magnitude, and opposite in sign (resonance shifts -7.11 GHz/0.0001 core index change). Index, rather than dimen-

sional, perturbation is used on account of the coarse discretization, but the results can be trusted as explained in Sec. 4.1.9. The simulated filter responses show the flat-top Chebyshev passband that was desired, with 30 dB in-band extinction (slight asymmetry shows ∼0.2 GHz residual mismatch). A transfer-matrix-method model, incorporating the individually modeled couplers and no net CIFS is overlaid confirming agreement. Coupler computations using FDTD and the modesolver (external Q) yield virtually identical results. The simulation confirms that CIFS was the only unaccounted impairment in the example filter of Fig. 4.2, and that its proper compensation enables the realization of the ideal filter response. In this example, only the net CIFS was compensated by modifying the middle ring, so the compensated filter center frequency remains slightly blue-shifted (Fig. 4.7(b)). This is sufficient because filters are generally desired to be tunable as a unit. Furthermore, in practice the center frequency is sensitive to variations and difficult to control. But in general, we may compensate all resonators to rigorously recover the exact desired response. Fabrication techniques allowing compensation of frequency shifts by pre-distortion are addressed in [90].

4.1.6 Higher-order CIFS effects

A second, higher-order CIFS-related effect in traveling-wave resonators deserves mention and may, at least in principle, impact performance. Traveling-wave resonators operate on the principle of two frequency-degenerate standing-wave resonances that are excited 90° out of phase to give unidirectional propagation. It has been shown that, based on this interpretation, traveling-wave-cavity-like filters can be mimicked by properly engineered pairs of standing-wave cavities [53, 54]. However, when a traveling-wave cavity is placed near a bus waveguide or a second cavity, the symmetry is broken and the two standing wave modes of the ring resonator may no longer be degenerate [91, 95]. CIFS for the even and odd standing-wave mode with respect to the coupling symmetry axis are in general different and will cause the splitting. A simple picture is given by the CMT-in-time treatment: the index perturbation of a bus waveguide has large overlap with the single field lump of the even mode, but smaller overlap with the odd mode which has a field null at the point of closest proximity of the coupled structures. Because the standing-wave modes are non-degenerate, the traveling-waves are no longer resonant eigenmodes of the system. From the traveling wave viewpoint, the directional coupler is a periodically phase-matched scatterer into the backward propagation direction, thus building up the reverse resonance and splitting the supermodes. In practice, this splitting is small as it is a difference of the CIFS for the two similar standing-wave modes. However, sidewall-roughness-induced contra-directional coupling has been predicted to lead to deleterious resonance splitting [96]. CIFS splitting due to couplers is much smaller than the CIFS itself and the filter bandwidth, but it may impact one's ability to reach high extinction

levels in higher-order filters. CIFS splitting will be greatest in high-index-contrast cavities with tight bend radii (e.g. in silicon waveguides), where the difference of overlap integrals can be more pronounced. A solution here is to make a longer, weaker directional coupler that covers several propagation wavelengths of the ring mode, thus making the overlaps more similar and the difference smaller; or, to distort the resonator shape, e.g. a ring into a slightly ellipse-shaped resonator, to compensate for the splitting of the standing-wave modes.

4.1.7 CIFS scaling laws and CIFS-free resonator configurations

Detuning of a cavity resonance impairs the response of a multi-cavity filter if the detuning is of the order of the filter bandwidth. Thus, a CIFS-to-bandwidth ratio (CBR) best expresses scaling of the CIFS impairment with bandwidth and FSR, coupling geometry, index contrast, filter order. Through-port notch responses are particularly sensitive to variations [Fig. 4.2(b)], because they rely on precise suppression of the poles by zeros over the stopband. Using simple filter models [38], we find that a CBR must be well under 1/10 to avoid impairing high-extinction through-ports, independent of filter order $N > 1$.

For a fixed coupling geometry (gaps adjustable to vary bandwidth, but cavity/waveguide shapes fixed within coupling region), the CBR due to cavity-bus coupling is *independent* of bandwidth and FSR (globally scaled for all cavities). For cavity-cavity coupling it scales as

$$CBR_{cavity-cavity} \sim \left.\frac{BW}{FSR}\right|_{\text{fixedcouplinggeometry}} = \frac{1}{finesse} \tag{4.11}$$

We infer this using overlap integrals (4.14),(4.15) (or E-field overlaps in [78]) and the CMT model (4.3), and assuming evanescently coupled generic cavities. We retain only the basic index perturbation term M_{11}/W_{11} in μ_{11} from Eq. (4.4), disregarding the other terms as they are of same order. These contributions may cancel to make μ_{11} smaller or zero in magnitude (Fig. 4.4(b)), but the first term gives a reasonable scaling for extremal values.

To relate the coupling coefficients to bandwidth scaling, we note that the bandwidth of a high-order filter is determined by resonance splitting $\sim \mu_{i,j}$ from Eq. (4.2), and by line broadening $\mu_i^2 = \omega_o/Q_i$. Both are of the order of the bandwidth, so in flat-top bandpass filters the desired cavity-cavity coupling is second-order in cavity-bus coupling, $\mu_{i,j} \sim \mu_i^2$. For traveling-wave cavities, the FSRs are related as $\mu_i^2 = \kappa_i^2 FSR_1$, $\mu_{i,j}^2 = \kappa_{i,j}^2 FSR_i FSR_j$ for cavity-bus and cavity-cavity couplings [38][‡].

[‡]Note that in the translation of temporal coupling coefficients to spatial power coupling fractions, the "FSR" used in the conversion is its local approximation at the center frequency, $FSR \equiv c/(n_{\text{group}} L_{\text{roundtrip}})$, *not* the true FSR, if they are don't coincide. This is because the conversion actually entails the local group velocity [38].

Referring to an example cavity pair in Fig. 4.1, the self-coupling overlap integral that determines CIFS, M_{11}, depends on the overlap of the evanescent tail of cavity 1 field squared over the second cavity's core. Cavity-cavity coupling M_{21}, on the other hand, is first-order in the evanescent tail of the first cavity. Thus $M_{11} \sim M_{21}^2$ as gap is varied. This leads to the dependence (4.11). A similar consideration, and the different scaling of bandwidth with μ_i leads to the different conclusion for cavity-bus coupling. More generally, the CIFS for a cavity scales inversely with the FSR of adjacent cavities, but does not scale with FSR changes of the cavity itself (for constant bandwidth and coupling geometry).

The coupling geometry may also be varied for a fixed bandwidth and FSR. We assume synchronous couplers. For a fixed total coupling, the CIFS (and CBR) for a cavity scales as $1/L_{\text{eff}}$, the effective coupling length to either a cavity or bus waveguide,

$$CBR \sim \frac{\phi_{11}}{\kappa} = \frac{1}{L_{\text{eff}}} \sim \sqrt{\frac{\alpha}{R_{\text{eff}}}}\Bigg|_{\text{fixedBW,FSR}} \tag{4.12}$$

This also results from (4.15), where $M_{11} \sim M_{21}^2$ as gap is varied, while both M_{11}, M_{21} are linear in interaction length (area). For straight parallel directional couplers, L_{eff} is the length. For curved couplers (such as ring-bus waveguide couplers), the diverging coupler's curvature may be represented as a single effective radius $1/R_{\text{eff}} = 1/R_1 + 1/R_2$ [38]. Then, the effective length goes as $\sqrt{R_{\text{eff}}/\alpha}$, where α is the evanescent decay rate. Hence, a short, strong coupling region gives a larger CIFS than a long, weak one providing the same coupling. This compares a ring and a racetrack resonator. Curved coupling regions will generally be nonsynchronous, so a more accurate comparison requires consideration of non-synchronous phase slip in Eq. (4.10).

Higher index contrast cavity designs generally employ shorter, stronger couplers. Thus, CIFS will generally be larger in HIC designs of an equivalent bandwidth and FSR. For example, a higher group index n_g in HIC means that a smaller microring radius is required for a given FSR ($FSR = c/2\pi R n_g$), leading to a shorter stronger coupler, and greater CBR.

In some filters, including series-coupled resonators, not all cavities may need to be compensated. From the coupling coefficient relationship $\mu_{i,j} \sim \mu_i^2$ for flat-top filters, we may conclude that the cavities that are coupled to access waveguides contribute a greater CIFS than "interior" cavities coupled only to other adjacent cavities. From (4.11), this will be particularly true in high-finesse filters. To first order, compensating only the outermost rings may thus be sufficient. In the given example (Fig. 4.7), only the central ring was compensated instead.

Simple cavity design pre-distortion may not be sufficient in device designs where the resonant frequencies must remain unchanged over a range of dynamically variable coupling gap configurations, such as with MEMS-actuated switching of ring filters [97]. In these cases, a CIFS-free resonator design is desirable. Ob-

serving Fig. 4.4(b) or Fig. 4.5(a), it is evident that there exists a bus waveguide width where the CIFS is flattened to first order to near zero for all coupling gaps. Such designs may be of value where the cavity is not tunable.

4.1.8 Conclusions

Coupling-induced resonance frequency shifts were shown to arise in dielectric cavities, and to lead to severe impairment of multi-cavity filter responses in the absence of proper compensation in design. While series-coupled microring filters were used as an example, CIFS is present in other cavity types and multipole-filter geometries. CIFS is second order in coupling as gap spacing is varied, and is greater in short, strong coupling regions. The CIFS-to-bandwidth ratio is independent of bandwidth and FSR due to cavity-bus waveguide coupling, and scales as $1/finesse$ due to cavity-cavity coupling. Theory and rigorous simulations show that CIFS can be positive or negative depending on the dominant of a number of contributing factors including index perturbation, mode non-orthogonality and mode field distortion. Standing- and traveling-wave pictures of the CIFS were considered. A perturbative lossless directional coupler model contains all necessary, and just enough, degrees of freedom to describe CIFS in traveling-wave cavities. A typical microring-resonator filter without CIFS compensation had a severely distorted simulated response. With CIFS compensation, the ideal synthesized response was recovered and verified by simulation. Therefore, CIFS must be rigorously taken into account in filter design, in cases where the resonator frequencies cannot be individually tuned post-fabrication. CIFS-free resonators may be engineered to enable applications such as MEMS-actuated coupling strength control via gap change, without shifting the resonance.

4.1.9 Simulation methods and case study details

Details of the simulated examples are given here to enable one to reproduce the results, and to justify the prediction of small frequency shifts by coarsely-discretized simulations.

The ring resonator was designed to have a high-Q TE resonance in the C-band with an odd round-trip number of wavelengths. The former was desired to unambiguously ensure that any spectral distortion in all examples is due to CIFS only, because far-field interference due to radiation loss may also cause a skew in the response spectrum. The latter is important because the ring is not perfectly circular in the discretized computational domain. An odd resonance still has degenerate standing wave modes, thus supporting traveling wave operation as in an ideal ring; while an even resonance has slightly split standing-wave modes so that the grid discretization causes some backward wave coupling. The circular ring resonator has a 6 μm outer radius, and a waveguide width of 400 nm with a

core index of 2.5 and a cladding index of 1.5. The simple indices were chosen to permit the 2D model to approximately correspond to typical radii and FSRs (3.2 THz) seen in high-index-contrast SiN or Si filters [38, 88, 89].

Ring resonant modes and Q's, relevant to the discretized computational domain, were computed by the complex-frequency mode solver in Appendix D [91], solving the scalar wave equation (in the case of TE modes) on the 2D domain. Perfectly-matched-layer (PML) boundary conditions were used in the form of complex coordinate stretching, to absorb outgoing radiation and permit the computation of leaky (finite Q) resonances. The Q is ∼260k in the discretized domain (due to "grid roughness"), while the ideal ring structure has $Q \sim 10^9$ (found by numerical root-finding of a rigorous, Bessel-function 1D analytic model).

The directional coupler interaction regions (Fig. 4.6), and the complete filters (Figs. 4.2, 4.7) were simulated by 2D resonant mode solver and FDTD. Bus waveguides were also 400 nm wide, and the ring-bus and ring-ring coupling gaps were 280 nm and 660 nm, respectively.

The FDTD simulation of directional couplers involved three simulations: a simulation of the coupler, a simulation of the ring section alone, and a simulation of the bus section alone. The lumped point-coupler scattering parameters referenced to the single (red) reference plane are obtained from the scattering parameters referenced to planes on the walls of a box, of the three simulations above. Couplers were virtually lossless for all gaps, including contact (zero gap).

All simulations used discretization of $\Delta x = \Delta y = 20$ nm. The FDTD timestep was shorter than the CFL stability timestep by 1.1. The filter simulation was run for 1.5M timesteps for Fig. 4.2 (3M timesteps for Fig. 4.7). Wiggles in the response below -30 dB in Fig. 4.2 are due to premature termination in time of the simulation. Such large discretization cannot determine the absolute resonance frequencies with an error smaller than the CIFS. However, the relative frequencies, such as shifts caused by coupling (relevant to CIFS), are accurately defined. The resonators in the example of Figs. 4.2, 4.7 are made identical to remove discretization effects.

4.1.10 Vector-field coupled mode theory in time derivation

A number of derivations of the coupled-mode theory in time are possible, starting from Maxwell's equations, depending on the starting equation and choice of uncoupled basis modes. The approach in [78] gives the form (4.3) for degenerate cavities. In the general case, it does not explicitly show the perturbation and has a slightly more complicated form than Eqns. (4.3),(4.4). While the details are beyond the scope of this chapter, here outlined briefly is one general-case vector-field formulation consistent with (4.3),(4.4) for completeness. At the same time, a basis of H-fields of the uncoupled resonator modes is chosen. The E-fields may be derived from the curl equation of the total system. A choice of H-field basis set then ensures that Gauss' law is preserved in the supermode trial fields of the coupled

configuration. Starting from the vector-wave equation for the total H field,

$$\nabla \times \overline{\overline{\varepsilon}}^{-1} \cdot \nabla \times \vec{H} = \omega^2 \overline{\overline{\mu}} \cdot \vec{H} \tag{4.13}$$

the orthogonality condition is found from the adjoint operator. The total dielectric distribution (inverse) for each basis function n is written as the distribution $\overline{\overline{\varepsilon}}_n^{-1}$ for which the function is an eigenmode plus a perturbation: $\overline{\overline{\varepsilon}}^{-1} \equiv \overline{\overline{\varepsilon}}_n^{-1} + \overline{\overline{\Delta\varepsilon_n}}^{-1}$ in (4.13). The coupling matrix is projected out subsequently by applying the orthogonality condition to the equation. To make the matrices consistent with (4.3), the orthogonality matrix is pre- and post-multiplied by a diagonal frequency matrix:

$$W_{mn} \equiv \frac{\omega_n}{\omega_m} \iiint_{\widetilde{V}} \vec{H}_m^T \cdot \overline{\overline{\mu}} \cdot \vec{H}_n \, d\widetilde{v} \tag{4.14}$$

where both fields are unconjugated to allow for leaky modes. Accordingly the tilde indicates an integration domain extending into the complex physical-space plane. The coupling matrix is similarly,

$$M_{mn} \equiv \frac{\omega_n}{2} \iiint_{\widetilde{V}} \vec{D}_m^T \cdot \overline{\overline{\Delta\varepsilon_n}}^{-1} \cdot \vec{D}_n \, d\widetilde{v} \tag{4.15}$$

This formulation was shown to give results for ring-to-ring resonator coupling that are consistent with FDTD simulations, as published in [8].

Chapter 5

Global design rules for strong-confinement silicon waveguides and tunable resonators*

In this chapter, a systematic design study and global parameter optimization of silicon-core waveguides and resonators is presented. Novel designs of strongly confined silicon (Si) waveguides are described that are optimized for the realization of tolerant tunable microring-resonator filters and switchable interferometers in the strong-confinement regime. These designs differ considerably from the conventional 2:1-aspect-ratio cross-sections (e.g. 450×200 nm) typically used, with TE excitation, in sub-micron Si waveguides [99, Table 1 and 2].

Optimal designs of silicon-core waveguides with silica cladding are investigated, in terms of waveguide cross-section and the guided-mode polarization, with respect to an extensive set of practically relevant design criteria: sufficiently large lithographic feature sizes (e.g. coupling gaps); low sensitivity of resonance frequencies and waveguide-resonator couplings to dimensional variations; high Q and large FSR; small sensitivity to waveguide roughness that translates to propagation loss; efficient thermo-optic tuning and low optical absorption loss from proximate metallic microheaters; and low substrate leakage with typical undercladding thicknesses. With design criteria chosen to enable thermally tunable high-order microring resonator filters for telecom applications, the results indicate that dimensional sensitivity of the resonance frequency, and proximity of metallic heaters (causing optical absorption) ultimately determine the choice of design. The

*Work done in collaboration with T. Barwicz; aspects of this work are published in [98].

results give two very different optimal designs for the choice of TE or TM device operation (about 600×110 nm and 455×265 nm, respectively), for the particular design criteria selected here. In comparison, the Si waveguides typically employed for TE excitation (∼450×200 nm) are much more sensitive to lithographic dimensional error – with resonance frequency shifting by over 100 GHz with 1 nm waveguide width error – rendering high-order filters difficult to realize. More generally, the design plots provided are intended to map critical performance parameters in as compact and general a way as possible, and may be used for arriving at optimal designs for other choices of constraints.

The basic approach taken is to parametrize the design space by waveguide cross-section aspect ratio ($A_R \equiv w/h$, for width w and height h), and at each aspect ratio to consider the most strongly confined (largest cross-sectional area) waveguide having only one TE mode, and also that having only one TM (but allowing more than one TE) mode. The former is to be used with a TE excitation, the latter with a TM excitation. This limits the optimization to be over a manageable design space of two one-dimensional domains indexed by the aspect ratio. Such a rigorous study does not appear to have been previously reported for any type of optical waveguide.

In addition to the optimized waveguide designs, the study yields some interesting insights and general conclusions about strongly confined waveguides. First, it was found that there exist corresponding or *equivalent* TE and TM designs, in much of the range of aspect ratios of interest, that have virtually the same properties – FSR for a given minimum Q, sensitivity to width, height and sidewall and top/bottom-wall roughness, etc. These equivalent TE and TM designs are shown to exist when the TE waveguide is a maximally confined, single-TE mode guide while the TM waveguide is a maximally confined, single-TM mode guide (but has 2 TE modes). The equivalent TE and TM designs do not have the same aspect ratios. Discovery of this empirical equivalence is counter to conventional intuition that TM waveguide modes (in wide, flat guides) are less well confined and less suitable for strong confinement microphotonics applications. Secondly, it is noted that higher-order TE and TM modes are not degenerate in a square cross-section. This lack of mode crossing yields an interesting instance of a device capable of adiabatic apparent polarization rotation without symmetry breaking in the structure geometry. Third, ultra-*sensitive* waveguide designs are found that may be of use for sensing. Fourth, the Si microring-resonator cross-section with single-mode excitation is found that maximizes the FSR for a given Q (tall, narrow, TM). Fifth, an interesting symmetry is noted in the TE and TM bending losses even at small radii where no underlying physical symmetry enforces such equivalence.

In Section 5.3, the first experimental results of fabricated samples of the proposed TE silicon waveguide and resonator design are presented.

Before the systematic design study is presented, a brief summary of the choice

of silicon as the core material and of previous work with silicon and other strong-confinement waveguides is given.

Choosing silicon for tunable microphotonic filters

A number of mechanisms may be used for resonant wavelength tuning, including thermally induced index change [100–103], carrier-injection-induced index change (carrier plasma effect), quantum-confined Stark effect (QCSE) [104], the electrooptic effect [100, 103, 105] and microelectromechanical system (MEMS) based dielectric perturbations [31, 51, 106, 107].

The electrooptic effect and QCSE are fast, and are thus well suited to modulator applications, but provide relatively small index changes for practical applied voltages. For telecom tunable filter applications, considered here, wide tuning range is required (10's of nm, to cover the C band), while speed is non-essential with microsecond timescales more than sufficient to perform required operations. For such applications, requiring large index changes, thermooptic, carrier injection, or MEMS-actuated dielectric perturbation are best suited. Carrier injection (as well as QCSE) has an absorption that accompanies the index perturbation, while MEMS requires complex multilayer fabrication. Hence, we have chosen for the demonstration of tunable telecom grade filters to use thermooptic tuning, commonly used in industry in silica integrated optics [9].

The thermooptic coefficient of silica ($dn/dT = 1.5 \cdot 10^{-5}$/K) and even that of Si-rich SiN ($2 - 4 \cdot 10^{-5}$/K) is too small to permit thermooptic tuning of several THz (10's of nm) with practical on-chip temperatures up to the order of 500–1000°C, limited by the current and power handling capabilities of on-chip microheaters. Therefore, the SiN strong-confinement platform, used to demonstrate HIC add-drop filters in Appendix E and Sec. 7.1, is not well suited to photonic devices that rely on large thermooptic index (resonant-wavelength) tuning.

Materials with a high thermooptic coefficient (on the order of 10^{-4}/K) include semiconductors such as silicon and InP, and polymers. Silicon was chosen in this work because of well-developed fabrication technology, and because it readily forms strongly-confined waveguides when using silicon-on-insulator (SOI) wafers that can provide a high index contrast on all sides of the Si waveguide core, by virtue of having a silica undercladding layer. In contrast, polymers [108, 109] generally have a low refractive index, so that a large index contrast is difficult to form, except with an air cladding which cannot be placed on all sides of the core. Undercutting the core has been demonstrated [110], but this approach leads to otherwise poor dimensional control not suitable for telecom-grade filters. On the other hand, most III–V group semiconductors (InP, GaAs) do not have readily available low-index undercladding materials of substantial thickness (2–3 μm) needed for low-loss and strong confinement.

Therefore, to add wide tuning and switching capability to strong-confinement microphotonic filters, we move from Si-rich SiN to Si. The primary reason for this change is only the thermooptic tunability. The index contrast with a silica cladding is large enough in both SiN and Si to support telecom-grade photonic circuits such as filters with FSRs of 10's of nm. Moreover, the much larger index contrast of Si introduces additional apparent challenges in terms of extreme sensitivity to dimensional errors and waveguide wall roughness, and considerably larger nonlinear effects which are to be avoided in linear filtering applications for optical networks.

Previous work on Si and other strongly confined waveguides

High-index-contrast microring resonators, based on silicon- and SiN-core waveguides have typically employed a single polarization and relied on square [111] or wide-and-flat guides [17, 99, 112–114] of up to about 2:1 aspect ratio, likely in part due to available thicknesses of core layers in SOI and SiN of ∼200–300 nm[†]. In particular, silicon waveguide work has almost invariably relied on waveguide cross-sections of approximate dimensions 450×200 nm as reviewed in [99, Tables 1 and 2]. A few exceptions include square [111] and thinner waveguides [116] in Si microring resonators, as well as very wide multimode waveguides for low propagation loss [117, 118]. However, a systematic consideration of the optimal Si waveguide design, taking into account sensitivity, loss, etc., has been lacking.

Silicon-rich SiN has also been used, due to its high refractive index, to demonstrate wide-FSR, high-order microring filters in Appendix E and Sec. 7.1 [88, 89, 119] and can be obtained in layers as thick as 800 nm or more. In this case, thickness is not a limitation and air-clad, Si-rich nitride (index 2.2:1) guides of ∼2:1 aspect ratio were introduced in high-order microring-resonator filters in order to prevent polarization crosstalk and to reduce resonance frequency sensitivity to guide width [88, 89, 119]. Those designs took some initial steps toward the global optimization study presented here in the context of silicon waveguides.

5.1 General approach

The study consists of two steps: first, establishing a set of all possible silicon waveguide cross-sections to be considered; and second, evaluating the merit of these cross-sections in the context of a number of application-related criteria, including support for small bend radii and a wide cavity FSR with high radiation Q, low resonance frequency and coupling sensitivity to dimensional errors, low sensitivity to waveguide wall roughness, compatibility with lithographic resolution limitations, efficient thermooptic tuning, low metallic-microheater-induced

[†]Stoichiometric SiN (Si_3N_4) is limited to layer thicknesses of about 300 nm due to internal stress that causes cracking when thicker films are deposited [115].

optical loss and low substrate leakage radiation loss with practical undercladding thicknesses. The optimum designs are chosen from the reduced set of waveguide designs remaining after all constraints are applied.

The analysis is carried out using the three-dimensional, cylindrical and Cartesian coordinate, vector-field mode solver developed in Appendix D. For the present study, the complex coordinate stretching used at the domain edges to absorb outgoing radiation was extended to the interior of the structure (with a real stretching coefficient) to permit a simple approach to nonuniform grids. A nonuniform grid is necessary for zero-finding and optimization routines executed on the mode solver to find waveguide dimensions at certain mode cutoffs, and approximate directional coupler gap sizes for given coupling ratios.

Based on the rigorous mode computations, a very large number of further results can be obtained directly from the computed mode field distribution by various overlap integrals, including the modal effective and group index (Sec. 3.2), sensitivities to dimensional perturbations, index perturbations (tunability) and loss sensitivity. This makes the design computations relatively inexpensive – only one mode instance for each cross-section is needed.

To make the analysis manageable, a few assumptions and simplifications are made. First, a planar geometry is assumed, with all waveguides and resonators coupling laterally in the same waveguide layer. Secondly, a rectangular, silicon-core, silica-cladded waveguide is considered, nominally with no other material layers. Refractive indices of 3.48 and 1.45, respectively, are used, which are representative of these materials at the 1550 nm wavelength. Except where necessary (such as for computing bending loss), straight rather than bent waveguides are used, in order to obtain results independent of microring bend radius. This approximation is accurate for most bend radii where the mode shape is not substantially altered by the bending.

For directional coupler analysis, simple coupled-mode theory approximations are made[‡]. Some error can be expected when using CMT with high index contrast waveguides, but these results give a good guideline for noting trends and tradeoffs. The final silicon device designs, described in later chapters, that are based on the waveguides described here make use of rigorous mode solver and 3D FDTD simulations to evaluate and optimize the design near the chosen design point.

The results of this search for an optimal Si waveguide cross-section across the global parameter space are summarized in Tables 5.2 and 5.3. In the following sections, the various parts of the study are explained. In plots showing the results of the design study, typically black plot lines are used for TE modes and gray lines

[‡]Rigorous 3D FDTD simulations are not used at this step because they are too computationally intensive to be done for all possible designs in reasonable time. And, they step away from the general philosophy taken of computing modes of the waveguide cross-sections and extracting as much relevant data as possible from this information using computationally cheap overlap integrals and approximations.

for TM modes. In addition, solid dots mark plot lines belonging to maximally-confined, single-TE-mode (MC-STE) waveguide designs and hollow dots are used for maximally confined, single-TM-mode (MC-STM) designs.

5.2 Global waveguide geometry design and optimization

Strong confinement, based on high index contrast, is the distinguishing property of all waveguide devices addressed in this thesis. Strong confinement is important because it permits small bending radii with negligible radiation loss, in turn enabling resonators with small cavity length and large FSR. As a result a resonant system can address a large wavelength spectrum. Up to an order of magnitude or so, the FSR can be multiplied up by various Vernier schemes [120, 121] and more complex geometries when the through-port response is of interest (see Chaps. 8 and 9), as is the case in large-bandwidth optical network applications. Since $\Delta f_{\mathrm{FSR}} = c/(n_{\mathrm{group}} L_{\mathrm{roundtrip}})$, a round-trip cavity length of about 100 µm leads to technologically relevant FSRs of the order of a terahertz or more (group indices typically being between 1.5 and 4). For a microring resonator, this means a radius of 15 µm or smaller.

Fig. 5.1 shows the minimum bending radius vs. index contrast for a 2D single-boundary bend (whispering gallery mode in a cylinder) which gives the lower bound on bending radiation loss. Contours for several values of loss are shown – only a factor of 2 in radius changes loss 1000-fold. The plot shows that microring resonators with radii of the order of 15 µm require an index contrast of the order of $\delta n/n \approx 0.5$, which leads to use of high-index-contrast waveguides such as SiN and Si.

Polarization

Throughout this chapter, results are presented on optimization of a waveguide to be used with a single designed polarization state and a single mode. Polarization-independent structures, necessary for most devices that communicate via standard optical fibers, may be obtained by making use of dual, preferably identical, structures within a polarization diversity scheme [31, 33].

Fields polarized in the plane of the chip are referred to here as TE polarized, and fields polarized normally to the plane of the chip are referred to as TM polarized. High-index-contrast dielectric waveguides in general support modes with hybrid polarization (which may have a major and minor transverse polarization field) and not necessarily pure TE and TM modes. However, the waveguides considered here usually support modes of interest that are TE-like or TM-like. In this chapter, the nomenclature is simplified to TE and TM to refer to these modes. The analysis is carried out on silicon waveguides with a rectangular core cross-section and a uniform dielectric silica cladding, but the general conclusions hold for a range

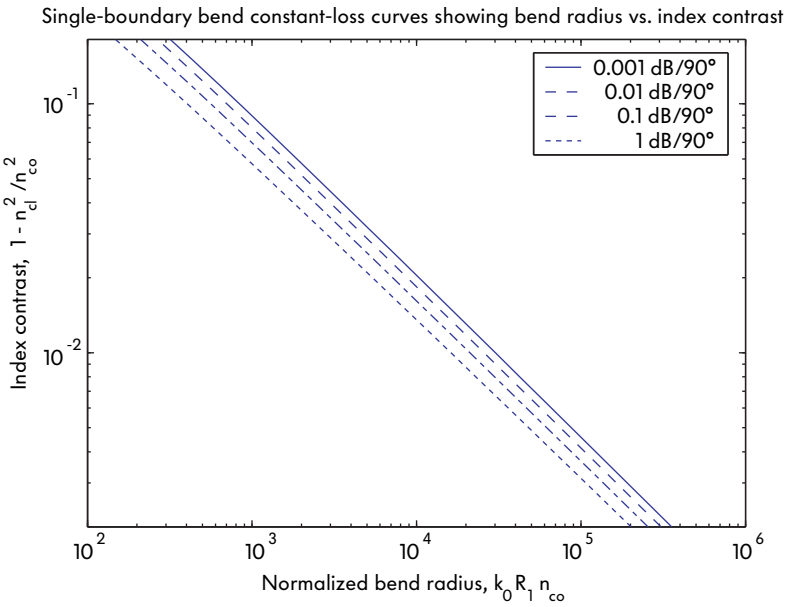

Figure 5.1: Normalized plot of bending-radiation-loss limited waveguide bend radius vs. index contrast, for the simplest model – a single interface bend in two dimensions, i.e. a slab cylinder (from [122, 123]). It shows that the critical bend radius is fairly strongly pinned to a particular value, and a factor of 2 change in radius changes the bending loss by three orders of magnitude.

of core and cladding indices of high index contrast, and other similar waveguide cross-sections.

More rigorously, the modes are classified as follows. In the examples presented, the waveguides have a symmetry about a horizontal reflection axis. In these cases, TE modes are defined as all modes having a PMC (perfect magnetic conductor) symmetry about a horizontal axis, i.e., having symmetric transverse electric and antisymmetric transverse magnetic fields; and TM modes as all modes having a PEC (perfect electric conductor) symmetry, i.e., having symmetric transverse magnetic and antisymmetric transverse electric fields[§]. This definition is not rigorously consistent with the naming convention "TE" and "TM", but it provides a physically consistent basis for labeling the fundamental and second-order mode of each polarization. The naming is consistent in wide-and-flat waveguides that turn out to be of primary interest. The labeling is also consistent with coupling being forbidden by symmetry between TE and TM modes of structures that are side-coupled in the plane of the chip (where the entire structure retains symmetry about a reflection plane that is horizontal - parallel to the chip surface). Throughout, reference is made to two waveguide designs, one design where the TE polarization is to be used, henceforth called the TE design; and one design where the TM polarization is to be used, henceforth called the TM design.

[§]Here, transverse means transverse to this symmetry plane, and the symmetric/antisymmetric property is relative to the direction normal to the symmetry plane.

5.2.1 Single-TE-mode and single-TM-mode silicon waveguides

The design space is chosen to be the set of all silicon-core, silica-cladded waveguides with rectangular cross-sections, of various width-to-height aspect ratios A_R, in two variants. The cross-section is symmetric about both a horizontal and vertical symmetry plane. The first variant are waveguides intended to operate in the fundamental TE mode. These waveguides have the largest possible area at each A_R that keeps the waveguide single-TE-mode (STE). They will be referred to as maximally confined, single-TE-mode (MC-STE) designs. The second variant are waveguides intended to operate in the fundamental TM mode, and must cut off the second TM mode. However, they may be allowed to support more than one TE mode, because we consider vertically symmetric waveguide structures, and lateral coupling between resonators and waveguides is nominally zero, as the TE and TM modes do not nominally interact (parasitic TE-TM coupling is investigated in Sec. 5.2.6). These designs are referred to as single-TM-mode (STM), and when the largest STM design is chosen for a given A_R they are referred to as maximally confined, single-TM-mode (MC-STM).

Map of Si waveguide cross-sections

Fig. 5.2 shows contours representing all Si waveguide MC-STE and MC-STM cross-sections, for aspect ratios $A_R = 1/30$ to $A_R = 30$, computed by a vector-field modesolver with an autogenerated non-uniform grid (see Appendix D), bootstrapped by a zero-finding algorithm. For example, all MC-STE designs have a rectangular cross-section with the lower left corner at the origin and the upper right corner on the MC-STE contour. All STE waveguides fit "under" this contour. Fig. 5.2(a) shows aspect ratio contours and also illustrates the two optimized TE and TM designs obtained for tunable 40 GHz-wide filters at the end of the analysis. The plot shows that wide TE waveguides become quite thin (sub-100 nm) to maintain STE operation, while wide TM waveguides remain STM even at ∼150 nm thickness.

Fig. 5.2(b) shows, at various points on the waveguide cross-section contours, the higher-order mode that is placed at cutoff for waveguide dimensions at the corresponding point on the contour. For wide, thin waveguides ($A_R > 1$), the second-order TE mode, TE_{21}, is at cutoff in the MC-STE design and the second-order TM mode, TM_{21}, is at cutoff in the MC-STM design. For tall, narrow waveguides ($A_R < 1$) the modes at cutoff are the 90° -rotated versions of those in the $A_R > 1$ case. Note that here our nomenclature is not strictly valid because the TE_{21} mode, for example, is primarily vertically (TM) polarized, but this mode is still the mode with PMC symmetry about a horizontal axis[¶].

[¶]For simplicity we continue to refer to them as TE and TM, rather than something more cryptic and more accurate like PMC-horizontal and PEC-horizontal.

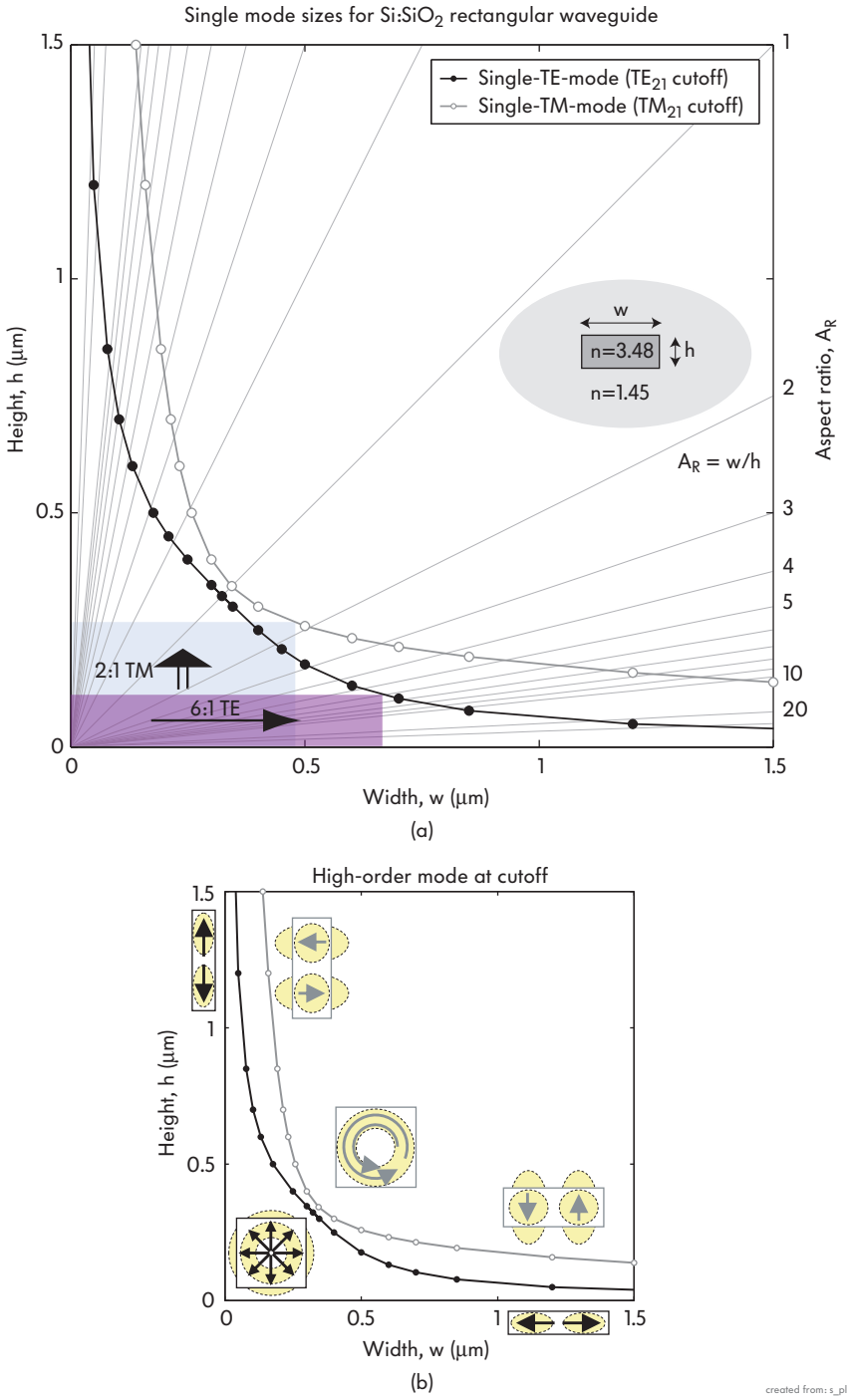

Figure 5.2: Map of maximally-confined single-TE and single-TM mode silicon waveguide cross-sections at each cross-sectional aspect ratio, A_R. (a) The contours show the top right corner of the waveguide cross-section when the bottom left corner is at the origin. In the TE designs, the contour indicates the cutoff condition for the second TE mode, TE_{21}. In the TM designs, the contour indicates the TM_{21} cutoff. The latter waveguide has 1 TM mode and 2 TE modes. (b) The dominant field distribution is illustrated in each waveguide to indicate what is referred to here as the TE_{21} mode and TM_{21} mode (published in [98]).

The reason why the nomenclature is kept is that at $A_R = 1$, where both the TE and TM designs are square, the fundamental modes are degenerate (TE_{11} for MC-STE design and TM_{11} for MC-STM design, as shown in the plot of effective indices in Fig. 5.5) but the second-order TE_{21} and TM_{21} modes, respectively in the TE and TM design, are *not* degenerate. Therefore, there is continuity of a single higher-order mode at cutoff along each of the two waveguide dimension contours, so the mode label must remain the same over all A_R values.

This lack of degeneracy occurs because, as illustrated in Fig. 5.2(b), the TE_{21} mode becomes a radially polarized mode (corresponding to the pure TM_{01} mode in a fiber), while the TM_{21} mode becomes azimuthally polarized (corresponding to the TE_{01} mode in a fiber). A simple numerical experiment of TE_{21} and TM_{21} effective index vs. waveguide width for $A_R = 1$ (square cross-sections), shown in Fig. 5.3, shows that the two modes reach a degeneracy well above the cutoff effective index, with different slopes, and therefore are cut off at different core sizes. An interesting aspect of this non-degeneracy is a conceptual possibility of adiabatic mode evolution from the wide second-order mode to the tall second-order mode by slowly varying the cross-section from $A_R \ll 1$ to $A_R \gg 1$ along the length of the waveguide, in a symmetric way so that the waveguide center is fixed. In particular, the evolution can be the set of MC-STM cross-sections along its dimension contour – which has a guided TE_{21} mode but a cut-off TM_{21} mode. Adiabatic mode evolution can occur because there are no mode crossings with modes that have non-zero coupling by symmetry with the second-order mode of interest (n_{eff} of TE_{21} crosses TM_{11} at $A_R \approx 3$ and TE_{11} at $A_R \approx 1/3$, see Fig. 5.5, but the modes are orthogonal with respect to the symmetric adiabatic perturbation so coupling is zero). In this case what occurs is a transformation of polarization from horizontal to vertical. However, in contrast with polarization rotation approaches such as [32], which require breaking of cross-sectional symmetry in both the horizontal and vertical direction, the present mechanism converts polarization slightly differently, by exchanging the roles of the major and minor field components in a horizontally and vertically symmetric structure. It is analogous to four conjoined polarization rotations, two clockwise and two anticlockwise, at the same time. However, because the light must be coupled into and out of the structure, into a single-mode (the fundamental mode) waveguide, the symmetry must eventually be broken at the input and output coupling from the structure. This particular conceptual structure has too complex a geometry for practical use. In addition, the small effective index detuning of the two second-order modes means that a large device length would be needed to meet the adiabatic condition. Nevertheless, this higher-order mode evolution mechanism seems interesting and may find an application.

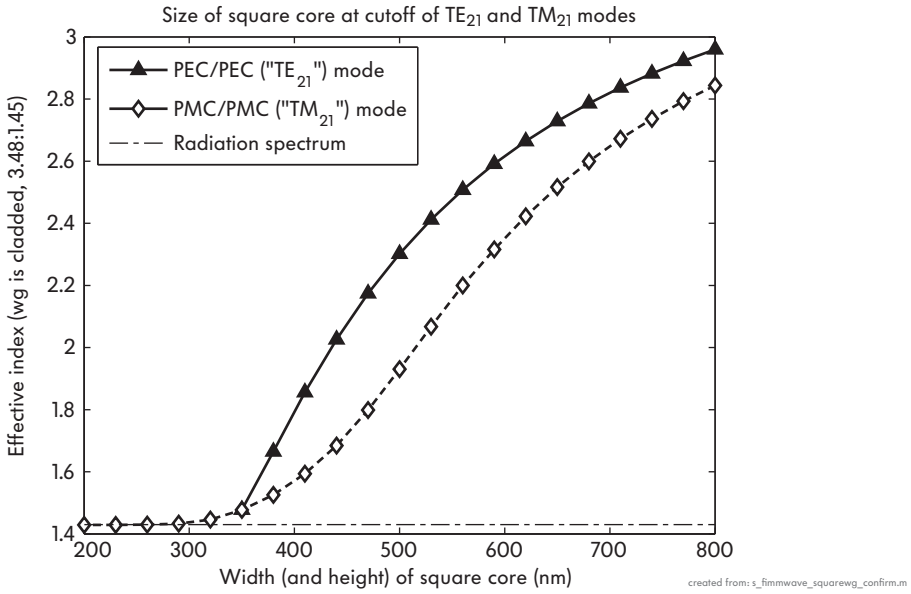

Figure 5.3: Verification that TE_{21} and TM_{21} modes have different cutoff sizes, with the TE_{21} cut off first. Effective index of both modes is plotted against the lateral dimension while keeping the cross-section square at all times.

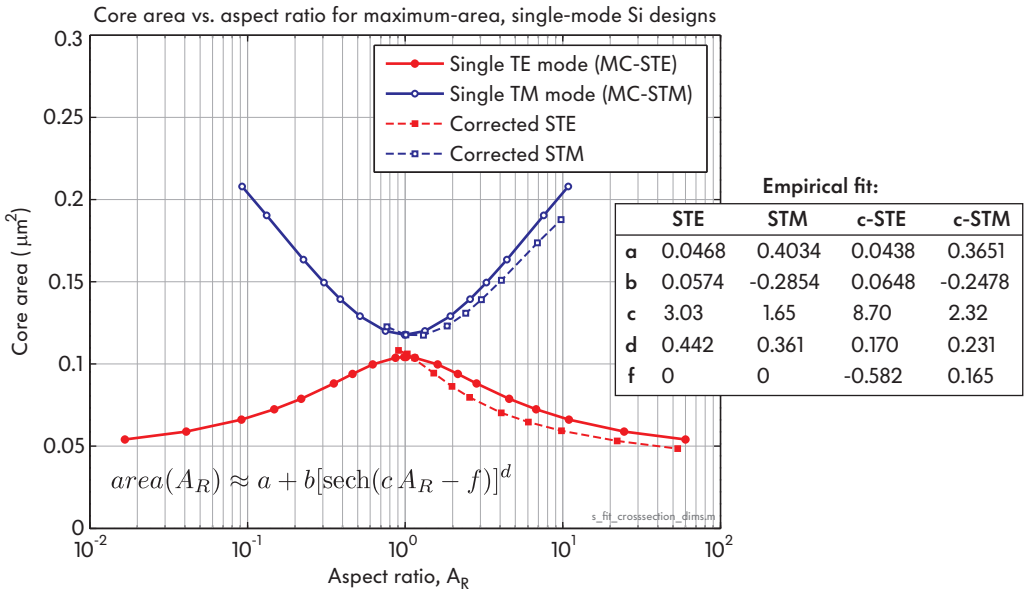

	STE	STM	c-STE	c-STM
a	0.0468	0.4034	0.0438	0.3651
b	0.0574	-0.2854	0.0648	-0.2478
c	3.03	1.65	8.70	2.32
d	0.442	0.361	0.170	0.231
f	0	0	-0.582	0.165

Figure 5.4: Map of maximally-confined silicon waveguide cross-sections shown as cross-sectional area vs. aspect ratio, A_R. A remarkably good fit of the function giving the single-mode TE and TM size for all A_R's is possible in this representation, shown as an inset with parameters.

Maximally-confined cross-sectional area vs. aspect ratio fit

The waveguide dimension contours are plotted in Fig. 5.4 in an alternative way, as cross-sectional area vs. aspect ratio A_R, for the MC-STE and MC-STM designs.

This representation lends itself to remarkably good empirical fits of the numerically computed results (indistinguishable in the plots from the data) using the functional form

$$\text{area}(A_R) = w \times h = a + b[\text{sech}(cA_R - f)]^d.$$

The fit parameters $\{a, b, c, d, f\}$ are given in the inset table for the nominal MC-STE and MC-STM designs, and allow the dimensions to be easily obtained ($w = \sqrt{\text{area} \cdot A_R}$, $h = \sqrt{\text{area}/A_R}$). Another set of dimension contours is shown (dashed lines), along with fits, which represent waveguide widths corrected to cut off a parasitic mode that occurs in directional couplers (labelled c-STE and c-STM in the figure). These contours are for ring-bus coupling for a 40 GHz-wide flat-top filter, and are described in more detail in Sec. 5.2.3.

Mode effective and group indices

Fig. 5.5 shows the effective and group indices of the modes of the MC-STE and MC-STM designs vs. aspect ratio A_R. Both the TE and TM fundamental modes are shown for each design – this is done in all plots. However, for most discussions here, only the TE mode of the MC-STE design and the TM mode of the MC-STM design will be of interest.

Effective and group index are defined in Sec. 3.1.1. The effective index, when compared with the core and cladding indices is indicative of level of mode confinement - the higher the effective index, the stronger the optical confinement (and the lower the bending loss in a curved waveguide of given radius, for example). The group index, on the other hand, enters into several important parameters, including the FSR, the loss Q as described in Eq. (5.1), as well as the wavelength tunability of a resonator, described by Eq. (3.1). A larger group index n_{group}, all other parameters staying equal, leads to a smaller FSR, higher cavity Q (for the same distributed losses per unit length), and smaller wavelength tunability.

Several conclusions may be drawn from Fig. 5.5(a), where the mode of primary interest is TE_{11}. First, the plot is symmetric about the $A_R = 1$ point on the horizontal axis because the TE_{11} mode in a 2:1 aspect-ratio, straight rectangular waveguide with uniform cladding is the same as the TM_{11} mode in a 1:2 aspect ratio waveguide, for example (the cross-section being only rotated 90°, which has no effect on the n_{eff}). Secondly, the dashed line confirms that the TE_{21} mode is at cutoff for all aspect ratios, having an effective index near the cladding index, as intended for the MC-STE designs. Third, the highest effective index and thus strongest confinement for the used TE_{11} mode in the MC-STE design is found to be for $A_R \approx 1.76$, i.e., for a waveguide cross-section of about width × height = 415×235 nm. This is near the typical dimensions used for silicon waveguides in literature, of about 400-500 nm wide by 200 nm tall. Fourth, the n_{eff} of the primary mode, TE_{11}, is fairly near the value for the cladding index when $A_R < 0.2$,

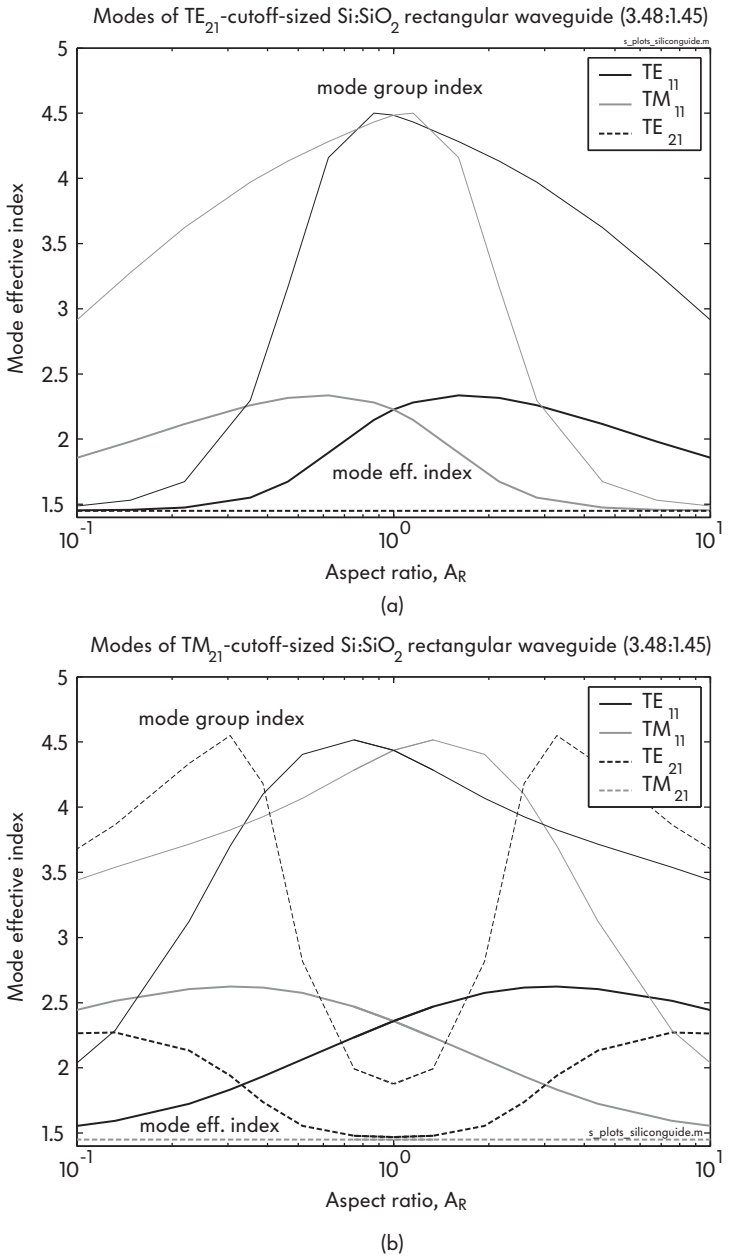

Figure 5.5: Maximally-confined Si waveguides: effective and group index vs. aspect ratio. (a) Maximally-confined single-TE-mode designs – MC-STE has strongest TE mode confinement at $A_R \approx 1.76$; (b) maximally-confined single-TM-mode designs have 1 TM and 2 TE guided modes. The propagation constant (effective index) crossing of TM_{11} and TE_{21}, i.e. $A_R \approx 3$, needs to be avoided (published in [98]).

indicating weak confinement, so that region of the design space ($A_R < 0.2$) may be excluded for the MC-STE design. For the TM_{11} mode, maximum confinement is near $A_R \approx 1/1.76 \approx 0.57$, i.e. for a 235×415 nm cross-section.

Fig. 5.5(b) shows the modal effective and group indices for the MC-STM designs

in Fig. 5.2. The intended excitation here is the TM_{11} mode. The TM_{21} mode is seen to be cut off, but there are two TE modes, TE_{11} and TE_{21}, in addition. Here, the TM_{11} mode has a low n_{eff}, near the cladding index, for $A_R > 10$, so that region of the design space may be excluded. The highest effective index and thus strongest confinement for the TM_{11} mode in the MC-STM design is for $A_R \approx 0.3$, i.e., a tall and narrow waveguide cross-section of about width $\times$ height = 215 $\times$ 700 nm. One important point is that the TE_{21} mode is degenerate with the TM_{11} mode, i.e., they have the same effective index, near $A_R = 3$. Although TE and TM modes are ideally orthogonal in this symmetric waveguide geometry, and nearly so more generally, when the modes are degenerate, the slightest perturbation can cause a large coupling between them (when extended over sufficient length). For example, unevenly slanted sidewalls in fabrication may couple TE and TM modes, or slanted sidewalls in coupling regions. This leads to crosstalk that may further be enhanced in resonators. Therefore, the $A_R = 3$ point is preferably avoided in the MC-STM design. Either sufficiently larger or smaller A_R is preferable. This constraint is reflected in Table 5.2.

Bending loss and FSR

After the mapping of effective and group indices, the resulting lateral optical confinement strength is investigated, as characterized in terms of minimum bending radii, and on the other hand the achievable FSR, for a given minimum bending-loss-associated microring radiation Q, for various A_R's for both design variants, MC-STE and MC-STM.

Fig. 5.6 shows the minimum waveguide bending radius allowed to achieve a bending loss low enough to support a bending loss associated radiation Q greater than 250,000. For a target Q that is 10 times larger or smaller, this plot is not significantly changed (compare Fig. 5.1). The Q is related to bending loss as (see Appendix B)

$$Q \approx \frac{40\pi^2 R\, n_{\text{group}}}{\lambda_o \ln 10\, L_{\text{dB90}}} \tag{5.1}$$

where R is the bend radius and L_{dB90} the bending loss in dB/90°. These plots show that TE_{11} modes in MC-STE designs support small bend radii with low bend loss, and large FSRs (order of 1 THz or more), for approximately $0.5 < A_R < 30$. TM_{11} modes in MC-STM designs do so for $A_R < 7$ or so, and on the lower end support $A_R = 0.1$ and lower aspect ratios. This is because the vertically polarized field is generally well confined in a tall waveguide even at very small aspect ratios and well suited to maintaining low radiation loss in bending in the plane.

Fig. 5.7 shows corresponding FSRs. It shows that high-Q (i.e., loss Q >250,000) rings can be made with large FSRs (around 1 THz or more) in MC-STE designs with $0.5 < A_R < 30$ and in MC-STM designs for $A_R < 7$. A 2 THz FSR is

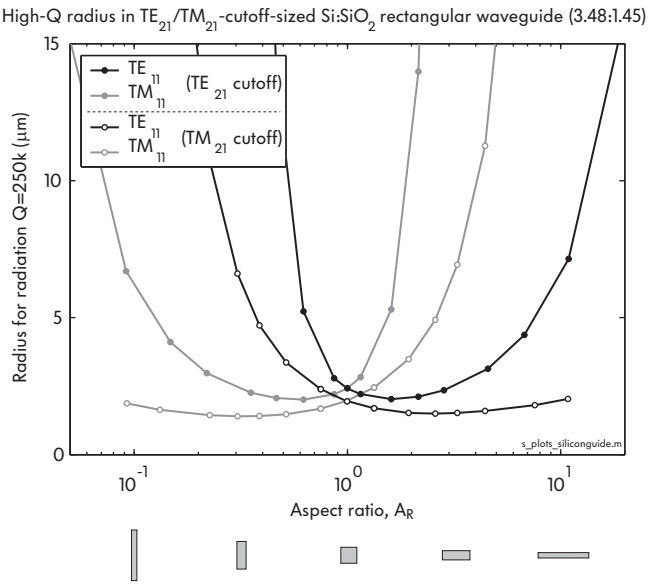

Figure 5.6: Minimum bend radius vs. aspect ratio for bend loss $Q > 250,000$ in a ring resonator. It is interesting that this plot is symmetric about the $A_R = 1$ axis (on the log scale), since the waveguides are strongly bent and there is therefore no symmetry that should produce similar bending losses for the wide-waveguide TE_{11} and corresponding tall-waveguide TM_{11} excitation, for example.

considered here, because the silicon-core thermooptic coefficient ($\sim 2 \cdot 10^{-4}$/K near 1550 nm) allows about that much wavelength tuning in a cavity with about 200°C temperature change. Larger effective tunable FSRs may be created using Vernier techniques in various embodiments (see Chaps. 8,9). Therefore for a 2 THz FSR, the MC-STE design is constrained to $0.5 < A_R < 15$, while the MC-STM design is constrained to about $0.05 < A_R < 3.2$ (even values below 0.05, not shown in the plot, may be permissible). For any other given minimum FSR, the range of admissible designs may be found from Fig. 5.7.

Correspondence of FSR and effective index

By comparing Fig. 5.5 and Fig. 5.7, it may be observed that the FSR is correlated with the mode effective index, by noting the aspect ratio for a given FSR, chosen mode (TE_{11} or TM_{11}) and design (MC-STE or MC-STM), and then finding the corresponding effective index at that aspect ratio, in Fig. 5.5(a) or Fig. 5.5(b). It may be noted that the radii and group indices are not necessarily the same for these corresponding TE and TM designs. This correlation of FSR and effective index holds primarily for wide flat designs, i.e., waveguides with $A_R > 1$, as shown in Fig. 5.8. These designs are also the designs of primary interest here, due to their favourable dimensional sensitivities, evaluated in the next section. This correspondence is evidence of equivalent TE and TM designs, and is further revisited later.

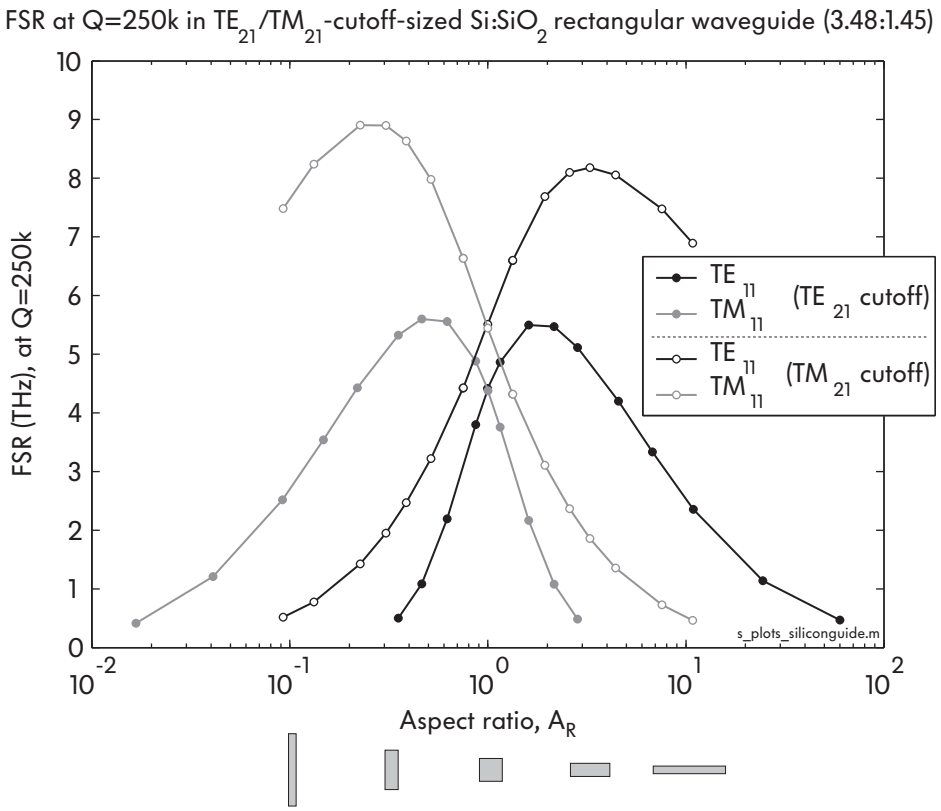

Figure 5.7: Maximum FSR with $Q > 250,000$ vs. aspect ratio of maximally confined Si waveguide. Both MC-STE (TE_{11}) and MC-STM (TM_{11}) designs show a considerably wide range of A_R's over which they support at least 2 THz (16 nm) of FSR that is relevant for telecom applications. This leaves a large design space for optimizing based on other critical parameters. This plot also shows that the largest achievable FSR in a silica-clad Si microring resonator, with single-mode excitation, is a tall and narrow MC-STM design, giving about 9 THz at $A_R \approx 0.25$.

Maximum FSR in silicon

In Fig. 5.7 it may be observed that the maximum achievable FSR for bend loss Q $\geq$ 250,000, for the TE_{11} mode excitation intended in the MC-STE design, is about 5.5 THz, or 44 nm, and occurs for $A_R \approx 1.9$ or a cross-section of $w \times h = 430 \times 225$ nm. This cross-section is similar to typically used Si cross-sections in literature today of 450×200 nm or so [99].

However this is not the highest achievable FSR in a uniformly clad silicon-core waveguide. If the TM_{11} mode is used, and the MC-STM design employed, which may be used when coupling is in the plane, then FSRs up to 9 THz, or 72 nm, may be achieved for $A_R \approx 0.25$ in principle, or a cross-section of $w \times h = 200 \times 790$ nm. This design corresponds to a bend radius as small as about 1.45 µm. This is the most strongly confined rectangular-core silicon waveguide design with uniform cladding, that does not support higher-order spurious modes that can couple substantially to the main TM_{11} mode when coupling laterally to structures

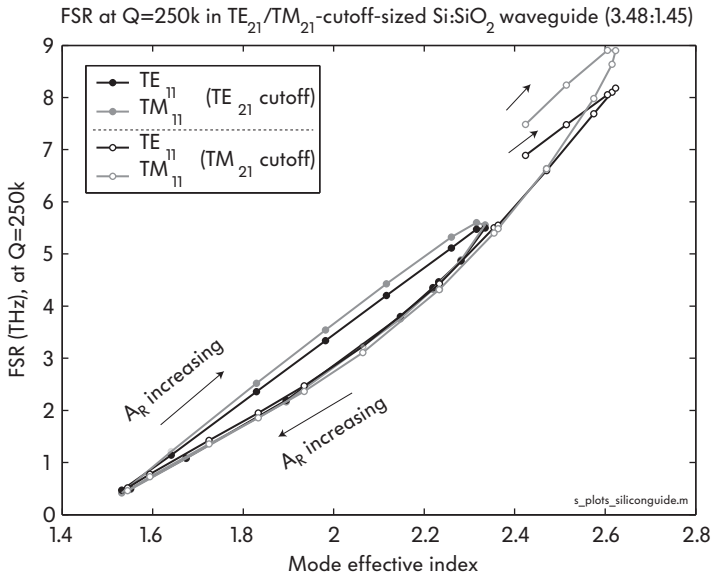

Figure 5.8: Contour plot illustrating discovered apparent correspondence of FSR and effective index, for *equivalent* TE and TM designs, in the region of interest $A_R > 1$. This correspondence contributes to establishing the existence of approximately *equivalent* TE and TM designs (of respectively different A_R's).

in the same lithographic layer. Achieving a maximum FSR for a given Q is desirable in some applications where either a large FSR is desired, or a large finesse is desired. For example, in nonlinear applications, large finesse means a large field enhancement in the cavity.

On the other hand, such tall, narrow waveguide designs have high sensitivity to lithographic dimensional errors as described in the following section, as well as to sidewall roughness, in addition to lithographic challenges due to the aspect ratio, and therefore are not ideal for high-fidelity filter applications.

5.2.2 Resonance frequency sensitivity and tunability

The most important comparison for all waveguide designs considered in this study is the sensitivity of the waveguide's optical properties to dimensional errors in fabrication (errors in width and height). This sensitivity may be measured in terms of the change in propagation constant, or alternatively in terms of shift in resonance frequency of a resonator formed of such a waveguide. In general, if a waveguide is turned into a closed loop traveling-wave cavity, or is made into a linear standing-wave cavity with 2-way propagation (such as a Fabry-Perot cavity), then the sensitivity of the resonance frequency to change in the propagation constant does not depend on the cavity length or the longitudinal resonance order, but only on the fractional error in propagation constant,

$$\frac{\delta\omega_o}{\omega_o} \simeq \frac{\delta\lambda_o}{\lambda_o} \simeq -\frac{n_{\text{eff}}}{n_{\text{group}}}\frac{\delta\beta_o}{\beta_o} \tag{5.2}$$

consistent with Eq. (3.1). Therefore, a resonance frequency error $\delta\omega_o$ is a scaled version of a propagation constant error $\delta\beta_o$, and their sensitivities to a perturbation are related in the same way.

The propagation constant sensitivity of a mode in a dielectric-core waveguide to width or height error depends on the electric field intensity on the sidewall interfaces or top and bottom wall interfaces, respectively, relative to the guided power. More field on the sidewalls means larger sensitivity. This sensitivity can be directly evaluated from the rigorously computed mode field distributions by line integrals along the perturbed waveguide walls. The sensitivity to width, for example, may be given by the overlap integral of the field along the perturbed sidewall edges of the waveguide (analogous to the ω integrals in [80]):

$$\frac{\partial\beta}{\partial w} = \frac{\int_{\text{sidewall}} \mathrm{dy} \left(\Delta\epsilon \left| \vec{E}_{\parallel}(x_{\text{wall}} = \pm w/2, y) \right|^2 - \Delta(\epsilon^{-1}) \left| \vec{D}_{\perp}(x_{\text{wall}} = \pm w/2, y) \right|^2 \right)}{\iint_{\text{cross-section}} \vec{E} \times \vec{H}^* + \vec{E}^* \times \vec{H} \cdot \hat{z} \mathrm{dA}}$$

where the overlap integral in the numerator is taken as a line integral along the height of each sidewall in the waveguide cross-section, while the normalization in the denominator is the guided power computed as an area integral over the waveguide cross-section (core and cladding). The waveguide width is w, y indicates the vertical (out of the chip plane) direction coordinate along sidewalls, and x is the lateral coordinate. In the numerator, $\Delta\epsilon = \epsilon_{\text{core}} - \epsilon_{\text{cladding}}$, $\Delta(\epsilon^{-1}) = \epsilon_{\text{core}}^{-1} - \epsilon_{\text{cladding}}^{-1}$, $\vec{D}_{\perp}$ is the electric displacement normal to the sidewall surface, and $\vec{E}_{\parallel}$ is the electric field parallel to the sidewall surface. The use of normal and parallel fields in different form in the overlap integral is a special form suitable for step-index discontinuities in high-index-contrast waveguides [80].

Fig. 5.9 shows the resonance frequency sensitivity to waveguide width error, vs. the aspect ratio A_R, of a ring resonator using the TE_{11} and TM_{11} modes of each of the MC-STE and MC-STM waveguide designs. The sensitivity is based on straight waveguide modes so that it is independent of bend radius of the waveguide, and is given in GHz frequency shift per nm error in waveguide width. The width error is assumed to be symmetric (see Fig. 5.9, inset). One may also read the sensitivity to error in height from the same plot, by interchanging the TE and TM mode labels within each design, and by letting $A_R \to 1/A_R$ (which amounts to reflecting the log-scale plot horizontally about the $A_R = 1$ point). Therefore the black solid line with solid dots gives the sensitivity of mode TE_{11} of the MC-STE design to width for aspect ratios A_R, as well as the sensitivity of mode TM_{11} of the MC-STE design to height for aspect ratios $1/A_R$.

Fig. 5.9 is one of the central figures in this design study, and several important conclusions may be drawn from it, specifically for the Si-core, uniformly clad waveguide under consideration, but also more generally.

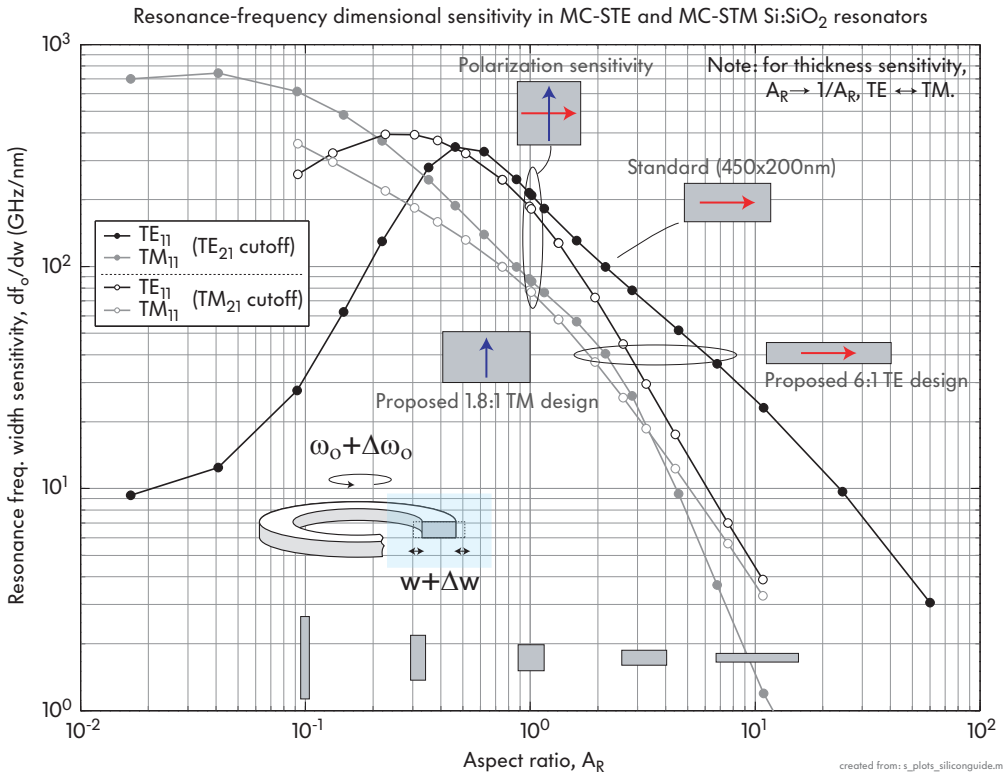

Figure 5.9: MC Si waveguides: resonance frequency sensitivity to waveguide width error. Sensitivity to height error is obtained by exchanging the $TE \leftrightarrow TM$ labels, and letting $A_R \rightarrow 1/A_R$. The plot shows that conventional Si waveguide designs (450x200 nm) have high sensitivity, while high-aspect-ratio TE designs and corresponding TM designs have much lower sensitivity. The MC-STM design TM_{11} mode is half an order of magnitude less sensitive to width error than the MC-STE design TE_{11} mode of equal A_R, but the *equivalent* designs have about the same sensitivity (see text). The figure also shows that use of square (or carefully tuned to degeneracy) cross-section waveguides for polarization-independent operation is impractical, as the sensitivities may require sub-atomic absolute dimensional control (published in [98]).

Extreme polarization sensitivity of SC waveguides

First, from Fig. 5.9 it can be concluded that polarization-insensitive resonators may require sub-atomic absolute lithographic dimensional control, due to the width sensitivity. Polarization-insensitive operation is a required property for many microphotonic systems that communicate via standard optical fibers, along which polarization is scrambled in time and wavelength. This happens due to the near degeneracy of the two polarization modes in the fiber, and the small natural shape deformations, strain variations, and temperature fluctuations that are sufficient to couple them.

Nominally, a square-cross-section, buried silicon waveguide with uniform cladding has degenerate fundamental TE and TM propagation constants and therefore aligned TE and TM resonances in a microring resonator formed of such a

waveguide[‖]. However, the TE and TM modes in such a resonator have highly different sensitivities of the resonant frequency to width.

For example, a maximally confined square silicon waveguide (with one TE and one TM guided mode) has a cross-section of ∼330×330 nm (see Fig. 5.2). In such a waveguide, the TE and TM propagation constant sensitivities to waveguide width are about 210 GHz/nm and 85 GHz/nm, respectively. The difference is about 125 GHz/nm, which means that even if TE and TM resonances in a ring resonator are frequency aligned for a given design, a 1Å error in ring waveguide width will misalign them by 12 GHz. For filters with 12 GHz bandwidth, this would clearly be intolerable Since 25 GHz is a standard ITU telecom spectrum channel spacing, this is not an unrealistic scenario.

Such atomic-scale dimensional control, required to align TE and TM resonances in a single device, is impractical and has led to a search for alternative solutions, and the demonstration of an integrated polarization diversity approach to polarization transparency in strong confinement waveguides [31, 33]. This approach relies on geometrical symmetry and replication of identical structures, a strong advantage of lithography. This justifies the approach taken in all of the work in this thesis – to pursue single-polarization designs to be used within a diversity scheme for polarization independent operation.

Sensitivity of conventional Si cross-sections, of improved cross-sections, and of TE vs. TM designs

Next, consider the typical 450×200 nm waveguide used with TE polarization only (aspect ratio of ∼2:1). The TE_{11} mode on the MC-STE design curve shows a width sensitivity of about 100 GHz/nm. Even if operating the device in a single polarization, this may still be a considerable challenge. This sensitivity makes very strict requirements on *relative* dimensional control between multiple ring resonators in the same device. Rings must be made with the same average width to a tolerance that provides much less frequency mismatch than the filter bandwidth (see also Sec. 4.1 on CIFS). In our demonstration of high extinction telecom-grade filters in SiN, the width sensitivity was on the order of 40 GHz/nm and posed an important challenge for fabrication [90].

In practice, the waveguide width is controlled by lithography and etching while the waveguide height is controlled by either material deposition or polishing. As the thickness of thin films may generally be measured before lithography, and adjusted more accurately than lateral dimensions introduced via lithography, waveguide height dimensions are considered much better controlled than lateral (e.g., width) dimensions in this work. Therefore, in illustrating optimum designs, the assumption

[‖]Rigorously, at small bend radii the symmetry is broken and the TE and TM modes deform and acquire slightly different propagation constants, but this may be corrected by adjusting the cross-section to be slightly rectangular, without changing our conclusions.

is made herein that the height may be well controlled, or accurately mapped prior to fabrication, and thus the sensitivity to width is to be reduced at the expense of sensitivity to height. Variations of height across a wafer may still need to be kept in bounds, or the sensitivity to height may need to be constrained for this uncertainty not to adversely impact device yield. This trade-off is easily accessed in Fig. 5.9.

Fig. 5.9 reveals that this width sensitivity of the standard 450×200 nm waveguide can be reduced in three ways. First, if the aspect ratio is increased, then the sensitivity is reduced. The log-log plot shows that width sensitivity is reduced by about an order of magnitude for an order of magnitude increase in aspect ratio A_R, in the region of interest $A_R > 1$.

Secondly, by moving to the TM polarization in a wide and flat waveguide design (i.e., $A_R > 1$), the sensitivity is reduced. The solid-dot TE_{11} and TM_{11} curves (MC-STE design) show that the TM_{11} mode has half the width sensitivity of the TE_{11} mode. Thirdly, using TM polarization in an in-plane circuit permits the use of a larger waveguide core while maintaining a single TM mode, because TE modes are orthogonal and will not excite a TM resonance in this configuration. This allows consideration of the MC-STM design (hollow dots in Fig. 5.9). The TM_{11} mode sensitivity is further reduced, while allowing a much higher achievable FSR at each aspect ratio and prescribed FSR, due to stronger confinement and less field on the sidewalls. These three steps may be combined, and in general for reduced width sensitivity, the highest usable aspect ratio is desired.

FSR-equivalent TE_{11} MC-STE and TM_{11} MC-STM designs

It may be noted that, for $A_R > 1$, for the same width sensitivity the TE_{11} mode of the MC-STE design and the TM_{11} mode of the MC-STM design have the same FSR and the same effective index. This correspondence is shown explicitly in Fig. 5.10, where the contours are parametrized by aspect ratio A_R. Note that the correspondence does not hold for the unused modes TM_{11} in the MC-STE design and TE_{11} in MC-STM design.

Although similar properties may be expected for similar conditions (cutoff of next like-polarized mode), it is interesting that there are thus far MC-STE designs and MC-STM designs with approximately equivalent performance in the aspect-ratio region $A_R > 1$. Their performance is equivalent in the sense that there is an A_R for the MC-STE design using the TE_{11} mode, and an A_R for the MC-STM design using the TM_{11} mode, where the maximum FSR and the sensitivity are both identical and correlate with the effective index (compare Figs. 5.9, 5.10, 5.7 and 5.8). The A_R's and the microring bend radii are not the same for the corresponding equivalent MC-STE and MC-STM designs, but for each frequency sensitivity value, there is such a pair of A_R's in the region $A_R > 1$. Which of the MC-STE and MC-STM designs is optimal will then need to be decided based upon other additional criteria.

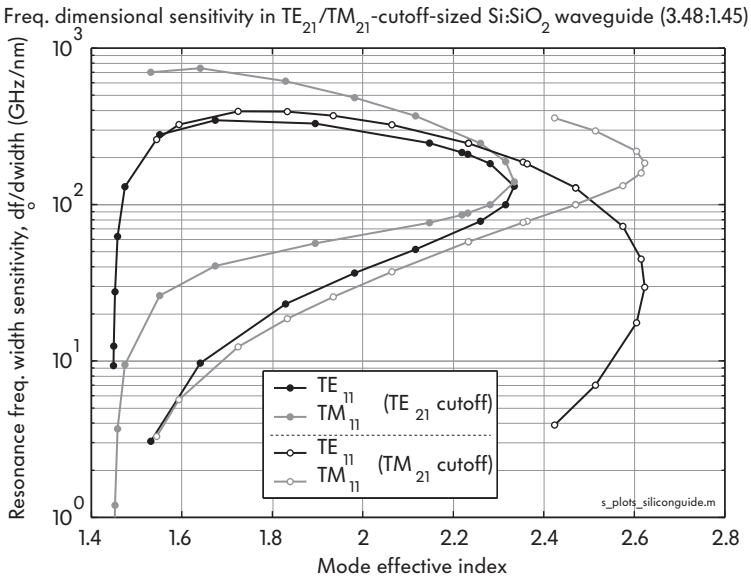

Figure 5.10: Contour plot illustrating the discovered apparent correspondence of sensitivity and effective index in the region of interest $A_R > 1$. This correspondence contributes to establishing the existence of approximately *equivalent* TE and TM designs (of respectively different A_R's).

Thermooptic tunability

Another important aspect of resonator design is wavelength tunability. Tuning may be effected by thermooptic means if the waveguide materials (core or cladding) have a high thermooptic coefficient. The effective index of the employed mode is changed by the tuning mechanism, thus changing the optical length of the resonator and shifting the resonant frequency as a result. Thermooptic tuning is one of the most common methods of tuning, where typically a heating element, such as a metallic or semiconducting strip, is resistively heated when current is passed through it and increases the temperature in the proximate optical waveguide.

The thermooptic tunability of the family of waveguide designs of Fig. 5.2 is examined. Fig. 5.11(b) shows a normalized tunability of the fundamental TE and TM guided mode due to a normalized change in the core index,

$$\frac{1}{n_{\text{group}}}\frac{\partial n_{\text{eff}}}{\partial n_{\text{core}}} \tag{5.3}$$

while Fig. 5.11(c) shows a normalized tunability of a guided mode due to change in the cladding index,

$$\frac{1}{n_{\text{group}}}\frac{\partial n_{\text{eff}}}{\partial n_{\text{clad}}}. \tag{5.4}$$

To arrive at the total tuning due to a particular tuning mechanism, using Eq. (3.1), factors (5.3) and (5.4) are multiplied by the core and cladding index changes

caused by the tuning mechanisms, respectively, and summed. For temperature tuning, this amounts to multiplying each by the thermooptic coefficient, and by the temperature change as in Eq. (3.5):

$$\frac{\delta\lambda_o}{\lambda_o} = \frac{1}{n_{\text{group}}}\frac{\partial n_{\text{eff}}}{\partial \text{core}} \cdot \frac{\partial n_{\text{core}}}{\partial T} \cdot \Delta T + \frac{1}{n_{\text{group}}}\frac{\partial n_{\text{eff}}}{\partial \text{clad}} \cdot \frac{\partial n_{\text{core}}}{\partial T} \cdot \Delta T. \tag{5.5}$$

Note more generally that for large tuning the thermooptic coefficient is temperature dependent and in device design a quadratic model is used here (see Fig. 6.2, Chap. 6).

Fig. 5.11(b) shows factor (5.3) for TE_{11} and TM_{11} modes of MC-STE and MC-STM designs of Fig. 5.2, for a range of A_R values. The temperature tunability for the primary modes (TE_{11} in MC-STE designs, and TM_{11} in MC-STM designs) is roughly similar over the range of A_R values that support a high FSR in each case ($0.5 < A_R < 15$ and $0.05 < A_R < 3.2$, for TE and TM respectively). The variation of the factor (5.3) is only up to about 50% within these ranges. Strongly confined designs will primarily have tuning due to this contribution, from the core index.

Fig. 5.11(c) shows factor (5.4), which is the sensitivity to the cladding index perturbation. Because a small amount of field is in the cladding in the strongly confined designs, this factor spans a larger range of values. Generally the more weakly confined designs at the edges of the plot, with a large fraction of guided power immersed in the cladding material, and with smaller FSRs, are strongly influenced by cladding index perturbation. However there are regions within the large-FSR range of A_R values that have significant sensitivity to cladding perturbation, such as the MC-STM design's TM_{11} mode at high A_R values (about $A_R = 2$ and above). This may be desirable where it is of interest to use a cladding material with a large thermooptic coefficient for tuning, such as a polymer which has a low refractive index (order of 1.3 to 1.7) but may have thermooptic coefficients as large as silicon and larger.

Since the thermooptic coefficient of polymers is typically negative, while that of semiconductors such as silicon is positive, designs may also be chosen to make athermal resonators that are insensitive to temperature, by balancing the thermooptic tuning effect of a silicon core and a polymer cladding. Such athermal design is common, for example, in silica arrayed waveguide grating (AWG) multiplexers [9]. Here, for example, Figs. 5.11(b,c) show that larger aspect ratios have a higher sensitivity to cladding index and lower sensitivity to core index, while maintaining maximally-mode-confining (MC-STE or MC-STM) cross-sectional dimensions. This means that for a given positive core material thermooptic coefficient, and a given negative cladding thermooptic coefficient, an aspect ratio can be found that provides an athermal waveguide design that is maximally confining (MC-STE or MC-STM). This may be useful for resonant filters operating in environments with large temperature fluctuations such as outdoor field environments, or densely integrated electronic environments such as microprocessors or graphics chips that

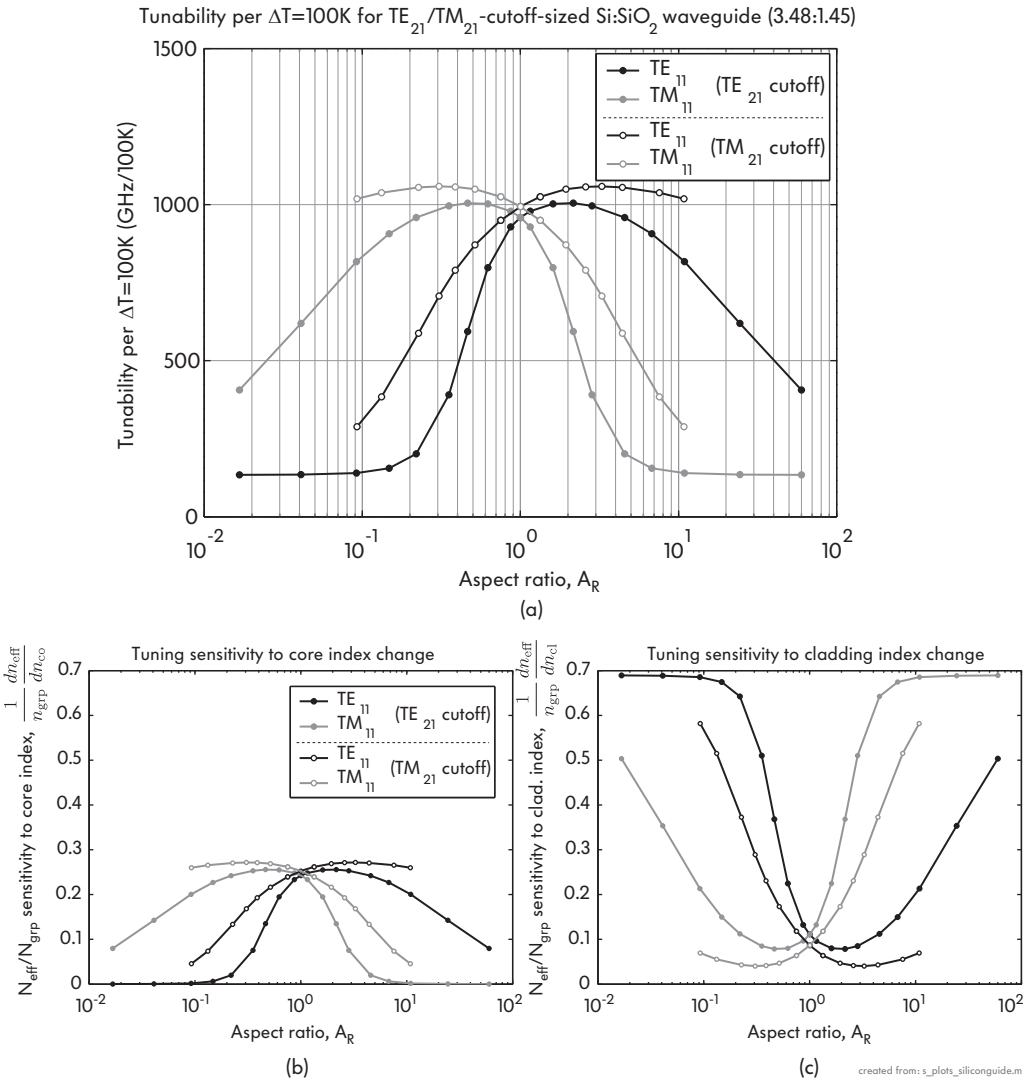

Figure 5.11: Thermooptic tunability of resonators based on maximally confined Si waveguides, vs. aspect ratio. (a) Real-frequency tuning per 100K temperature rise shows weak variation of the tuning efficiency with aspect ratio. Normalized plots of the (b) core tuning sensitivity and (c) cladding tuning sensitivity may be useful in considering other materials (such as polymer claddings that have a high, negative thermooptic coefficient). These plots use straight-waveguide data, hence are independent of ring radius.

generate a lot of heat, and where optical components may be incorporated to increase speed and memory bandwidth and reduce power consumption of communication links.

For the particular choice of the example in Fig. 5.2, with a silicon core and silica cladding, the results of Eqs. (5.3) and (5.4), i.e., Figs. 5.11(b) and (c), are combined with the thermooptic coefficients of silicon (core) and silica (cladding) – about $+2 \cdot 10^{-4}/^\circ\,\mathrm{C}$ and $+1 \cdot 10^{-5}/^\circ\,\mathrm{C}$, respectively. The result, equivalent to Eq. (5.5), is shown in Fig. 5.11(a), showing the total thermal resonance-frequency

tunability of a resonator in GHz per +100° C change in temperature. The plot shows that the MC-STE design with the TE_{11} mode excited has about 1 THz/100° C tunability or nearly so for a fairly large range of A_R values, about $0.8 < A_R < 7$. The MC-STM design with TM_{11} mode excited has about 2/3 as much tunability at the highest usable A_R of about 3.2 – about 700 GHz/100° C, and larger tunability for smaller A_R values. Therefore, the tunability is reasonably similar and the tunability consideration does not narrow the usable range of A_R's considerably from the ranges constrained by the FSR requirement of 2 THz and the dimensional sensitivity.

5.2.3 Loss and coupling sensitivities and limitations

Several other important factors in the Si waveguide and resonator design depend on the level of optical confinement, including optical absorption by a heating element that may serve as a resistive heater for thermooptic tuning, and optical mode leakage into a wafer substrate material.

In the first case, a metallic or a semiconductor heating element is preferably placed close enough to an optical resonator to efficiently heat the dielectric materials where optical intensity is substantial, but far enough away in order to avoid significant overlap of the optical field with the heating element that may lead to significant optical absorption losses in the resonator. The heating element may consist of a metal, such as chromium, or a semiconductor such as silicon. The same issues apply to sections of waveguide used for interferometer arms.

In the second case, low index undercladdings have a limited thickness separating the high index core region from a typically high index substrate such as bulk Si. For example, an SOI wafer may have 2-3 microns of silica undercladding separating the silicon device layer and the silicon substrate. If the optical mode in the waveguide has a lower effective index than the core index of the substrate (for Si, $n = 3.48$ at 1550 nm), then the mode becomes leaky and some optical power is lost by tunneling leakage into the substrate (e.g. see modesolver analysis in [122, 124]). Since the leakage loss is through an optical tunneling process via the evanescent mode field which has an exponential decay with distance from the core region, increasing the undercladding thickness decreases leakage loss exponentially.

In the substrate loss, heating element absorption and coupling gap analysis, only the range $A_R > 1$ is considered where the width sensitivities are small.

Metallic membrane optical absorption

In this section, absorption due to a metallic membrane is considered. Metals tend to be absorptive at optical frequencies (wavelengths) of excitation. The complex optical refractive index characterizes this optical loss, and is given in Table 5.1 for

Table 5.1: Optical constants of metals [125]

Metal	Complex refractive index at 1550 nm (0.8 eV) $n + i\,k$
Chromium	$3.8 + i\,3.7$
Gold	$0.5 + i\,0.9$
Nickel	$3.3 + i\,7$
Titanium	$3.9 + i\,3.7$
Molybdenum	$1.6 + i\,7$
Palladium	$2.9 + i\,8$
Vanadium	$2.5 + i\,5.5$
Tungsten	$2.4 + i\,4.5$

a few metals suitable for fabricating microheaters for microphotonics applications. Although the level of absorption varies in general among different metals, the behaviour is similar and generally within the same order of magnitude in absorption. Here, chromium (Cr) is used as an example for illustrative purposes, but the conclusions apply more generally to gold, titanium, nickel, molybdenum, palladium, vanadium, tungsten, and other metals that may be used.

Fig. 5.12(a) shows the cross-section of an exemplary microring resonator configuration considered in this analysis, showing a 100 nm thick chromium heating element, displaced vertically by a distance d from the ring waveguide. Fig. 5.12(b) shows the total loss Q due to absorption vs. aspect ratio for the MC-STE designs. For computational efficiency, a symmetric structure with a metal slab both above and below the ring, symmetrically placed is considered. The loss also includes the bending loss at the radius required for a bend loss Q of 250,000.

The case of the bent waveguide is used because the waveguide mode in a bent waveguide is pushed radially outward and becomes less well confined in the vertical (out of the chip-plane) direction in comparison to its straight counterpart waveguide. Therefore, the bent-waveguide case gives a worst case scenario for coupling to a substrate or conductive absorber (heating element) above or below the waveguide. The total Q is given in dotted line (which does not exceed 250,000, limited by the bending loss Q set by the design), while the solid line gives the disembedded loss Q due only to absorption in a single heating element, e.g., a metallic or semiconducting slab. The latter is the loss Q of interest.

It is of interest to place the heating element as close to a resonator as possible without spoiling the resonator Q by the heating element optical absorption, in order to minimize temperature drop from the heater to the resonator waveguide. Hence, the displacement of the heating element is an important consideration in the design, and is directly related to the chosen aspect ratio, A_R. This design consideration favors choosing as small an aspect ratio as possible, in the region

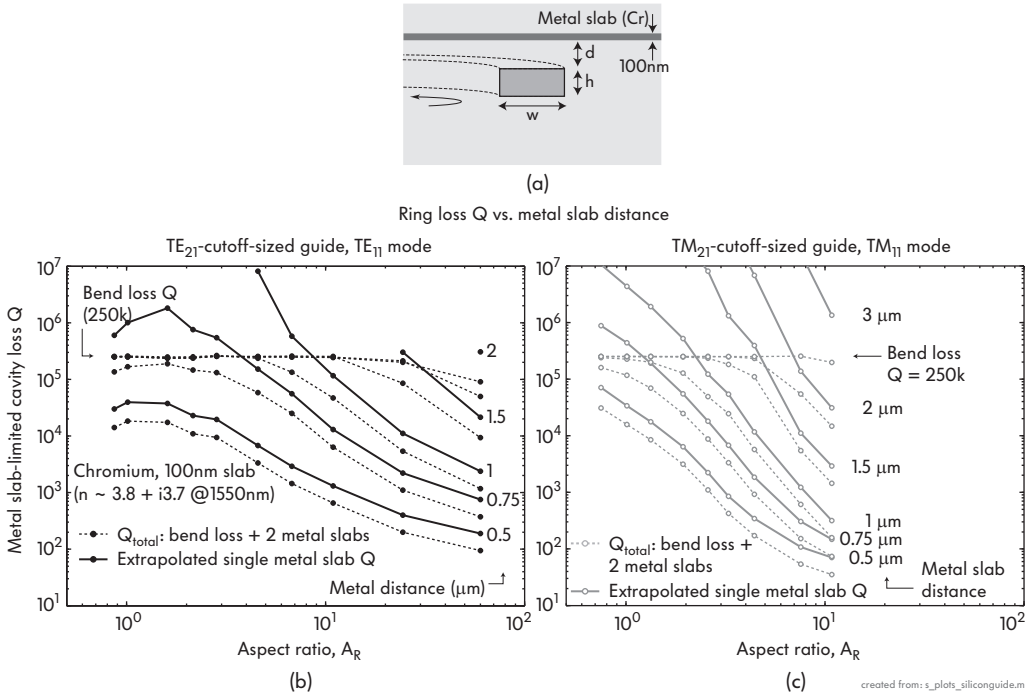

Figure 5.12: Overhead metal slab (microheater) absorption losses in maximally confined Si waveguides. (a) The geometry under study assumes a 100 nm-thick Chromium ($n = 3.8 + i3.7$ at $\lambda = 1550$ nm) forming a material layer that is raised a distance d above the top surface of the silicon ring, for optical decoupling; (b) MC-STE design, TE_{11} mode loss vs. A_R, (c) MC-STM design, TM_{11} mode loss vs. A_R. The plots show that $A_R = 6$ TE design and $A_R = 1.8$ TM design, which are *equivalent* in that they have equal sensitivities for example (Fig. 5.9), also both require about a $d = 1$ μm microheater displacement to keep optical loss low enough for a $Q > 250,000$ (published in [98]).

of A_R values plotted, so that the heating element may be placed closer to the resonator waveguide without inducing absorption losses sufficient to spoil the Q. This means seeking as high an optical confinement as possible.

On the other hand, Fig. 5.2 showed that high aspect ratios are favored for low sensitivity to dimensional error, and as discussed further later (see Fig. 5.18) also for low propagation loss due to sidewall roughness. Therefore, for thermally tuned resonators heated by a resistive heating element, the optimum design will need to trade off these two requirements according to their importance in the particular case.

Fig. 5.12(c) shows that the same constraint on the undercladding thickness for the MC-STM designs using the TM_{11} mode. For example, in the MC-STE, TE_{11} case with $A_R \approx 6$, undercladdings of about 0.9 μm thickness and up are sufficient; while in the MC-STM, TM_{11} case the same undercladding thickness is sufficient for up to about $A_R = 2$. Since MC-STE (TE_{11}) with $A_R \approx 6$ and MC-STM (TM_{11}) with $A_R \approx 2$ are "equivalent designs" as already described, in terms of sensitivity, achievable high-Q FSR and effective index, the metal absorption overlap requirement does

not point strongly in favor of one design or the other, but is rather in keeping with their equivalence in this respect also. This is despite the intuition one may have that TM modes are more extended in the vertical direction and thus may have higher substrate losses – this weaker confinement is compensated by the lower width sensitivity of TM at lower aspect ratios and larger allowable cross-sectional area.

Substrate leakage loss

The second loss mechanism considered is substrate leakage loss. Fig. 5.13(c) shows computed substrate leakage loss (in dotted curves) for a symmetric, bent waveguide, having two high index "substrate" regions, symmetrically placed above and below the waveguide core at a distance from the core indicated next to each plot curve (again a dual symmetric structure is used for computational efficiency). The bend radius used is the radius that gives a bend loss Q of 250,000, consistent with the example case used thus far.

The propagation loss is plotted in Fig. 5.13(c) in dotted line for various displacements of two semi-infinite half-spaces of index 3.48 (modeling a bulk silicon substrate). This curve includes bending loss as well as substrate leakage loss to each of the two halfspaces. By removing the effect of bending loss, and dividing by two, the substrate loss due to a single substrate is disembedded. This is shown in the solid line. It may be seen that the total propagation loss (dotted line) is limited to stay above about 3 dB/cm, which corresponds to a bend loss Q of 250,000. The extrapolated single-substrate loss (solid line) is the figure of interest. In integrated optical circuits it is preferable that waveguide propagation losses be kept well below 10 dB/cm, and ideally below 1 dB/cm. Therefore the loss due to substrate leakage in general waveguiding circuits (straight waveguides, bends, etc.) needs to be well below 1 dB/cm, preferably below 0.1 dB/cm. From Fig. 5.13(c), for all MC-STE design (TE_{11} mode) aspect ratios with usable FSRs, $0.5 < A_R < 15$, an undercladding thickness of about 2 μm or larger ensures below 0.1 dB/cm leakage loss.

Fig. 5.13(d) shows the same calculation for the MC-STM design employing the TM_{11} mode. Here, also, a silica undercladding of thickness 1.8 μm or larger is sufficient to guarantee less than 0.1 dB/cm substrate leakage in the relevant MC-STM design range of aspect ratios, $0.05 < A_R < 3.2$.

Because the cavity Q is not directly related to propagation loss, but scales with the group index (refer to Fig. 5.5), for resonator design the results of Figs. 5.13(c),(d) are shown again in Figs. 5.13(a),(b), with loss expressed in terms of resonator loss Q due to substrate leakage. Dotted lines show the total cavity loss Q due to bending loss and two symmetrically placed substrates (above and below) at various displacements from the core, and solid lines show the disembedded loss Q due to a single substrate half-space, which is the value of interest. Since Q's due to

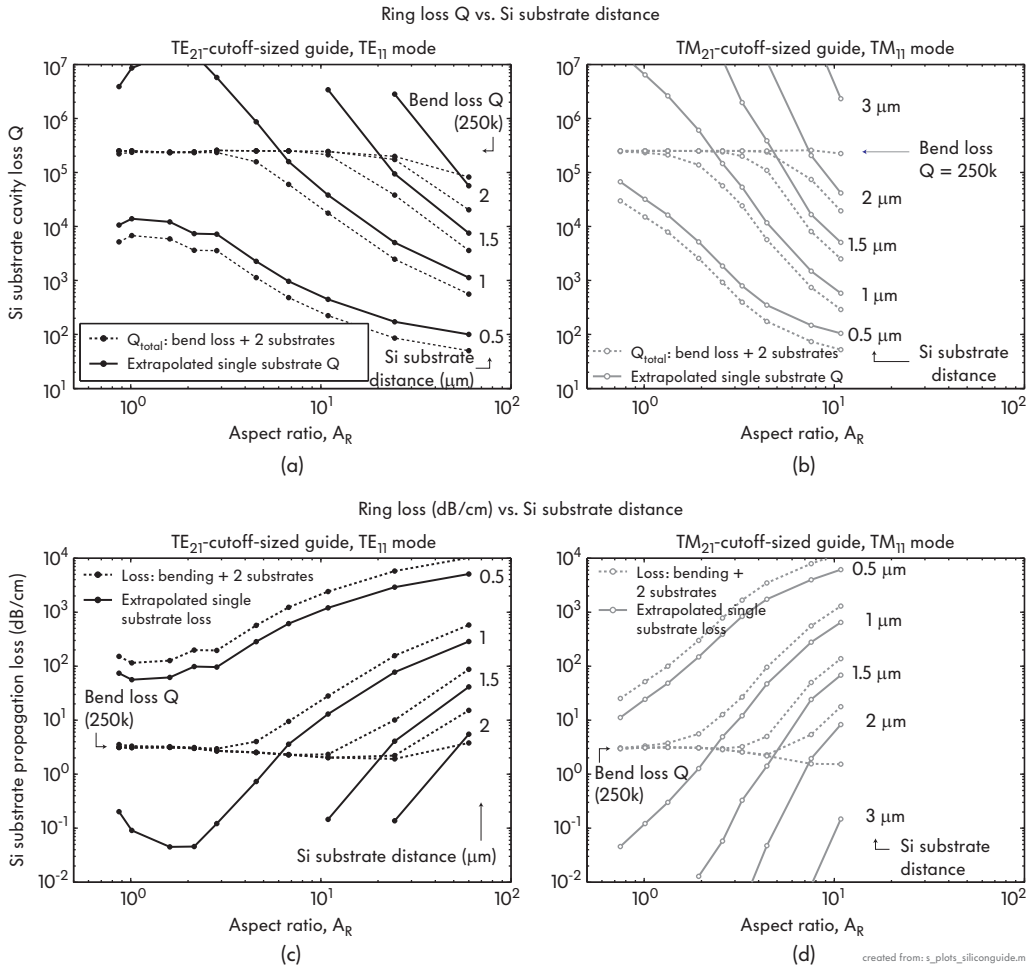

Figure 5.13: Substrate leakage loss in maximally confined Si waveguides vs. aspect ratio and undercladding thickness: (a) substrate-loss Q vs. aspect ratio for TE_{11} mode of MC-STE design, and (b) for TM_{11} mode of MC-STM design; (c,d) same data in waveguide propagation loss units (dB/cm).

various loss mechanisms combine to yield a lower total Q, it is desirable to select substrate displacements large enough that the total Q is not significantly reduced from the bending loss Q of 250,000. For MC-STE designs (TE_{11}), for aspect ratios $0.5 < A_R < 15$, an undercladding thickness of 1.2 μm or larger is sufficient to ensure that the substrate loss has negligible effect on the cavity Q, i.e., does not reduce it substantially below 250,000. Fig. 5.13(b) shows that for MC-STM (TM_{11}) designs, the *same* undercladding thickness requirement (about 1.2 μm) ensures that the Q is unaffected in the relevant range of aspect ratios $0.05 < A_R < 3.2$.

In this situation too, we encounter similar characteristics in the "equivalent" MC-STE and MC-STM designs. In the context of design of isolated resonators, it has been discovered that a set of equivalent MC-STE and MC-STM designs exists, with different aspect ratios, but largely matching performance in terms of achievable high-Q FSR, sensitivity, tunability, substrate leakage and heating

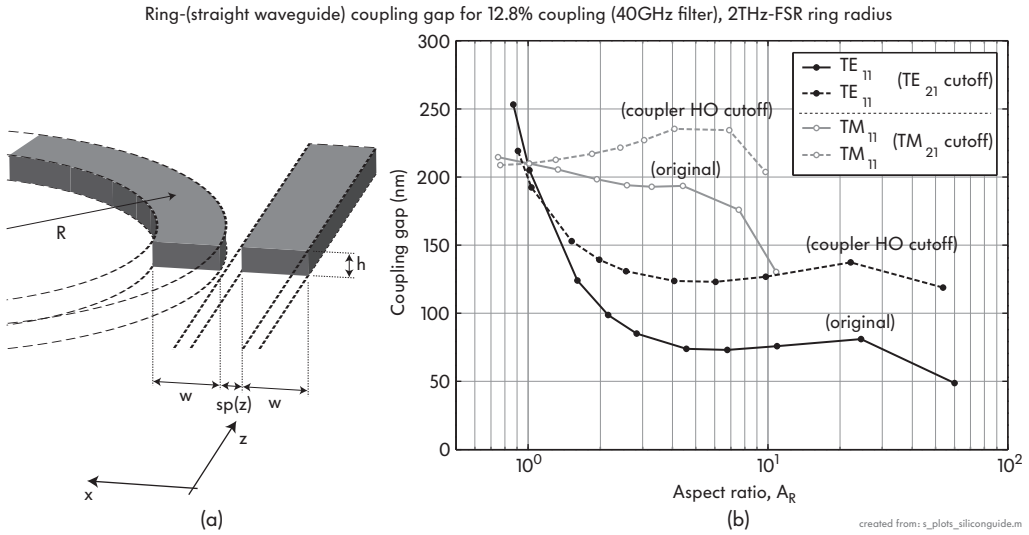

Figure 5.14: Coupling gap vs. aspect ratio of MC-STE and MC-STM designs, for a circular ring coupling to a straight bus waveguide of same cross-sections: (a) geometry, (b) the coupling gap is chosen to provide a 12.8% cross-state power coupling at a radius that provides a 2 THz FSR and therefore supports an exemplary telecom-compatible third-order SCC filter design with a 40 GHz bandwidth. All designs require no less than a 100 nm gap, and TM designs have gaps that are twice as wide, but also waveguides that are taller.

element absorption losses.

5.2.4 Directional coupler design and parasitic mode suppression

In general, in the construction of resonator-based devices, excitation of a resonant cavity entails direct or evanescent coupling to other resonators or waveguides. Next, minimum coupling gaps for in-plane evanescent coupling and coupling coefficient sensitivity to error in waveguide width and height are examined.

Minimum coupling gap size (for a 40 GHz microring filter)

Continuing with designs in Fig. 5.2, ring-to-straight-bus waveguide coupling gaps are considered, for various aspect ratios, that provide 12.8% ring-bus power coupling coefficient. This ring-bus power coupling coefficient is necessary to realize a 40 GHz-wide, 3rd-order (3-microring) bandpass filter with a 2 THz FSR. Fig. 5.14(a) shows the ring-bus waveguide coupling geometry considered. For each aspect ratio, as usual, the TE_{11} mode of the MC-STE design and the TM_{11} mode of the MC-STM design are considered. For each case, the bend radius is chosen to be that provides a 2,THz FSR (not the minimum radius for a bend loss Q of 250,000). Then, the coupling gap is found that gives 12.8% single pass power coupling.

Here, for the computation of each data point an optimization problem must be solved to find that coupling gap which provides the desired power coupling coefficient. Therefore, the computation has been done using a semi-analytical

approximation, using accurate, numerically solved mode distributions, and accounting for the bent coupling region in an analytical way, using coupled mode theory, to allow the estimate to be computed in reasonable time for a large number of coupling gap values. This means that the values may be inaccurate even on the order of 50%, but the dependence, relative comparison and scaling are trustworthy, and therefore useful information may be extracted from these computations.

Fig. 5.14(b) (solid lines) shows the estimated coupling gap vs. aspect ratio that is needed. This plot shows the first significant difference found between otherwise equivalent MC-STE and MC-STM designs. For $A_R > 1$, the coupling gap does not change very strongly with aspect ratio for either design, but the MC-STM gaps (on the order of 200 nm) are twice as wide as the MC-STE gaps (on the order of 100 nm).

Minimum coupling gap sizes are an important consideration for several reasons associated with fabrication technology. First, in lithography, at this scale wider coupling gaps are easier to realize, and therefore MC-STM designs may be better suited to lower-resolution lithography, such as conventional photolithography and deep-UV lithography. Both designs are suitable for scanning electron beam lithography (SEBL). Secondly, in the context of etching, the aspect ratio of the gaps, measured as the waveguide height to gap width ratio, is more relevant. This is a measure relevant for the ability to create such gaps by etching, as well as for the ability to fill these gaps with an overcladding material, such as a spin-on glass, in cases where an overcladding is to be used. In this second category, the MC-STE and MC-STM designs are again approximately on par, since the gap in the MC-STM cases is about twice as large, but at the same time equivalent MC-STM designs are generally about twice as tall as the corresponding MC-STE designs (as shown also by specific example below).

Elimination of reconfined parasitic supermode in couplers

For efficient, low-loss filter designs, a correction must be made in the waveguide cross-sections that is specific to high-index-contrast directional coupler regions, to eliminate a parasitic high order supermode. If one designs an HIC waveguide cross-section to support only one TE and one TM mode, as in the MC-STE designs of Fig. 5.2, this ensures no spurious higher-order modes are present to couple to and cause crosstalk and loss. When two such waveguide are placed in close proximity side-by-side, in addition to two supermodes that emerge from coupling (a symmetric and an antisymmetric mode, if the coupler is symmetrical), a third mode may become guided. This is shown by an example in Fig. 5.15(a), showing the dominant electric field of an $A_R \approx 6$ MC-STE design TE_{11} symmetric coupler mode, and a parasitic third-order TE_{31} mode also confined at a gap of about 100 nm.

This confinement of a higher-order mode to provide a larger number of guided modes in the collective system than the sum of guided modes of the two individual

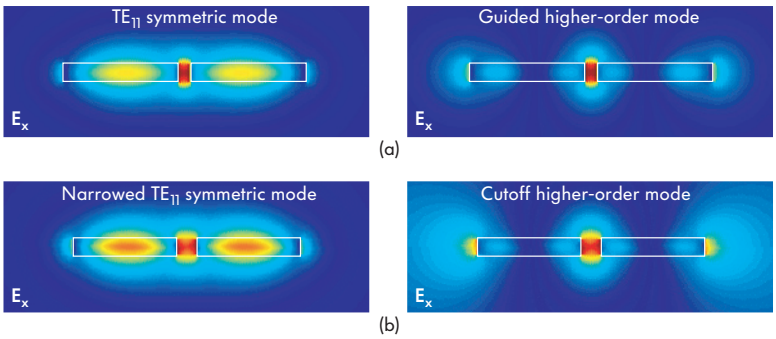

Figure 5.15: Mode field profiles of the fundamental symmetric TE mode (TE_{11}) and the parasitic, third TE mode (TE_{31}) that forms in a directional coupler formed of two (single-mode) MC-STE design waveguides. A coupling gap is chosen that gives TE_{11} mode coupling of 12.8% (for a 40 GHz passband filter with 2 THz FSR) with one straight guide and one at the minimum bend radius in Fig. 5.6. (a) TE_{11} and TE_{31} supermodes in coupler formed of nominal waveguide designs from Fig. 5.2, (b) TE_{11} and TE_{31} supermodes in coupler with waveguide width narrowed (adjusting the gap to maintain prescribed coupling) by numerical modesolver to drive supermode TE_{31} at minimum gap to cutoff.

waveguides occurs in the strong coupling regime. For example, if the waveguides are placed immediately next to each other to form a single waveguide that is twice as wide (a zero gap), the lateral dimension may be more strongly confined at the expense of slightly weaker confinement in the vertical dimension, such that a third mode, that is near cutoff, may become guided. This is counter to intuition one might take from the behaviour of slab waveguides, which have an analytical solution, and do not show this effect. Namely, the number of modes in a slab waveguide is given by the V-number divided by $\pi/2$, where the slab V-number is defined as $V = k_o w/2\sqrt{n_{\text{core}}^2 - n_{\text{clad}}^2}$, w is the slab width, and k_o is the free-space wavenumber. Thus the number of guided modes in a slab waveguide is

$$N = \left\lfloor \frac{V}{\pi/2} \right\rfloor = \left\lfloor \frac{w}{\lambda_o/2}\sqrt{n_{\text{core}}^2 - n_{\text{clad}}^2} \right\rfloor$$

where $\lfloor \cdot \rfloor$ indicates rounding down to the nearest integer. Now if one takes a slab waveguide with one guided mode, such that its second mode is at cutoff, it's V number equals $\pi/2$. If two such waveguides are placed adjacent each other with small gaps, they will have strong coupling and at least two modes (one for each waveguide) with propagation constant splitting of these supermodes representing the coupling. If the gap is zero, the two slab waveguides touch, and one obtains a single waveguide of twice the width. This wider waveguide, according to the above expression, has twice the V number. Since the V number of the original waveguide is $\pi/2$ (having only one mode), the V number of the new waveguide is π and it

has exactly and no more than 2 modes. This is independent of polarization. Thus, appearance of the additional modes seen in 3D HIC waveguide couplers requires the additional physics allowed by the vertical degree of freedom for confinement available in 3D waveguides.

A way to justify the existence of the confined supermode is to account for the fact that coupling of degenerate modes causes splitting in effective index – larger with stronger coupling. The fundamental modes split and form the symmetric and antisymmetric coupler supermodes. If each waveguide is at cutoff of the second-order mode, the latter have an effective index equal to the cladding index. When the waveguides are coupled, these modes at cutoff are degenerate and may be thought to split due to coupling. In doing so, one of them goes up in effective index and becomes guided, while the other dives further down into the radiation spectrum and is further from cutoff. Of course, this analogy gives only plausibility as there is a common-mode effective index shift which may shift both modes up or down in effective index due to coupling, as occurs with the slab case described.

This existence of the higher-order, spurious modes is undesirable, and the ring, the bus waveguide or both may be made narrower to cut off such modes even in the coupled configuration (at the design coupling gap). In the present discussion, the ring and bus waveguide are symmetrically narrowed (i.e. both equally narrowed) to ensure the absence of the higher order mode. Fig. 5.15(b) shows the corrected MC-STE coupler design at an $A_R \approx 6$ – the TE_{11} symmetric coupler mode, and the cutoff parasitic third-order TE_{31} mode field extending indefinitely in lateral extent.

The dotted lines in Fig. 5.14(b) show the modified coupling gap curves. Since the waveguides are narrower, the field is slightly more expelled from the core and the coupling is stronger for a given coupling gap, hence the gaps increase for the given required coupling. The sensitivities also slightly change, since these do not represent the maximally confined (MC) waveguide designs. These designs are below and to the left of the corresponding (MC-STE or MC-STM) curve in Fig. 5.2, and they are shown in Fig. 5.16 for the particular coupling strength chosen in Fig. 5.14(b). Fig. 5.16 shows a directional coupler designed using each waveguide aspect ratio, with width adjusted to ensure the absence of a third (parasitic) mode, the first and second modes being the usual symmetric and antisymmetric modes of interest in the coupler. The increase in coupling gap as a result of modifying the waveguide cross-section is limited, but the TM designs still have about twice the coupling gap for most aspect ratios in the range $A_R > 1$.

In the case of the corrected designs shown in Fig. 5.16, the width is narrowed by between 0 and 10% (in both the MC-STE and MC-STM designs) in order to cut off the relevant coupler mode, in the case of aspect ratios $A_R > 1$ (aspect ratios $A_R < 1$ are not strongly susceptible to gaining extra parasitic modes under lateral coupling, so no substantial correction is needed). For example, the MC-STE design with a ∼6:1 aspect ratio Si–SiO_2 rectangular waveguide (Fig. 5.2) has

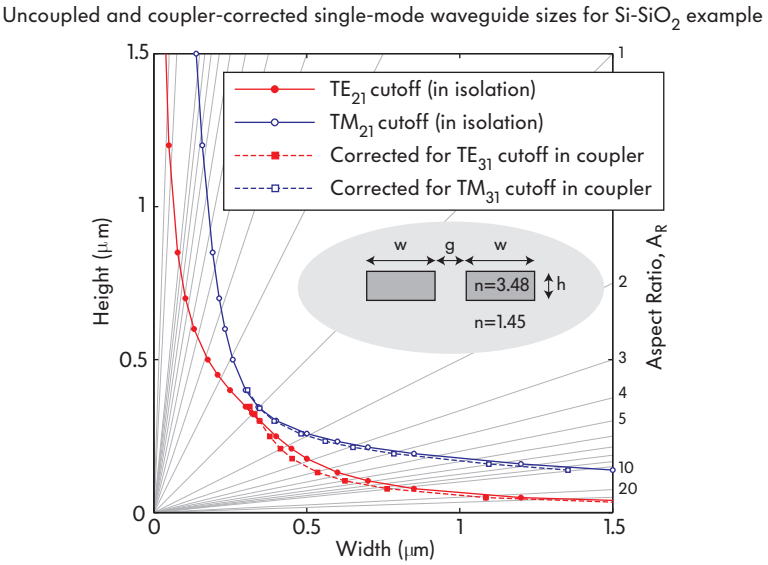

Figure 5.16: Map of maximally-confined single-TE and single-TM mode silicon waveguide cross-sections at each cross-sectional aspect ratio, with a second set of contours showing dimensions with waveguide width corrected at each aspect ratio to eliminate the third (parasitic) coupler mode at the corresponding minimum bend radius for each A_R and the coupling gap that gives a 12.8% coupling (see also Fig. 5.2). Data also shown in different form in Fig. 5.4.

about 675 nm width and 110 nm height. In order to produce a 12.8% coupler used in the example of a 40 GHz-bandwidth filter with 2 THz FSR, the width is narrowed to about 605 nm, consistent with Fig. 5.16. Similarly, in the case of an MC-STM design of aspect ratio 1.8:1 the nominal cross-section is 480×265 nm, but is narrowed to about 455×265 nm in the 12.8% coupler. These examples illustrate the correction applied to width for couplers, as shown in Fig. 5.16.

Since all TE waveguide designs have similar coupling gaps and all TM designs have similar coupling gaps, all being realizable using scanning-electron-beam lithography (SEBL) and the TM design also being suitable for photolithography in this example, the coupling gap does not select among the remaining admissable aspect ratios or mark a set of designs in the parameter space to be excluded, for the 40 GHz telecom filter design case considered here. Narrower filters will have wider coupling gaps, so the minimum coupling gap is unlikely to play a strong constraint in most applications.

Ring-waveguide coupling dimensional sensitivity

Next, the coupling coefficient sensitivity to waveguide width and height error is considered, for the coupling gaps in Fig. 5.14(b). Fig. 5.17(a) shows the width sensitivity of the power coupling coefficient corresponding to the four coupling gap cases shown in Fig. 5.14(b). Plotted is the fractional error in the power coupling coefficient (nominally 12.8%) per nm width error.

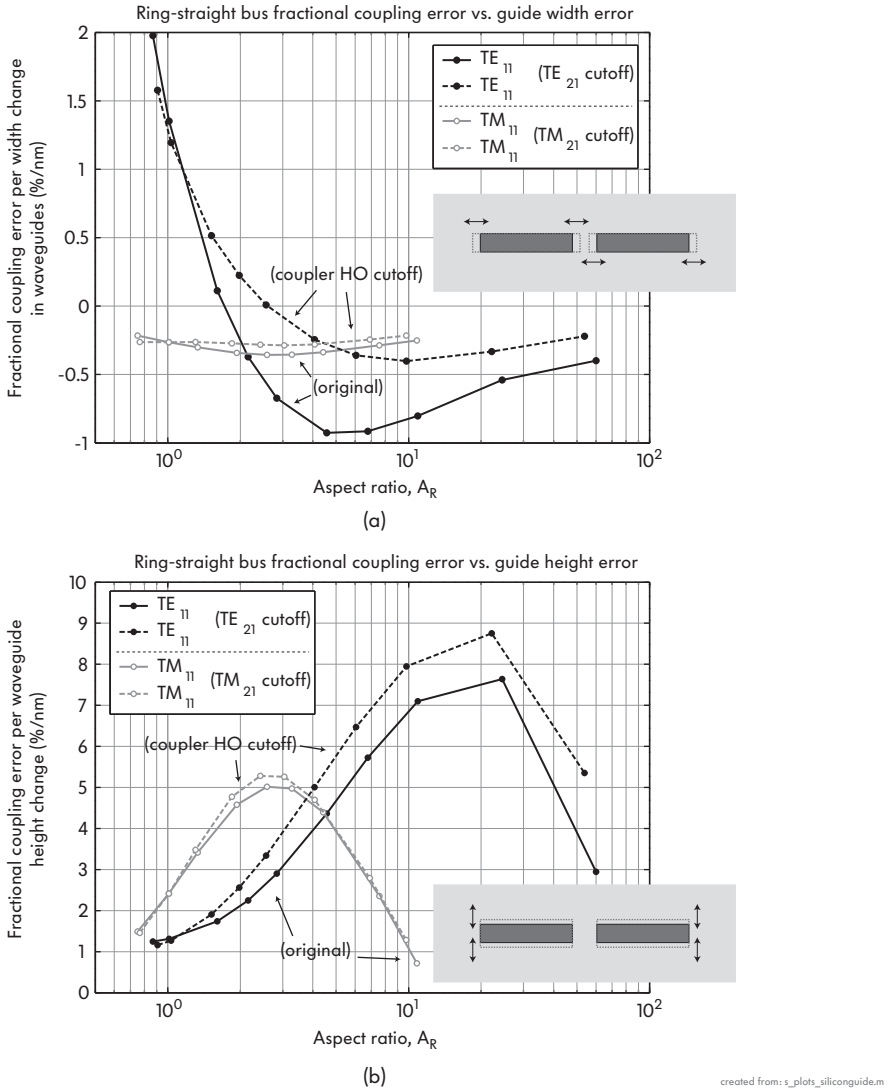

Figure 5.17: Ring-bus coupling sensitivity to waveguide (a) width and (b) thickness, vs. aspect ratio.

The zero point of sensitivity is attractive because the coupling coefficient there is insensitive to first order to errors in waveguide width. This occurs only for the MC-STE design for the plotted aspect ratios, around $A_R \approx 2.5$ for the higher-order-cutoff-corrected MC-STE case. In both corrected designs (i.e., dotted lines), for a typical width uncertainty of about 10 nm, which is achievable in SEBL, the coupling coefficient may be in error by about 4% of its value, which is generally an acceptable variation. Therefore, the waveguide-width sensitivity of the coupling coefficient does not select strongly over the field of remaining MC-STE or MC-STM designs.

The height sensitivity is more of a concern, as shown in Fig. 5.17(b). There, the fractional error in the coupling coefficient per nm error in waveguide height

is plotted corresponding to the four cases shown in Fig. 5.14(b). The MC-STE and MC-STM designs are corrected for the higher-order-mode cutoff in couplers (i.e., dotted lines). The TM design has larger sensitivity at a given A_R, but if *equivalent* MC-STE and MC-STM designs are selected, then the sensitivity of the TM and TE design is about the same for A_R up to about 3 in the TM case, and the corresponding A_R for TE up to about 6-7. Above $A_R \approx 3$, the TM design is less sensitive than TE, but the TM design at high aspect ratios also has very small FSRs, as described in Sec. 5.2.1.

The height sensitivity of the coupling coefficient is considerable for both the TE and TM designs, reaching on the order of 50% change in the power coupling coefficient per 10 nm error in thickness. However, thickness is very well controlled in fabrication, and may in addition be measured to high precision prior to the lithography step. For this reason, in the presented designs sensitivities to height are sacrificed in favour of optimizing sensitivities to width. Any designs will only need to be tolerant enough to height (i.e., core layer thickness) error to work properly within tolerances set by stochastic errors in measurement and on the wafer surface, and to tolerate slow variations of the height across the wafer, if the latter cannot be mapped. Typical values for thickness variation across a usable part of an SOI wafer may reach on the order of 1–2 nm (and 5 nm is guaranteed by SOI wafer manufacturers [126]). Hence reasonably large sensitivity to height may be tolerable, in comparison to width sensitivities.

5.2.5 Summary of optimized Si waveguide designs

Based on the analysis in the previous sections, Table 5.2 summarizes the constraints imposed by each consideration, for the MC-STE and MC-STM design, with reference to the relevant figures that are the source for each constraint. The constraining criteria in the example studied – a 40 GHz-wide add-drop filter with 2 THz FSR for telecom applications – are the resonance frequency sensitivity to lithographically defined, lateral dimensions on the low-A_R side ($A_R > 6$ for MC-STE and $A_R > 1.8$ for MC-STM); and the metallic heater optical absorption on the high-A_R side ($A_R < 7$ for MC-STE and $A_R < 2.5$ for MC-STM). They are indicated in bold in the table.

Concrete proposed Si waveguide designs

These computed bounds impose a fairly tight range on the usable aspect ratios that meet the chosen design constraints. Within this range, for the silicon devices demonstrated in this thesis, we chose the lowest possible A_R's to minimize heater loss (due to greater uncertainty in the realization of the microheaters). Hence, a MC-STE design with $A_R = 6$ and a MC-STM design with $A_R = 1.8$ is selected based on these criteria. The waveguide dimensions are summarized in Table 5.3.

Table 5.2: Summary of constraints on silicon waveguide design for tunable filters

Parameter	Condition	from Fig.	Waveguide aspect ratio constraints	
			TE (of MC-STE)	TM (of MC-STM)
Effective index	no crossing	5.5(a,b)	$A_R \neq 3$	$A_R \neq 3$
FSR	>2 THz	5.7	$0.5 < A_R < 15$	$A_R < 3.2$
Frequency vs. width	<40 GHz/nm	5.9	$\mathbf{6} < A_R$	$\mathbf{1.8} < A_R$
Thermal tunability	2 THz with ΔT =300° C	5.11(a)	$0.5 < A_R < 20$	$A_R < 3.5$
Si substrate loss	2 µm undercladding, Q ≥250k	5.13(a,b)	$A_R < 20$	$A_R < 5$
	<0.1 dB/cm	5.13(c,d)	$A_R < 20$	$A_R < 5$
Metal (Cr) heater loss	100 nm thick, Q ≥250k	5.12(b,c)	$A_R < \mathbf{7}$	$A_R < \mathbf{2.5}$
Coupling gap litho. compat.	40 GHz bandwidth, 2 THz FSR	5.14(b)	any	any (×2 TE gap size)
Gap sensitivity to guide width	<0.5%/nm	5.17(a)	$1.5 < A_R$	any (×2 TE gap size)
Gap sensitivity to guide height	(known/unif. to <5 nm, no cond.)	5.17(b)	challenging	challenging

Table 5.3: Dimensions of optimized silicon waveguides

Parameter	Waveguide design			
	MC-STE (TE_{11})	MC-STM (TM_{11})	Standard TE	units
Dimensions and optical properties				
Waveguide cross-section	675×110	480×265	440×220	nm
Aspect ratio	6.16	1.82	2	
Effective index	2.01	2.09	∼2.32	
Group index	3.36	4.43	4.17	
Radius for 2 THz FSR	7.1	5.4		µm
FSR for bend loss Q>250k	3.4	3.2		THz
Cr heater distance for Q ∼200k	1	1		µm
Ring-bus coupler correction				
Corrected size	605×110	455×265		nm
Gap for 40 GHz BW, 2 THz FSR	120	215		nm

The resultant A_R ranges represent an example of equivalent TE and TM designs as described in previous sections. Remarkably, these equivalent TE and TM designs have very similar performance on all criteria, except the gap sizes and other physical dimensions. The fabrication of silicon devices related to this work was done by electron-beam lithography, so both designs are acceptable with respect to constraints on minimum feature size.

Two further considerations are taken into account to decide between the TE and TM design: sensitivity to propagation loss due to waveguide surface roughness, and sensitivity of TE-TM mode parasitic coupling in the overmoded MC-STM design which may cause unwanted TE parasitic resonant peaks, since the overmoded TM design has two guided TE modes. This latter concern may prevent use of the TM design, at least without restricting further the overmoded approach taken here, if the polarization crosstalk is too large or resonantly enhanced.

Propagation loss sensitivity to roughness

The sensitivity to roughness for the chosen MC-STE ($A_R = 6$) and MC-STM ($A_R = 1.8$) waveguides is evaluated, and compared to the conventional 2:1 aspect ratio TE designs used in literature.

To evaluate sensitivity to roughness, results from a theoretical three-dimensional propagation loss model [127], which provides normalized loss maps for silicon waveguides, are used. The waveguide propagation loss sensitivity to waveguide roughness is estimated from normalized maps of roughness-induced loss vs. waveguide dimensions, shown in Fig. 5.18, reproduced from [127]. The waveguide designs presented here, the standard Si waveguide and the square, "polarization-independent" waveguide (see Fig. 5.9) are overlaid in the figure.

A loss estimate computation is shown in Table 5.4 for the MC-STE and MC-STM designs and for a standard cross-section Si waveguide. Estimates for expected sidewall roughness and top/bottom wall roughness in fabrication processes available to the projects associated with this work are included in the table**. While several approximations and empirical guesses were made, an attempt was made to provide reasonable estimations of the relative merits of the waveguide designs, as well as some plausible projections of the achievable propagation losses.

The results show that both optimized waveguide designs, MC-STE and MC-STM, should allow waveguide losses of the order of 1 dB/cm to be obtained, with the estimated roughness parameters (where worst case bolded values were used, see Table 5.4). This is over 3 times lower loss than the standard Si waveguide design, estimated at about 3.5 dB/cm with the assumed loss parameters. The latter is consistent with published propagation losses in Si waveguides of standard dimensions [99, Table 1],[117]. Although more recent results have shown lower losses of about 1.7 dB/cm [128] in similar 2:1 aspect ratio TE waveguides, this should

**Estimated by T. Barwicz.

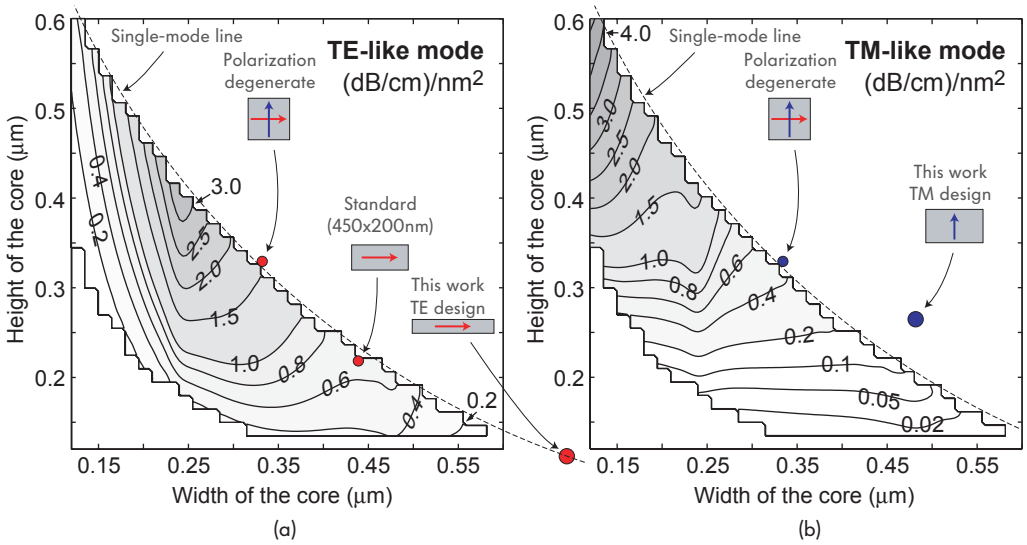

Figure 5.18: Propagation loss sensitivity to waveguide sidewall and top/bottom surface roughness vs. aspect ratio: (a) TE polarized modes, (b) TM polarized modes. The map of roughness-induced loss vs. waveguide dimensions is based on a rigorous 3D model and is reproduced directly from [127] (provided by T. Barwicz). The proposed waveguide designs are indicated on the map.

be accountable to better roughness numbers than assumed in the estimates done here, and accordingly the proposed waveguide designs will improve accordingly with such better fabrication.

Corresponding to the estimated losses, loss-limited Q's of 500,000 should be achievable even with the somewhat pessimistic roughness characteristics assumed. It is worth noting that glass reflow techniques on free-standing silica resonators have yielded Q's that are orders of magnitude larger – 100 million [129] – but such reflow approaches lead to poor dimensional control that is not suitable for high-fidelity filtering components that require 10 nm-scale absolute dimensional control and small coupling gaps on the order of 100–200 nm.

Competition of unused guided modes under perturbation

Another important consideration is the competition of unwanted modes in resonators based on the proposed waveguide designs. Table 5.4 also shows the Q's of the other guided modes in each design. In the microring resonators based on the MC-STE design, with a radius of 7 μm for a 2 THz FSR, the unused fundamental TM mode has a Q of only 10, limited by the bending loss. This Q is low enough that the resonance can be considered quenched and should not pose as a substantial loss mechanism to TE resonant structures. Furthermore, the excitation of TM resonances by perturbations will be weak due to the nominal orthogonality of the TE excitation and the TM resonant mode, which further suppresses its excitation.

In the MC-STM design, there are two unused TE modes – the fundamental TE_{11}

Table 5.4: Estimated losses of optimized silicon waveguides (where a range is given the bold value is used)

Parameter		Waveguide design			
		MC-STE (TE_{11})	MC-STM (TM_{11})	Standard TE	units
Waveguide cross-section		675×110	480×265	440×220	nm
Primary mode loss		TE_{11}	TM_{11}	TE_{11}	
Guess roughness σ^2	sidewall		∼5		nm^2
	topwall		∼0.01-**0.1**		nm^2
Roughness loss coefficient, x	sidewall	0.05< x <**0.1**	0.1< x <**0.2**	0.7	(dB/cm)/nm^2
(from [127, Fig. 12])	topwall	x >6	x ∼3	1.75	(dB/cm)/nm^2
Estimated roughness loss	sidewall	0.5	1	3.5	dB/cm
	topwall	0.6	0.3	0.175	dB/cm
	total	1.1	1.3	3.675	dB/cm
Achievable roughness-limited loss Q	total	530,000	595,000	200,000	
Bending-loss limited Q		∼10^8	∼10^8		
Secondary mode loss		TM_{11}	TE_{11}		
Group index		1.58	4.09		
Roughness loss coefficient, x	sidewall	x <0.005	**0.4**< x <0.7		(dB/cm)/nm^2
(from [127, Fig. 12])	topwall	x ∼0.2	**1**< x <1.5		(dB/cm)/nm^2
Estimated roughness loss	sidewall	0.025	2		dB/cm
	topwall	0.02	0.1		dB/cm
	total	0.045	2.1		dB/cm
Achievable roughness-limited loss Q	total	6,000,000	340,000		
Bending-loss limited Q		∼10 (dead)	∼10^{14}		
Higher-order mode loss		n/a	TE_{21}		
Bending-loss limited Q		n/a	∼20 (dead)		

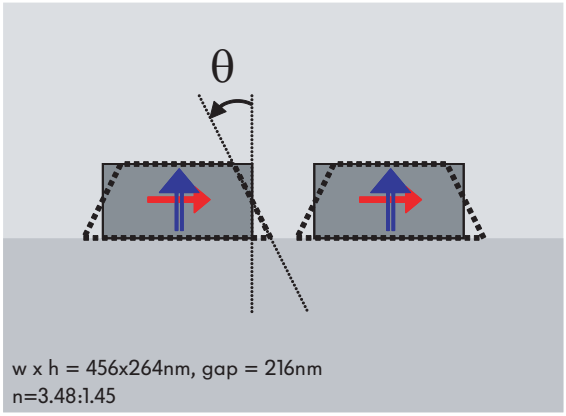

Figure 5.19: Waveguide wall-slant geometry for evaluation of parasitic polarization crosstalk in directional couplers of proposed MC-STM waveguide designs.

mode, and the higher-order, guided TE_{21} mode. Table 5.4 shows that the higher-order mode bending-loss limited Q is ∼20, due to its weak confinement. On the other hand, the fundamental TE mode is not limited by bending loss, and with the assumed roughness parameters can have a loss-limited Q in the hundreds of thousands (300,000 in Table 5.4). This means that the TE mode will be present, but in principle unexcited due to the orthogonality with the TM excitation. However, any perturbations that break the symmetry, such as sidewall slant in the directional coupler, will couple the polarizations and cause crosstalk. The magnitude of this crosstalk is evaluated in the next section in order to find whether the TM variant is usable under practical conditions.

5.2.6 Polarization crosstalk sensitivity of overmoded TM design

In this section, an example third-order channel add-drop filter using the MC-STM waveguide design is used to investigate the effect of wall slant on polarization crosstalk and cross-polarized resonant effects, and estimate their practical detrimental significance for the MC-STM Si waveguide designs. Figure 5.19 shows the cross-section of a directional coupler in such a filter. The wall slant angle is θ, with vertical sidewalls for $\theta = 0$, and a non-zero θ giving a symmetric camber.

The same filter considered thus far is investigated, having a 40 GHz-wide passband with 2 THz FSR. The coupling gaps are chosen to provide a flat, Chebyshev-shaped passband with 0.05 dB ripple over 33 GHz (∼20 dB through-port extinction) in the ideal case.

Computing TE-TM crosstalk due to wall slant

The TE and TM crosstalk coupling is computed using numerically computed modes of the ideal (vertical-walled) directional coupler, where the effect of wall slant is computed perturbatively using coupled mode theory, formulated in a suitable way

for high-index-contrast waveguides. This is necessary because the relevant wall slants in practice are very small (typically $\leq 5^\circ$, e.g., 1-5°), and the Cartesian discretization of the computational domain would lead to excessive errors when trying to compare waveguides with small differences in wall slant. For small angles $\theta < 20^\circ$, the derivative of the coupling coefficient between two (super)modes in the waveguide or coupler, i and j, due to perturbative wall slant can be computed, $\partial\kappa_{i,j}/\partial\theta$. The wall-slant-induced coupling introduces a linear term in the vertical coordinate into the overlap integral, and can be shown to evaluate as

$$\frac{\partial\kappa_{i,j}}{\partial\theta} = \frac{\frac{1}{4}\int_{\text{sidewall}} \mathrm{dy}(y-y_o)\left(\Delta\epsilon\vec{E}^*_{i\parallel}\vec{E}_{j\parallel} - \Delta(\epsilon^{-1})\vec{D}^*_{i\perp}\vec{D}_{j\perp}\right)}{\iint_{\text{cross-section}} \vec{E}_j\times\vec{H}^*_i + \vec{E}^*_i\times\vec{H}_j\cdot\hat{z}\mathrm{dA}}$$

Here, y_o is the position at the mid-point of the vertically symmetric structure, so that a wall-slant does not introduce an average width change to first order (treated separately). Then, coupling coefficient $\kappa_{i,j}$ is approximately found for small angles as

$$\kappa_{i,j} = \left.\frac{\partial\kappa_{i,j}}{\partial\theta}\right|_{\theta=0}\cdot\theta$$

For $\theta = 0^\circ$, the uncoupled case is recovered whose modes are the basis modes, and coupling is zero. This model is later rigorously justified in Fig. 5.21(b).

Regular TM filter operation

For illustration, it is assumed that the filter of interest operates in TM mode ideally, as intended in the MC-STM design. It is also assumed that the microring cavities have TE resonances, as they are likely to have, at a different but nearby frequency. First, operation is considered when TM input excites the TM resonances [Fig. 5.20(a)] and when TE input excites the TE resonances [Fig. 5.20(b)], before considering crosstalk (TM input exciting TE resonances) illustrated in Fig. 5.20(c).

Fig. 5.20(a) illustrates TM input at a wavelength near the resonant TM passband of the filter, showing excitation of the TM microring resonances, and TM through and drop port outputs. An exemplary drop and through port response of this filter is computed by coupled mode theory in time, with crosstalk coupling coefficients supplied by the perturbative computation described in the previous section. The response for various TM input wavelengths near the passband, using TM input and measuring the TM polarized light in the through and drop port outputs shows the normal intended operation of such a filter, based on the MC-STM waveguide design.

Fig. 5.20(b) illustrates TE input at a wavelength near the TE resonances of the microring cavities comprising the filter, showing the excited TE resonances of the microring resonators. These resonances are formed of the unwanted secondary TE_{11} waveguide modes of the MC-STM design. It is assumed for the moment that both the TE and TM resonances are lossless – the worst case scenario for crosstalk.

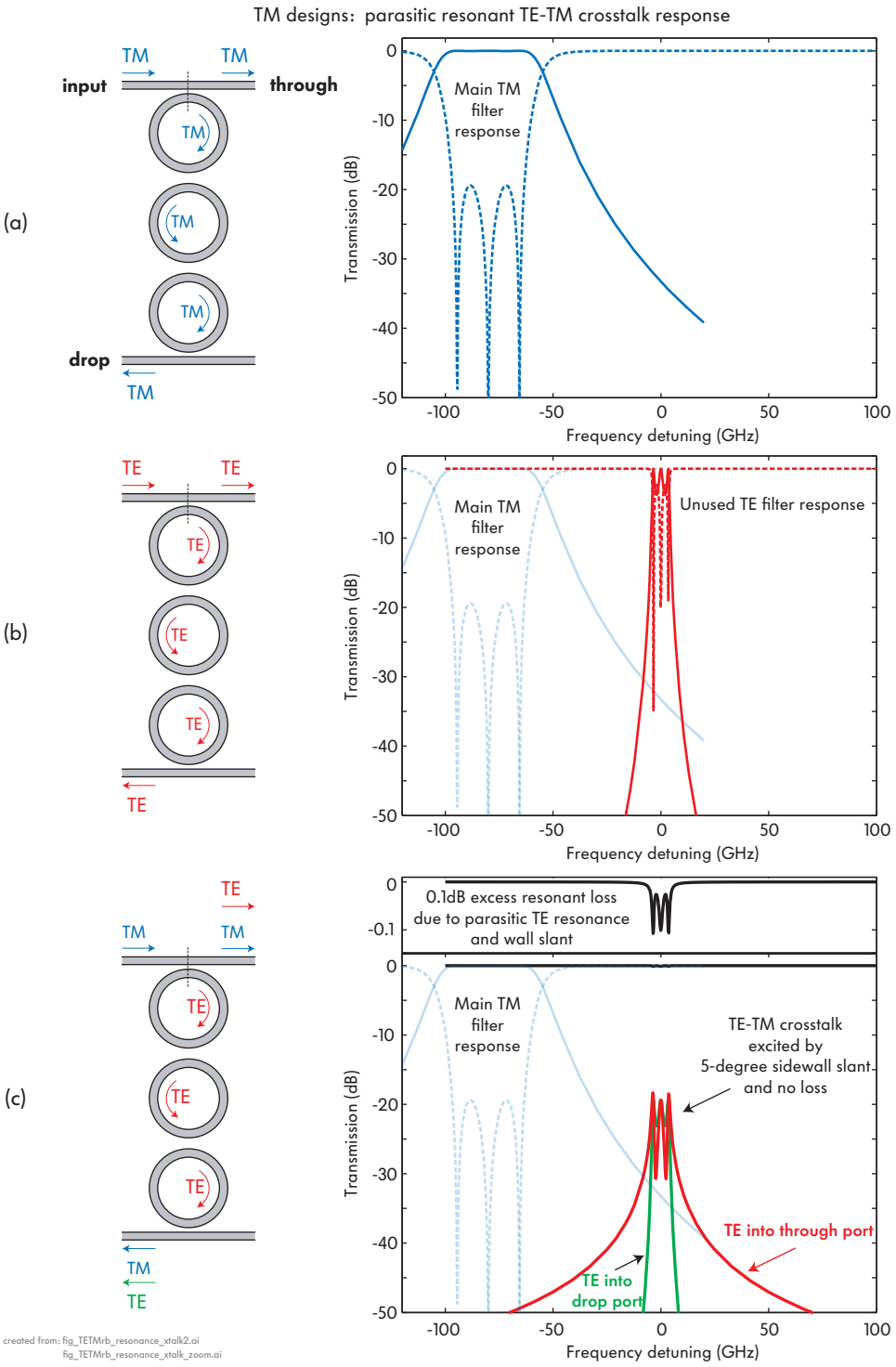

Figure 5.20: Parasitic TE response in MC-STM filter due to wall-slant-induced polarization coupling: (a) exciting TM resonances by a TM input produces the primary desired response; (b) exciting TE resonances by a TE input produces a narrow TE response (this way of exciting the structure is not a normal mode of operation as this is a TM device); (c) exciting TE resonances by the primary TM input signal, due to wall-slant-induced polarization crosstalk in the directional coupler, leads to spurious TE resonant responses which mix with the main TM signal. The TE parasitic response is below -20 dB for wall slant $\theta < 5^\circ$.

The filter response is as shown is narrower in bandwidth and has high ripple, unusable as a filter. This is because the coupling gaps were designed to provide a flat-top passband for the TM polarization. Since the TE polarization is more strongly confined, the coupling is weaker and therefore the bandwidth is narrower. However, the transmission to the drop port, when on resonance with each of the supermodes, is still nearly 100%, because zero loss was assumed and the critical coupling condition is satisfied. This response is not of particular concern, because the filter is intended to have only TM input. However, it illustrates that if excited by TE light, the filter drops 100% of it at certain wavelengths.

Filter operation with polarization crosstalk

With this in mind, the polarization crosstalk situation can be considered. Fig. 5.20(c) illustrates monochromatic TM input at a wavelength near the TE resonances of the microring cavities comprising the filter, showing excited TE resonances due to the crosstalk from TM to TE in the input directional coupler. A 5° wall slant is assumed. A wall slant of 2-3° can be easily achieved with present-day fabrication techniques. Polarization crosstalk in the other couplers may be ignored as it contributes second order effects (once TM excites TE in the resonator, most of the light stays TE rather than converting back to TM).

The amount of TE and TM light transferred to the through port and to the drop port should be considered. If there is significant TM light dropped into the drop port, unwanted crosstalk at the TE resonant frequency results. If there is significantly less than 100% of TM light passing to the through port, it also means that a significant amount of conversion to TE is acting as a loss mechanism and extracting TM power - thus potentially attenuating and distorting a through-port channel. TE light leaving the through and drop ports is undesired but is of less concern because it may easily be cleaned up by passing the through-port output through a polarizer (bulk or waveguide integrated). Since the used polarization is TM, TE will be filtered by the polarizer. Integrated waveguide polarizers are well known and designs are readily available in literature for HIC waveguides [130]. Furthermore, such polarizers are already an intrinsic part of a polarization divesity scheme [20, 33] as polarization splitters serve this function too; hence, no additional components are needed to reject the cross-polarized light (to the degree of extinction of the polarization splitter).

Fig. 5.20(c) shows the drop and through port responses when TE and TM polarized output light is observed, near the TE resonant frequency of the resonant cavities comprising the filter. In this case, the transmission of the TE light excited by the TM input is of a similar passband shape to the TE resonance, but is considerably attenuated. The reason follows. The TE-TM coupling is much smaller than the also small TE-TE coupling, because in the former near polarization orthogonality weakens the coupling. However, the TE light resonating in the rings due to cross-

polarization excitation from the TM input is primarily leaving the rings through the much stronger TE-TE ring-waveguide coupling, to the drop and through waveguide TE modes. Therefore the Q (bandwidth) of the filter is determined by TE-TE couplings, and thus the filter drop-port response shape is similar to the TE-excited response in Fig. 5.20(b). The amplitude of the response is proportional to the input coupling, i.e., the fraction of light coupled in from the input port. Since the TM-TE crosstalk coupling is much weaker than TE-TE coupling, the response is attenuated by 20 dB. Since the input side ring-bus coupling and the output side ring-bus coupling are equal, the intensity and shape of resonant response dropped into the TE polarization in each port is about the same (i.e., at about -20 dB).

Since 1% of power is converted to each of a TE signal in the through port and a TE signal in the drop port on resonance, it is of interest to evaluate the loss to the TM input. The through port shows a flat TM transmission, indicating that little power is lost. A closer look shows about 0.1 dB loss at TE resonant wavelengths, which amounts to about 98% transmission, accounting for all input power. There is no significant power dropped into the TM polarization in the TM port, which would constitute crosstalk. This is because the TE-TM coupling of the output is much weaker than TE-TE coupling, thus the TM response is at least 20 dB below the TE response, i.e., around -40 dB.

Scaling of polarization crosstalk with wall-slant angle

The above analysis considered 5° wall slant. It is of interest to consider how the amplitude of the transfer function representing the polarization crosstalk scales with wall slant. The spurious crosstalk, i.e., TE output due to TM input, approximately scales as

$$|H_{\text{spurious}}|^2 \sim \frac{k^2_{\text{TE,TM}}}{k^2_{\text{TE,TE}}} = \frac{Q_{\text{TE,TE(loss)}}}{Q_{\text{TE,TM(external)}}}$$

where $k^2_{\text{TE,TM}}$ and $k^2_{\text{TE,TE}}$ are respectively the polarization crosstalk and the TE-TE power coupling fractions in one pass of the input directional coupler, and $Q_{\text{TE,TM(external)}}$ and $Q_{\text{TE,TE(loss)}}$ are the respective associated ring external Q's (the latter acting as a loss Q). Therefore if the ratio of TE-TM polarization crosstalk coupling to TE-TE coupling is increased by a factor of 2, the total crosstalk simply increases by a factor of 2, i.e., by 3 dB.

Therefore, next it is investigated how TE-TM crosstalk depends on the wall-slant angle. A second way that in practice an asymmetry may be introduced is due to an unequal refractive index in top and bottom cladding. The polarization crosstalk coupling depends on them as follows:

$$k^2_{\text{TE,TM}} \propto \theta^2, \Delta\epsilon^2_{\text{clad(top-bottom)}} \tag{5.6}$$

where θ is the wall-slant angle, or where $\Delta\epsilon^2_{\text{clad(top-bottom)}}$ is the difference between the relative dielectric constants (i.e., square indices) of the overcladding (top)

and undercladding (bottom). If the wall-slant angle is reduced by half, crosstalk drops by a factor of 4, and the spurious crosstalk response is reduced by a factor of 4, or 6 dB. With respect to top and bottom cladding index matching, it can be calculated that the square-indices have to differ by about 4.5 to contribute the same level of crosstalk coupling as a 5° wall slant. This is a very large square index difference (between the top and bottom cladding) and it may be concluded that asymmetry between the overcladding and undercladding refractive indices is unlikely to play a significant role in polarization crosstalk, unless the index difference is purposefully made very substantial.

Coupled-mode computations of polarization crosstalk

TM-TE polarization crosstalk is much smaller than the TE-TE coupling in this analysis. Fig. 5.21 illustrates this by a coupled mode theory analysis. Fig. 5.21(b) shows the TE-TE and TM-TM power coupling coefficients in a directional coupler with symmetric waveguide cross-sections, one being a curved ring and the other a straight bus waveguide. Power coupling is plotted vs. wall-to-wall coupling gap, arrived at as follows. First, the coupling coefficient at the narrowest point is computed in two ways: exactly, by computing the supermodes of the coupler, and second, approximately by coupled mode theory. This result is then extrapolated to a total coupling through a curved coupling region by an analytical approximation [38, Appendix] in both cases. For each of the TM-TM and TE-TE couplings, the both results are plotted, showing very good agreement between coupled mode theory and exact modesolver results.

Fig. 5.21(a) shows the TM-TE crosstalk computed using coupled mode theory, and the analytical extrapolation, in two different ways. An exact modesolver result cannot be obtained for this geometry. However, the agreement between coupled mode theory and the modesolver result in Fig. 5.21(a) gives one confidence that this computation may be trusted for the purposes of crosstalk, where high accuracy is not required. The polarization-crosstalk power coupling, per 1 radian wall slant, is plotted vs. coupling gap as obtained from the two different coupled mode theory computations. Agreement is reasonable. The coupling for any wall slant angle may be obtained by scaling according to Eq. 5.6.

The 40 GHz filter design used as an example throughout (Fig. 5.20) requires a 215 nm ring-bus coupling gap in the MC-STM design. At that coupling gap, Fig. 5.21 shows that the TE-TM power coupling per 1 rad of wall slant is about 0.006 to 0.01, whereas TE-TE coupling is 0.006, about the same value. However, 1 rad (57°) is a very large wall slant. For a realistic 5° wall slant used so far, the TE-TM coupling is seen to be about 100-150 times smaller than the TE-TE coupling. Thus, the crosstalk TM resonant response at the TE resonance is about 20-25 dB lower than the TE crosstalk response (in the drop port).

This analysis shows that polarization crosstalk is large enough to be a concern

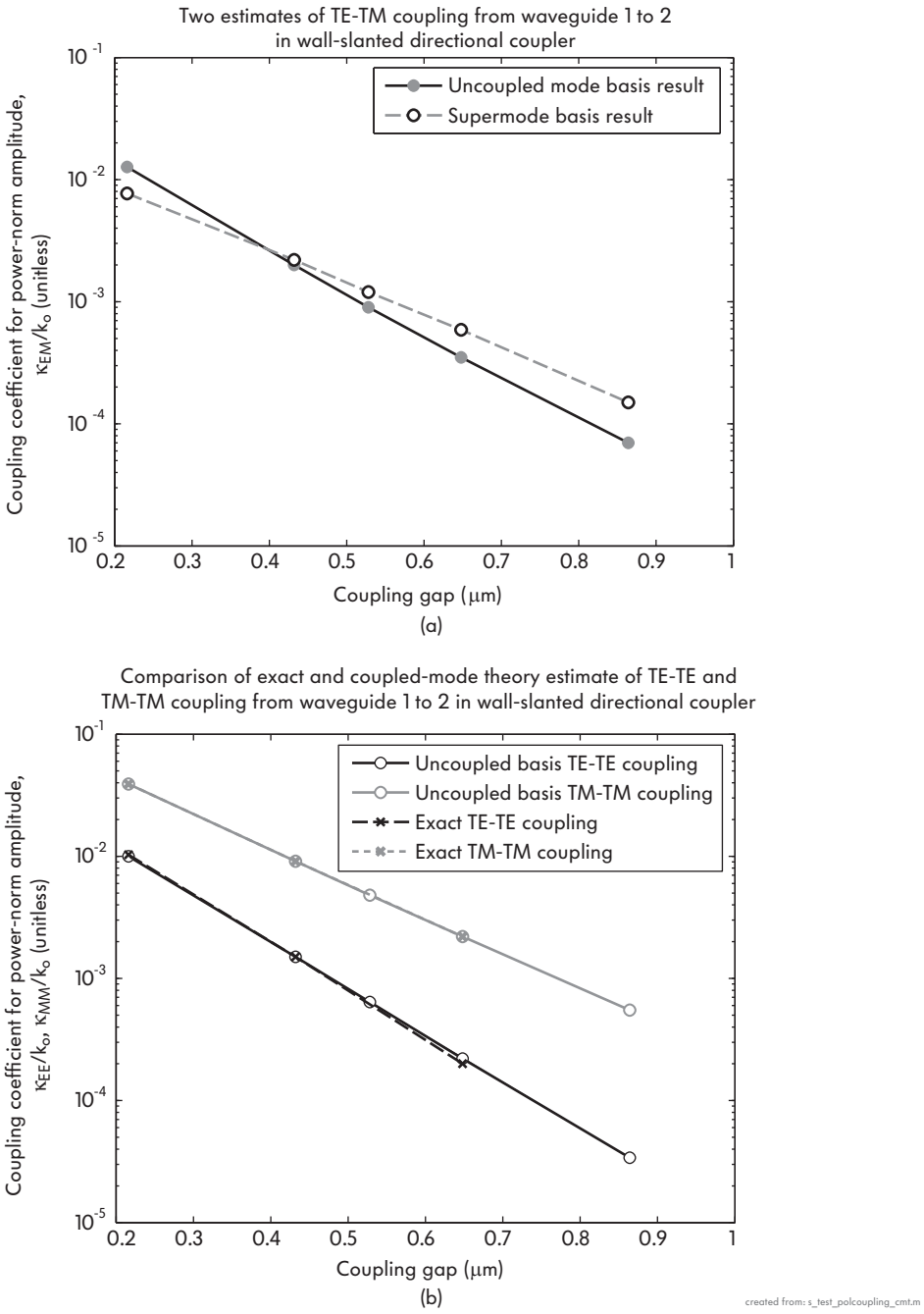

Figure 5.21: Polarization coupling due to wall slant by coupled-mode theory: (a) TE-TM coupling using an uncoupled mode basis, and using a supermode basis; and (b) TE-TE coupling and TM-TM coupling by coupled mode theory compared with numerical mode solver solutions for verification.

in the MC-STM design, but small enough that it can be tolerated with proper engineering, depending on the particular design. Therefore, on the one hand the MC-STM (TM polarized, overmoded) design has the advantage of larger coupling

gaps with all other performance metrics similar (high-Q FSR, sensitivities, tunability, etc.) to the MC-STE design, but the MC-STM design also has the drawback that the unwanted, well-confined fundamental TE mode must be carefully sidestepped in engineering to avoid excessive crosstalk and parasitic resonant losses.

Two other issues may be addressed in this context. First, if the TE and TM resonances of the resonators are co-resonant (i.e., at the same wavelength), crosstalk may be significantly enhanced, and may prevent a successful TM design. Therefore, care must be taken in misaligning the TE and TM resonances adequately in the TM design, where resonance placement sensitivity, i.e., resonance frequency sensitivity to perturbations will be important.

Second, the polarization crosstalk study in Fig. 5.20 used lossless resonances. However, introducing losses to reduce the polarization-crosstalk-induced loss in the TM through port, seen in Fig. 5.20(c), does not pay off greatly. The loss Q of the resonators must be reduced to about 15,000 in order to cut the through-port loss in half, i.e., to about 0.05 dB maximum and about 0.025 dB average across the passband. This would be a very large reduction in Q, and would cause significant losses and primary-mode (TM) filter shape distortion in the 40 GHz filter. Therefore, introduction of loss does not greatly help to quench the polarization crosstalk. The reason for this is that the TE-TE coupling, which is the loss mechanism determining the bandwidth of the spurious TE resonance, is already reasonably strong, and very large intracavity loss must be introduced to make an impact on the filter shape further by dominating over the TE-TE coupling as the primary loss mechanism.

5.3 Experimental results

In this section, the first and preliminary experimental results of fabricated Si waveguides and resonators based on the designs in this chapter are presented. Designs based on the MC-STE design, with a slightly modified 600×106 nm cross-section, are used, with and without overhead microheaters. Propagation losses of 2–2.5 dB/cm and loss Q's exceeding 250,000 are demonstrated in Si microring cavities with a central radius of ∼6.7 μm and an FSR of 2 THz. With microheaters at a 1 μm overhead displacement, the loss Q is reduced to ∼115,000, still well within the necessary bounds for the realization of low-loss high-order microring-resonator add-drop filters for telecom applications.

The structures used for experimental demonstration were waveguides and microring resonators in the undercoupled regime for accurate loss evaluation (see Appendix A). The heaters were formed of titanium metal rather than chromium as used in simulations, but their complex refractive indices at optical wavelengths are the same (Table 5.1) so a direct comparison can be made. Another difference from design is the overcladding – for practical reasons, rather than silica ($n = 1.445$) the overcladding used was hydrogen sesquisiloxane (HSQ) [131], with an index

$n \approx 1.38$. The loss ring method for cavity loss evaluation uses very weak ring-bus waveguide couplings and therefore large coupling gaps, which minimizes coupling region geometrical distortion in fabrication and associated optical losses, so that the intrinsic cavity losses dominate. First, the fabrication is summarized; then the optical characterization results described, together with the coupled-mode theory fitting model used to disembed the intrinsic losses and the results.

5.3.1 Fabrication of Si waveguides and resonators

The devices were fabricated[††] on a Unibond silicon-on-insulator (SOI) wafer with 3 μm buried oxide undercladding and a 220 nm silicon layer, thinned to 106 nm by calibrated steam oxidation and HF stripping. The thickness was measured after thinning, and all device designs adjusted for the 106 nm thickness.

The waveguides were defined by e-beam lithography using 60-nm-thick hydrogen silsesquioxane (HSQ) as e-beam resist and mask for reactive-ion etching (RIE) in pure HBr. HSQ was used as a hardmask because a detailed study showed that many metal hardmasks react with the Si waveguide core material to form thin metal silicides which introduce prohibitively high optical absorption losses [132].

After defining the waveguides by RIE, the e-beam exposed HSQ was removed and the structure was spin coated with a 1 μm layer of HSQ used as overcladding [131]. Next, 100-nm-thick titanium (Ti) heaters were formed on top of the HSQ by aligned contact photolithography, e-beam evaporation and liftoff. A second photolithography and liftoff step defined 100-nm-thick gold contact pads. The prepared chips were mounted on a designed copper thermal mass mount, and wire-bonded to specially designed circuit boards. A 100 nm layer of silicon oxide was sputtered as a crude passivation layer to slow down the oxidation of the Ti heaters at high operating temperature.

A scanning electron micrograph of an example 500 nm-wide (106 nm thick) Si bus waveguide is shown in Fig. 5.22(a).

5.3.2 Q measurement by the loss-cavity method

The waveguide loss and resonator loss Q were characterized by the loss ring method, where weakly coupled single-ring add-drop filters are designed whose linewidth is dominated by their intrinsic loss rather than external coupling. A measurement of the linewidth then gives a direct measurement of the internal cavity Q, and thus internal losses, with little uncertainty. A coupled-mode theory in time model is used to fit the experimentally obtained spectra.

Fig. 5.22(b) shows a typical drop-port response of a high-Q (weakly coupled) microring resonator. The drop port response is intentionally about 15-20 dB below

[††] All process design and development for the silicon device fabrication, and the device fabrication, was done by T. Barwicz. A brief summary of the fabrication is given here.

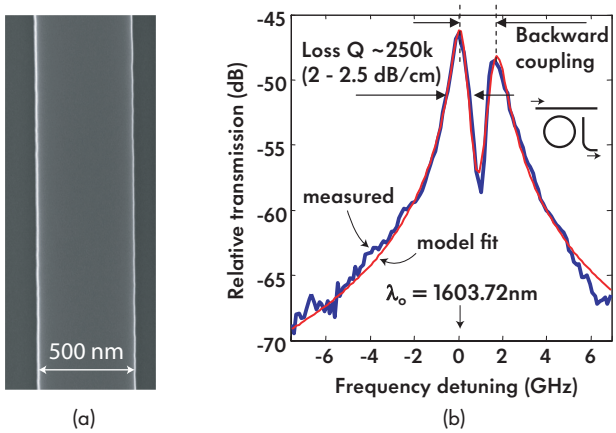

Figure 5.22: (a) Scanning electron micrograph (SEM) of fabricated Si waveguide, and (b) fitting of Si "loss microring" experimental response for experimental determination of loss Q .

the through-port response in these devices because the external coupling is weak and loss dominates. The linewidth, here on the order of GHz is directly indicative of loss. However, the lineshape is not Lorentzian, as typically found in single-mode resonators, but rather has a dual peak.

The double-peak is a signature of contradirectional coupling in the ring resonator directly, or indirectly via the waveguide coupled to the resonator. This is possible because microring resonators have two degenerate counter-propagating resonances at each longitudinal order. Roughness, surface scattering defects and shape non-idealities can couple the two counter-propagating modes.

Note that this contradirectional coupling happens in such narrow resonant cavities as these – used for loss testing. However, in a 40 GHz-wide filter, for which these cavities are designed, the small splitting due to contradirectional coupling will largely be suppressed by the line broadening due to strong coupling to external waveguides.

Taking this as all the essential physics in these spectra, a simple model fit is used to disembed the internal loss and contradirectional coupling.

CMT fitting model of microring cavity with contradirectional coupling

A simple single-cavity, two-mode coupling of modes in time model is used for fitting the experimental data, shown in Fig. 5.23(a), having two degenerate counter-propagating resonant modes, a_1 and a_2, coupled by an abstract coupling parameter μ_{12}. An input and output waveguide have coupling rates r_i and r_o, respectively, with each of the two modes.

The contradirectional coupling model can also be represented by an equivalent photonic circuit in Fig. 5.23(b), using only reflectionless (unidirectional) propagation. This makes more apparent the CMT equations for the model (reduced to only

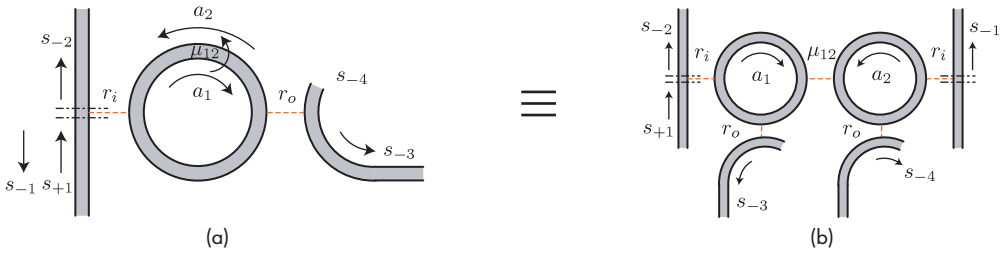

Figure 5.23: (a) Coupled-mode theory in time model of contradirectional coupling in a microring resonator filter, used for fitting high-Q microring cavity response spectra to disembed losses. (b) Equivalent photonic circuit in hybrid (reflectionless 4-port) form of the structure in (a), using unidirectional reflectionless propagation in all structures.

the input/output ports used) as follows:

$$\frac{\partial}{\partial t}\begin{bmatrix} a_1 \\ a_2 \end{bmatrix} = j\begin{bmatrix} \omega_o + j(r_i + r_o + r_l) & -\mu_{12} \\ -\mu_{21} & \omega_o + j(r_i + r_o + r_l) \end{bmatrix} \cdot \begin{bmatrix} a_1 \\ a_2 \end{bmatrix} - j\mu_i s_{+1}$$

$$s_{-3} = -j\mu_o a_1$$

where r_l is the cavity loss rate associated with each traveling wave mode, i.e. related to round-trip propagation loss. As usual in CMT, the decay rates are related to the couplings as $\mu_i^2 = 2r_i$, $\mu_o^2 = 2r_o$, and the intercavity coupling can be set as symmetric $\mu_{12} = \mu_{21}$ by assuming an appropriate reference plane. Then the measured response s_{-3}/s_{+1} of the system is

$$\frac{s_{-3}}{s_{+1}} = \frac{-2\sqrt{r_i r_o}}{j\delta\omega + r_{\text{tot}} + \frac{\mu_{21}\mu_{12}}{j\delta\omega + r_{\text{tot}}}}$$

where $\delta\omega \equiv \omega - \omega_o$, and the total cavity mode decay rate is $r_{\text{tot}} \equiv r_i + r_o + r_l$ due to the two ports and internal loss. This model has only 4 independent parameters, in addition to frequency: an arbitrary amplitude $r_i r_o$ (scaled by other transmission losses in the chip); a total decay rate that determines the Q, r_{tot} ($Q \equiv \omega/(2r_{\text{tot}})$); and a complex-valued coupling $\mu_{21}\mu_{12}$ that splits the modes, comprising a frequency splitting $|\mu_{21}\mu_{12}|$ and a "Q-splitting phase" $\phi_Q \equiv \angle\mu_{21}\mu_{12}$. The phase of the coupling is important. It determines the relative amplitudes of the two peaks in Fig. 5.22(b) and the overall shape. By fitting this phase over a wavelength range, an associated group delay can be disembedded that gives information about the physical position of the effective contradirectional-coupling scatterer. This will be addressed further elsewhere. Here, ϕ_Q is referred to as a Q-splitting phase because it can be shown that the supermodes of the system have complex resonance freqencies and Q's

$$\omega_{+,-} = \frac{\omega_o}{2} \pm \sqrt{|\mu_{21}\mu_{12}|}\cos(\phi_Q/2) + j\left(r_l \pm \sqrt{|\mu_{21}\mu_{12}|}\sin(\phi_Q/2)\right)$$

$$Q_{+,-} = \frac{\omega_o}{2}\frac{1}{r_l \pm \sqrt{|\mu_{21}\mu_{12}|}\sin(\phi_Q/2)}.$$

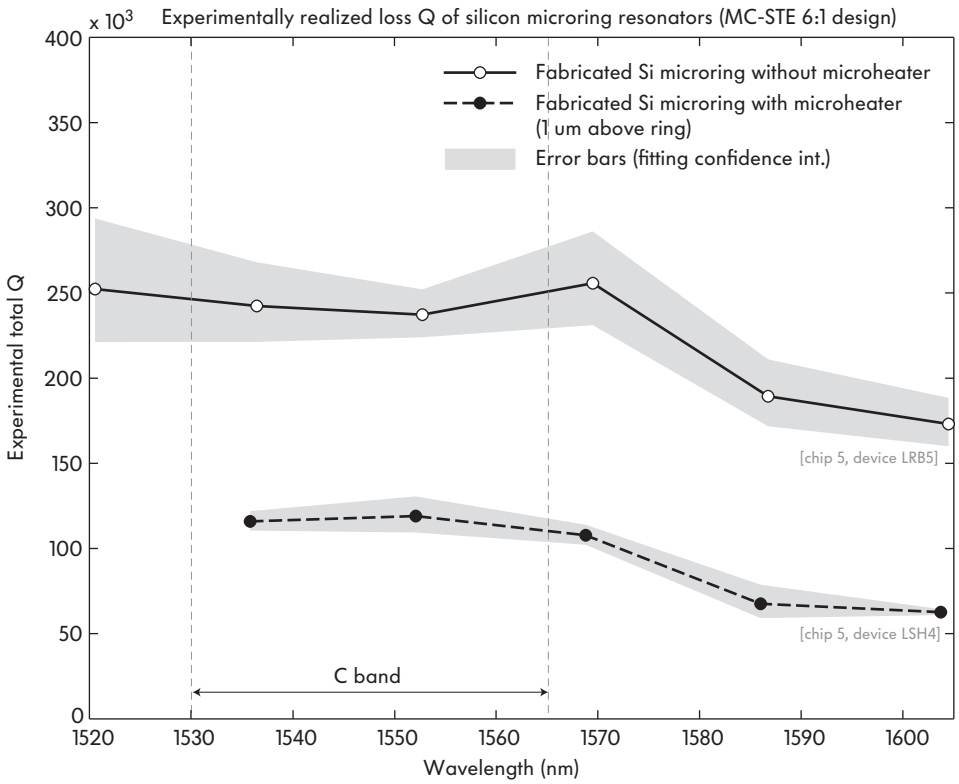

Figure 5.24: Preliminary experimentally measured loss Q of Si microring resonators based on the MC-STE design (Table 5.3). The actual design dimensions used here for the ring cross-section are 600×106 nm. The loss Q data is obtained by the "loss ring" method (see Appendix A), and extracted by fitting to a CMT model with backward coupling.

Returning to fitting the double-peak Lorentzian, the four parameter model can be used in amplitude form only, since the amplitude response is most easily measured in experiment, and fitted to extract the four parameters[‡‡]. If the ring is weakly coupled enough, the round trip loss will be much larger than the coupling to waveguides ($r_l \gg r_i, r_o$), and the total Q also gives the intrinsic loss Q.

Experimental measurements of Q

Results obtained in this way from two microring resonators, one with no overhead microheater and one with a titanium microheater at 1 μm displacement above it, are shown in Fig. 5.24. The microrings have an FSR of 2 THz (16 nm), so the Q and intrinsic loss is evaluated at six wavelengths from 1520 to 1605 nm. Lines show the fit disembedded results for the intrinsic loss Q, and the gray regions are the 95% confidence interval of the fit.

[‡‡]Since the used system drop-port response is minimum-phase, the amplitude and phase responses are uniquely related by the Kramers-Kronig relationship. Hence there is no extra information (fit improvement) to be gained by including the phase response in the model fit.

The results show that a metal-free Si ring cavity has a loss Q of 250,000 across the C-band telecommunications window (1530–1570 nm). This translates, through the group index to an effective propagation loss of 2–2.5 dB/cm (see Appendix B). With a microheater present, the Q is reduced to about 120,000 in this wavelength range. This would imply a Q associated with the metallic heater absorption of about 250,000, as designed, since it reduces the heater-free ring Q by a factor of two. These results agree remarkably well with the design estimates for loss (Table 5.4), in fact much more so than justified by the error bars in our estimations, and the changes and substitutions introduced between design and experiment. Nevertheless, the first attempt at demonstration gave agreeable results, consistent with the design, and it is hoped that process optimization will demonstrate further merits in these waveguide designs.

Furthermore the demonstrated waveguide loss and resonator loss Q's are sufficiently high to enable the demonstration of high-fidelity, telecom-grade resonant filtering devices, and they are therefore used in the design of Si filters in following chapters.

5.4 Conclusions

In this chapter, a systematic and rigorous design study of silicon-core, strongly confined microphotonic waveguides was presented and novel waveguide designs optimized for tunable microphotonic filters were proposed. Against a set of relevant criteria, wide and flat (6:1-aspect-ratio) TE and overmoded, 1.8:1-aspect-ratio TM designs were found to provide optimal properties, including sensitivity comparable to previously demonstrated, lower index contrast SiN resonators, and losses about 3 times smaller than conventional Si waveguide designs.

It was discovered that there exist corresponding sets of MC-STE (TE) and MC-STM (TM, overmoded) waveguide designs that have equivalent performance for TE and TM polarizations, respectively, in terms of frequency sensitivity, FSR, propagation loss sensitivity to surface roughness, metallic microheater optical overlap absorption, substrate leakage loss, sensitivity of ring-waveguide coupling to dimensional errors, etc. The equivalent designs generally have correspondingly equal effective indices. It is interesting, however, that their dimensions are different – waveguide width and height, resonator radius, coupling gap widths.

The TM design was found to support sufficient rejection of parasitic TE modes under perturbations to make it a relevant alternative design.

Finally, initial experimental demonstrations of fabricated TE waveguides and resonators showed microring cavity loss Q's of 250,000, corresponding to propagation losses of 2–2.5 dB/cm, and Q's ∼120,000 with a proximate metallic heater. These preliminary results validate the proposed designs and agree closely with the expected performance. They are well suited to enable high-fidelity microphotonic

tunable and reconfigurable filters in silicon, for chip-scale optical signal processing in rigorous telecom applications.

Chapter 6

Widely tunable strong-confinement channel add-drop filters

In this chapter, the rigorous design and first demonstration of widely tunable, wide-FSR channel add-drop filters, based on strongly confined silicon microring resonators, are described. Based on novel, optimized waveguide designs proposed in Chap. 5, low loss and sensitivities suitable to high-fidelity microphotonic devices for telecom-grade applications are demonstrated. Efficient, wide thermooptic tuning and amplitude response shapes independent of the tuned wavelength are demonstrated. The first telecom-grade, higher-order tunable channel add-drop filters are experimentally demonstrated with performance characteristics suitable for up to about 25 Gb/s channels in densely wavelength division multiplexed (DWDM), high-bandwidth optical networks.

First, the basic considerations of tuning silicon resonators are addressed, including the enhancement available due to the increase of the silicon thermooptic coefficient with temperature. The realization of microheaters integrated with waveguide designs from Chap. 5, and the experimental demonstration of wide (20 nm) thermooptic tuning of silicon microring cavities are described. Second, the strategy and architecture for creating C-band, widely tunable resonant channel add-drop filters is described. Methods to design tunable filter passbands that do not change spectral shape with tuned wavelength are addressed, including "resonant-frequency-independent coupling". Rigorous design of a fourth-order test filter is described based on 3D complex-frequency mode solver [91] and 3D finite-difference, time-domain (FDTD) [68] simulations, including coupling strength, minimization of coupler scattering loss and accounting for CIFS (Sec. 4.1). Simulated sensitivities of the coupling coefficients to temperature and dimensional error are discussed and exploited in the design, and prototype filter designs presented. Finally, the

experimental demonstration of these fourth-order tunable filters is presented. The experimentally demonstrated filters meet rigorous telecom-grade specifications, including over 20 dB through-port extinction ratio per stage (projecting 40 dB in a 2-stage design like those demonstrated in Sec. 7.1 [119]) and about 1 dB drop loss.

6.1 Maximizing the thermooptic tuning range of silicon resonators

In this section, maximization of the thermooptic tuning range of Si microring cavities is addressed and the demonstration of 20 nm-wide, full-FSR tuning of microring resonators with a 16 nm FSR is described, with a tuning efficiency of about 20 μW/GHz. This is a prerequisite for the construction of high-order, telecom-grade widely tunable and switchable channel add-drop filters, described thereafter. In addition, the switching speeds are evaluated, for applications using switchable filters proposed in Chaps. 8 and 9. Switching times of the order of 10 μs, typical of thermooptic actuation, are sufficient for tunable/reconfigurable-filter applications.

6.1.1 Basic design considerations

Thermooptic resonant-wavelength tuning in highly dispersive propagation media must take into account two effects: change of effective index with wavelength, and change of effective index with temperature. These two effects add or compete (depending primarily on the sign of the thermooptic coefficient), and must be accounted in order to find the new resonant-wavelength condition resulting from an applied temperature change. For this reason, the thermooptic tuning formula (3.1), derived for strongly confining (dispersive) structures, involves the perturbation in *effective* index and normalization in the *group* index. Finally, practical considerations are briefly discussed that limit the maximum on-chip temperature, which in turn limits the tuning range.

Fig. 6.1 shows the dependence of crystalline silicon index with wavelength. A quadratic fit, shown in the figure, is used for device designs from here on, in the range of 1500 to 1600 nm. In strongly confined guided structures considered here, however, the waveguide dispersion dominates the wavelength dependence, and this dependence is contained to first-order in the guided group index. A larger group index reduces the tuning range and the FSR for a fixed thermooptic index change and microring radius.

For wide tuning (here, by wide tuning we mean 10's of nm, or several THz), substantial on-chip temperature changes are required. From the thermooptic coefficient of $2\cdot10^{-4}/^{\circ}$ C, one may project about 100° C temperature change to provide about 1 THz (8 nm) of tuning, i.e. 10 GHz/$^{\circ}$ C. However, when large temperature changes are used, the temperature dependence of the thermooptic coefficient of

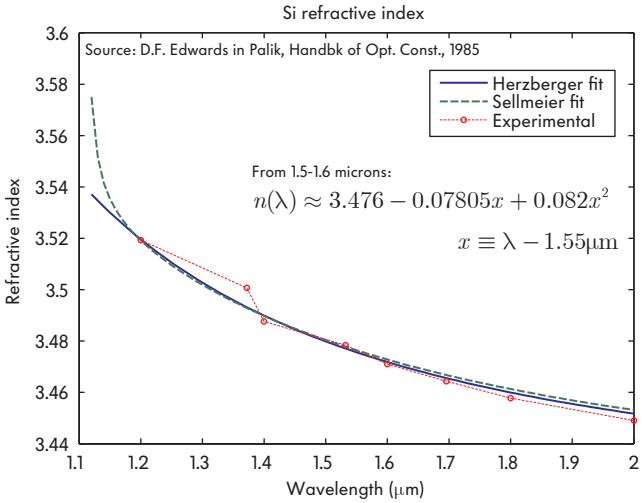

Figure 6.1: Silicon refractive index vs. wavelength (data from [133]). A quadratic fit about $\lambda = 1550\,\text{nm}$ is used for the present device designs.

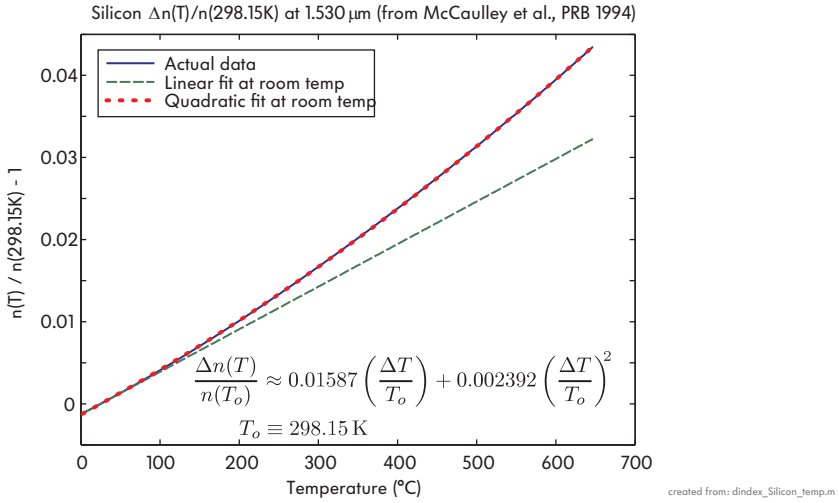

Figure 6.2: Silicon thermooptic coefficient quadratic enhancement with temperature (data from [134]). The quadratic fit shown is used in the present tunable resonator designs.

silicon needs to be accounted [134], and provides a substantial enhancement of tunability. The normalized thermooptic index change in bulk silicon is plotted vs. temperature in Fig. 6.2. It shows for example that at about $\Delta T = +400^\circ\,\text{C}$, the nonlinear thermooptic coefficient provides about 20% larger index tuning than extrapolation from the room-temperature linear thermooptic coefficient would suggest. Therefore, in the device designs in this work, a quadratic fit of the thermooptic index change, shown in the figure, is used.

The maximum temperature of on-chip microheaters will be limited by oxidation, which rapidly increases at high temperatures, and electromigration damage in the microheater metal (or doped semiconductor), which increases at high current

densities and high temperatures. For this reason, the waveguide designs used here were optimized (in Chap. 5) for proximity of the microheater and optical structure with low optical loss, to maximize tuning with on the order of 200° C temperature change. This low temperature tuning was assumed because the microring temperature may be considerably reduced (on the order of a factor of 2) in relation to the microheater temperature, due to their 1 µm relative displacement. This partially depends on the thermal design, briefly summarized in the experiment section.

6.1.2 Experimental demonstration

This section describes the experimental demonstration of wide, full-FSR thermooptic tuning of silicon resonators in three subsections. First, the thermal analysis and design of the Ti microheater is briefly described*. Second, the fabrication is summarized. Third, the experimental demonstration results of wavelength tuning range and electrical power, and switching speed are shown.

The waveguide cross-section and material stackup used for all of the silicon devices described in this section (single tunable rings and fourth-order filters), as well as those in sections that follow (Sec. 9.3), is shown in Fig. 6.3. The replacement of SiO_2 overcladding (used in design) with HSQ modifies the experiment in two ways. First, the overcladding index is slightly lowered. Second, the thermal conductivity of HSQ is a factor of 2–3 lower than that of silica. Therefore, the temperature drop from the heater to the silicon microring is considerably larger. If one-dimensional heat flow is assumed from the heater downward through the ring and cladding to the Si substrate, then temperature at the ring can be expected to increase by as much as a factor of 2 with the use of a SiO_2 overcladding.

Thermal and microheater design

The filters are tuned thermally. Titanium microheaters were designed using finite-element heat flow simulations to raise the microring core temperature to about 250°, permitting tuning a full FSR using on the order of 40 mW per ring. The microheaters are shown in Figs. 6.3 and 6.4(a).

The heater temperature is the tuning limiting parameter. Metal heaters cannot be made arbitrarily thick because of fabrication constraints that limit metal layers here to thicknesses of the order of 100 nm [135]. Hence, the current density cannot be decreased arbitrarily and then electromigration sets a limit on the operating temperature and current density of the heater.

As a result, a maximum ring temperature for a fixed maximum heater temperature, and therefore the widest tuning range, is achieved by designing the heaters to approximate a 1D heat flow in the vertical direction through the ring. Avoiding

*This work was primarily done by colleague Fuwan Gan, in collaboration with T. Barwicz and the author.

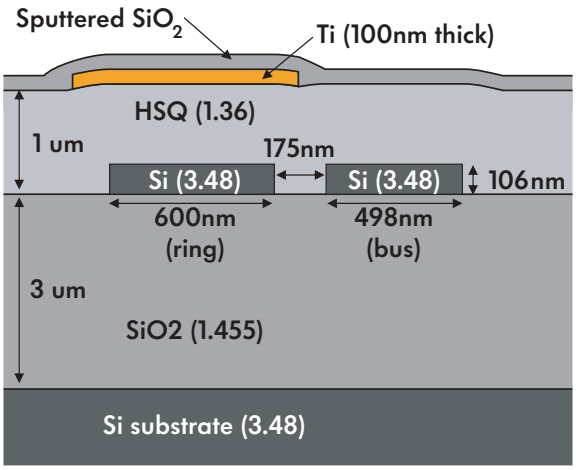

Figure 6.3: Design cross-section of material, waveguide and microheater stackup used for experimental demonstration of silicon tunable filters. The MC-STE Si ring waveguide design from Chap. 5 is used. The bus waveguide is adjusted for reduced coupler scattering loss.

"diffraction"-like spreading from a narrow heater wire avoids excessive temperature drop from the heater to the Si ring resonator core. In the 1D case, the temperature drop is linear in a region of constant thermal resistance. This is accomplished by making the heater strip considerably wider than its distance (1 μm) to the Si waveguide beneath it. This means that maximizing the tuning range comes at the expense of some inefficiency in use of the heat flux and lower power efficiency.

The heater is formed of multiple concentric wires for practical reasons, in order to provide around 2 kΩ resistance, which leads driving voltages and currents under 10 V and 10 mA, respectively. The wire width is 0.8–1 μm and the gap between wires is 0.8 μm for compatibility with contact photolithography.

Fabrication

The fabrication of the silicon rings is described in Sec. 5.3.1 and [135, 136]. The 100-nm-thick Ti heaters were formed on top of the HSQ overcladding by aligned contact photolithography, e-beam evaporation and liftoff. A second photolithography and liftoff step defined 100-nm-thick gold contact pads. The prepared chips were mounted on a designed copper thermal mass mount, and wire-bonded to specially designed circuit boards. A 100 nm layer of silicon oxide was sputtered as a crude passivation layer to slow down the oxidation of the Ti heaters at high operating temperature.

Fig. 6.4(a) shows an optical micrograph of a single Si microring cavity symmetrically coupled to an input and a drop waveguide on a first layer and the titanium microheater on a second lithographic layer, 1 μm above. The particular device shown has a central radius of 6.735 μm (outer radius of ∼7 μm shown in figure),

both the ring and the bus have nominal widths of 605 nm, and a coupling gap of about 855 nm. The heater leads are widened on the left side of the micrograph to reach a very low resistivity usable for contact leads to the heater (which are not to dissipate any power).

Device tuning demonstration

The drop-port response spectrum of the microring resonator was measured for several drive voltages across the heater. Resulting spectra are shown in Fig. 6.4(b), along with the estimated tuning power. The microring cavity was successfully tuned across its full FSR with about 40 mW of power applied to the microheater, reaching a maximum tuning of 20 nm at 44 mW. The low-temperature (low-power) tuning efficiency is about 30 mW/THz, while the overall (full-range) tuning efficiency is about 20 mW/THz. This allows the tuning of about 20–30 independent elements across a full FSR with 1W of power – sufficient to construct a fully reconfigurable optical add-drop multiplexer based on ring-resonator filters. This experiment confirmed that the cavity-microheater design and tuning capability are sufficient to permit their use for demonstration of complex higher-order filters with switching and multiple-FSR selection and tuning capability[†].

A second experiment of importance is the switching speed. For this experiment, an unbalanced Mach-Zehnder interferometer was constructed using two 3 dB couplers of adiabatic (broadband) design, unequal arm lengths and a linear microheater design, as shown in the optical micrograph in Fig. 6.5(a). Fig. 6.5(b) shows the time response, measured by applying a square-wave voltage to the heater. The heater changes the temperature in one arm and induces a phase difference between the two arms of the MZI to shift the nulls of its sinusoidal frequency response. This MZI heater has the same cross-section as the microring heater discussed above. The square shape of the current response means that the driving circuits don't contribute notable capacitance or inductance that can be a limitation to the switching speed at this scale. Therefore, the measured time response, with decay rates visible in the optical response, is mainly from the heat flow process in the devices. The rise and fall times are 8 μs and 15 μs, respectively. This response time is short enough to permit the application of these structures in telecom chip-scale reconfigurable and tunable OADMs.

[†]Higher tuning efficiencies can be expected by some simple improvements to the thermal configuration. First, using silica overcladding (such as TEOS) will increase the overcladding thermal conductivity in comparison to the presently used HSQ, and potentially increase tuning by the order of a factor of 2. Furthermore, it is of interest to investigate low index, high thermal conductivity overcladdings, that may make thermal contact between the resonator and the heater, while confining the optical mode away from the heater metal. Patterning such a structure may be needed to avoid lateral thermal crosstalk between various optical components on the chip, such as multiple resonators.

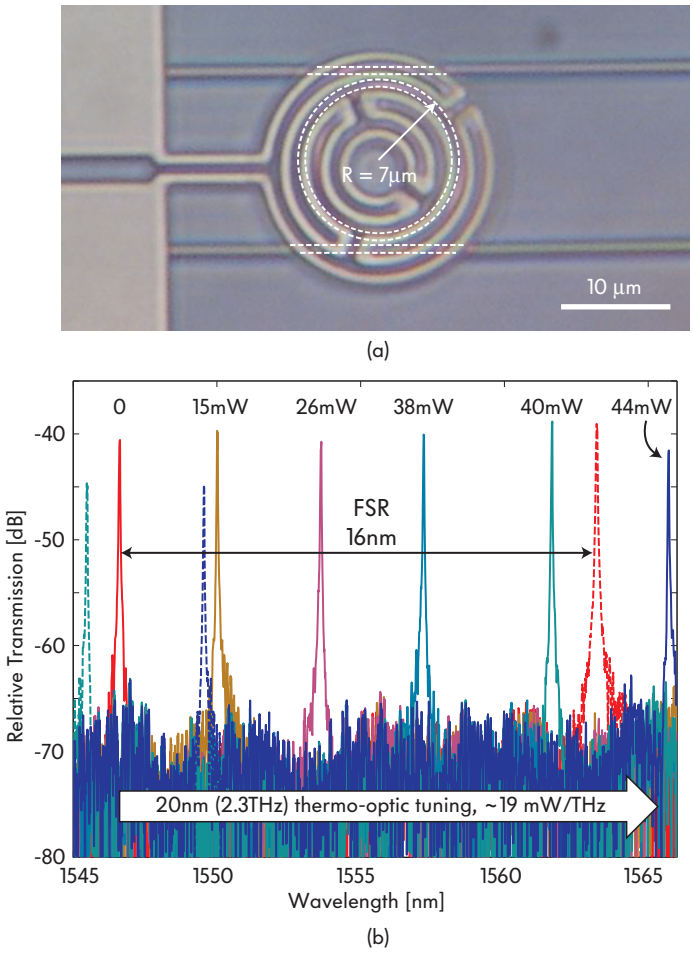

Figure 6.4: Demonstration of widely tunable silicon microring resonator: (a) optical micrograph of fabricated thermally tunable silicon microring resonator, based on the proposed Si waveguide design; (b) drop-port response spectra demonstrating 20 nm of resonant-wavelength tuning with under 50 mW.

6.2 Widely tunable, high-order silicon add-drop filters

In this section, the general approach, rigorous electromagnetic design and demonstration of fourth-order tunable microring resonator filters is described. They are designed to meet rigorous telecom spectral requirements at all wavelengths in their tuning range across the 30 nm C-band.

6.2.1 Two-band tuning approach

In order to make use of a single resonant band of a tunable wavelength filter across a larger tuning range than its FSR, typically a Vernier scheme is employed [120, 121]. Such schemes select only one of every several resonant passbands and create a larger effective FSR. However, these schemes are dispersive in the through-port response, and therefore are not well suited for channel add-drop filters, where all

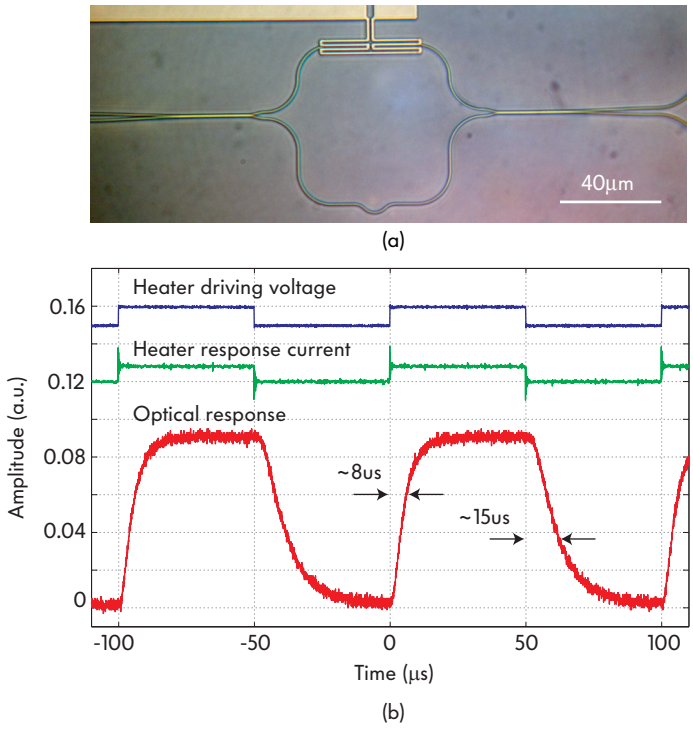

Figure 6.5: Thermooptic switching speed of silicon microphotonics: (a) optical micrograph of fabricated thermally switchable silicon Mach-Zehnder-interferometer (switching speed test structure); (b) applied heater voltage, heater current response showing that the electrical circuit is not band-limited at this switching speed, and the optical transmission response, showing a 8 μs rise time and 15 μs fall time due to thermal constants in the structure (published in [135]).

through-port channels (not being dropped) must remain unaffected by the filter. For this purpose, device designs and architectures are proposed and demonstrated, in Chaps. 8 and 9 in this thesis, that permit dispersion free FSR multiplication. Here, the silicon tunable filters are designed having such an architecture in mind to select among the passbands. Hence, here a filter with a passband that does not vary substantially over the tuning range is demonstrated.

The microring-resonator waveguide was designed to meet a number of design constraints in Chap. 5. To permit sufficient freedom for such designs (and to keep finesse and intracavity field enhancement low, to avoid nonlinear impairments), the maximum possible FSR was not used; instead a 16 nm (2 THz) FSR was deemed sufficient. Therefore FSR doubling is sufficient to provide a reach of 32 nm to cover the C-band. The heaters were designed to maximize the tuning range and cover one full FSR of the resonator. Therefore, the objective is to select two longitudinal resonances of the filter, as illustrated in Fig. 6.6. The lower-wavelength resonance is tuned a full FSR first, then is brought back to the starting point and the second resonance is tuned across its FSR to cover the second part of the spectrum. At these wavelengths the spectral shape is to be maintained.

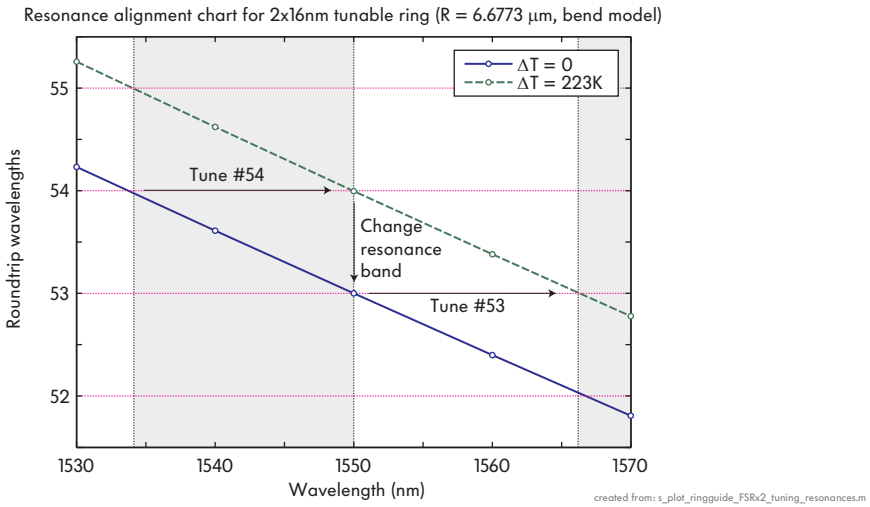

Figure 6.6: Two-band tuning approach to covering the C band with a 16-nm FSR resonator-based filter. The filter is designed to simultaneously meet the filtering criteria with multiple longitudinal resonance orders (in this case two adjacent resonances). The first resonance is tuned a full FSR to cover half the total tuning range, and the second resonance is tuned a full FSR to cover the rest of the tuning range. A resonance selection mechanism is required that allows suppression of all resonances to a "fully transparent" state, except the one currently active. Such designs are presented in Chap. 8 and 9.

6.2.2 Resonance-frequency-independent coupling and spectral response shape

Maintaining a fixed spectral shape means maintaining the CMT-in-time "energy coupling coefficients" that determine the spectral response shape. Since the various ring-bus and ring-ring power coupling ratios of directional couplers (e.g. κ_{rb} and κ_{rr}) scale with the FSR as [38]

$$\kappa_{\mathrm{rb}} = \frac{\mu_{rb}^2}{2\Delta f_{\mathrm{FSR}}}$$
$$\kappa_{\mathrm{rr}} = \frac{\mu_{rb}^2}{\Delta f_{\mathrm{FSR}}^2}$$

and the FSR, Δf_{FSR}, depends on the group index, then the power coupling to group index ratio is the quantity that must be unchanging near the resonant frequency as the resonant frequency is tuned.

Note that this requirement does not mean that the directional coupler power ratios must be wavelength-independent, but rather may be wavelength dependent also, so long as the value of coupling at and near the passband wavelength, at all tuning positions, remains the same. This property is referred to here as *resonant-*

frequency-independent coupling, and calls for the requirement:

$$\left.\frac{\kappa_{\mathrm{rb}}}{n_{\mathrm{group}}}\right|_{\omega_o(q)} = \text{const.}$$
$$\left.\frac{\kappa_{\mathrm{rr}}}{n_{\mathrm{group}}^2}\right|_{\omega_o(q)} = \text{const.}$$

for all q, where q parametrizes the tuning states.

In strongly confined waveguides, both the power coupling ratios $\kappa(\omega, q)$ and group indices $n_{\mathrm{group}}(\omega, q)$ change both with wavelength and with temperature. However, an interesting observation is that in silicon, whose thermooptic coefficient is positive, the temperature and wavelength contributions cancel so that the overall wavelength dependence is reduced. Higher temperature shifts the resonant mode to longer wavelengths, where the guided mode is less well confined, so the effective index is reduced, and the couplings increase. On the other hand, the temperature increases the core index, so the mode is better confined and couplings decrease. In principle, a waveguide cross-section may be chosen that cancels the two.

6.2.3 Rigorous design simulations

Rigorous 3D FDTD simulations were carried out to find the models for the ring-bus and ring-ring couplers. For a set of coupling gaps, the simulations yield cross-coupling power ratio, CIFS, and coupler loss. In the case of non-symmetric couplers, such as ring-bus couplers with a straight bus and a bent ring, the coupler loss for a bus-side input excitation and for a ring-side input excitation may be different. Here, only the more critical ring-side loss is computed.

Fig. 6.7 shows a schematic of the ring-bus coupler, and time snapshots of the out-of-plane magnetic field during a FDTD simulation for the 105 nm gap. Fig. 6.8 shows a schematic of the ring-ring coupler, and time snapshots of the out-of-plane magnetic field during a simulation for the 100 nm gap. The results of these simulations are shown in Fig. 6.9(a) and (b), respectively. Each parameter is plotted at three wavelengths – the leftmost end of the target spectrum (1534 nm), the middle (1550 nm) and the rightmost end (1566 nm).

The bus waveguide was chosen to be narrower, at 495 nm, in order to suppress the formation of any spurious higher-order coupler modes that are associated with coupler scattering loss [89, 119]. The ring-bus coupling plots show that the loss is 25 dB below the coupling fraction – essentially negligible in the context of the filter. A narrower bus also means larger coupling gaps (compare this data – about 200 nm gap for 12.8% coupling – to the CMT estimates for identical 600 nm waveguides in Fig. 5.14(b) which give about 120 nm). The ring-ring coupling shows a higher coupler loss, but still 15 dB below the coupling ratio, which is also very low.

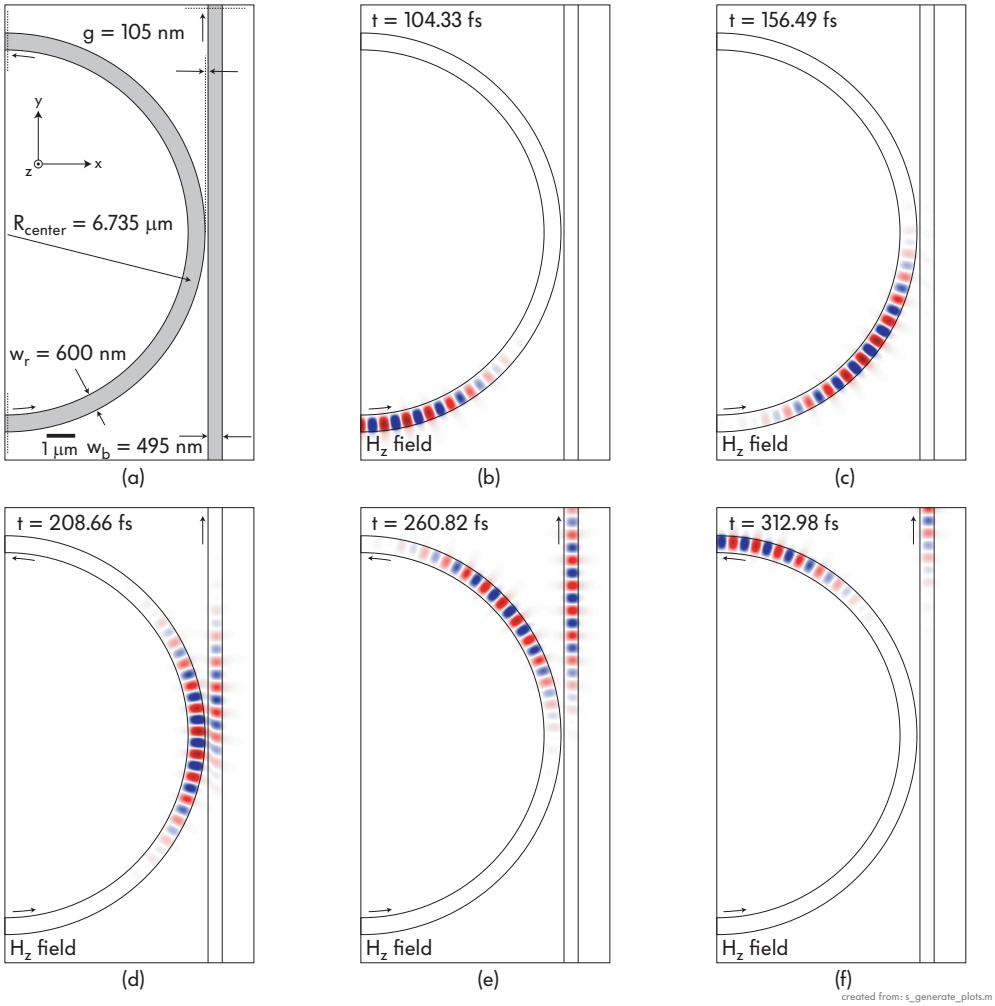

Figure 6.7: Rigorous 3D FDTD simulation of a ring-bus coupling region for the design of silicon tunable filters: (a) configuration and dimensions, (b-f) H_z field snapshots at several points in time showing the test pulse traversing the structure. The simulation yields cross- and bar-state coupled power ratio and phase shifts. A set of simulations with varying coupling gaps yields coupling ratio, coupler loss and CIFS vs. gap. A narrower bus is used to achieve low coupler loss [89, 119].

The coupling, loss and CIFS plots may be used to design resonant filters and structures based on the chosen waveguide design and ring radius. The simplest way to use this data is to perform linear or low-order polynomial fitting of the simulated data on the semilog scale as plotted. Such simple fits can then be used to enter the coupling, loss and phase shift parameters into the directional coupler models for various choices of coupling gap.

The fourth-order filter geometry is illustrated in Fig. 6.12(a). The filter is designed based on these criteria, and was chosen to have a 3 dB bandwidth of 75 GHz. This was done to reduce loss and to ensure that the 40 GHz channel window falls within the low-dispersion region of the filter response. A fourth-

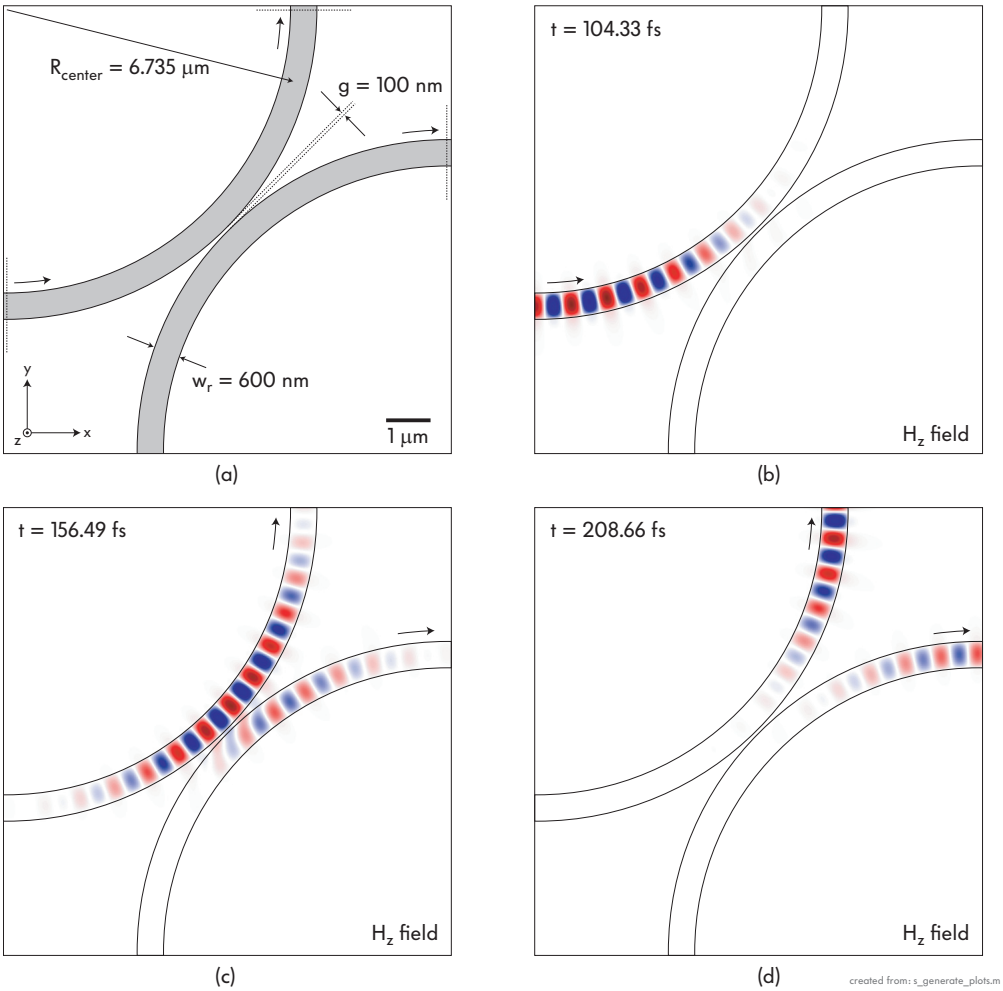

Figure 6.8: Rigorous 3D FDTD simulation of a ring-ring coupling region for the design of silicon tunable filters: (a) configuration and dimensions, (b-d) H_z field snapshots at several points in time showing the test pulse traversing the structure. The simulation yields cross- and bar-state coupled power ratio and phase shifts. A set of simulations with varying coupling gaps yields coupling ratio, coupler loss and CIFS vs. gap.

order filter can accommodate such a wide passband and still roll off to -30 dB at +80 GHz detuning from center, at the edge of the adjacent channel. The designed electromagnetic and physical parameters (coupling coefficients and dimensions) for the filter are given in Tables 6.1 and 6.2. Because the wavelength dependence of the couplings and group index varies the response between the first and second resonant passband under consideration, the designed filter shape is not standard Chebyshev. Rather, it is a slight modification, where the 1550 nm cold passband has the middle of the three through-port extinction lobes suppressed by 28 dB, and the two side lobes suppressed by about 24 dB. This is discussed further in the wavelength and tuning dependence.

The coupling simulations just described were all done assuming room-temperature

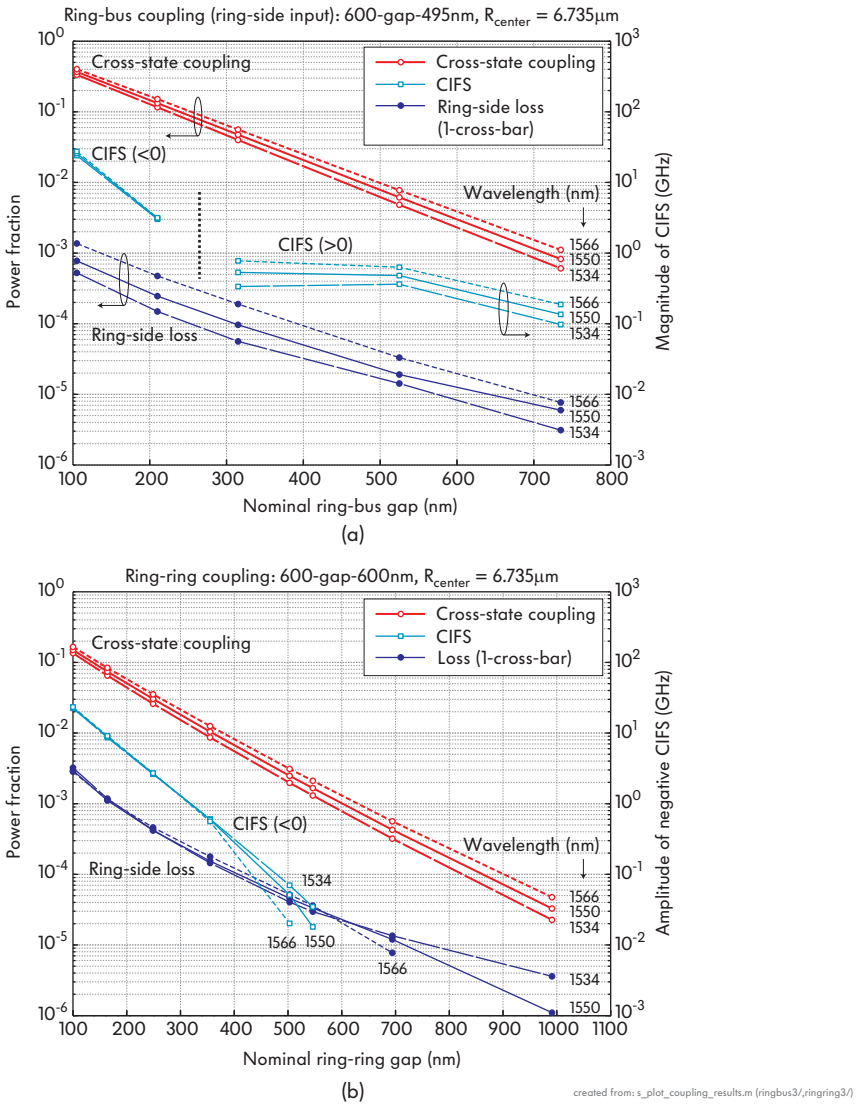

Figure 6.9: 3D FDTD-computed design plots showing cross-state power coupling, ring-side coupler loss and CIFS for a range of wall-to-wall coupling gaps and for (a) ring-bus and (b) ring-ring coupling. The computations were done for 600×106 nm ring waveguides with 6.735 µm central radius, and 495×106 nm bus waveguides.

refractive indices. The simulations were also repeated in two other scenarios: when the temperature is 223° C above room temperature, which is the projected full-FSR-tuning temperature actuation for the chosen MC-STE design; and at room temperature but with a width error on all waveguides of +30 nm. This data gives the wavelength-dependent temperature and dimensional error perturbations to the coupling. The coupling ratios, only for the gaps in Table 6.2, are plotted against wavelength for two different temperatures in Fig. 6.10(a-c). The shaded regions indicate the range of coupling coefficient for ±30 nm error in the waveguide width. The dimensional errors are assumed to be symmetric about the center of the waveg-

Table 6.1: Electromagnetic parameters of fourth-order, wide-tunable microring add-drop filter

FSR	$(d\gamma/df)^{-1}$	2125 GHz
Input/output coupler cross-state coupling	$\kappa_{(i,o)}$	0.186
Input/output coupler ring-side loss	$l_{(i,o),rr}$	$3.7 \cdot 10^{-4}$
Ring 1-ring 2 coupling	κ_{rr1}	0.0065
Ring 1-ring 2 loss	l_{rr1}	$9.6 \cdot 10^{-5}$
Ring 2-ring 3 coupling	κ_{rr2}	0.0036
Ring 2-ring 3 loss	l_{rr2}	$5.8 \cdot 10^{-5}$
Ring 3-ring 4 coupling	κ_{rr3}	0.0065
Ring 3-ring 4 loss	l_{rr3}	$9.6 \cdot 10^{-5}$
Ring 4-ring 1 coupling	κ_{rr4}	(0)
Resonant order (at λ_o =1550 nm)	γ_o	53 and 52
Assumed propagation loss		8 dB/cm (0.0338 dB/r.t.)

Table 6.2: Physical dimensions of fourth-order, wide-tunable microring add-drop filter

Height of all waveguides		106 nm
Ring center radius	R	6.732 m
Ring waveguide width	w_r	600 nm
Bus waveguide width	w_b	498 nm
Input coupler gap	g_i	175 nm
Ring 1-ring 2 gap	g_1	404 nm
Ring 2-ring 3 gap	g_2	463 nm
Ring 3-ring 4 gap	g_3	404 nm
Output coupler gap	g_o	175 nm
Ring 4-ring 1 gap	g_4	1637 nm

uide – therefore, for example, 30 nm narrower waveguides mean a 30 nm wider coupling gap. This is the most relevant type of error in lithography and etching.

Fig. 6.10(a) also shows a dotted line that shows the approximate coupling coefficient at the center wavelength of the filter, when the filter is tuned to that wavelength. One longitudinal resonance is used from 1534 nm to 1550 nm, then the next passband from 1550 nm to 1566 nm. As described, the thermooptic index change offsets the wavelength dependence of the coupling coefficient to recover a flatter overall dependence represented by the dotted "resonance-frequency-dependence" of the on-resonance coupling. Therefore the coupling zigzags between two bounds over a fairly limited range.

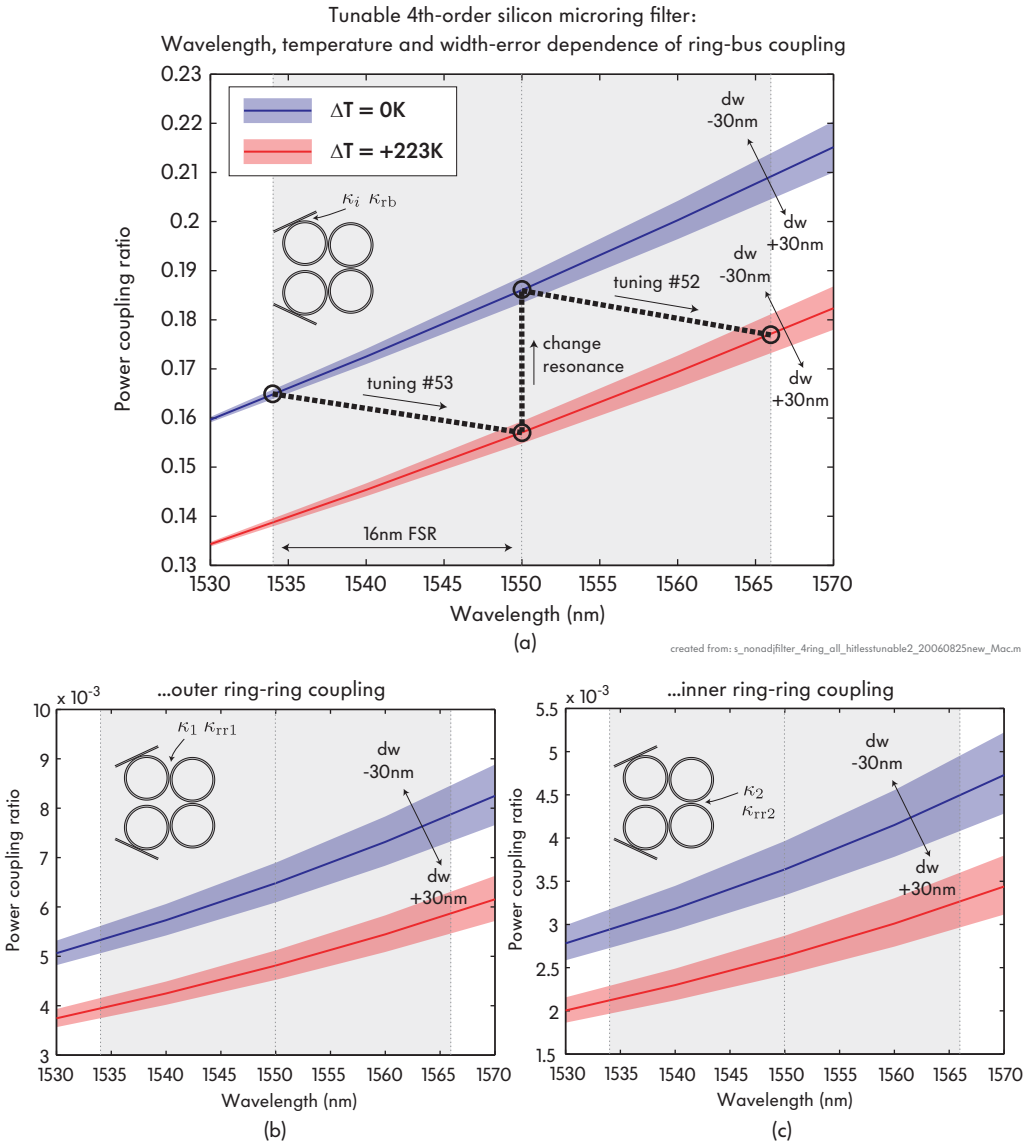

Figure 6.10: Resonant-frequency-independent coupling: 3D FDTD-computed (a) ring-bus and (b,c) first and second ring-ring couplings vs. wavelength, temperature and symmetric waveguide width error, dw. The nominal design at 1550 nm has power couplings $\{\kappa_{\rm rb}, \kappa_{\rm rr1}, \kappa_{\rm rr2}\} = \{18.6, 0.648, 0.364\}\%$ (the structure is symmetrical and SCC, not loop-coupled as devices in Chap. C, so $\kappa_{\rm rr4} \approx 0$). Note that the coupling coefficient *on resonance* at different temperatures, as the filter is tuned, is shown by the dotted line. This dependence is about $3\times$ weaker than the plain frequency dependence as the thermooptic effect and wavelength dependence cancel each other.

The predicted spectral response at the four critical points of the tuning spectrum – the cold state of the 1534 nm resonance and 1550 nm resonance, and the "hot state" (at 223K above room temperature) – is shown in Fig. 6.11. Fig. 6.11(a) shows both resonant passbands in the cold state (at room temperature), and Fig. 6.11(b) shows them in the hot state. The target response is shown in solid line, while the

shaded bars around the response show the variation of the response with ±30 nm width variation in all waveguides.

The spectral response is remarkably unchanged between the first and second resonance, and in particular between the cold state and the hot state (there is a very slight narrowing in the latter). The through-port extinction ratio, the most sensitive part of the filter, is maintained above ∼22 dB in all tuning states.

The filter design meets typical telecom specifications at all channels – 30 dB adjacent channel rejection, <3 dB loss, >30–35 dB extinction in the through port (see Table 1.1). To achieve a high through port extinction, these filters are designed to use a two-stage configuration, as demonstrated in Sec. 7.1 [119]. Multistage configurations provide sufficient robustness in the through-port response to enable high extinction ratios in practical devices, and at least two stages are required to use the standard add-after-drop configuration typically used in industry (though in general these stages need not be identical). This is done in order to avoid the need to impose an extremely high extinction ratio from add to drop port, since the add port typically has a high-power signal at the start of a link, whereas a drop port is handling an arriving signal that may be highly attenuated. Therefore add-to-drop extinction must be considerably larger than the input-to-through-port extinction.

The simulated filter design responses here are computed using a spatial scattering state-variable model (similar to that in Sec. 9.3.1), where each scattering point is a directional coupler modeled by the canonical form in Figs. 2.5, 2.6, 2.7, 2.10. The parameters for the model of each coupler are obtained from the 3D FDTD simulations, summarized in Fig. 6.9 and 6.10.

6.2.4 Experimental demonstration

The experimental demonstration of the fourth-order tunable filter was realized in the waveguide cross-section shown in Fig. 6.3. The geometry of the filter is shown in Fig. 6.12(a), and an optical micrograph of the fabricated device is shown in Fig. 6.12(b). The rings are arranged in a folded geometry (rather than in a linear arrangement as in [38]) in order to localize all resonators to the middle of the e-beam tool writing field, and to balance fabrication proximity effects to some degree. Note that microring 1 and 4 are not coupled in the design, and in the realization are placed far enough apart (1.6 µm) that the coupling is effectively nil. This is in contrast to loop-coupled structures, proposed in Appendix C of this thesis, where ring 1 and 4 might be coupled so as to establish a cavity coupling loop.

Whereas in the demonstration of SiN filters [90, 119] care was taken to calibrate for resonance frequency shifts due to CIFS and fabrication-related proximity effects (in a first fabrication run), and apply those corrections in the device run, this was not done here due to lack of time. It was not of critical concern since all resonators have individual heaters and can be lined up by thermal tuning.

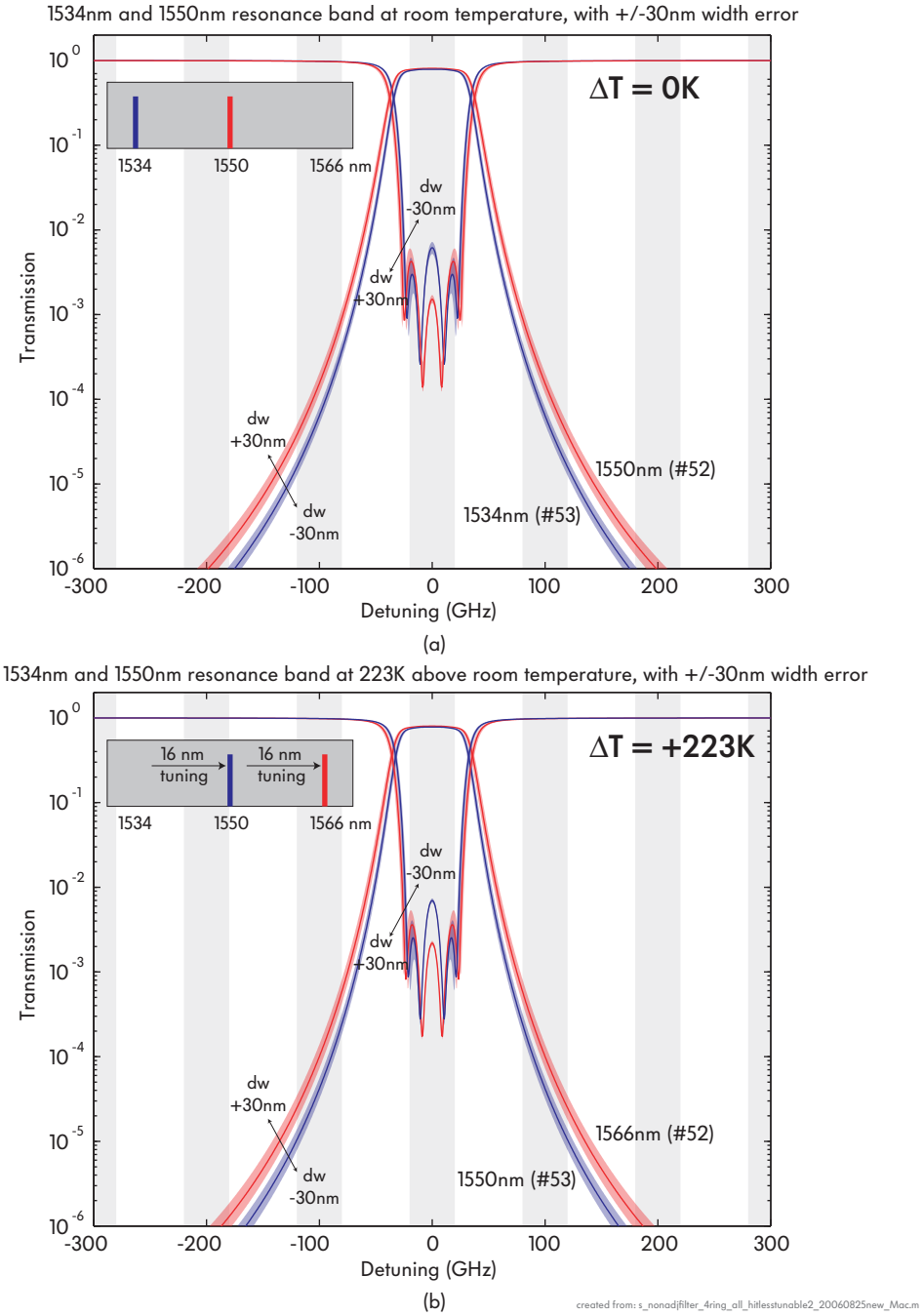

Figure 6.11: Fourth-order tunable silicon microring-resonator filter theoretical passband shape vs. wavelength tuning. (a) At room temperature, resonant passbands # 53 and # 52 are at 1534 nm and 1550 nm, respectively. Wavelength dependence of the coupling coefficients and symmetric width errors of ± 30 nm cause very little passband shape variation. (b) At $\Delta T = +223$K above room temperature, both passbands tune by a full FSR to 1550 nm and 1566 nm, respectively, showing virtually no change in passband shape while tuning, due to the small on-resonance coupling variation shown in Fig. 6.10.

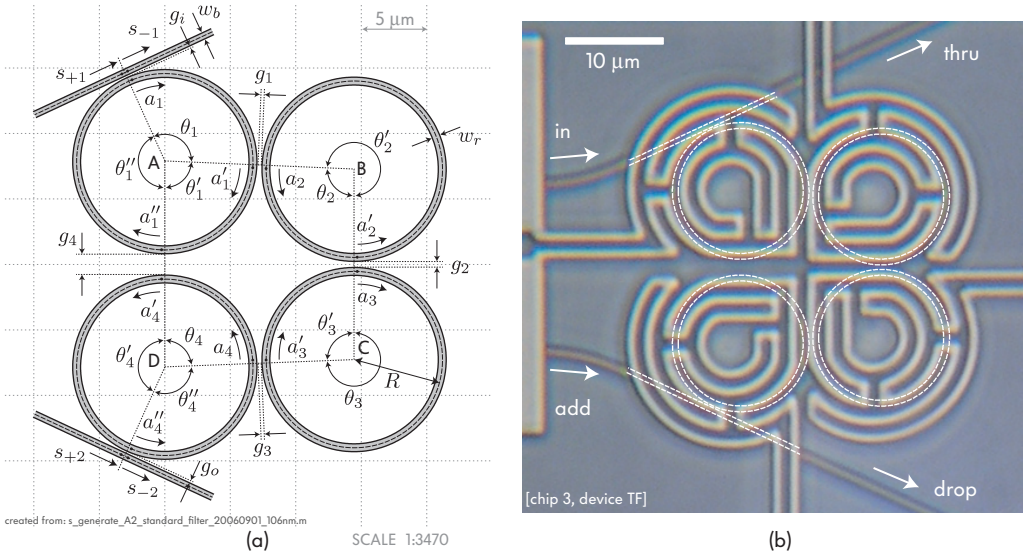

Figure 6.12: Fourth-order, tunable series-coupled-cavity add-drop filter in silicon (4^{th}-order): (a) design layout of actual device, (b) optical micrograph of fabricated add-drop filter in silicon.

The experimentally measured through and drop port responses are shown in Fig. 6.13. The microheaters are actuated to align the filter with a number of ITU grid specified channels, shown in gray boxes for a 40 GHz clear window and 100 GHz channel spacing. Fig. 6.13(a) shows a 16 nm FSR. Fig. 6.13(b) shows a close view of the drop and through port responses showing a cold state and three tuned states, at 2, 4 and 6 channel spacings away from the cold state. The theoretical response of the nominal design is shown overlaid with the experimental responses, showing good agreement. The filter shows on the order of 1 dB loss, 30 dB out-of-band rejection and 20 dB in-band extinction in the through port. This enables 40 dB extinction in a two-stage configuration. This is the first demonstration of high-order, tunable microring-resonator filters capable of channel add-drop filtering. They show a substantial in-band extinction response.

The passbands were tuned by no more than six channels in the initial experiment over concerns that the microheaters may burn out by oxidation at the higher powers (40–50 mW). A part of the tuning range was used to compensate a 400 GHz misalignment of the resonances of the first and fourth ring relative to the second and third. The reason for this misalignment is likely fabrication-related proximity effects (CIFS was evaluated to be small, see Fig. 6.9). In this fabrication, a calibration run for frequency matching was not performed due to lack of time. However, this technique, previously applied to SiN filters [90, 119], can easily be applied in Si designs. Nevertheless, the demonstration of full-FSR tuning in single-ring cavities of identical design gives confidence that the four ring filters demonstrated should be tunable across their full FSR. More careful experiments, and additional passivation, should allow the demonstration of full-FSR tuning in these devices.

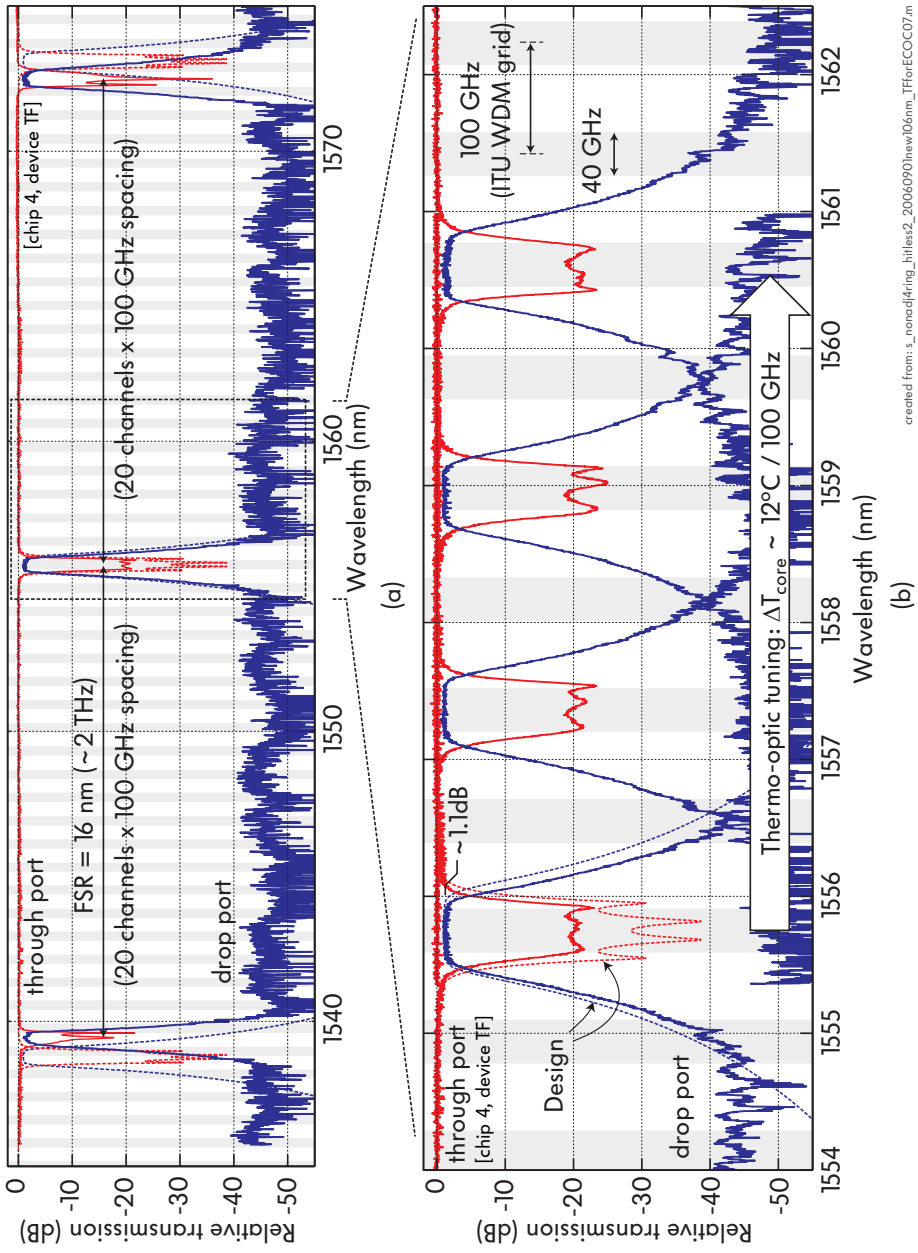

Figure 6.13: Experimental and design spectra of fourth-order, tunable series-coupled-cavity add-drop filter in silicon (4^{th}-order): (a) spectrum over 2 FSRs, (b) demonstration of tuning by 6 channel spacings.

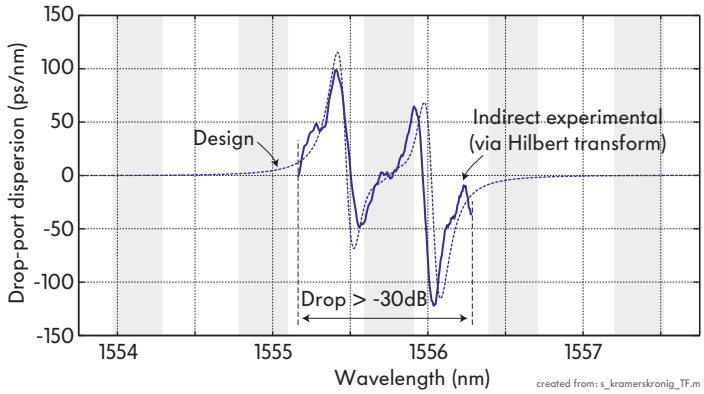

Figure 6.14: Dispersion of fabricated telecom-grade (4^{th}-order, series-coupled-cavity) microring resonator add-drop filter in silicon. The dispersion is extracted by Hilbert transforming a smoothed experimental amplitude response [Fig. 6.13(b)].

Besides the amplitude response, a key criterion for WDM telecom network applications is dispersion. For a 40 GHz channel window, less than 20 ps/nm of dispersion is typically required (Table 1.1). The filter in this section was designed to have a wide bandwidth in order to place the channel window away from its dispersion peaks which are at band edges.

The phase response of the fabricated filter was evaluated using the Kramers-Kronig (Hilbert transform) approach to extracting the amplitude from phase response and vice versa. Fig. 6.14 shows the design drop and through port dispersion (they are identical), and the "experimental" drop-port dispersion extracted from the experimental amplitude response data, with some smoothing to remove high frequency noise. The agreement is good, and the dispersion is estimated to be at most 50–60 ps/nm at the very edges of the channel, and considerably less inside.

6.3 Conclusions

In this chapter, the first demonstration of wide full-FSR tuning of silicon resonators was described. Rigorous design of filters for wide tunability was discussed, including resonance-frequency-independent passband response shape (i.e. nearly resonance-frequency-independent coupling). Fourth-order, tunable silicon microring resonator add-drop filters were designed and demonstrated, having passbands that are substantially independent of the tuned resonant frequency. The filters show 1 dB of drop loss and high extinction ratios in the drop and through port responses that make them suitable for telecom channel add-drop applications for chip-scale R/T-OADMs.

Part III

Optical circuit synthesis and architectures

Chapter 7

Resonant filter synthesis and design

7.1 Multistage filters*

7.1.1 Introduction

High-index-contrast (HIC) microring resonators support high-Q modes with a large free spectral range (FSR) that enables planar microphotonic filters to operate over the multi-terahertz channel spectra of densely wavelength-division multiplexed (DWDM) networks. Previous work on high-order (multi-cavity) resonant filters was focused on achieving flat-top drop-port responses with a sharp rolloff (>30 dB at closely spaced adjacent channels), low loss (<3 dB) or a wide FSR [38, 88, 137]. Equally important for add-drop applications is a high-extinction, box-like *notch* response across the channel band in the through port – in excess of 30 dB – to avoid so-called *coherent crosstalk* between the *drop* and *add* data. Critical coupling enables a high-extinction notch response from a lossy cavity, but it is sensitive to variations and insufficiently selective for high-spectral-efficiency applications. And, the technique does not trivially generalize to high-order filters. Rigorous design and resonance matching techniques have enabled the demonstration of 3^{rd}-order filters with 14 dB notch extinction [89]. Higher extinctions require overcoming the response sensitivity to resonance alignment and coupling errors. Such notch filters have other important applications in optical single-sideband modulation, fluorescence spectroscopy, astronomy and quantum encryption schemes.

In this section, high-order add-drop filters based on strongly confined SiN waveguides are described, constructed by feed-forward (FF) cascading of reduced-order stages. The resulting through-port responses are less sensitive to the fine dimensional tolerances for coupling coefficients and resonance frequencies associated with HIC. The latter make it difficult to achieve high through-port extinction

*This section reproduced, with modifications, from the published version of this work in [136].

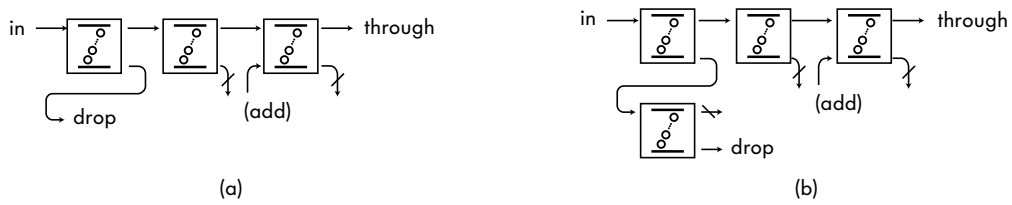

Figure 7.1: Multistage add–drop filters: incoherently cascaded stages in (a) the through-port path, and (b) the through and drop port paths.

in a single high-order, series-coupled-cavity (SCC) filter [38]. Multistage filters also permit lower drop loss due to partial divorce of the drop- and through-port synthesis. The design and experimental demonstration of one-, two-, and three-stage filters using identical 3-ring stages, fabricated in Si-rich SiN, is described. They exhibit a 20 nm FSR, a 40 GHz passband with 2 dB drop loss, 30 dB adjacent channel rejection, and reach >50 dB in-band extinction in the through port.

7.1.2 Sensitivity of the through-port-response extinction

Fig. 7.1 illustrates multistage arrangements of arbitrary filter blocks forming a cascade in the in-to-through signal 'path' only (a) or in both the through and drop paths (b). In previous work, cascading of single rings enabled sharper resonant lines and increased through-port extinction [138], but flat passbands are not possible without prohibitive insertion loss resulting from the necessary detuning. On the other hand, cascaded higher-order thin-film filters have been employed to increase extinction [139]. This approach has merit, and integrated filters present further advantages of negligible cascading loss, controllable stage-to-stage variation, and high-Q cavities. With non-identical stages further advantages are found for the design of multiport responses in the presence of loss.

In multistage filters, synthesis for multiple response functions is partially decoupled, unlike SCC designs. In Fig. 7.1(a), the first-stage parameters influence the in-to-through and in-to-drop responses, the last stage is shared by in-to-through and add-to-through responses, while intermediate stages affect only the in-to-through response. With at least two stages, add and drop ports are isolated in the common add-after-drop arrangement. Were the first stage a broadband 3 dB splitter, drop and thru response shape design would be fully decoupled, at the cost of a 3 dB loss in each. Hence, there is a tradeoff between spectral design decoupling, which permits separate optimization, and loss.

Separate design leads to lower drop stage order and lower loss. A flat-top response with both high out-of-band drop-port rejection and high in-band through-port extinction requires a filter of higher order than one meeting either single requirement. The minimum order N of a bandpass filter is determined by a spectral fill factor on the one hand (channel bandwidth to channel spacing ratio, BSR), and approximately by the sum of desired in-band (R_i) and out-of-band

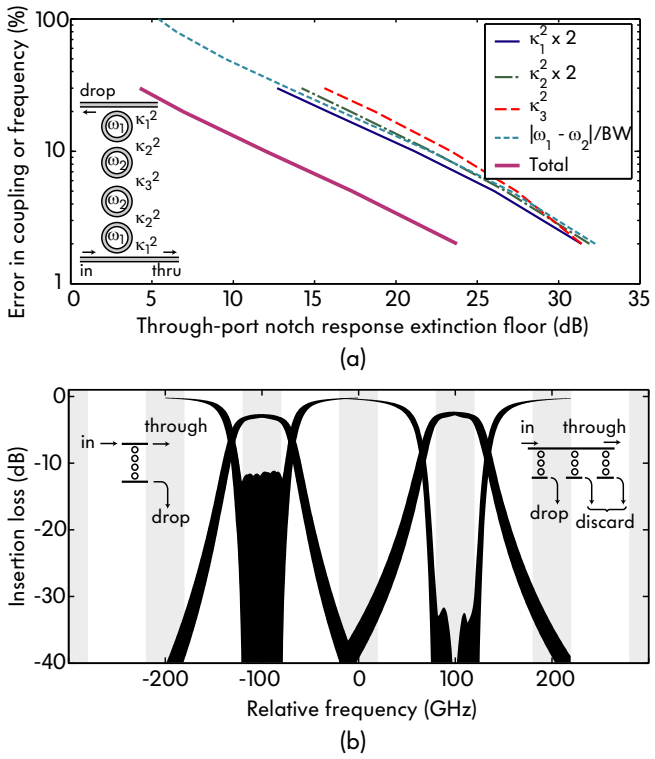

Figure 7.2: (a) Normalized through-port response sensitivity to fractional error in coupling and resonance frequencies; (b) loss and tolerance to errors of a comparable single-stage filter and (c) multistage filter.

(R_o) rejection levels in dB: $N \approx (R_i + R_o)/[20\log_{10}(2/\mathrm{BSR} - 1)]$ for maximally flat filters (similarly for equiripple). Since the allowable passband ripple is up to large fractions of a dB (typically < 1 dB in-band rolloff), drop-port criteria *alone* could be met by a lower order filter. Conversely, an SCC filter with 30 dB in-band extinction in the through port requires, by power conservation, a corresponding drop response with $<$0.004 dB passband ripple. This calls for a high order filter, leading to high drop loss. Conversely, since the allowable passband ripple in add-drop filters is up to large fractions of a dB, drop-port criteria *alone* could be met by a lower order filter.

Through-port extinction in SCC filters is particularly sensitive to errors, and a high extinction is much more difficult to realize in practice than a sharp rolloff in the drop port. Drop-port rejection through a chain of N co-resonant coupled resonators is guaranteed to roll off at a rate of $6N$ dB per octave of detuning, independent of the precise details of coupling and frequency matching. Passband flatness does depend on these parameters but is also fairly robust to variations ([46], see also Chap. 4.1). On the other hand, both precise matching and coupling control are required for a high extinction through port to be achieved. Alternative, parallel-coupled ring geometries [140] provide higher tolerance of through-port extinction but lower tolerance of drop-port out-of-band rejection.

Sensitivity of the through port extinction may be estimated analytically using a coupled-mode model [38]. In passbands and stopbands, where one response function is near unity, flat-top passive filters are first-order insensitive to parameter errors. Therefore we consider a parabolic normalized measure of sensitivity, $S_{H(\omega),\alpha} \equiv \partial^2|H(\omega;\alpha)|^2/\partial(\ln\alpha)^2$ where the parameter α may represent error in coupling coefficients (fractional), or frequency mismatch (normalized to bandwidth). In Fig. 7.2a, the through-port sensitivity is computed theoretivally for a 4^{th}-order filter example that meets typical WDM criteria, for the four relevant parameter types: inner and outer ring resonance frequencies and couplings (each category carrying approximately uniform values in flat-top filters). A Chebyshev filter with R_i ~35 dB in-band extinction and a normalized bandwidth of 1 rad/s employs energy couplings $\{\mu_1^2, \mu_2^2, \mu_3^2\} = \{1.5, 0.36, 0.18\}$ (proportional to power coupling coefficients, κ_i^2, $i = 1, 2, 3$) [38]. The plot shows the worst-case through-port extinction within the channel band due to fractional error in each of the coupling coefficients and due to resonance frequency mismatch (between outer and inner resonators) as a fraction of the filter bandwidth, separately; and the total extinction floor due to the net effect of all parameters. The symmetric geometry is assumed to be preserved when errors are introduced. This is the most likely case in fabrication. All parameters contribute similarly, and an error of 15% in all parameters leads to an extinction floor at 10 dB. While response sensitivity to each parameter is of the same order, the expected uncertainty of the frequency mismatch is typically greater than that of the coupling coefficients.

We may compare the 4^{th}-order SCC filter, suitable for a 100 GHz-spaced WDM channel grid, with a multistage filter meeting comparable requirements. Incorporating finite cavity loss Q's of 25,000, Fig. 7.2(b) shows 1000 overlaid responses representing a uniformly distributed random fractional error in power couplings and in frequency mismatch as a fraction of bandwidth ($\pm 15\%$ in both cases). The extinction is limited by the random perturbations to ~10 dB. By comparison, in a multistage filter [Fig. 7.2(b), right] a 3^{rd}-order first stage is sufficient (and others are set identically), resulting in lower drop loss (here, 2.5 dB instead of 3 dB), and provides a partial decoupling of the design variables with respect to the response functions, and a more robust total through-port extinction of 30 dB. In higher order filters, multistage designs provide a greater reduction of the drop loss.

7.1.3 Rigorous electromagnetic design

For experimental demonstration, one-, two- and three-stage filters [Fig. 7.1(a)] were designed for 40 GHz channels on a 100 GHz WDM grid. Identical 3^{rd}-order stages were employed to simplify stage-to-stage resonance alignment. Each stage has a drop passband with 0.05 dB ripple, rolling off to 0.2 dB at the channel band-edges and 30 dB rejection 80 GHz from center-band; and a through-port extinction of 22 dB over mid-channel (15 dB near band edges). For a three-stage filter, the

extinction is thus 66 dB (45 dB). A 20 nm FSR calls for 8 μm ring radius, and ring-bus and ring-ring couplings of 10.3%, 0.22%.

The electromagnetic design follows Ref. [89] and was tailored to measured core and cladding indices (2.181, 1.455) and core-layer thickness, 396 nm. Wide, thin waveguide cross-sections reduce ring sensitivity to width tolerances and sidewall roughness, and curb polarization mixing [89]. The filter is designed for TE input. An integrated polarization diversity scheme is to be used for polarization-independent operation [20, 31, 33]. In previous work, we found 1.5 dB drop loss intrinsic in design (bending, coupler scattering) [89]. Here, we chose a wider (900×396 nm) ring waveguide with a deeper (200 nm) overetch, increasing the radiation Q of the fundamental (TE_{11}) resonance associated with bending loss to ∼250,000 at 1530 nm. Spurious TM_{11} and TE_{21} resonances were kept to low Q's under 2000 and 25, respectively, to prevent them from contributing to coupler losses [89]. With narrower, 702 nm bus waveguides, rigorous three-dimensional finite-difference time-domain (FDTD) simulations produced design ring-bus and ring-ring gap spacings of 120 nm and 372 nm (rounded to the 6 nm e-beam step size) corresponding to the desired coupled-power ratios. Coupler loss was reduced by 5× from Ref. [89] and 10× from Ref. [88]. With total "design insertion loss" at 0.35 dB, coupler loss accounts for 0.1 dB, bend loss for 0.25 dB.

7.1.4 Fabrication and optical characterization results

One-, two- and three-stage filters were fabricated by a process based on direct-write scanning-electron-beam lithography (SEBL), described in Ref. [90]. The pattern was defined in 200 nm of poly-methyl-methacrylate (PMMA) using a Raith 150 SEBL system at 30 keV. A hardmask was formed by evaporating and lifting off a thin film of Ni. Waveguides were formed by a 590 nm-deep conventional reactive-ion etching step using a gas mixture of CHF_3 and O_2. Finally, the Ni hardmask was removed. Fig. 7.3(a) shows a scanning electron micrograph (SEM) of a 3-stage device.

Care was taken to prevent lithographic distortions. The exposure pattern was designed for lithographic field distortions to affect the filter stages in common mode, such that they remain frequency aligned. To compensate for the resonance frequency mismatch reported in Ref. [88, 90], a 3.8-4.2% higher e-beam dose was applied to the middle ring of each stage to increase its dimensions and match its frequency to the outer rings.

Figs. 7.3(b-d) show measured drop- and through-port responses, for TE-polarized input, of one-, two- and three-stage frequency-compensated filters. Care was taken during characterization to ensure that the drop- and through-port responses have a consistent relative insertion loss scale. Measurement of high-extinction through ports necessitated filtering the laser line pedestal in the characterization setup by a narrowband following filter [21]. Fig. 7.3(b) shows close agreement between

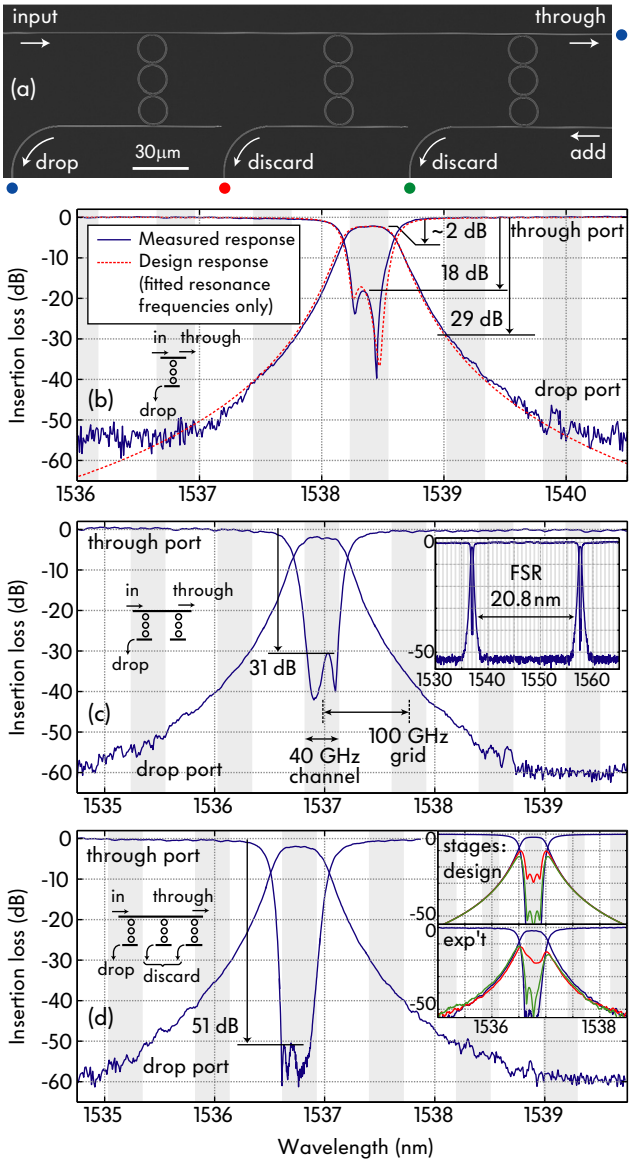

Figure 7.3: (a) SEM of fabricated three-stage filter. Measured response spectra of (b) one- (with design plot), (c) two- (inset shows FSR) and (d) three-stage filter showing high in-band extinction (inset: individual stage responses, design and experiment, showing <5 GHz stage alignment).

the intended design and measured result for a single-stage filter, validating the design and demonstrating the fabrication accuracy. The only fitted parameters were the center wavelength of 1538.36 nm, and the middle-to-outer ring resonance frequency mismatch of 2.3 GHz. Excess ring propagation loss of 12 dB/cm was extracted by independent measurement and included in the theoretical model plot. Improving on Ref. [89], the single-stage filter has a 40 GHz 1 dB-passband with 2 dB drop loss, 30 dB out-of-band rejection, and 18 dB through-port extinc-

tion – the highest reported in a high-order microring filter – owing to the frequency matching and low loss. Evidence suggests that the propagation loss is associated primarily with material absorption in Si-rich SiN. In-band dispersion is zero near center-band with an average wavelength slope of $\sim 0.3\,\mathrm{ns/nm^2}$. In the design, it varies from +40 ps/nm to -40 ps/nm across the 40 GHz passband.

The two-stage filter [Fig. 7.3(c)] shows a similar drop response with increased through-port extinction of over 30 dB across the channel, meeting typical requirements for WDM add-drop filtering. The inset shows a realized FSR above 20 nm. While theory predicts an extinction >60 dB for compensated 3-stage filters, the observed extinction [Fig. 7.3(d)] is above 51 dB across a 32 GHz window, limited by intra- and inter-stage frequency mismatch. Rings in compensated filters are synchronous to ∼2 GHz, corresponding to a matching of average ring widths to better than 70 pm. The 3-ring filter stages are frequency aligned to <5 GHz (∼12% of the bandwidth; see Fig. 7.3(d), inset), a critical requirement for practicability of multistage filters without post-fabrication trimming or active adjustment of individual rings. Adjacent channel insertion loss in the through port of a single stage is <0.3 dB. This puts a limitation on the number of stages that can be tolerated.

Drop and through port cascading

Multistage filters based on symmetric 2-ring stages were also designed and fabricated. They do not require frequency compensation and are less sensitive to variations, but require cascading in both the drop and the through paths [Fig. 7.1(b)] to meet similar drop-port rolloff criteria. They are also limited in range of applicability to WDM applications with coarse requirements. These structures will be described in greater detail elsewhere.

7.1.5 Asymmetric stages and loss-compensated multistage filters

The separation of functions afforded by the multistage design offers further advantage when substantial cavity losses are accounted. In particular, asymmetrical filter designs can be used to advantage. First, the concept of asymmetrical series-coupled-cavity filters for the purposes of loss-compensated flat-top responses and impedance-mismatched partially dropping filters (e.g. channel monitors) is presented. Second, the application of asymmetric filters as stages in a multistage arrangement is summarized by an example.

Asymmetrical series-cavity filters for loss compensation and channel monitors

Series-coupled cavity (SCC) high-order resonators [38] have a symmetric distribution of coupling coefficients to produce flat-top (maximally flat or equiripple) responses. However, when losses are introduced into the cavities, as is necessary to model realistic situations, the effect of the loss is to round passband edges. Large

rounding of the passband can affect the amplitude spectrum of the filtered signal, or introduce loss dependent on the wavelength alignment of the filter with the signal channel.

In this work, asymmetrical series-coupled-cavity filter designs are proposed. They are found to enable pole-preserving designs that can compensate for the passband shape distortions of cavity losses at the expense of larger midband insertion loss.

SCC filters have all-pole drop-port responses. Therefore, the algorithm proposed to arrive at a loss-compensated filter design is one that preserves the pole positions (which determine filter shape) of the lossless filter as cavity loss is smoothly introduced into the design. One starts with a lossless filter design, and gradually introduces loss, then corrects the coupling coefficients to preserve all the pole positions. It turns out that an N^{th}–order (N-cavity) filter has N poles, but $N+1$ coupling coefficients including input and output couplings to bus waveguides. This is in contrast to the low-pass electrical circuit (ladder-network) prototype that is equivalent to this filter[†] which, for fixed access port impedances, has exactly N inductive and capacitive elements.

Therefore, even after meeting all requirements to keep the pole positions fixed after the introduction of loss, there is one degree of freedom remaining. This degree of freedom is equivalent to impedance matching. Let us choose the first coupling coefficient (of the first ring coupling to the input waveguide) as the free parameter. Then, if the input coupling is varied, while the other couplings are adjusted to keep the pole positions fixed either when the input coupling is modified, or when loss is introduced, or both, the result is that the filter passband shape is maintained. When the input coupling is varied, the overall insertion loss level of the filter response changes however, as its analogy with impedance matching would imply.

This has two consequences. First, it allows one, in a lossy filter, to find the lowest loss design (among the possible cases parametrized by adjusting the additional degree of freedom) in addition to maintaining the flat-top filter shape. There is indeed a minimum-loss design and it generally turns out to have an asymmetrical distribution of coupling coefficients in higher-order filters. Incidentally, it has been suggested in previous literature that the critical coupling condition maximizes drop-port response transmission in a *single-ring* add-drop filter [55, 141]. This claim is not true. It can be simply proven that for a fixed bandwidth Lorentzian response, the lowest drop-port loss is arrived at, in fact, in a design with equal input and output coefficients. While it is well known and true that critical coupling is optimal in one sense in that all power is extracted from the input waveguide, in this case, more power is given up to the loss mechanism, so overall the drop loss is higher than in the symmetric case. However, the generalization described here to higher-order filters does indeed typically lead to asymmetrical distributions of

[†]This correspondence was briefly described by the author in [8].

couplings.

The second consequence of the extra degree of freedom is that it allows new flat-top filter designs even in substantially lossless resonant filters. For example, by lowering the input coupling, and adjusting the remaining couplings to maintain the flat-top filter shape, an impedance-mismatched flat-top filter is designed that drops only a fraction (e.g. 10%) of the input signal, and leaves the remainder to continue into the through port. If the input coupling was lowered from the nominal value, then the filter is in the undercoupled regime, which means it provides lower out of band dispersion in the through port, and also has a larger coupling gap and lower group delay for through-port channels. These factors mean that it can be used as an efficient channel monitor that introduces very low excess losses and dispersion into through-port channels.

It should be noted that flat-top responses may not be optimal for telecom applications. For example, Bessel filters with rounded passbands provide linear phase (no dispersion) in the passband of SCC filters. It turns out that asymmetrical designs can be used to arrive at these designs too. When loss is introduced into a flat-top filter, the passband rounds where it is most sensitive to loss, i.e. at the band edges where high-Q supermodes are found. Then, one may fix the passband shape, remove the loss and vary the coupling distribution to preserve the shape in a lossless case. For filters rounder than a Butterworth response, the couplings will typically be asymmetric.

Further details, analysis and examples of this work are described at greater length in [142].

Asymmetrical stages in multistage filters

In the presence of substantial cavity losses, passbands are rounded. A multistage configuration (Fig. 7.4) can further enable independently designed asymmetric first and last stages to maintain flat-top input-to-drop and add-to-through responses, while the intermediate stage ensures a maximum rejection across the channel band in the through (input-to-through-port) response. The first and last stage couplings are the same: $\{6.8, 0.084, 0.22, 1.9\}\%$, designed to maintain a flat-top filter shape in a 3-ring SCC filter with 3 THz FSR (realizable with low bend loss in SiN microring resonators) and a loss Q of 15,000 in the cavities. The middle stage, on the other hand, is designed to compensate the deteriorated through port that results in the first and third stages and has the couplings: $\{8.2, 0.16, 0.16, 15.6\}\%$. The resulting response, shown in the figure, demonstrates a flat-top drop-port response and a flat extinction in the through port in a filter with substantial finite losses. Of course there is an insertion loss, but this aspect cannot be avoided.

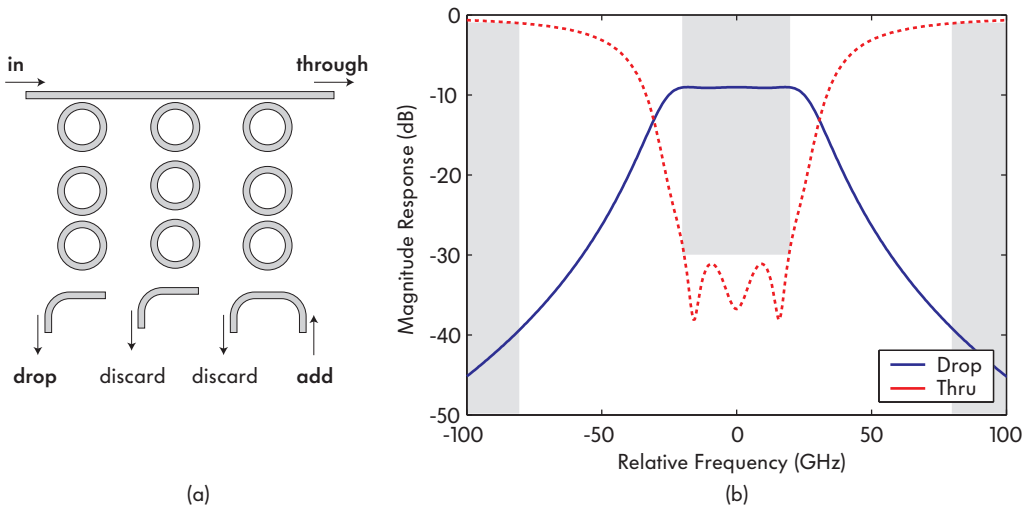

Figure 7.4: Multistage filters based on asymmetric, loss-compensated filter stages: (a) Loss-compensated multistage filter simulation. Non-identical stages give (b) flattened lossy passband and high-extinction through-port (published in [142]).

7.1.6 Conclusions

Multistage add-drop filters based on HIC, third-order microring-resonator stages were experimentally demonstrated. They showed tight stage-to-stage resonance alignment and accurate realization, matching design, of 40 GHz flat-top responses with $\sim$ 30 dB in-band extinction and 20 nm FSR. The filters satisfy basic requirements for a 100 GHz WDM grid, without the need for post-fabrication trimming or active adjustment of individual cavities.

The presented multistage add-drop filters demonstrate the first high-extinction, rectangular notch spectra achieved experimentally in microring resonators, exceeding 50 dB. These are also the first microphotonic filters to show low-loss, high-fidelity flat-top responses that meet the full spectral requirements of WDM add-drop filtering. The ease of increasing complexity in microphotonic circuits promises a path to higher extinction levels and spectral selectivity where macroscale approaches are limited.

Asymmetrical SCC filters were described that allow flat-top filters compensated for loss, minimum-loss design, as well as lossless flat-top filters with impedance mismatch and low dispersion for fractional-power dropping for channel monitoring applications. Multistage filters based on asymmetrical stages allow both through and drop port responses compensated for the spectral response distorting effects of loss.

It is shown in other parts of this work (Chaps. 8 and 9) that these filters are in principle suitable for hitless tuning [143], an important capability for wavelength routing networks that is difficult to achieve in bulk-optical technologies.

Part IV

Transparent switching of the amplitude and phase response of resonant systems

Chapter 8

Universally balanced interferometers as bypass schemes

In this section, a new class of interferometers is proposed in which the spectrum entering one input port may be split among the interferometer arms in an arbitrarily chosen wavelength- and/or time-dependent manner, but is fully recombined in a single corresponding output port by symmetry. On account of the guaranteed constructive interference, the proposed devices are referred to as universally balanced interferometers (UBIs). They are a generalization of a bypass switch proposed by Haus [143] and summarized in Sec. 8.2.1. The types of interferometers that have proven useful in optics (Mach-Zehnder, Fabry-Perot, Michelson) have generally entailed fixed-reflectivity mirrors and adjustable arm lengths. In UBIs, illustrated in Fig. 8.1, the "mirror" design is largely arbitrary [and may contain couplers, resonators, switches, and non-reciprocal elements – see Fig. 8.2(a)], while the interferometer arms are fixed. Hence, they are primarily suitable for microphotonic circuit realization.

An important application of UBIs is as a general bypass scheme for photonic devices. A generic UBI modified by an inserted optical processing device F in one interferometer arm is shown in Fig. 8.1. This configuration permits the device access to a part of the input spectrum routed to it by input mirror A. The part of the spectrum passing unaffected through the device F is recombined with the bypass signal in a single output port (of A'). New generalized filter designs emerge that address hitless tuning [143] and dispersion-free multiplication of the free spectral range (FSR) of microresonators [63, 144], enabling their introduction into chip-scale tunable wavelength routers.

First, I describe the physical principle of operation and show that UBIs guarantee broadband constructive interference into one output port, for a general class of

input mirror choices. This principle is represented as a simple conceptual "lossless UBI rule", and a second generalization, the "lossy UBI rule". Next, sensitivities of UBIs to loss, phase error, and asymmetric actuation are described. Then, folded UBIs – using non-reciprocal delay lines – are described, along with their potential applications.

Among several novel applications of UBIs, I propose a spectrum slicing UBI that suppresses undesired resonances and provides a new way to multiply the effective FSR and wavelength tunability of a microphotonic add-drop filter, without adding excess dispersion. I outline a geometrical proof, based on canonical representations described in Sec. 2.2, that UBIs using arbitrary cascaded Mach-Zehnder lattice filters [145] as mirrors contribute zero excess dispersion in general, even when the splitter and combiner are each dispersive.

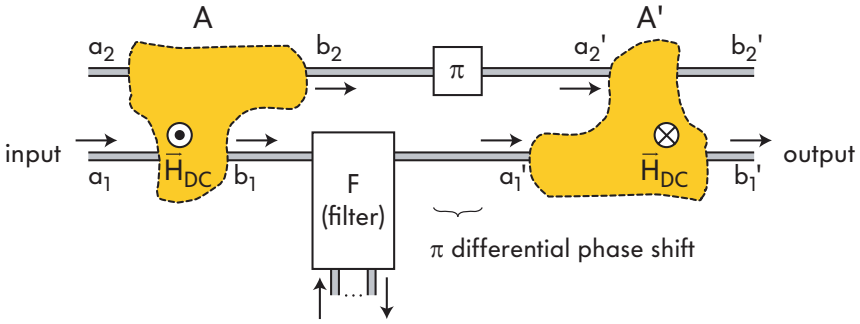

Figure 8.1: Conceptual representation of general universally balanced interferometer (UBI), with a filter inserted in one arm and excited from one input port, recombines all unfiltered spectrum in one output port (published in [63]).

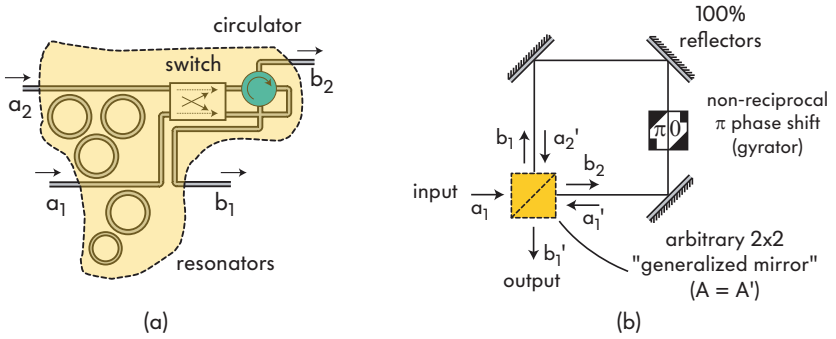

Figure 8.2: (a) Illustrative example to show that the UBI splitting "mirror" A may be of arbitrary design (and may even be non-reciprocal); (b) a folded UBI arrangement, in a free-space representation. A folded UBI requires a non-reciprocal π differential phase shift. A non-reciprocal phase shift corresponds to the action of a gyrator element [48] (published in [63]).

8.1 Theory of UBIs

8.1.1 Principle of operation: a physical viewpoint

Consider a generic interferometer with a splitter "mirror" A and a combiner mirror A' (Fig. 8.1 without filter F), each having 2 input and 2 output ports. In a folded embodiment in Fig. 8.2(b), A and A' are coincident. Sufficient conditions to construct a UBI are that: combiner A' operate as a time-reversed and *port-complementary** replica of the splitter A; each be a substantially lossless and reflectionless (LR) 4-port; and the interferometer arms be fixed with a π differential phase shift (DPS). Referring to Sec. 2.2.1, a general 4-port optical hybrid A that is LR can be represented by a 2×2 unitary transfer matrix $\overline{\overline{\mathbf{U}}}$ (with $\bar{b} = \overline{\overline{\mathbf{U}}}\cdot\bar{a}$) of the most general form (2.10). Factorized into a form more suitable for a physically intuitive description, $\overline{\overline{\mathbf{U}}}$ is

$$\begin{aligned}\overline{\overline{\mathbf{U}}} &= e^{i\theta_o}\begin{bmatrix}\sqrt{1-\kappa}\,e^{i\theta_1} & i\sqrt{\kappa}\,e^{i\theta_2}\\ i\sqrt{\kappa}\,e^{-i\theta_2} & \sqrt{1-\kappa}\,e^{-i\theta_1}\end{bmatrix} \\ &= \begin{bmatrix}e^{i(\theta_1+\theta_2)} & \\ & 1\end{bmatrix}\begin{bmatrix}\sqrt{1-\kappa} & i\sqrt{\kappa}\\ i\sqrt{\kappa} & \sqrt{1-\kappa}\end{bmatrix}\begin{bmatrix}e^{-i\theta_2} & \\ & e^{-i\theta_1}\end{bmatrix}e^{i\theta_o}\end{aligned} \tag{8.1}$$

symmetrized so that $\theta_o \equiv (\phi_{11}+\phi_{22})/2$, $\theta_1 \equiv (\phi_{11}-\phi_{22})/2$ and $\theta_2 \equiv (\phi_{12}-\phi_{21})/2$; where elements of $\overline{\overline{\mathbf{U}}}$ are labeled $u_{mn} \equiv |u_{mn}|\,e^{i\phi_{mn}}$. One coupling ratio and three phases remain as free parameters, the fourth phase having been fixed by the requirement of unitarity (2.7) that $\phi_{11}+\phi_{22}-\phi_{12}-\phi_{21} = \pm\pi$.

This π unitary phase condition contributes in an essential way to the construction of a UBI. Otherwise, design of the "mirror" A is arbitrary, and may contain couplers, resonators, switches, and non-reciprocal elements (circulators, gyrators). Its T-matrix, $\overline{\overline{\mathbf{U}}}$, may be wavelength-dependent and controllable in time (such as a tunable filter or switch), i.e. $\overline{\overline{\mathbf{U}}} \equiv \overline{\overline{\mathbf{U}}}(\lambda, p)$, where p parametrizes the possible (switch) configurations. The λ and p dependence is understood and omitted henceforth.

A general physical argument for the design of a UBI can be given by considering a canonical physical model for splitter A (see Sec. 2.2.1). Only the left-most two matrices in the factorization in Eq. (8.1) are physically relevant to interference in Fig. 8.1. Thus, arbitrary splitter A may at any *one* (λ, p) be described as an ideal directional coupler with coupling ratio κ and a characteristic phase shift $\phi_o \equiv \theta_1 + \theta_2$ in one output arm. This is illustrated in Fig. 8.3(a) excited from one port.

With the objective of recombining all signal power from the interferometer arms into one waveguide, it is instructive to think in terms of time reversibility of

*A "port-complementary" replica here means a replica that is excited from the opposite input port (of two input ports) with respect to the original structure.

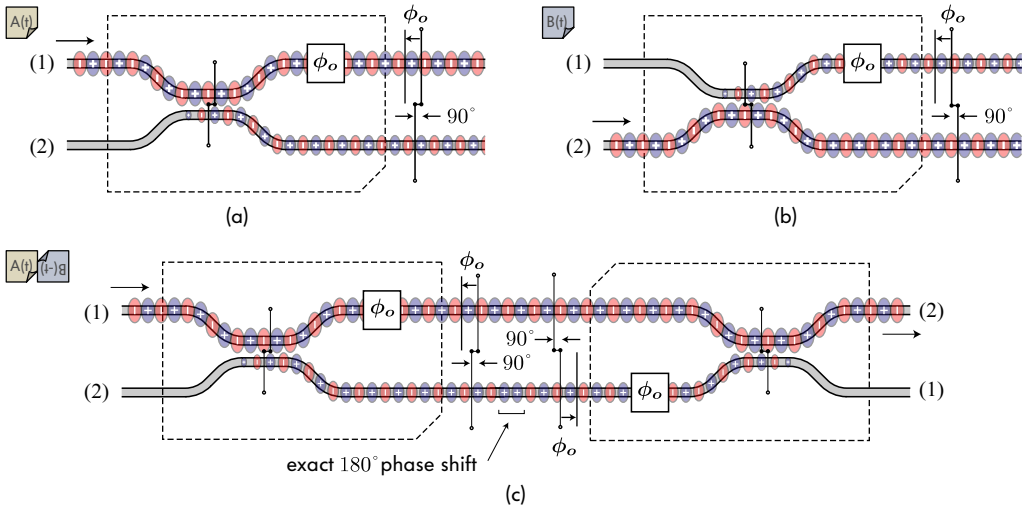

Figure 8.3: Canonical models of arbitrary LR 4-port mirrors, and of a constructed UBI. (a),(b) Excitation at port 1 or 2 gives respectively $\pi/2 \mp \phi_o$ differential phase at the outputs; (c) cascading splitter from (a) and the time-reversed and 180° rotated version of (b) cancels arbitrary phase ϕ_o. If the remaining π differential phase shift is compensated, perfect constructive interference is obtained, i.e. a UBI is derived (published in [63]).

Maxwell's equations. Reversing time shows that properly phased arm excitations re-enter the upper waveguide to the left. This conclusion might suggest using a $\mathcal{V}$-reflected mirror-image (see Fig. 2.4) replica device in cascade at the output to recombine the signal. However, an interferometer constructed from a splitter A, and a combiner that is a $\mathcal{V}$-mirror-image replica of A with respect to a vertical reflection axis (flipped left-to-right on page) is inconvenient in the general case. This is because the arm lengths have a phase difference of $2\phi_o$, dependent on the arbitrary design of A, that must be compensated; and ϕ_o may be wavelength (or time) dependent (a few specific designs that have intrinsically $\phi_o = 0$ are presented later in the chapter). In general, a more profitable approach is to consider the same splitter A excited from the *complementary* input port [Fig. 8.3(b)]. The splitting ratio is the same, but the phase difference between higher and lower intensity outputs, as illustrated, is now $\pi/2 + \phi_o$ instead of $\pi/2 - \phi_o$. This is enforced by the unitary phase condition (2.7). Now, we take the time-reversed operation of Fig. 8.3(b), mirror imaged with respect to both a vertical ($\mathcal{V}$) and horizontal ($\mathcal{H}$) axis of reflection, to represent output combiner A'. This is equivalent to a rotation of splitter A by 180° ($\mathcal{HV}$ operation) in the plane of the chip. Then, the arbitrary phases ϕ_o cancel and only a π differential phase shift remains [Fig. 8.3(c)]. If the π-radian DPS is compensated by inserting a broadband π phase shift in one arm, a general UBI device of the form of Fig. 8.1(a) is derived.

The matrix formalism shows this rigorously. In the time-reversed solution (subscripted by *tr*) corresponding to a particular excitation of splitter A, the outputs become the inputs ($\bar{b}^* \rightarrow \bar{a}_{tr}$), the inputs become the outputs ($\bar{a}^* \rightarrow \bar{b}_{tr}$) and

the time-reversed transfer matrix is $\overline{\overline{\mathbf{U}}}_{tr} = [\overline{\overline{\mathbf{U}}}^{*}]^{-1}$ (in the time-reversed solution, material-response phasor tensors are conjugated as $\overline{\bar{\epsilon}} \rightarrow \overline{\bar{\epsilon}}^{*}$ and $\overline{\bar{\mu}} \rightarrow \overline{\bar{\mu}}^{*}$). Note that time reversal corresponds to conjugation of the field phasors or mode amplitudes [67, p. 82]. For a splitter A and combiner A' comprising lossless ($\overline{\bar{\epsilon}} = \overline{\bar{\epsilon}}^{\dagger}, \overline{\bar{\mu}} = \overline{\bar{\mu}}^{\dagger}$) and reciprocal ($\overline{\bar{\epsilon}} = \overline{\bar{\epsilon}}^{T}, \overline{\bar{\mu}} = \overline{\bar{\mu}}^{T}$) media, the time-forward and time-reversed solutions are supported by one and the same structure. For non-reciprocal lossless media, the time-reversed solution is supported by a structure with a reversed orientation of the built-in (and any applied) DC bias magnetic fields ($\bar{H}_{DC} \neq 0$ in Fig. 8.1). Thus, A and A' may be non-reciprocal and still form a valid UBI structure, except in a folded arrangement [Fig. 8.2(b)] where they are coincident and must therefore be reciprocal. This is a rare if not unique application of the time-reversal principle for the design of a device, where it is not used in the context of a *symmetry* under time reversal (which leads to reciprocal devices), because the "time-forward" and "time-reversed" operation occur in separate copies of a device.

8.1.2 The UBI rule

The total transfer matrix of the UBI in Fig. 8.1 involves [from right to left in eq. (8.2)] the splitter A (matrix $\overline{\overline{\mathbf{U}}}$), a π differential phase shift matrix, and the matrix of the second, time-reversed element ($\overline{\overline{\mathbf{U}}}_{tr}$), sandwiched by Pauli matrices here representing reflection about a horizontal axis ($\mathcal{H}$ operation):

$$\overline{\overline{\mathbf{T}}} = \begin{bmatrix} 0 & 1 \\ 1 & 0 \end{bmatrix} \overline{\overline{\mathbf{U}}}_{tr} \begin{bmatrix} 0 & 1 \\ 1 & 0 \end{bmatrix} \begin{bmatrix} 1 & 0 \\ 0 & e^{i\pi} \end{bmatrix} \overline{\overline{\mathbf{U}}}. \tag{8.2}$$

From unitarity, $\overline{\overline{\mathbf{U}}}_{tr} \equiv [\overline{\overline{\mathbf{U}}}^{*}]^{-1} = \overline{\overline{\mathbf{U}}}^{T}$, as described in Sec. 2.2 (Fig. 2.4). This, and the form (8.1) for $\overline{\overline{\mathbf{U}}}$ lead to the simplified total matrix

$$\overline{\overline{\mathbf{T}}} = e^{i2\theta_o} \begin{bmatrix} 1 & 0 \\ 0 & -1 \end{bmatrix}. \tag{8.3}$$

Thus, all signal entering an input port recombines in one output port, regardless of the splitting ratio and phase relationship within the interferometer determined by the splitter A. No assumptions about the particular design of splitter A were made beyond unitarity of $\overline{\overline{\mathbf{U}}}$. It is interesting, from (8.2) and (8.3), to see that A', preceded and followed (not shown) by a π-radian differential phase shift, is a kind of *inverse* – in the sense of amplitude only – to the arbitrary unitary operator corresponding to splitter A; however, a common-mode phase spectrum $\theta_o(\lambda, p)$ is not canceled by A' in general.

This property may be summarized in a different but equivalent manner by noting that the cascade (i.e. matrix product) of this "inverse" of A and the T-matrix of the splitter A itself, is the identity matrix, to within a phase-factor (which may be wavelength- and time-dependent), as illustrated in Fig. 8.4. This property will

be referred to as the *UBI rule*, and more specifically as the *lossless UBI rule*, as its derivation relied on energy conservation (but holds valid for non-reciprocal as well as reciprocal devices). This rule is helpful for analysis of interferometer structures and is used here to derive a proposed dispersionless Vernier filter scheme, as well as to derive an alternative lossy UBI rule in other parts of this chapter.

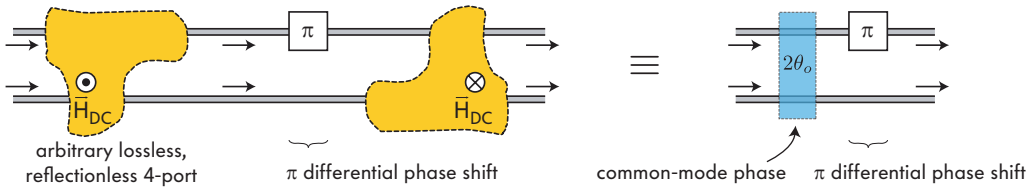

Figure 8.4: The *lossless UBI rule*: a UBI with lossless (reciprocal or non-reciprocal) splitter A and combiner A' is equivalent to a pair of non-interacting waveguides with a π differential phase shift and a common-mode phase θ_o, as per Eq. (8.3).

8.1.3 Broadband π differential phase shifts and UBI sensitivities

From the derivation of the UBI rule it is clear that the π differential phase shift plays an essential role. Therefore, in this section, first the sensitivity of UBI operation to deviations from a π phase shift in this principal parameter is shown to be reasonably weak. Since, for broadband operation, a π DPS must be substantially maintained over the entire operating wavelength range, designs of an ultra-broadband π DPS are next analyzed and proposed. Finally, the sensitivity of UBIs to non-idealities in other important parameters such as finite loss of the splitter A, and asymmetry between elements A and A', are addressed and UBIs are shown to be remarkably tolerant in principle and in the appropriately defined sense in each case.

Previous work using interferometers with a π DPS

We briefly address previous work that exhibits most similarity to UBIs in principle of operation. Haus' hitless switch [143] relies on this principle, and thus belongs to the general class of UBIs, as summarized later in Sec. 8.2.1. In earlier work, Henry *et al.* employed a π differential phase shift to flatten the wavelength response of a Mach-Zehnder Bragg grating filter [146]. In addition, considerable work exists in integrated-optics literature on so-called cascaded-MZI, or lattice, filters [66, 145], including ones using point-symmetric configurations [66] like UBIs. However, the previous use of point-symmetric structures for flattened *cross-state* passbands [66] does not rely on a π DPS, and therefore does not fall in the UBI class of devices. Furthermore, to avoid confusion it should be restated here that UBIs may contain arbitrary reflectionless 4-port photonic circuits in splitter A, and are not limited to cascaded-MZI configurations, though several applications of UBIs may employ them. Further to this point, it is worth restating that Fig. 8.3 is an abstract

canonical representation of an arbitrary lossless UBI (at a fixed wavelength λ and configuration p), and does not refer solely to a concrete directional coupler. It may indeed represent devices comprising resonators, magnetooptic devices such as circulators, etc.

UBI sensitivity to π differential phase shift error

In Fig. 8.5(a), the effect of error in the differential phase shift of π radians on the UBI transmission is plotted. The range of possible insertion losses due to incomplete recombination of output signals by the combiner device A' is indicated for a range of fractional error in the π DPS. It is shown that less than 1 dB loss in recombination at the combiner A' is obtained for up to 30% deviation from the ideal π DPS, substantially less than 0.2 dB for less than 10% deviation, and virtually no excess loss for under 5% deviation. A gray region between two contours shows all possible loss values, for various relative amplitude ratios of the two signals entering A'. This gives a general requirement for physical realizations of the DPS. Ideally, the DPS should be between 0.95π and 1.05π over the operating wavelength range. The largest loss in recombination is seen when the splitting ratio of the splitter device A is near $1:1$, shown as the bottom limit of the gray region of possible losses in Fig. 8.5(a). In contrast, virtually no signal is lost in operating regimes where the splitter device substantially transfers all power to one or the other optical path, because the interferometric character of the device is not important in that case (represented as the top boundary of the gray loss region).

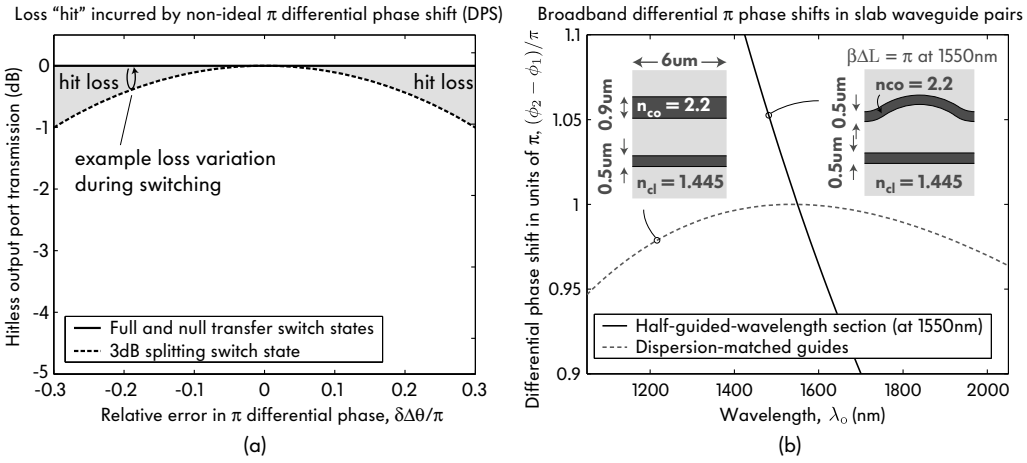

Figure 8.5: (a) Tolerability of lossless UBI transmission efficiency to error in the π differential phase shift, showing corresponding signal recombination loss, equivalent to "hit loss" for UBI-based hitless switch implementations; (b) deviation from a π phase shift of a standard half-guided-wavelength and an ultra-broadband π DPS design. (published in Ref. [143])

Design of broadband π differential phase shifts

Since UBIs employ arbitrary splitter A and combiner A' (subject to their required relative configuration), they operate in a regime with nearly perfect signal recombination at a single output port over a bandwidth that is only as broadband as the π differential phase shift realization employed. The most straightforward physical realization of a π DPS is a half-guided-wavelength arm length difference (at a given wavelength) in the waveguide pair connecting splitter A and combiner A'. The guided wavelength of the propagating mode is related to its propagation constant β as $\lambda_{\text{guided}} = 2\pi/\beta$. A half guided-wavelength may be equivalent to a π DPS at a select wavelength, but waveguide dispersion (and plain frequency dependence of the propagation constant) causes the DPS to vary with wavelength. Nevertheless, the short length guarantees a reasonably large bandwidth. For example, identical cross-section slab waveguide arms with core index 2.2, cladding index 1.445 and thicknesses of 0.5 μm (TE) give less than 5% deviation in the π DPS from its nominal value over 140 nm bandwidth, as shown in Fig. 8.5(b). This is sufficient bandwidth to cover optical communication bands, with negligible loss in recombining the total power and negligible "hit" loss (if used for hitless switching).

Next, an approach is proposed for designing ultra-broadband DPS sections. For cases where wider bandwidth or lower hit loss is required, the dispersion of the waveguides in the two interferometer arms of the UBI may be engineered by using non-identical waveguide cross-sections. If the two waveguides 1 and 2 have lengths L_1 and L_2, then in the ideal case, for a π DPS to be established the following needs to hold for all frequencies of interest, ω: $\beta_1(\omega)L_1 - \beta_2(\omega)L_2 = \pi + 2\pi m$, with m integer. In a band of interest near ω_o, a first-order Taylor-series expansion of $\beta(\omega)$ in frequency detuning $\delta\omega$ yields two requirements (from the zeroth and first order terms in $\delta\omega$):

$$\beta_1(\omega_o)L_1 - \beta_2(\omega_o)L_2 = \pm\pi + 2\pi m$$
$$\left.\frac{\partial\beta_1}{\partial\omega}\right|_{\omega_o} L_1 - \left.\frac{\partial\beta_2}{\partial\omega}\right|_{\omega_o} L_2 \equiv \left.\frac{L_1}{v_{\text{g1}}}\right|_{\omega_o} - \left.\frac{L_2}{v_{\text{g2}}}\right|_{\omega_o} = 0$$

The first equation requires that there be a π DPS at the reference frequency. The second equation requires that the group delays across the two sections be matched. Such waveguide designs are realizable. For sake of illustration, again a two-dimensional example is given – a pair of slabs as above, this time of identical lengths $L_1 = L_2 = 6.5\,\mu\text{m}$, but having widths of $0.5\,\mu\text{m}$ and $0.9\,\mu\text{m}$, respectively. The pair yields a π DPS within 5% over more than 900 nm, as shown in Fig. 8.5(b). It is interesting to note that two waveguides with different widths and otherwise identical design may have the same transit time and (since they have equal lengths) equal group velocities (to within 0.05%), even though their propagation constants differ by over 5%. This match, of course, exists only at the design wavelength of 1550 nm. With guides of non-identical design, in practice propagation loss in the

two arms (e.g., sidewall-roughness-induced loss [127]) can be different and cause imbalance in the UBI. Care is required in design to ensure balanced arm losses. For short-length waveguides this may not pose a problem, and otherwise it can be compensated.

A second, more important issue is that a functional device that is inserted into the UBI (see Fig. 8.1), such as a channel add/drop filter, may alter the phase balance. If the device adds phase and dispersion over the wavelength range over which UBI operation is expected, it may be compensated by design in the second arm (by altering the design of that waveguide or inserting a designed phase-compensating device) to restore the π DPS. This issue is demonstrated in hitless switch designs in Sec. 8.2.1, and was the driving factor for novel designs in Chap. 9 which address and circumvent this problem.

UBI sensitivity to antisymmetric perturbations

UBIs rely on identical splitter A and combiner A' (except for their orientation and any bias magnetic field in the non-reciprocal case). Therefore, common-mode perturbations of the splitter and combiner – ones which change both in the same way – do not alter ideal UBI operation in the sense that complete constructive interference into a single output port is preserved, although the spectrum splitting response into the two UBI arms between the splitter and combiner will be accordingly affected.

On the other hand, antisymmetric perturbations to A and A' directly affect the overall constructive interference that characterizes UBIs. Here, sensitivity of UBI operation to antisymmetric perturbations of splitter A and combiner A' is considered.

The splitter and combiner have T-matrices that are cross-transposes[†] of each other, and may be represented in standard form (2.10). Referring to the canonical representation for LR 4-ports in Fig. 2.6, for the lossless splitter A, it may be observed by inspection that antisymmetric perturbations to θ_o, θ_1 or θ_2 in A and A' lead effectively to an error in the DPS between the splitter and combiner, the sensitivity to which was addressed in Fig. 8.5(a). Therefore, here only antisymmetric perturbation of the coupling ratio is considered.

Now, suppose that we introduce an arbitrary antisymmetric error to the coupling ratio κ in the transfer matrices of the splitter and combiner. The coupling ratio in the splitter A is increased by δ_κ, such that $\kappa \rightarrow \kappa + \delta\kappa$, and the coupling ratio in the combiner A' is decreased by $\delta\kappa$. Since perturbations cannot increase κ to first order when $\kappa = 1$ (nominally) or decrease it when $\kappa = 0$, let us first rewrite the coupling ratio in terms of a beat length so that $\sqrt{1-\kappa} \equiv \cos(\theta_\kappa)$ and $\sqrt{\kappa} \equiv \sin(\theta_\kappa)$. The phase θ_κ has physical significance as an optical beat length in a synchronous directional coupler, for example, and therefore errors in θ_κ are an

[†]see definition (2.5) in Chap. 2.

appropriate way to characterize error sensitivity at all nominal values of κ. The nominal transfer matrix of the splitter can then be rewritten as

$$\overline{\overline{\mathbf{U}}}_{\mathrm{A}} \equiv \overline{\overline{\mathbf{U}}}^{C}_{\mathrm{A}'} = e^{i\theta_o} \begin{bmatrix} \cos(\theta_\kappa)e^{+i\theta_1} & i\sin(\theta_\kappa)e^{+i\theta_2} \\ i\sin(\theta_\kappa)e^{-i\theta_2} & \cos(\theta_\kappa)e^{-i\theta_1} \end{bmatrix}$$

If an antisymmetric error is introduced (e.g. due to limitations in device fabrication), then $\theta_\kappa \rightarrow \theta_\kappa + \delta\theta$ in the splitter A, and $\theta_\kappa \rightarrow \theta_\kappa - \delta\theta$ in the combiner A'. The T-matrix of the total UBI, comprising the perturbed splitter A, an ideal π DPS, and the perturbed combiner A' is

$$\overline{\overline{\mathbf{T}}} = \overline{\overline{\mathbf{U}}}_{\mathrm{A}'} \cdot \begin{bmatrix} 1 & 0 \\ 0 & e^{i\pi} \end{bmatrix} \cdot \overline{\overline{\mathbf{U}}}_{\mathrm{A}} \tag{8.4}$$

$$= e^{i2\theta_o} \begin{bmatrix} \cos(2\delta\theta) & -ie^{+i(\theta_1+\theta_2)}\sin(2\delta\theta) \\ ie^{-i(\theta_1+\theta_2)}\sin(2\delta\theta) & -\cos(2\delta\theta) \end{bmatrix}. \tag{8.5}$$

A few conclusions may be drawn from this transmission response of the asymmetrically perturbed UBI. First, it is independent of the nominal coupling phase θ_κ, which means that the UBI sensitivity to antisymmetric perturbation $\delta\theta$ is the same for all nominal values of θ_κ (this is reasonable as there is no reason why there should be a special coupling phase value). Secondly, if the antisymmetric coupling perturbation is zero, $\delta\theta \rightarrow 0$, the combiner A' is identical to the splitter A and the total transfer matrix is the ideal UBI transfer matrix in eq. (8.3).

On the other hand, if finite asymmetry is present due to fabrication errors, then $\delta\theta \neq 0$. The matrix elements T_{11} and T_{22}, that have unity magnitude in an ideal UBI and are the response functions of interest, are reduced from unity to second-order in $\delta\theta$. This is evident from a Taylor-series expansion of the matrix in eq. (8.5) in orders of $\delta\theta$, so that $T_{11} = \cos(2\delta\theta) = 1 - 2\,\delta\theta^2 + \mathcal{O}(\delta\theta^4)$. Therefore the UBI transmission response function of interest is first-order insensitive to small asymmetric perturbations in the coupling ratio of the splitter A and combiner A'.

This insensitivity can be restated in terms of the power coupling ratio κ. For $\kappa + \delta\kappa = \sin^2(\theta_\kappa + \delta\theta)$, and for small $\delta\theta$, the coupling ratio error $\delta\kappa$ and corresponding coupling phase error $\delta\theta$ are related by: $\delta\kappa = 2\sqrt{\kappa}\sqrt{1-\kappa}\,\delta\theta$. Therefore, a given error in the coupling phase θ_κ results in the largest absolute perturbation to the coupling ratio κ when $\kappa = 1/2$, i.e. at the 3 dB coupling ratio point. This is consistent with sensitivity to the errors in the DPS, which was also shown to be most acute at the equal splitting ratio point.

A further comment is in order regarding the sensitivity to antisymmetric coupling ratio perturbations. Even though the recombining response T_{11}, as shown, is first-order insensitive to antisymmetric perturbations to the coupling ratios of the splitter A and combiner A' at any particular wavelength in the wavelength range of interest, this cannot be translated to a conclusion that all UBI designs are highly

tolerant to *dimensional* errors. In some possible device designs for a splitter A, the $\delta\kappa$ (or $\delta\theta$) perturbation of the ideal T-matrix, if resulting from a dimensional error for example, can be highly sensitive to that dimensional error. In this case, a minute dimensional error can cause a large $\delta\kappa$, and thus the demonstrated first-order insensitivity in $\delta\kappa$ will be insufficient to preserve successful operation. An important example are high-Q (narrow-band) resonators. A resonant filter, such as a microring-based channel add-drop filter, supports drop-port responses that have narrow resonant lineshapes. The sensitivity of the resonant frequency to dimensional error can be very large, as shown in Chap. 5 (Fig. 5.9). For example, typical microring resonators formed of SiN single-mode waveguides in Appendix E and Sec. 7.1 were shown to have approximately 40 GHz/nm sensitivity of the resonance frequency to the width of the waveguide. The width is lithographically defined and therefore typically a larger contribution to resonance error than waveguide thickness. Based on this information, only a 1Å error in ring-waveguide width will shift a resonance by 4 GHz. If the bandwidth of the resonant response of interest is on the order of 4 GHz, clearly the transmission of the device can change from nearly 100% to nearly 0% at one wavelength, due to the dimensional error. The resulting $\delta\kappa$ in the coupling ratio of a splitter A containing such a resonator is of order 1, and thus no first or even higher order insensitivity would help make the operation robust to such errors.

This is a fundamental limitation of UBIs. However, this problem is eliminated by the inherent symmetry in folded UBIs, proposed in Sec. 8.3, which use the same device as the splitter and combiner element.

UBI sensitivity to loss

For practically relevant devices, the impact of finite loss on the operation of UBIs must also be considered. Recall that the initial derivation of the UBI principle in Sec. 8.1.1 relied on the assumption of lossless devices in two ways: first, in the use of time reversibility in the analysis; and second, in making use of the unitary phase condition (2.7).

Loss may be introduced into the splitter A and combiner A', into the pair of waveguides connecting them (including the π DPS), or both. Arbitrary common-mode loss, gain or phase modulation in the two waveguides is permitted and does not impair the operation of an UBI. Common-mode operations on the optical signals in the two waveguides "commute" with the splitter A and combiner A', so the common-mode loss, gain or phase shift may be moved from inside the UBI to outside, i.e. before the splitter, or after the combiner, without affecting the overall response of the device.

Antisymmetric loss in the waveguide arms cannot be tolerated, but if it can be predicted at the design stage it may still be compensated by adding a balancing loss element in the lower-loss waveguide arm.

When small but finite loss is introduced into the splitter A and combiner A', on the other hand, not only is loss introduced, but the unitary phase condition (2.7) is violated. However, it was shown in Sec. 2.2.4 that passive reflectionless 4-ports satisfy a bound (2.29) on the characteristic phase, that is analogous to the unitary phase condition, the bound being tighter for lower maximum loss values. Referring to Fig. 2.11(c), for example, we may infer that for an arbitrary passive splitter A with no more than $10:1$ maximum splitting ratio from one port, and 1 dB of loss, the characteristic phase is π to within about $\pm 10\%$. For larger splitting ratios, the characteristic phase is less well bound. However, it was shown that UBIs are most sensitive to phase errors at balanced splitting ratios of the splitter and combiner, near $1:1$, and very weakly sensitive at high splitting ratios of the order of $10:1$ or more. Therefore, UBIs are not highly sensitive in general to reasonably small losses of the order of 1 dB. It is noted that here the impact of loss on the time-reversal aspect was disregarded, and in the future this should be accounted to complete this analysis.

8.1.4 Reciprocal passive/active UBIs by SVD and the lossy UBI rule

The argumentation regarding sensitivity of UBIs to small losses in the previous section holds in the context of reciprocal and non-reciprocal splitter A and combiner A' elements. An exact generalization of the UBI principle may be derived that is valid for passive and active devices with arbitrarily high loss or gain, if the scope is restricted to reciprocal devices only.

UBIs that use a highly lossy splitter A and combiner A' elements cannot be expected to recombine all input signal energy at the output, since some signal energy is lost to the particular loss mechanisms present in A and A'. These loss (or gain) mechanisms may be broadband or arbitrarily wavelength dependent. Under these constraints, the best possible outcome in terms of proper UBI operation would be for all *remaining* signal to be recombined into a single output port. This may be accomplished by lossy UBIs when splitter A and combiner A' are reciprocal. It is first demonstrated briefly using the T-matrix transformations in Fig. 2.4, and then shown in a more physically intuitive way using the SVD canonical form in Fig. 2.10.

If the transfer matrix of the splitter A is $\overline{\overline{\mathbf{U}}}$, then for a reciprocal device, the combiner A' – being a 180° rotated copy of A – has the T-matrix, according to Fig. 2.4,

$$\overline{\overline{\mathbf{U}}}_{A'} = \overline{\overline{\mathbf{U}}}_{A}^{C} = \begin{bmatrix} u_{22} & u_{12} \\ u_{21} & u_{11} \end{bmatrix}.$$

Although this passive-device derivation is based on reciprocity, while the lossless derivation was based on time reversal, the total transfer matrix of the UBI comprising a reciprocal, lossy splitter A, a pair of optical waveguides with a π-radian DPS,

and a corresponding combiner A' as described above is of identical form to (8.2) and results in:

$$\overline{\overline{\mathbf{T}}} = \overline{\overline{\mathbf{U}}}_{A'} \cdot \begin{bmatrix} 1 & 0 \\ 0 & e^{i\pi} \end{bmatrix} \cdot \overline{\overline{\mathbf{U}}}_{A} = \begin{bmatrix} u_{11}u_{22} - u_{21}u_{12} & 0 \\ 0 & -u_{11}u_{22} + u_{21}u_{12} \end{bmatrix}.$$

Therefore, although the diagonal elements show that recombining output may in general have lossy and wavelength dependent constructive interference, the zero off-diagonal elements show that this is the best that can be done with the given lossy splitter and combiner devices as all remaining power is recombined into one output port. As a result, the general property of UBIs to recombine arbitrarily split input signal is shown to hold for arbitrarily large losses in the case of reciprocal splitter A and combiner A', in the sense that all remaining power is recombined into one output port.

More generally, a *lossy/gainy UBI rule* can be found, that holds for passive and active splitters and combiners that are reciprocal, as shown in Fig. 8.6(a), by analogy with the *lossless UBI rule* (Fig. 8.4). It is found by considering the SVD canonical form of Fig. 2.10 for the splitter A and combiner A', and offers greater insight than that afforded by the straightforward reciprocity derivation above.

Fig. 8.6(b) shows the SVD canonical form of a UBI architecture (Fig. 8.4) having an arbitrary passive or active splitter and combiner, each being represented by the SVD canonical form for an arbitrary reflectionless 4-port (Fig. 2.10). Each of the splitter A and combiner A' accordingly comprises two lossless abstract directional couplers, separated by a maximum and minimum gain section, along with the phase degrees of freedom.

We may use the established *lossless UBI rule* (Fig. 8.4) to simplify this form by inspection, by noting that the output coupler of the splitter, the central π DPS, and the input coupler of the combiner form a lossless UBI. The latter may be replaced by a π DPS section to collapse the structure to that shown in Fig. 8.6(c). Now, each waveguide arm in the middle of the device has the same gain equal to the product of the maximum and minimum SVD gain of the splitter, $g_{\max}g_{\min}$. Since this is a common-mode gain, it "commutes" with the lossless couplers, and may be pulled out of the middle, either in front of the splitter, or behind the combiner, as shown in Fig. 8.6(d), without affecting the transmission response of the structure. Finally, now the left-hand side of the remaining structure is again a lossless UBI, and may be replaced by a plain π DPS. As a result, the structure on the right-hand side of Fig. 8.6(a) is obtained, and the *lossy/gainy UBI rule* is derived. Therefore, we have used the lossless UBI rule to derive the lossy/gainy UBI rule.

An interesting observation from the lossy/gainy UBI rule, based on the SVD, that is not made apparent by the reciprocity derivation, is that UBIs not only ensure maximal constructive interference into one port when using reciprocal splitters and combiners, but also that the loss is "smoothed" as the transmission is the geometric

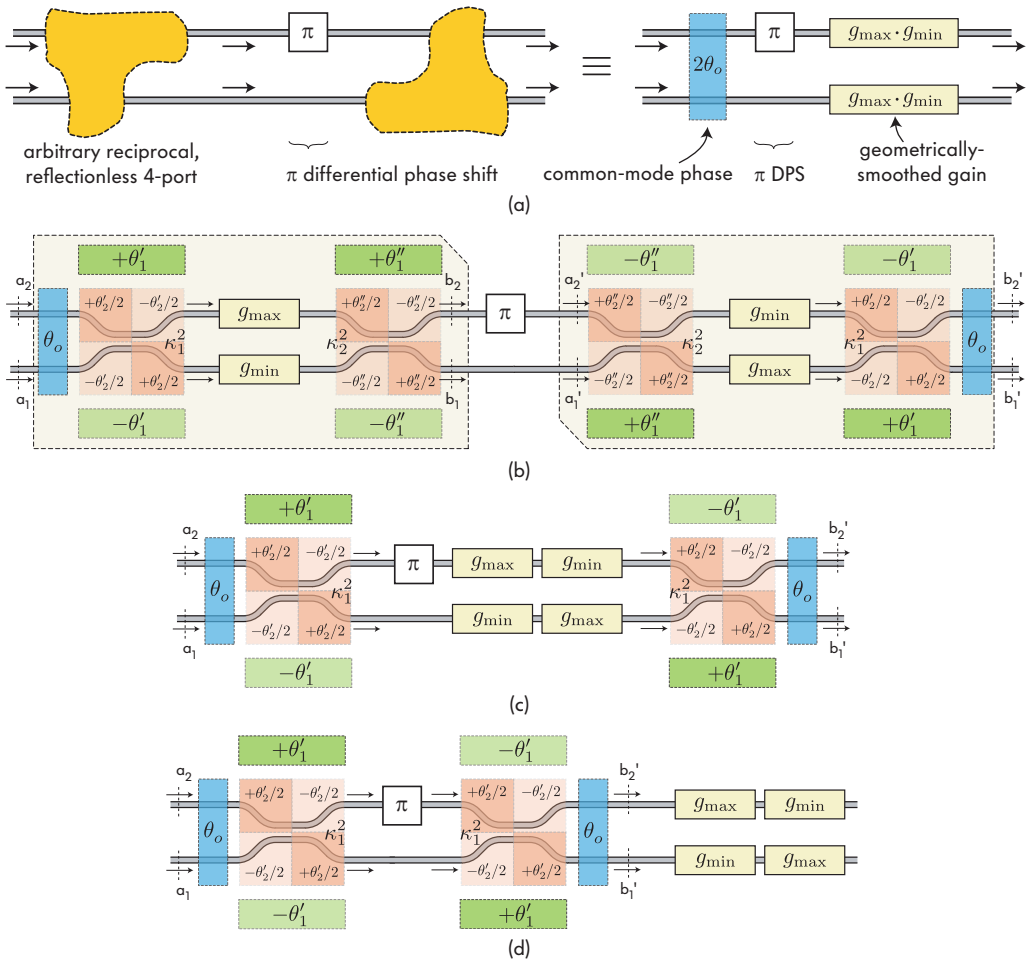

Figure 8.6: (a) The *lossy/gainy UBI rule* (restricted to the reciprocal case): a UBI comprising reciprocal splitter A, a π-radian DPS, and combiner A' is equivalent to a pair of non-interacting waveguides with a π DPS, a common-mode phase $2\theta_o$, and a common-mode gain that is the geometric average of the SVD min/max gains of splitter A; (b) canonical representation of an arbitrary lossy/gainy UBI using canonical form in Fig. 2.10; (c,d) reduced forms after applying the lossless UBI rule (Fig. 8.4) and rearranging "commuting" sections.

average of the maximum and minimum SVD gain (or loss) of the individual splitter or combiner.

8.1.5 Approximating inverse physical operations of R 4-ports

Since the lossless and lossy UBI rules show the construction of devices that resemble the inverse operation of a R 4-port, it is of interest to consider whether an exact inverse may be constructed.

In UBIs based on lossy/gainy reciprocal 4-ports, while all output power is in one port, this may be more or less than the total input power, depending on the loss/gain of the system. To obtain a unity magnitude output response of the UBI

and obtain an "identity matrix" in magnitude, a modification may be made to the UBI principle. Referring to Fig. 8.6(b), the combiner A' may be altered so that its SVD gains are not equal but related to those of the splitter A, as follows: $g_{\min}(A') = 1/g_{\max}(A)$, $g_{\max}(A') = 1/g_{\min}(A)$. That is, if a passive (lossy) splitter A has maximum and minimum "gains" less than unity in magnitude, the combiner A' must be an active structure with positive gain, i.e. $g_{\min}(A'), g_{\max}(A') > 1$. Referring to Fig. 8.6(a), clearly by this action the general UBI is reduced to the form of the lossless UBI (Fig. 8.4). What this relationship between the combiner A' and the splitter A means in physical terms, and whether a simple, symmetry-preserving action exists that can implement this transformation is left for future investigations.

Besides an identity magnitude response, an ideal inverse combiner must cancel the phase response of the splitter device. However, there is a fundamental limitation to our ability to construct an ideal inverse to an optical system, including both lossless and passive/active splitter/combiners A,A', which is rooted in the phase response, and calls for violating causality. That is, the common-mode phase response θ_o of splitter A must be replaced by $-\theta_o$ in the combiner A' for a true inverse operation. This is not possible, in general, in physical terms as a positive group delay in A would call for a negative group delay in A'. A simple thought experiment that confirms this is to consider a splitter A comprising parallel, uncoupled waveguides, each with a single-microring-resonator all-pass filter. The combiner would then require rings with negative (unphysical) circumference, i.e. round-trip time, to cancel the group delay.

Therefore, the closest possible approximation to a true inverse would be an approximation of the true inverse to within a constant group delay. This may be accomplished by using combiner A', sandwiched by a π-radian DPS on each side, as already described, where A and A' have the same θ_o, and following the combiner A' with a set of ideal all-pass filters to flatten the group delay spectrum. While there exist efficient algorithms that permit the approximation of a desired group-delay spectrum to arbitrarily high order [147–149], these schemes break the symmetry of the UBI, and the all-pass filters will in practice have additional loss, which requires attention in engineering. Nevertheless, such schemes may be of interest as the generation of various operator functions in physical (and in particular optical) systems is of interest in quantum computation and quantum information processing [150], and the inverse is a fundamental operation. In addition, as fabrication technology improves, microphotonic circuits may become of interest in these fields.

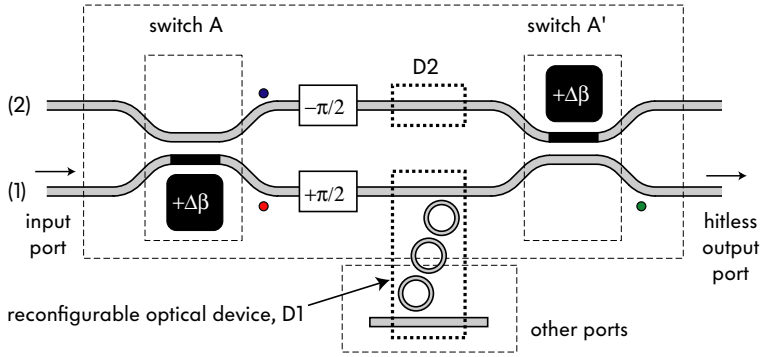

Figure 8.7: Basic waveguide geometry and configuration of hitless switch based on $\Delta\beta$ switches, with embedded reconfigurable device, $D1$ [143].

8.2 Applications and novel devices based on UBIs

8.2.1 Haus hitless switch and generalizations

In this section, a new microphotonic "hitless switch" is described (Fig. 8.7). It was proposed by Prof. H. A. Haus [143], predates the work on the general UBI principle described in the rest of this chapter, and was the direct motivation for the author to consider the latter, more fundamental generalization[‡]. Hence the presentation is chronologically out of order. However, this arrangement is preferable because the "Haus switch" turns out to be an instance of the general class of UBIs, and can be understood based on the developed UBI rule [Figs. 8.4, 8.6(a)]. In the original work [143], the switch was treated by coupled-mode theory, in the context of $\Delta\beta$ switches, and that more specific analysis will be omitted here.

The switch, illustrated in Fig. 8.7, is a solution to the hitless filter tuning problem. By enabling continuous, uninterrupted transition of an optical input signal to a bypass path, it permits tuning of wavelength add-drop filters without disturbing intermediate channels. The scheme comprises two symmetrically actuated, 2×2 $\Delta\beta$-type optical switches, anti-symmetrically cascaded in a balanced Mach-Zehnder configuration, and a π differential phase shift in the interferometer arms. By symmetry, it provides for wavelength-independent hitless operation before, during and after switch reconfiguration, permitting slow switching (slower than the bit period), independent of bitrate, to be used. Compact implementations using high-index-contrast, MEMS-actuated switches were proposed.

To circumvent switch-state-dependent phase introduced by $\Delta\beta$ switches, the

[‡]The original memo on the switch was written by H.A. Haus in March 2003, with the author and colleague M.R. Watts as contributors. It was last revised by him the day before his death, May 20, 2003 [151]. The paper [143] was put together in Nov. 2004 based on this memo, and consideration of the fundamental principles at work led the author to the UBI principle and various generalizations presented in this chapter. The problem of hitless tuning, addressed first by this result, and now by other work in this thesis as well, was brought to the authors' attention in February 2003 by L. Socci and M. Romagnoli of Pirelli Labs, Italy.

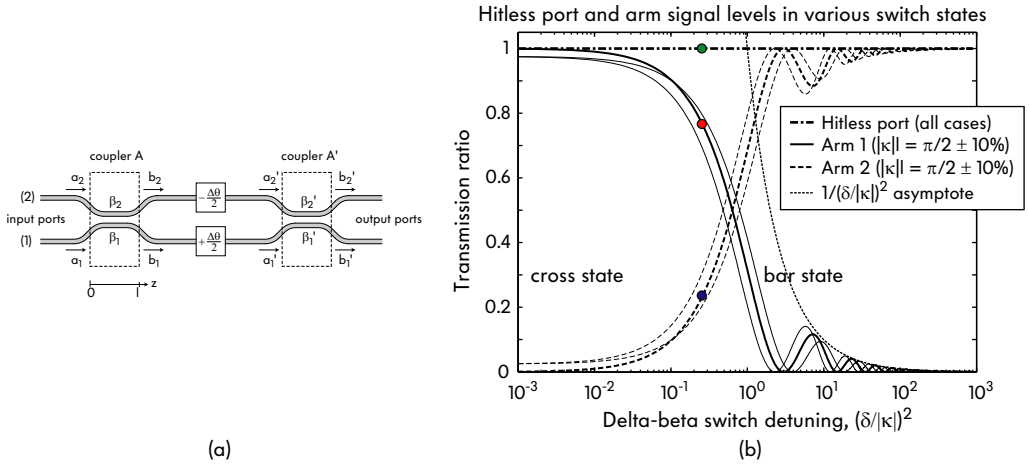

Figure 8.8: Response in the interferometer arms and at the "hitless" output port in various states of the symmetrically actuated $\Delta\beta$ switches. A symmetric error in coupling $|\kappa|l$ of $\pm$ 10% affects individual arm responses (hence filter extinction), but the hitless output remains unaffected with unity transmission.

inputs of the second switch are reversed with respect to the inputs of the first; and, a π differential phase shift is introduced in the interferometer arms [Fig. 8.7(a)]. For hitless operation, the switches are synchronously actuated. This is in contrast to approaches that imply feedback control or careful adjustment of a phase element and/or one switch state depending on the state of the other [28, 29]. For express channels, the hitless scheme proposed is as broadband as the π phase shift introduced, independent of the bandwidth of the individual switches, as may be concluded from the UBI rule.

In the proposed hitless switching scheme, one arm of the interferometer contains the device to be reconfigured – a wavelength-tunable channel add/drop filter – and the other arm is free. First, leaving out the filter, the behaviour of the switch interferometer alone [Fig. 8.8(a)], based on generic $\delta\beta$ switches, is considered [Fig. 8.8(b)]. It shows that, in different switch states of the $\Delta\beta$ switches, the fraction of power in each arm may vary, but the output is uniformly 100% in one port (in the lossless case). In addition, an error in the optical coupling length that is common-mode in the two switches (as might be expected in lithography) affects output to each arm but not the signal recombining property of the interferometer. These are consistent with the properties of UBIs described in Sec. 8.1.3.

Now, for a hitless-switchable filter, the filter ($D1$ or $D2$ in Fig. 8.7) is inserted in one arm of the switch. Then, a second concern is that the inserted device, e.g. an add/drop filter, may alter the phase balance by virtue of its own wavelength-dependent phase response. If the device adds excessive parasitic phase and dispersion over the wavelength range that requires hitless operation for through-port channels, this phase must be compensated by design in one of the arms to restore a π phase shift.

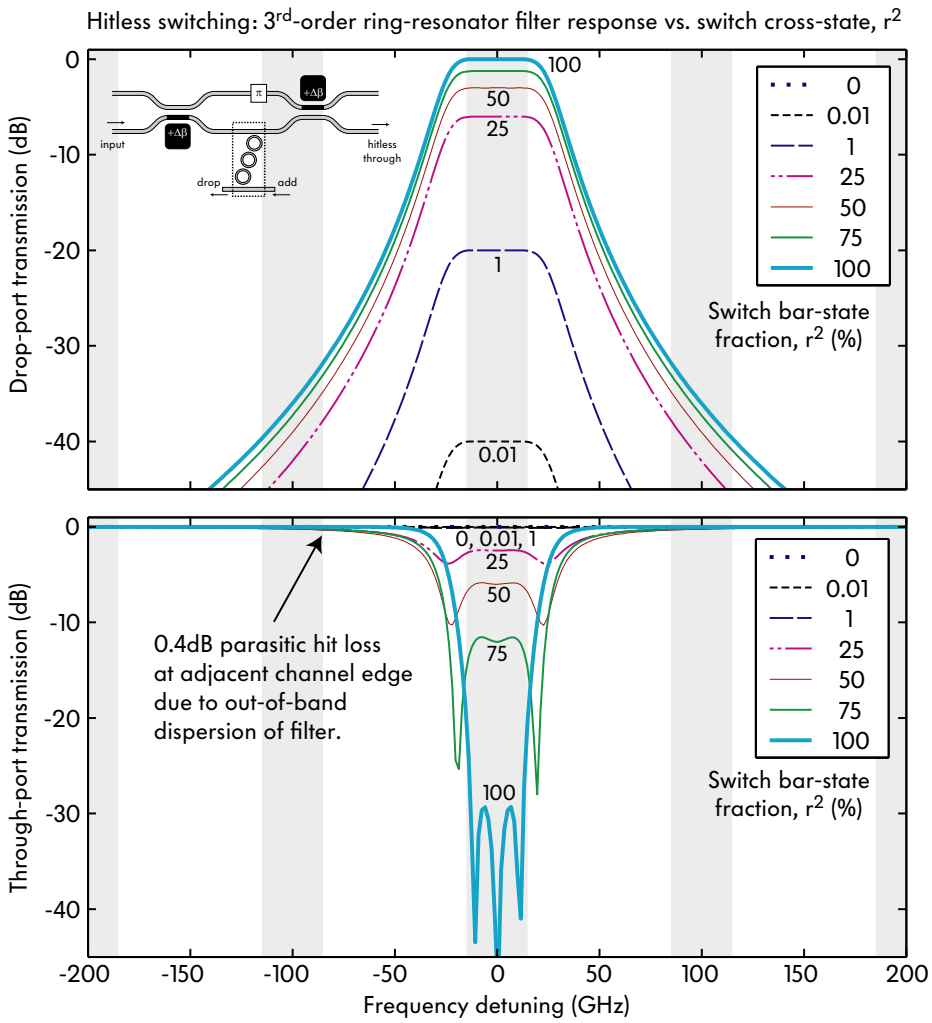

Figure 8.9: Hitless switching of a 3^{rd}-order microring-resonator add-drop filter: (a) drop- and (b) through-port amplitude responses vs. the bar-state, r^2, of a single $\Delta\beta$ switch.

Fig. 8.9 shows simulated drop- and through-port responses of a third-order microring-resonator example filter within a hitless switch for various switch states, r^2. The filter, shown on a 100-GHz channel grid, has 4 THz FSR and ring-bus and ring-ring couplings of $\{7\%, 0.08\%\}$. Hitless switching from a first state – dropping a channel – to a second state – complete bypass – is shown, whereupon the filter may be tuned to a new channel. The resonant filter has excess dispersion outside its channel window that is larger at smaller detunings from the passband. This dispersive response contributes a phase that unbalances the DPS in the switch and leads to a parasitic hit loss of 0.4dB at adjacent channel edges.

When multistage filters are considered, the hit loss can be larger. In this example, a cascade of two identical stages leads to 0.9 dB hit loss, and of three stages to 2.2 dB.

In some present telecom applications such levels of hit loss may be tolerable

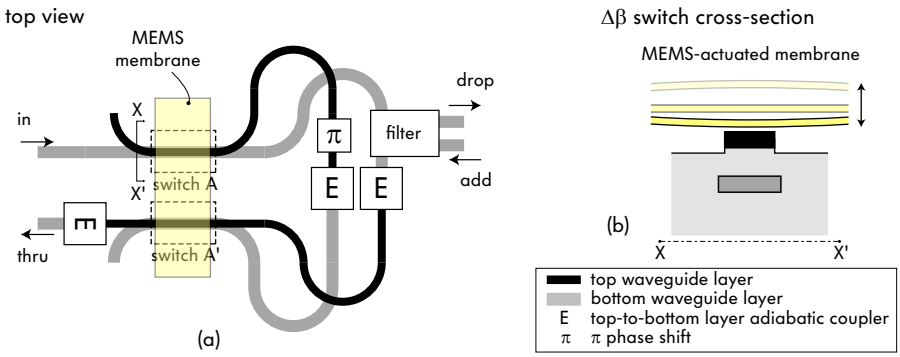

Figure 8.10: MEMS-actuated hitless switch implementation: (a) multi-layer waveguide switch layout, in folded geometry using one membrane, (b) a vertically-actuated MEMS $\Delta\beta$ switch cross-section.

because the switch can be actuated gradually, and because there may be sufficient tolerance in the link budget. On the other hand, requirements on power balancing between channels, and increases in data rate and channel density may eventually reduce the tolerability of this hit. In general it is desirable to reduce this transient loss to much lower levels. This hit loss may be reduced in a number of ways, including improved designs of the filter that is embedded, such as low-dispersion designs proposed in [142], and briefly described in Sec. 7.1.5.

For the hitless switching application broadband switches are required. Broadband $\Delta\beta$ switches were not required for hitless recombining, as the UBI rule tolerates arbitrary splitters. However they are necessary in order to route the operating spectrum fully to the tunable filter or to the bypass path across the wavelength of interest for filtering.

MEMS implementations

A number of approaches exist to broadband directional couplers [152] and switches. Here, a MEMS-based implementation is described. The compact implementation employs a HIC waveguide switch with MEMS-actuated dielectric slab β perturbation[§] Due to exponentially vanishing evanescent fields of a guided mode, short, strong couplers are more broadband than long, weakly-coupled ones. This is because a small wavelength-dependent change in propagation constant will affect the field amplitude at larger distances from the core exponentially, while the length contributes linearly. For full switching $\kappa l = \pi/2$, and for strong coupling high index contrast is desirable. Then, large $\Delta\beta$ is in turn required to achieve switching. A dielectric slab that interacts with the evanescent field of a waveguide and can

[§]In this work, MEMS-actuated $\Delta\beta$ switches (and resonator tuning by similar evanescent MEMS actuation) were proposed by colleague M. R. Watts. The folded switch arrangement employing a single MEMS actuator was proposed by the author. In previous work, MEMS-actuated switches and tunable resonators have been investigated, for example by Magel [107] and Marcatili [51].

be physically positioned by a MEMS assembly into proximity or contact with the waveguide can provide strong $\Delta\beta$ perturbation. Operation of one such switch, in a vertical geometry where the coupler waveguides are in different lithographic layers and the slab moves up and down, is illustrated in Fig. 8.10(b). In addition to a strong $\Delta\beta$ detuning, the slab "pulls" the guided mode of the top waveguide toward it, thus also reducing the coupling κ and further increasing the δ/κ ratio that is relevant for switching. A disadvantage of a two-layer configuration is that the waveguides must swap layers in the intermediate arms in order to provide an opposite $\Delta\beta$ for the second switch as required. This requires inter-layer optical coupling that can be achieved with adiabatically tapered coupler designs. A symmetric hitless switch design with equal lengths of each layer guide ensures balanced losses and optical length. A folded geometry may then be used to provide symmetric switch actuation, where one MEMS slab acts over both the input and output switch-coupler [Fig. 8.10(a)].

The given MEMS implementation is an example. Alternatively, single-lithographic-layer MEMS-perturbation schemes may be pursued akin to similar ones used for variable resonator coupling [97]. More generally, any realization of a $\Delta\beta$ switch and a π phase shift will work.

Generalizations

The coupled-mode theory analysis in [143] and the physical symmetry of the hitless switch in Fig. 8.7 does not bear out the general form of the UBI principle either in terms of the most general symmetry and orientation of the splitter and combiner, or the generality of the splitter device. For example, the symmetric form of the T-matrix in [143] for each switch implies (referring to Fig. 2.5) an implicit assumption of a longitudinal (or $\mathcal{V}$-) symmetry of each switch.

The physical derivation of the UBI principle, including the lossless and lossy UBI rules, in Sec. 8.1.1 showed a more general class of structures having similar properties which hold for non-reciprocal, strongly wavelength-dependent, and lossy or gainy structures (i.e. splitter devices) of arbitrary symmetry. Haus' hitless switch belongs to this family of structures.

Therefore, although some generalizations may be made by inspection from the form in Fig. 8.7, by appealing to the UBI principle it can be concluded that the $\delta\beta$ switches may be replaced with virtually any form of optical switch, and the same operation may be maintained provided that the arrangement follows Fig. 8.1.

8.2.2 Filter FSR multiplication and dispersionless Vernier schemes

In this section, I propose a number of novel filter architectures for the purpose of multiplying the effective FSR of a microphotonic channel filter – that are based on the UBI principle. The channel filter may be, for example, a WDM channel

add-drop filter, a channelized dispersion compensating filter, or a channelized modulator. Parts of this work have been published in Refs. [61–63, 144].

The proposed architectures, which are modified "Vernier" schemes, offer improvements and new capabilities over the state of the art, in that they provide – in the ideal case – perfect transmission at suppressed resonant passbands and, in some architectures, furthermore virtually no excess dispersion at suppressed resonances. The latter is particularly important for add-drop filters for tunable and reconfigurable optical add-drop multiplexers.

Resonator-based structures are ideally suited for the engineering of narrowband responses for such filters. On the other hand, in dielectric resonators – even ones with strong confinement based on high index contrast – the minimum size of the resonator is limited according to the tolerable radiation loss Q; for example, in microring resonators, this limitation is due to the bending loss and it imposes a minimum ring radius for a given index contrast and waveguide design. The lower bound on microring radius sets in turn a lower limit on the cavity length, and therefore an upper limit on the FSR. In strong-confinement SiN and Si microring resonators, FSRs of the order of 20 to 40 nm have been demonstrated (in our work in Sec. 7.1, Appendix E and Chaps. 5, 6; and by others [128, 141, 153–157]). However, as shown in Chap. 5, for high-performance filters optimal waveguide designs may limit the FSR to lower values (on the order of 20 nm in silicon) in order to provide other beneficial properties including low sensitivity to roughness and dimensional error tolerance. Furthermore, independent of the particular value of the FSR of a resonator, this FSR is limited by the index contrast and waveguide design, and does not provide a path to scaling up the usable spectrum to arbitrarily large values that can approach the 20 THz or more of low-loss usable bandwidth in an optical fiber.

Therefore, it is important to devise methods to extend the FSR of resonator-based and other narrowband filters by permitting the suppression of some of the resonant passbands, ideally in both the amplitude and phase responses.

Previous work

A straightforward way to suppress resonances and extend the effective FSR of a resonant response is the so-called Vernier method, previously used to select a single longitudinal mode in laser cavities [158]. The Vernier approach has also been employed to extend the FSR of resonant filters [120, 121, 159, 160], but the primary focus of these methods has been the drop-port response – used as a 2-port transmission filter. Oda *et al.* [121] and Yanagase *et al.* [120] take a conventional approach where the ring radii differ and resonant transmission is established only at wavelengths at which all cavities are simultaneously (synchronously) resonant. Tormen *et al.* [159, 160], on the other hand, use Mach-Zehnder interferometer based variable couplers to introduce loss and destructive interference at various

resonances. In either case, if the effective FSR has been enlarged beyond the FSR of any one cavity, then there will be suppressed resonances that form an unwanted, dispersive all-pass response in the through port – as there will be at least some cavities resonant with the input at the suppressed resonances.

Proposed architectures

On the other hand, in WDM systems by far the most important response function is the through-port response, which affects all channels except the dropped channel, whereas the drop-port response affects only the dropped channel. Therefore significant impairments in the through-port are much less tolerable.

In the context of our project to realize a microphotonic R-OADM, the author has pointed out in particular that dispersion at suppressed resonances of a Vernier scheme is not tolerable in many cases, it being further enlarged by the cascading of filters, and impairs transmission. None of the above-cited FSR extension approaches address this problem.

This work proposes two novel filter architectures, based on the UBI principle, that offer substantial improvement over the prior art. The first offers a near-ideal through-port amplitude transmission, without a spurious resonant loss signature in the spectrum that accompanies suppressed resonances in many of the previously cited schemes. The second proposed architecture further nearly eliminates dispersion at suppressed resonances. Various example designs are presented illustrating extendability of the scheme to higher orders to achieve larger FSR multiplication, or higher suppression of unwanted resonances.

For the purposes of demonstration of the various architectures that follow, an example 3$^{\text{rd}}$ order microring-resonator filter will be used as a reference, as shown in Fig. 8.11. In all cases it is designed to have a 40 GHz Chebyshev passband with 0.05 dB ripple (nearly 20 dB in-band extinction in the through port), giving a flat-top passband suitable for (the relatively standard) 100 GHz WDM channel spacing. For the several architectures involving cascaded-MZI splitters/combiners, a ring-filter FSR of 20 nm (2565 GHz) is chosen, resulting in power coupling coefficients for the filter of $\{\kappa_{\text{rb}}, \kappa_{\text{rr}}, \kappa_{\text{rr}}, \kappa_{\text{rb}}\} = \{0.089, 0.0017, 0.0017, 0.089\}$. These are the parameters achievable in high-index-contrast, strongly confined waveguides and demonstrated in the SiN add-drop filters described in Appendix E.2 [89]. For the resonator-splitter Vernier schemes in the next section only, somewhat smaller FSRs (800 GHz and 1 THz) are used for illustration and the corresponding couplings are given there.

UBI improvements to conventional Vernier add-drop filters

In this section, I propose a UBI-based structure for FSR multiplication that provides improved transmission properties over previous designs such as Ref. [161]. First, a

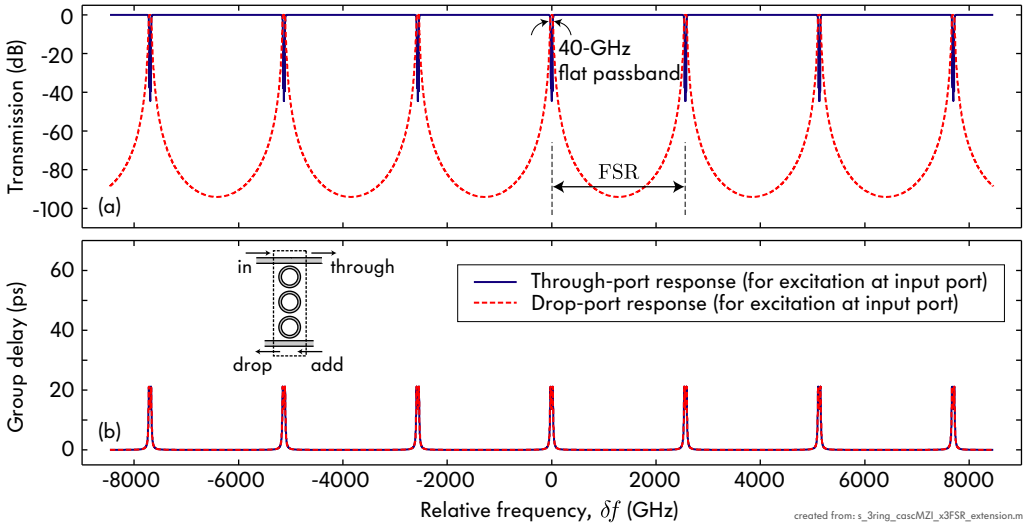

Figure 8.11: Third-order microring-resonator add-drop filter example: (a) calculated amplitude and (b) group delay spectral responses for comparison with FSR multiplication schemes. The filter has a 40 GHz bandwidth and an FSR of 2565 GHz (20 nm).

workable conventional Vernier approach for add-drop filters is described, and its limitations discussed. Then the improved design is presented.

The conventional structure is illustrated in Fig. 8.12(a). The idea is to use a splitting microring-resonator filter A and combining filter A' which have one FSR, FSR_1, and an embedded channel dropping filter B having a second, different FSR, FSR_2. Here, the dropping filter is multistage (see Sec. 7.1) having a second stage, B'. When a spectrum of WDM channels enters input port a_2, the splitter filter A drops channels separated in frequency by FSR_1 to port c_1, while the remaining channels continue in the through port c_2 of A. Those channels in the bottom arm c_1 that are frequency-aligned with a resonant passband of the embedded filter B (and B') are dropped to the drop port, d_3. Since the FSR of filter B, FSR_2, is different from FSR_1, filter B will drop only one of every number of channels in c_1 (in Fig. 8.12(b), one of every four). The remaining channels that pass on to port d_1 will be dropped by the combining filter A' (identical to A) and recombined with the through-passing channels in the top waveguide from c_2.

This straightforward approach has been considered previously, for example by M. Margalit in 2002 [161], and independently by the author and colleague L. Socci in 2004. Its typical performance is illustrated in Fig. 8.12 by a example design simulated with parameters relevant for WDM telecom applications.

Vernier stages A, A' have $FSR_1 = 1\,\text{THz}$, and add-drop filter stages B, B' have $FSR_2 = 800\,\text{GHz}$, giving a total effective FSR, $FSR_{\text{eff}} = 4\,\text{THz}$ (their lowest common multiple). This permits, for example, an operating wavelength range of the filter which covers a spectrum of 40 WDM channels at 100 GHz channel spacing. All four filters (A, A', B, B') are chosen to have a Chebyshev passband

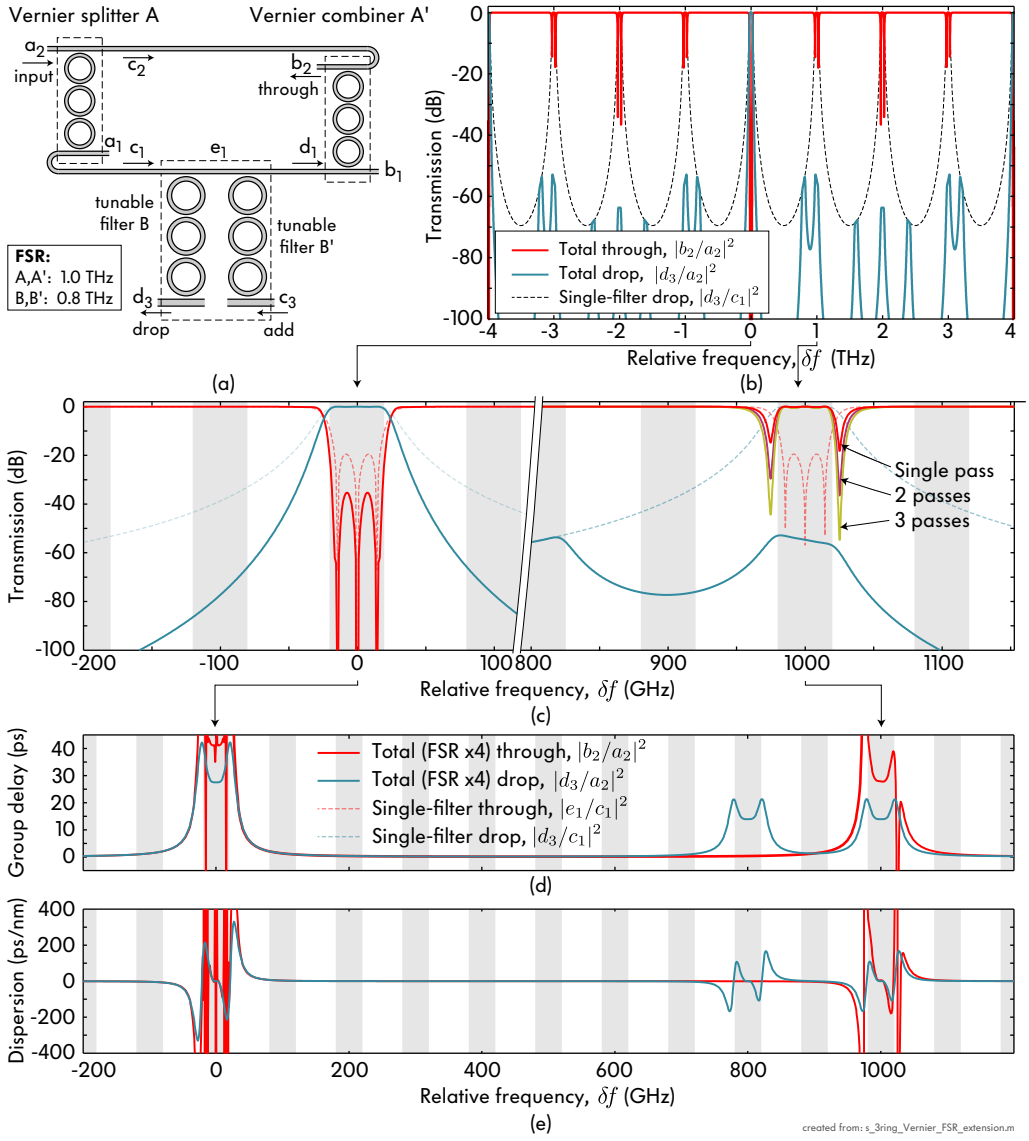

Figure 8.12: Conventional architecture for Vernier multiplication of the FSR of a resonator-based channel add-drop filter ($B - B'$), showing non-ideal amplitude transmission: (a) schematic showing splitter A, multistage add-drop filter $B - B'$, and combiner A'; (b) total amplitude response showing 4 THz effective FSR, with suppressed passbands below -50 dB; (c) dropped-channel passband and worst-case suppressed passband (showing undesirable band-edge transmission dips), and corresponding (d) group delay and (e) dispersion spectra.

characteristic with a 0.25 dB bandwidth of 40 GHz, 0.05 dB passband ripple (corresponding to 19.5 dB in-band extinction in the through port, with no loss) and 33 dB rolloff at 80 GHz detuning from the channel central wavelength, so as to permit 100 GHz channel spacing. The resulting filter design has a symmetric geometry and employs ring-to-bus-waveguide power couplings of 21.2% and ring-to-ring power couplings of 1.11% for filter stages A and A'. For the same filter shape and bandwidth, respective couplings of 25.8% and 1.74% are required in filter stages

B and B' due to their smaller FSR.

Fig. 8.12(b,c) shows the amplitude drop-port responses of splitting stage A alone (dashed line), and the drop- and through-port responses of the complete device (solid line). The through-port response shows that all channels (indicated by gray bars in the zoomed plots) over one effective FSR of 4 THz, other than the dropped channel at $\delta f = 0$, are recombined in the through port b_2. Fig. 8.12(c) shows an enlarged view of the selected channel-dropping resonance and the adjacent suppressed resonance (which has the worst case drop-port out-of-band rejection). Typical requirements for telecom OADMs are met by the complete device, with its >35 dB in-band extinction in the through-port response, and >60 dB out-of-band rejection of adjacent channels 100 GHz away in the drop port. Fig. 8.12(c) (right side) shows an enlarged view of the worst-case suppressed drop-port resonance centered at +1 THz relative to the selected drop resonance. The unwanted resonance is suppressed by >50 dB in the drop port and the channel is reinserted in the through port by stage A' after passing by stages B and B'. This approach has advantages over some Vernier schemes that employ a different radius for each cavity within a single filter [120, 121], in that the group delay seen by all through-port channels is relatively flat, as shown in Fig. 8.12(d), or at least not worse than typical filter drop ports, which must be designed to have tolerable dispersion. Since dispersion is zero at center-band, for sufficiently narrowband signals, the dispersion, shown in Fig. 8.12(e), can be tolerated.

There is a number of drawbacks in this design. First, sharp dips in transmission near the band edges of some channels are visible [Fig. 8.12(b,c)], which can be a cause of signal degradation. These dips occur at the band edges of through-port channels which are dropped by A and reinserted by A', and result from interference. At most wavelengths, nearly all signal passes in the top waveguide. At wavelengths within a passband of filters A and A', nearly all signal is dropped by A, passes the bottom waveguide and, with the exception of wavelengths dropped by B and B', reenters the through port b_2 via A'. However, at the 3 dB corner frequency of filters A and A', half of the signal traverses each path, and at a particular wavelength fully destructive interference is seen in the through port [as low as ~ -20 dB in Fig. 8.12(b)]. This effect rounds the passbands of through-passing channels. Since a signal may pass as an express channel through many filters, this passband narrowing worsens with cascading [see Fig. 8.12(c) (right side) for 1, 2, and 3 passes] and may cause signal degradation. This problem occurs because previous designs have not treated the device as an interferometer but rather as a cascade of filters that are fully-on or fully-off resonance at wavelengths of interest and transmit each signal in only one path (c_2 or c_1).

This problem can be solved by treating the structure as an interferometer, and recognizing that the structure in Fig. 8.12(a) can be modified to be a UBI, as shown in the proposed design in Fig. 8.13(a). The new structure, leaving out for the

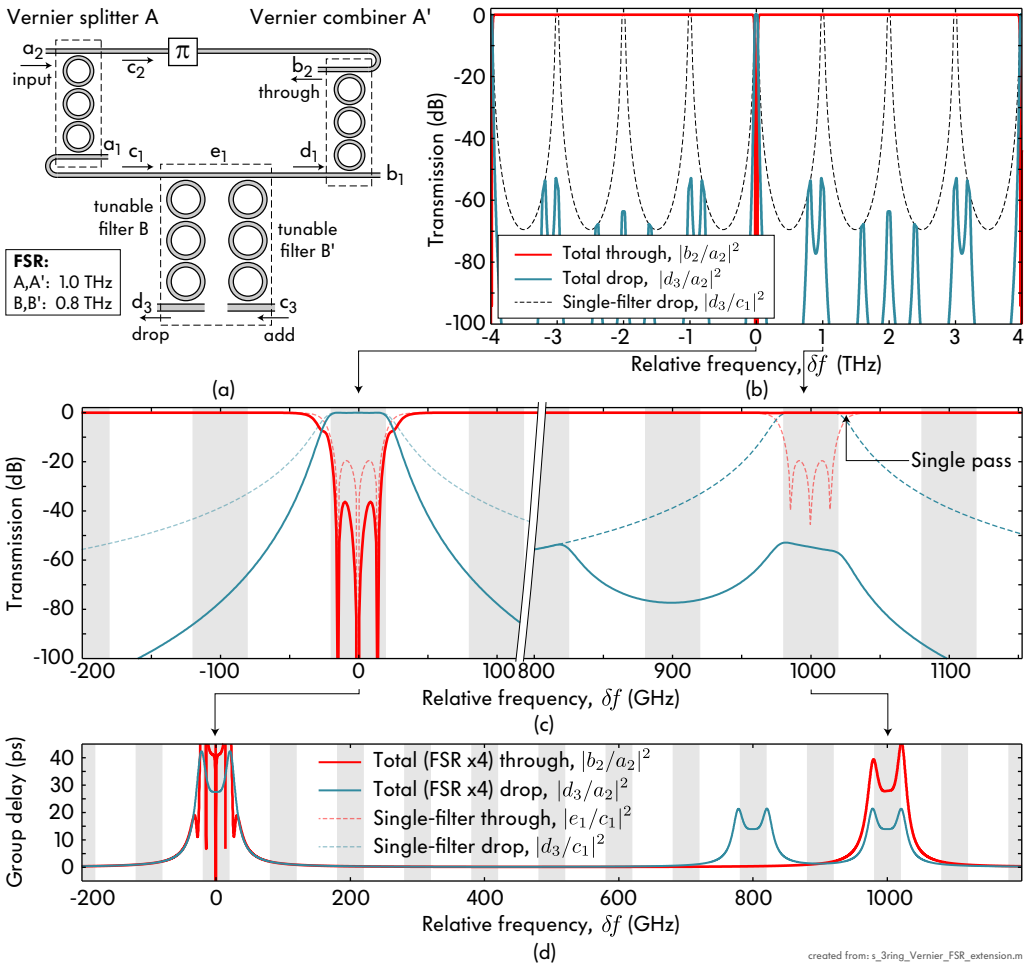

Figure 8.13: Improved, UBI-based architecture for Vernier multiplication of the FSR of a resonator-based channel add-drop filter ($B - B'$), showing ideal out-of-band through-port transmission: (a) schematic showing splitter A, π-radian DPS, multistage add-drop filter $B - B'$, and combiner A'; (b) total amplitude response showing 4 THz effective FSR with flat through port; (c) dropped-channel passband and worst-case suppressed passband, and (d) corresponding group delay spectrum.

moment filters B and B', comprises a splitter A, and π DPS, and a combiner A' that is a 180° -rotated replica of A as required (see Fig. 8.1). Therefore, full transmission is expected to the through port at all wavelengths in the absence of B and B', for lossless A and A' (and the best possible recombination of signals in the lossy case, per the lossy UBI rule, Fig. 8.6). When channel dropping filters B and B' are introduced in one arm of the bypass scheme, full extraction of a channel is made possible at the resonant passbands of B, B', but the device continues to function as a UBI at all wavelength detunings large enough so that the dispersive response of B, B' does not introduce a substantial phase shift between the interferometer arms.

In practice, the performance of such a scheme, simulated with the same param-

eters those of as Fig. 8.12, is shown in Fig. 8.13(b-d). Fig. 8.13(b,c) shows that the destructive interference nulls near the suppressed resonant passbands have been eliminated. The device has near-unity transmission at all wavelengths except the selected passband. It should be noted that the selected resonance at $\delta f = 0$ has a slightly different through-port response shape near the band edges when compared to Fig. 8.12(c), due to the π DPS, but these small transmission bumps are in the transition band and far from the adjacent channels. The group delays have remained similar as expected. Therefore the UBI-based Vernier filter is advantageous in comparison to the conventional design.

Lastly, the choice of third-order microring filters has required a somewhat complicated waveguide routing in Fig. 8.12(a) and Fig. 8.13(a), and may require a waveguide crossing to route the through and add ports out of the filter. However, even-order filter stages provide a simpler topology while alternatively efficient, low-crosstalk waveguide crossings may be readily designed, as shown in Appendix. F.

Referring to Fig. 8.12(d), a second drawback of this architecture is that, although channels are split into two paths may be fully recombined, the through port channels that are dropped twice (by stages A and then A'), bypassing the filters B and B', experience the group delay and dispersion of the drop-port passbands of stages A and A', because they traverse them on-resonance. Because these are narrowband resonant filters, the on-resonance group delay, $\tau_{\mathrm{g}}(\delta\omega = 0)$, is substantial, and is comparable to half of the inverse of the filter bandwidth, times the filter order N, $\tau_{\mathrm{g}}(\delta\omega = 0) \sim 2N/(\pi^2 \delta f_{3\mathrm{dB}})$ where $\delta f_{3\mathrm{dB}}$ is the 3 dB bandwidth in Hertz. A substantial group delay also means that these channels have greater sensitivity to intrinsic loss in the filters. This is a problem not only in terms of insertion loss, but also in terms of channel power balancing across the spectrum, the specifications for which typically tolerate no more than 1–2 dB variation. The UBI-based Vernier microring bypass design in Fig. 8.13(a) does not help in this respect because it is the group delay of splitter A and combiner A' that contributes the group delay and dispersion at suppressed passbands.

This type of Vernier FSR extender, however, offers large FSR multiplication factors of the order of $FSR/\delta f_{3\mathrm{dB}}$. These may be extended to even larger multipliers by nesting the Vernier scheme, i.e. using several levels of bypass.

Another advantage intrinsic to Vernier schemes is the enhancement of wavelength tunability. The complete filter may be tuned across the entire effective FSR, FSR_{eff}, by tuning each filter stage only across its own substantially smaller FSR, by lining up resonant passbands of A, A' and B, B' as appropriate. Therefore the effective tuning range is multiplied by the same factor as the FSR. This is not in itself a new result, and simply translates to the new proposed schemes as a result of their validity for conventional Vernier schemes.

The tuning range enhancement also simplifies control of resonance frequencies. For a filter with a fixed passband width, a larger and larger effective FSR and tuning

range means a larger and larger ratio of FSR to bandwidth (for higher-order filters, a generalized *finesse*). The resonant wavelength control must, on the one hand, be able to reliably arrive at and stabilize to a value within a fraction of the filter bandwidth. On the other hand, it is expected permit tuning the full FSR. As a result, with increasing effective FSR, a single resonant-wavelength control variable would require increasingly large "dynamic range", i.e. increasingly finer granularity – to be able to control a value to within 1 part in 100, 1000, 10000. . . Vernier schemes provide multiple control variables – one for the splitter/combiner A and one for the filter B, like digits in a decimal number. As a result, the relative control required for each control variable may be kept within bounds. This result, too, is not new and holds for previous Vernier schemes. However, it is strong justification for why the present improved Vernier schemes for FSR multiplication are an efficient approach to large-FSR filters, enabling addressable-spectrum scalability.

Dispersionless FSR doubler for channel add-drop filters

In this and the next two sections, another novel, UBI-based Vernier architecture is proposed that nearly completely eliminates excess group delay and dispersion at suppressed resonances. The latter are the major drawback of Vernier architectures using resonant splitters and combiners, including UBI-based ones, described in the previous section. The proposed structures instead employ feed-forward filters with a slowly varying spectrum as splitter and combiner elements which, in a UBI implementation, are shown to cancel each other's excess dispersion.

First, reasons for the presence of substantial group delay and dispersion at the suppressed resonances in the FSR multiplier designs such as Fig. 8.12(a) are considered. Delay and dispersion is significant in those through-port channels that are dropped by resonant splitter A and reinserted by combiner A'. Such Vernier schemes are designed under the assumption that the splitter element A must route each channel fully either to one or the other output port (c_1 or c_2), and in no channel is the signal to be substantially divided between the two bypass-interferometer paths. This is done to avoid interference of a channel with itself at the output, but it imposes a strong requirement on the design. It implies that the splitter A must change its amplitude transmission from nearly 100% to nearly 0% in one port over a frequency range corresponding to the spacing between two adjacent WDM channels. As a result, the splitter A (and combiner A') are narrowband filters, which leads to their construction using resonators and to the large suppressed-resonance group delay determined by their narrow bandwidth. The latter translates into substantial loss sensitivity, and dispersion in comparison to other through-port channels (which pass in the top waveguide, c_1, in Fig. 8.12(a) for example). The spectral shape of the group delay and dispersion seen by "dropped-and-reinserted" channels is fixed by the flat-top shape of the passband amplitude response of A, because these resonant filters are typically *minimum phase* [56, 71],

and therefore have amplitude and phase responses that are directly related by the Kramers-Kronig relationship (Hilbert transform) [57, 162]. The magnitude of the group delay and dispersion spectrum is, on the other hand, determined by the narrow bandwidth of A and A' according to an inverse proportionality relationship. Wider splitter/combiner filters would reduce the group delay, and filters with less sharp rolloff (less box-like passbands) would impose smaller dispersion.

The UBI-based resonant FSR multiplier design proposed in Fig. 8.13 ensured that even at the passband edges, when the signal is divided between the two waveguides (c_1 and c_2), it recombines fully in the through port, at all wavelengths and configuration states, according to the UBI rule. Since the UBI configuration ensures constructive interference regardless of the design of the splitter, this approach enables the consideration of schemes where splitting and recombining devices are permitted to split the channels in arbitrary proportion between the two (top and bottom) waveguides. In particular, the narrowband requirement for A and A' may be removed, and the splitter and combiner need a rolloff that is only fast enough to pass one resonance and reject another that is one FSR away – a considerably less strict demand. Then, to reduce group delay and dispersion introduced by the splitter/combiner devices, it is desirable that they have the following properties: (1) use wideband, smoothly varying passbands; and (2) avoid use of feedback interference (resonance) which produces a non-linear phase spectrum giving rise to dispersion. This approach is in contrast to band-splitting schemes, including the narrowband splitter Vernier approaches in Figs. 8.12-8.13, where each channel must be fully routed either via one or the other bypass-interferometer waveguide. In particular, in a UBI-based scheme it would appear to be of advantage to use substantially linear phase filters for splitter and combiner devices, to reduce dispersion and have uniform group delay. However, it will be shown that even the use of non linear-phase filters for A and A' can result in a FSR multiplier which has substantially linear phase to the final output, and thus contributes nearly no excess dispersion and flat group delay. This is the case if the filters in A and A' are feed-forward-type filters.

Feed-forward-interferometer-type filters (also referred to as lattice, or cascaded-MZI, filters [57, 145]) typically have rounder, less selective passbands with slower rolloff than resonant filters of comparable complexity and size. The former are typically too large, sensitive to phase errors and slow-rolloff for narrowband WDM applications for which they were initially considered [71], but they are ideally suited – in physical size, spectral selectivity and passband shapes – for selection of resonances among several FSRs. The present diversity scheme enables consideration of such filters as splitter and combiner devices A and A' because it enables channels which are partially split among the top and bottom optical paths to be fully recombined. Thus the slow rolloff characteristic of such devices may be tolerated without penalty so long as they can provide full transmission to one

optical path at one filter resonance, and a transmission null at the adjacent filter resonance.

In the presented designs that follow, only dispersion due to the structure of the filtering elements in the splitter and combiner devices and in the add-drop filter is considered, because dispersion induced by such elements is typically the dominant source of dispersion. The designs presented reduce the structural dispersion of the filter. Waveguide dispersion is ignored because it is much smaller and more spectrally uniform. As a result of this focus, some of the "zero-dispersion" designs that follow in fact have small residual waveguide dispersion (as does almost any waveguided device of comparable length).

In general, the proposed dispersionless FSR multiplication interferometers comprise a feed-forward filter (e.g. cascaded MZI) as splitter and combiner of a UBI, and an embedded resonant filter. In the feed-forward-type (FF) interferometers in the following examples, only R 4-port directional couplers and interconnecting waveguide lengths are used to engineer a spectral response.

In example shown in Fig. 8.14, a FSR doubling interferometer design is described. It makes use of the simplest FF interferometer – an MZI – shown as splitter A in Fig. 8.14(a). The MZI comprises two 3 dB couplers ($\kappa_1 = \kappa_2 = 1/2$) connected by waveguide arms of different lengths. If the length difference, ΔL, is such that the period (i.e. FSR) of the MZI sinusoidal spectral response is twice the FSR of the 3-ring resonant filter B, then the MZI splitter A can be used to suppress every second resonance of the filter B and effectively double its FSR. This is accomplished by permitting spectral content coincident with every other resonance to bypass the filter in the top waveguide, c_2, of the device.

If the waveguides used in the MZI splitter device and in the ring resonator are of the same cross-section design, or even of different cross-section designs but having the same group effective index, then the required arm length difference for the MZI filter A to facilitate doubling of the FSR of add-drop filter $B - B'$ is

$$\Delta L = \pi R = \frac{c}{n_{\text{group}}\, FSR_{\text{mzi}}} = \frac{1}{2}\frac{c}{n_{\text{group}}\, FSR_{\text{ring}}}$$

or half the ring circumference. More generally, the right hand side expressions hold if the FSR of embedded filter $B - B'$ is FSR_{ring} (in units of frequency, e.g., Hz), the spectral period of the MZI is FSR_{mzi}, and a separate effective group index, n_{group}, value may be assigned to the MZI and the ring waveguides. For an FSR-doubling bypass interferometer, the FSR of the MZI filter in the splitter A is twice the spacing of the add-drop filter $B - B'$ passbands.

If a WDM input spectrum is inserted at port a_2 in, MZI-based splitter A separates it among the top and bottom waveguides with a sinusoidal wavelength dependence [Fig. 8.14(b)] at ports b_2 and b_1, respectively. All power at $\delta f = 0, \pm 2\, FSR_{\text{ring}}, \ldots$ are passed to the bottom, add-drop filter arm, while all power at $\delta f = \pm FSR_{\text{ring}}, \pm 3\, FSR_{\text{ring}}, \ldots$ bypass the filter in the top arm. Be-

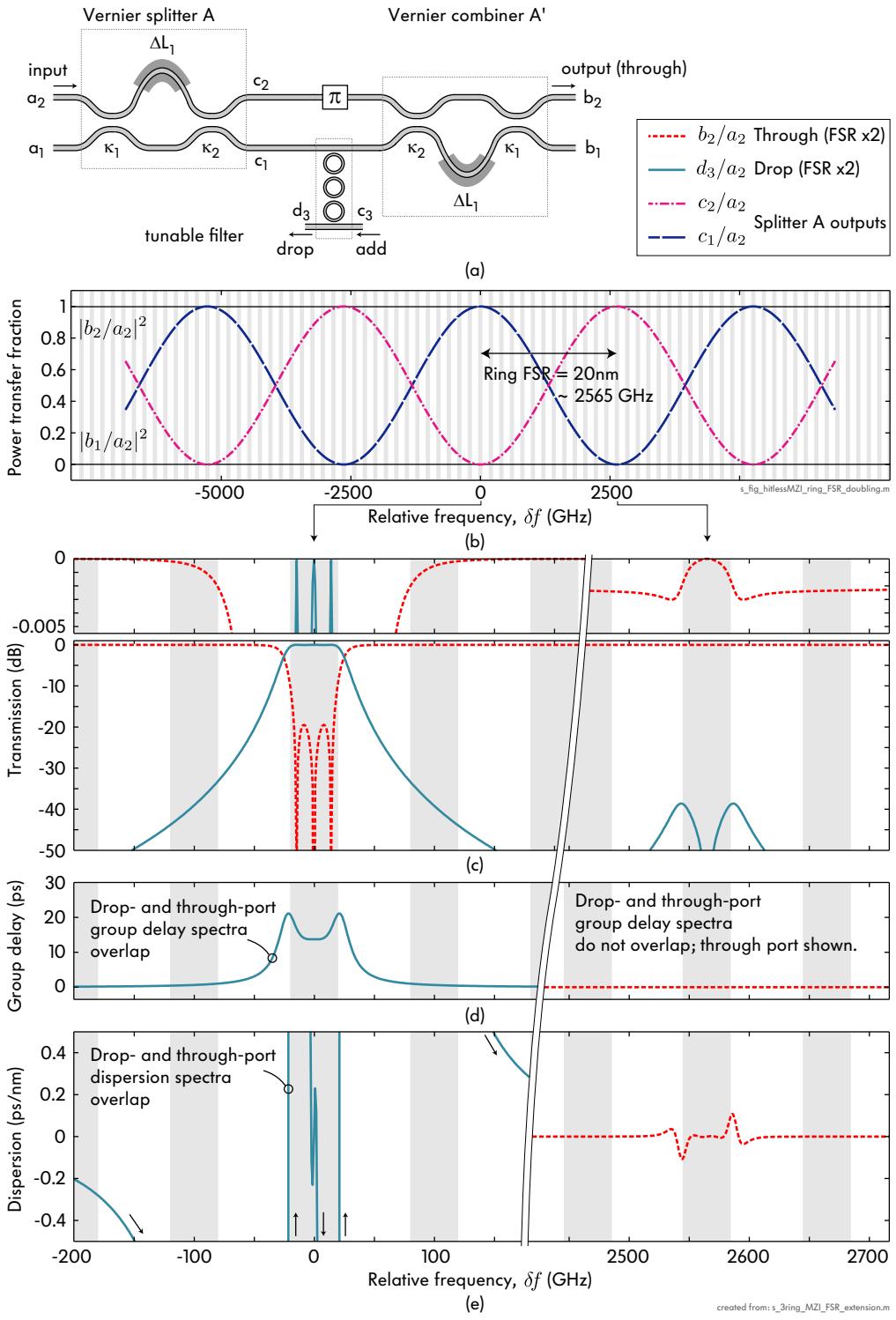

Figure 8.14: UBI-based non-dispersive FSR doubler for a resonator-based add-drop filter: (a) schematic of MZ splitter/combiner and 3-ring microring filter in one arm; (b) MZ splitter/combiner response; (c) amplitude response of total through and drop ports ($|b_2/a_2|^2$ and $|d_3/a_2|^2$, respectively); corresponding (d) group delay and (e) dispersion spectra show negligible group delay and dispersion at the suppressed resonances at $\delta f = \pm 2565\,\text{GHz}$.

cause the MZ response is slowly varying, the entire passband of a channel near a maximum or minimum of the splitter response can be substantially routed to just one arm. The characteristics of the dropped and bypassing resonant channels, at $\delta f = 0$ and $\delta f = +2565$ GHz respectively, are detailed further in Fig. 8.14(c-e).

Fig. 8.14(c) shows the drop- and through-port amplitude responses. The drop resonance passband at $\delta f = +2565$ GHz is suppressed by > 35 dB, and the through-port response is close to unity across the spectrum near the suppressed resonance. The through-port dispersion of the 3-ring filter $B - B'$ should be low enough (or compensated in design) to avoid substantially modifying the π DPS in the bypass interferometer that ensures complete recombination in a single output waveguide at port b_2. That this phase (without any special compensation) has little impact on the response is shown in the top of Fig. 8.14(c), which shows an enlarged portion of the spectrum, making visible the spectral features between 0 dB and -0.005 dB. It indicates that the unwanted out-of-band phase response contributed by the add-drop ring filter leads to less than 0.003 dB loss in recombination at the through port b_2 (or $> 99.9\%$ transmission).

The more important consideration here is the group delay and dispersion to the through port b_2 at the suppressed resonance. Fig. 8.14(d) shows the group delay of the drop- and through-port responses at the dropped and the suppressed resonances. The drop port shows a group delay of ~ 15 ps, as expected for a 40 GHz-wide filter passband. The through-port response at the suppressed resonance has virtually no group delay (computed at less than 0.002 ps). This may be compared to the usual drop-port picosecond-scale group delays in filters of such bandwidth. Therefore, the device should see virtually no excess loss at the suppressed resonance, if the drop port has reasonable loss levels. Furthermore, in Fig. 8.14(d), the dispersion in the through-port b_2 of the total device at the suppressed passband is shown to be < 0.1 ps/nm at channel edges and far less within the 40-GHz channel band, well below tolerable dispersion levels for telecom add-drop applications, which are in the 10's of ps/nm for through ports of filters with this order of bandwidth, i.e. symbol rate.

Channels not at the maximum or minimum of the sinusoidal MZ response in Fig. 8.14(b) are split between both arms of the bypass interferometer, but fully recombine in the output b_2. This happens according to the UBI rule at wavelengths that are at large detunings from resonant passbands of the add-drop filter, at which the filter does not disturb the π DPS substantially with its dispersive response (which extends to about two channel spacings on either side). On the other hand, for channels that are near the resonant passbands of the add-drop filter, where its dispersive response may be substantial, the MZ has a near unity or zero amplitude response, so maintaining the π DPS is not necessary (or there is more tolerance for deviation, see Sec. 8.1.3) because the channel passes primarily in one arm of the interferometer. This is the reason why all channels recombine in the output

without substantial degradation. The impairment in the UBI that is induced by the out-of-band dispersion of an inserted resonant filter, which is seen in the hitless switch designs, is not found is the present UBI-based FSR multiplier architectures.

The compound FSR-doubled filter has a doubled wavelength-tuning range for a given actuation level (effective index change), akin to other Vernier schemes. To tune the selected drop-channel resonance across the entire 40 nm effective FSR, the add-drop filter B passband needs to be wavelength tuned by up to 20 nm, to move the closest filter resonance, the resonances being spaced by $FSR_{\text{ring}} = 20$ nm, to the desired wavelength. The MZI-based splitter, on the other hand, must be tuned over the entire 40 nm, because its spectral response is periodic with 40 nm. The MZI splitter A is tuned so as to track one resonance of the add-drop filter B and suppress another adjacent resonance over the first 20 nm, and is tuned further to do the reverse, tracking a second resonance and suppressing the previous, over the second 20 nm range. That the MZIs A and A' need to be tuned 40 nm is not a drawback. This is because the MZI arms can be made as long as desired, permitting accumulation of sufficient phase to tune 40 nm with a comparably small change in effective index in the waveguide. For example the MZI could be thermally tuned by 40 nm with the same temperature change as needed to tune a ring by 20 nm. Tuning phase shifters are schematically indicated by gray bars along the longer MZ arms, and are also implicit in each ring resonator.

The conclusion is that the device in Fig. 8.14(a) provides FSR and tuning range multiplication with an amplitude response of similar quality to that of the device in Fig. 8.13(a), but it also virtually eliminates by virtue of its design configuration the group delay and dispersion that is normally present in the latter devices.

This scheme, based on feed-forward interferometers, is not limited to the simple MZI for splitter and combiner devices A and A' used in the present. More advanced FF interferometers may be employed, such as cascaded MZIs (consisting of multiple cascaded directional couplers and waveguide arms of different lengths). The increased interferometer order may be employed to achieve two advantages. First, it may be used to suppress a greater number of adjacent resonances of the ring filter, thereby extending the FSR by a factor of three, four, etc. Second, it may be used to make the suppression of a particular resonance of higher order (e.g., maximally flat), such that the resonance is more strongly suppressed and the resonance suppression is more robust to wavelength misalignments. Or, it may be used to achieve a combination of both. Examples of such higher-order designs are given next.

The "parasitic" or unwanted loss and dispersion, albeit very small, increase when lower finesse resonant filters are used. However, the simulated choice of parameters assumes a reasonable index contrast and typical dimensions for practical strong-confinement photonic circuits, and it may be expected that similar designs used in practice will show comparable performance to that predicted here.

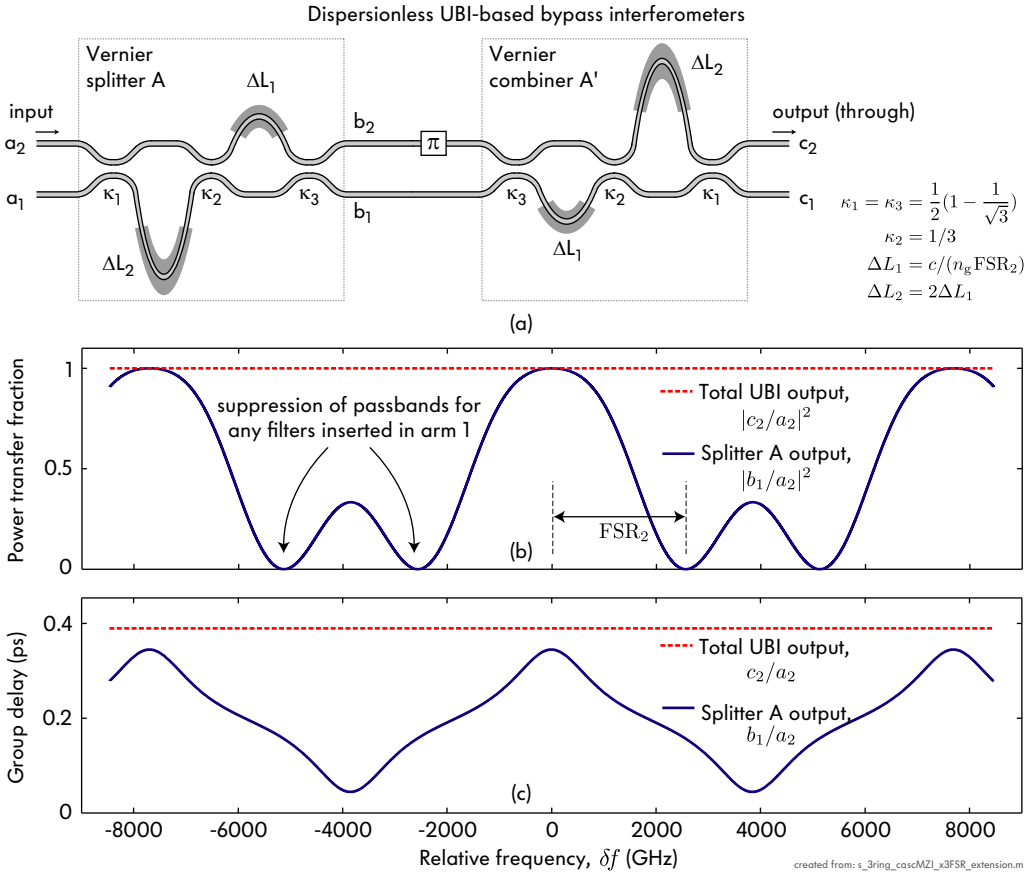

Figure 8.15: Non-dispersive UBI based on *dispersive* splitter A and combiner A', for dispersionless FSR tripling: (a) UBI based on lattice-filter splitter/combiner, showing coupling fractions and arm lengths for an FSR-tripling interferometer; (b) amplitude response of the splitter A alone, and of the complete UBI; (c) group delay of the dispersive splitter A, and of the complete UBI, showing flat group delay and no dispersion at the output.

The first FSR-doubled microring-resonator filter of this type has been designed and fabricated using silicon-core waveguides of the design in Chaps. 5 and 6, and this result awaiting experimental optical characterization.

Dispersionless FSR tripler for channel add-drop filters

In this section, it is shown that a higher-order cascaded-MZI splitter may be used to achieve larger FSR multiplication factors in a dispersionless FSR-multiplier scheme. In a similar way to the previous section, an example simulated design is proposed. Furthermore, it is shown that a dispersive splitter A does not contribute to through-port dispersion through the UBI. A geometrical proof using the lossless (or lossy) UBI rule is given that shows that the splitter and combiner dispersive spectra cancel, if the splitter and combiner are cascaded MZI devices.

The proposed splitter/combiner design and UBI is shown in Fig. 8.15 and the complete example filter device is shown in Fig. 8.16(a). It multiplies the FSR and

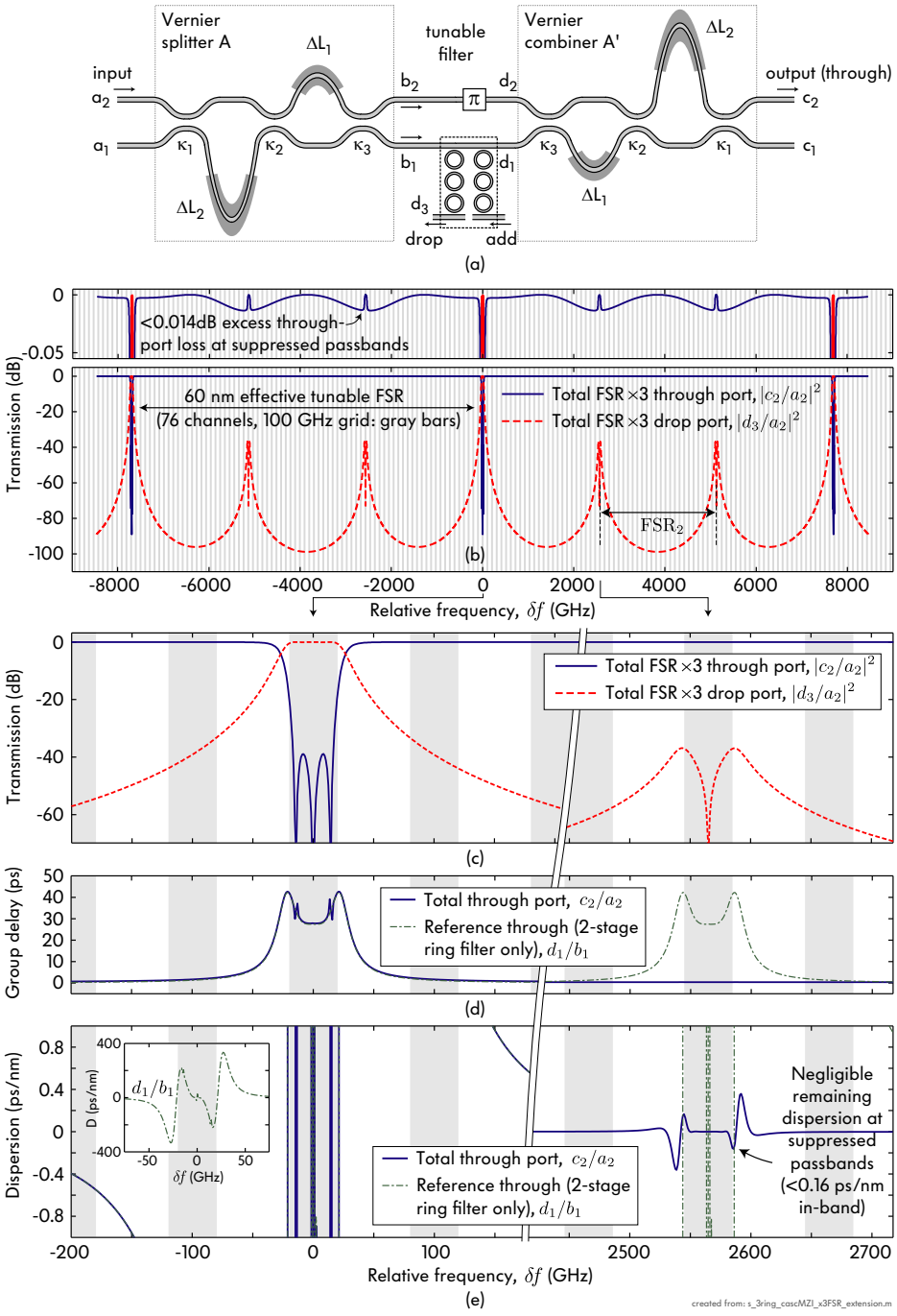

Figure 8.16: Non-dispersive FSR multiplier (×3) for an add-drop filter: (a) UBI based on lattice-filter splitter/combiner, augmented with an embedded 2-stage microring filter in one arm; (b) drop- and through-port amplitude response of the complete device (with enlarged view on the dB-scale) showing suppression of unwanted passbands by > 35 dB to provide a 60 nm effective FSR; (c) enlarged view of a dropped and a suppressed passband; (d) corresponding group delay, and (e) dispersion, showing less than 0.2 ps/nm dispersion within suppressed passbands.

tuning range (for a given index change) of a microring-resonator add-drop filter by a factor of 3. The microring filter used is that shown in Fig. 8.11. Here, splitter A and combiner A' are lattice filters having a transmission maximum aligned with one ring filter resonance, and transmission nulls aligned with *two* adjacent ring-filter resonances in one spectral period of the splitter, as shown in Figs. 8.15,8.16. For this to be the case, a two-stage cascaded-MZI splitter A suffices with the following coupling ratios and arm lengths[¶]:

$$\begin{aligned}\kappa_1 = \kappa_3 &= \frac{1}{2}\left(1 - \frac{1}{\sqrt{3}}\right)\\ \kappa_2 &= 1/3\\ \Delta L_1 &= \frac{2}{3}\frac{c}{n_{\text{group}}\text{FSR}_2} = \frac{2\pi R}{3}\\ \Delta L_2 &= 2\Delta L_1\end{aligned}$$

Fig. 8.15(c) shows that the slow-rolling passbands of this MZ filter give minimal group delay and dispersion (compare to the drop-port group delay of the 40-GHz ring filter of $\sim 15\,\text{ps}$). Without a ring filter inserted, all signal reaches one final output port [Fig. 8.15(b)]. When inserted, the ring filter has access to channels at one of every three resonant wavelengths, while the other two resonant channels bypass in the top arm, b_2.

Similarly to the FSR doubling case, these wavelengths are suppressed in the drop port by over 35 dB [Fig. 8.16(c)]. Through-port excess loss for through-port channels, due to the arrangement, is $< 0.015\,\text{dB}$ [Fig. 8.16(b)], due to parasitic out-of-band ring filter phase modifying the π phase shift.

The group delay in the through port is negligible at the suppressed resonances [Fig. 8.16(d)]. Note that at the dropped channel ($\delta f = 0$) only the through-port group delay is shown, and is twice the drop-port delay of $\sim 15\,\text{ps}$ due to the two-stage arrangement in the through-port path. The dispersion, shown in Fig. 8.16(e) is below 0.16 ps/nm at the wings of the suppressed channel (reaching a maximum of less than 0.4 ps/nm between channels), and no more than about 0.005 ps/nm across most of the spectrum, which is negligible in comparison to typical tolerable levels of the order of 20 ps/nm for such (40-GHz-wide) channels in telecom applications.

Therefore, a usable add-drop filter with a three-fold multiplied effective FSR and tunability (for a given index change) is achieved.

An interesting part of this example is the result, shown in Fig. 8.16(c), that the final output of the UBI (without the ring filter in the bottom arm) has flat group delay and contributes identically zero excess dispersion, even though the splitter A and combiner A' are dispersive. It can be proven by a simple geometrical argument, using the UBI rule (Fig. 8.4) that UBIs in general contribute no structural dispersion to the output (through) port, if the splitter A is a lattice-type (cascaded-MZI) filter.

[¶]Design techniques for lattice filters are well known [71] and will not be detailed here.

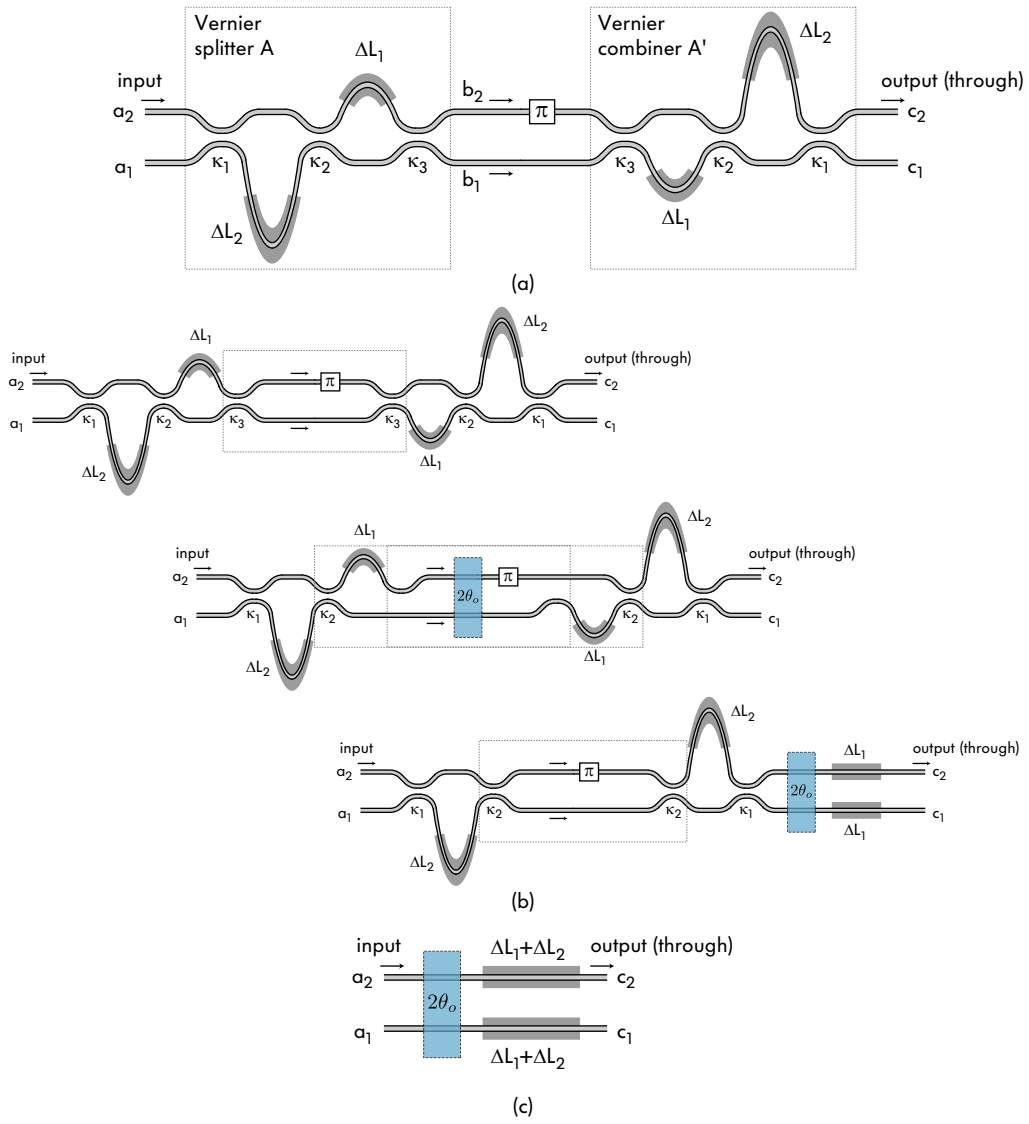

Figure 8.17: Pictorial proof, based on the UBI rule, that a UBI based on dispersive, cascaded-MZI splitter A and combiner A' is "dispersionless" (has no *structural* dispersion): (a) the UBI of interest, (b) a 3-step single iteration of the proof by reduction shows that: first, the inner couplers κ_3 and π DPS are an UBI and can be collapsed to a common-mode phase $2\theta_o$ and a π DPS; second, the waveguide lengths ΔL_1 and common-mode phase may be taken outside the interferometer; (c) the collapsed equivalent structure after 3 iterations – if the couplers and waveguides (i.e. θ_o) are not dispersive then the UBI is not dispersive.

A single iteration, comprising three steps, of this geometrical proof by induction is sketched in Fig. 8.17(b).

The innermost couplers (κ_3 in Fig. 8.17(b), top structure) and interferometer arms are themselves a UBI and, according to the UBI rule, may as a unit be replaced by a π DPS (and a common-mode phase $2\theta_o$ of the directional couplers), resulting in the middle structure in Fig. 8.17(b). Now, the center of the interferometer has

uncoupled waveguides with common-mode lengths ΔL_1 and phases $2\theta_o$. Since these "commute" with an arbitrary remaining splitter or combiner on either side, they can be taken out of the middle of the interferometer to the outside, as shown in the bottom structure in Fig. 8.17(b). Repeating the procedure collapses the entire structure, after three iterations, into the equivalent structure in Fig. 8.17(c). The only dispersion in the structure is therefore any waveguide dispersion in the total waveguide length in the structure and the additional lengths ΔL_1 and ΔL_2, and dispersion of the combined common-mode phases of the three directional couplers, $2\theta_o$. All "structural" dispersion of the cascaded-MZI filter, shown in Fig. 8.15(c), cancels in the UBI configuration. Since directional couplers and waveguides have weak dispersion in comparison to narrowband filters, it can be ignored in the context of filters.

Higher-order dispersionless FSR doubler

There are other ways in which higher-order MZ filters can be employed, besides the multiple passband suppression per period that was shown in Fig. 8.16(a). Another application of a higher-order MZ filter is to create a double zero at a single frequency, and by doing so create a second-order, maximally flat suppression of a single passband. In that case, the higher-order structure increases the suppression of the passbands, and makes it more tolerant to detuning errors.

The single-zero MZI used in Fig. 8.14(a) has a zero at the center frequency of a suppressed passband, and therefore the worst-case suppression is at the passband edges where the MZ response has departed most from an exact zero (in the ideal case).

The example proposed structure in Fig. 8.18(a) is an FSR doubler, like Fig. 8.14. In the present structure, however, a second-order cascaded-MZI splitter is used. In this case, a second-order, maximally-flat transmission zero is created, as shown in Fig. 8.18(b), by choosing the couplings and arm lengths as

$$\begin{aligned}
\kappa_1 = \kappa_3 &= \frac{1}{2}\left(1 - \frac{1}{\sqrt{2}}\right) \approx 0.1464 \\
\kappa_2 &= 1/2 \\
\Delta L_1 &= \frac{1}{2}\frac{c}{n_{\text{group}}\text{FSR}_2} = \pi R \\
\Delta L_2 &= \Delta L_1.
\end{aligned}$$

In this case, the geometrical symmetry of the splitter A results in a linear-phase response the splitter itself (and of the UBI without the filter $B - B'$ inserted).

Fig. 8.18(d) shows the amplitude response of the FSR doubled filter, showing that the suppressed passband is rejected by over 70 dB in this design, due to the double zero. The through-port loss is below 0.02 dB at all wavelengths. The

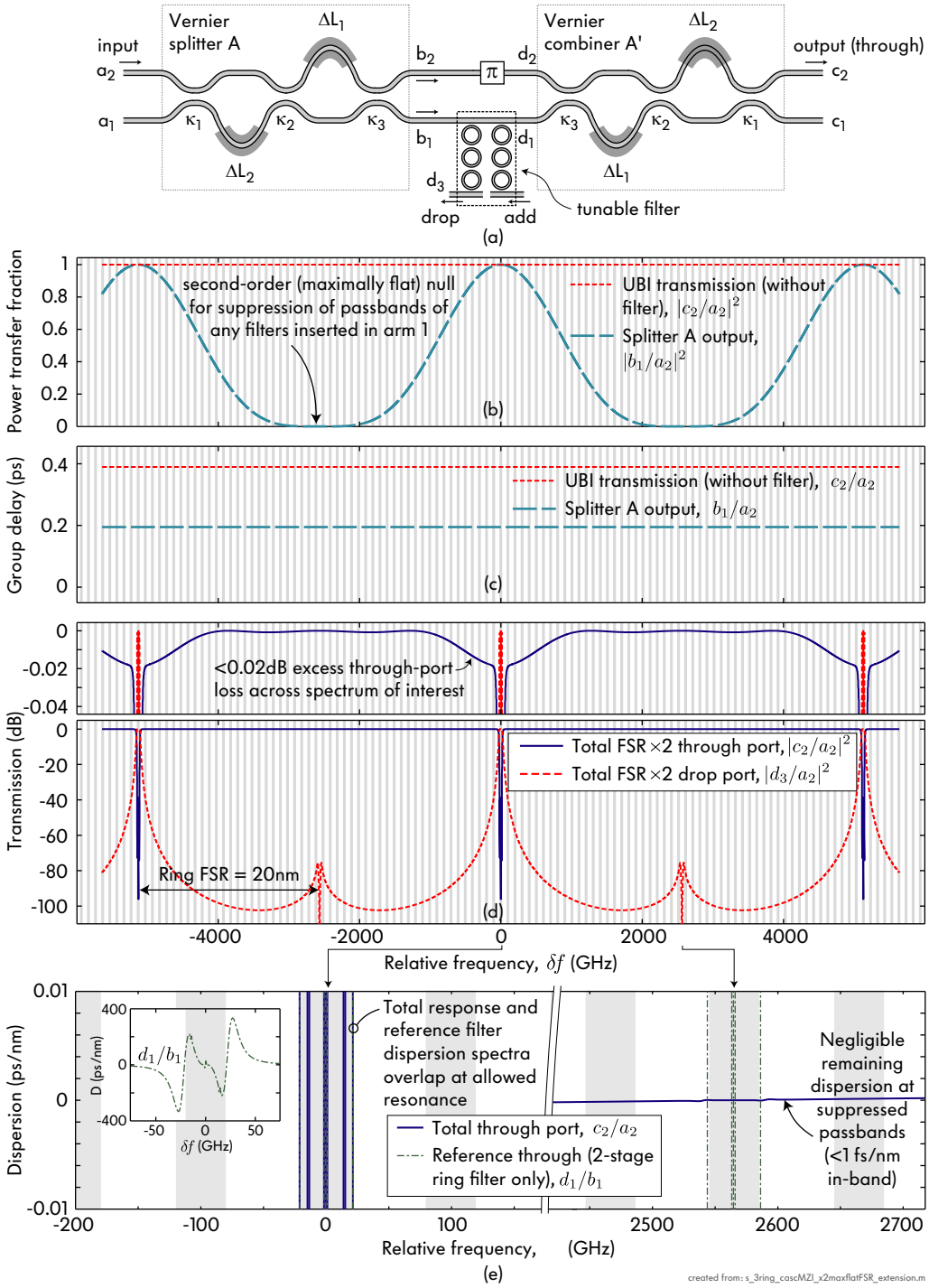

Figure 8.18: (a) Non-dispersive, UBI-based FSR doubler for an add-drop filter; (b) amplitude and (c) group delay responses of the splitter A to the filter path, and of the complete UBI without the ring filter; (d) amplitude and (e) dispersion spectral responses of the complete FSR-doubled filter.

dispersion at the suppressed resonance is negligible, at less than 1 fs/nm, owing to the maximally flat suppression.

Conclusions

The FSR multiplication architectures proposed in this section, based on the UBI principle, were shown to permit the multiplication of the FSR of a resonant filter by suppressing some of the resonant passbands in amplitude and phase. In particular, the improved *resonant-splitter* Vernier schemes based on UBIs, that are interferometric, show near-ideal through-port amplitude transmission at suppressed resonances. These architectures are suitable for achieving large FSR multiplication factors. On the other hand, FSR multipliers based on cascaded-MZI splitter and combiner structures within the UBI scheme were proposed to eliminate the group delay and dispersion seen at suppressed passbands when resonant-splitter Vernier schemes are used. These ideally solve the FSR multiplication problem. In Figs. 8.16 and 8.18, 2-stage ring-based filters were used to demonstrate FSR doubling and tripling of a telecom-grade filter response.

An alternative strategy to hitless switching and resonance suppression is proposed in Chapter 9. Both approaches have applications, and in some cases need to be combined, for example to achieve both hitless tuning and FSR multiplication in a filter.

8.3 Folded UBIs

In this section, *folded UBIs* are proposed. Their implementation is unique in that they require magneto-optic (non-reciprocal) components to realize the π DPS that is required in UBIs. At the expense of this complication, they offer intrinsic insensitivity to asymmetric perturbations of the splitter and combiner that may be of concern in some particularly sensitive UBI designs (e.g. ones with narrowband resonances in the splitter/combiner, such as Fig. 8.13). This insensitivity offers two benefits: first, insensitivity to fabrication errors; and second, in dynamically configurable UBIs such as ones involving switches or tuning elements, it eliminates the need for synchronism in actuation between the splitter and combiner. The latter quality permits UBI implementations with very fast modulation speeds.

A generalization of folded UBIs provides *dual folded UBI devices* which provide two UBIs that operate on the same embedded device, one in each propagation direction through the device. For reciprocal embedded devices this may be exploited for calibration and control purposes in UBI photonic circuits. Based on dual folded UBIs, a novel system application is proposed, referred to as "hot-swapping" of photonic circuits, whereby UBIs may be configured to host ports for pluggable microphotonic-chip subsystems that operate on a through-passing optical spectrum. The UBIs permit such subsystems to be removed and replaced

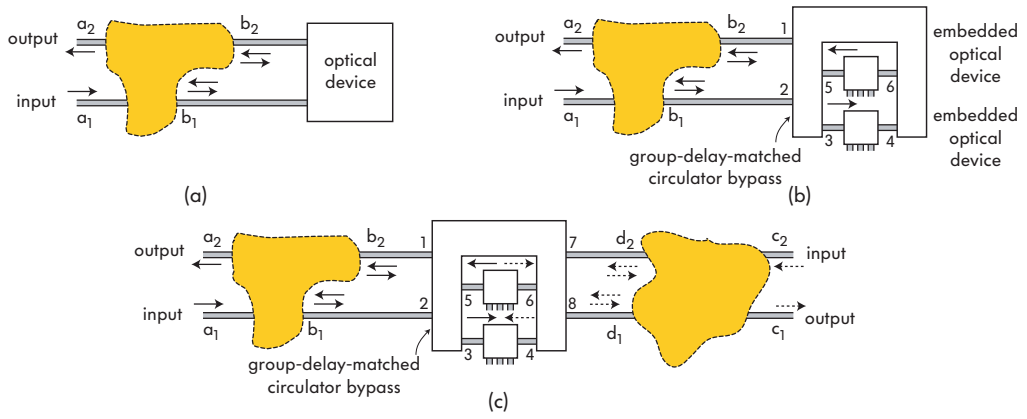

Figure 8.19: Folded universally balanced interferometers (UBIs): (a) general structure of a folded UBI comprising a reciprocal splitter/combiner element, and a non-reciprocal bypass block (NRBB) that effects equal loss and group delay in both traversal directions and a non-reciprocal phase shift such that $b_2 \rightarrow b_1$ has π DPS with respect to $b_1 \rightarrow b_2$; (b) folded UBI modified by inclusion of embedded devices within two traversal paths in the NRBB in addition to the non-reciprocal π DPS; (c) dual folded UBIs share the same NRBB but incident signal from the two traverses the embedded devices in opposite directions.

in a manner that is hitless to parts of the optical spectrum not operated on by the subsystem. By using the symmetry properties of UBIs, such functionality can be achieved with reasonable photonic and electronic circuit complexity that should become available in the near future.

8.3.1 Group-delay-balanced non-reciprocal bypass

A generic folded UBI is illustrated in Fig. 8.19(a), as a more general representation of the free-space folded UBI shown in Fig. 8.2. The splitter A and combiner A' are the same device in this case, and the desired operation is as follows: port a_1 is the input, port a_2 is the UBI output, and ports b_1 and b_2 are bidirectional where the two directions of propagation comprise the two interferometric paths inside the UBI. To satisfy the UBI rule, signal exiting port b_1 to the right must re-enter the splitter/combiner at port b_2, and signal leaving port b_2 to the right must re-enter port b_1 to the left. In addition, the two propagation paths $b_2 \rightarrow b_1$ and $b_1 \rightarrow b_2$ must have balanced insertion losses and group delays, but a relative π DPS. Therefore the device block connecting b_2 and b_1 must be non-reciprocal. For this reason, we refer to such a generic photonic circuit block as a non-reciprocal bypass block (NRBB).

Because the splitter element and the combiner element are the same device – a splitter/combiner element (SCE) – folded UBIs can *only* have a reciprocal splitter/combiner (here the time-reversal design rule for UBIs reduces to the requirement of a *symmetry* under time reversal for the splitter/combiner).

Furthermore, to maintain a π DPS over a reasonable bandwidth, the group delays in the two propagation directions need to be matched. We'll refer to such

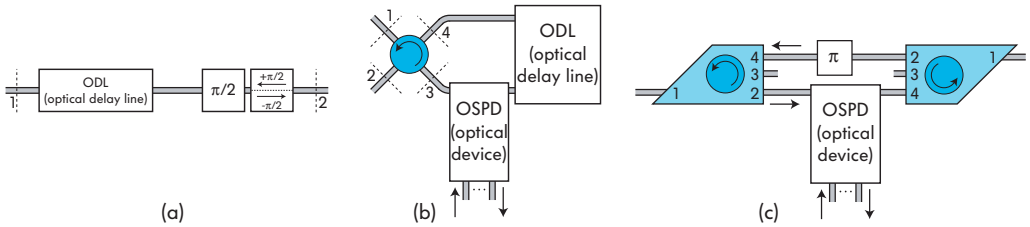

Figure 8.20: Non-reciprocal bypass blocks: (a) plain non-reciprocal phase shift ($\leftarrow \pi, \rightarrow 0$) rad (this would be an optical gyrator [48, p. 300]); (b) group-delay-matched non-reciprocal bypass (GDM-NRBB) comprising a circulator, with an embedded optical signal processing device; (c) NRBB that is GDM, loss-matched and provides a π DPS by symmetry – with arbitrary circulator designs.

a generic NRBB as a group-delay-matched bypass or GDM-NRBB. Fig. 8.20 illustrates some possible realizations of GDM-NRBBs. The first is a plain bidirectional waveguide with a non-reciprocal π differential phase shift (an optical gyrator [48, p. 300]), which is the minimum that can be contained in the NRBB in Fig. 8.19(a) to form a valid UBI. However, to make use of an UBI's properties a signal processing device is typically inserted into one path of the interferometer, such as an add-drop filter (this breaks the UBI rule over a limited bandwidth by design). A generic NRBB comprising such an embedded device requires an optical circulator and is shown in Fig. 8.20(b).

While integrated optical circulators are not readily available in indutrial use at the time of this writing, they have been proposed and demonstrated in research [43, 163, 164], and it is expected that with time they will become available in commercial photonics technology. Then folded UBIs will become practical.

The latter NRBB architecture is unwieldy because the circulator must be designed to balance loss and group delay in the two directions, and to support a π DPS. In addition, this property has to be established over an operating wavelength range of the device. A simple way in which broadband, balanced operation can be intrinsically achieved by use of symmetry is shown in Fig. 8.20(c). The particular design of the circulator is not important here, but the orientation of the two circulators ensures balanced transmission in the two directions in different optical paths. Note that the arrangement in Fig. 8.20(c) is *not* a UBI (and not intended to be), because the magnetic bias field (i.e. the sense of signal "rotation" between ports) is not reversed in one circulator with respect to the other (as required by the lossless UBI rule).

The proposed symmetrized geometry of a folded UBI is shown in Fig. 8.21. For efficient operation, a broadband and reasonably low-loss and low-reflection circulator design is desirable.

The reader may note that the circulators suggested in Figs. 8.20(c) and 8.21 are 4-port, whereas 3-port circulators would in principle suffice. The reason for using 4-port circulators is the risk in practice that parasitic reflection into the reverse

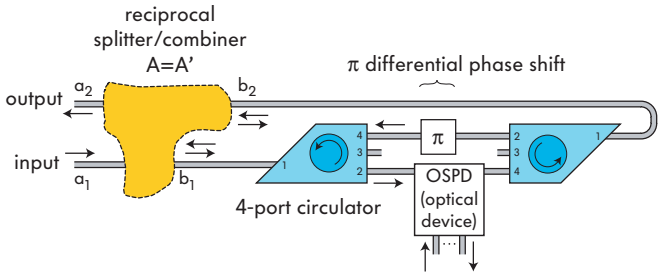

Figure 8.21: Symmetrized general form of folded UBI including arbitrary circulator designs, and an embedded optical signal processing device in one propagation direction.

propagation direction within the UBI interferometer arms would build up a high-Q resonance fed clockwise between the two circulators. The fourth port on each circulator acts as a high-loss mechanism for reverse propagation, to stop resonant buildup. The fourth port is further utilized in dual folded UBI schemes in Sec. 8.3.2.

A worthwhile comment is that a folded UBI is not equivalent to an optical loop mirror [165]. A loop mirror is a section of waveguide or optical fiber that is folded forming a directional coupler with itself. A loop mirror will return all signal entering a port to that same port, and only when the directional coupler is a 3 dB coupler; otherwise the signal is divided between the two outputs. A folded UBI takes all input from one input port, and channels into into the second output port at all wavelengths, configuration states, and for all possible splitter designs (subject to them being reciprocal R 4-ports).

Folded UBIs have all the functional properties of lossless UBIs that have been utilized here, and can therefore be used for all the same applications. They provide the same tolerances in most respects as standard UBIs, but they eliminate sensitivity to antisymmetric mismatch between the splitter and combiner and reduce control and tuning circuit complexity.

Fig. 8.22 shows folded-UBI implementations of the hitless switch, resonant UBI-based Vernier FSR multiplier and dispersionless, cascaded-MZI FSR multiplier proposed in the previous sections (Figs. 8.7, 8.13 and 8.16).

8.3.2 Dual-folded UBIs and hot-swapping of microphotonic subsystems

It may be noted, referring to the generic folded UBI in Fig. 8.21, that a second splitter/combiner of arbitrary design may be connected to the two open ports of the 4-port circulators (both labeled 'port 3' in Fig. 8.21). Then, two independent UBIs are formed, each with its own splitter/combiner, as illustrated in Fig. 8.19(c) in abstract form, and in Fig. 8.23(a) in a general symmetric implementation.‖ The shared feature between these two UBIs is a shared NRBB, i.e. a shared embedded

‖Note that the circulators in Fig. 8.23(a) are drawn with a different routing arrangement between input and output ports than in previous illustrations, in order to better correspond to the port arrangement that is typically obtained in microphotonic circulator realizations (see [43]).

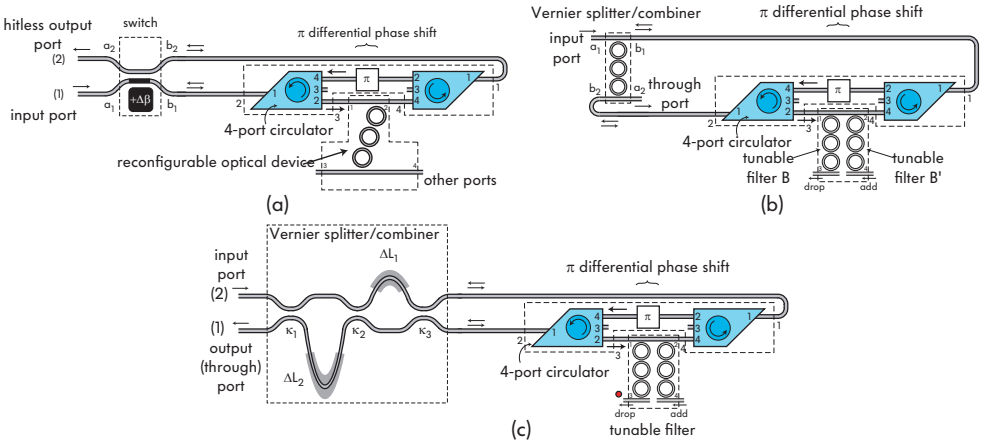

Figure 8.22: Folded UBI implementations of (a) a hitless switch, (b) a resonant Vernier FSR multiplier and (c) a dispersionless cascaded-MZI FSR multiplier, for an add-drop filter. Compare proposed standard-UBI structures in Figs. 8.7, 8.13 and 8.16.

optical device, which may be an add-drop filter, for example. However the two UBIs access the same device in opposite directions of propagation.

If in practice parasitic reflections in the circuit can be kept low enough to prevent substantial crosstalk between the two propagation directions, this geometry may offer some useful capabilities. For example, if the embedded device is reciprocal (as most optical devices are) the two UBIs will independently be able to sample the same spectral response without interfering with each other. This could be used for dynamic control, for example, where one UBI passes a primary optical WDM spectrum through the device, while the second UBI may be used to launch a low-power test signal through the device to probe its properties without interfering with the main signal. For example, this may be used for feedback control, and in the context of a filter, the secondary circuit may dynamically track its resonant wavelength, spectral shape, etc., which may be used in a feedback loop to actuate tuning controls of the device to stabilize its spectral shape to a reference.

One potential new application that is made simpler by such a "dual-folded" UBI is a generic access port where complex microphotonic subsystems may be hot-swapped into and out of a high-density optical network in a hitless manner. The rationale is roughly as follows. Integrated optical circuits are generally inserted into an offline network, and the network is then made live. Thus, replacement of integrated optical components, for failure replacement or upgrade, currently requires temporary interruption of network service passing through the device and a down time, since the device ports must be disconnected from the network. Since a WDM network carries a multitude of channels, the majority of which may not be processed by the device being replaced, the device replacement unnecessarily causes a service interruption on a number of express channels. As photonic circuit capability and complexity is scaled up and as WDM networks scale to larger

numbers of wavelength channels, accommodated by a wider spectral range of wavelengths and/or a higher spectral efficiency and utilization of the spectrum, disrupting the majority of channels at a single point will cause greater disturbance to the overall network. Therefore, it may be of interest to find an approach to "hot-swap" an optical signal processing component within the network, that is, to replace it without interrupting service to channels which are physically passing through the optical component being replaced, but are functionally bypassing the component as so-called express channels. Such a "swappable" optical signal processing component may not be only an add-drop filter but a more complex integrated photonic subsystem on a chip.

Such a generic, hitless access port that allows "hot swapping" is schematically shown in Fig. 8.23(b), based on the architecture in Fig. 8.23(a). The splitter/combiner A/A' of the primary circuit is a variable coupler (a continuous switch) which connects the primary optical spectrum to the device of interest in a hitless switch arrangement of the type proposed in Fig. 8.7. A pair of connecting ports is shown where the arbitrary embedded device, such as a filter, is to be connected. These ports are illustrated by vertical fiber-chip grating couplers here, which are a promising technology for coupling light into and out of microphotonic circuits [166–168], and can facilitate flip-chip type insertion of the embedded device where the two chips with vertical couplers are aligned one on top of the other.

Therefore, before removing and replacing the embedded optical device (labeled D in Fig. 8.23), the main hitless switch on the optical network side is actuated to route all optical wavelength channels that were not affected by the failure of device D to a bypass state in the top waveguide arm of the NRBB. Then, the optical device D may be removed and another inserted (which may serve the same or another function).

Insertion of the new device D into the circuit provides a few other complications. The device D itself may have a group delay between the input and "through" port that is not accurately known, and in practice, seating the chip will have a positional uncertainty that places another variation on the group delay. Therefore, the differential phase shift and group delays in the NRBB are not in general balanced when an arbitrary device is inserted to form a valid folded UBI on the optical network side.

A control circuit and the second folded UBI are provided to permit automatic adjustment of a variable group delay, phase shift, and possibly gain or loss, in order to form a balanced interferometer and a folded UBI without disturbing the optical network side of the circuit. A variable switch, or a fixed coupler, on the local control side in Fig. 8.23(b) may be used to launch a weak optical test signal continuously through the NRBB, and may determine the optical path length and gain from the fringes of the optical transmission. With feedback control of the group delay, phase and potentially gain/loss to compensate for the inserted device

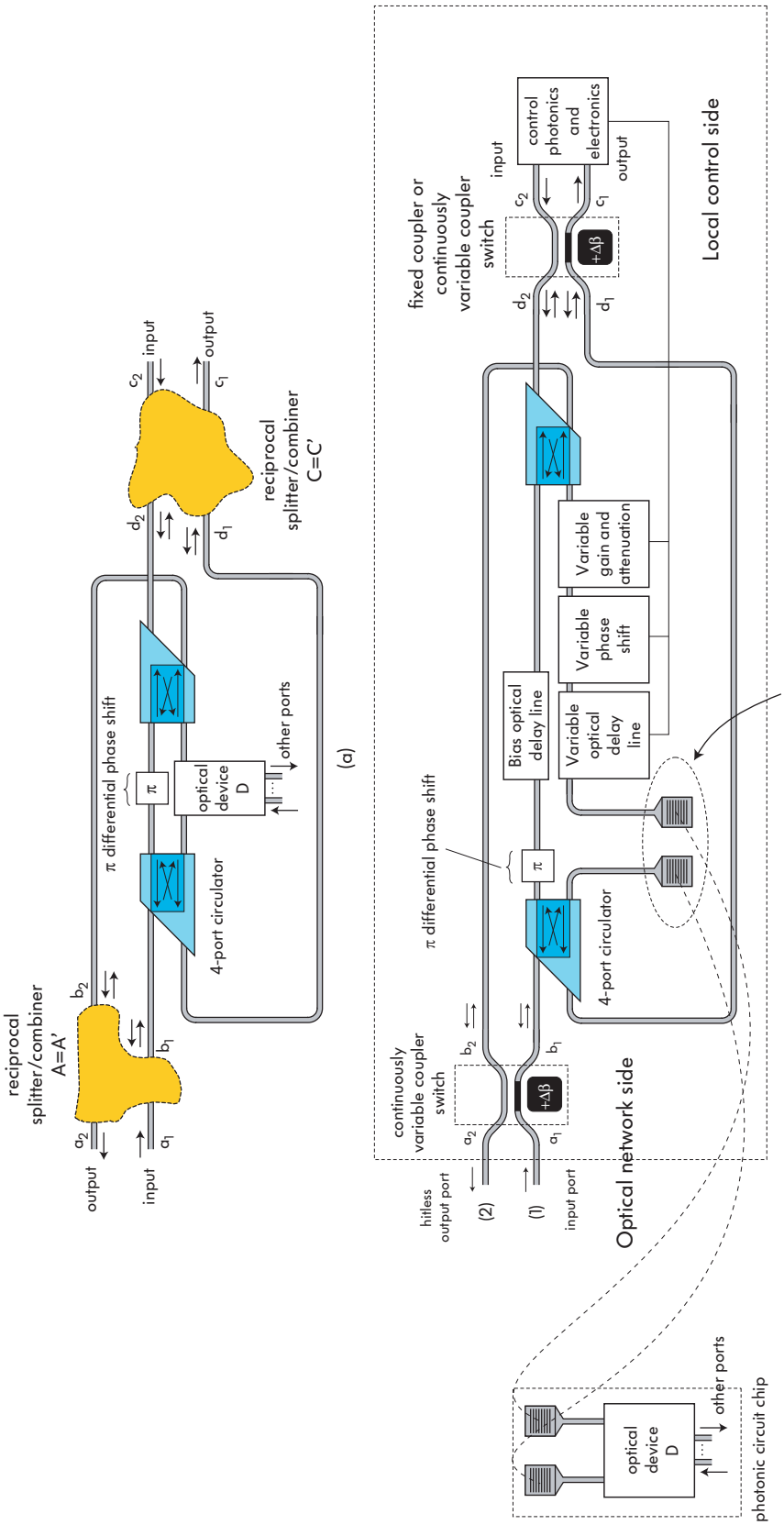

Figure 8.23: (a) Proposed general dual UBI, showing two splitter/combiners sharing a single NRBB, comprising an embedded optical device D (which may be an add-drop filter). Circulators are schematically represented with a port arrangement that corresponds to usual microphotonic implementations (see [43]); (b) Application of dual UBI for a generic UBI-based access port that permits "hot-swapping" of microphotonic subsystems.

unbalancing the interferometer, a broadband π DPS can be established for folded UBI operation on the optical network side. Then the hitless switch on the optical network side can be actuated to bring the device seamlessly back into the network.

8.4 Zero-DPS bypass interferometers (ZDBI)

In this section, alternatives to the UBI principle are investigated for bypass interferometers. Folded UBIs were shown in Sec. 8.3 to provide important advantages over conventional UBIs in terms of reduced sensitivity and control complexity. However, the requirement of integrated non-reciprocal elements – optical circulators – increases the complexity and challenge of their realization with present technology. Here it is shown that in a very limited subset of device designs similar functionality to folded UBIs can be obtained without use of any non-reciprocal elements.

Referring to Figs. 8.1(a) and 8.21, it can be observed that there are two reasons why non-reciprocal elements are needed in folded UBIs. The first is the π DPS between the two paths, where one path must see a π phase shift with respect to the other. It is of interest to see whether general bypass interferometers can be built using other phase shifts, in particular a zero DPS. Previous work on hitless switching has already demonstrated zero-DPS unfolded devices of particular implementations (e.g., see [169, Fig. 11(a)])** The second problem is that the embedded device such as a filter should be seen to only one of the two optical paths in the interferometer, while the other should be a bypass path. Both of these problems are addressed in order.

The guiding principle will be to seek forms with as much symmetry as possible, for the same tolerance and bandwidth benefits as those offered by UBIs, and at the same time with as much generality of admissable splitter/combiner elements as possible.

First, bypass interferometers of different DPS are investigated. Fig. 8.24(a) shows a general form of bypass interferometer that will be investigated, having an arbitrary DPS of $\Delta\Theta$ (UBIs have $\Delta\Theta = \pi$). With completely arbitrary splitters and combiners, a rule similar to the UBI rule cannot be found for arbitrary $\Delta\Theta$. Therefore we will impose two restrictions. First, we will restrict the form of the splitters and combiners to be generic Mach-Zehnder interferometers, which are a relevant splitter form, as shown in the proposed hitless switching and FSR multiplier devices in the previous sections. Second, the "splitter" and "combiner" of the MZI in each splitter will be restricted to be identical, though they may be arranged

**The cited device cannot be a UBI because it only has one input port and one output port, whereas UBIs have input at one of two ports, but the output signal in the combiner is at the opposite corresponding port, as shown in Fig. 8.1(a). If a π DPS were introduced in the here-cited device, the output would be lost to a radiation mode (or coupled to a higher-order guided mode).

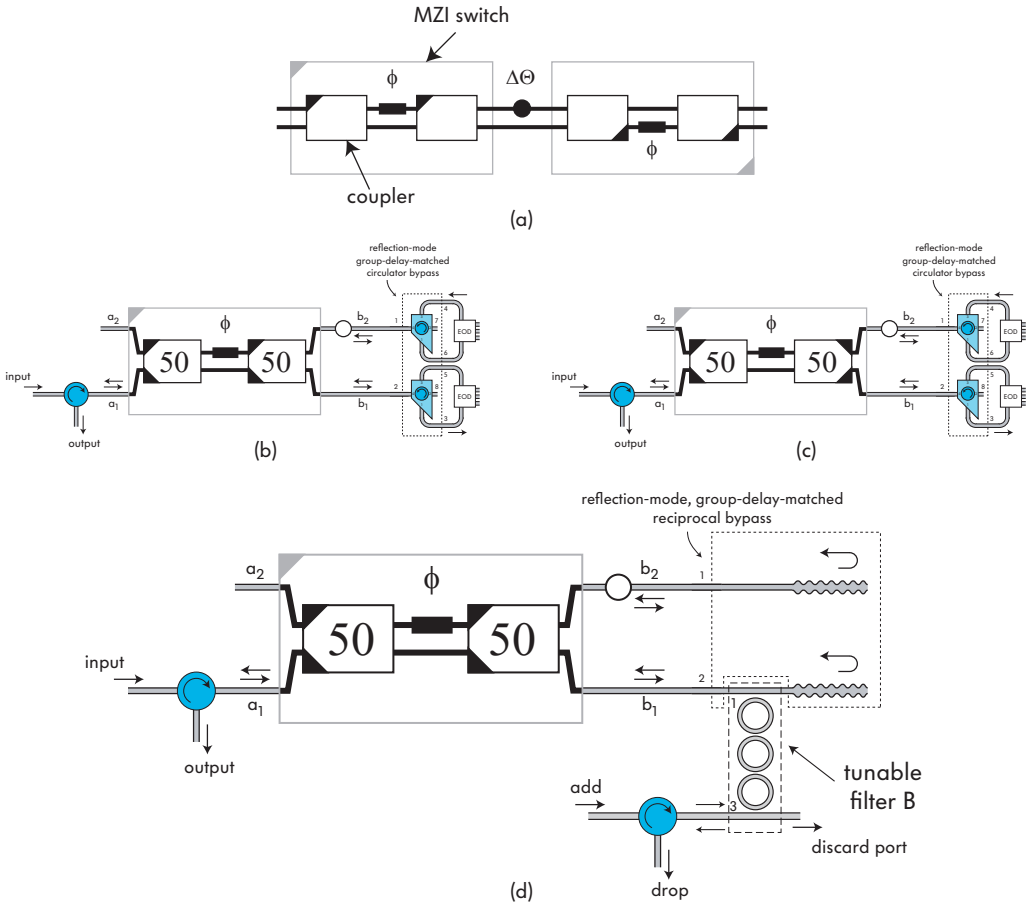

Figure 8.24: Zero-DPS bypass interferometers (ZDBIs): (a) general structure of bypass interferometer with an arbitrary DPS of $\Delta\Theta$, and splitter and combiner elements restricted to be generic Mach-Zehnder interferometers; (b,c) the two symmetry-forms of splitter/combiner that permit a folded bypass interferometer with zero DPS; (d) such a folded ZDBI can be used to make a hitless bypass for a ring filter without embedded circulators (circulators are required outside but may be off-chip). A two-stage filter is obtained from a passing twice by the reciprocal single filter stage.

in various relative orientations, and may have various (including continuously variable) DPS, ϕ, between them.

The output of these generic interferometers is studied by an exhaustive search through three parameter spaces:

- the set of all four relative orientations (Fig. 2.4) of the combiner with respect to the splitter;
- the set of all four relative orientations, within the splitter, of its embedded combiner relative to its splitter;
- the set of two possible DPS in the main circuit, $\Delta\Theta = 0$ and $\Delta\Theta = \pi$.

In order to permit useful applications, the interferometer must recombine all input from one input port into only one output port for all possible values of the MZI phase ϕ in the splitter (to permit hitless tuning, etc.).

By taking the canonical forms of reflectionless 4-ports of various symmetries and orientations and computing their general transmission matrix, the set of successful bypass interferometers was found, and is summarized in Fig. 8.25. The left two-column group shows $\Delta\Theta = \pi$ cases, while the right two-column group shows $\Delta\Theta = 0$ (ZDBI) cases. Note that for $\Delta\Theta = 0$ interferometers, it is furthermore necessary that the power splitting be 3 dB $(50 : 50)$, as indicated in the figure. Rows show different relative orientations of splitter and combiner inside a MZI splitter, while the columns show different orientations of combiner relative to splitter in the main circuit. There are only two columns per group because the other two symmetries in each group ($\mathcal{T}$ and $\mathcal{V}$ for $\Delta\Theta = \pi$, and $\mathcal{H}$ and $\mathcal{HV}$ for $\Delta\Theta = 0$) have no valid cases.

In each case, the most general symmetry of MZI splitter and combiner is shown that provides a valid bypass interferometer (see Fig. 2.5). The left column are recognized all to be UBIs. Some redundancy is present in the various symmetry restrictions. The yellow shaded devices are the only three unique forms found. The first is the general class of UBIs. The other two are ZDBIs comprising a splitter and combiner that are each MZIs comprising themselves a 3 dB splitter and combiner where the combiner is a translation ($\mathcal{T}$) copy of the splitter and both have a $\mathcal{H}$ symmetry, or where the combiner is a 180° -rotated ($\mathcal{HV}$) copy of the splitter with no requirement on symmetry of each.

Since UBIs have been discussed, we will investigate briefly the two forms of ZDBI found in Fig. 8.25. Since they have a zero DPS, they may be formed into a folded bypass interferometer without requiring a non-reciprocal phase shift. Referring to Fig. 8.19(a), there are two ways one may envision forming such an interferometer – we'll call them *swap mode* and *reflection mode*. In *swap mode*, signal exiting the splitter/combiner and entering the embedded optical device in the bottom port (b_1) returns via the top port of the embedded device to the splitter/combiner; while a signal entering the embedded optical device on the top exits on the bottom. In this case, the unfolded form of the folded interferometer has a combiner that is a 180° rotated copy of the splitter. In *reflection mode*, signal entering the bottom port exits the bottom port, and signal entering the top port exits the top port. In this case, the unfolded form of the folded interferometer has a combiner that is a horizontally reflected ($\mathcal{H}$) copy of the splitter. Swap mode has the drawback that non-reciprocal devices would still be required to address the second issue – having only one of the two optical paths see the embedded optical device such as a filter. In reflection mode, the two paths may be physically separated without magnetooptics. Therefore we consider the latter form of bypass block in the context of ZDBIs. The two generic forms of ZDBIs, according to

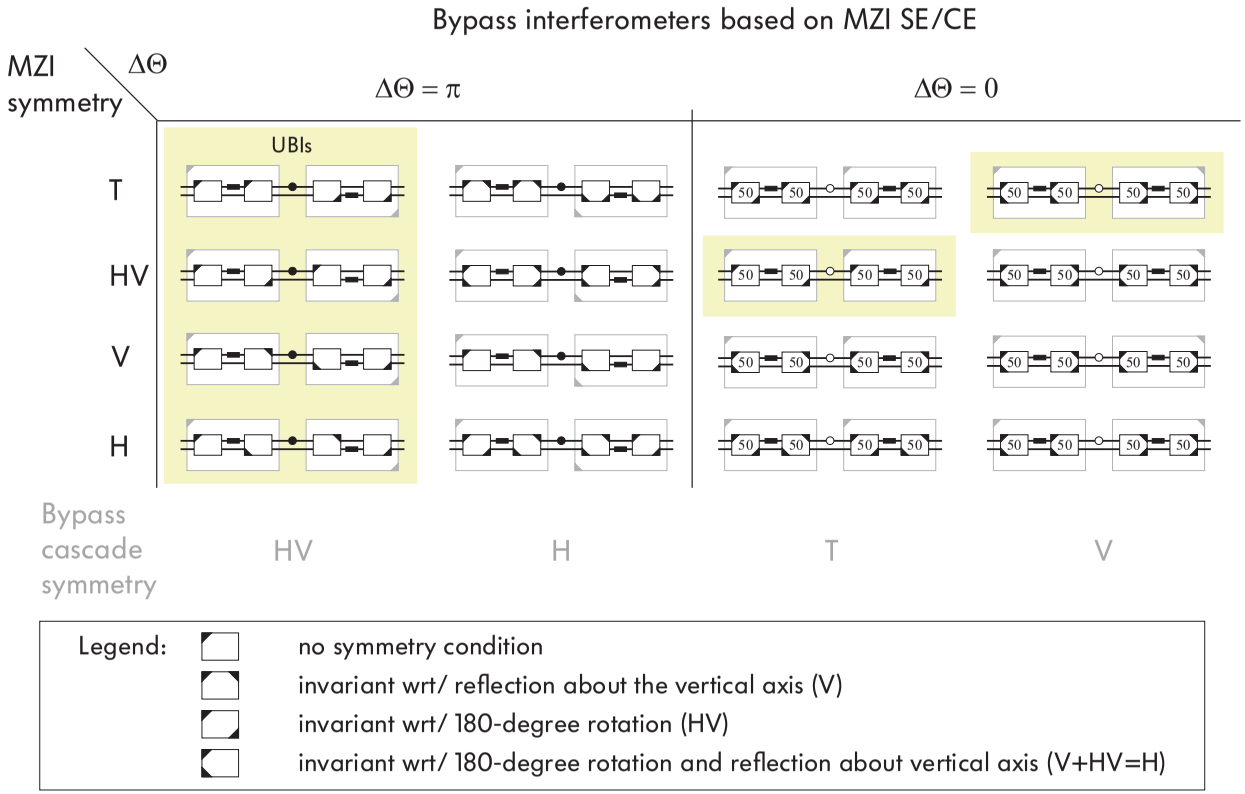

Figure 8.25: Table of valid bypass interferometers with a splitter and combiner of generic Mach-Zehnder form. The left two-column group shows $\Delta\Theta = \pi$ cases, while the right two-column group shows $\Delta\Theta = 0$ cases. Rows show different relative orientations of splitter and combiner within a MZI splitter, while the columns show different orientations of combiner relative to splitter in the main circuit. In each case, the most general symmetry of MZI splitter and combiner is shown that provides a valid bypass interferometer. There are only two columns per group because the other two symmetries in each group have no valid cases. The left column are all UBIs. The yellow shaded devices are the only three unique forms.

Fig. 8.25, are illustrated in Fig. 8.24(b,c). Note that, because of the folding, the symmetry of the couplers in the implementation in Fig. 8.24(b) is more limiting than the unfolded form in Fig. 8.25.

To use unidirectionally-excited embedded devices, i.e. optical hybrids, such as microring-resonator add-drop filters in their typical use configuration, circulators are still needed. However, implementations without circulators on the chip may provide useful functionality. One such example is illustrated in Fig. 8.24(d). It shows a hitless tunable add-drop filter based on microring resonators. Each path in the reciprocal bypass block is terminated by a perfect mirror, which may be a Bragg-based reflector as illustrated, or may be a waveguide loop mirror. For high-index-contrast microphotonic implementations, the latter is proposed as a simpler alternative. Note that the complete device is equivalent to an unfolded filter with *two* 3-ring stages, because the filter is passed twice, once from left to right and once from right to left. In addition, the same port being used for drop and add results effectively in the commonly used "add-after-drop" decoupling geometry as the add signal does not couple to the drop, if the waveguide is properly terminated in a lossy or radiative element.

This implementation of a hitless filter still requires circulators off chip to split the in and through, and the add and drop signals. However, off-chip circulators are readily available devices. Therefore this scheme is a viable alternative to UBIs in scenarios where integrated circulators are not practical.

Chapter 9

Switching resonant systems into a fully transparent reflection state*

In the first part of this chapter, I propose a general approach for directly switching a resonant system into a "fully transparent" reflection state. The approach involves a continuously variable coupling coefficient at the access (input) port to a resonator and, in general, an artificial loss mechanism (that may also be variable), introduced into all supermodes, i.e. into one or more resonant cavities. The resonant system is switched into a minimum-phase transparent reflection state that is dispersionless. The outcome of this approach is a robust pole-zero cancellation at all system poles.

Concept designs are described that enable new capabilities for telecom applications, including variants involving time-variable coupling coefficients that enable hitless-tunable filters switchable to a fully transparent state; and wavelength-variable coupling coefficients that enable FSR multiplication of resonant circuits, including FSR doubling, where the suppressed resonances are dispersion free.

By contrast with this direct approach, in Chapter 8, an indirect approach was described where a bypass interferometer is used to route the input signal away from a resonant system by transferring, in a continuous way, the signal from the input-output-port optical path of the resonant device to a bypass path (maintaining coherence between the paths by the geometry of the interferometer). The latter approach is general with respect to the type of bypassed device (filter), but has drawbacks including physical size of the interferometer, added loss of the splitter and combiner elements, and constraints on the allowable dispersive response of the embedded bypassed device (see Fig. 8.9 and description).

In the second part of the chapter, the first experimental demonstrations of devices based on these concepts are described, carried out as part of a team ef-

*Aspects of this work are published in [136].

fort to demonstrate technology for a tunable microphotonic OADM based on SC waveguides[†]. Transparently switchable first-order and telecom-grade, fourth-order microring-resonator add-drop filters, based on strongly confined silicon waveguides, are demonstrated. These structures are the first truly hitless microring-resonator add-drop filters, in that they have nearly full transmission and effectively no dispersion (for the relevant data rate) in the off-state through port response.

Full transparency

Full transparency, as defined here, refers primarily to the spectral shape of the amplitude and group-delay responses. In passing through a linear system that has broadband transparency, understood in the conventional sense, it is expected that the amplitude spectrum of an incoming signal will remain unchanged in shape, as well as absolute amplitude level; however, the phase response may be distorted and accordingly the time-domain waveform will not remain unchanged – an input pulse may exit the device broadened and/or torn apart by dispersion.

We will define *full transparency* as a generalization of the typical meaning of transparency extended to both amplitude and phase. A system is fully transparent over a wavelength range if an input signal entering an input port exits an output port with the amplitude spectrum unchanged, and the group delay spectrum unchanged in shape with the exception of a constant delay. Therefore, a lossless Gires-Tournois interferometer or all-pass filter is transparent, but not fully transparent.

Full transparency in the off state is not a requirement for present telecom add-drop filters. A degree of loss and dispersion, potentially varying in time during switching and tuning, may be tolerated so long as the variation is slow and does not substantially impact the bit-error rate. However, such constraints introduce further constraints into the design. Also, as data rates increase, as spectral efficiency and bandwidth utilization is pushed closer to 100%, and as the number of wavelengths and WDM network nodes on an all-optical path grow, such device non-idealities are likely to become substantial impairments in at least some applications. It is the author's belief that providing a microphotonic technology capable of fully transparent switching will enable new capabilities and new levels of scaling to large aggregate data rates and spectral densities in WDM optical networks, in addition to providing a better alternative to the conventional hitless tuning approaches such as cavity detuning [170–172].

[†]This project (2005–2007) was led by the author and Tymon Barwicz. Device design was done by the author; process design and development, and fabrication by T. Barwicz; heater design primarily by Fuwan Gan; experimental characterization primarily by Marcus Dahlem; mounting, wire bonding and passivation by Charles Holzwarth.

Relationship to previous work

The resonance suppression approach described in this chapter builds upon previous work on switching of resonators [31, 71, 97, 173–175], but several new elements are introduced. First, the functionality targeted – full transparency in the reflection (through-port) response[‡] of a resonator – itself appears to be new. Previous work on optical switching using resonators has focused on amplitude switching, and on the transmission (drop-port) response. There, simply detuning a Lorentzian resonant response leads to a substantial reduction of amplitude (various implementations include microring resonators [173] and photonic crystals [175]).

On the other hand, switching off a resonant system to full transparency in the reflection response is considerably more demanding. The entire input spectrum, except for wavelengths near resonances, is reflected (or passes to the through-port) with substantially little attenuation and phase distortion (dispersion)[§]. Wavelengths near critically-coupled resonances are partially or fully dropped from the input spectrum (usually into another port), while wavelengths near strongly-overcoupled resonances experience dispersion, with smaller or no attenuation. Switching off the resonant system implies returning the amplitude response to 100% at all wavelengths (in the spectrum of interest) in reflection. Because the off-switching is to a full-transmission rather than to a null-transmission state, it is necessary in addition that the phase response be non-dispersive (a broadband phase shift and group delay is of no consequence) for the resonant system to be considered truly "off". This is achieved in a "fully transparent" system.

In previous literature, two approaches to switching of resonators have been taken: switching by control of cavity loss [17, 31, 159, 174] and switching by control of the coupling strength [97]. These approaches have several drawbacks. Both require, as shown in the following section, 30-40 dB switching contrast in the actuation mechanism to switch fully between the on and off state. Changing cavity loss from very high to very low can be a substantial practical challenge. Furthermore, in the case of microring and other finite-FSR cavities, the loss control approach has a broadband residual loss in the reflection (through-port) response equal to the single-pass input coupled power (or about the inverse of the finesse), which cannot be tolerated in the majority of applications. Smaller-FSR devices have larger broadband loss, and practical SC microring filters for telecom applications have on the order of 2-20% depending on finesse. In previous approaches

[‡]The reflection response refers to the diagonal response functions in the S-matrix of an N-port, or to the diagonal elements (so-called through-ports) in the T-matrix of a $2N$-port optical hybrid (see Sec. 2.1.1). We consider systems where, when resonances are unexcited, the S-matrix of the N-port or T-matrix of the hybrid is diagonal (ideally unity amplitude). This means excluding structures that may have substantial direct (non-resonant) coupling between ports.

[§]Waveguide and material dispersion for propagation to and from ports is excluded – we assume collocated input and output port reference planes, so that all phase response is due to excitation of the resonant system.

making use of coupling strength variation, an additional drawback has been the actuation approach which does not necessarily lead the system to a minimum-phase off state, and therefore may or may not produce substantial through-port dispersion. In this chapter these issues and designs that solve them are rigorously addressed.

Fully transparent switching is illustrated in Fig. 9.1 as part of the expected operation of a truly hitless-tunable channel add-drop filter for T-OADMs and WDM networks. In steps 1–3, the add-drop filter is switched to a fully transparent state – the drop-port amplitude response is extinguished, the through-port response recovered to full transmission at all wavelengths, and the through-port dispersion (due to resonant group delay variation) eliminated. In steps 4–5, the filter is tuned while maintaining full transparency. Therefore it has no effect on live wavelength channels through which its resonant wavelength may be tuned. In step 6, the filter is brought back into the on state at a new target wavelength. This is the desired operation to be achieved.

9.1 Disabling the amplitude and phase response of a resonance

In this section, the basic approach is described for disabling resonant systems to a fully transparent state in the reflection response. It is shown that a large contrast between off-state and on-state input-coupling-to-internal-loss ratio is needed for complete switching. A combination of variable input coupling and variable loss mechanism solves two problems: it makes practical switching dynamic ranges sufficient to achieve full switching, and it eliminates single-pass loss seen in conventional schemes. It also permits putting the system into a robust minimum-phase fully transparent state, by placing pole-zero cancellation far from the real frequency axis.

To establish the requirements for fully transparent switching, a generic resonance is considered which has an access port and a loss mechanism. This simple model also covers higher-order resonant systems, as we may for general insight consider each supermode of the system separately[¶]. All losses and any output ports (other than the access port) are all lumped into the abstract "loss" parameter.

Such a generic resonance is illustrated in Figs. 9.1(a,b), as a 1-port and as a 2-port hybrid with a traveling-wave resonance (e.g. relevant to reflectionless devices based on ring resonators). There the cavities are lossless and the lumped loss is represented explicitly as an output port within the resonant system. In the general coupling of modes in time (CMT) formalism [67], the resonance has a resonant

[¶]If the supermodes are close in frequency and input coupling is strong (coupling rate on the order of their frequency difference), strictly they must be considered together; however, general insight for purposes of fully transparent switching does not require us to go to such lengths.

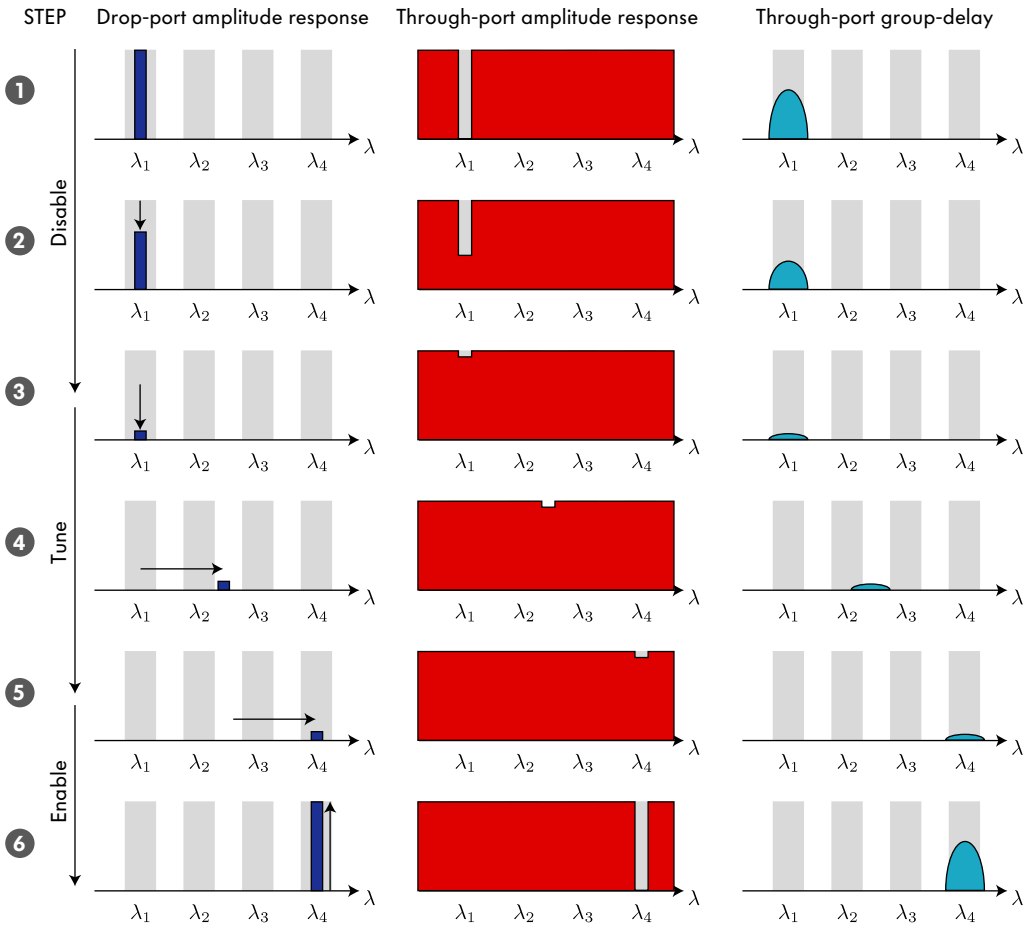

Figure 9.1: Illustration of the required behaviour of a truly hitless-tunable filter, with switching to a fully transparent state. The drop-port amplitude response, and the through-port amplitude and group-delay responses are schematically represented. The tuning operation is carried out in 3 steps: (1) the filter is disabled, so that no power is dropped, all power is passed to the through port, and the through-port group delay is eliminated; (2) the filter, in the off state, is tuned to a new target wavelength; (3) the filter is re-enabled at the new wavelength returning to a state substantially dropping the target channel from the through port spectrum.

frequency ω_o and energy amplitude a such that $|a|^2$ is the stored energy. When free running, the energy amplitude decays with rate $r_e \equiv 1/\tau_e$ into the access port, and with rate $r_o \equiv 1/\tau_o$ due to the loss mechanism (τ_e and τ_o are the corresponding time constants). The system is described by the CMT equations of state

$$\frac{d}{dt}a = (j\omega_o + r_e + r_o)a - j\mu_e s_+$$
$$s_- = -j\mu_e a + s_+$$

where $\mu_e = \sqrt{2r_e}$ [8, 67]. For the frequency response, $d/dt \to j\omega$, and we characterize the resonant reflection (or through-port) response of the 1-port in

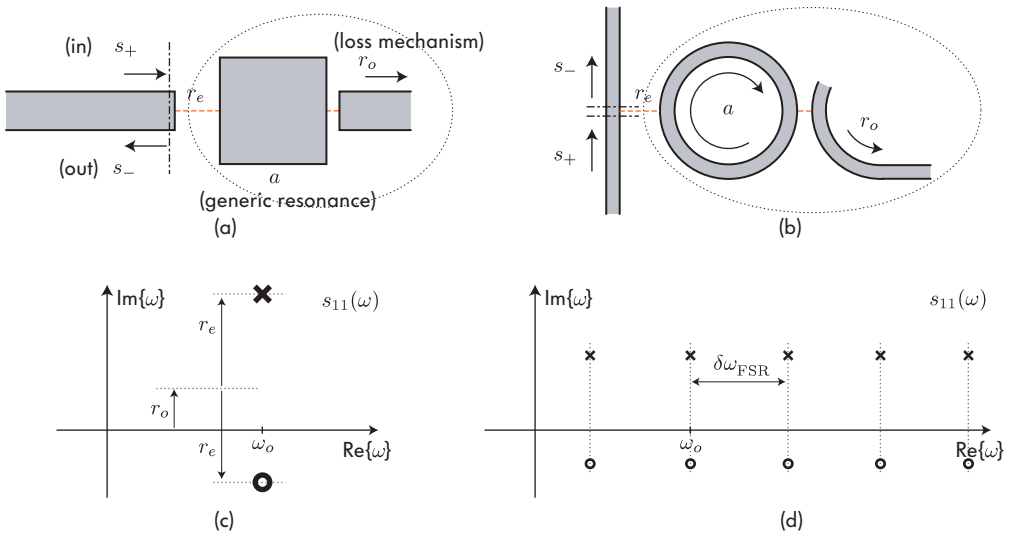

Figure 9.2: An abstract resonator is a generic 1-pole resonance. It is shown coupled to an access port with an external decay rate r_e, and comprising a loss mechanism giving rise to "internal" decay rate r_o: (a) standing-wave resonance and standard access port form, (b) traveling-wave resonance and hybrid (see Sec. 2.1.1) access port form.

terms of the detuning $\delta\omega \equiv \omega - \omega_o$ as [67, p. 205]

$$s_{11}(\omega) \equiv \frac{s_-}{s_+} = \frac{j\delta\omega + r_o - r_e}{j\delta\omega + r_o + r_e}$$

The reflection response of this single (abstract) resonant mode has a single pole and a single zero in the complex-ω plane, as shown in Fig. 9.1(c). For physical resonators having multiple modes spaced by an FSR (such as Fabry-Perot cavities or microring resonators), in general this pole zero pattern repeats in frequency with the FSR [Fig. 9.1(d)], if the adjacent resonances are not substantially coupled and if the FSR and decay rates are independent of frequency; but, a single resonance of interest provides the insight required for switching. In these plots, one can also see by inspection the conditions for critical coupling ($r_e = r_o$), overcoupling (maximum-phase zeros, $r_e > r_o$) and undercoupling (minimum-phase zeros, $r_e < r_o$).

Several pieces of information that are important for fully transparent switching can be extracted from this simple model. First, the amplitude switching, on-resonance where the contrast ratio is largest, is given in terms of external and loss Q's as

$$\left|\frac{s_-}{s_+}\right|^2_{\delta\omega=0} = \left(\frac{Q_e/Q_o - 1}{Q_e/Q_o + 1}\right)^2$$

where $Q_x \equiv \omega_o\tau_x/2 = \omega_o/(2r_x)$, $x \in \{e, o\}$. This normalized relationship is shown in Fig. 9.3(a). The switching characteristic depends only on the ratio of the input coupling coefficient (represented by an external Q, Q_e) to the internal loss (loss Q,

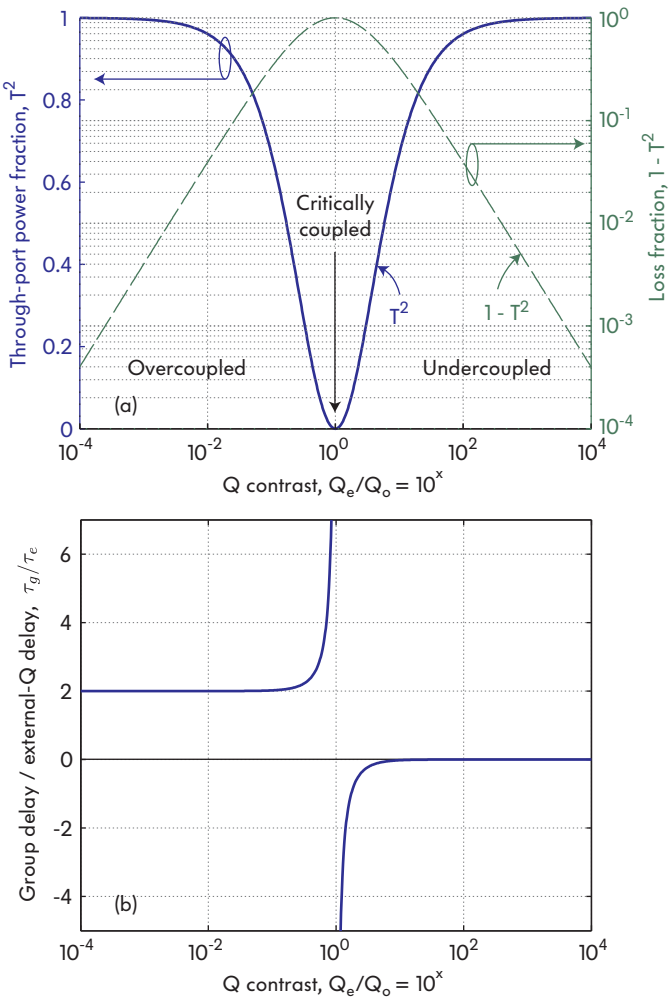

Figure 9.3: Switching characteristics of a single abstract resonance: (a) Amplitude and (b) normalized group delay of the response function on-resonance for a range of input-to-internal decay time contrasts, or Q contrasts, relevant to dispersionless switching.

Q_o). For scalability to a large number of cascadable devices, reflection (through) port losses much lower than 1% – on the order of 0.1% or smaller – are desirable. Then, switching contrasts $\chi \equiv 10\log_{10}(Q_e/Q_o)$ of at least +30 to +40 dB or -30 to -40 dB are required. For example, for $\chi = \{0, 10, 20, 30\}$ dB, the on-resonance residual loss in the through-port is respectively $\{100, 33, 4, 0.4\}$%. This implies that either the input coupling coefficient must change by 3–4 orders of magnitude between a full on state and a full off state, or the loss must be varied by 3–4 orders of magnitude. Such switching contrasts can be challenging to achieve in practice, particularly in sensitive SC photonic circuits.

An improved approach is to include a variable input coupling as well as a variable loss mechanism, and to split the switching contrast between them. For the on-state the external coupling r_e sets the bandwidth and the loss r_o is set to

a minimum value; in the off-state the external coupling is reduced towards zero as much as possible, and the intracavity loss is increased. In this regime of operation, high-fidelity switching is obtained with a switching contrast of 20 dB or better in each parameter. Such switching contrasts are on the order of the contrasts achievable experimentally in typical broadband optical switches without feedback control [176, 177] (for high-extinction-ratio optical switches typically require a cascade of stages [178], particularly in high index contrast [177]). Therefore the combination of variable input coupling and loss mechanisms provides more tolerant designs that can achieve high switching contrasts with simple, experimentally viable optical structures.

The second relevant piece of information we consider in the CMT model is switching of the phase response of $s_{11}(\omega)$,

$$\phi_{11}(\delta\omega) \equiv \angle s_{11}(\delta\omega) = \tan^{-1}\left(\frac{j\delta\omega}{r_o - r_e}\right) - \tan^{-1}\left(\frac{j\delta\omega}{r_o + r_e}\right)$$

The phase response gives a group delay response $\tau_g \equiv -\partial\phi_{11}/\partial\omega$, which on-resonance and normalized to the input coupling decay time τ_e is

$$\left.\frac{\tau_g}{\tau_e}\right|_{\delta\omega=0} = -\frac{2\tau_e}{\left(\frac{\tau_e}{\tau_o}\right)^2 - 1} = -\frac{2\tau_e}{\left(\frac{Q_e}{Q_o}\right)^2 - 1}$$

and is shown in Fig. 9.3(b). At large Q contrasts ($Q_e/Q_o \ll 1$ or $\gg 1$), the group delay is directly related to the external coupling on the left side of the plot (over-coupled regime), whereas it is reduced to a zero fraction of the input coupling on the right (under-coupled regime). Since group delay is a direct measure of the sensitivity of the amplitude transmission to absorption loss introduced into the system, and since it does not forbid dispersion, the over-coupled (all-pass filter) regime is undesirable, and the ideal operating point is the undercoupled, right-hand-side half of the plots.

As a related side-note, that the group delay on-resonance is negative for $Q_e/Q_o > 1$ should not be cause for concern over causality. This is because the group delay-bandwidth product is fixed at zero in the reflection-mode under-coupled regime, so the average group delay is no less than zero. Furthermore, the transmission is less than unity at those frequencies at which group delay is negative (larger loss at larger negative group delays). Group delay is a direct measure of sensitivity to internal loss. Therefore, the negative group delay in reflection can be interpreted as a statement about impedance matching – it says that transmission (into the reflection response) *increases* when loss is introduced into the cavity [Fig. 9.3(b)]. While this may appear counter to intuition at first, it is simply a statement that loss turns off the resonance (by Q spoiling) and therefore the reflection-response loses the resonant dip. At critical coupling, transmission is zero; if loss is changed to either higher or lower values, the transmission increases.

So negative group delay is related to impedance mismatch in the undercoupled regime.

A final useful matter to note is that the group delay-bandwidth (GB) product in reflection (per system pole) is dependent on whether the system has minimum or maximum phase zeros. Typically, the GB product is represented as a fixed function of the resonator order [179–181]. But in general, in the reflection response it depends on the number of maximum-phase zeros. In the case of a single pole-zero pair system,

$$\begin{aligned}\mathbb{I}_{\mathrm{gb}} &\equiv \int_{-\infty}^{+\infty} \tau_g(\delta\omega)\,\mathrm{d}\delta\omega = -\phi_{11}\Big|_{\delta\omega\to+\infty} + \phi_{11}\Big|_{\delta\omega\to-\infty} \\ &= \begin{cases} 0, & \text{for } r_o > r_e \text{ (undercoupled)} \\ 2\pi, & \text{for } r_o < r_e \text{ (overcoupled)} \end{cases}\end{aligned}$$

In Fig. 9.1(c), this can be understood by following the phasors of a pole and zero as the real frequency axis is tracked. A lower-half-plane (maximum phase) zero adds to the phase of the pole, while an upper-half-plane (minimum phase) zero subtracts from it. For linear phase zeros (at the critical coupling condition, $r_e = r_o$), the product above is undefined but this is of no importance because the critical coupling condition never represents an off state, which is of interest here.

In a higher-order resonator, the group delay-bandwidth product is $\mathbb{I}_{\mathrm{gb}} = 2\pi m$ where m is the number of maximum-phase (lower half-plane) zeros. In a cavity with a finite FSR, the GB product is therefore 2π per cavity, per FSR, for each maximum-phase zero.

Although optical filters, including hitless-tunable ones, typically need to switch both the through-port response and drop-port response, the focus in this chapter is on switching the through-port, which is more difficult to achieve. Fig. 9.3(a) shows that, if the internal loss rate r_o is all representative of a coupled drop port, the drop port amplitude is suppressed to less than -30 dB in the off state for $Q_e/Q_o \gg 35$ dB, and the phase response is not relevant. Switching of the drop port(s) is not of fundamental concern, however, because only resonant wavelengths pass to the drop port and all need to be switched off. Therefore cascading broadband optical switches with each drop port can in principle provide arbitrarily large signal suppression. In practice, it is still of advantage to find designs that support strong suppression of drop-port amplitudes without added components for lower device complexity – therefore this subject is briefly revisited in Sec. 9.4 in relation to higher-order filters switchable to a fully transparent state.

9.1.1 Robust resonance suppression to a minimum-phase state

The approach to switching to full transparency described is intrinsically robust with respect to non-idealities. The requirement of a large Q_e/Q_o, i.e. r_o/r_e, contrast for effective pole-zero cancellation can be interpreted physically to reach

this conclusion. Referring to Fig. 9.3(c), the displacement between the pole and zero is $2r_e$ so $r_e \to 0$ is desirable. In practice there will be a residual coupling, δr_e, and imperfect pole-zero cancellation. Then, we note that both the amplitude and dispersive response of the pole-zero pair is "observed" from the real-frequency axis. Therefore, for a given parasitic displacement δr_e between the pole and zero in the off state, the effect on the spectral response is smallest when r_o is made large, $r_o \gg \delta r_e$, so that from the vantage point of the real-ω axis, the pole and zero "look overlapped".

A channel-dropping amplitude filter is obtained for $r_e = r_o$ [38, 55, 67], where its 3 dB bandwidth $\delta\omega_{3\text{dB}}$ is determined by the overall decay rate $r_{\text{total}} \equiv r_e + r_o$ as $\delta\omega_{3\text{dB}} = 2r_{\text{total}}$. Since the device will be used with signals of this order of bandwidth, switching to off states will need to keep dispersion below levels relevant for such signal rates. This means increasing r_o above its nominal on-state value, while decreasing r_e below its nominal on-state value, in addition to reaching the required r_o/r_e ratio.

In the context of this design philosophy, two previous approaches can be commented. First, a MEMS-based design that mechanically displaces both the input and the drop-port waveguide from a resonator [97] leads to $r_e \to 0$ and $r_o \to r_{\text{internal}}$ since the output port is also decoupled, r_{interal} being the remaining internal cavity loss. If $r_{\text{internal}} \ll r_o$, which is normally the case with low-loss filters, then the r_o/r_e contrast may not be sufficiently large. The pole and zero are both located near the real-frequency axis, relative to the on-state pole $\delta\omega_p = \omega_o + j(r_o + r_e)$, making the spectral response sensitive to small errors δr_e in the switch off state. In practice, it can be challenging to turn off an optical variable-coupler-based switch (e.g. an MZI-based one) by more than on the order of 20 dB – i.e. switching off to a residual signal lower than 1%. However, in the MEMS-actuated case where the coupling gap is varied, the coupling strength varies exponentially with the gap so such ratios could be achieved with sufficient motion. The downside of MEMS devices is their fabrication complexity. A planar approach with relatively few material layers is preferable. In planar approaches involving interferometric switches the discussed sensitivity is more problematic. On the other hand, a switching approach based on variable intracavity loss [173] leaves a residual loss in the reflection (through-port) response when finite-FSR, small finesse cavities are used such as Fabry-Perot and microring-resonators. Finesses of 30 and lower have substantial single-pass loss.

9.2 Broadband and wavelength dependent variable couplers

In this section, physical implementations for variable input coupling in traveling-wave and standing-wave resonators are proposed. They all rely on the use of phase shifts to make the incident mode field distribution in the access port either

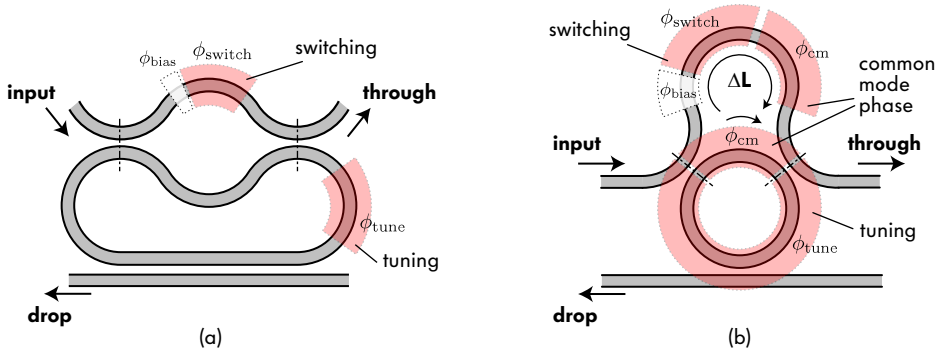

Figure 9.4: Hitless single-ring filter concept, switchable to complete transparency (amplitude and phase disabling) by varying input coupling to undercoupled state: (a) Ideal, broadband variable input coupler; (b) unbalanced (wavelength dependent) MZ coupler may be required to work with a high-Q, circular ring cavity. In the latter case, if several resonances (spaced by the FSR) are to be switched, then the MZ FSR and ring FSR are related.

maximally overlapped or orthogonal to the resonant mode field in the cavity. In the traveling-wave (ring-resonator) case, a simpler way to view the variable coupling is as an interferometric (e.g. MZ based) directional coupler.

9.2.1 Variable excitation of traveling-wave cavity modes

Fig. 9.4 shows variants of a single-cavity, traveling-wave add-drop filter with a variable input coupler. The MZ input coupler, comprising two identical directional couplers with power coupling κ and a differential phase $\Delta\phi$, can be replaced by an effective abstract directional coupler with a point transfer matrix [see Fig. 2.7(c)]

$$\overline{\overline{\mathbf{T}}} = e^{i\frac{\Delta\phi}{2}} \left[\begin{array}{c|c} t'_{11} & t'_{12} \\ \hline t'^{*}_{12} & t'^{*}_{11} \end{array}\right] \tag{9.1}$$

where

$$t'_{11} \equiv (1-2\kappa)\cos\frac{\Delta\phi}{2} + i\sin\frac{\Delta\phi}{2} \tag{9.2}$$

$$t'_{12} \equiv i2\sqrt{\kappa(1-\kappa)}\cos\frac{\Delta\phi}{2} \tag{9.3}$$

$$\Delta\phi \equiv \phi - \theta = \beta\Delta L = \Delta\phi_o + \frac{\Delta L}{v_g}\delta\omega. \tag{9.4}$$

Here, $\Delta\phi_o$ represents a substantially broadband phase shift, while $v_g/\Delta L \equiv \Delta f_{\mathrm{FSR,MZ}}$ is the FSR in Hertz and represents the slope of a frequency dependent phase shift. Since a traveling-wave cavity has multiple longitudinal resonances spaced by the FSR, the ideal configuration for an interferometric coupling would be Fig. 9.4(a) where $\Delta L = 0$ and the effective input coupling ratio is frequency-independent. This means that the response is the same for all longitudinal resonances (or all within the frequency range within which this assumption holds), and

they can be simultaneously disabled by taking the broadband differential phase shift $\Delta\phi_o = \phi_{\text{switch}} + \phi_{\text{bias}}$ to π.

Since the MZ coupler contains part of the resonant cavity, a $\Delta L = 0$ design has the disadvantage of requiring a non-circular cavity. This is because, in practice, the MZ interferometer arms will require some physical spacing to accommodate a physical phase shifting mechanism in one arm, such as a thermo-optic phase shifter, or biasing or carrier-injecting electrodes. On the other hand, a circular ring resonator can be shown to have the lowest bending loss (highest Q) for a given waveguide cross-section design and traveling-wave cavity round-trip length. To use a circular microring resonator, the input coupler needs to make use of an unbalanced MZ coupler [Fig. 9.4(b)]. In this case, the input coupling coefficient is wavelength dependent. When a broadband phase shifter ϕ_{switch} is actuated, the sinusoidal spectral response of the MZ coupler shifts in wavelength, thereby modulating the effective coupling ratio at each wavelength.

If we assume that the MZ and ring have waveguides of identical group index for the guided mode at all points, then for $\Delta L = 2\pi R m$, m non-negative (real or integer), the MZ has an FSR related to the ring resonator FSR as

$$\Delta f_{\text{FSR,MZ}} = \frac{\Delta f_{\text{FSR,ring}}}{m}$$

For $m = 0$, the MZ FSR is infinite and the broadband case [Fig. 9.4(a)] is obtained. For m integer, the coupling spectrum is co-periodic with the ring resonance condition so that all resonances have the same behavior. This is relevant for switching all longitudinal orders to a fully transparent state (in a wavelength range of interest). Finally for $m = 1/2$, the FSR of the MZ is twice the FSR of the ring resonator. Then, every second ring resonance has zero input coupling and is switched to a fully transparent off state, while the remaining resonances have maximum coupled power ($\sim 4\kappa$) as determined by the MZ and can form filtering passbands. This allows a compact and efficient approach to the effective doubling of the FSR of a resonant filter (an alternative to the designs presented in Sec. 8.2.2).

9.2.2 Variable excitation of standing-wave cavity modes

Analogous implementations of variable input couplings can be devised for standing-wave cavity modes (Fig. 9.5). We will consider N-port standing-wave-resonator circuits where each port is a waveguide terminated by a perfect reflector in the absence of coupling to cavities. Then, the through-port response at each access port is in reflection, and when no resonant cavity is excited all signal is reflected. This also means that a standing-wave pattern is established in the waveguide near the terminating end-mirror. When resonances are excited, resonant tunneling from an access port to a second port gives the drop-port response.

Here the strategy for variable input coupling is as follows. The input waveguide is coupled to a cavity mode, and its standing-wave field pattern is coupled to the

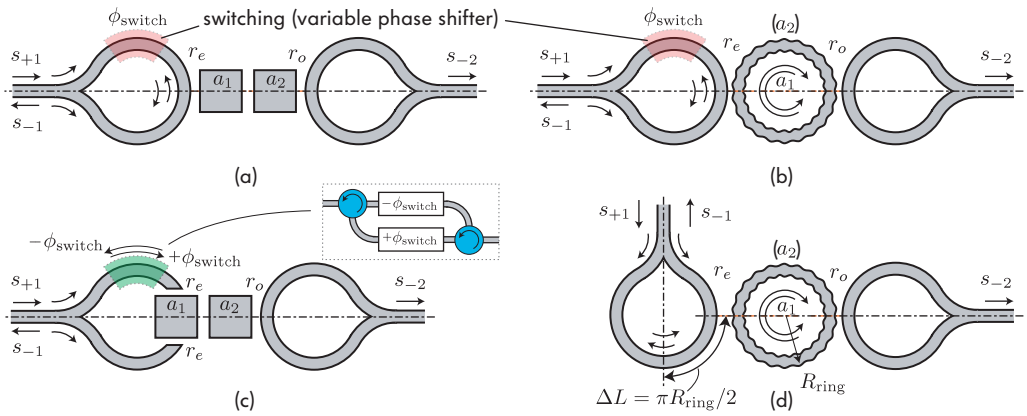

Figure 9.5: Illustration of some proposed hitless switching and FSR doubling approaches for standing-wave-cavity systems. Switching of the excitation is based on mode-symmetry (mis)matching of the resonator mode and waveguide/port mode. A loop-mirror is an efficient realization of a waveguide termination for a standing-wave resonator access port, as shown in examples for (a) hitless switching of generic standing-wave resonators, and (b) of standing-wave excitations of ring resonators; in order to permit switching, the degenerate ring modes need to be detuned, as done here by a weak corrugation with the same periodicity as the mode of interest – one period per wavelength. (c) An alternative excitation may use a pair of reflective excitation waveguides that may be configured with a phase shifter to excite the resonant mode in or out of phase. However, for proper (lossless) operation the phase shifter in this variant must be non-reciprocal and produce the opposite phase shift in reflection. Hence this is included only as a conceptual example. (d) A configuration for FSR doubling of a standing-wave ring-resonator – the length of the loop-mirror arc is related to the ring radius to suppress the adjacent resonance.

standing-wave field pattern of the cavity mode. The overlap of the field patterns with the dielectric distribution gives the coupling coefficient (see, e.g., [78],[46, App. B]). Now, the idea is that in the on state, the input waveguide field pattern should have a large overlap with the cavity field pattern, while in the off state, a phase shift should be introduced so that the waveguide standing-wave field pattern is orthogonal to the cavity-mode field pattern.

A particularly straightforward and practical implementation of a reflecting waveguide is a loop mirror [shown as part of Figs. 9.5(a,b)]. It consists of a broadband 3 dB Y-splitter the outputs of which are joined. Such waveguide terminations are realizable in strongly confined, high-index-contrast (e.g. Si or SiN) waveguides in compact form, as minimum bend radii with low bending loss in Si waveguides can be as small as 2-3 μm. For switching, the waveguide loop mirror has a controllable phase shifter, ϕ_{switch}.

For a broadband variable coupling, the cavity is aligned symmetrically to the center of the loop mirror as shown in Figs. 9.5(a,b). We consider the loop to be of length L, and assign a position variable x to parameterize distance along the loop, with $x = 0$ at the center of the loop, and $x = \mp L/2$ as the reference planes for the top and bottom Y-junction outputs (at the junction). Disregarding

the cavity, if the incident waveguide mode to the loop mirror has amplitude s_{+1} at the junction $x = \mp L/2$, so that total incident power is $|s_{+1}|^2$, then the waveguide mode amplitude distribution in the loop mirror is

$$\begin{aligned} f(x) &= \frac{s_{+1}}{\sqrt{2}} e^{-j\beta(x+\frac{L}{2})} e^{-j\phi_{\text{switch}}} + \frac{s_{+1}}{\sqrt{2}} e^{+j\beta(x-\frac{L}{2})} e^{+j\phi_{\text{switch}}} \\ &= s_{+1}\sqrt{2} e^{-j(\beta L + \phi_{\text{switch}}/2)} \left[\cos\left(\beta x + \frac{\phi_{\text{switch}}}{2}\right)\right]. \end{aligned} \tag{9.5}$$

For $\phi_{\text{switch}} = 0$, the waveguide mode forms a symmetric standing-wave pattern about $x = 0$. If the cavity mode [with energy amplitude a_1 in Fig. 9.5(a,b)] is also symmetric about $x = 0$, then the input coupling coefficient is maximized and the resonant filter is on. Setting $\phi_{\text{switch}} = \pi$ changes the access waveguide pattern to antisymmetric about $x = 0$ and orthogonal to the cavity mode field pattern, thereby making the input coupling coefficient zero and taking the device into the off state.

If the cavity mode a_1 is instead antisymmetric about $x = 0$, the reverse behavior will be seen with $\phi_{\text{switch}} = 0$ giving the off state and $\phi_{\text{switch}} = \pi$ giving the on state. More generally, the cavity mode need not have any particular symmetry. So long as the resonator is reciprocal[‖] and a single resonance is considered, there will be a ϕ_{switch} state for which the overlap integral with the cavity mode is zero, and can therefore disable the resonance.

Fig. 9.5(a) shows a schematic representation of a second-order channel dropping filter using standing-wave cavities (abstract representations are used, which could be for example square pillbox resonators [14, 16] or photonic crystal cavities.

In Fig. 9.5(b), a standing-wave-cavity filter is built from a corrugated microring resonator. Reciprocal microring resonators have two degenerate modes at a resonant frequency, which can be seen as two traveling-wave modes propagating in opposite directions or as a symmetric and antisymmetric standing-wave mode with respect to an axis of symmetry, e.g. the horizontal symmetry axis in the figure. Switching the symmetry of excitation in the input waveguide loop mirror would then simply switch between one and the other microring resonance. In order to permit switching off the resonant system, one of the two resonant modes must be either quenched by reducing the Q considerably or detuned to another frequency. In this example, a weak corrugation with a periodicity equal to a guided wavelength in the ring (i.e. number of wiggles in the corrugation equal to the number of wavelengths around the resonator – the resonance order) is used to split the resonant frequencies of the two modes. Because there is interaction with the corrugation along the entire circumference of the microring, a substantial

[‖] A non-reciprocal (magneto-optic) ring resonator can have a single traveling-wave resonance that is not degenerate with another counter-propagating one. In that case no choice of ϕ_{switch} will turn off the resonance and a more complex input coupler would be needed in general.

splitting should be achievable with very small perturbation, and therefore without substantially coupling to radiation modes or lowering the radiation Q.

Fig. 9.5(c) shows an alternative conceptual implementation of a variable input coupling, which is in practice unattractive because it requires a non-reciprocal phase shifter. In this case each waveguide is perfectly reflecting. In order to ensure that all signal entering as s_{+1} exits in the waveguide after constructive interference as s_{-1}, the phase shift imposed upon incidence needs to be undone after reflection, so that the phase shifter needs to apply a phase delay ϕ_{switch} in one direction and $-\phi_{\text{switch}}$ in the other. This requires a magnetooptic material to realize, which is unnecessary because reciprocal implementations exist such as the loop-mirror approach.

A final example, shown in Fig. 9.5(d), illustrates how a wavelength dependent variable input coupling can be achieved. This can be used to suppress an adjacent resonance, for example for FSR doubling. If the cavity mode is coupled off center to the waveguide loop mirror, then the standing-wave-mode pattern will compress with increasing wavelength, and will slide along the waveguide everywhere except at the center point. To suppress resonances on each side of a resonant mode that are $\Delta\omega$ away, a coupling point (displaced from the center by ΔL) must be chosen on the loop mirror at which a frequency detuning of $\Delta\omega$ leads to a 90° phase shift of the standing-wave pattern. In eqn. (9.5), $x \to x - \Delta L$, so that the required condition for FSR doubling ($\Delta f_{\text{FSR,LM}} = 2\Delta f_{\text{FSR,ring}}$) is

$$\beta\Delta L\Big|_{\omega_o} - \beta\Delta L\Big|_{\omega_o+\delta\omega} = \pm\pi/2$$
$$\frac{\Delta L}{v_g}\delta\omega = \pm\pi/2.$$

To change from full to null coupling across one ring FSR, $\Delta f_{\text{FSR,ring}} \equiv v_g/(2\pi R_{\text{ring}})$, $\delta\omega \to 2\pi\Delta f_{\text{FSR,ring}}$ and the length offset needs to be

$$\Delta L = \frac{\pi R_{\text{ring}}}{2}.$$

Note that in the case of microring resonators being used – even corrugated ones – the present scheme provides the general approach but may not be sufficient by itself to build an FSR doubler for standing-wave resonators with a somewhat ordered resonance spectrum. This is because the detuned resonances of one and the other symmetry will both be located somewhere in the FSR of the corrugated ring, for example. Therefore, to avoid addressing one of the two resonances, it is preferable to provide a symmetry-selective loss mechanism, such as a decay waveguide that only couples to one of the two standing-wave ring modes (a single-mode waveguide radially oriented and evanescently coupled at its end, for example).

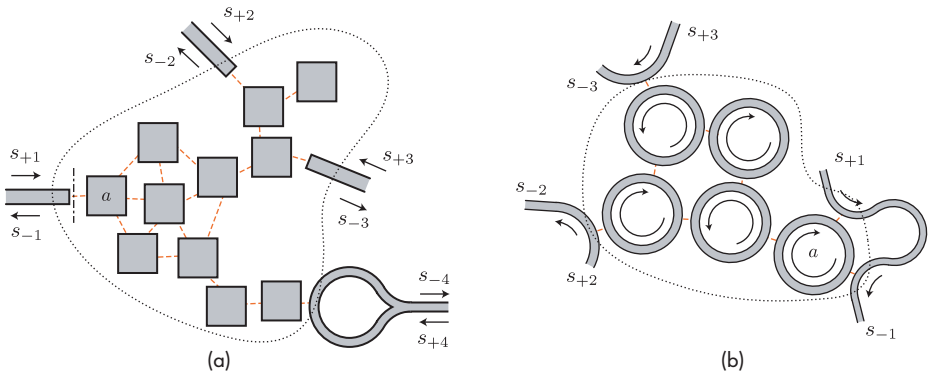

Figure 9.6: Illustration of generic hitless resonant systems of arbitrary order, switchable to complete transparency (amplitude and phase disabling), based on (a) standing-wave cavities (hitless at port 4), (b) traveling-wave (microring) cavities (hitless at port 1).

9.2.3 Transparent switching of high order multiport resonators

Fully transparent switching in a higher-order resonator is illustrated in Fig. 9.6 for standing-wave and reflectionless, traveling-wave variants. Those ports in which switching to a fully transparent off state in reflection is required need to use a loop-mirror or interferometric coupling. In the off state, furthermore variable loss mechanisms need to be introduced that substantially broaden the linewidth of *all* supermodes of the system near the wavelength of interest. Coupled drop ports may be sufficient, or artificial loss mechanisms may be turned on, as discussed in forthcoming sections.

9.3 Single-pole transparently hitless tunable add-drop filter

In this section, a proposed design and experimental demonstration is described of a hitless tunable channel add-drop filter based on switching a tunable filter to a fully transparent off state. This is the first demonstration of the complete disabling of both the amplitude and phase response of a resonant filter. The concept demonstration employs a single ring resonator, and extension to higher-order designs necessary to meet telecom-grade filtering specifications is described in the following section.

For the first-order case of interest here, first, the concept design and simulated switching characteristics are described. Then the experimental realization is shown, including a brief discussion of heater topology, thermal design and fabrication, and the optical performance results that demonstrate fully transparent switching.

9.3.1 Concept and design

A concrete geometry for a single-cavity hitless tunable add-drop filter is shown in Fig. 9.7(a). In this design, we will set the FSR of the MZ variable coupler to

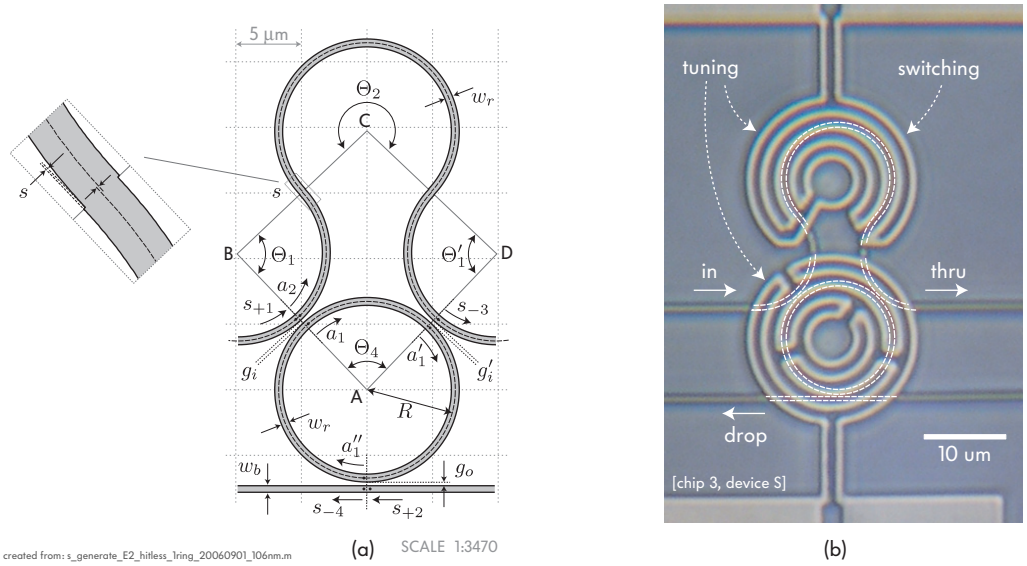

Figure 9.7: Device concept geometry and experimental demonstration of single-ring hitless filter switching to full transparency: (a,b) electromagnetic ports, state variables and parameters, and physical design layout and dimensions; (c) optical micrograph of fabricated silicon single-ring transparent-hitless filter showing silicon waveguides on a lower layer, and titanium microheaters on an upper layer.

be equal to the FSR of the ring resonator. This means that the variable coupling will have the same spectral periodicity as the ring resonances. As a result all resonances are simultaneously disabled (in the wavelength range within which the design approximations hold). To achieve this, the MZ has an arm length difference equal to the ring circumference if all waveguides have the same guided group index. Such an MZ coupler accommodates a circular (high Q) ring resonator, and also provides sufficient physical displacement between the outer MZ arm and the ring to avoid thermal crosstalk between thermally actuated MZ switching and ring cavity tuning – where each is actuated by a separate microheater.

Geometry

The physical geometry of the MZ coupler can be rigorously fixed by choosing to use circular waveguide arcs of identical radii and cross-sections to form the coupler. This provides symmetry in design as the group and effective mode indices are matched, so the FSR matching in the spectral response will be primarily determined by geometry and will be first-order insensitive to waveguide cross-section.

The MZ geometry is fully determined by the arc/ring central radius R, four angles Θ_1, Θ_2, Θ_1' and Θ_4, input coupling gaps g_i and g_i', and bend-to-bend offsets s. The points A, B, C and D in Fig. 9.7(a) are the centers of the arcs and ring structure. The geometry is derived from the optical properties which in addition need to take into account the waveguide propagation constant and group index.

Since circular arcs are used, we will use an angular propagation constant γ such that the mode propagates around the azimuthal angle Θ as $e^{-j\gamma(\omega)\Theta}$.

We will assume the two coupler gaps to be equal ($g_i = g_i'$), leading to equal coupling coefficients. This is the desirable situation for any lossless, balanced or unbalanced MZ to have a spectral response to at least one port (the cross port) with periodic nulls**. In the case of larger loss in propagation or scattering at bend-to-bend junctions in the longer MZ arm, the MZ with two equal couplers will not provide an overall input-coupler response with periodic nulls. The second coupler may then in principle be made stronger (smaller gap) in order to return the overall input coupler to a response with periodic nulls. Because the lengths differences are so short (on the order of a ring circumference which may be on the order of 50 µm), even as high as a 10 dB/cm propagation loss translates only to on the order of 1% loss. Therefore, here the differential loss is assumed negligible, and equal couplers are used. Furthermore, since the two input coupler gaps are equal and the radii are all the same, then $\Theta_1' = \Theta_1$ here.

Furthermore, it is well known that tight waveguide bends push the energy in the guided mode to larger radii toward the outer waveguide wall. This mode shift means that junctions of bent waveguides with opposite bend orientations require a lateral offset to maximize the overlap integral of the modes, and thereby optimally match (with minimum loss) coupling from one bend to the next. Even at the offset with optimum match, transmission is not 100% because the mode shapes of a left and right turning waveguide bend with tight radii differ. In principle, the MZ arm consisting of the three arcs Θ_1, Θ_4 and Θ_1' should be designed as a curved waveguide with smoothly varying curvature, so that the mode shape continuously evolves along the bend. In this case the group index matching with the ring is lost since radii are not equal everywhere, and the benefit was not deemed large enough to use this approach in this design.

The dimensions of the MZ variable coupler will depend on the desired arm length difference, which we will express in terms of the number of guided wavelengths, n_λ. The geometrical and optical parameters of the MZ coupler are then related by three relationships: first, the required difference in propagation lengths; second, the relationship of Θ_1, Θ_2 and Θ_4 whose vertices form a triangle; and third, the sine rule relating the angles and edge lengths of the triangle:

$$\begin{aligned} \gamma(2\Theta_1 + \Theta_2 - \Theta_4) &= \Delta\phi_{\text{desired}} = 2\pi n_\lambda \\ \Theta_1 + \frac{2\pi - \Theta_2}{2} + \frac{\Theta_4}{2} &= \pi \\ \frac{\sin\left(\frac{2\pi-\Theta_2}{2}\right)}{2R + \bar{g}_i} &= \frac{\sin\left(\frac{\Theta_4}{2}\right)}{2R + s} \end{aligned}$$

**For example, this can be seen by the UBI rule (see Chap. 8) which shows no cross-state coupling (to the ring) at those wavelengths at which the MZ arms have a π differential phase shift.

where, for waveguide width w,

$$\bar{g}_i \equiv w/2 + g_i + w/2$$

is the center-to-center waveguide spacing. From these three equations the angles can be derived if R, s, $\bar{g}_i$, γ and the desired arm length difference n_λ are known. The geometry angles are given by

$$\Theta_1 = \frac{\Delta\phi_{\text{desired}}}{4\gamma} = \frac{\pi n_\lambda}{\gamma} \tag{9.6}$$

$$\Theta_4 = 2\cot^{-1}\left[\frac{\frac{2R+\bar{g}_i}{2R+s} - \cos\Theta_1}{\sin\Theta_1}\right] \tag{9.7}$$

$$\Theta_2 = \frac{\Delta\phi_{\text{desired}}}{2\gamma} - \Theta_4. \tag{9.8}$$

The given form of solution is valid when $(2R + \bar{g}_i)/(2R + s) > 1$, which generally holds for all designs of interest because the junction offset s will be smaller than a waveguide width, w, while the coupler waveguide spacing $\bar{g}_i$ will always exceed w (for a gap $g_i > 0$). Once the angles are known all other dimensions, such as positions of the centers of all waveguide arcs, can be straightforwardly computed.

For simultaneous hitless switching of all longitudinal resonances, the FSR of the MZ should be infinite, equal to the FSR of the ring, or an integer fraction of it. Therefore, $n_\lambda = m\gamma$, for m non-negative integer. For $m = 0$ [illustrated in Fig. 9.4(a)], the present geometry has no solution because the ring is assumed circular. In this design, $m = 1$, so $n_\lambda = \gamma$ and $\Theta_1 = \pi/2 = 90^\circ$.

State-variable propagation matrix model

A state-variable propagation matrix model can be used to both analyze the basic properties and to simulate the expected response of the designed device (using parameters obtained from FDTD simulations). It is assumed that backreflections can be neglected and therefore a reflectionless 4-port model is used (Chap. 2). Fig. 9.7(a) shows the electromagnetic input and output port variables (s_{+1}, s_{+2}, s_{-1}, s_{-2}) and internal state variables (a_1, a_1', a_1'', a_2); the waveguide directional-coupler coupling matrices $\overline{\overline{\mathbf{Q}}}_i$, $\overline{\overline{\mathbf{Q}}}_i'$ and $\overline{\overline{\mathbf{Q}}}_o$; and the physical parameters sufficient to describe the geometry – the angles Θ_i, $i \in \{1, 2, 1', 4\}$. Dots show the reference planes for the port and state variables, with collocated input and output ports at each coupler.

The system response is described by the state-variable equations

$$\vec{a} = \overline{\overline{\mathbf{M}}} \cdot \overline{\overline{\mathbf{P}}} \cdot \vec{a} + \overline{\overline{\mathbf{K}}}_i \cdot \vec{s}_+$$

$$\vec{s}_- = \overline{\overline{\mathbf{K}}}_o \cdot \overline{\overline{\mathbf{P}}} \cdot \vec{a} + \overline{\overline{\mathbf{R}}} \cdot \vec{s}_+$$

where

$$\vec{a} \equiv \begin{pmatrix} a_1 \\ a_1' \\ a_1'' \\ a_2 \end{pmatrix}, \vec{s}_+ \equiv \begin{pmatrix} s_{+1} \\ s_{+2} \end{pmatrix}, \vec{s}_- \equiv \begin{pmatrix} s_{-1} \\ s_{-2} \end{pmatrix}.$$

Here, $\vec{a}$, $\vec{s}_+$ and $\vec{s}_-$ are mode amplitudes normalized so that the square magnitude of each component is the guided power at the given reference plane.

All internal state variables, $\vec{a}$, are defined at reference planes at the beginning of a propagation region, i.e. at the output of a coupler (scatterer). Matrix $\overline{\overline{\mathbf{P}}}$ represents propagation for all these internal-state-variable mode amplitudes to propagate them to the reference planes at the input of the next scattering region:

$$\overline{\overline{\mathbf{P}}} = \begin{bmatrix} e^{-j\gamma\Theta_4} & & & \\ & e^{-j\gamma(\pi-\Theta_4/2)} & & \\ & & e^{-j\gamma(\pi-\Theta_4/2)} & \\ & & & c_{\text{jctn}}^2 e^{-j\gamma(\Theta_1+\Theta_2+\Theta_1')} \end{bmatrix}$$

where $\gamma(\omega)$ is the angular propagation constant of the guided mode in the circular waveguide at radius R, and c_{jctn} is the transmission amplitude (including amplitude and any phase shift) across each bend-to-bend junction in the long MZ arm.

Matrices $\overline{\overline{\mathbf{M}}}$, $\overline{\overline{\mathbf{K}}}_i$, $\overline{\overline{\mathbf{K}}}_o$ and $\overline{\overline{\mathbf{R}}}$ represent scattering coefficients between the various ports and internal state-variable modes. Therefore all directional couplers are represented in these matrices. Each directional coupler can be modeled by the general lossless or general lossy reflectionless 4-port representations in Figs. 2.7, 2.6, 2.10. The elements of their 2×2 T-matrices are contained in these larger matrices.

The total coupling matrix $\overline{\overline{\mathbf{H}}}$ for this structure is:

$$\overline{\overline{\mathbf{H}}} \equiv \left[\begin{array}{c|c} \overline{\overline{\mathbf{M}}} & \overline{\overline{\mathbf{K}}}_i \\ \hline \overline{\overline{\mathbf{K}}}_o & \overline{\overline{\mathbf{R}}} \end{array}\right] = \left[\begin{array}{cccc|cc} 0 & 0 & q_{i,11} & 0 & q_{i,12} & 0 \\ q_{i,11}' & 0 & 0 & q_{i,12}' & 0 & 0 \\ 0 & q_{o,11} & 0 & 0 & 0 & q_{o,12} \\ 0 & 0 & q_{i,21} & 0 & q_{i,22} & 0 \\ \hline q_{i,21}' & 0 & 0 & q_{i,22}' & 0 & 0 \\ 0 & q_{o,21} & 0 & 0 & 0 & q_{o,22} \end{array}\right].$$

Here, the input couplers have a geometrical $\mathcal{H}$-symmetry (Fig. 2.5) so, for example, the top-left coupler in Fig. 9.7(a) has matrix $\overline{\overline{\mathbf{Q}}}_i$

$$\overline{\overline{\mathbf{Q}}}_i \equiv \begin{bmatrix} q_{i,11} & q_{i,12} \\ q_{i,21} & q_{i,22} \end{bmatrix} = e^{i\theta_o} \begin{bmatrix} \sqrt{1-\kappa_i - l_{i,rr}} & i\sqrt{\kappa_i} \\ i\sqrt{\kappa_i} & \sqrt{1-\kappa_i - l_{i,rr}} \end{bmatrix}$$

where κ_i is the cross-state coupled power fraction, $l_{i,rr}$ is the fractional total power loss when the coupler is excited from either input, and θ_o is the coupling-induced

phase shift (CIPS) from each side (see Sec. 4.1). The output coupler only has a geometrical $\mathcal{V}$-symmetry, so its matrix $\overline{\overline{\mathbf{Q}}}_o$ has the form

$$\overline{\overline{\mathbf{Q}}}_o \equiv \begin{bmatrix} q_{o,11} & q_{o,12} \\ q_{o,21} & q_{o,22} \end{bmatrix} = e^{i\theta_o} \begin{bmatrix} \sqrt{1-\kappa_o-l_{o,bb}}\, e^{i\theta_1} & i\sqrt{\kappa_o} \\ i\sqrt{\kappa_o} & \sqrt{1-\kappa_o-l_{o,rr}}\, e^{-i\theta_1} \end{bmatrix}$$

where κ_o is the cross-state power fraction, $l_{o,rr}$ is the ring-side total coupler loss, and $l_{o,bb}$ is the bus-side total coupler loss. CIPS from the ring and bus sides is $\phi_{11} \equiv \theta_o + \theta_1$ and $\phi_{22} \equiv \theta_o - \theta_1$.

The complete transmission matrix, $\overline{\overline{\mathbf{T}}}$, of the reflectionless 4-port filter is then found from the state variable equations directly as,

$$\overline{\overline{\mathbf{T}}} = \overline{\overline{\mathbf{K}}}_o \cdot \left[\overline{\overline{\mathbf{I}}} - \overline{\overline{\mathbf{M}}} \cdot \overline{\overline{\mathbf{P}}}\right]^{-1} \cdot \overline{\overline{\mathbf{K}}}_i + \overline{\overline{\mathbf{R}}}. \tag{9.9}$$

In an equivalent 2-port, such as Fig. 9.5(a), $\overline{\overline{\mathbf{T}}}$ is instead the scattering matrix.

Theoretical design switching characteristics

For a hitless tunable filter, switchable to a fully transparent state at all resonances, we match the MZ FSR and the ring FSR by letting $\Theta_1 + \Theta_2 + \Theta_1' - \Theta_4 = 2\pi$ (the arm-length difference is one full round-trip of the ring). Since the coupling-induced phase shifts are equal in the two arms in each coupler, they do not need to be accounted in the MZ switching here, but they modify the preceding relation in general. For the theoretical switching curves, we disregard bend-to-bend junction scattering as small, and set $c_{\rm jctn} \to 1$.

Switching is done by changing the propagation constant in the long MZ arm or ring section between the two input couplers, while passband wavelength tuning is done by changing the propagation constant in the ring resonator. To consider switching and tuning more explicitly, the thermooptically induced phase shifts can be disembedded from the propagation constant $\gamma(\omega, T)$ by representing the latter as the sum of a nominal-temperature propagation constant $\gamma_o \equiv \gamma(\omega, T_o)$ and thermooptically-induced phase shifts defined as $\phi \equiv (\gamma - \gamma_o)\Theta$, as illustrated in Fig. 9.4. There, the switching MZ arm phase is broken down into a static bias phase $\phi_{\rm bias}$, and a dynamic switching phase $\phi_{\rm switch}$, one or both of which may be due to the MZ heater [top in Fig. 9.7(b)]. In addition, cavity tuning is done by a tuning phase shift $\phi_{\rm tune}$ in the ring, which does not affect the MZ input coupler. If the ring heater heats the part of the ring that is between the two input couplers (covered by angle Θ_4), then both switching and tuning is actuated, because the MZ arm length differential phase is altered, as well as the round-trip ring-resonator phase. Therefore, if the ring is uniformly heated, to prevent switching an equivalent excess phase shift to that accumulated between the two couplers needs to be effected in the longer MZ arm to common-mode out the offset and avoid switching the

Table 9.1: Electromagnetic parameters of the single-ring hitless filter

FSR	$(d\gamma/df)^{-1}$	2125 GHz
(Total input power coupling)		0.0689
Input coupler cross-state coupling	$\kappa_i (= \kappa_i')$	0.0172
Input coupler loss	l_i	$2.46 \cdot 10^{-4}$
Output coupler cross-state coupling	κ_o	0.0574
Output coupler ring-side loss	$l_{o,rr}$	$1.29 \cdot 10^{-4}$
Resonant order (at λ_o =1550 nm)	γ_o	53
Assumed propagation loss		8 dB/cm (0.0338 dB/r.t.)

MZ response while tuning the ring cavity. This phase is denoted by ϕ_{cm} in the illustration in Fig. 9.4.

The single-ring filter is designed to have a 40-GHz 3 dB bandwidth, of relevance for telecom applications. The electromagnetic parameters – coupling coefficients including coupler loss, expected propagation constant and FSR – are given in Table 9.1. Because this work was the first attempt in our group to realize working devices in silicon waveguides, a conservative 8 dB/cm propagation loss was assumed in the design, based on our best results in SiN[††]. The input couplers were chosen to give a total input power-coupling ratio of 6.9% in the on-state, which is larger than the output coupling in order to put the device into a near-critically coupled state with the loss accounted.

The switching characteristics of the described example device are shown in Fig. 9.8 for six possible states of the ϕ_{switch} phase shifter, including the fully off state and fully on state. Here, ϕ_{bias} is set (by trimming, half-wave longer waveguide length in design, or thermal bias) so that the device is "normally off" (that is, it is off with $\phi_{\mathrm{switch}} = 0$).

Fig. 9.8(a) shows a wide spectral view showing 2 FSRs. The main part of the figure shows the drop- and through-port responses (T_{21} and T_{11} in Eq. 9.9, respectively) of the single-ring filter, and the MZ input power-coupling coefficient vs. wavelength. In the on state *a*, the drop port has nulls at a half-FSR detuning from resonance because the MZ input coupling has a maximum coupling ($\sim 6.9\%$) on resonance, and nulls at half-FSR ($\sim$1 THz) detuning in each direction. By changing the switching phase from $\phi_{\mathrm{switch}} = 0$ to $\phi_{\mathrm{switch}} = \pi$, the detuned nulls of the input coupling coefficient tune into the resonance as the filter goes into the off state *f*. In this case the input coupling is maximum ($\sim 6.9\%$) now at half-way wavelengths

[††]In SiN, waveguide loss was limited by intrinsic material losses of the Si-rich SiN. Bulk crystalline silicon is in principle nearly lossless at 1550 nm, but smaller waveguide cross-sections and higher index contrast contribute to higher loss due to sidewall and surface roughness, so this conservative estimate was taken. Other groups previously demonstrated on the order of 3 dB/cm or better in Si [99, Table 1].

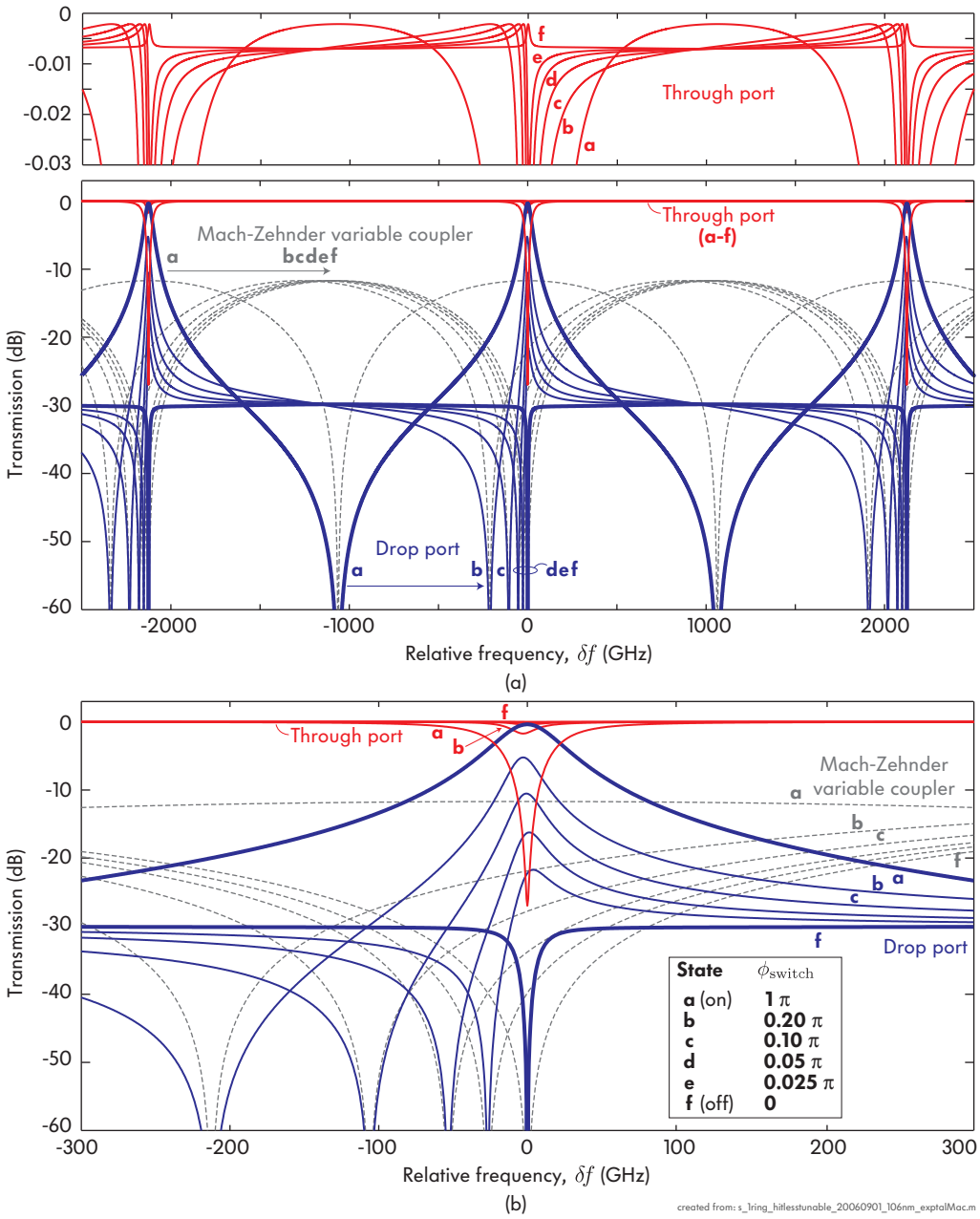

Figure 9.8: Theoretical switching characteristics of silicon single-ring hitless filter design, switchable to full transparency state, based on variable input coupling: (a,b) amplitude switching characteristics of the drop-port and through-port responses, and of the wavelength-dependent, variable input coupling ratio. . . (continues on next page)

between resonances, so the off-state maximum drop-port transmission is the same as that of an equivalent single-ring filter having a broadband coupling coefficient of the maximum coupling ratio here, i.e. the on-state linewidth. The top part of Fig. 9.8(a) shows that off-state (state f) loss in the through port response is less than 0.01 dB far from resonance. Furthermore, this off-state loss is related to the

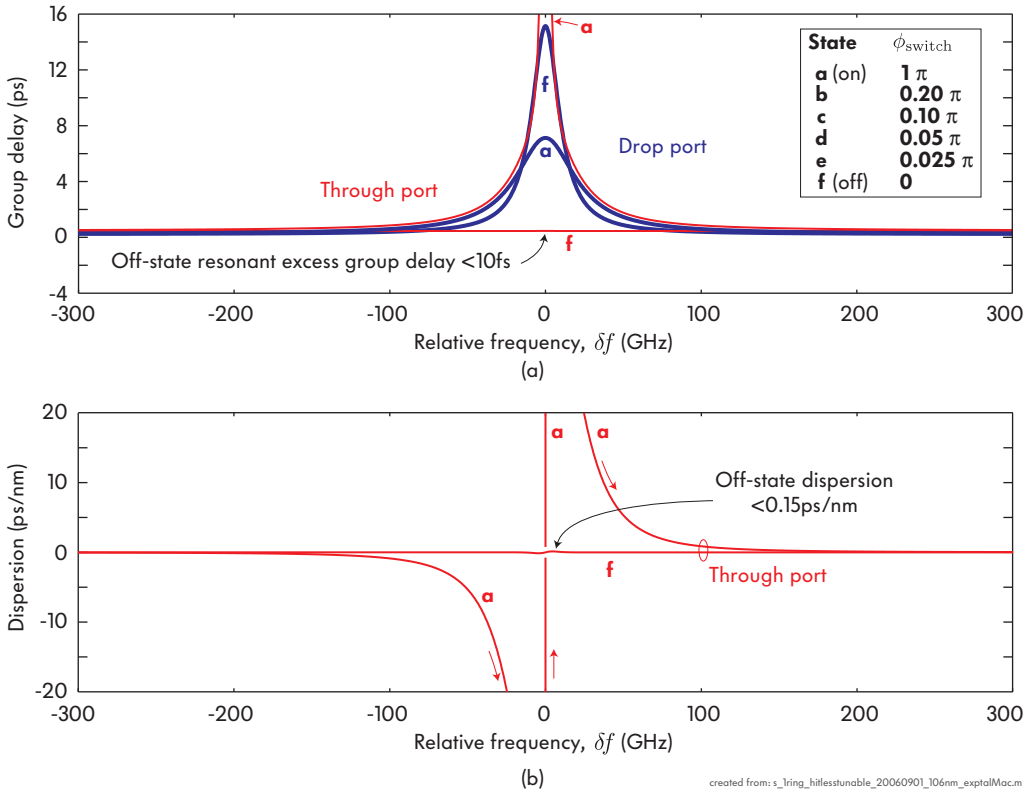

Figure 9.8 (continued) . . . (c) group delay and (d) dispersion spectra of the through port response. All responses are shown for switch states $\phi_{\text{switch}} = \{0, 0.8, 0.9, 0.95, 0.975, 1\}\pi$. The design parameters of this device are given in Table 9.1.

drop-port roll-off at half-FSR detuning, when maximum input coupling is present at that wavelength. Therefore, higher-order filters promise lower off-state loss far from resonance.

Fig. 9.8(b) shows in closer detail the suppression of the resonance from on state *a* to off state *f*. Fig. 9.8(c) shows the on-state and off-state group delay spectral responses in the through and drop ports. For ideal critical coupling, the on state (state *a*) drop- and through-port group delay spectra would be identically equal, because they share a single pole, and the through-port response zero is on the real-frequency axis, contributing no phase response. In this plot they diverge because of a slight mismatch – the through-port response group delay on resonance is sensitive to structure parameters due to the strong amplitude suppression of the signal near resonance. Due to the latter, it is also unimportant. In the off state *f*, the through-port group delay is nearly zero (less than 10 fs) across the wavelength range of interest, when compared to the bandwidth-determined on-state group delay of about 6 ps. The drop-port group delay is not of interest because the drop port is suppressed to less than -30 dB. It has half the linewidth and twice the maximum group delay because the Q has been doubled by turning off the input coupling, while leaving on the output coupling, the two being nearly equal (see

Table 9.2: Physical dimensions of the single-ring hitless filter

Height of all waveguides		106 nm
Ring/arc center radius	R	6.732 µm
Ring/arc waveguide width	w_r	600 nm
Output bus waveguide width	w_b	498 nm
Input coupler gap	$g_i (= g_i')$	306 nm
Output coupler gap	g_o	296 nm
Bend-bend offset	s	30 nm
Geometry angles	$\Theta_1 (= \Theta_1')$	90.0° (89.13°)
[for normally ON (OFF)]	Θ_2	266.4° (265.48°)
	Θ_4	86.4° (87.21°)

Table 9.1).

Fig. 9.8(d) shows the computed dispersion spectrum, showing less than 0.15 fs/nm of worst-case dispersion in the spectrum, in the off state. For telecom-grade filters operating on 10 Gb/s data streams, dispersion specifications (depending on modulation format) typically require less than 20 ps/nm. Therefore, in the context of this filter bandwidth, the off-state dispersion is essentially zero.

Dimensions for the silicon single-ring hitless device design

For a physical realization of this device in silicon, the electromagnetic parameters in the previous section can be translated to physical device characteristics and dimensions. The structure is realized using the TE, 6:1 aspect-ratio waveguide design proposed in Chap. 5 for the microring cavity and for the input waveguide including the longer MZ arm. A narrower, 500 nm-wide waveguide is used for the output bus, for low coupler loss and a large gap (as explained in Sec. 4). Electromagnetic simulations of the directional couplers were done in Chap. 6 (Fig. 6.9) for tunable filters and are reused here.

Two additions are made here to arrive at the physical parameters for the device design. First, the bend-to-bend junction offset s is evaluated to minimize junction loss. Then, the various dimensions are extracted – gaps from previous simulations (Chap. 6) and geometry angles from the formulas (9.6–9.8).

Based on the electromagnetic coupler simulations, the coupling gaps for the coupling ratios in Table 9.1 are found. The physical dimensions are shown in Table 9.2[‡‡]. Based on these coupling gaps, the corresponding coupler loss is found and included in the electromagnetic model parameters in Table 9.1.

[‡‡]The fabrication layout used a 498 nm bus waveguide width due to a 6 nm step size, but simulations were done using a 495 nm width (Chap. 6).

Normally-on and normally-off variants

The design described so far is "normally on", that is, the drop-port passband is enabled when the switching phase $\phi_{\mathrm{switch}} = 0$. This is not the most advantageous configuration for operating a hitless tunable filter, because the filter must be tuned in the off state. The switching phase ϕ_{switch} is the only one that needs to be actuated to change by $\pm\pi$ radians in order to turn on or off the resonant response. On the other hand, both ϕ_{switch} and ϕ_{tune} must be varied in unison to tune the resonant wavelength of the filter while keeping it in the off state. This is because ϕ_{tune} tunes the resonant frequency of the ring, while ϕ_{switch} tunes the wavelength-dependent coupling ratio spectrum along with it. If the device is in the normally on configuration, it needs first to switch off (π phase shift to ϕ_{switch}), and then both ϕ_{tune} and ϕ_{switch} need to be varied across another 2π to tune up to a full FSR (to address any channel). This means that a normally on filter requires 3π of actuation in ϕ_{switch} when the phase shifting mechanism can only shift the phase (effective index) in one direction.

The desired configuration for hitless tuning is therefore a "normally off" design. This means introducing an additional fixed π phase shift into the MZ arm in design to set the filter into the off state when all control phases are not zero. Then ϕ_{switch} and ϕ_{tune} must each only be capable of covering a range of 0 to 2π radians when actuated in order to tune to any wavelength over one FSR, and then turn on the filter at that wavelength, and turn it off again to allow tuning to another wavelength again.

For a normally off design, a design with a half-guided-wavelength shortened long MZ arm is given in Table 9.2 (in parentheses). Angle Θ_1 is not 90° because the desired arm length difference on resonance is the circumference of the ring (in guided wavelengths) minus 1/2 guided wavelength.

9.3.2 Experimental demonstration

In this section, the experimental realization of the single-ring hitless tunable filter is described. The waveguide cross-sections and layouts used for tunable filters in Chap. 5 are the same for this device. The fabrication process and heater design is also the same. For the present device, however, it was necessary to choose a geometry with a large enough MZ arm length difference to prevent substantial thermal crosstalk between the switching arm heater and the ring heater (and the corresponding optical structures underneath them). An MZ input coupler with an FSR equal to the ring FSR was sufficient. Both the normally on and the normally off (better) variants of the design were fabricated.

An optical micrograph of a fabricated device is shown in Fig. 9.7(b). It shows silicon waveguides and the ring resonator on a lower layer, and titanium micro-heaters – one over the switching arm and one covering the ring – on an upper

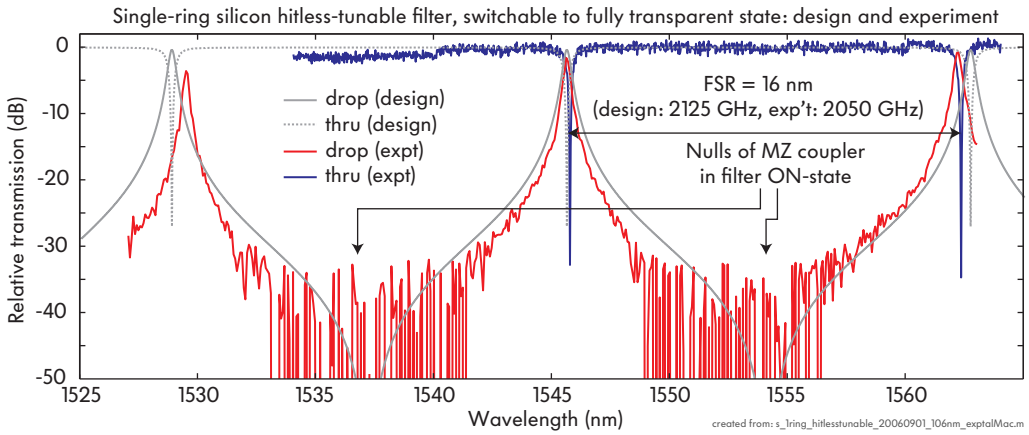

Figure 9.9: Spectral response of a silicon single-ring hitless filter, switchable to full transparency: design and experiment.

layer. This is a normally on variant of the device. Its experimentally measured spectral responses, with no heaters actuated, are shown in Fig. 9.9 together with the design responses. The experimentally measured FSR of 2050 GHz is in good agreement with the designed FSR of 2125 GHz, with the difference likely attributable to slightly different waveguide dimensions than designed.

To demonstrate hitless tuning with a fully transparent off state, the filter was turned off at its nominal wavelength, tuned to a new channel at a 500 GHz longer wavelength, and re-enabled at the new wavelength channel. The experiment is shown in Fig. 9.10. The approximate power applied to each of the switching arm and ring heaters is shown on the right of each step.

In Fig. 9.10, steps (a)-(f) show disabling the filter from a fully on to a fully off state, by applying 39 mW to the switching heater. Step (f) shows the on state in step (a) overlaid, showing that the resonance has shifted only 5 GHz in the off state. This is a direct confirmation of the low thermal crosstalk. Simulated results of the thermal crosstalk done by F. Gan, for the designed structure, reasonably agree with the experiment and are described in [135].

In the off state in step (f), the drop port response is suppressed by 25 dB, while the through port response shows full transmission with no sign of a resonant response dip. Since we know that the off state is minimum phase, the phase responses of both the drop port and the through port are related to their respective amplitude responses by the Kramers-Kronig relation, i.e. the Hilbert transform. The response is by design strongly minimum phase in the off state, so experimental verification of this fact is not necessary, except in the presence of extremely large errors in realization. Then, since the through port is flat, this can be taken as evidence of a linear phase and no substantial dispersion across the spectrum.

Steps (f)-(j) show tuning of the resonance by 500 GHz or 2 channels as indicated on the plot. The FSR of 16 nm (2 THz) was divided into 8 channels spaced by 250 GHz as the single ring filters show 25-30 dB adjacent channel rejection in the

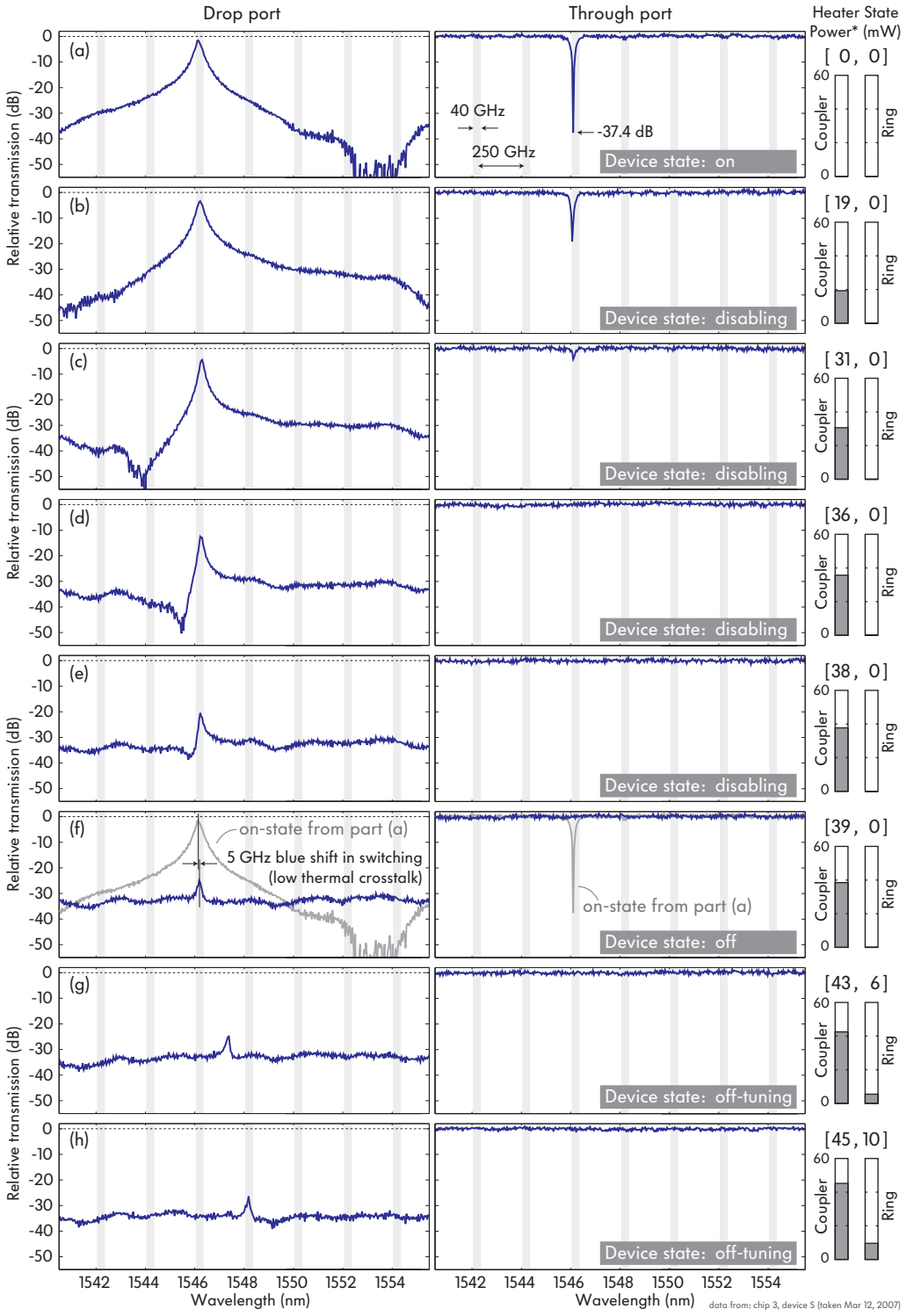

Figure 9.10: Experimental switching spectra demonstrating a silicon single-ring hitless filter, switchable to full transparency, based on thermo-optic tuning and switching: (a-f) disabling the filter, (f-j) tuning the filter in the off state, . . . (continues on next page)

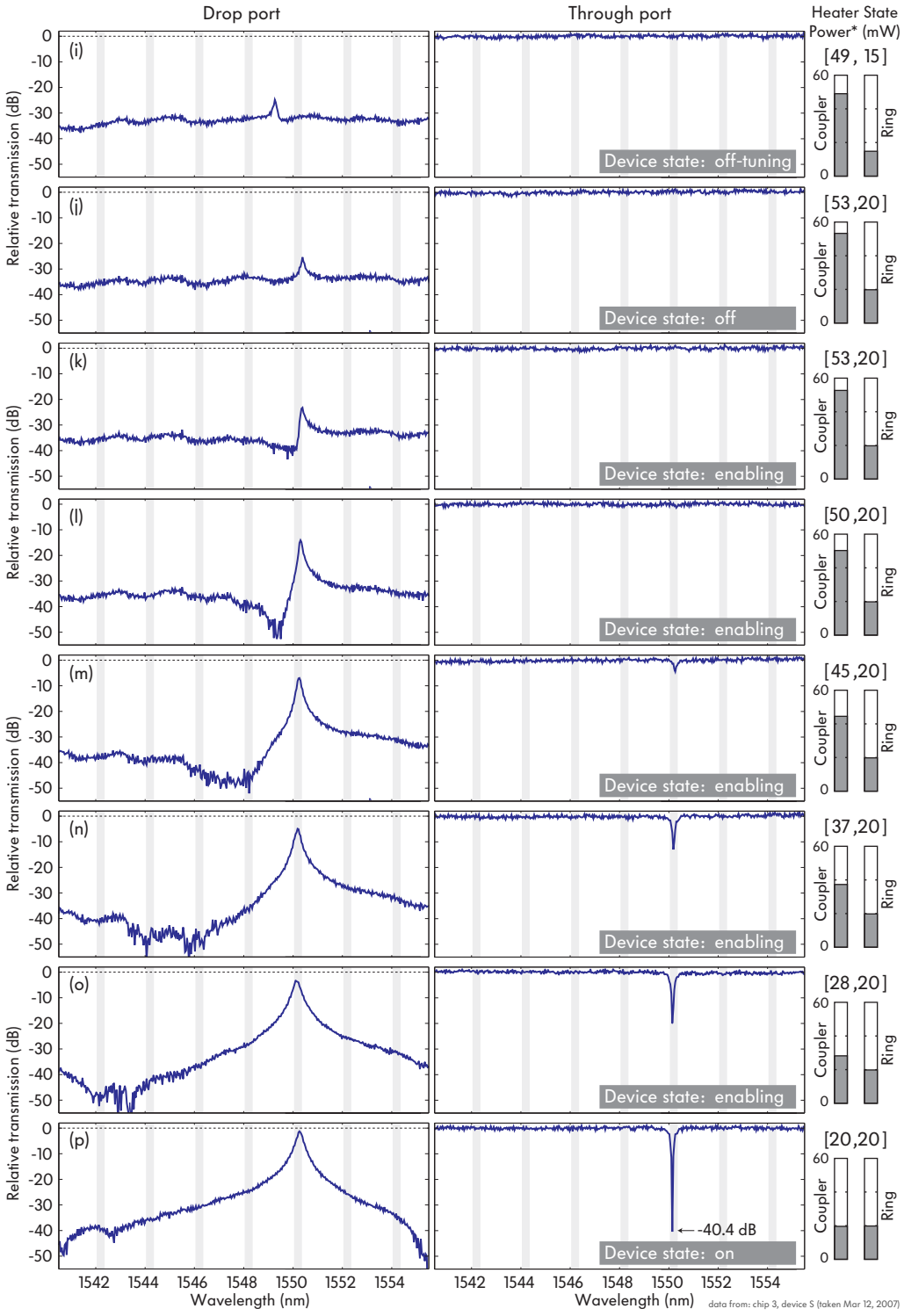

Figure 9.10 (continued) . . . (j-p) enabling the add-drop filter at a new wavelength channel.

drop port with such a spacing, so this device can be used as an add-drop filter in such an example application. The wavelength tuning required the addition of about 14 mW to the switch heater (already starting at 39 mW), and the addition of 20 mW to the ring heater in order to tune in unison. The reason why the added powers are not equal is that the heated areas of the switching arm under the switch heater and of the ring under the ring heater are not perfectly balanced. Further, the thermooptic coefficient changes with temperature (see Chap. 6). Since the switch heater is biased to 39 mW in state (f), the added powers cannot be expected to equal, and a lower additional power is expected in the switch heater.

Steps (j)-(p) show the re-enabling of the filter at the new channel wavelength of about 1550 nm. The re-enabling involves changing the power applied to only the switch heater. Both heaters are at about 20 mW in the on state at the new channel. This shows a low-temperature-rise tuning efficiency of about 40 mW/THz (the efficiency increases at higher temperatures due to the thermooptic coefficient temperature dependence).

The fabricated device was designed for hitless tuning across its entire 16 nm FSR. This experiment has yet to be performed at the time of this writing because further attention needs to be paid to passivation of the microheaters, to avoid their burnout by oxidation at higher temperatures, i.e. higher powers. However, the basic capability of wide tuning was demonstrated by the tuning experiment on an identical microring resonator without switching capability in Chap. 6.1, so the combination of these two experiments demonstrates the complete functionality. In order to hitless tune to and switch at any channel in the FSR with only the maximum power required to tune the full FSR, the "normally off" design variant must be used. This design, with only a half-wavelength shorter MZ arm, was also fabricated and is to be evaluated in forthcoming work.

9.4 Higher-order-resonator transparent switching

In this section, the single-cavity design in the previous is extended to higher-order resonators. Higher-order resonators provide flat-top passbands that meet typical transmission system specifications (Sec. 1.1). Generalization of the approach to higher order is necessary in order to realize fully transparent off states in telecom-grade channel add-drop filters. In this section we will consider only higher-order resonant systems where each input-output port is coupled to only one cavity mode (or ring mode).

Near a resonance frequency of interest, a higher-order resonator supports multiple supermodes, where the resonant frequencies split into bands – sometimes used as filter passbands of a device (see [38, 49]). To switch the resonant system into a fully transparent state, it is necessary that *all* supermodes in the passband of interest (and the entire wavelength of interest) be switched off, each like the

single-ring filter in Sec. 9.3.

If a broadband input coupler is used [Fig. 9.4(a)] then in principle all supermodes forming the passband of a system can be suppressed in the same way as in a single cavity system. More practical systems use a long switching arm to accommodate a circular ring resonator and to permit sufficient thermal isolation of the switching and tuning phase shifters (e.g. Fig. 9.7 – and have a wavelength-dependent input coupling. In this case, since the supermodes resonate at different resonance frequencies, the sinusoidal input-coupling spectrum can only provide one complete null in the passband and fully suppress only one supermode. The other supermodes at detuned wavelengths see a small residual coupling away from the coupling null, leaving a residual drop-port excitation and through-port dispersion signature.

An additional feature – a variable loss mechanism – can be added to a cavity to kill the supermode Q. Judicious placement of the controlled loss on a particular cavity maximally quenches the Q and enables full suppression of the response. The idea is to kill the Q of those modes that are most detuned from the coupling null and thus see the largest excitation.

First, a coupling of modes in time model is developed for resonant filters with MZ interferometer based variable couplers. This permits study of the general switching characteristics without attention to details of the FSR. Then, the extension of wavelength-dependent variable coupling to high-order passbands is described, and illustrated through examples. Finally, a concrete silicon-waveguide design is described, and preliminary experimental results shown.

9.4.1 Coupling of modes in time model

A coupled-mode-theory-in-time (CMT in time) model can be derived for a resonator with interferometric input coupling. Although its derivation is less straightforward than a spatial propagation scattering model, CMT in time provides useful physical insight into the device operation because it describes only the resonant mode of interest (whereas a spatial model describes all longitudinal resonances and has more complex analytic form).

The CMT state-variable-form model for a single ring resonator with a MZ interferometric input coupler [Fig. 9.11(a)] is

$$\frac{d}{dt}a = \left(j\omega_o - \frac{1}{\tau'}\right)a - j\mu_i' s_+$$
$$s_- = -j\mu_o' a + R s_+$$

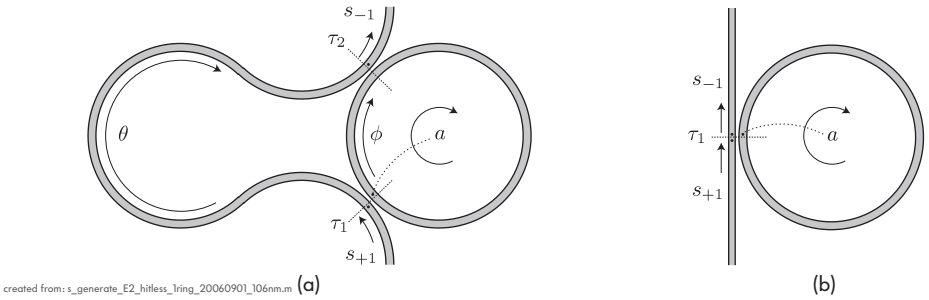

Figure 9.11: Coupled-mode theory in time model parameters for (a) interferometric, variable input coupling to a resonator, (b) regular input coupling for comparison.

where

$$\frac{1}{\tau'} = \frac{1}{\tau_1} + \frac{1}{\tau_2} + \sqrt{\frac{4}{\tau_1 \tau_2}} e^{j(\theta-\phi)} \tag{9.10}$$

$$\mu_i' = \sqrt{\frac{2}{\tau_1}} + \sqrt{\frac{2}{\tau_2}} e^{j(\theta-\phi)} \tag{9.11}$$

$$\mu_o' = \mu_i'^* e^{-j\phi} = \mu_i'^* R \tag{9.12}$$

and a is the resonant mode energy amplitude, ω_o the resonant frequency, τ_1 is the energy-amplitude decay rate via coupler 1 alone, τ_2 is the decay rate via coupler 2 alone, ϕ is the accumulated propagation phase around the long coupler arm between coupling points 1 and 2, and θ is the accumulated propagation phase around the part of the ring resonator between coupling points 1 and 2.

Then τ' is the effective decay rate, which depends on the interferometric coupler's differential phase. If $\tau_1 = \tau_2$, then for $\theta - \phi = 0$ the decay rate is $1/\tau' = 4/\tau_1$ – four times the decay rate $1/\tau_1$ with a single coupler. This is because fields add, and energy goes as the square. This quadrupling is valid for weak directional couplers, which are found in high-finesse designs (FSR $\gg$ bandwidth). If instead $\theta - \phi = \pm\pi$, then the input coupler is in the off state, and decay rate $1/\tau' = 0$. The resonance is then "infinite Q" and has no decay, zero linewidth and infinite group delay on resonance (while preserving a 2π group delay-bandwidth product) for a lossless cavity. Therefore even when the input coupler is zero, formally the device isn't off. It is necessary to introduce an infinitesimal loss into the cavity first, to push the zero into the minimum-phase half-plane together with the pole and permit pole-zero cancellation that leads to a dispersionless response. In practice, as discussed in Sec. 9.1, larger off-state cavity loss is desirable in order to secure a sufficient contrast between the input coupling and loss for switching to an effectively fully transparent state.

Keeping with notation in other CMT analyses [8, 38, 67], μ_i' here is the effective coupling from the input wave to the resonant mode, while μ_o' is the effective output coupling from the resonant mode to the output wave, and R is the direct coupling ("reflection") of the input to the output wave when the resonator is not excited;

here, in absence of other ports, it has magnitude 1. These parameters satisfy the conditions for CMT parameters imposed by power conservation [182].

This model was derived with some assumptions. First, there is the standard CMT assumption of high Q (i.e. a system bandwidth much smaller than the center frequency). Second, it is assumed that, in decay, the transit time around the longer MZ arm is much shorter than the decay time of the resonator, so that the two interfering signal amplitudes are of equal magnitude even though the resonator amplitude is decaying. This is equivalent to assuming that the FSR of the MZ is much larger than the resonator bandwidth, an assumption valid in nearly all cases of interest. In principle, excess propagation loss in the MZ arm can be taken into account in the model, but here it is disregarded because the structure is small.

This is a self-contained model of the interferometric input coupling and can be applied to more general resonant structures. For example a structure such as Fig. 9.11(a) but having an additional drop port simply requires an additive decay rate in the resonator that represents the drop port. Similarly additional resonators can be coupled to construct higher-order designs without affecting the coupler model.

For comparison, the for the resonator with plain (non-interferometric) input coupling in Fig. 9.11(b), the effective couplings in the model eqns. (9.10)–(9.12) are: $\tau' = \tau_1$, $\mu_i' = \mu_1 \equiv \sqrt{\frac{2}{\tau_1}}$, $\mu_o' = \mu_i'$ and therefore $R = 1$ [8, 67].

9.4.2 Push-pull switching concept and supermode suppression

In this section, the combination of variable input coupling and a variable loss mechanism introduced into some cavities is described as an effective approach to extend fully transparent switching capability to higher-order resonators. This is accomplished by quenching the Q of the least suppressed supermodes with the introduced variable loss mechanism. The concept is illustrated with examples.

In a higher-order resonator, the supermode resonance frequencies are distributed across the passband. For example, a maximally-flat (Butterworth) series-coupled-cavity (SCC) channel dropping filter [38] has supermode frequencies distributed on a circle in the complex-frequency plane [49, 56], the diameter of which is its bandwidth. Then, it can be expected that a switching mechanism of the kind described in Sec. 9.4.1 will only disable fully the resonances nearest in frequency to the input coupling null, and may leave more detuned supermodes incompletely suppressed. This can be illustrated by an example filter, shown in Fig. 9.12.

A series-coupled-cavity, third-order filter is used as the example for comparison of several filter geometries, designed to provide 40 GHz-wide channel windows (passbands) with a 100 GHz channel spacing, and 30 dB out of band rejection of the adjacent channel (at the channel edges at $\pm$80 GHz detuning). This is accomplished by a Chebyshev filter design with 17.5 dB in-band extinction across the 40 GHz channel window, realized as a SCC resonant fil-

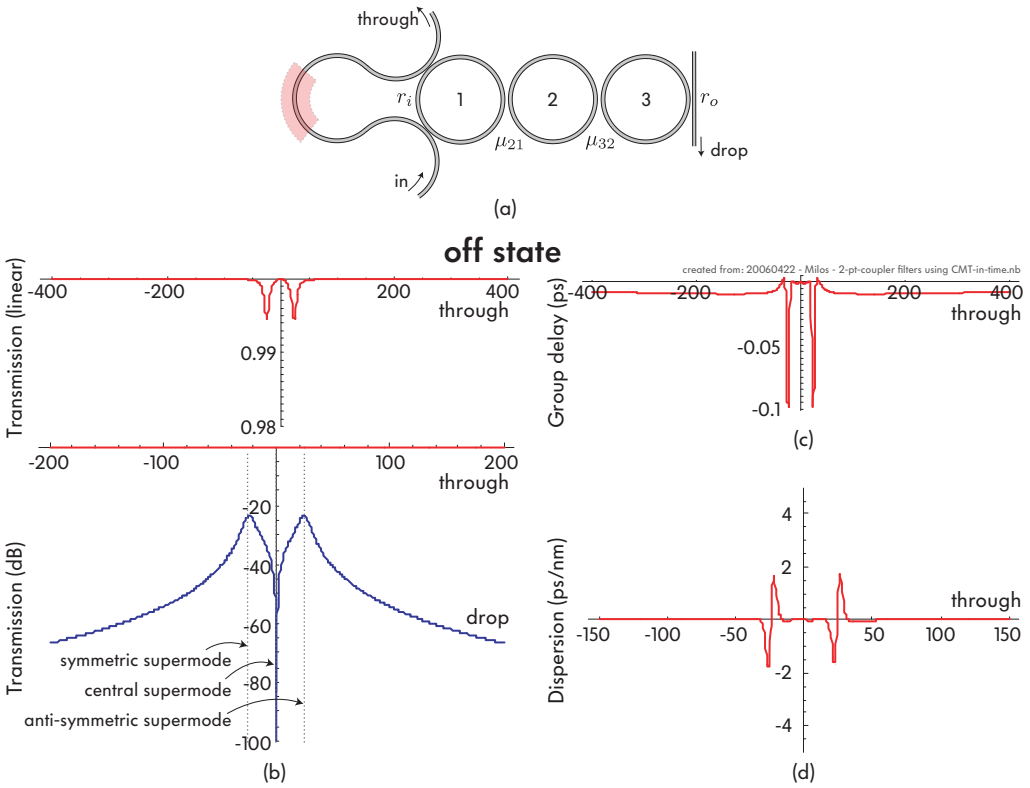

Figure 9.12: Switching higher-order resonators to transparency: (a) third-order resonator example with variable input coupler; (b-d) amplitude, group delay and dispersion response spectra in the off state.

ter. The temporal-CMT coupling coefficients to synthesize this response are $\{r_i, \mu_{21}, \mu_{32}, r_o\} = \{129.2, 119.5, 119.5, 129.2\}$ Grad/s [38, 49]. An intrinsic cavity loss Q limited to 200,000 is assumed, which corresponds to about 2-4 dB/cm in typical strongly confined Si or SiN waveguides with a group index between 2 and 4 (Appendix B), which are values consistent with typical propagation losses in present state-of-the-art Si and Si-rich SiN waveguides.

A straightforward CMT analysis of this filter can be carried out by CMT as done in [38]. In this situation we replace the input coupler with an interferometric, variable coupler [Fig. 9.12(a)], by using the model developed in Sec. 9.4.1 and simply substituting in the expressions for effective decay rate and couplings for the input coupler in the CMT model. The variable coupler is assumed to be wavelength dependent with an FSR of 2.5 THz (or 20 nm range near 1550 nm central wavelength) – a typical FSR for Si and SiN microring resonators. Typical loss is included so that insertion loss that results from high-Q group delay spectrum spikes in the off state of some non-ideal designs can be seen.

Only the off state of the filter is shown in Fig. 9.12. The amplitude response shows that the central of the three supermodes of the filter is fully suppressed to zero drop-port response amplitude since the MZ input coupler null is located at $\delta f = 0$

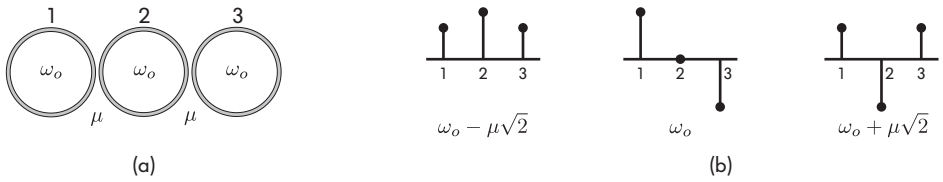

Figure 9.13: Supermodes of a 3-cavity, symmetrically coupled SCC resonator: (a) third-order resonator with degenerate cavities (ω_o) and equal coupling rates (μ); (b) supermode resonant frequencies and energy amplitude distribution in the cavities (each vector is real to within a constant common-mode phase). The energy distribution is the square of these amplitudes, i.e.: $\{1/4, 1/2, 1/4\}$, $\{1/2, 0, 1/2\}$ and $\{1/4, 1/2, 1/4\}$.

in the off state. The lower and higher frequency supermodes, on the other hand, see non-zero input coupling due to the latter's sinusoidal frequency dependence with a 2.5 THz period (FSR). Therefore, here they show spurious resonant peaks in the off state, suppressed from the on state by only about 23 dB. This means that about 0.5% of the light is dropped at the two spurious peak wavelengths, producing loss and remnant dispersion [Fig. 9.12(d)] in the through port which is in the low ps/nm, which is still relevant for bitrates compatible with this filter bandwidth. Fig. 9.12(c) shows a group delay spectrum that is negative – as previously discussed this means that adding loss into cavities will generally increase through-port transmission, not decrease it, due to the introduction of impedance mismatch between the input wave and cavity.

In order to suppress the spurious modes, to completely eliminate through-port loss and dispersion in the off state, an artificial loss mechanism may be added to those supermodes that are not sufficiently suppressed, in order to drastically lower their internal (loss) Q and thus suppress their resonant excitation. Here, there are just two detuned supermodes, symmetrically arranged about the center wavelength. In general, one would first quench the supermodes that are most detuned (if their effective input couplings are all roughly of the same order). A fixed artificial loss is generally not a good solution, because the cavities must have an internal cavity loss much smaller than the effective input coupling in order to provide high fidelity resonant filter characteristics; while they need to have internal cavity losses much higher than the input coupling in order to suppress the resonant excitation. Therefore we will use the interferometric input coupler described in Sec. 9.4.1 also as a variable loss mechanism that can be added to any cavity.

The most convenient approach is to add a variable loss mechanism to individual cavities rather than to try to interferometrically address supermodes. Furthermore, it is desirable to use as few controllable components as possible in the interest of efficiency. Therefore, since the objective is to quench the Qs of particular supermodes, while the variable loss will be introduced on a per-cavity basis, it is of interest to investigate what the optimal placement of loss mechanisms should be.

A good guideline is to introduce the variable loss mechanism into the cavity

having the highest energy amplitude for the supermodes to be quenched. For the example considered in this section, this is illustrated in Fig. 9.13(a). The three supermodes of a structure such as that in Fig. 9.12(a), with ports disconnected are illustrated (the ports send the resonances into the complex-frequency plane, but they don't change the symmetry of the system so the basic conclusions are the same). The energy amplitude in each cavity is illustrated in Fig. 9.13(b) for each of the three supermodes having resonance frequencies $\omega_o - \mu\sqrt{2}$, ω_o and $\omega_o + \mu\sqrt{2}$. This is simply obtained from the eigenvectors and eigenvalues of the coupling matrix for three symmetrically coupled degenerate cavities: $[\omega_o - \mu 0; -\mu\omega_o - \mu; 0 - \mu\omega_o]$. This picture suggests that for an interferometric loss coupler with a coupling gap that provides a certain cavity decay rate (power loss per unit time per unit of stored energy), the optimal approach is to place the loss coupler on the cavity with the highest mode amplitude, as that results in the highest loss rate for the supermode.

The lowest and highest frequency supermodes both have the maximum amplitude in the middle cavity. Therefore, the variable loss mechanism should be placed on the second cavity. It should be noted that the middle supermode does not receive virtually any loss from this loss mechanism, because the middle cavity has no amplitude (for finite-FSR cavities this amplitude is small but non-zero).

Fig. 9.14 shows such a design and its on state and off state characteristics. This is proposed to be the correct approach to completely suppresses the dispersion to negligible levels and minimizes insertion loss in transmission. The off state dispersion is less than 0.1 ps/nm, the group delay variation below 0.01 ps (in comparison to 20 ps group delay in the on state), the residual through-port loss in the off state is less than 0.2% in this example, and the drop-port response suppressed by over 33 dB. This design provides a good approximation to a fully transparent off state in higher-order resonators with wavelength-dependent variable coupling, and is suitable for telecom-grade filters.

There is a second way to arrange two variable couplers, that is in principle less advantageous. It is shown in Fig. 9.15. This approach suppresses the drop-port response similarly as the previous example because the output coupler is turned off in the off state as well. However, neither coupler is used as a loss mechanism, and furthermore both the input and output port are decoupled, so that the resonator supermode Qs all increase greatly (up to a Q limited by their internal losses). As a result, the drop-port response has very sharp peaks, shows large group delay (several ps) and dispersion (20 ps/nm) near the band edges. This also leads to a substantial insertion loss at band edges of over 2% (0.1 dB). If the internal losses of the cavities are more substantial, the insertion loss may be reduced due to impedance mismatch, but the response is as a result sensitive to the value of the internal loss, which is undesirable as devices tend towards lower waveguide loss. Nevertheless, this design uses one fewer waveguide than that in Fig. 9.14, because

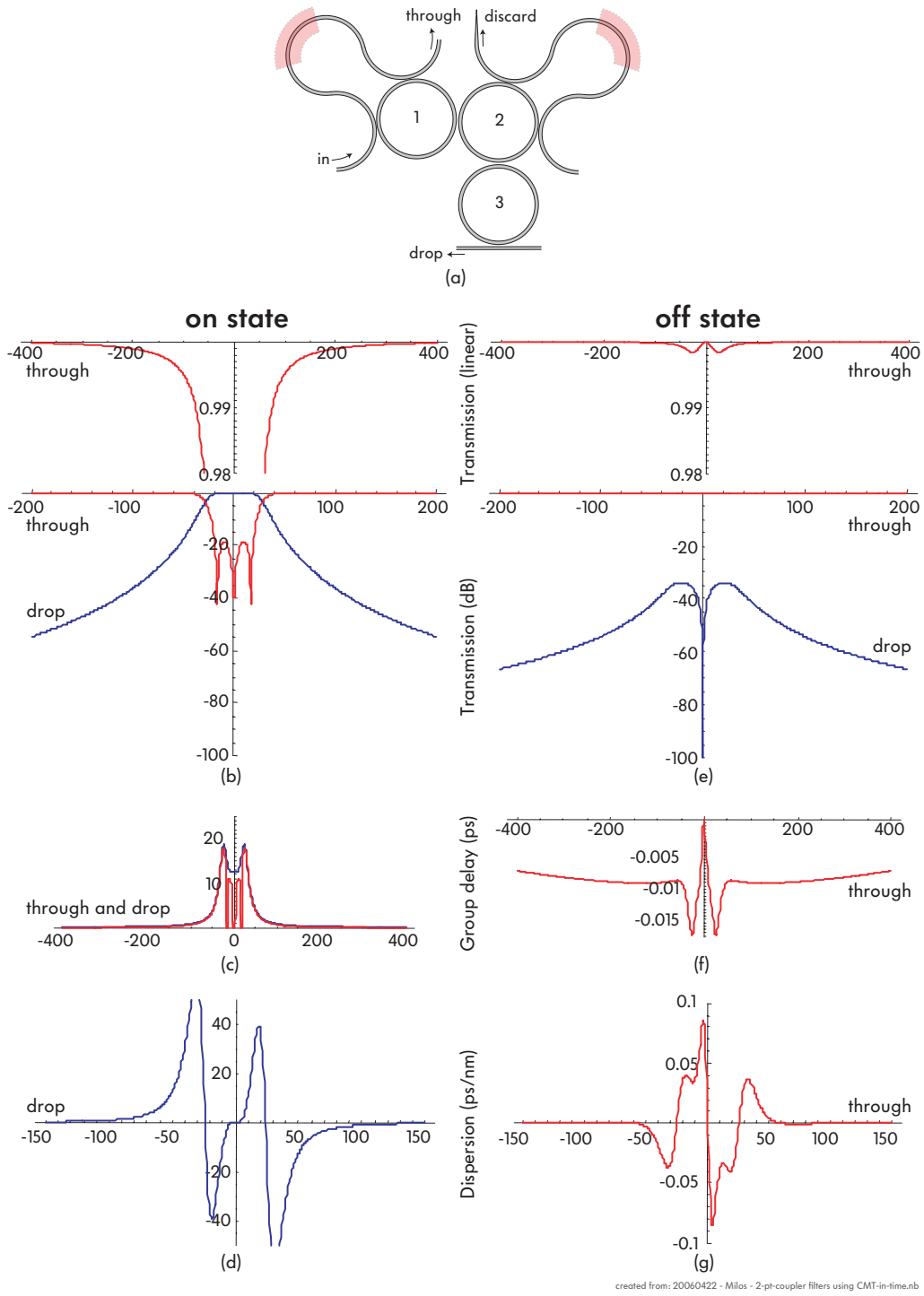

Figure 9.14: Switching higher-order resonators to transparency (best approach): (a) third-order resonator example with variable input coupler and loss mechanism on internal (second) cavity; (b-d) amplitude, group delay and dispersion response spectra in the on state; (e-g) amplitude, group delay and dispersion response spectra in the off state.

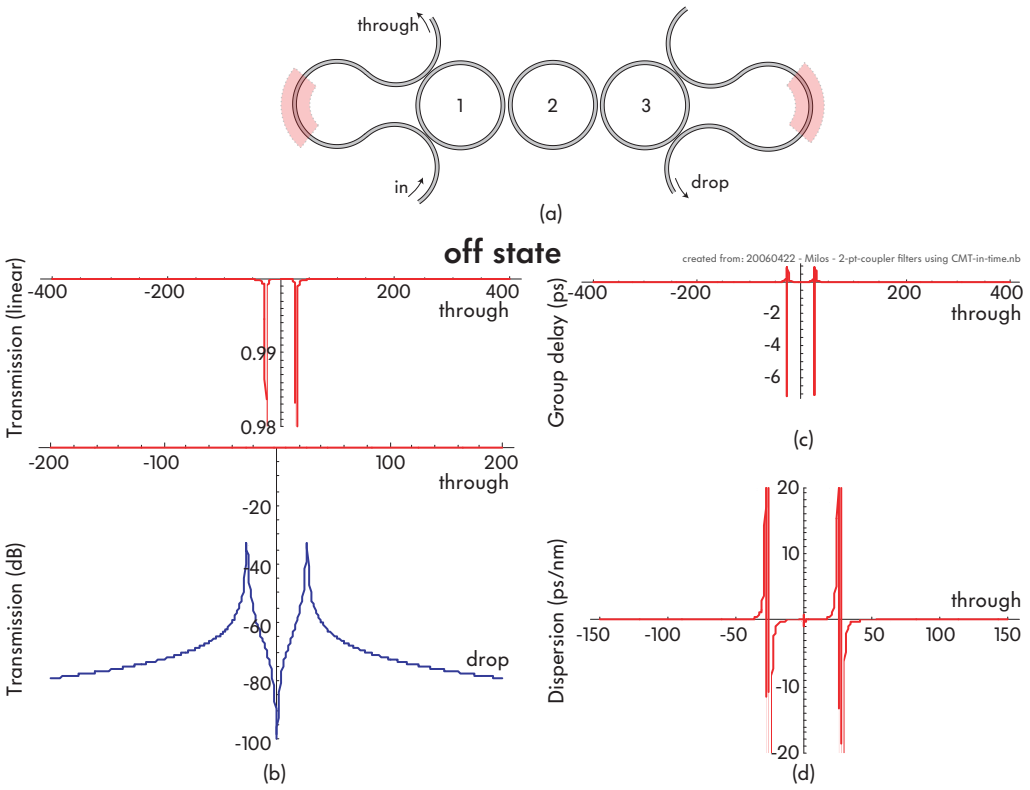

Figure 9.15: Switching higher-order resonators to transparency: (a) third-order resonator example with variable input and output couplers; (b-d) amplitude, group delay and dispersion response spectra in the off state.

a simple drop bus is avoided. Therefore it may be practical in some applications that can tolerate the moderately dispersive phase sidebands.

The response may generally be improved by introducing more than one variable loss coupler, e.g. one to each cavity. This raises the complexity level. It also has to be done with care. Fig. 9.16 shows a 3-ring filter as in the previous examples with the input and output couplers variable, as well as a variable loss coupler on the middle ring – all three introduce the same decay rate into the cavity when switched on. It turns out that in this particular symmetric configuration with three cavities, the design with a larger number of variable couplers does not offer an advantage. The drop-port response is suppressed further than in the other examples to about -60 dB. However, the through-port transmission loss is not reduced in comparison with the preceding simpler designs. Furthermore, the dispersion is slightly larger, and has a narrowband spike at the center wavelength. This is because the central supermode has lost all line-broadening mechanisms – the input and output coupler are off, and the middle supermode has no substantial amplitude in the middle cavity, so the variable loss coupler on the second cavity has no substantial effect. In this example, therefore this design is not useful. However, in general a larger number of variable couplers, used judiciously can lead to greater suppression at

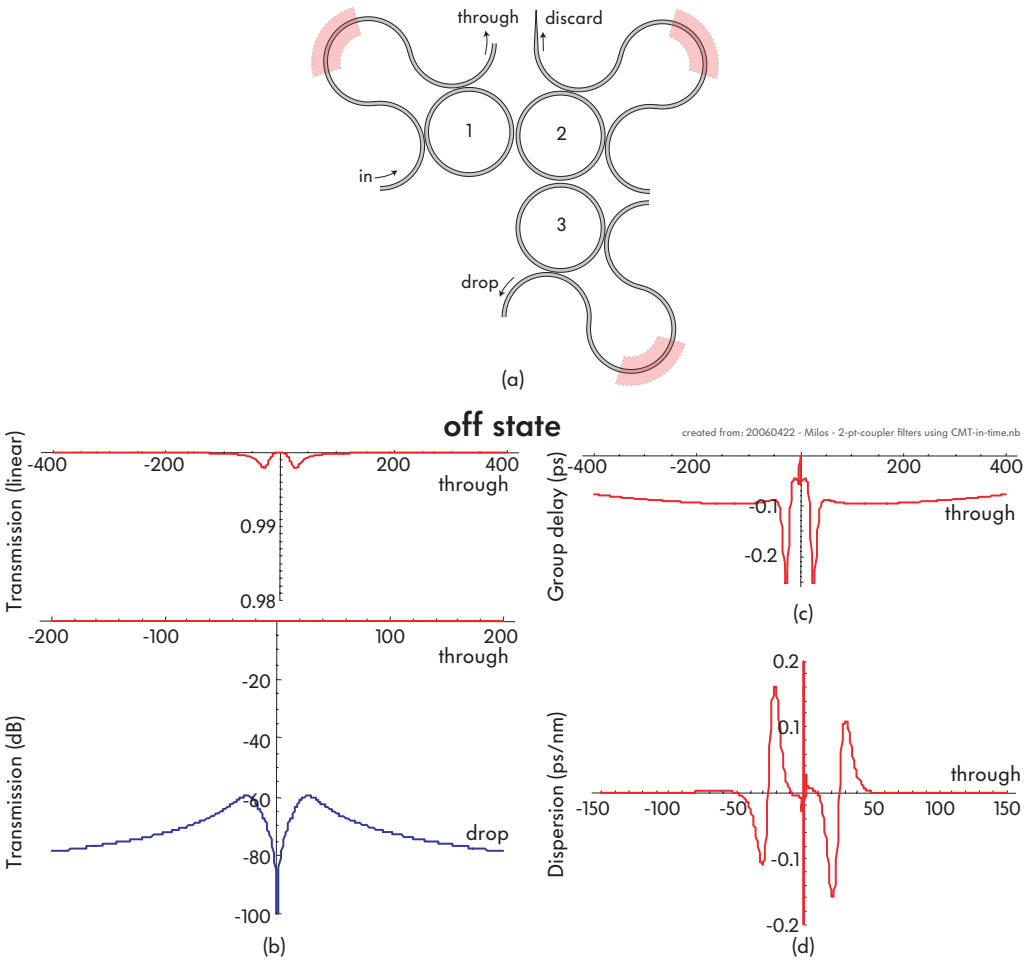

Figure 9.16: Switching higher-order resonators to transparency: (a) third-order resonator example with variable input and output couplers and loss mechanism on internal (second) cavity; (b-d) amplitude, group delay and dispersion response spectra in the off state.

the expense of added device complexity. For example, a symmetric fourth-order SCC filter will have no supermodes with null amplitude in any one cavity, so this approach would be more robust in that case. It should be noted that both Fig. 9.14 and Fig. 9.16 provide suitable performance for telecom applications with bitrates matched to the considered filter bandwidth.

Conclusions

It was shown that the variable input coupling and loss-mechanism approach to fully transparent off states can be extended to higher-order resonators, in practical structures that use wavelength-dependent couplers, by introducing variable loss to cavities that have maximum energy amplitudes in supermodes most detuned from the passband center and therefore having largest spurious resonant response in the off state.

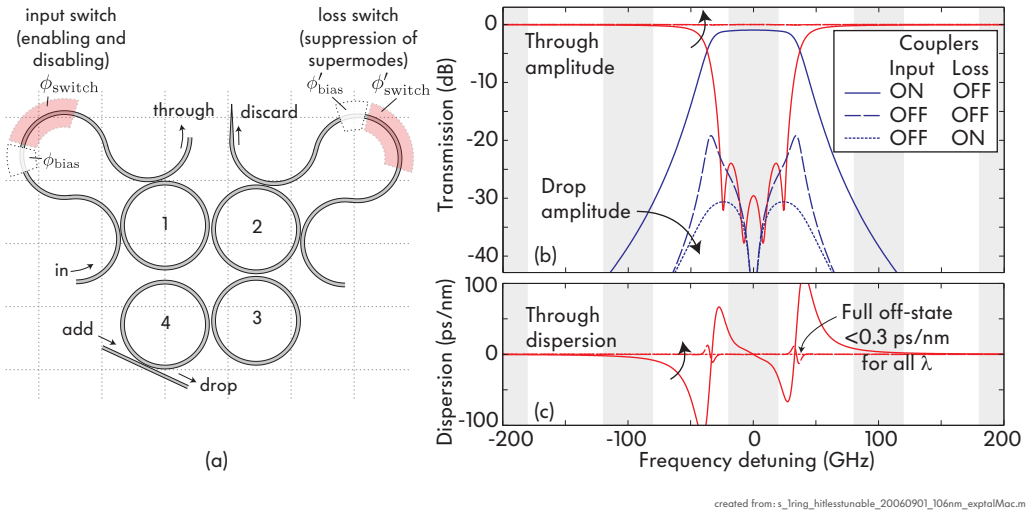

Figure 9.17: (a) Concept and (b) theoretical switching response of proposed hitless-tunable high-order (multicavity) filter, based on "push-pull mode" variable couplers. It enables telecom-grade transmission characteristics (here 4^{th}-order, series-coupled-cavity microring resonator), and is switchable to a fully transparent state. The input switch brings the filter into a minimum-phase off state. The loss switch broadens the most detuned supermodes to suppress their excitation and remove residual through-port dispersion peaks.

9.5 Experimental demonstration of 4^{th}-order hitless add-drop filter

In this section, the experimental demonstration of a telecom-grade, fourth-order add-drop filter is described. The demonstration device is based on silicon-core microring resonator designs in Chap. 5 and variable input and loss couplers in the configuration of Fig. 9.14(a). The complete electromagnetic design and physical structure are described, and the expected design response is shown based on the state variable model supported by rigorous complex-frequency mode solver computations and 3D FDTD simulations. Preliminary results of the fabricated, thermally tunable silicon-core device are shown.

The basic device design is illustrated in Fig. 9.17(a). In addition to a variable input coupler (top left) and a variable loss coupler (top right), each of which has a bias phase shift and a thermally actuated switching phase shifter, each microring is also thermally tunable by a microheater, as in Chap. 6. For optimal use of thermal power for switching and tuning – to achieve maximum switchable tuning range – the bias phase shifts are set to make the variable input coupler off and the variable loss coupler on in the cold state of the filter with all heaters off. Then the filter may be tuned to any wavelength by actuating all six heaters (two for couplers and four for rings). If the destination wavelength is in the first half of the filter FSR, then the variable couplers are heated further by a half FSR to add a π-radian phase shift to each and switch their states to turn on the filter. If the destination wavelength

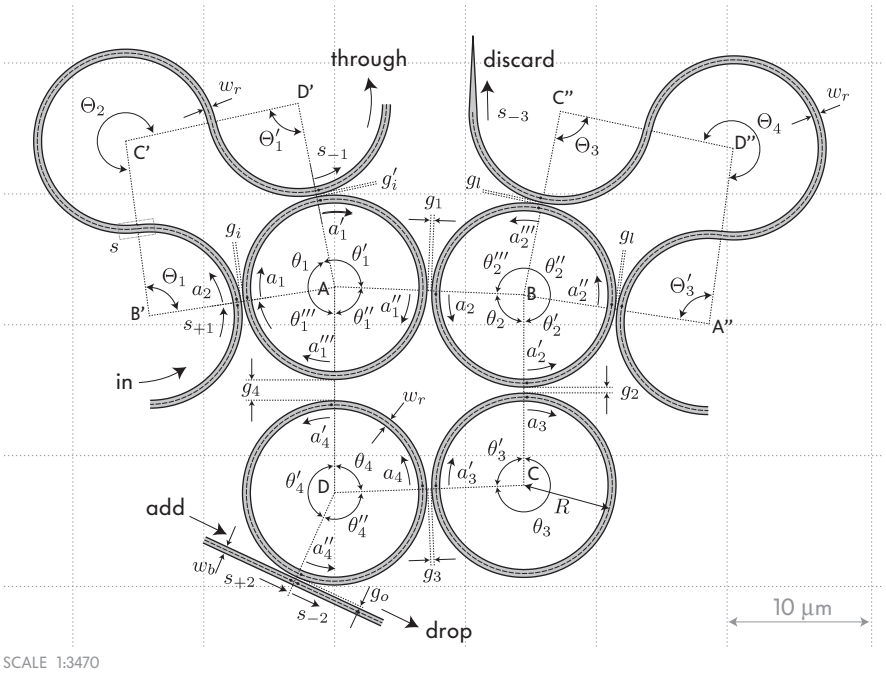

Figure 9.18: Concept and theoretical response of proposed hitless-tunable high-order (multicavity) filter, based on "push-pull mode" variable couplers. It enables telecom-grade transmission characteristics (here 4^{th}-order, series-coupled-cavity microring resonator), and is switchable to a fully transparent state.

is in the second half of the filter FSR, then all heaters, including the MZ couplers, have been actuated to tune beyond one half of the FSR. In this case, the variable coupler heaters can be cooled down to shift by one half the FSR to turn on the filter. Reversing this operation returns the filter to the fully transparent off state, after which it may be tuned to a new channel.

The final design switching characteristics are shown in Fig. 9.17(b). When the input is on and the loss mechanism off, a flat-top telecom-grade response is expected. The passband shape design, having a higher extinction on the middle lobe of the through-port extinction than on the outside lobes, is for higher tolerance to fabrication variations and wavelength tuning, and is identical to that demonstrated in the high-order silicon SCC tunable add-drop filters described in Chap. 6. When the input is switched off, the response shows spurious sidebands at about -20 dB and 10-20 ps/nm of dispersion at the band edges. Once the variable loss mechanism is switched on in addition, the outside resonances are broadened, the response is further suppressed in the drop port, the through port is completely flattened to near unity transmission and the dispersion is negligible at below 0.3 ps/nm at the band edges and smaller elsewhere.

The details of the device that gives this simulated performance are shown in Fig. 9.18 and Table 9.3. The figure shows all of the relevant electromagnetic and physical variables for the state-variable spatial scattering model that gives the

Table 9.3: Physical dimensions of the fourth-order microring hitless filter (normally-off design)

Height of all waveguides		$106\,\mathrm{nm}$
Ring/arc center radius	R	$6.732\,\mathrm{m}$
Ring/arc waveguide width	w_r	$600\,\mathrm{nm}$
Output bus waveguide width	w_b	$498\,\mathrm{nm}$
Input coupler gap	$g_i (= g_i')$	$209\,\mathrm{nm}$
Ring 1–ring 2 gap	g_1	$407\,\mathrm{nm}$
Ring 2–ring 3 gap	g_2	$462\,\mathrm{nm}$
Ring 3–ring 4 gap	g_3	$407\,\mathrm{nm}$
Ring 4–ring 1 gap	g_3	$1637\,\mathrm{nm}$
Loss coupler gap	$g_l (= g_l')$	$209\,\mathrm{nm}$
Output coupler gap	g_o	$175\,\mathrm{nm}$
Bend-bend offset	s	$30\,\mathrm{nm}$
Geometry angles	$\Theta_1 (= \Theta_1')$	89.13°
	Θ_2	265.87°
	θ_1	87.60°
	$\Theta_3 (= \Theta_3')$	90°
	Θ_4	266.79°
	θ_2''	86.79°
	θ_1''	87.70°
	θ_2	92.30°
	θ_3'	92.30°
	θ_4	87.70°

simulated response. The physical dimensions for the device, obtained from 3D FDTD simulations are shown in Table 9.3. The electromagnetic parameters of the device are shown in Table 9.4.

The device was fabricated in silicon-core waveguides of the cross-section in Chap. 5, as described in Sections 5.3.1, 6.1.2. An optical micrograph is shown in Fig. 9.19, showing the silicon waveguide structure on a lower layer and the titanium microheaters on an upper layer.

The first optical characterization of these fabricated devices is presently under way at the time of this writing. The interested reader is advised to consult forward references from this document, in the short term, when any obtained results are likely to be available.

Table 9.4: Electromagnetic parameters of the fourth-order microring hitless filter

FSR	$(d\gamma/df)^{-1}$	2125 GHz
(Max. variable-input coupled power)		0.186
Input-coupler cross-state coupling	$\kappa_i (= \kappa_i')$	0.0465
Input-coupler loss	l_i	$7.00 \cdot 10^{-4}$
(Max. variable-loss coupled power)		0.0465
Loss-coupler cross-state coupling	$\kappa_l (= \kappa_l')$	0.0172
Loss-coupler loss	l_l	$7.00 \cdot 10^{-4}$
Output coupler cross-state coupling	κ_o	0.186
Output coupler ring-side loss	$l_{\mathrm{o,rr}}$	$3.7 \cdot 10^{-4}$
Ring 1–ring 2 cross-state coupling	κ_{rr1}	0.0063
Ring 1–ring 2 coupler loss	l_{rr1}	$9.4 \cdot 10^{-5}$
Ring 2–ring 3 cross-state coupling	κ_{rr2}	0.0037
Ring 2–ring 3 coupler loss	l_{rr2}	$5.9 \cdot 10^{-5}$
Ring 3–ring 4 cross-state coupling	κ_{rr3}	0.0063
Ring 3–ring 4 coupler loss	l_{rr3}	$9.4 \cdot 10^{-5}$
Ring 4–ring 1 cross-state coupling	κ_{rr4}	$3 \cdot 10^{-7}$
Ring 4–ring 1 coupler loss	l_{rr4}	n/a (zero)
Resonant order (at λ_o =1550 nm)	γ_o	53
Assumed propagation loss		8 dB/cm (0.0338 dB/r.t.)

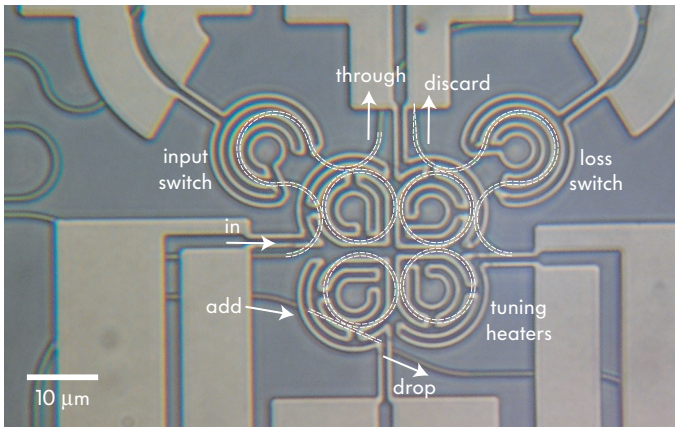

Figure 9.19: Optical micrograph of fabricated hitless-tunable fourth-order microring filter, based on "push-pull mode" variable couplers.

Chapter 10

Conclusions

Summary of accomplishments

In this thesis, the theoretical and design challenges of strong-confinement, high-index-contrast microphotonic circuits were addressed, arriving at complete models and efficient device designs, and novel device architectures were proposed and demonstrated that show proof of principle solutions to all of the key impediments to the wide acceptance of SC microphotonics in telecom and other high-fidelity optical signal processing applications. These impediments were: the lack of rigorously complete design models that include all potential impairments; extreme sensitivity to dimensional errors and surface roughness; extreme polarization sensitivity; the need for wide wavelength tuning and an approach to dispersion-free hitless switching; and the need to efficiently compensate the strongly dispersive response of narrowband channel add-drop filters in order to approach tight channel spacing and reach the limits of spectral utilization.

All of these issues were addressed rigorously. Coupling-induced resonance frequency shifts (CIFS), a resonant-mode misaligning effect that is part of linear coupling was identified, systematically studied, and compensated in SiN high-order microring-resonator filters to show the first frequency aligned higher-order filters [89, 90]. Further, ring and directional coupler mode reconfinement issues, that result in leakage and scattering loss in couplers, were identified and corrected showing as a result greatly reduced loss, and essentially loss-free couplers in SiN and Si microring filters [119, 136]. Multistage filter designs were proposed and demonstrated as a robust way to achieve high through-port extinction ratio [119], a key requirement for telecom applications not previously demonstrated in high-order microring resonator add-drop filters. These were also the first telecom-grade microring resonator channel add-drop filters demonstrated, showing an in-band extinction ratio exceeding 50 dB, well beyond telecom requirements. Canonical

models for lossless and lossy directional couplers (and 4-ports, in general) were proposed, clarifying the number of degrees of freedom depending on the physical symmetry properties of the 4-port. These are used for the modeling of microring-based and general structures, and can be used as a template for extracting physically meaningful data from numerical simulations of ring filter couplers, for example.

Widely tunable and switchable filters were demonstrated in silicon, taking advantage of its large thermooptic coefficient and its quadratic enhancement at high temperatures. To address the extreme sensitivity of silicon micron-scale waveguides, a systematic design study was carried out to find the optimum silicon waveguide designs for tunable filter applications, against an extensive set of relevant criteria. Novel TE and TM waveguide designs were proposed, having a high aspect ratio or overmoded cross-section, respectively, which are equivalent and which provide lower sensitivity and lower loss than conventional cross-sections by a factor of about 3. Extensive design maps are provided. These waveguide designs were also experimentally demonstrated, showing 2 dB/cm loss and microring unloaded Q's exceeding 250,000. Based on these Si waveguide designs, tunable microring filters were designed and experimentally demonstrated, showing the largest demonstrated (20 nm) full-FSR tuning covering the 16 nm cavity FSR, and enabling C-band scale wavelength tuning with the aid of FSR doubling and multiplication approaches. Further, fourth-order, telecom-grade silicon microring filters were designed for a 100 GHz ITU grid of 40 GHz channel windows. The filter was designed with a passband shape nearly independent of the tuned resonant frequency, and successfully demonstrated, showing $\sim$1 dB loss, 20 dB of through-port extinction per stage, $>$30 dB rejection of adjacent channels, and a flat-top response.

In order to facilitate the scaling of the wavelength range accessible to finite-FSR filters, a number of architectures and designs were proposed for FSR doubling and multiplication, and for hitless switching – switching off the resonant response during tuning to avoid disturbing intermediate channels. First, universally balanced interferometers (UBIs) – a new, general class of photonic interferometers – were proposed, their properties derived and numerous applications described, including dispersion-free suppression of resonant passbands for FSR doubling and multiplication. Silicon proof of principle structures were designed (and fabricated). Second, another general approach was proposed for switching a resonant passband to a "fully transparent" state – i.e. a state where passing light sees neither substantial amplitude response nor phase/dispersive response. This too has applications for hitless switching and FSR doubling. Implementations based on variable and interferometric input couplers are discussed, and strategies that involve the joint switching of a variable input coupler and a loss coupler, which enable the full suppression of a resonant response. The first "truly hitless" microring resonator based add-drop filter, having a fully transparent response (no amplitude or phase

distortion) was demonstrated using a single-ring device. A telecom grade, fourth order truly hitless design was also fabricated, and is awaiting characterization.

When filters with high-fidelity responses can be realized on chip in silicon, it becomes of great importance to mitigate the Kramers-Kronig-limited dispersive response of sharp, flat-top filters that are needed for high spectral efficiency and tight channel packing in the spectrum. In this thesis, a new class of optical structures – loop-coupled resonators – has been proposed that allows non-minimum-phase (non-Kramers-Kronig-limited) responses, and supports optimally sharp responses with linear in-band phase response over 80% of the channel bandwidth. On the one hand these structures enable optical designs to benefit from a wealth of microwave design literature dealing with equivalent structures. On the other hand, it is found that microring-based (traveling-wave) loop-coupled structures have more general responses than reciprocal standing-wave cavities typically used in microwave design. A new parameter, called the loop-coupling phase, is defined to index this difference and to quantify the key parameters of loop coupled resonators. Furthermore, high-order optical resonator designs based on the introduced loop-coupling concept were shown that operate as optical delay lines and allow, in principle, over 3,000,000 bitslots of delay without substantial distortion of the pulse shape. With optimally sharp and phase-linearized responses it is believed that these structures will find important applications in telecom add-drop filters, as well as in microwave photonics as satellite transponder channelizers, sensors due to the sharp possible response edges, and other applications.

When microphotonic circuits of this complexity are assembled into a complete system on a chip, such as a chip-scale tunable OADM, the number of devices makes inevitable in-plane waveguide crossings. In this work, a novel approach to waveguide crossing design is described based on searching for a low-loss Bloch wave with a matched periodicity to the structure. The resulting crossing array designs predict 0.04 dB of loss per exemplary crossing, and have smaller loss in arrays than in individual cascaded crossings.

A paramount issue for all of the described functionality is the extreme polarization dependence of HIC structures. It was shown in the analysis in Chap. 5 that individual structures tailored for polarization independent operation may require atomic-scale absolute dimensional control to maintain the polarization degeneracy against remaining fabrication errors. This makes polarization transparency nearly impossible to engineer into such a device. Instead, a symmetry based integrated polarization diversity approach, associated with this work, was demonstrated and is described in [20, 33].

In sum, efficient solutions have been found to all of the major challenges to passive strong confinement photonics, and it is expected that SC photonic circuits, with the major benefits they offer, will soon begin gaining acceptance in wider practical applications, with support from some of the presented results. The

developments in this thesis have demonstrated the design techniques, waveguide design strategies and device topologies that enable strong confinement photonics to reach their potential.

Future work

The work presented in this thesis leaves further avenues to be pursued in future work in several ways. The future work is divided into three categories: relatively immediate, unfinished (design or experimental) work on the concepts and designs presented in this work some of which are under way, work on more sophisticated device designs suggested here which require new future projects, and less immediate and less well defined general new research directions suggested by this work.

First, owing to time and thesis length constraints, many of the results of this work are presented here in abbreviated form, such as the work included in appendices, including the mode solver, loop-coupled resonators, low-loss Bloch-wave structures, SiN filters, asymmetric SCC filter designs, and contradirectional coupling model used for cavity loss extraction. Also, the design approaches used to arrive at the results are sometimes left out all together, and brief feasibility arguments given to the reader. The latter include topics such as the filter synthesis methods used, which in some cases are new or have novel aspects, and other results that simply include more convenient forms of known results; the electromagnetic design analysis (state-variable CMT and space scattering methods), finite difference simulations and contributions to the simulation methods, and in particular the complex-frequency mode solver; the physical effects that give rise to coupler loss and efficient approaches for reducing coupler loss (as used in Sec. 7.1). One of the most important topics that was not explicitly covered is general approaches for combining both hitless tuning and FSR multiplication functionality in a resonant filter, based on a combination of UBIs, interferometric coupling and other approaches. One goal for future work will be to provide a more complete account of these parts of this work.

Custom, rigorous simulation tools have been developed for this work, including a rigorous mode solver for leaky resonant cavities, and an integrated finite-difference-based mode-matching solver that efficiently optimizes adiabatic structures. Another worthwhile pursuit would be the conditioning of these tools for public release*.

Second, several experimental results have been presented in preliminary form, with further optical characterization planned, particularly in the later, more complex devices. In particular, a complete T-OADM channel add-drop filter has been

*At the time of writing, some of the tools – the complex-frequency mode solver, and soon the mode-matching code – are available by request from the author.

designed and fabricated in silicon is awaiting testing. Similarly, simple proof-of-principle experimental demonstrations of broadband, adiabatic couplers, broadband Mach-Zehnder interferometers, and UBI-based ring FSR multiplication have been prepared in the same silicon platform used for the Si devices presented here, and await optical characterization. Furthermore, in the presented devices, it is of interest to carry out an experimental characterization of the thermal properties (temperature profiles and limiting factors to maximizing speed and temperature), and electromigration and oxidation limitations in the microheaters. Some characterization remains for the results presented, such as directly carrying out full-FSR tuning of the tunable fourth-order microring filters, in order to compare the experimental passband shapes vs. tuned wavelength to the behaviour expected from design. The first experimental demonstration of loop-coupled resonators is also included among the devices such as the fourth order tunable filter, with a smaller gap between ring 1 and 4, and an appropriate geometry tilt (see Appendix C). This characterization work is to be brought to completion[†].

Third, and most importantly, this work has left unaddressed many problems that the investigations here suggest, some of which were indicated in the corresponding chapters. With reference to work in Chap. 2, it is of interest to investigate the characteristic phase bound for other classes of devices such as active 4-ports, and to further investigate symmetry-based approaches to the approximation of a general optical inverse operator. It is also of interest to consider the applicability of the UBI to other fields of study in which coherent wave systems are dealt with, such as quantum computation. With reference to work in Chap. 4, it is of interest to further investigate the design methods and applications for CIFS-free resonator designs. With reference to work in Chap. 5, it is of interest to consider applications for the polarization rotation mechanism that (at least locally) avoids the necessity of symmetry breaking. Furthermore, for the experimental Si work in this thesis we opted for the optimized TE design from Chap. 5 due to uncertainty over issues arising in practice with polarization crosstalk in the TM designs. It would be of interest to experimentally evaluate the merits of the proposed TM (MC-STM) designs, as they offer equal performance to optimized TE designs presented here, but have critical dimensions of twice the size (better), and are easily suitable for fabrication by deep-UV lithography. With reference to Chap. 8 on UBIs, it is of interest to consider in greater detail the practical feasibility of folded UBIs that require integrated circulators, and also of the proposed photonic circuit hot-swapping concept. Experimental demonstrations would be ideal vehicles to carry out such an evaluation.

[†]We obtained some preliminary results on similar fourth-order loop-coupled structures in 2004, in the same fabrication run as the multistage filters in Sec. 7.1, using SiN microrings. In these devices, the microrings were not successfully frequency compensated, so a flat-top passband was not obtained, but the physical spectral signatures of the basic loop coupling concept were already demonstrated in this experiment.

Finally, some of the concepts presented here, such as UBIs, loop-coupled resonators, and switching resonant systems into minimum-phase transparent states are very general. This makes it not entirely straightforward to predict all of their future applications. It is hoped that the most interesting concepts and devices based on the work presented here will yet result from its continuation by other researchers.

Bibliography

[1] A. L. Schawlow and C. H. Townes, "Infrared and optical masers," *Phys. Rev.*, vol. 112, no. 6, pp. 1940–1949, Dec 1958. [cited on p. 15]

[2] T. H. Maiman, "Stimulated optical radiation in ruby," *Nature*, vol. 187, no. 4736, pp. 493–494, Aug. 1960. [Online]. Available: http://dx.doi.org/10.1038/187493a0 [cited on p. 15]

[3] C. H. Townes, "Obituary: Theodore H. Maiman (1927-2007)," *Nature*, vol. 447, no. 7145, pp. 654–654, June 2007. [Online]. Available: http://dx.doi.org/10.1038/447654a [cited on p. 15]

[4] M. L. Povinelli, M. Lončar, M. Ibanescu, E. J. Smythe, S. G. Johnson, F. Capasso, and J. D. Joannopoulos, "Evanescent-wave bonding between optical waveguides," *Opt. Lett.*, vol. 30, pp. 3042–3044, Nov. 2005. [cited on p. 15]

[5] M. Eichenfield, C. P. Michael, R. Perahia, and O. Painter, "Actuation of micro-optomechanical systems via cavity-enhanced optical dipole forces," *Nat. Photon.*, vol. 1, no. 7, pp. 416–422, July 2007. [Online]. Available: http://dx.doi.org/10.1038/nphoton.2007.96 [cited on p. 15]

[6] P. T. Rakich, M. A. Popović, M. Soljačić, and E. P. Ippen, "Trapping, corralling and spectral bonding of optical resonances via optically induced potentials," *Nature Photonics*, 2007, accepted for publication. [cited on p. 15]

[7] L. V. Hau, S. E. Harris, Z. Dutton, and C. H. Behroozi, "Light speed reduction to 17 metres per second in an ultracold atomic," *Nature*, vol. 397, no. 6720, pp. 594–598, Feb. 1999. [Online]. Available: http://dx.doi.org/10.1038/17561 [cited on p. 16]

[8] H. A. Haus, B. E. Little, M. A. Popović, S. T. Chu, M. R. Watts, and C. Manolatou, "Optical resonators and filters," in *Optical Microcavities*, ser. Advanced Series in Applied Physics, K. Vahala, Ed. Singapore: World Scientific, 2004. [cited on p. 17, 34, 73, 92, 178, 239, 266, 267, and 329]

[9] T. Miya, "Silica-based planar lightwave circuits: passive and thermally active devices," *IEEE J. Select. Topics Quantum Electron.*, vol. 6, no. 1, pp. 38–45, Jan. 2000. [cited on p. 17, 95, and 115]

[10] W. R. Headley, G. T. Reed, F. Gardes, A. Liu, and M. Paniccia, "Enhanced polarization-independent optical ring resonators on silicon-on-insulator," in *Proceedings of the SPIE, Optoelectronic Integration on Silicon II*, J. A. Kubby and G. E. Jabbour, Eds., vol. 5730, no. 1. SPIE, 2005, pp. 195–202. [Online]. Available: http://link.aip.org/link/?PSI/5730/195/1 [cited on p. 18]

[11] S. John, "Strong localization of photons in certain disordered dielectric superlattices," *Phys. Rev. Lett.*, vol. 58, no. 23, pp. 2486–2489, June 1987. [cited on p. 18]

[12] E. Yablonovitch, "Inhibited spontaneous emission in solid-state physics and electronics," *Phys. Rev. Lett.*, vol. 58, no. 20, pp. 2059–2062, May 1987. [cited on p. 18]

[13] H. A. Haus, "Micro ring add-drop filters," MIT Optics and Quantum Electronics Group, Research Memo, 1994. [cited on p. 18]

[14] C. Manolatou, S. G. Johnson, S. Fan, P. R. Villeneuve, H. A. Haus, and J. D. Joannopoulos, "High-density integrated optics," *J. Lightwave Technol.*, vol. 17, no. 9, pp. 1682–1692, Sept. 1999. [cited on p. 18, 36, 248, 325, 328, and 345]

[15] B. E. Little, S. T. Chu, and H. A. Haus, "Micro-ring resonator channel dropping filters," in *Proceedings of the 8th Annual Meeting of the IEEE Lasers and Electro-Optics Society*, vol. 2. San Francisco, CA, USA: IEEE, Oct 1995, pp. 233–234. [cited on p. 18]

[16] C. Manolatou and H. A. Haus, *Passive components for dense optical integration*. Boston, MA: Kluwer Academic Publishers, 2002. [cited on p. 18, 248, 325, 328, and 330]

[17] B. E. Little, J. S. Foresi, G. Steinmeyer, E. R. Thoen, S. T. Chu, H. A. Haus, E. P. Ippen, L. C. Kimerling, and W. Greene, "Ultra-compact Si-SiO_2 microring resonator optical channel dropping filters," *IEEE Photon. Technol. Lett.*, vol. 10, no. 4, pp. 549–551, 1998. [cited on p. 18, 96, and 237]

[18] D. Rafizadeh, J. P. Zhang, S. C. Hagness, A. Taflove, K. A. Stair, S. T. Ho, and R. C. Tiberio, "Waveguide-coupled AlGaAs/GaAs microcavity ring and disk resonators with high finesse and 21.6-nm free spectral range," *Opt. Lett.*, vol. 22, no. 16, pp. 1244–1246, 1997. [cited on p. 18]

[19] T. Barwicz, "Accurate nanofabrication techniques for high-index-contrast microphotonic devices," Ph.D. dissertation, Massachusetts Institute of Technology, Cambridge, MA, USA, 2005. [cited on p. 18]

[20] M. R. Watts, "Polarization independent microphotonic circuits," Ph.D. dissertation, Massachusetts Institute of Technology, Cambridge, MA, USA, 2005. [cited on p. 18, 137, 175, 281, and 345]

[21] P. T. Rakich, "Optical studies of photonic crystals and high-index-contrast microphotonic circuits," Ph.D. dissertation, Massachusetts Institute of Technology, Cambridge, MA, 2006. [cited on p. 18, 175, and 305]

[22] T. E. Murphy, "Integrated optical grating-based matched filters for fiber-optic communications," Master's thesis, Massachusetts Institute of Technology, Cambridge, MA, Feb. 1996. [cited on p. 19 and 34]

[23] R. Ramaswami and K. N. Sivarajan, *Optical Networks: A Practical Perspective*, 2nd ed. San Francisco, CA: Morgan Kaufmann Publishers, 2002. [cited on p. 19 and 21]

[24] C. R. Giles and M. Spector, "The wavelength add/drop multiplexer for lightwave communication networks," *The Bell System Technical Journal*, pp. 207–229, Jan.–Mar. 1999. [cited on p. 22]

[25] T. Shiragaki, N. Henmi, M. Fujiwara, M. Misono, T. Shiozawa, and S. Suzuki, "Optical cross-connect system incorporated with newly developed operation and management system," *IEEE J. Select. Areas Commun.*, vol. 16, no. 7, pp. 1179–1189, Sept. 1998. [cited on p. 22]

[26] C. R. Doerr, L. W. Stulz, D. S. Levy, R. Pafchek, M. Cappuzzo, L. Gomez, A. Wong-Foy, E. Chen, E. Laskowski, G. Bogert, and G. Richards, "Wavelength add-drop node using silica waveguide integration," *J. Lightwave Technol.*, vol. 22, no. 12, pp. 2755–2762, 2004. [cited on p. 22]

[27] R. E. Scotti, C. K. Madsen, C. H. Henry, G. Lenz, Y. P. Li, H. Presby, and A. White, "A hitless reconfigurable add-drop multiplexer for WDM networks utilizing planar waveguides, thermo-optic switches and UV-induced gratings," in *Technical Digest of the Optical Fiber Communication Conference (OFC)*, San Jose, CA, 1998, pp. 142–143. [cited on p. 22]

[28] M. Margalit and E. Cohen, "Hitless filter tuning," United States Patent Application US2003/0156780A1, 2003. [cited on p. 22 and 199]

[29] B. Meekers and R. Maerz, "Arrangement for the implementation of an add/drop method in wavelength division multiplex transmission of optical signals," U.S. Patent 6,025,943, 2000. [cited on p. 22 and 199]

[30] K. Buse, F. Havermeyer, W. Liu, L. Moser, and D. Psaltis, "Holographic filters," in *Photorefractive Materials and Their Applications*, P. Gunter and J. P. Huignard, Eds., vol. 2–3. Springer, 2006. [cited on p. 22]

[31] M. R. Watts, "Wavelength switching and routing through evanescently induced absorption," Master's thesis, Massachusetts Institute of Technology, Cambridge, MA, 2001. [cited on p. 23, 95, 98, 112, 175, 237, and 339]

[32] M. R. Watts and H. A. Haus, "Integrated mode-evolution-based polarization rotators," *Optics Letters*, vol. 30, no. 2, pp. 138–140, May 2005. [Online]. Available: http://www.opticsinfobase.org/abstract.cfm?URI=OL-30-2-138 [cited on p. 23 and 102]

[33] T. Barwicz, M. R. Watts, M. A. Popović, P. T. Rakich, L. Socci, F. X. Kärtner, E. P. Ippen, and H. I. Smith, "Polarization-transparent microphotonic devices in the strong confinement limit," *Nature*, vol. 1, no. 1, pp. 57–60, Jan. 2007. [cited on p. 23, 98, 112, 137, 175, 281, and 345]

[34] F. X. Kärtner, S. Akiyama, G. Barbastathis, T. Barwicz, H. Byun, D. T. Danielson, F. Gan, F. Grawert, C. W. Holzwarth, J. L. Hoyt, E. P. Ippen, M. Kim, L. C.

Kimerling, J. Liu, J. Michel, O. O. Olubuyide, J. S. Orcutt, M. Park, M. Perrott, M. A. Popović, P. T. Rakich, R. J. Ram, H. I. Smith, and M. R. Watts, "Electronic photonic integrated circuits for high speed, high resolution, analog to digital conversion," in *Proceedings of the SPIE, Silicon Photonics*, J. A. Kubby and G. T. Reed, Eds., vol. 6125, no. 1. SPIE, 2006, p. 612503. [Online]. Available: http://link.aip.org/link/?PSI/6125/612503/1 [cited on p. 24]

[35] F. X. Kärtner, R. Amatya, G. Barbastathis, H. Byun, F. Gan, C. W. Holzwarth, J. L. Hoyt, E. P. Ippen, O. O. Olubuyide, J. S. Orcutt, M. Park, M. Perrott, M. Popović, P. T. Rakich, R. J. Ram, H. I. Smith, S. Takahashi, M. Geis, M. E. Grein, T. M. Lyszczarz, S. J. Spector, and J. U. Yoon, "Silicon Electronic Photonic Integrated Circuits for High Speed Analog to Digital Conversion," in *Proceedings of 3rd IEEE International Conference on Group IV Photonics (GFP2006)*, Ottawa, Canada, 2006, pp. 203–205. [cited on p. 24]

[36] V. Belevitch, *Classical Network Theory*. San Francisco: Holden-Day, 1968. [cited on p. 32, 34, 37, and 38]

[37] E. A. J. Marcatili, "Dielectric rectangular waveguide and directional coupler for integrated optics," *The Bell System Technical Journal*, vol. 48, pp. 2071–2102, Sept. 1969. [cited on p. 33]

[38] B. E. Little, S. T. Chu, H. A. Haus, J. Foresi, and J.-P. Laine, "Microring resonator channel dropping filters," *J. Lightwave Technol.*, vol. 15, no. 6, pp. 998–1005, June 1997. [cited on p. 33, 35, 36, 39, 73, 74, 75, 76, 84, 88, 89, 91, 139, 157, 164, 171, 172, 174, 177, 244, 264, 266, 267, 268, 317, 319, 320, 322, 325, 327, 332, 333, and 349]

[39] H. J. Carlin and P. P. Civalleri, *Wideband Circuit Design*. Boca Raton, FL: CRC Press, 1998. [cited on p. 33 and 34]

[40] C. R. Giles, "Lightwave applications of fiber bragg gratings," *J. Lightwave Technol.*, vol. 15, no. 8, pp. 1391–1404, Aug. 1997. [cited on p. 34]

[41] C. Madsen and G. Lenz, "Optical all-pass filters for phase response design with applications for dispersion compensation," *IEEE Photon. Technol. Lett.*, vol. 10, no. 7, pp. 994–996, July 1998. [cited on p. 34]

[42] M. J. Khan, M. Lim, C. Joyner, T. Murphy, H. A. Haus, and H. I. Smith, "Integrated Bragg grating structures," in *Digest of the LEOS Summer Topical Meeting on WDM Components*, Copper Mountain, CO, 2001. [cited on p. 34, 36, and 81]

[43] N. Sugimoto, T. Shintaku, A. Tate, H. Terui, M. Shimokozono, E. Kubota, M. Ishii, and Y. Inoue, "Waveguide polarization-independent optical circulator," *IEEE Photon. Technol. Lett.*, vol. 11, no. 3, pp. 355–357, Mar. 1999. [cited on p. 34, 35, 224, 225, and 228]

[44] R. Levy and S. B. Cohn, "A history of microwave filter research, design, and development," *IEEE Trans. Microwave Theory Tech.*, vol. 32, no. 9, pp. 1055–1067, Sept. 1984. [cited on p. 34 and 318]

[45] E. Torgow, "Equalization of waveguide delay distortion," *IEEE Trans. Microwave Theory Tech.*, vol. 13, no. 6, pp. 756–762, Nov. 1965. [cited on p. 34]

[46] M. A. Popović, C. Manolatou, and M. R. Watts, "Coupling-induced resonance frequency shifts in coupled dielectric multi-cavity filters," *Opt. Express*, vol. 14, pp. 1208–1222, Feb. 2006. [Online]. Available: http://www.opticsinfobase.org/abstract.cfm?URI=oe-14-3-1208 [cited on p. 35, 73, 74, 173, 247, 337, 338, and 340]

[47] M. Tormen and M. Cherchi, "Wavelength-flattened directional couplers for mirror-symmetric interferometers," *J. Lightwave Technol.*, vol. 23, no. 12, pp. 4387–4392, Dec. 2005. [cited on p. 35]

[48] R. E. Collin, *Foundations for Microwave Engineering*, 2nd ed. Wiley-IEEE Press, 2001. [cited on p. 35, 36, 184, and 224]

[49] A. Melloni and M. Martinelli, "Synthesis of direct-coupled-resonators bandpass filters for WDM systems," *J. Lightwave Technol.*, vol. 20, no. 2, pp. 296–303, Feb. 2002. [cited on p. 35, 73, 74, 76, 264, 267, 268, and 349]

[50] D. M. Pozar, *Microwave Engineering*, 2nd ed. New York, NY: Wiley, 1998. [cited on p. 36]

[51] E. A. J. Marcatili, "Optical frequency filters using disk cavity," 26 Jan. 1971, US Patent 3,558,213. [cited on p. 36, 95, and 201]

[52] S. Fan, P. R. Villeneuve, J. D. Joannopoulos, and H. A. Haus, "Channel Drop Tunneling through Localized States," *Physical Review Letters*, vol. 80, no. 5, pp. 960–963, Feb. 1998. [cited on p. 36]

[53] S. Fan, P. R. Villeneuve, J. D. Joannopoulos, M. J. Khan, C. Manolatou, and H. A. Haus, "Theoretical analysis of channel drop tunneling processes," *Phys. Rev. B*, vol. 59, pp. 15 882–15 892, June 1999. [cited on p. 36, 73, 81, and 87]

[54] M. J. Khan, C. Manolatou, S. Fan, P. R. Villeneuve, H. A. Haus, and J. D. Joannopoulos, "Mode-coupling analysis of multipole symmetric resonant add/drop filters," *IEEE J. Quantum Electron.*, vol. 35, no. 10, pp. 1451–1460, Oct. 1999. [cited on p. 36, 73, 74, 87, and 325]

[55] C. Manolatou, M. J. Khan, S. Fan, P. R. Villeneuve, H. A. Haus, and J. D. Joannopoulos, "Coupling of modes analysis of resonant channel add-drop filters," *IEEE J. Quantum Electron.*, vol. 35, pp. 1322–1331, Sept. 1999. [cited on p. 36, 81, 178, 244, and 325]

[56] J. G. Proakis and D. G. Manolakis, *Digital signal processing: principles, algorithms, and applications*. Upper Saddle River, NJ: Prentice-Hall, 1996. [cited on p. 37, 210, and 267]

[57] G. Lenz, B. J. Eggleton, C. R. Giles, C. K. Madsen, and R. E. Slusher, "Dispersive properties of optical filters for WDM systems," *IEEE J. Quantum Electron.*, vol. 34, no. 8, pp. 1390–1402, Aug. 1998. [cited on p. 39 and 211]

[58] A. W. Snyder and J. D. Love, *Optical Waveguide Theory*. London, UK: Chapman and Hall, 1983. [cited on p. 41 and 69]

[59] J. Makhoul, "Author's reply to "comments and corrections to 'on the eigenvectors of symmetric toeplitz matrices' "," *IEEE Trans. Acoust., Speech, Signal Processing*, vol. 33, no. 3, pp. 737–738, June 1985. [cited on p. 41]

[60] H. A. Haus, M. A. Popović, and M. R. Watts, "Hitless switch for high-density integrated optics," U.S. Patent Application US 2005/0275921, filed Jan 2004. [cited on p. 41]

[61] M. A. Popović, "Wide free-spectral-range, widely tunable and hitless-switchable optical channel add-drop filters," International Patent Application WO2007014218, filed July 2005. [cited on p. 41 and 203]

[62] ——, "Group-delay-balanced bypass circulators and folded universally balanced interferometers," U.S. Provisional Patent App., MIT case 12289, filed Aug 2006. [cited on p. 41 and 203]

[63] M. A. Popović, E. P. Ippen, and F. X. Kärtner, "Universally balanced photonic interferometers," *Optics Letters*, vol. 31, no. 18, pp. 2713–2715, Sept. 2006. [cited on p. 42, 183, 184, 186, and 203]

[64] H. J. Carlin, "The Scattering Matrix in Network Theory," *IRE Transactions on Circuit Theory*, vol. 3, no. 2, pp. 88–97, June 1956. [cited on p. 42]

[65] H. J. Carlin and A. B. Giordano, *Network Theory: An Introduction to Reciprocal and Non-reciprocal Circuits*. Englewood Cliffs, NJ: Prentice-Hall, 1964. [cited on p. 42]

[66] K. Jinguji, N. Takato, Y. Hida, T. Kitoh, and M. Kawachi, "Two-port optical wavelength circuits composed of cascaded Mach-Zehnder interferometers with point-symmetrical configurations," *J. Lightwave Technol.*, vol. 14, no. 10, pp. 2301–2310, Oct. 1996. [cited on p. 42 and 188]

[67] H. A. Haus, *Waves and Fields in Optoelectronics*. Englewood Cliffs, NJ: Prentice-Hall, 1984. [cited on p. 43, 45, 75, 84, 85, 187, 238, 239, 240, 244, 266, and 267]

[68] A. Taflove, *Computational electrodynamics: the finite-difference time-domain method*. Boston, MA, USA: Artech House, 1995. [cited on p. 44, 149, and 326]

[69] A. Yariv, "Universal relations for coupling of optical power between microresonators and dielectric waveguides," *Electron. Lett.*, vol. 36, pp. 321–322, Feb. 2000. [cited on p. 45 and 84]

[70] A. E. Siegman, *Lasers*. Sausalito, CA: University Science Books, 1986. [cited on p. 45]

[71] C. K. Madsen and J. H. Zhao, *Optical filter design and analysis: a signal processing approach*. New York: Wiley, 1999. [cited on p. 45, 73, 76, 82, 84, 210, 211, 218, 237, and 317]

[72] L. N. Trefethen and D. Bau III, *Numerical Linear Algebra*. SIAM: Society for Industrial and Applied Mathematics, 1997. [Online]. Available: http://web.comlab.ox.ac.uk/oucl/work/nick.trefethen/text.html [cited on p. 49]

[73] G. H. Golub and C. F. Van Loan, *Matrix Computations (Johns Hopkins Studies in Mathematical Sciences)*. The Johns Hopkins University Press, October 1996. [Online]. Available: http://www.amazon.ca/exec/obidos/redirect?tag=citeulike04-20{\&}path=ASIN/0801854148 [cited on p. 49 and 56]

[74] O. Nevanlinna, *Meromorphic Functions and Linear Algebra*, ser. Fields Institute Monographs. American Mathematical Society, 2003, vol. 18. [cited on p. 49]

[75] A. Edelman and N. R. Rao, "Random matrix theory," *Acta Numerica*, vol. 14, pp. 233–297, 2005. [cited on p. 57]

[76] K. Zyczkowski and M. Kus, "Random unitary matrices," *Journal of Physics A: Mathematical and General*, vol. 27, no. 12, pp. 4235–4245, 1994. [cited on p. 57]

[77] M. L. Mehta, *Random Matrices*, 3rd ed., ser. Pure and Applied Mathematics. Academic Press, 2004, vol. 142. [cited on p. 57]

[78] H. A. Haus and W. P. Huang, "Coupled-mode theory," *Proc. IEEE*, vol. 79, pp. 1505–1518, Oct. 1991. [cited on p. 69, 75, 78, 79, 80, 85, 88, 91, and 247]

[79] C. Vassallo, *Optical Waveguide Concepts*, ser. Optical Wave Sciences and Technology. Amsterdam: Elsevier Science Publishers, 1991. [cited on p. 69]

[80] S. G. Johnson, M. Ibanescu, M. A. Skorobogatiy, O. Weisberg, J. D. Joannopoulos, and Y. Fink, "Perturbation theory for Maxwell's equations with shifting material boundaries," *Physical Review E*, vol. 65, no. 6, p. 066611, June 2002. [cited on p. 69 and 110]

[81] S. Blair and Y. Chen, "Resonant-enhanced evanescent-wave fluorescence biosensing with cylindrical optical cavities," *Appl. Opt.*, vol. 40, pp. 570–582, Feb. 2001. [cited on p. 73]

[82] P. P. Absil, J. V. Hryniewicz, B. E. Little, P. S. Cho, R. A. Wilson, L. G. Joneckis, and P.-T. Ho, "Wavelength conversion in GaAs micro-ring resonators," *Opt. Lett.*, vol. 25, pp. 554–556, Apr. 2000. [Online]. Available: http://www.opticsinfobase.org/abstract.cfm?URI=ol-25-8-554 [cited on p. 73]

[83] B. Liu, A. Shakouri, and J. E. Bowers, "Passive microring-resonator-coupled lasers," *Applied Physics Letters*, vol. 79, no. 22, pp. 3561–3563, 2001. [Online]. Available: http://link.aip.org/link/?APL/79/3561/1 [cited on p. 73]

[84] M. Lončar, T. Yoshie, A. Scherer, P. Gogna, and Y. Qiu, "Low-threshold photonic crystal laser," *Applied Physics Letters*, vol. 81, no. 15, pp. 2680–2682, Oct. 2002. [Online]. Available: http://link.aip.org/link/?APL/81/2680/1 [cited on p. 73 and 81]

[85] H. A. Haus, "Microwaves and photonics," in *OSA TOPS 23 Symposium on Electro-Optics: Present and Future*, H. A. Haus, Ed. Washington and DC: Optical Society of America, 1998, pp. 2–8. [cited on p. 73]

[86] R. Orta, P. Savi, R. Tascone, and D. Trinchero, "Synthesis of multiple-ring-resonator filters for optical systems," *IEEE Photon. Technol. Lett.*, vol. 7, no. 12, pp. 1447–1449, Dec. 1995. [cited on p. 73, 74, 76, 82, and 84]

[87] C. Manolatou, M. A. Popović, P. T. Rakich, T. Barwicz, H. A. Haus, and E. P. Ippen, "Spectral anomalies due to coupling-induced frequency shifts in dielectric coupled-resonator filters," in *Technical Digest of the Optical Fiber Communication Conference*, vol. 1, Los Angeles, CA, 23–27 Feb. 2004, paper TuD5. [cited on p. 74, 76, 337, and 338]

[88] T. Barwicz, M. A. Popović, P. T. Rakich, M. R. Watts, H. A. Haus, E. P. Ippen, and H. I. Smith, "Microring-resonator-based add-drop filters in SiN: fabrication and analysis," *Optics Express*, vol. 12, pp. 1437–1442, Apr. 2004. [Online]. Available: http://www.opticsinfobase.org/abstract.cfm?URI=oe-12-7-1437 [cited on p. 74, 91, 96, 171, 175, 331, 333, 335, 338, 339, and 340]

[89] M. A. Popović, M. R. Watts, T. Barwicz, P. T. Rakich, L. Socci, E. P. Ippen, F. X. Kärtner, and H. I. Smith, "High-index-contrast and wide-FSR microring-resonator filter design and realization with frequency-shift compensation," in *Technical Digest of the Optical Fiber Communication Conference*, Anaheim, CA, 6–11 Mar. 2005, paper OFK1. [cited on p. 74, 91, 96, 158, 159, 171, 175, 176, 204, 279, and 331]

[90] T. Barwicz, M. A. Popović, M. R. Watts, P. T. Rakich, E. P. Ippen, and H. I. Smith, "Fabrication of add-drop filters based on frequency-matched microring resonators," *J. Lightwave Technol.*, vol. 24, no. 5, pp. 2207–2218, May 2006. [cited on p. 76, 87, 112, 164, 166, 175, 279, and 343]

[91] M. Popović, "Complex-frequency leaky mode computations using PML boundary layers for dielectric resonant structures," in *Proceedings of the Integrated Photonics Research Conference*, Washington, DC, 17 June 2003. [cited on p. 77, 87, 91, 149, 325, 327, and 340]

[92] A. D. Berk, "Variational principles for electromagnetic resonators and waveguides," *IRE Trans. Antennas Propag.*, vol. 4, no. 2, pp. 104–111, Apr. 1956. [cited on p. 80]

[93] H. A. Haus, W. P. Huang, and A. W. Snyder, "Coupled-mode formulations," *Opt. Lett.*, vol. 14, pp. 1222–1224, Nov. 1989, http://www.opticsinfobase.org/abstract.cfm?URI=ol-14-21-1222. [cited on p. 80]

[94] J. Scheuer and A. Yariv, "Two-dimensional optical ring resonators based on radial Bragg resonance," *Opt. Lett.*, vol. 28, pp. 1528–1530, Sept. 2003, http://www.opticsinfobase.org/abstract.cfm?URI=ol-28-17-1528. [cited on p. 81]

[95] S. V. Boriskina, T. M. Benson, P. Sewell, and A. I. Nosich, "Effect of a layered environment on the complex natural frequencies of 2D WGM dielectric-ring resonators," *J. Lightwave Technol.*, vol. 20, pp. 1563–1572, Aug. 2002. [cited on p. 87]

[96] B. E. Little, J.-P. Laine, and S. T. Chu, "Surface-roughness-induced contradirectional coupling in ring and disk resonators," *Opt. Lett.*, vol. 22, pp. 4–6, Jan. 1997. [Online]. Available: http://www.opticsinfobase.org/abstract.cfm?URI=ol-22-1-4 [cited on p. 87]

[97] M. M. Lee and M. C. Wu, "MEMS-actuated microdisk resonators with variable power coupling ratios," *IEEE Photon. Technol. Lett.*, vol. 17, no. 5, pp. 1034–1036, May 2005. [cited on p. 89, 202, 237, and 244]

[98] M. A. Popović, T. Barwicz, E. P. Ippen, and F. X. Kartner, "Global design rules for silicon microphotonic waveguides: sensitivity, polarization and resonance tunability," in *Proceedings of the Conference on Lasers and Electro-Optics (CLEO)*, Long Beach, CA, 21–26 May 2006, paper CTuCC1. [cited on p. 93, 101, 105, 111, and 119]

[99] Y. Vlasov and S. McNab, "Losses in single-mode silicon-on-insulator strip waveguides and bends," *Optics Express*, vol. 12, no. 8, pp. 1622–1631, Apr. 2004. [cited on p. 93, 96, 108, 131, and 256]

[100] P. Rabiei and W. H. Steier, "Polymer microring resonators," in *Optical Microcavities*, ser. Advanced Series in Applied Physics, K. Vahala, Ed. Singapore: World Scientific, 2004. [cited on p. 95]

[101] S. T. Chu, B. E. Little, V. Van, J. V. Hryniewicz, P. P. Absil, F. G. Johnson, D. Gill, O. King, F. Seiferth, M. Trakalo, and J. Shanton, "Compact full C-band tunable filters for 50 GHz channel spacing based on high order micro-ring resonators," in *Technical Digest of the Optical Fiber Communication Conference (OFC)*, vol. 2, Los Angeles, CA, 23–27 Feb. 2004, postdeadline paper PDP9. [cited on p. 95]

[102] I. Christiaens, D. Van Thourhout, and R. Baets, "Low-power thermo-optic tuning of vertically coupled microring resonators," *Electronics Letters*, vol. 40, no. 9, pp. 560–561, Apr. 2004. [cited on p. 95]

[103] P. Rabiei, W. H. Steier, C. Zhang, and L. R. Dalton, "Polymer micro-ring filters and modulators," *J. Lightwave Technol.*, vol. 20, no. 11, pp. 1968–1975, Nov. 2002. [cited on p. 95]

[104] M. V. Kotlyar, L. O'Faolain, A. B. Krysa, and T. F. Krauss, "Electrooptic tuning of InP-based microphotonic Fabry-Perot filters," *J. Lightwave Technol.*, vol. 23, no. 6, pp. 2169–2174, June 2005. [cited on p. 95]

[105] R. Grover, T. A. Ibrahim, S. Kanakaraju, L. Lucas, L. C. Calhoun, and P.-T. Ho, "A tunable GaInAsP-InP optical microring notch filter," *IEEE Photon. Technol. Lett.*, vol. 16, no. 2, pp. 467–469, Feb. 2004. [cited on p. 95]

[106] P. T. Rakich, M. A. Popović, M. R. Watts, T. Barwicz, H. I. Smith, and E. P. Ippen, "Ultrawide tuning of photonic microcavities via evanescent field perturbation," *Optics Letters*, vol. 31, no. 9, pp. 1241–1243, May 2006. [cited on p. 95 and 327]

[107] G. A. Magel, "Integrated optic devices using micromachined metal membranes," in *Proceedings of the SPIE: Integrated Optics and Microstructures III*, M. Tabib-Azar, Ed., vol. 2686, no. 1. SPIE, Mar. 1996, pp. 54–63. [Online]. Available: http://link.aip.org/link/?PSI/2686/54/1 [cited on p. 95 and 201]

[108] L. Eldada, "Organic photonics," in *Microphotonics: Hardware for the information age*, L. C. Kimerling, Ed., Cambridge, MA, USA, 2005. [cited on p. 95]

[109] L. Eldada and L. W. Shacklette, "Advances in polymer integrated optics," *IEEE J. Select. Topics Quantum Electron.*, vol. 6, no. 1, pp. 54–68, Jan. 2000. [cited on p. 95]

[110] W.-Y. Chen, R. Grover, T. A. Ibrahim, V. Van, W. N. Herman, and P.-T. Ho, "High-finesse laterally coupled single-mode benzocyclobutene microring resonators," *IEEE Photon. Technol. Lett.*, vol. 16, no. 2, pp. 470–472, Feb. 2004. [cited on p. 95]

[111] J. Niehusmann, A. Vörckel, P. H. Bolivar, T. Wahlbrink, W. Henschel, and H. Kurz, "Ultrahigh-quality-factor silicon-on-insulator microring resonator," *Optics Letters*, vol. 29, no. 24, pp. 2861–2863, Dec. 2004. [cited on p. 96]

[112] V. R. Almeida, C. A. Barrios, R. R. Panepucci, and M. Lipson, "All-optical control of light on a silicon chip," *Nature*, vol. 431, no. 7012, pp. 1081–1084, 2004. [cited on p. 96]

[113] J. Guo, G. A. Vawter, M. J. Shaw, G. R. Hadley, P. Esherick, A. Jain, C. R. Alford, and C. T. Sullivan, "Characterization of Si_3N_4/SiO_2 planar lightwave circuits and ring resonators," in *Proceedings of the SPIE: Optical Components and Materials*, M. J. F. Digonnet and S. Jiang, Eds., vol. 5350, no. 1. SPIE, June 2004, pp. 13–22. [Online]. Available: http://link.aip.org/link/?PSI/5350/13/1 [cited on p. 96]

[114] K. K. Lee, D. R. Lim, L. C. Kimerling, J. Shin, and F. Cerrina, "Fabrication of ultralow-loss Si/SiO_2 waveguides by roughness reduction," *Opt. Lett.*, vol. 26, no. 23, pp. 1888–1890, Dec. 2001. [cited on p. 96]

[115] M. Melchiorri, N. Daldosso, F. Sbrana, L. Pavesi, G. Pucker, C. Kompocholis, P. Bellutti, and A. Lui, "Propagation losses of silicon nitride waveguides in the near-infrared range," *Applied Physics Letters*, vol. 86, no. 12, p. 121111, Mar. 2005. [Online]. Available: http://link.aip.org/link/?APL/86/121111/1 [cited on p. 96]

[116] T. Baehr-Jones, M. Hochberg, C. Walker, and A. Scherer, "High-Q ring resonators in thin silicon-on-insulator," *Applied Physics Letters*, vol. 85, no. 16, pp. 3346–3347, Oct. 2004. [Online]. Available: http://link.aip.org/link/?APL/85/3346/1 [cited on p. 96]

[117] S. J. Spector, M. W. Geis, D. M. Lennon, R. C. Williamson, and T. M. Lyszczarz, "Hybrid multi-mode/single-mode waveguides for low loss," in *Proceedings of the Integrated Photonics Research Conference*, San Francisco, CA, June 2004, paper IThE5. [cited on p. 96 and 131]

[118] A. Säynätjoki, S. Arpiainen, J. Ahopelto, and H. Lipsanen, "High-index-contrast Optical Waveguides on Silicon," in *Physics of Semiconductors: 27th International Conference on the Physics of Semiconductors – ICPS-27*, J. Menéndez and C. G. V. de Walle, Eds., vol. 772, no. 1. AIP, 2005, pp. 1537–1538. [Online]. Available: http://link.aip.org/link/?APC/772/1537/1 [cited on p. 96]

[119] M. A. Popović, T. Barwicz, M. R. Watts, P. T. Rakich, L. Socci, E. P. Ippen, F. X. Kärtner, and H. I. Smith, "Multistage high-order microring-resonator add-drop filters," *Optics Letters*, vol. 31, no. 17, pp. 2571–2573, Sept. 2006. [cited on p. 96, 150, 158, 159, 164, 166, 279, 317, and 331]

[120] Y. Yanagase, S. S. Suzuki, Y. Kokubun, and S. T. Chu, "Box-like filter response and expansion of FSR by a vertically triple coupled microring resonator filter," *J.*

Lightwave Technol., vol. 20, no. 8, pp. 1525–1529, Aug. 2002. [cited on p. 98, 155, 203, 207, 332, and 338]

[121] K. Oda, N. Takato, and H. Toba, "A wide-FSR waveguide double-ring resonator for optical FDM transmission systems," *J. Lightwave Technol.*, vol. 9, no. 6, pp. 728–736, June 1991. [cited on p. 98, 155, 203, and 207]

[122] M. A. Popović, "Air trenches for dense silica integrated optics," Master's thesis, Massachusetts Institute of Technology, Cambridge, MA, USA, 2002. [cited on p. 99 and 117]

[123] E. C. M. Pennings, "Bends in optical ridge waveguides: Modeling and experiments," Ph.D. dissertation, T.U. Delft, The Hague, Netherlands, 1990. [cited on p. 99]

[124] M. Popović, K. Wada, S. Akiyama, H. A. Haus, and J. Michel, "Air trenches for sharp silica waveguide bends," *J. Lightwave Technol.*, vol. 20, no. 9, pp. 1762–1772, Sept. 2002. [cited on p. 117 and 328]

[125] "n, k database," in *New Semiconductor Materials Archive*. Ioffe Physico-Technical Institute, St. Petersburg, Russian Federation, 2007. [Online]. Available: http://www.ioffe.rssi.ru/SVA/NSM/nk/index.html [cited on p. 118]

[126] "General specifications for 300 mm standard UNIBOND™ SOI wafers," *Soitec Online Product Information*, 2007. [Online]. Available: http://www.soitec.com/en/products/p_6.htm [cited on p. 128]

[127] T. Barwicz and H. A. Haus, "Three-Dimensional Analysis of Scattering Losses Due to Sidewall Roughness in Microphotonic Waveguides," *J. Lightwave Technol.*, vol. 23, no. 9, p. 2719, Sept. 2005. [cited on p. 131, 132, 133, and 191]

[128] F. Xia, L. Sekarić, and Y. Vlasov, "Ultracompact optical buffers on a silicon chip," *Nat. Photon.*, vol. 1, no. 1, pp. 65–71, Jan. 2007. [Online]. Available: http://dx.doi.org/10.1038/nphoton.2006.42 [cited on p. 131 and 203]

[129] D. K. Armani, T. J. Kippenberg, S. M. Spillane, and K. J. Vahala, "Ultra-high-Q toroid microcavity on a chip," *Nature*, vol. 421, no. 6926, pp. 925–928, Feb. 2003. [Online]. Available: http://dx.doi.org/10.1038/nature01371 [cited on p. 132]

[130] M. R. Watts, H. A. Haus, and E. P. Ippen, "Integrated mode-evolution-based polarization splitter," *Optics Letters*, vol. 30, no. 9, pp. 967–969, May 2005. [Online]. Available: http://www.opticsinfobase.org/abstract.cfm?URI=OL-30-9-967 [cited on p. 137]

[131] C. W. Holzwarth, T. Barwicz, and H. I. Smith, "Optimization of hydrogen silsesquioxane films for photonic applications," in *Proceedings of the 51st International Conference on Electron, Ion and Photon Beam Technology and Nanofabrication*, Denver, Colorado, May 2007, paper PA-10. [cited on p. 141 and 142]

[132] T. Barwicz, C. W. Holzwarth, P. T. Rakich, M. A. Popović, E. P. Ippen, F. X. Kartner, and H. I. Smith, "Metallic-contamination-induced optical loss in passive silicon waveguides and resonators," in *Proceedings of the Conference on Lasers and Electro-Optics (CLEO)*, Baltimore, MD, 10 May 2007, paper CTuG5. [cited on p. 142]

[133] D. F. Edwards, "Silicon (Si)," in *Handbook of Optical Constants of Solids*, E. D. Palik, Ed., vol. 1. Academic, 1985, pp. 547–569. [cited on p. 151]

[134] J. A. McCaulley, V. M. Donnelly, M. Vernon, and I. Taha, "Temperature dependence of the near-infrared refractive index of silicon, gallium arsenide, and indium phosphide," *Phys. Rev. B*, vol. 49, no. 11, pp. 7408–7417, Mar. 1994. [cited on p. 151]

[135] F. Gan, T. Barwicz, M. A. Popović, M. S. Dahlem, C. W. Holzwarth, P. T. Rakich, H. I. Smith, E. P. Ippen, and F. X. Kärtner, "Maximizing the thermo-optic tuning range of silicon photonic structures," in *Proceedings of the IEEE/LEOS Photonics in Switching Conference*, San Francisco, CA, Aug. 2007, paper TuB3.3. [cited on p. 152, 153, 156, 261, and 331]

[136] M. A. Popović, T. Barwicz, F. Gan, M. S. Dahlem, C. W. Holzwarth, P. T. Rakich, H. I. Smith, E. P. Ippen, and F. X. Kärtner, "Transparent wavelength switching of resonant filters," in *Postdeadline Papers of the Conference on Lasers and Electro-Optics (CLEO)*, Baltimore, MD, 10 May 2007, paper CPDA2. [cited on p. 153, 171, 235, 279, and 331]

[137] B. E. Little, S. T. Chu, P. P. Absil, J. V. Hryniewicz, F. G. Johnson, F. Seiferth, D. Gill, V. Van, O. King, and M. Trakalo, "Very high-order microring resonator filters for WDM applications," *IEEE Photon. Technol. Lett.*, vol. 16, no. 10, pp. 2263–5, Oct. 2004. [cited on p. 171, 332, and 338]

[138] S. T. Chu, B. Little, W. Pan, T. Kaneko, and Y. Kokubun, "Cascaded microring resonators for crosstalk reduction and spectrum cleanup in add-drop filters," *IEEE Photon. Technol. Lett.*, vol. 11, no. 11, pp. 1423–1425, Nov. 1999. [cited on p. 172]

[139] M. Scobey and R. Hallock, "Hybrid thin film WDM and optical switch devices for optical add/drop," in *Technical Digest of the Optical Fiber Communication Conference (OFC)*, vol. 2, Baltimore, MD, 7–10 Mar. 2000, pp. 335–337. [cited on p. 172]

[140] B. E. Little, S. T. Chu, J. V. Hryniewicz, and P. P. Absil, "Filter synthesis for periodically coupled microring resonators," *Opt. Lett*, vol. 25, no. 5, pp. 344–346, Mar. 2000. [cited on p. 173 and 337]

[141] A. Vörckel, M. Mönster, W. Henschel, P. H. Bolivar, and H. Kurz, "Asymmetrically coupled silicon-on-insulator microring resonators for compact add-drop multiplexers," *IEEE Photon. Technol. Lett.*, vol. 15, no. 7, pp. 921–923, July 2003. [cited on p. 178 and 203]

[142] M. A. Popović, "Optical coupled-resonator filters with asymmetric coupling," WIPO Patent Application WO2005010582 (U.S. Patent App. US/2006 0159392/A1), filed July 2003. [cited on p. 179, 180, and 201]

[143] H. A. Haus, M. A. Popović, and M. R. Watts, "Broadband hitless bypass switch for integrated photonic circuits," *IEEE Photon. Technol. Lett.*, vol. 18, no. 10, pp. 1137–1139, May 2006. [cited on p. 180, 183, 188, 189, 198, and 202]

[144] M. A. Popović, H. A. Haus, and M. R. Watts, "General approach to hitless switching and FSR extension for resonators in integrated photonic circuits," in *Technical Digest*

of the Optical Fiber Communication Conference (OFC), Anaheim, CA, 5–10 Mar. 2006, p. 3, paper OWI66. [cited on p. 183 and 203]

[145] K. Jinguji and M. Kawachi, "Synthesis of coherent two-port lattice-form optical delay-line circuit," *J. Lightwave Technol.*, vol. 13, no. 1, pp. 73–82, Jan. 1995. [cited on p. 184, 188, and 211]

[146] C. H. Henry, C. K. Madsen, and T. A. Strasser, "Article comprising a Bragg reflective Mach-Zehnder filter of reduced coupled dependence," US Patent 5,889,899, 30 Mar. 1999. [cited on p. 188]

[147] G. R. Reddy and M. N. S. Swamy, "Digital all-pass filter design through discrete hilbert transform," in *IEEE International Symposium on Circuits and Systems*, vol. 1, 1–3 May 1990, pp. 646–649. [cited on p. 197]

[148] K. Rajamani and Y.-S. Lai, "A novel method for designing allpass digital filters," *IEEE Signal Processing Lett.*, vol. 6, no. 8, pp. 207–209, Aug. 1999. [cited on p. 197]

[149] G. Jovanović-Doleček and J. Diaz-Carmona, "Digital all-pass filter design method based on complex cepstrum," *Electronics Letters*, vol. 39, no. 8, pp. 695–697, Apr. 2003. [cited on p. 197]

[150] M. Reck, A. Zeilinger, H. J. Bernstein, and P. Bertani, "Experimental realization of any discrete unitary operator," *Phys. Rev. Lett.*, vol. 73, no. 1, pp. 58–61, July 1994. [cited on p. 197]

[151] H. A. Haus, M. A. Popović, and M. R. Watts, "A hitless switch," MIT Optics and Quantum Electronics Group, Research Memo, revised May 20, 2003. [cited on p. 198]

[152] B. E. Little and T. E. Murphy, "Design rules for maximally flat wavelength-insensitive opticalpower dividers using Mach-Zehnder structures," *IEEE Photon. Technol. Lett.*, vol. 9, no. 12, pp. 1607–1609, Dec. 1997. [cited on p. 201]

[153] P. Dumon, G. Roelkens, W. Bogaerts, D. Van Thourhout, J. Wouters, S. Beckx, P. Jaenen, and R. Baets, "Basic photonic wire components in silicon-on-insulator," in *Proceedings of the 2nd IEEE International Conference on Group IV Photonics*, Antwerp, Belgium, 21–23 Sept. 2005, pp. 189–191. [cited on p. 203, 345, and 346]

[154] P. Dumon, W. Bogaerts, D. Van Thourhout, G. Morthier, R. Baets, P. Jaenen, S. Beckx, J. Wouters, T. Farrell, N. Ryan, E. Grivas, E. Kyriakis-Bitzaros, G. Halkias, and I. McKenzie, "A nanophotonic 4/spl times/4 wavelength router in silicon-on-insulator," in *Optical Fiber Communication Conference, 2006 and the 2006 National Fiber Optic Engineers Conference*, 5-10 March 2006, p. 3pp. [cited on p. 203]

[155] P. Dumon, G. Priem, L. R. Nunes, W. Bogaerts, D. van Thourhout, P. Bienstman, T. K. Liang, M. Tsuchiya, P. Jaenen, S. Beckx, J. Wouters, and R. Baets, "Linear and nonlinear nanophotonic devices based on silicon-on-insulator wire waveguides," *Jpn. J. of Appl. Phys.*, vol. 45, pp. 6589–6602, 2006. [cited on p. 203]

[156] W. Bogaerts, R. Baets, P. Dumon, V. Wiaux, S. Beckx, D. Taillaert, B. Luyssaert, J. Van Campenhout, P. Bienstman, and D. Van Thourhout, "Nanophotonic waveguides in silicon-on-insulator fabricated with cmos technology," *Lightwave Technology, Journal of*, vol. 23, no. 1, pp. 401–412, Jan. 2005. [cited on p. 203]

[157] W. Bogaerts, P. Dumon, D. V. Thourhout, D. Taillaert, P. Jaenen, J. Wouters, S. Beckx, V. Wiaux, and R. G. Baets, "Compact wavelength-selective functions in silicon-on-insulator photonic wires," *IEEE J. Select. Topics Quantum Electron.*, vol. 12, no. 6, pp. 1394–1401, Nov.–Dec. 2006. [cited on p. 203 and 345]

[158] B. Liu, A. Shakouri, and J. E. Bowers, "Wide tunable double ring resonator coupled lasers," *IEEE Photon. Technol. Lett.*, vol. 14, no. 5, pp. 600–602, May 2002. [cited on p. 203]

[159] M. Tormen, "Passive optical integrated components for telecommunication," Ph.D. dissertation, l'Universite de Nice-Sophia Antipolis, Nov. 2003. [cited on p. 203 and 237]

[160] M. Tormen, M. Cherchi, and H. A. Haus, "Optical add-filtering switching device," World Intellectual Property Organization Patent Application WO 2005/036793 A1, Sept. 2003. [cited on p. 203]

[161] M. Margalit, "Tunable optical filtering device and method," US Patent 6,839,482, Jan. 4 2005. [cited on p. 204 and 205]

[162] H. W. Bode, *Network analysis and feedback amplifier design*. New York, NY: Van Nostrand, 1945. [Online]. Available: http://amazon.com/o/ASIN/B0007FC9XO/ [cited on p. 211]

[163] T. Zaman, X. Guo, and R. J. Ram, "Integrated optical circulator in InP," in *Proceedings of the Conference on Lasers and Electro-Optics (CLEO)*, vol. 2, Baltimore, MD, 22–27 May 2005, pp. 1321–1323. [cited on p. 224]

[164] T. R. Zaman, X. Guo, and R. J. Ram, "Proposal for a polarization-independent integrated optical circulator," *IEEE Photon. Technol. Lett.*, vol. 18, no. 12, pp. 1359–1361, June 2006. [cited on p. 224]

[165] N. J. Doran and D. Wood, "Nonlinear-optical loop mirror," *Opt. Lett.*, vol. 13, no. 1, pp. 56–58, Jan. 1988. [cited on p. 225]

[166] D. Taillaert, P. Bienstman, and R. Baets, "Compact efficient broadband grating coupler for silicon-on-insulator waveguides," *Optics Letters*, vol. 29, no. 23, pp. 2749–2751, Dec. 2004. [cited on p. 227]

[167] F. van Laere, G. Roelkens, J. Schrauwen, D. Taillaert, P. Dumon, W. Bogaerts, D. van Thourhout, and R. Baets, "Compact grating couplers between optical fibers and silicon-on-insulator photonic wire waveguides with 69% coupling efficiency," in *Technical Digest of the Optical Fiber Communication Conference (OFC)*, Anaheim, CA, 5-10 Mar. 2006, pp. 1–3. [cited on p. 227]

[168] F. van Laere, M. Ayre, D. Taillaert, D. Van Thourhout, T. F. Krauss, and R. Baets, "Compact and efficient fibre-to-waveguide grating couplers in InP-membrane," in *Electronics Letters*, vol. 42, no. 6, Mar. 2006, pp. 343–345. [cited on p. 227]

[169] L. Eldada, "Hitless errorless trimmable dynamic optical add/drop multiplexer devices," US Patent 7,221,821, May 2007. [cited on p. 229]

[170] L. Domash, M. Wu, N. Nemchuk, and E. Ma, "Tunable and switchable multiple-cavity thin film filters," *J. Lightwave Technol.*, vol. 22, no. 1, pp. 126–135, Jan. 2004. [cited on p. 236]

[171] Y. Goebuchi, T. Kato, and Y. Kokubun, "Fast and stable wavelength-selective switch using double-series coupled dielectric microring resonator," *IEEE Photon. Technol. Lett.*, vol. 18, no. 3, pp. 538–540, Feb. 2006. [cited on p. 236]

[172] ——, "Multiwavelength and multiport hitless wavelength-selective switch using series-coupled microring resonators," *IEEE Photon. Technol. Lett.*, vol. 19, no. 9, pp. 671–673, May 2007. [cited on p. 236]

[173] B. E. Little, H. A. Haus, J. S. Foresi, L. C. Kimerling, E. P. Ippen, and D. J. Ripin, "Wavelength switching and routing using absorption and resonance," *IEEE Photon. Technol. Lett.*, vol. 10, no. 6, pp. 816–818, June 1998. [cited on p. 237 and 244]

[174] G. Nielson, D. Seneviratne, F. Lopez-Royo, P. Rakich, Y. Avrahami, M. Watts, H. Haus, H. Tuller, and G. Barbastathis, "Integrated wavelength-selective optical MEMS switching using ring resonator filters," *IEEE Photon. Technol. Lett.*, vol. 17, no. 6, pp. 1190–1192, June 2005. [cited on p. 237]

[175] M. Notomi, A. Shinya, S. Mitsugi, G. Kira, E. Kuramochi, and T. Tanabe, "Optical bistable switching action of Si high-Q photonic-crystal nanocavities," *Optics Express*, vol. 13, no. 7, pp. 2678–2687, Apr. 2005. [cited on p. 237]

[176] Y. Li, J. Yu, S. Chen, Y. Li, and Y. Chen, "Submicrosecond rearrangeable nonblocking silicon-on-insulator thermo-optic 4×4 switch matrix," *Optics Letters*, vol. 32, no. 6, pp. 603–604, Mar. 2007. [cited on p. 242]

[177] Z. Wang, Z. Fan, J. Xia, S. Chen, and J. Yu, "Rearrangeable nonblocking thermo-optic 4×4 switching matrix in silicon-on-insulator," *IEE Proc.-Optoelectron.*, vol. 152, no. 3, pp. 160–162, June 2005. [cited on p. 242]

[178] M. P. Earnshaw, J. B. D. Soole, M. Cappuzzo, L. Gomez, E. Laskowski, and A. Paunescu, "Compact, low-loss 4×4 optical switch matrix using multimode interferometers," *Electronics Letters*, vol. 37, no. 2, pp. 115–116, Jan. 2001. [cited on p. 242]

[179] M. F. Yanik and S. Fan, "Stopping and storing light coherently," *Phys. Rev. A*, vol. 71, no. 1, p. 013803, Dec. 2005. [Online]. Available: http://link.aps.org/abstract/PRA/v71/e013803 [cited on p. 243]

[180] G. Lenz, B. J. Eggleton, C. K. Madsen, and R. E. Slusher, "Optical delay lines based on optical filters," *IEEE J. Quantum Electron.*, vol. 37, no. 4, pp. 525–532, Apr. 2001. [cited on p. 243]

[181] Z. Wang and S. Fan, "Compact all-pass filters in photonic crystals as the building block for high-capacity optical delay lines," *Phys. Rev. E*, vol. 68, no. 6, p. 066616, Dec. 2003. [cited on p. 243]

[182] W. Suh, Z. Wang, and S. Fan, "Temporal coupled-mode theory and the presence of non-orthogonal modes in lossless multimode cavities," *IEEE J. Quantum Electron.*, vol. 40, no. 10, pp. 1511–1518, Oct. 2004. [cited on p. 267]

[183] R. Regener and W. Sohler, "Loss in low-finesse Ti:$LiNbO_3$ optical waveguide resonators," *Appl. Phys. B: Lasers and Optics*, vol. 36, no. 3, pp. 143–147, Mar. 1985. [cited on p. 305 and 306]

[184] L. S. Yu, Q. Z. Liu, S. A. Pappert, P. K. L. Yu, and S. S. Lau, "Laser spectral linewidth dependence on waveguide loss measurements using the Fabry–Perot method," *Applied Physics Letters*, vol. 64, no. 5, pp. 536–538, Jan. 1994. [Online]. Available: http://link.aip.org/link/?APL/64/536/1 [cited on p. 305 and 307]

[185] D. F. Clark and M. S. Iqbal, "Simple extension to the Fabry-Perot technique for accurate measurement of losses in semiconductor waveguides," *Optics Letters*, vol. 15, no. 22, pp. 1291–1293, Nov. 1990. [cited on p. 306]

[186] W. J. Tomlinson and R. J. Deri, "Analysis of a proposed extension to the Fabry-Perot technique for measurements of loss in semiconductor optical waveguides," *Optics Letters*, vol. 16, no. 21, pp. 1659–1661, Nov. 1991. [cited on p. 306]

[187] M. A. Popović, "Sharply-defined optical filters and dispersionless delay lines based on loop-coupled resonators and 'negative' coupling," in *Proceedings of Conference on Lasers and Electro-Optics (CLEO)*, Baltimore, MD, 6–11 May 2007, paper CThP6. [cited on p. 317]

[188] C. K. Madsen, "Efficient architectures for exactly realizing optical filters with optimum bandpass designs," *IEEE Photon. Technol. Lett.*, vol. 10, no. 8, pp. 1136–1138, Aug. 1998. [cited on p. 317 and 318]

[189] J. B. Khurgin, "Expanding the bandwidth of slow-light devices based on coupled resonators," *Optics Letters*, vol. 30, no. 5, pp. 513–515, Mar. 2005. [cited on p. 317 and 320]

[190] J. D. Rhodes, "A low-pass prototype network for microwave linear phase filters," *IEEE Trans. Microwave Theory Tech.*, vol. MTT-18, no. 6, pp. 290–301, June 1970. [cited on p. 318, 319, 320, 321, 323, and 356]

[191] A. E. Atia and A. E. Williams, "Nonminimum-phase optimum-amplitude bandpass waveguide filters," *IEEE Trans. Microwave Theory Tech.*, vol. MTT-22, no. 4, pp. 425–431, Apr. 1974. [cited on p. 318 and 319]

[192] R. Levy, "Filters with single transmission zeros at real or imaginary frequencies," *IEEE Trans. Microwave Theory Tech.*, vol. MTT-24, no. 4, pp. 172–181, Apr. 1976. [cited on p. 318]

[193] R. Levy, R. V. Snyder, and G. M. Matthaei, "Design of microwave filters," *IEEE Trans. Microwave Theory Tech.*, vol. 50, no. 3, pp. 783–793, Mar. 2002. [cited on p. 318]

[194] R. J. Cameron, "General coupling matrix synthesis methods for chebyshev filtering functions," *IEEE Trans. Microwave Theory Tech.*, vol. 47, no. 4, pp. 433–442, Apr. 1999. [cited on p. 318]

[195] A. E. Atia, A. E. Williams, and R. W. Newcomb, "Narrow-band multiple-coupled cavity synthesis," *IEEE Trans. Circuits Syst.*, vol. CAS-21, no. 5, pp. 649–655, Sept. 1974. [cited on p. 318]

[196] H. A. Bethe, "Theory of diffraction by small holes," *Phys. Rev.*, vol. 66, no. 7/8, pp. 163–182, Oct. 1944. [cited on p. 318]

[197] M. A. Popović, "Optical coupled-resonator structures based on loop-coupled cavities and loop-coupling phase," US Patent Application, filed 4 May 2007. [cited on p. 322]

[198] S. G. Johnson, C. Manolatou, S. Fan, P. R. Villeneuve, J. D. Joannopoulos, and H. A. Haus, "Elimination of cross talk in waveguide intersections," *Opt. Lett.*, vol. 23, no. 23, pp. 1855–1857, Dec. 1998. [cited on p. 325]

[199] J.-P. Berenger, "A perfectly matched layer for the absorption of electromagnetic waves," *Journal of Computational Physics*, vol. 114, no. 2, pp. 185–200, Oct. 1994. [cited on p. 326]

[200] K. Radhakrishnan and W. C. Chew, "An efficient Krylov-subspace-based algorithm to solve the dielectric-waveguide problem," *IEEE Trans. Microwave Theory Tech.*, vol. 49, no. 7, pp. 1345–1348, July 2001. [cited on p. 326]

[201] F. L. Teixeira and W. C. Chew, "PML-FDTD in cylindrical and spherical grids," *IEEE Microwave Guided Wave Lett.*, vol. 7, no. 9, pp. 285–287, Sept. 1997. [cited on p. 326]

[202] W. P. Huang, C. L. Xu, W. Lui, and K. Yokoyama, "The perfectly matched layer boundary condition for modal analysis of optical waveguides: Leaky mode calculations," *IEEE Photon. Technol. Lett.*, vol. 8, no. 5, pp. 652–654, May 1996. [cited on p. 326]

[203] W. C. Chew, "Electromagnetic theory on a lattice," *Journal of Applied Physics*, vol. 75, no. 10, pp. 4843–4850, May 1994. [cited on p. 326 and 327]

[204] N. N. Feng, G. R. Zhou, C. Xu, and W. P. Huang, "Computation of full-vector modes for bending waveguide using cylindrical perfectly matched layers," *J. Lightwave Technol.*, vol. 20, no. 11, pp. 1976–1980, Nov. 2002. [cited on p. 327]

[205] M. A. Popović, T. Barwicz, M. S. Dahlem, F. Gan, C. W. Holzwarth, P. T. Rakich, H. I. Smith, E. P. Ippen, and F. X. Kärtner, "Tunable, Fourth-Order Silicon Microring-Resonator Add-Drop Filters," in *Proceedings of European Conference on Optical Communication (ECOC)*, Berlin, Germany, 17 Sept. 2007, paper 1.2.3. [cited on p. 331]

[206] B. E. Little, "Advances in microring resonators," in *Proceedings of Integrated Photonics Research Conference*, Washington, DC, USA, 2003, pp. 16–20. [cited on p. 332]

[207] J. V. Hryniewicz, P. P. Absil, B. E. Little, R. A. Wilson, and P.-T. Ho, "Higher order filter response in coupled microring resonators," *IEEE Photon. Technol. Lett.*, vol. 12, no. 3, pp. 320–322, Mar. 2000. [cited on p. 332, 333, and 338]

[208] B. E. Little, "A VLSI Photonic Platform," in *Proceedings of the Optical Fiber Communication Conference (OFC)*, vol. 2, 2003, pp. 444–445. [cited on p. 332 and 338]

[209] T. Barwicz and H. I. Smith, "Evolution of line-edge roughness during fabrication of high index-contrast microphotonic devices," *J. Vac. Sci. Technol. B*, vol. 21, no. 6, pp. 2892–2896, Nov.–Dec. 2003. [cited on p. 334]

[210] M. A. Popović, E. P. Ippen, and F. X. Kärtner, "Low-loss Bloch waves in open structures and highly compact, efficient Si waveguide-crossing arrays," in *Proceedings of the 20th Annual Meeting of the IEEE Lasers and Electro-Optics Society (LEOS)*, Lake Buena Vista, Florida, Oct. 2007, paper MF5. [cited on p. 345]

[211] M. A. Popović, T. Barwicz, M. R. Watts, P. T. Rakich, M. S. Dahlem, F. Gan, C. W. Holzwarth, L. Socci, H. I. Smith, F. X. Kärtner, E. P. Ippen, and H. I. Smith, "Strong-confinement microring resonator photonic circuits (Invited)," in *Proceedings of the 20th Annual Meeting of the IEEE Lasers and Electro-Optics Society (LEOS)*, Lake Buena Vista, Florida, Oct. 2007, paper TuCC3. [cited on p. 345]

[212] T. Fukazawa, T. Hirano, F. Ohno, and T. Baba, "Low Loss Intersection of Si Photonic Wire Waveguides," *Japanese Journal of Applied Physics*, vol. 43, no. 2, pp. 646–647, Feb. 2004. [cited on p. 345 and 346]

[213] W. Bogaerts, P. Dumon, D. Van Thourhout, and R. Baets, "Low-loss, low-crosstalk crossings for SOI nanophotonic waveguides," *Opt. Lett.*, accepted for publication. [cited on p. 345 and 346]

[214] H. R. Stuart, "Waveguide lenses with multimode interference for low-loss slab propagation," *Optics Letters*, vol. 28, no. 22, pp. 2141–2143, Nov. 2003. [cited on p. 345 and 346]

[215] H. Liu, H. Tam, P. K. A. Wai, and E. Pun, "Low-loss waveguide crossing using a multimode interference structure," *Optics Communications*, vol. 241, no. 1-3, pp. 99–104, 2004. [cited on p. 345 and 346]

[216] H. Chen and A. W. Poon, "Low-loss multimode-interference-based crossings for silicon wire waveguides," *IEEE Photon. Technol. Lett.*, vol. 18, no. 21, pp. 2260–2262, Nov. 2006. [cited on p. 345 and 346]

[217] G. Goubau and F. Schwering, "On the guided propagation of electromagnetic wave beams," *IEEE Trans. Antennas Propagat.*, vol. 9, no. 3, pp. 248–256, May 1961. [cited on p. 345 and 346]

Appendices

Appendix A

Loss characterization methods

This appendix describes two practical loss characterization methods that were tailored to provide accurate estimates of loss in strongly confined, high-index-contrast waveguides in the experimental SiN and Si photonic device demonstrations described in this work. These are the Fabry-Perot method, and a weakly-coupled-cavity method. Comments are made on both that are relevant for the accurate characterization of losses in high index contrast photonic circuits.

Several methods were used for experimentally characterizing losses in the waveguides and devices described elsewhere in this work*: the Fabry-Perot method [183, 184], the cutback method, direct camera imaging of the decay length [21], and a weakly-coupled-cavity method. The cutback method and camera method are straightforward and provide trustworthy results for large enough levels of loss, in practice on the order of 10 dB/cm and above for chips on the order of 0.5 cm in length. In the former case, the limitation is resolving the difference in losses between two lengths of waveguide, while in the latter the decay length must be on the order of the camera window size, or a few of them, and certainly not substantially larger than the chip length. These methods are not described further because they are unchanged in the context of high index contrast waveguides.

The remaining two methods, the Fabry-Perot method and the weakly-coupled-cavity method, enable characterization of a large range of losses including very low propagation losses, and have aspects that are worth addressing in the context of high index contrast in the following sections.

The first is the well-known Fabry-Perot method, where light launched into a chip-integrated waveguide reflects from the end-facets, and the fringe contrast together with an predicted end-facet reflectivity is used to estimate the loss. Here, the sensitivity of the Fabry-Perot method is analyzed and the optimal round-trip loss is found for high-accuracy determination of loss. Based on this result, the

*The loss characterizations were done primarily by P.T. Rakich.

facet-to-facet waveguide length can be chosen based on an estimated expected level of propagation loss.

The second method makes use of a single-ring-cavity drop filter that is weakly coupled so that the loss Q of the cavity dominates the total Q of the structure. This provides a direct measurement of internal cavity loss, which may be extrapolated to waveguide propagation loss. This method is an improvement over the typically used critically-coupled resonator approach for two reasons. First, it is shown that only two resonators are needed per order of magnitude in detectable loss range, whereas critically coupled resonators require a greater number of devices, and rely on the quality of fitting through-port data. Second, the weakly-coupled-cavity method has a waveguide-cavity coupling that is much lower than the round trip loss, whereas they are equal in the critically-coupled resonator. Waveguide-cavity coupling may, by itself, be lossy and may incur losses typically an order of magnitude smaller than the coupling itself, or larger, without careful design, as described briefly in Sec. 5.2.3, Chap. 6, Appendix E and Sec. 7.1.

Fabry-Perot method for strong-confinement waveguides

Propagation loss of waveguides on a planar photonic chip with reflective end facets can be determined by the so-called Fabry-Perot method [183].The waveguide and reflective chip end-facets form a (typically low-Q) cavity. The fringe contrast in the transmission spectrum is measured and the loss extracted from an estimated (measured or calculated) waveguide length and end-facet reflection coefficients. One of the drawbacks of the Fabry-Perot method is its sensitivity to uncertainty or error in the reflection coefficient, for example due to uncertainty in the quality of the facet cleave. Although it has been proposed that the need for knowing reflection coefficients can be eliminated with a modified Fabry-Perot technique that uses transmission and reflection data [185], this approach has been shown to be applicable in only a very limited range of parameters [186].

In this section, two issues related to the Fabry-Perot method are addressed. First, sensitivity of the loss estimate to error in observed fringe contrast is derived, and it is found that there is an optimum round-trip loss level in the waveguide that provides the lowest relative error. Second, it is pointed out that the facet reflection coefficients must be considered from a rigorous standpoint, and Snell's law calculations based on the effective index method of the waveguide and air index can give errors as large as a factor of 2. A physical explanation for this is that strongly-confined waveguides with sub-wavelength mode cross-sections have an effective index on the air side of the facet that is not 1.0 but well below 1.0 due to their strong lateral confinement at the facet. A simple formula is given that corrects this to first order.

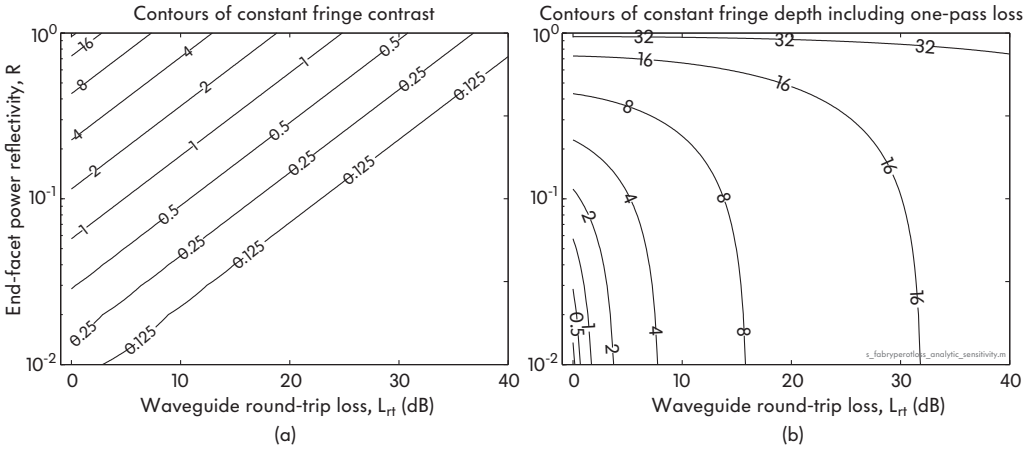

Figure A.1: Fabry-Perot waveguide loss measurement method: (a) contours of constant fringe contrast for various waveguide round-trip losses and end-facet reflectivities; (b) contours of constant fringe depth, including single-pass loss.

Error sensitivity of Fabry-Perot waveguide loss method

The loss rate, L_{dBcm}, is determined by three parameters: chip length l_{cm}, end-facet power reflectivity R (for different facets 1 and 2, $R \equiv \sqrt{R_1 R_2}$), and fringe intensity contrast $I_{\max}/I_{\min}$. The round trip waveguide loss in dB, L_{dBrt}, is [184]

$$L_{\mathrm{dBrt}} = -20 \log_{10} \left(\frac{1}{R} \frac{\sqrt{\frac{I_{\max}}{I_{\min}}} - 1}{\sqrt{\frac{I_{\max}}{I_{\min}}} + 1} \right)$$

Given waveguide length l_{cm}, the propagation loss rate L_{dBcm} (in dB/cm) can be found from $L_{\mathrm{dBrt}} \equiv 2 L_{\mathrm{dBcm}} l_{\mathrm{cm}}$. Figure A.1(a) shows contours of constant fringe contrast, $I_{\max}/I_{\min}$ in dB, vs. reflectivity and waveguide round-trip loss. Large enough fringe contrast, that exceeds the signal-level measurement uncertainty, is needed for small measurement error. The fringe pattern also has an absolute insertion loss, and must stay above the optical background noise floor. Figure A.1(b) shows contours of maximum insertion loss of the fringe pattern (assuming $T = 1 - R$).

It is important to estimate the sensitivity of the error in computed loss rate L_{dBcm} to errors in the three input parameters ($I_{\max}/I_{\min}$, R and l_{cm}) in order to place error bars on the resulting loss and design better experiments for loss characterization. The sensitivity is computed by first-order perturbation. For error analysis, the "true" values of physical variables are subscripted with a nought (x_{o}), experimentally obtained values are left unsubscripted (x), and the error (δx) is the difference such that $x \equiv x_{\mathrm{o}} + \delta x$.

Sensitivity to relative errors in inputs

Let us define the fringe contrast in dB as $\Delta I_{\mathrm{dB}} \equiv 10\log_{10}(I_{\max}/I_{\min})$. The relative errors are related to first order in the input errors by

$$\begin{aligned}\frac{\delta L_{\mathrm{dBcm}}}{L_{\mathrm{dBcm,o}}} &\approx -\frac{\delta l_{\mathrm{cm}}}{l_{\mathrm{cm,o}}} - \frac{1}{\ln\left(\frac{\ln 10}{40}\frac{\Delta I_{\mathrm{dB,o}}}{R_{\mathrm{o}}}\right)}\left(\frac{\delta R}{R_{\mathrm{o}}} - \frac{\delta\Delta I_{\mathrm{dB}}}{\Delta I_{\mathrm{dB,o}}}\right)\\ &\approx -\frac{\delta l_{\mathrm{cm}}}{l_{\mathrm{cm,o}}} - \frac{8.686}{L_{\mathrm{dBrt,o}}}\left(\frac{\delta R}{R_{\mathrm{o}}} - \frac{\delta\Delta I_{\mathrm{dB}}}{\Delta I_{\mathrm{dB,o}}}\right)\end{aligned}$$

The "loss magnification" coefficient with respect to fringe contrast is an approximation valid for $R_{\mathrm{o}} \cdot 10^{-L_{\mathrm{dBrt,o}}/20} \ll 1$ (it's twice smaller at ~ 0.8). The error magnification with respect to reflectivity and fringe contrast errors is large if the true round trip loss $L_{\mathrm{dBrt,o}} \ll 8.686\,\mathrm{dB}$. To minimize relative errors, measuring a large round trip loss is optimal.

Sensitivity to absolute dB error in fringe contrast

"Absolute" error $\delta\Delta I_{\mathrm{dB}}$ in the dB fringe contrast, ΔI_{dB}, represents a *relative* error in the fringe intensity ratio $I_{\max}/I_{\min}$, so it's relevant to explicitly state its effect on the *relative* error in computed loss:

$$\begin{aligned}\frac{\delta L_{\mathrm{dBcm}}}{L_{\mathrm{dBcm,o}}} &\propto -\frac{1-\left(R_o 10^{-L_{\mathrm{dBrt,o}}/20}\right)^2}{2R_o 10^{-L_{\mathrm{dBrt,o}}/20} L_{\mathrm{dBrt,o}}}\delta\Delta I_{\mathrm{dB}}\\ &\approx -\frac{1}{2R_o 10^{-L_{\mathrm{dBrt,o}}/20} L_{\mathrm{dBrt,o}}}\delta\Delta I_{\mathrm{dB}}.\end{aligned} \tag{A.1}$$

Here, the magnification factor is *minimized*, i.e. optimal, for $L_{\mathrm{dBrt,o}} \approx 8.686\,\mathrm{dB}$ (with a value $-0.156/R_o$). For large waveguide round trip losses ($\gg 8.686$ dB/rt), the fringes wash out (small contrast), and errors thus become large. Small waveguide losses ($\ll 8.686$ dB/rt), on the other hand, give large fringe contrast, but the fringe contrast is dominated by the "loss" due to the end-facet mirrors. The relative error of the total round trip loss (including mirror loss) would thus be smaller, but translates to a higher relative error in the extracted waveguide loss which is now a small fraction of the round trip loss.

Figure A.2 shows exactly computed contours of constant error magnification coefficient in equation (A.1) vs. reflectivity and waveguide round trip loss. The blue dash-dot line indicates the error-minimizing round-trip loss with respect to an absolute error in the dB fringe contrast for each value of end-facet reflectivity ($\sim 8.686\,\mathrm{dB}$ for small reflectivities). The red lines give the range of round-trip losses which give within a factor of 2 of the minimum error magnification, for each reflectivity.

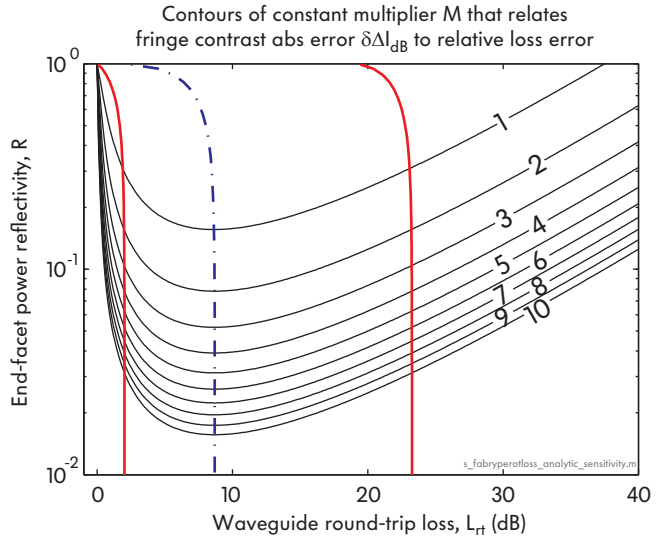

Figure A.2: Fabry-Perot waveguide loss method: contours of constant error magnification factor for the relative error in the $L_{\mathrm{dB/cm}}$ loss value show that the lowest error is obtained for a round-trip waveguide loss of about 8.7 dB.

Effect of noise floor on fringe contrast $\delta\Delta I_{\mathrm{dB}}$

One source of a *relative error* in $\delta\Delta I_{\mathrm{dB}}$ is a constant optical noise floor N dB below the bottom of the fringes. Such a noise floor contributes a reduction in fringe contrast

$$\frac{\delta\Delta I_{\mathrm{dB}}}{\Delta I_{\mathrm{dB,o}}} \approx \frac{1}{1+10^{N/20}} \approx 10^{-N/20}.$$

Conclusions

For accurate Fabry-Perot measurement of waveguide propagation loss, it is desirable to have a large fringe contrast in order to minimize uncertainty in its determination, but also a waveguide round-trip loss that is comparable to or larger than the end-facet reflection "loss". It appears that a round-trip waveguide loss of ~9 dB is optimal with as high a reflectivity as can be achieved.

Perhaps there is a down side to too high a fringe contrast, where an optical noise floor would deteriorate the measurement. This is to be quantified.

A second issue is that in low loss waveguides extending the length to obtain the optimal 9 dB loss per round trip will make the fringe free-spectral range (FSR) narrower and make measurement more difficult.

Weakly-coupled cavity method

In this section, a particularly suitable method for characterizing the loss in strongly confined waveguides is proposed. Such waveguides are capable of making micron-

scale bends with negligible loss. Therefore using weakly (under-) coupled microring resonators, where the loss Q dominates, gives a direct route to evaluating loss.

This method is particularly useful when scanning electron beam lithography (SEBL) is used. SEBL introduces stitching errors at field boundaries during exposure. As a result the waveguide loss comprises stitching loss and waveguide propagation loss due to roughness, absorption, etc. Since microring resonators typically fit within a field, the relevant loss for their loss Q values should exclude stitching.

A simple coupled-mode theory in time model can be used to model a microring resonator weakly coupled to an input waveguide and a bus. The idea is to have waveguide couplings weaker than the round-trip ring losses, so that the linewidth is dominated by the loss, and an experimental measurement of the linewidth provides a direct loss Q measurement (which can be translated to the equivalent propagation loss). However, the waveguide coupling cannot be too weak as the signal level in the drop port would be too low.

Fig. A.3(a) shows three design curves which can be used to design a loss measurement experiment using ring resonators. Plotted against the external Q (waveguide coupling) to loss Q (internal propagation losses) ratio are the on-resonance transmission in the drop port, the fraction of power lost on-resonance in the through port, and the fraction by which the true intrinsic linewidth associated with loss is overestimated by the actual linewidth that includes waveguide coupling.

To have an error in intrinsic linewidth of less than 20%, the figure shows that we need $Q_e/Q_o > 10$ (this means the drop-port response must be at least 15 dB below the off-resonance through-port signal level). Of course, the intrinsic linewidth could be disembedded from the total linewidth by computing the expected couplings, but the idea is not to require precise knowledge of the coupling gaps and coupling strengths. This is because such a loss characterization method is typically used in the early stages of a process development for making waveguides, when the uncertainty on dimensions and coupling strengths may be large. Furthermore, it is desirable not to require rigorous numerical simulations (and accurate knowledge of the refractive indices and dimensions) to compute the coupling coefficients.

The second limitation is signal level. If we assume that about 15–20 dB of contrast is required in the drop-port response to define a Lorentzian response with high quality for a good linewidth fit, and we assume a reasonable measurement dynamic range of 35–40 dB below the through-port signal level, then the response peak should not dip lower than about 25 dB below the through-port. This requires $Q_e/Q_o < \sqrt{100} \sim 30$.

Finally, it is desirable that the through-port response not exhibit excessive on-resonant loss from the loss cavities if several cavities are to be cascaded on one waveguide (Fig. A.4), to allow accurate measurement of loss over several orders of magnitude in possible propagation loss values. The on-resonant loss might

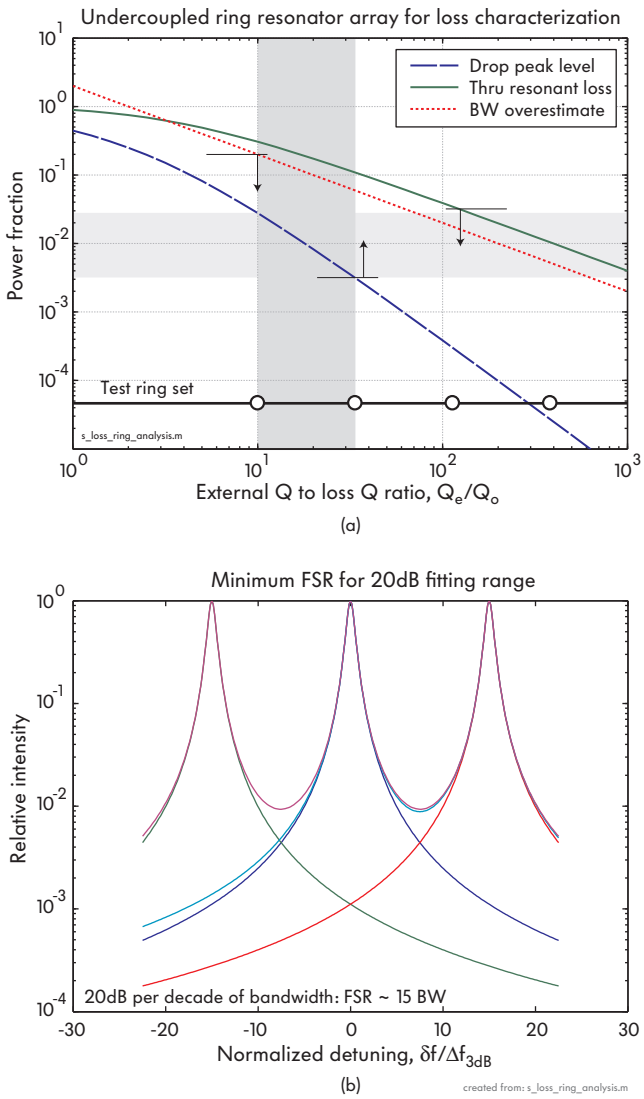

Figure A.3: (a) Contours of on-resonance drop-port insertion loss, through-port fractional power lost and bandwidth estimation error set limitations on the waveguide coupling to internal loss ratios for which a ring provides a reliable loss measurement. (b) The ring's FSR must be at least 15 times its linewidth to resolve the adjacent resonances by at least 20 dB. These constraints determine how many rings are needed per order of magnitude in the measurable loss range, and their maximum size for the loss experiment.

distort the spectral response shape of cavities down the line and make accurate extraction of linewidth from Lorentzian fits more difficult. This constraint is difficult to reconcile with the others if very low through port losses are tolerated [e.g. ~3%, shown in the Fig. A.3(a)], so we will guide the design of such an experiment using the first two. If rings are cascaded as in Fig. A.4, they can be nominally staggered in resonant frequency across the FSR to avoid substantial impact of one response on the next.

In the arrangement of Fig. A.4, the first ring has the weakest coupling and

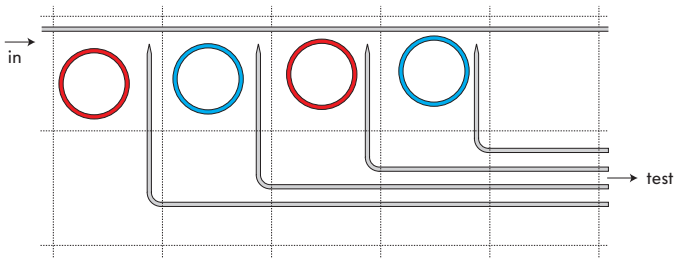

Figure A.4: A weakly-coupled-ring array loss characterization device takes up little chip area, and facilitates accurate measurement of losses spanning several orders of magnitude in Q (or dB/cm). The first ring has the weakest coupling, and subsequent rings have stronger coupling. If the first ring drop port doesn't show a measurable signal, its through port also shows no substantial distortion, and once can move onto the next ring. The first ring to show a resolvable resonance provides the loss measurement.

thus the lowest drop-port transmission and lowest through-port on-resonance loss. Further rings are progressively more strongly coupled. The first ring that shows a high enough signal level in the drop port to resolve a resonance provides the loss measurement, subject to meeting the requirements set out above (i.e. being at least 15 dB below the through port).

How many rings are needed to cover possible loss levels in a certain range? Based on the empirical estimates and assumptions described above, Fig. A.3(a) shows that two rings are needed per order of magnitude in loss (in dB/cm), since the loss Q, Q_o, is directly related to $L_{\mathrm{dB/cm}}$ (see Appendix B). Therefore to measure any propagation loss between 1 and 10 dB/cm two rings are needed, and to measure any loss between 1 and 100 dB/cm four rings are needed. To cover uncertainties an additional ring may be added. However, the number of cavities needed is fairly small to cover a wide range of possible losses.

A final consideration is how large the ring resonators should be. Initially, one may wish to make the rings very large to approximate a straight waveguide. In practice several considerations place an upper bound on the ring size. First, if scanning electron beam lithography (SEBL) is used to fabricate the structures, a ring should be smaller than a single writing field. Secondly, depending on the expected loss level, the FSR needs to be at least large enough to permit adjacent resonances of the ring cavity to be well enough resolved. Fig. A.3(b) shows that resolving each resonance to 20 dB below the peak requires the FSR to be about 15 times wider than the 3 dB bandwidth of the resonance, which is related to the expected loss Q and propagation losses ($Q \equiv \omega_o/\Delta\omega$). Since there is a lower bound on the FSR, there is an upper bound on the ring radius. Therefore this measurement method is well suited for strong-confinement waveguides, based on high index contrast, where relatively small bend radii can be achieved (10's of microns) without substantial distortion of the waveguide mode shape in comparison to the straight waveguide mode shape.

This loss characterization method has proven to be the most reliable in the SiN

and Si microring resonator and waveguide loss characterization associated with this work.

Appendix B

Conversion formulas

This section provides handy conversions between various ways of specifying the optical loss in a traveling-wave resonator - in terms of a loss Q, a propagation loss in dB per cm ($L_{\mathrm{dB/cm}}$) or in dB per round-trip ($L_{\mathrm{dB/rt}}$), the field attenuation coefficient α (power $\sim e^{-2\alpha z}$), or the imaginary part of the complex mode effective index.

Table B.1: Conversions for ring resonator loss (radius R and wavelength λ_o in meters)

	$\times L_{\mathrm{dB/cm}}$	$\times L_{\mathrm{dB/rt}}$	$\times \alpha(\mathrm{m}^{-1})$	$\times 1/Q$	$\times \Im\{n_{\mathrm{eff}}\}$
$L_{\mathrm{dB/cm}} =$	1				
$L_{\mathrm{dB/rt}} =$	$200\pi R$	1			
$\alpha(\mathrm{m}^{-1}) =$	$\frac{\ln 10}{0.2}$	$\frac{\ln 10}{40\pi R}$	1		
$1/Q =$	$\frac{\lambda_o}{\pi n_{\mathrm{group}}}\frac{\ln 10}{0.2}$	$\frac{\lambda_o}{\pi^2 n_{\mathrm{group}}}\frac{\ln 10}{40R}$	$\frac{\lambda_o}{\pi n_{\mathrm{group}}}$	1	
$\Im\{n_{\mathrm{eff}}\} =$	$\frac{\ln 10}{0.4\pi}\lambda_o$		$\frac{\lambda_o}{2\pi}$		1

Appendix C

Loop-coupled resonators: sharply-defined optical filters and dispersionless delay lines based on coupling loops and "negative" coupling*

In this appendix, a new class of optical resonant structures based on loop-coupled cavities is proposed. The proposed coupled-optical-microcavity geometries incorporate loop coupling and "negative" ("inductive") coupling, enabling new compact microring filters and slow-light delay lines that circumvent Kramers-Kronig causality constraints, allowing optimally square-amplitude and linear-phase response over more than 80% of the passband.

Notwithstanding advances in microphotonic resonant structures [38, 71, 119, 188, 189] there is a continuing need to develop both highly spectrally efficient (sharp amplitude responses and linear phase) and compact-footprint resonant structures, motivated in part by emerging applications like photonic networks on a microprocessor. Slow-wave structures for optical delay lines and nonlinear applications also require high bandwidth utilization to permit the greatest delay in pulse lengths and enhancement. For both scenarios, series-coupled-cavity filters [38] give suboptimal, all-pole flat-top responses, and are highly dispersive over much of the passband as limited fundamentally by the Kramers-Kronig constraint (for filters, remedied by adding dispersion compensator cavities [188, 189]). Another

*This appendix reproduced nearly verbatim from my paper [187].

architecture [188] allows optimally sharp (elliptic) passbands, but its extinction is sensitive to achieving broadband 3 dB directional couplers.

In this appendix, new optical coupled-cavity geometries are proposed that allow the sharpest fundamentally achievable passbands, for a given number of used resonances, in a very compact footprint. They are also shown to support an optimal flat-top and linear-phase response, in the sense defined by Rhodes [190], over more than 80% of the passband, without compensators and with lower (minimal) filter order – responses not demonstrated previously, to the author's knowledge, in any optical device. The new salient features of these structures are:

- loop-coupling of resonators (Figs. C.1 and C.2),
- phase-sensitive (negative) coupling achieved through geometrical configuration and use of high-order resonances Fig. C.1(b)],
- optional (weak) direct coupling between the input and output waveguides,
- existence of a direct mapping of optical parameters to synthesis of linear-phase flat-top passbands in [190].

Analogs of these devices are known in several aspects in circuit theory and microwave design [190, 191], but these concepts have not yet been utilized in optics, including the different approach for flattening dispersion (than all-pass stages) discussed in [190]. Furthermore, it can be shown that optical structures based on (reciprocal) ring resonators can realize more general responses with non-symmetric distributions of transmission zeros (see Sec. 2.1), which cannot be realized in reciprocal standing-wave or lumped resonators typically used in microwaves or electronic circuits. Therefore, while a great deal of previous microwave work [44, 192–195] can be applied to the proposed photonic structures, in microring (and other hybrid) structures there appear to also be opportunities for new response types not previously investigated in the microwave field.

In metallic microwave cavities, "positive" or "negative" coupling is possible due to opposite signs of effective polarizabilities of coupling apertures placed at electric and magnetic field maxima [196]. Magnetic coupling is not possible in high-Q dielectric optical resonators for the lack of good metals and a substantial magnetic response in dielectrics at optical frequencies. However, it is still possible to achieve effective negative (inductive) coupling of optical cavities. It is proposed here to use higher-order resonant modes (at least 1 node in the electric field mode pattern), with a geometry that couples cavities in a loop, as shown in Fig. C.1(a,b). This is not a disadvantage since optical cavities often operate at high order to achieve high Q (e.g. microrings). In Fig. C.1(a), four traveling-wave (microring) resonators are coupled, each to two neighbors, arranged in a square, showing all positive couplings (by inspection of overlap integrals). By tilting this geometry by $\sim 1/8^{\text{th}}$ of the guided wavelength, fields in cavity 1 and 4 are phase-aligned so

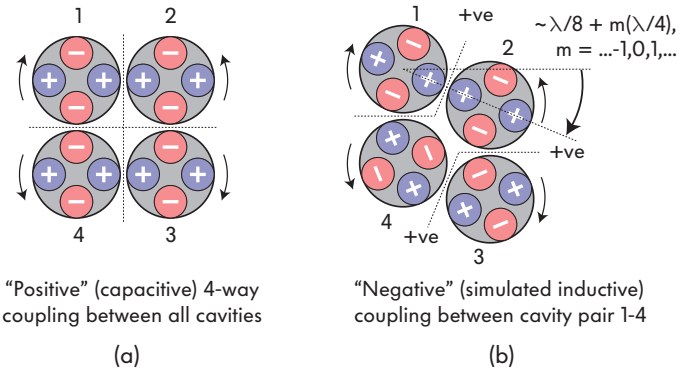

Figure C.1: Proposed loop-coupled cavity structures (couplings: 1–2, 2–3, 3–4, 4–1) based on high-order modes (traveling-wave modes illustrated). Uniquely defined product of coupling coefficients can be of either sign. Example using 4 traveling-wave cavities shows: (a) square geometry giving all positive couplings (and product), (b) one phase-reversed, "negative" coupling created by $\lambda/8$ shear-mode rotation of the coupling axis geometry.

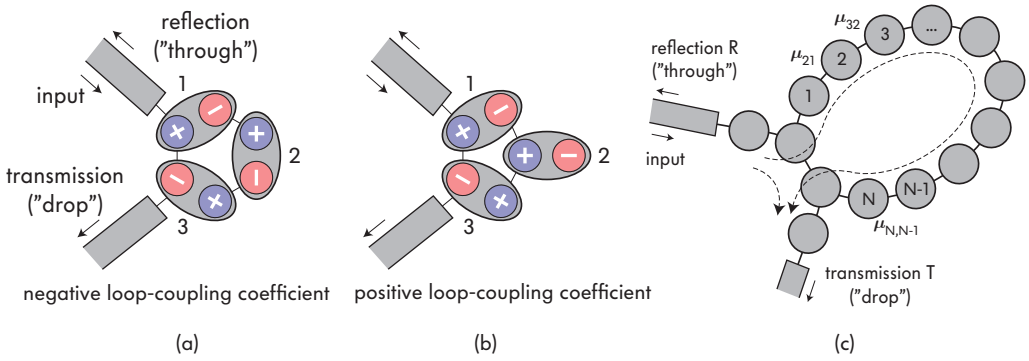

Figure C.2: Proposed loop-coupled cavity structures based on high-order cavity modes (standing-wave modes illustrated). Uniquely defined product of coupling coefficients can be of either sign. Example using 3 standing-wave cavities shows: (a) a configuration with a positive loop coupling (zero loop-coupling phase), (b) with one cavity mode rotated, "negative" coupling created by the product of couplings.

that one negative coupling is achieved [Fig. C.1(b)]. Loop coupling and negative coupling sign have nontrivial consequences for the range of realizable spectral responses [190, 191] – nulls and non-minimum-phase.

One implementation of a structure based on multiple, phase-sensitive coupling in Fig. C.1(a) is shown in Fig. C.4(a), with two rows of resonators coupled horizontally as well as vertically. With non-zero vertical couplings, a generalization of series-coupled cavities [38] is obtained that is not subject to Kramers-Kronig. This structure is extremely useful and optimal in the sense that it supports the most selective (quasi-elliptic) amplitude responses given a resonance order. Fig. C.4(b) shows how an equivalent implementation based on single-mode (non-traveling-wave), such as photonic crystal, cavities can be constructed. One 4^{th}-order filter example in Fig. C.3, based on Fig. C.1(a), shows a quasi-elliptic response (with

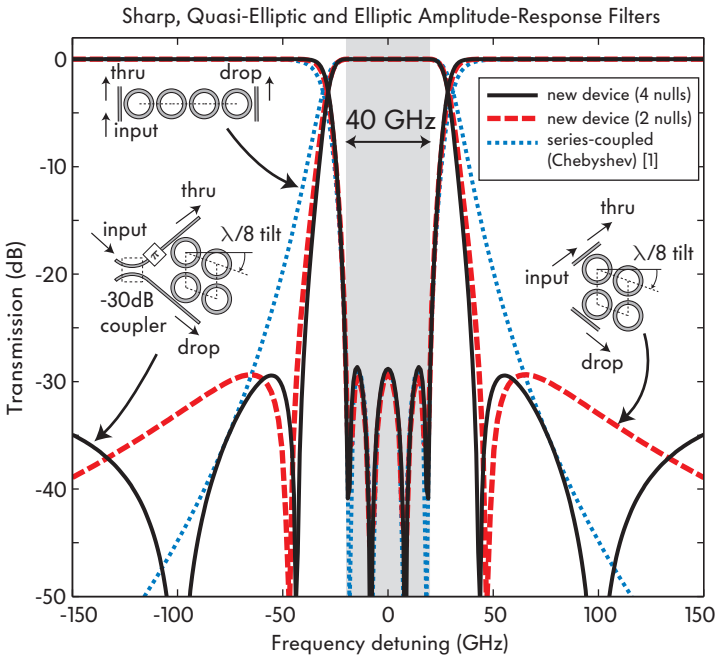

Figure C.3: (a) Compact 4th-order resonant filters with "negative" coupling between rings 1 and 4 allow realization of the sharpest achievable (quasi-elliptic) responses for a given number of used resonances, shown compared with a series-coupled cavity [38] (all designed for a 30 dB stopband). Input-output waveguide coupling is needed for the sharpest filters.

2 transmission zeros) compared to a series-cavity [38]. To achieve the sharpest possible (elliptic) transition band (here with 4 nulls), it suffices to add a properly phased, weak directional coupler directly between the input and drop waveguides, at the level of the stopband ripple (e.g. -30 dB in Fig. C.3).

Furthermore, Fig. C.4(a) can directly implement an "equidistant linear-phase polynomial" response function, proposed in [190], which simultaneously provides optimally flattened amplitude and group-delay responses. This is generally done with fewer resonators than required in an equivalent cascade of an all-pole filter followed by an all-pass dispersion compensator. A second use may be for slow-light optical delay lines. It was shown by Khurgin that adding side-coupled cavities to a series-cavity structure can cancel the lowest-order dispersion term [189]. The present structure provides optimally flattened dispersion to high order in the sense of the minimizing polynomial [190], and uses no extra resonators [see Fig. C.5(a-c)].

Fig. C.5(a) compares the new optical structure (ripple A = 1, see [190]) with a typical maximally-flat series-coupled-cavity filter [38], both of order N = 30 rings. The passband flatness and rolloff is the same. However, the new structure using the prototype in [190] sacrifices rolloff beyond 30 dB extinction, in this case, to allow optimally flattened dispersion. The difference is enormous - dispersion is

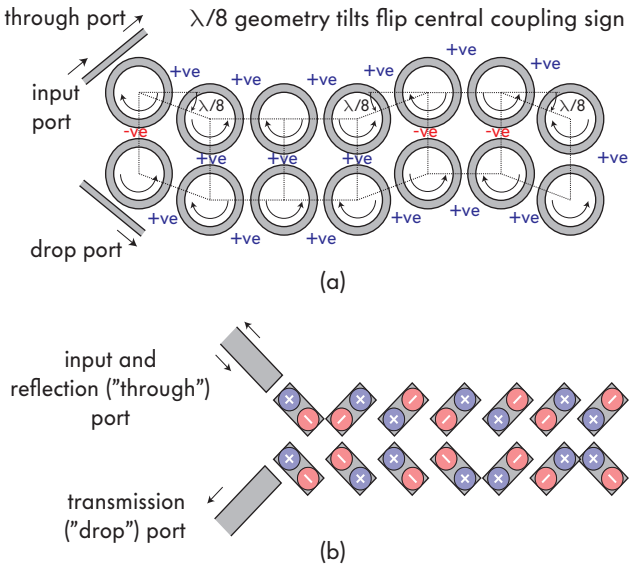

Figure C.4: Optical structures using loop-coupled resonators based on (a) traveling-wave (microring), and (b) standing-wave (e.g. PhC) cavities. High order modes with at least one electric field node are needed. The structures admit "positive" or "negative" (capacitive or simulated inductive) coupling, by proper choice of the geometry, as shown. Ring-loop tilts or standing-wave cavity rotations reverse global phase.

<20 ps/nm (typical telecom requirement) over 6% of the bandwidth in the standard design, and over 80% of the bandwidth in the new structure (and less than 0.05 ps/nm over 75% bandwidth!). A 20 ps pulse is delayed by ∼15 pulse widths, with no substantial dispersion. An exact mapping of Rhodes' prototype circuit [190] to a coupled-mode theory in time (CMT) model of this optical structure was found, as illustrated in Fig. C.6, that makes the synthesis of this type of optical device immediately accessible to practitioners:

$$\mu_{n,n+1}^2 = \mu_{N-n,N-n+1}^2 = \frac{1}{C_n C_{n+1}} \tag{C.1}$$

$$1/\tau_{in} = 1/\tau_{out} = \frac{1}{C_n} \tag{C.2}$$

$$\mu_{n,N-n+1} = \frac{K_n}{C_n} \tag{C.3}$$

for $n = 1..N/2$, where N is the filter order. The device has a symmetric coupling coefficient distribution. These formulas are used to design the structure in Fig. C.5.

In this appendix, the goal was to summarize and give a physically intuitive explanation of the principles proposed and their basic implications - loop-coupling of cavities and negative coupling coefficients (i.e. π-radian loop-coupling phase), input-output waveguide coupling, and the unique way in which dispersion flattening is achieved [190].

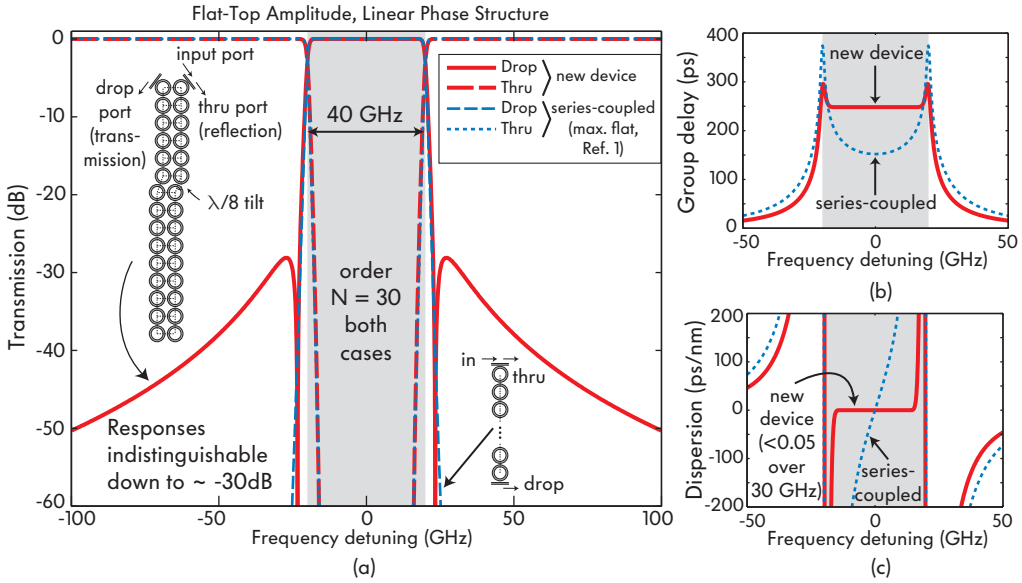

Figure C.5: Slowing light without dispersion: proposed coupled-resonator optical delay line that is dispersionless in transmission, compared with a standard series-coupled-cavity structure[38], each using $N = 30$ ring resonators. (a) amplitude responses are nearly identical above -30 dB; (b) group delay is flat and (c) dispersion near zero over 80% of the bandwidth for the new structure. The new structure can delay a pulse by over 15 pulse lengths with negligible dispersion, while simultaneously maintaining a flat, high-efficiency amplitude transmission in the resonant passband.

A more detailed description of the proposed structures, which defines a new physical parameter – the *loop-coupling phase* – and shows a few other designs is described in [197].

The proposed structures are expected to have important applications. Potential applications include: channel add-drop filters for high spectral efficiency photonic networks for telecommunication applications as well as for intrachip photonic networks for next-generation microprocessors; dispersion-compensated filters; slow-wave resonator-based structures for sensors, channelized modulators, amplifiers, wavelength converters, and coupled-cavity nonlinear optics in general. Another example application is in microwave photonics, where the flat-top, linear-phase microphotonic filters may be used in combination with an optical modulator to replace microwave satellite transponder filters, thereby reducing the size and weight of the payload. The flat-top, linear-phase microphotonic filters may also be used in terrestrial microwave filtering, such as in spectral slicing filters in cellular telephone towers. These optical filter designs provide added degrees of freedom, accommodating the topology in the planar microphotonics platform, and optimum filter responses which are inaccessible to bulk technologies such as thin-film filters. These filter designs do not appear to have any substantial drawbacks in comparison to series-coupled-cavity filters, to offset the benefits. Therefore it is expected that they will replace SCC filters in at least some microphotonic filtering applications.

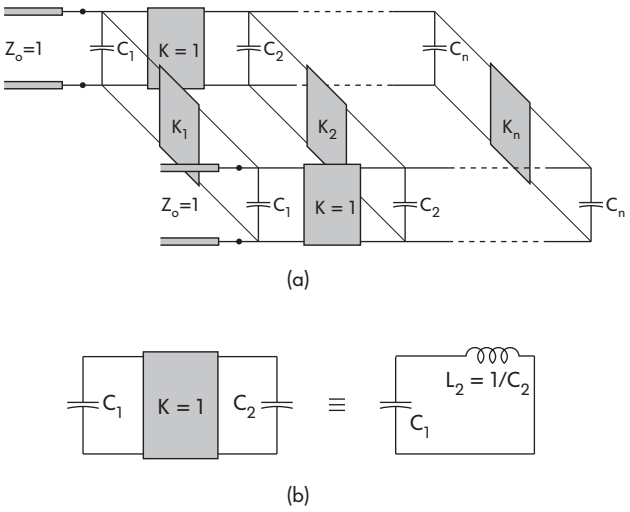

Figure C.6: (a) Symmetric, cross-coupled low-pass ladder network [190] that supports optimal flat-top, linear-phase transmission band. This circuit may be directly mapped to the optical structure in Fig. C.4; capacitors are "DC" resonators. (b) CMT coupling coefficients may be found by inspection, by considering the resonance frequency of each isolated pair of capacitors connected by an immitance inverter, which is equivalent to an LC resonator; the resonance frequency is the beat frequency at which the energy is exchanged between the capacitors (resonators).

Appendix D

Complex-frequency leaky mode solver for dielectric resonant structures*

In this appendix, a complex-frequency and complex-propagation-constant vector field mode solver is summarized, that was developed for the rigorous simulation of high-index-contrast optical waveguides and resonators described in this thesis. Perfectly matched layers are used for finite-difference computation of complex-frequency leaky modes of resonant dielectric structures in cylindrical and Cartesian coordinates. Examples of dielectric-halfspace-perturbed 3D ring resonators and 2D round, square and coupled resonators are given.

Resonant dielectric structures play an instrumental role in high-density integration of optical channel add/drop filters. Dielectric resonators coupled mutually and to waveguides can give sharp, box-like complementary bandpass and bandstop frequency responses desired in channel add/drop filters [38, 54]. Resonators are also found in proposals for high index contrast (HIC) low-crosstalk crossings [198], sharp bends [14], and fiber-chip couplers [16].

Coupling of modes in time (CMT) has been a successful theory for dealing with coupled resonant cavity modes, e.g. in ring [38] or square-resonator filters [14, 16, 54, 55]. Complex-frequency supermodes, where the imaginary frequency component accounts for decay in the case of a finite Q, are the natural solutions which result from a CMT treatment of coupled resonators with no driving term.

A mode solver for the complex-frequency modes of a resonant structure can be used to find the individual resonator parameters (modes of interest, frequencies, Q's) for a CMT analysis. It also allows comparison of the exact supermodes with the

*This appendix reproduced nearly verbatim from my paper [91].

CMT result. Studying the mode structure gives insight into the physical operation of the device and can be of help in fine-tuning the predictions of approximate analytic methods like CMT. Some effects of resonator coupling not usually included in first-order CMT include coupling-induced resonance frequency shift (CIFS, see Chap. 4.1) and a coupling-modified supermode radiation Q. These are accessible to computation.

Energy modes of dielectric resonators, even in lossless dielectric media, have a fundamental radiation loss – a finite unloaded Q. Thus methods to compute them must handle outgoing radiation and a complex resonant frequency representative of the decay, where the quality factor is directly extracted from the complex frequency, $Q \equiv -\omega_{\mathrm{R}}/(2\omega_{\mathrm{I}})$ ($Q > 0$ for loss in the $e^{j\omega t}$ convention).

I present the use of PML boundary layers [199] for the direct computation of leaky mode complex frequencies and field distributions for dielectric resonant structures. The full-vector Maxwell's equations for the transverse electric field, cast as an eigenvalue problem with complex-frequency (squared) eigenvalue, are solved on a 2D domain of interest bound by radiation-absorbing PMLs. Here, the domain can be a $\rho - z$ cross-section of a cylindrically symmetric 3D resonant structure (with radial dimension ρ and axial dimension z), the cross-section of a 3D Cartesian-geometry waveguide, or the $x - y$ plane of a 2D resonant system.

The cylindrical finite-difference (FD) formulation in this paper is on the Yee grid, similar to the finite-difference time-domain (FDTD) method [68], but in the frequency domain as in [200]. PMLs, extended to cylindrical coordinates in [201], are used to pad the edges of the computational domain. Huang *et al.* first applied PMLs to a 1D, Cartesian complex propagation constant FD modesolver [202].

Using Chew's notation [203] for difference equations on the Yee grid, the cylindrical-geometry eigenvalue equation solved here for leaky modes is (assuming a diagonal, spatially-varying permittivity tensor $\bar{\bar{\epsilon}}$ and a constant, scalar permeability μ)

$$\left[\begin{array}{c|c} -\hat{\partial}_z\tilde{\partial}_z - \frac{1}{\rho^2_{m+\frac{1}{2}}}\tilde{\partial}_\rho \frac{\rho_m}{\epsilon^{\phi\phi}_{\mathbf{m}}}\hat{\partial}_\rho \rho_{m+\frac{1}{2}}\epsilon^{\rho\rho}_{\mathbf{m}} & \hat{\partial}_z\tilde{\partial}_\rho - \frac{1}{\rho^2_{m+\frac{1}{2}}}\tilde{\partial}_\rho \frac{\rho^2_m}{\epsilon^{\phi\phi}_{\mathbf{m}}}\hat{\partial}_z \epsilon^{zz}_{\mathbf{m}} \\ \hline \frac{1}{\rho_m}\hat{\partial}_\rho \rho_{m+\frac{1}{2}}\tilde{\partial}_z - \frac{1}{\rho_m}\tilde{\partial}_z \frac{1}{\epsilon^{\phi\phi}_{\mathbf{m}}}\hat{\partial}_\rho \rho_{m+\frac{1}{2}}\epsilon^{\rho\rho}_{\mathbf{m}} & -\frac{1}{\rho_m}\hat{\partial}_\rho \rho_{m+\frac{1}{2}}\tilde{\partial}_\rho - \tilde{\partial}_z \frac{1}{\epsilon^{\phi\phi}_{\mathbf{m}}}\hat{\partial}_z \epsilon^{zz}_{\mathbf{m}} \end{array}\right] \cdot \left[\begin{array}{c} E^\rho_{m+\frac{1}{2},n} \\ E^z_{m,n+\frac{1}{2}} \end{array}\right] =$$
$$= \left(\omega^2\mu \left[\begin{array}{c|c} \epsilon^{\rho\rho}_{\mathbf{m}} & \\ \hline & \epsilon^{zz}_{\mathbf{m}} \end{array}\right] - \gamma^2 \left[\begin{array}{c|c} \frac{1}{\rho^2_{m+\frac{1}{2}}} & \\ \hline & \frac{1}{\rho^2_m} \end{array}\right]\right) \cdot \left[\begin{array}{c} E^\rho_{m+\frac{1}{2},n} \\ E^z_{m,n+\frac{1}{2}} \end{array}\right]. \tag{D.1}$$

Grid points are marked by $\mathbf{m} = (m, n)$, $(m + 1/2, n)$ or $(m, n + 1/2)$ in the 2D domain; the tilde ($\sim$) and caret ($\hat{}$) identify forward and backward differences on the grid [203]. Here, γ is the angular propagation constant of a mode of the cylindrical structure (propagation $e^{-j\gamma\phi}$), and equals the order of the resonance; ω is the resonant frequency; ρ and z are interpreted as complex coordinates, as defined in [201].

For complex-frequency modes, Eq. (D.1) is rearranged so that ω^2 is the eigenvalue on the RHS of the equation. By rearranging to isolate γ^2 instead, a complex-propagation-constant eigenvalue problem for power modes is obtained. The latter form has applications in evaluating full-vector complex-β modes of bent waveguides in cylindrical coordinates. The complex-β variant, in a similar formulation, was published by Feng *et al.* [204] independently of this work [91]. Some differences exist between the two formulations in that the present work uses the Yee grid formulation [203] which affords rigorously consistent adjoint operators and overlap integrals (to be shown elsewhere). In view of this work, here the will focus be placed primarily on the computation of complex-frequency modes.

The eigenmode equation (D.1) is adapted to Cartesian geometry if one interprets z as y, ϕ as z, γ as β, and ρ as x in the derivatives only and $\rho \to 1$ elsewhere. This is used to simulate straight waveguides. In the frequency domain, as used here, the PML boundary condition acts as complex coordinate stretching. By extending the PML from being confined to the edges of the computational domain to covering the entire computational domain, and by allowing a real coefficient in the PML that provides real coordinate stretching, a simple and smooth non-uniform grid generation is obtained. This is used for accurate, inexpensive computation of high-index-contrast waveguide cross-sections, and particularly for optimization problems where waveguide dimensions are varied by minute amounts by a zero-finding algorithm, as used in Chap. 5.

Here, the utility of this mode solver is demonstrated with a number of examples of practical interest. The structures shown are designed for low radiation Q here, so that radiation absorbed by the PML is visible in the plots. In practice, of course, high Q is desirable.

The first example given is a 3D air-clad ring resonator on a slight undercladding pedestal (Fig. D.1), perturbed by a high-index dielectric halfspace in proximity[†]. The ring could be part of a coupled-ring channel add/drop filter, e.g. of a topology as in [38]. The core and cladding indices are 2.2 and 1.445, and the waveguide dimensions are a 1.05 μm width, 0.33 μm core height on a pedestal 0.1 μm above the cladding surface, and a 4.25 μm outer radius. In the absence of the dielectric, the resonant frequency of the TE-like mode is 1552 nm with a radiation Q of 1706 (not shown). Lowering the high-index (n = 2.0) dielectric halfspace to a 250 nm displacement from the ring produces a second leakage path [Fig. D.1(a)]. The loss Q is reduced to 91, with a small shift in the resonant frequency to 1555 nm. The structure supports also a TM-like mode, shown in Fig. D.1(b), which experiences a slightly smaller effect due to polarization charge screening; its Q drops from 153 to 94. It becomes the lower loss resonant mode in this case.

Other 3D cylindrical structures that have been simulated with this formulation

[†]Since the publication of this work, such a structure has been experimentally investigated in [106].

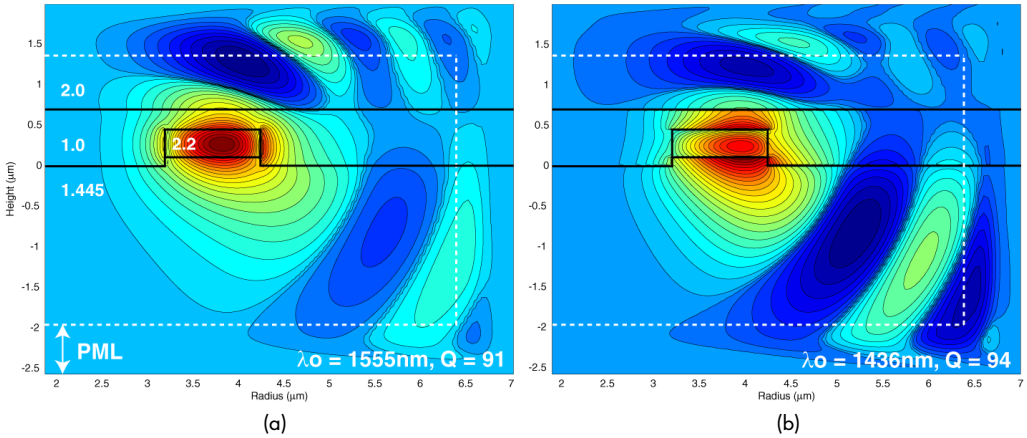

Figure D.1: Leaky modes of a 3D ring resonator in proximity to a high index dielectric halfspace: (a) E_ρ of the TE-like mode, (b) E_z of the TM-like mode. Contours are assigned quadratic spacing to show more low-amplitude detail.

include stacked coupled rings and straight and bent air trench waveguides [124] with bending and substrate leakage loss. High-index-contrast, strongly confining microring resonators with loss Q's in excess of 10^8 have been simulated and verified against other methods.

Small resonators (a few wavelengths in size) of various geometric shapes are of interest in high index contrast [14, 16]. In the second set of examples, the standalone TM modes of a disk and square resonator are shown in 2D, and the CIFS, frequency splitting and coupling-induced loss-Q modification of a coupled resonator pair are investigated. This is accomplished by adapting the complex-frequency solver variant to Cartesian coordinates as explained above, and setting the propagation constant γ (i.e. β) to zero.

Figs. D.2(a,d) show one of two degenerate high-Q modes, near 1550 nm, of a disk of diameter 1.66 μm (refractive indices 3:1), and a lower-Q, higher-order mode chosen to show the PML absorbing outward radiation. Resonant frequencies are 1623.5 nm and 1453.8 nm, with Q's of 2238 and 91. Figs. D.2(b,e) shows coupled disks spaced by 1/10 of their diameter, 0.166 μm. Four relevant modes are now found, symmetric and antisymmetric about each of the x and y axes. The new resonant frequencies are all different: (1611.9, 1611.1 nm) and (1618.5, 1619.7 nm). The major frequency splitting due to coupling of the resonators is seen between pairs of the supermodes. However, the smaller frequency difference within the pairs indicates reflection and backward coupling. Circulating traveling waves are not modes of the new structure, and there is an inherent contradirectional coupling due to the self-phase-matched nature of the scattering from the coupling region "scatterer", which occurs periodically every round trip (this being an integer number of wavelengths on-resonance). This effect is only pronounced in the large index contrast and strong coupling demonstrated here for illustration.

A further important effect, not discussed here in detail, is coupling-induced Q

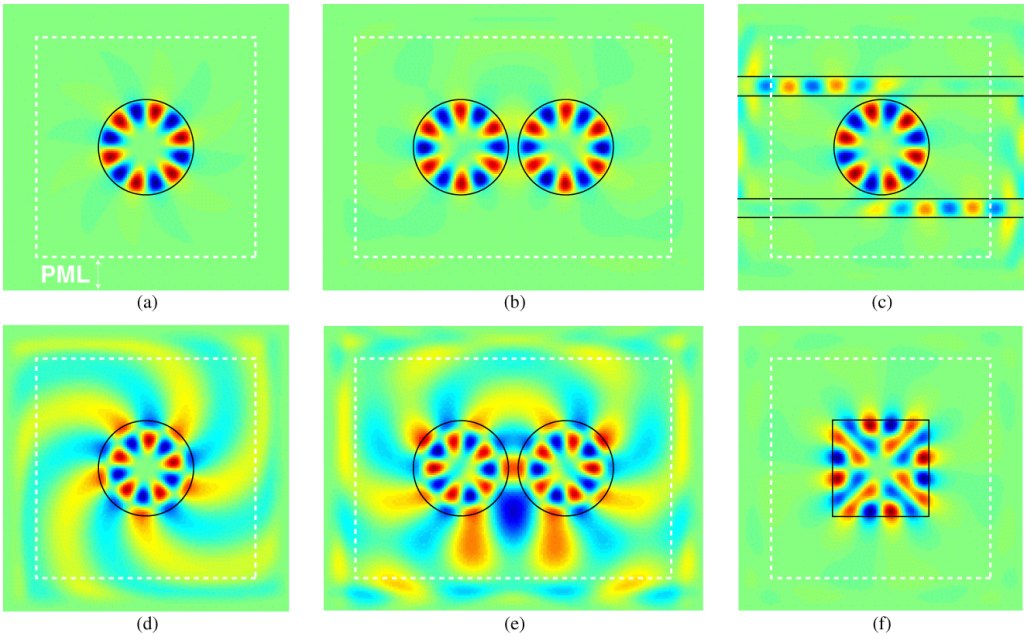

Figure D.2: Leaky modes of 2D resonators (TM, H_z field): (a) high-Q disk mode, (b) high-Q coupled-disk supermode, (c) waveguide-loaded disk mode, (d) low-Q disk mode, (e) low-Q coupled-disk supermode, (f) high-Q square resonator mode (TE, E_z).

enhancement. Coupled resonant modes see far-field radiative cancellation and show a higher radiation Q supermode than either of the uncoupled cavity resonant modes. This effect will be addressed elsewhere. Coupling of modes in time has complex-coefficient degrees of freedom (coupling-induced interferometric decay constants) that can account for this phenomenon. It is analogous to the way we have modeled the variable Q (decay rates) of the single ring cavity with an interferometric input coupling in Sec. 9.4.1, but here the decay mechanism is to the radiation field, whereas in the hitless ring filter it is to the bus waveguide (which has a more restricted mode spectrum). The radiation Q enhancement effect has been observed in early simulations of devices comprising CIFS, shown in Ref. [8, Fig. 5], where we fitted it using the complex CMT model.

In Fig. D.2(c), the superposition of two almost degenerate leaky modes of a loaded resonator shows decay of power from the resonator primarily through coupled waveguides in the counter-clockwise direction. The resulting Q of ∼150 is represents what is normally termed the external Q, i.e. the Q due to decay into ports, and it is much lower (faster decay) than the unloaded Q above. The degeneracy of the even and odd standing wave modes is broken by the presence of the waveguides, and their resonant frequencies are shifted to 1626.9 nm and 1627.8 nm. Neither the shift nor the frequency splitting is predicted by first-order CMT, which only gives a change in the total Q. There is a fundamental, if small, back-reflection in a ring channel-drop filter. Some further comments by the author on this issue are in [8].

Fig. D.2(f) shows a standing-wave mode of a square resonator (edge 1.66 μm, indices 3:1) proposed in [16]. The high-Q mode is found to be at 1556 nm with a Q of 2800 for TE, matching the result obtained in [16] by time-domain FDTD simulation, and at 1415 nm for TM with a Q of 4800.

These examples illustrate the problems that can be solved with this mode solver. It has been applied to solve cylindrical and Cartesian symmetry modes of lossless and lossy/leaky waveguides, as well as to compute the transmission of adiabatic structures by combining the mode solver with film-matching method overlap integrals. All SiN and silicon microring resonator designs associated with this thesis work were designed using this complex frequency solver.

Appendix E

Resonance-frequency-matched strong-confinement filters*

In this section, the rigorous design and first demonstration of channel add-drop filters based on strong-confinement silicon nitride waveguides and microring resonators are described. This work laid the groundwork for the subsequent demonstrations of telecom-grade multistage filters in SiN (Sec. 7.1, [119]), and tunable filters in Si (Chaps. 5, 6 and 9, [135, 136, 205]). In the first section, the first low-loss (3 dB), flat-top and wide-FSR channel dropping filters are described. The frequency mismatch between cavities (including CIFS, see Sec. 4.1) is addressed. In the second section, the first higher-order true channel add-drop filters are demonstrated in strongly confining waveguides, being "true add-drop" insofar as they show a through-port response with a practical in-band extinction, here of 15 dB. This is accomplished by calibration and resonance frequency matching of the ring cavities to compensate for CIFS and fabrication related mismatch. These are also the first reported microring resonator filters realized based on a fully rigorous design taking into account rigorous numerical models of the ring cavities and coupling regions, with model parameters obtained by 3D modesolver and FDTD simulations.

E.1 Low-loss channel add-drop filters in strong-confinement SiN microrings

In this section, third-order add-drop filters based on series-coupled microring resonators are described. They were fabricated in silicon-rich silicon nitride with

*This section was reproduced nearly verbatim from papers [88] and [89]. Device design was done in collaboration with M. R. Watts, all structures were fabricated by T. Barwicz, and optical characterization was done by P. T. Rakich.

accurate dimensional control and negligible sidewall roughness. For the first time, a low 3 dB drop loss is demonstrated with a wide 24 nm free-spectral-range in a high-order microring filter without using the Vernier effect. The spectral response is matched by rigorous numerical simulation, and non-idealities in the drop- and through-port responses are shown to be of design origin and to be correctable.

Introduction

Microring resonators allow for compact channel add-drop filters [38]. They have an important application in optical add-drop multiplexers (OADMs), key components for modern optical networks. Add-drop filters in OADMs must show low loss, flat passbands, and a wide free-spectral-range (FSR) that covers a significant part of the C-band. Recently, sixth-order microring resonator filters have been demonstrated in moderate index-contrast ($\sim$17%) with low drop loss ($<$ 2 dB) and flat passbands [206]. However, these filters suffer from a narrow FSR of about 6.4 nm, which is inadequate for OADMs where an FSR of about 30 nm is desired. For some applications, Vernier operation (rings of different radii) can be used to suppress non-synchronous ring resonances and extend the FSR, as in [120]. However, this technique introduces intolerable dispersion into through channels at the suppressed resonances. Thus, it cannot be used for add-drop filters in OADMs where the through-port response is of critical importance. To increase the FSR, a higher index contrast ($>$100%) must be used to reduce the ring radius while keeping bending loss within acceptable bounds. Unfortunately, high index contrast (HIC) invites a number of difficulties in design and fabrication, and previous attempts at demonstrating high-order filters have met limited success [207].

In this section, we report on third-order series-coupled microring add-drop filters fabricated in silicon-rich silicon nitride (SiN). For the first time, low drop loss (3 dB) and a wide FSR (24 nm) are demonstrated in high-order HIC filters without using the Vernier effect. The drop loss is improved by 10 dB over previously reported wide-FSR filters [207]. The FSR is improved by more than a factor of 2 over moderate-index-contrast filters with only a 2 dB penalty in the drop-loss [137, 208]. Further, the spectral response of the filter is matched to excellent agreement by rigorous numerical simulations. The latter show that the remaining filter shortcomings are not due to the material system or fabrication limitations, but are rather of design origin and are correctable. Therefore, this work demonstrates that HIC, SC resonators are a promising approach to add-drop filters.

Design

Our objective was to design add/drop filters with a 40 GHz passband and a 24 nm FSR in the C-band. Sensitivity of resonance frequencies and bus-ring and ring-ring coupling to dimensional variations makes polarization-independent operation

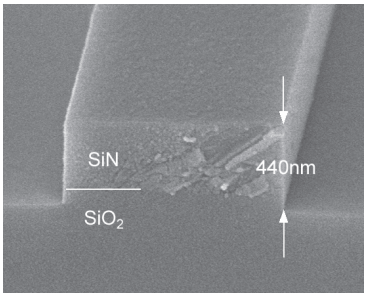

Figure E.1: Scanning-electron micrograph (SEM) showing the cross-section of a fabricated SiN waveguide. See Table E.1 for waveguide parameters (published in [88]; figure SEM by T. Barwicz).

Table E.1: First SiN high-order filter waveguide parameters

Parameter	Designed	Measured
SiN thickness	330 nm	314 nm
SiN refractive index	2.200 at $\lambda = 1.55\,\mu$m	2.217 at $\lambda = 1.55\,\mu$m
SiO_2 thickness	2.50 µm	2.53 µm
SiO_2 refractive index	1.445 at $\lambda = 1.55\,\mu$m	1.455 at $\lambda = 1.55\,\mu$m
Etch depth	430 nm	440 nm

difficult to achieve in HIC. Therefore, we designed filters to operate in only the TE polarization (electric field in the plane of the substrate). We rely on a polarization-diversity scheme to obtain polarization-independent operation. It involves splitting the polarizations and rotating one to obtain identical on-chip polarizations [6].

A waveguide cross-section is shown in Fig. E.1. A single core layer of SiN on a SiO_2 cladding was used for bus waveguides and rings, with air top and side cladding. Designed and measured waveguide parameters are presented in Table E.1. The rings were designed to support a high-Q (about 30,000) fundamental TE mode, but to suppress TM and higher-order TE resonant modes within the desired spectral range. Rings were chosen instead of racetrack resonators [207] as they have a higher uncoupled radiation Q for a given resonator path length. Using known synthesis techniques [38], the third-order filters were designed with a flat-top (Chebyshev) drop-port response. A simplified coupled-mode theory (CMT), based on that in the appendix of [38] but in 3D, was used to convert desired power couplings to bus-ring and ring-ring coupler spacings.

Fabrication

Fabrication[†] of HIC microring resonators requires high-resolution lithography, strict dimensional control, and smooth sidewalls. Consequently, our fabrication process was based on direct-write scanning-electron-beam lithography (SEBL) and non chemically-amplified resist. In addition, the process was optimized to reduce sidewall roughness using the scheme described in [209].

Silicon wafers were first thermally oxidized to form the SiO_2 cladding. Then, the SiN core was deposited by low-pressure chemical-vapor-deposition (LPCVD) in a vertical thermal reactor using a gas mixture of SiH_2Cl_2 and NH_3. This deposition method yields a SiN with low stress and low hydrogen-content. Hence, the material exhibits low birefringence and negligible absorption in the telecommunication bands. The vertical thermal reactor provides excellent on wafer uniformity and a repeatable wafer-to-wafer distribution of film thicknesses and indices of refraction. The discrepancy between the designed and the employed SiN thickness (Table E.1) is due to a problem with the optical characterization tool used in the clean room to select the device wafer. Next, 200 nm of poly-methyl-methacrylate (PMMA) and 40 nm of Aquasave were spun on. PMMA is a positive e-beam resist while Aquasave is a water-soluble conductive polymer from Mitsubishi Rayon used to prevent charging during SEBL. The PMMA was exposed at 30 keV using a Raith 150 SEBL system. The Aquasave was removed, and the PMMA developed. Next, 50 nm of Ni was evaporated on the structure, and a liftoff performed by removing the non-exposed PMMA. Using the Ni as a hardmask, the waveguides were defined by conventional reactive-ion-etching (RIE). Vertical and smooth sidewalls where obtained with a gas mixture of CHF_3-O_2 in a 16:3 flow-ratio. To obtain an accurate etch depth, the RIE was performed in several steps, between which the etch depth was measured with a profilometer. Finally, the Ni was removed using a nitric-acid-based commercial wet Ni etchant. A third-order microring filter is presented in Fig. E.2.

This process yielded high resolution, accurate dimensional control, and smooth sidewalls. Ring-to-bus gaps as small as 50 nm were successfully fabricated with good repeatability. Strict dimensional control was confirmed by feature size measurements using the Raith 150 in scanning-electron-microscope (SEM) mode. Accurate measurements were obtained by calibrating the deflection of the electron beam to the movement of the interferometric stage. During fabrication, the e-beam dose was selected to generate a correct bus waveguide width at the coupling region. This width was found to be accurate within the error of the measurement (about 5 nm). However, as proximity effect corrections were not applied, repeatable waveguide-width errors reaching 20 nm were observed on parts of the structure.

[†]All process development and device fabrication was done by T. Barwicz. This section provides a summary of the fabrication.

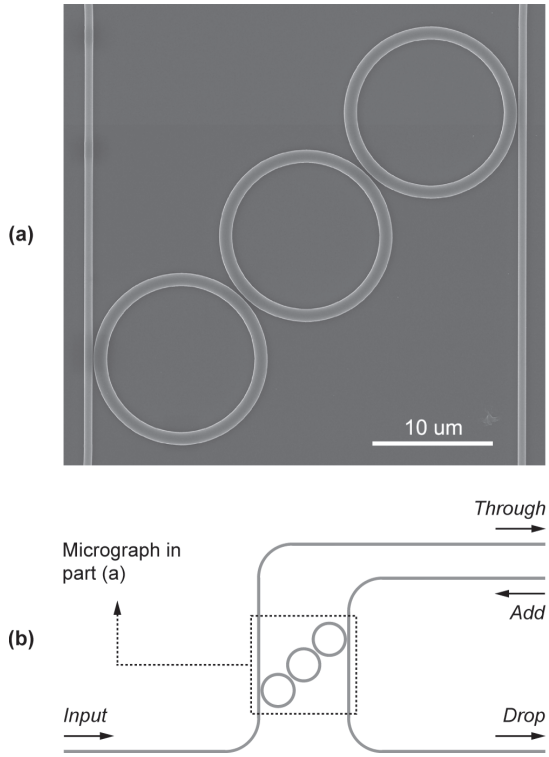

Figure E.2: (a) Scanning-electron micrograph (SEM) of third-order SiN microring resonator add-drop filter with 25 nm FSR; (b) layout of the structure (by Tymon Barwicz).

Optical characterization

Transmission measurements[‡] were performed using a modulated tunable laser coupled to the input facet of each waveguide from an optical fiber using a high-numerical-aperture-lens assembly. The output signal was detected with a large-area Ge photodetector through a non-dispersive microscope objective and filtered using a lock-in amplifier.

As input-to-drop loss is extracted by comparing the drop and through responses, these two measurements were performed under similar conditions and repeated several times with two different collection methods. A measurement of the response of a third-order microring filter is shown in Fig. E.3. The filter shows 3 dB drop loss, a 24 nm FSR, a 1dB-bandwidth of 88 GHz and 7.5 dB of in-band rejection.

Initial Fabry-Perot loss measurements, performed on several straight waveguides, found an upper bound for propagation loss of 3.6 dB/cm reported in the initial publication [88]. A review of this data, and later rigorous loss measurements of later SiN devices (those in Sec. E.2 and Sec. 7.1) gave propagation loss estimates on the order of 10 dB/cm, which was the final concluded propagation loss value for Si-rich SiN waveguides used here. The lower (erroneous) loss reported here

[‡]Done by P. T. Rakich.

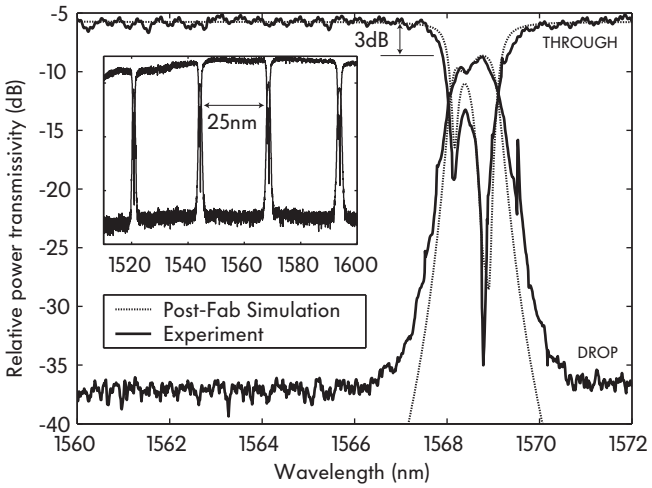

Figure E.3: Experimental results demonstrating the first low-loss higher-order add-drop filters based on strong-confinement photonics. Simulated drop- and through-port responses match the experiment if a 22 GHz resonant-frequency mismatch is assumed.

was most likely caused by an omission in estimating the facet reflectivity for the Fabry-Perot loss method. The effective index method cannot be used in strong-confinement waveguides and rigorous finite-difference time-domain simulations of the facets are required. A rigorously computed facet reflectivity and a review of the Fabry-Perot data placed this waveguide loss around 11 dB/cm. Returning to the propagation loss for the present devices, numerical simulations indicate that some of the loss is due to e-beam field-stitching errors. A rotational error in the field calibration created a 30 nm offset of the bus waveguides every 100 μm, resulting in a loss of 0.021 dB/junction or 2.1 dB/cm.

Discussion

Post-fabrication simulations were performed to understand the observed response of the fabricated third-order filter using the measured dimensions and refractive indices[§]. Ring-ring and ring-bus coupling coefficients were calculated using three-dimensional finite-difference time-domain (FDTD) simulations. A cylindrical mode solver yielded bend losses and ring effective and group indices. The ring resonant frequencies were chosen to fit the data. These parameters, inserted into a transfer-matrix model for the filter, show agreement between theory and experiment (Fig. E.3). The remaining difference may be explained by dimensional measurement errors.

The FDTD simulations indicate that additional losses were present in each of the rings due primarily to coupling to a lossy higher-order transverse mode of the ring waveguide at the couplers. The waveguides support a single mode of each polarization when straight, but when bent regain the second-order TE mode as

[§]Done by M. R. Watts.

a leaky resonance with high bend loss. This occurs because bending increases lateral confinement on the inner edge of the mode in addition to forcing leaky behavior beyond the radiation caustic. A higher-order mode can be tolerated if its loss is engineered to be high enough to ensure that no coupling to it from the fundamental mode is present and that it is not resonant. In our design, the 7 dB/90° of bending loss predicted for the second-order TE mode was sufficient to suppress its resonance, but turned out to be too low to forbid excitation of the mode at the couplers by the fundamental resonance. This excitation translates to coupler losses, which are higher in the outer rings since the ring-bus coupling is stronger than the ring-ring coupling. The realized dimensions and indices give an expected radiation Q, due to bend loss, of 22,000. The coupler losses reduce the radiation Q's to about 10,000 (outer rings) and 13,000 (central ring). This reveals coupler scattering to be a significant loss mechanism. It and bend loss fully account for the observed drop loss (Fig. E.3).

The spectral asymmetry, clear in the through-port response, is indicative of unequal, symmetrically distributed resonance frequencies, with the central ring having a higher frequency than the outer rings by 22 GHz. The effect is partially explained by coupling-induced frequency shifting (CIFS) of resonators [46, 87] due to the index perturbations caused by adjacent ring and bus waveguides. The CIFS calculated by FDTD is 43 GHz. Frequency shifts are also expected to result from dimensional variations in the rings due to e-beam proximity effects and e-beam discretization errors. While dimensional measurement uncertainty prevents a proper estimate of these effects, simple calculations reveal these effects to be of the same order as the CIFS. Proximity effects should contribute a shift of the same sign as the CIFS. Thus, we believe e-beam discretization errors are significant in reconciling the calculated CIFS with the experimentally-observed frequency shift.

The frequency mismatch can be corrected by properly predistorting the device design [46]. In practice, a slight, deliberate increase of e-beam dose on the middle ring could be applied. This would make the middle ring slightly wider and lower its resonant frequency to match it to the outer rings. We note that the deleterious impact of uncompensated frequency mismatch will be less pronounced in filter designs that are intrinsically less sensitive to resonance frequency variations, such as those based on parallel-cascaded resonators [140]. These filters would also exhibit frequency shifts, but their geometry may give these designs the advantage of a smaller net frequency mismatch to begin with. Despite the accurate fabrication of our filters, the measured 88 GHz bandwidth was more than twice the intended 40 GHz bandwidth. The matching of simulation results and experimental data supports the validity of the numerical simulations, and the discrepancy is attributed to the simple CMT design model used. A larger-than-intended passband ripple limited the in-band (through-port) rejection to 9 dB, instead of an intended 13 dB. The resonant frequency mismatch further reduced this to 7.5 dB. These factors can

be compensated to produce symmetric responses with stronger in-band rejection.

Conclusion

SiN microring-resonator-based add-drop filters were fabricated and characterized. These were the first low-loss filters to be demonstrated in HIC, wide-FSR (25 nm) microring resonators. Low filter loss and a large FSR were obtained without employing the Vernier effect. The filter response was measured and compared with rigorous post-fabrication simulations. Scattering at the ring-to-bus gaps and resonant frequency mismatch between the rings were found to degrade the filter response and to be correctable. A fabrication process yielding high resolution, accurate dimensional control and smooth waveguides was demonstrated. SiN has been shown to be a well-suited material for microring resonators.

E.2 Frequency-matched, high-order SiN microring resonator add-drop filters

In this section, rigorous electromagnetic simulations are used to design high-index-contrast microring-resonator filters. The first fabricated third-order filters compensated for passband distortion due to coupling-induced and fabrication-related frequency shifts demonstrate a 20 nm FSR and the highest reported thru-port extinction (14 dB).

Introduction

Coupled-microring filters are a promising approach to planar integrated-optical add/drop filters for wavelength-division multiplexed (WDM) networks [87, 88, 120, 137, 207, 208]. Coupled cavities enable narrow, frequency-selective line-shapes with flat passbands while traveling-wave-cavity operation facilitates a natural separation of ports. Low-loss drop-only filters have been demonstrated [137, 208] using microrings with a free spectral range (FSR) of $\sim$6 nm. True add/drop filtering of a single WDM channel requires large resonator FSR spanning the optical band in use ($\sim$30 nm), and strong extinction of the dropped channel in the thru-port. Vernier schemes [120] can extend a small FSR, but tend to introduce intolerable dispersion into some thru channels. High index contrast (HIC) enhances confinement reducing bend loss in small-radius rings thereby enabling low-loss and wide-FSR filters directly [88]. Yet, HIC adds considerably to cavity design and fabrication challenges. Coupling-induced resonance frequency shifting (CIFS) [46, 87] and excess losses due to coupler scattering [88] must be overcome in a successful design. Fabrication-related distortions of cavities (e.g. proximity effects) must also be countered. Detailed consideration of these issues and use of rigorous electro-

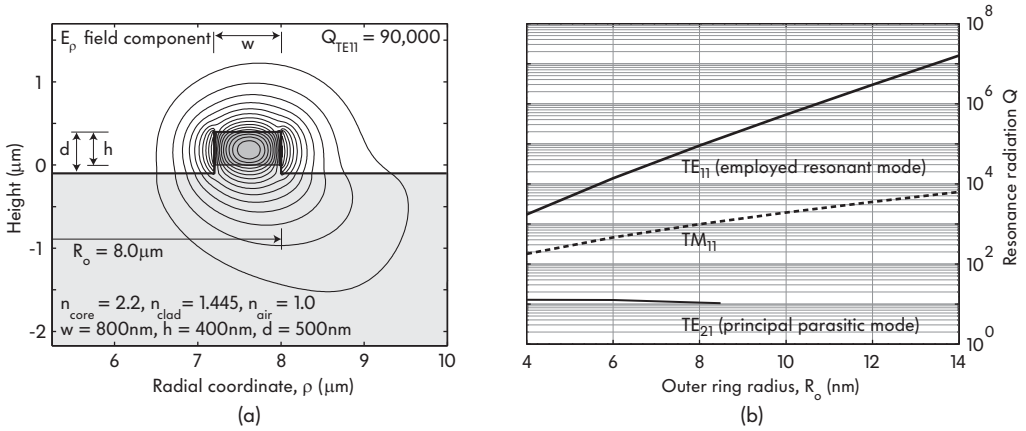

Figure E.4: (a) HIC microring waveguide cross-section with overlaid horizontal electric field pattern; (b) Q vs. radius and FSR for the fundamental TE_{11} and spurious TE_{21} and TM_{11} modes, showing bending-induced reconfinement of the spurious mode.

magnetic design, the importance of which we pointed to in [88], was absent in the literature at the time of this work.

We present design considerations for efficient HIC filters and rigorous analysis using three-dimensional, finite-difference cylindrical mode-solver and time-domain codes and experimental results on the first fabricated filters compensated for coupling-induced and fabrication-related cavity resonance shifts. The filters exhibit a 20 nm FSR and, as a result of the compensation, 14 dB in-band extinction in the thru-port, the highest reported result in third order microring filters. Measured results closely match the design response.

Design of HIC waveguides and resonators

The challenges in HIC design and fabrication are outlined through an example filter with a drop response having a flat-top, 40 GHz passband with $\geq$30 dB rejection 80 GHz from the passband center, and 20 dB extinction of the dropped channel across 40 GHz in the thru-port.

Differences in propagation and coupling strength between TE and TM modes make achieving polarization independence in HIC difficult. Hence, a single-polarization filter is designed to be used within a balanced polarization-diversity scheme [31]. A wide, thin cross-section [Fig. E.4(a)] waveguide was chosen. The geometry more tightly confines the intended TE mode, reduces the ring's sensitivities to sidewall roughness and its frequency dependence on waveguide width while providing a substantial mismatch between the propagation constants of the TE and TM modes. The mismatch inhibits crosstalk between the modes due to unintended perturbations by allowing the modes a chance to de-phase before substantial coupling takes place.

A 40-GHz filter corresponds roughly to an external Q of 4,000. For low filter

losses a radiation Q $\sim$ 100,000 is sought in the fundamental TE_{11} resonance. To analyze the ring modes, a full-vector cylindrical mode-solver is employed [91]. To arrive at a wide-FSR design, the ring radius is minimized while keeping the TE_{11} Q $\sim$ 100,000. The TM_{11} mode is also confined by the structure, but its presence is less of a concern since coupling to it is inhibited by the near-orthogonality of the cross-polarized modes in the coupling regions. However, the tight bend radii required to achieve large FSRs tend to re-confine modes that are cutoff in a straight guide, admitting spurious leaky resonances. The TE_{21} mode is of particular concern and must be suppressed, as it couples strongly to the TE_{11} mode in coupling regions resulting in excess loss [88]. The guide cross-section is adjusted to strongly suppress the undesired TE_{21} resonance. Qs of the TE_{11}, TM_{11} and TE_{21} resonances are shown in Fig. E.4(b). An 800$\times$400 nm ring core with 100 nm overetch yields a 20 nm FSR and a Q $\sim$ 90,000 for the TE_{11} resonance (order 52) at 1544.5 nm while suppressing the TE_{21} and TM_{11} resonances to Qs of 10 and 980, respectively. Identical cross-sections were used for bus waveguides.

To synthesize the prescribed response, a third-order resonator requires 8.9% ring-bus and 0.17% ring-ring coupled power ratios. Complex coupling coefficients for various separations yield the power coupling, the excess cavity losses due to the interaction, and the coupling-induced resonance frequency shifts [46]. Rigorous 3D finite-difference time-domain (FDTD) simulations of the coupler regions were used to determine the complex ring-bus and ring-ring coupling coefficients at the resonant wavelength. The results, accompanied by exponential fits, are shown in Fig. E.5. Rounded to a 6 nm scanning-electron-beam lithography (SEBL) system pixel size, 102 nm ring-bus and 492 nm ring-ring separations were chosen corresponding to the above couplings. With these separations the net CIFS in the outer rings is +38 GHz, which is comparable to the filter bandwidth. Clearly, the filter would not work without compensation of the frequency mismatch. The middle ring may be slightly pre-distorted in resonance frequency by the negative of the shift without changing appreciably any of the coupling parameters. An ideally compensated response shown in Fig. E.6(c) (dash) gives a flat passband, 38 GHz 1 dB bandwidth, 19 dB thru-port extinction, and 1.5 dB loss due to bending and coupler scattering.

Fabrication and optical characterization results

The devices were fabricated using direct write SEBL. The fabrication process is similar to the one described in [88]. The pattern was defined in 200 nm of polymethyl-methacrylate (PMMA) using a Raith 150 SEBL system at 30 keV. A hardmask was formed by evaporating and lifting off a thin film of Ni. The waveguides were created by a 500-nm-deep conventional reactive-ion etching step using a gas mixture of CHF_3 and O_2. Finally, the Ni hardmask was removed. The e-beam dose to the center ring of several identical filters was varied to slightly enlarge the

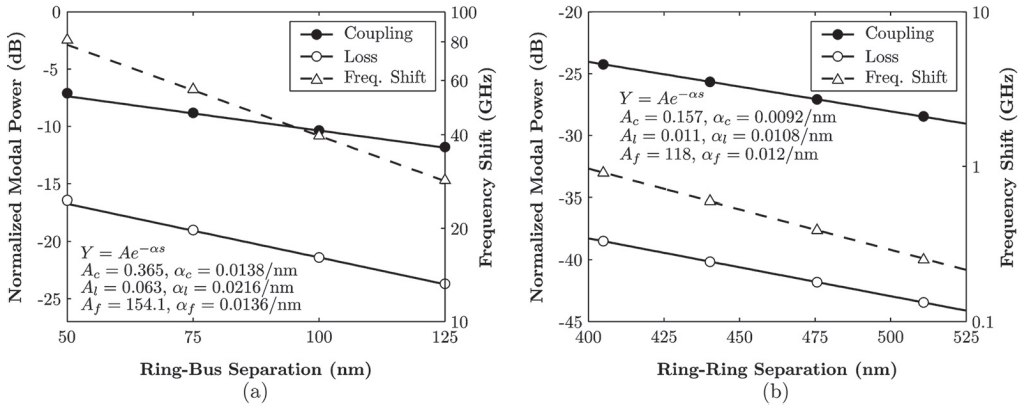

Figure E.5: 3D FDTD determined (a) ring-bus and (b) ring-ring coupling, loss and coupling-induced frequency shifts (simulations by M. R. Watts).

center ring to tune it into resonance with the other rings in the filter. Fig. E.6(a) is a micrograph of a fabricated filter.

Measured responses of the uncompensated and successfully compensated fabricated filters are shown in Figs. E.6(b) and E.6(c). Care was taken to ensure that the drop- and thru-port responses have the same insertion loss scale. A fit to the uncompensated filter response indicated that the frequency of the center ring differed by 170 GHz from that of the rings adjacent to the bus waveguides. A 4.5% increase in the electron-beam dose to the center ring was required to compensate the frequency shift. The resulting compensated filter exhibits a 30 GHz-wide 1 dB passband in the drop port, with a rolloff that provides 25 dB extinction 58 GHz from the channel center. In addition, a ∼14 dB in-band rejection of the dropped channel in the thru-port was achieved, the highest reported for a high-order microring filter, and a crucial requirement for add/drop filters.

Higher than expected drop loss of 6 dB rounds the compensated filter passband. Total ring loss was extracted by fitting the uncompensated response indicating an excess waveguide propagation loss of ∼15 dB/cm. Accounting for this loss in the design model gives agreement with the measured filter response. The loss breakdown is 20% due to bending, 20% due to excess coupler scattering and 60% attributed to loss in SiN and roughness. The high propagation loss was also verified by the Fabry-Perot method using FDTD-computed facet reflectivity.

The higher than expected propagation loss is mainly attributed to an imperfect Ni liftoff. The Ni evaporation produced a thicker film (62 nm) than expected (45 nm) and a coarse microstructure, which amplified the line-edge-roughness of the Ni hardmask and translated to larger sidewall roughness and higher than expected scattering losses.

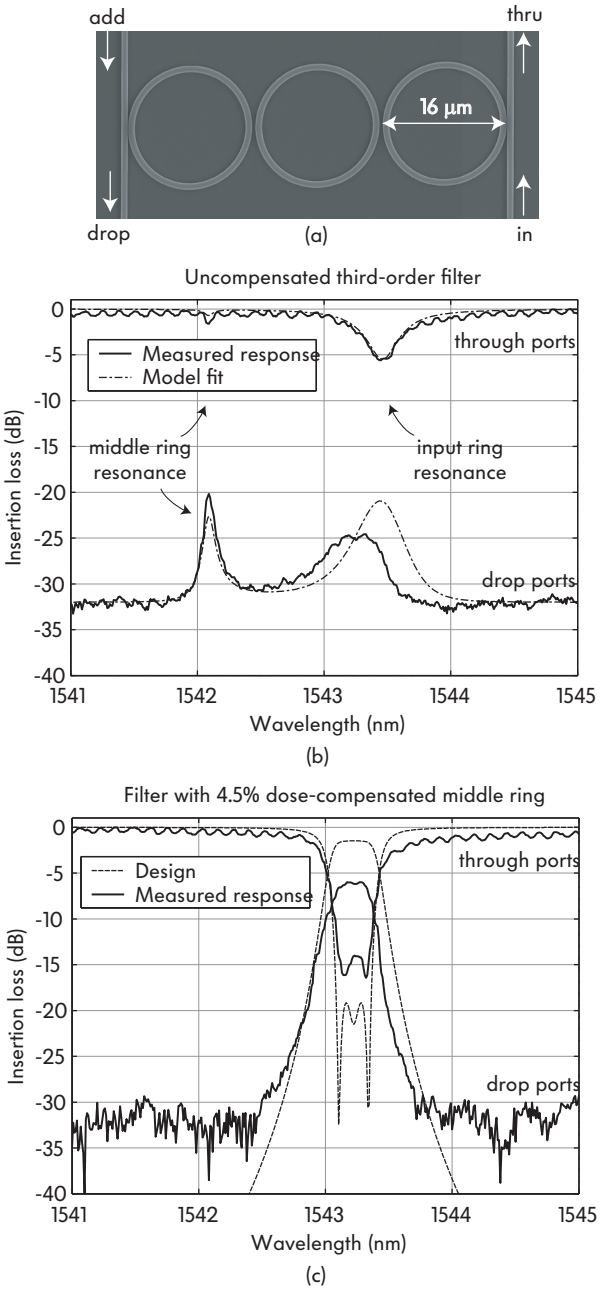

Figure E.6: (a) Micrograph of a compensated filter with 4.5% incremental dose applied to the middle ring; (b) drop- and thru-port responses of 3-ring filter without compensation - experiment (solid) and fit (dotted); (c) drop- and thru-port responses of compensated filter - theory (dash), theory with 15 dB/cm waveguide loss (dotted) and experimental (solid).

Conclusions

Rigorous electromagnetic analysis is needed for HIC filter design. Fabricated filters with proper compensation of coupling-induced and fabrication-related frequency mismatch in fabrication are shown. This compensation is necessary for successful

realization of HIC microring filters with high extinction in the thru port. Dose compensation in e-beam fabrication was applied to demonstrate the first frequency-compensated filters, yielding 14 dB extinction in the thru port, and matching design predictions. Further results on the fabrication-related aspects including resonance-frequency compensation by dose adjustment are published in [90].

Appendix F

Low-loss Bloch waves in open structures and compact, efficient silicon waveguide-crossing arrays*

In this appendix, low-loss, compact, broadband silicon-waveguide crossing arrays and active structures are proposed based on periodicity-matched multimode focusing. Simulations show loss of 0.045 dB/crossing and >200 nm bandwidth in a typical example. Correspondence to low-loss, structure-matched Bloch-waves is demonstrated.

Strong-confinement (SC) waveguides based on high index contrast support dense photonic device integration, promising complex microphotonic circuits such as on-chip wavelength multiplexers [33, 157, 211] or entire photonic networks on a microprocessor die. As device density and complexity increase in a planar photonic circuit, efficient waveguide crossings quickly become of paramount importance because the number of waveguide crossings required rises quickly and tolerable levels of loss and crosstalk per crossing accordingly drop to very small limits.

Straightforward crossing of single-mode SC waveguides leads to strong diffraction losses [14], and a number of improvements have been proposed [14, 20, 33, 153, 212–217]. Low-Q resonator based Si waveguide crossings [14] give in theory ∼0.2 dB loss, but have limited, 10-15 nm low-loss bandwidth, and challenging critical dimensions and fabrication sensitivities. On the other hand, waveguide crossings using mode expanders (to widen the effective aperture and minimize diffraction losses) are broadband and tolerant, but large [20, 33], or not optimally efficient giving on the order of 0.4 dB loss in theory and experiment [153, 212],

*This appendix reproduced nearly verbatim from my paper [210].

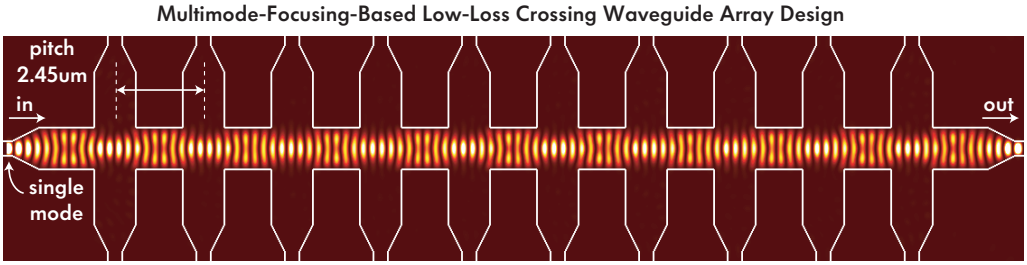

Figure F.1: Low-loss waveguide crossings and crossing arrays based on multimode focusing, low-loss Bloch waves: design of 10 crossing cascade in Si-SiO_2 waveguides shows intensity of light focusing across each crossing to avoid diffraction losses.

or 0.2 dB with a multi-layer structure [213]. To reduce diffraction losses, multimode interference-based crossings that mimic focusing have been investigated [214–216], but though more compact in size, their predicted losses remain on the order of 0.2 dB per crossing [215]. While such losses may seem small, they are not acceptable in dense circuits where one may thus accumulate 10-20 dB of loss after 50 crossings.

In this work, ultra-low loss waveguide crossing arrays are proposed by combining the multimode focusing concept with matching of the field pattern and dielectric structure periodicities to produce a low-loss Bloch wave. This crossing array is a unified structure (Fig. F.1) that permits 10s or 100s of crossings at a dense pitch of only a few microns. Two-dimensional FDTD simulations (valid since diffraction is in the plane) of an example silica-clad, Si-core waveguide crossing array show ∼0.04 dB/crossing (Fig. F.2), with the remaining loss accounted by the input/output tapers. This is 5-10 times lower loss than previously proposed designs in nearly identical waveguides and material systems [153, 212, 215]. These crossing arrays also provide the most compact waveguide-crossing footprint, for a non-resonant crossing, known to the author with a spacing of 2.45 μm. Considering minimum spacing between waveguides for low crosstalk, these designs approach the limit of compactness for crossing arrays. In addition to a more compact footprint, an advantage of a crossing array over a cascade of single crossings is that the input/output tapers can have losses of the same order as the crossing region, and therefore the array has considerably lower loss. Since the designs are broadband, they are also expected to be tolerant to fabrication errors.

This concept is not without previous analogue; in the 1960's Goubau and Schwering proposed so-called beam waveguides composed of a periodic array of confocal lenses in free space [217]. In the proposed periodic structures, the crossing regions correspond to the free-space regions in the beam waveguide, and the waveguide regions correspond to the lenses. However, the microphotonic structure has virtually no reflection at each period and can approach very low losses, unlike the beam waveguide, where the lenses produce reflection loss.

The confocal principle in the beam waveguides is generalized to looking for

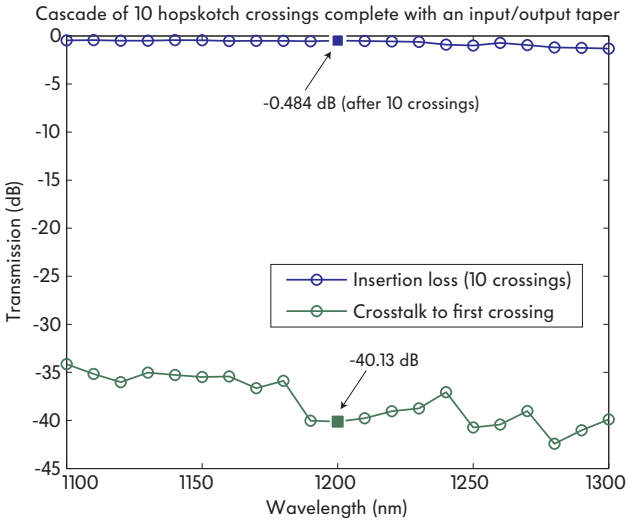

Figure F.2: Spectral transmission properties of the set of 10 crossings in Fig. F.1, showing <0.05 dB/crossing loss, with -35 to -40 dB crosstalk over 200 nm bandwidth.

a structure-matched low-loss Bloch wave, as illustrated in Fig. F.3. Here, input and output tapers are left out, and the fundamental mode of the wider, multimode waveguide is excited. Launching the fundamental mode into the structure causes large diffraction losses at the first two crossings, shedding the part of the field pattern that has high losses, and leaving behind a field configuration that eventually finds the low-loss Bloch-mode, after the first couple of crossings, and thereafter has dramatically lower loss per crossing, as seen from the field pattern. An efficient design is achieved in Fig. F.1 by providing a short (non-adiabatic) taper that immediately excites this low-loss field configuration and thereby provides low loss right from the first crossing. This is done by exciting the appropriate ratio of the fundamental and third mode, which beat to simulate the focusing pattern, finding the phase relationship that places the focus-like point at the center of each waveguide crossing. By varying the few available parameters in Fig. F.3, an optimum configuration is obtained with the lowest-loss Bloch mode. Then the matching tapers are simply added.

Furthermore, devices based on multimode interference where the mode beat pattern self-confines may be useful for other novel devices such as modulators with low optical loss due to contacts and low contact resistance. This work will be further described elsewhere.

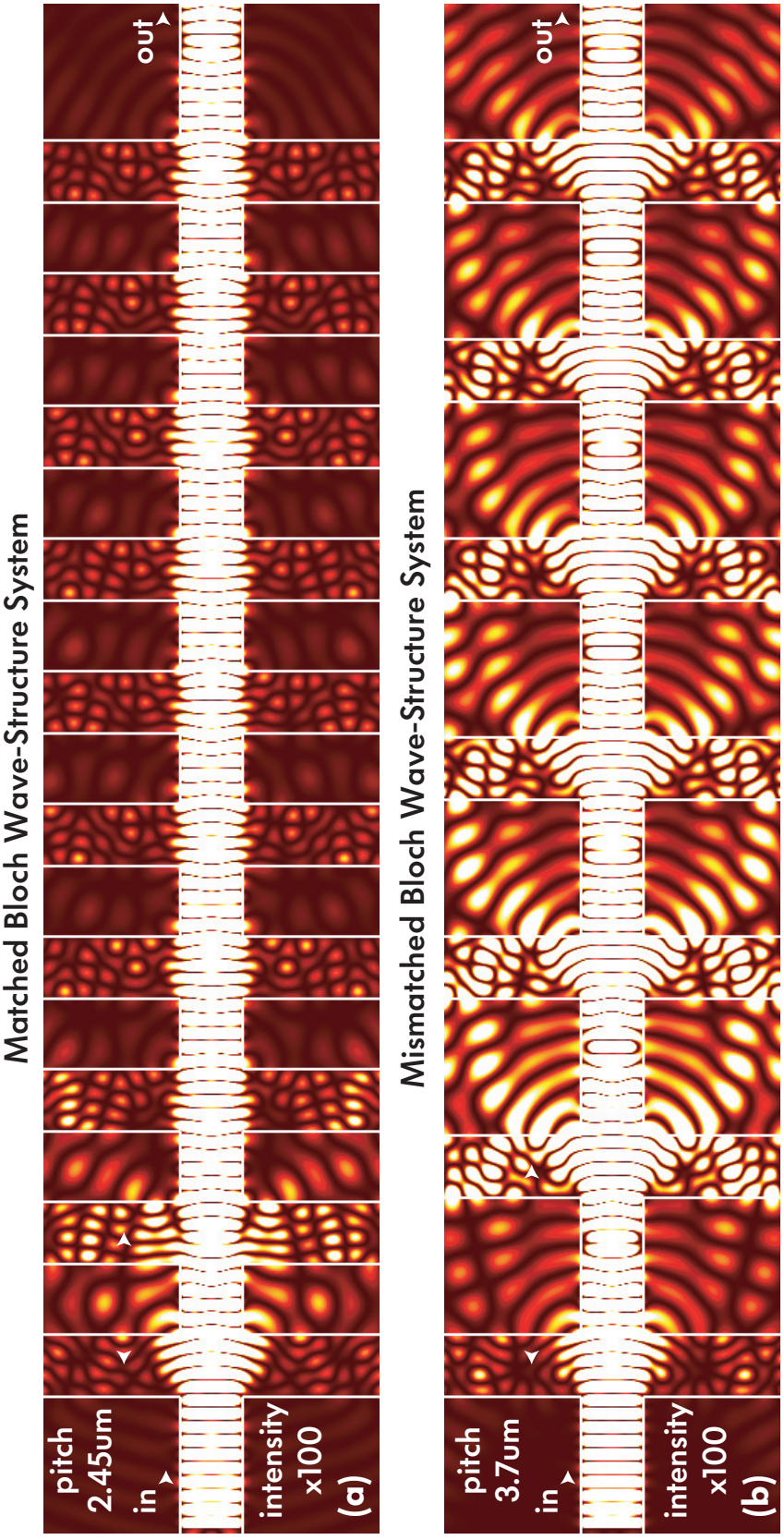

Figure F.3: Low-loss Bloch modes: (a) simulated periodic crossing structure with period of Fig. F.1, showing that a matched focusing field pattern period and structure period gives low (0.04 dB) loss per crossing; while (b) mismatched periods cause 15 times larger (0.65 dB per crossing) losses.

List of Symbols and Abbreviations

Abbreviation	Description	Definition
CMT	Coupling of modes in time	page 75
CIFS	Coupling-induced resonance frequency shift	page 73
DWDM	Dense wavelength-division multiplexing	page 18
FDTD	Finite-difference time-domain (simulation method)	page 74
FSR	Free spectral range (of a resonant cavity)	page 17
ITU	International Telecommunications Union (standards body)	page 20
MC-STE	Maximally confined, single-TE-mode (referring to waveguide)	page 98
MC-STM	Maximally confined, single-TM-mode (referring to waveguide)	page 98
NRBB	Non-reciprocal bypass block	page 223
OADM	Optical add-drop multiplexer	page 18
Q	Quality factor, Q (of a resonant mode)	page 17
R	Reflectionless (e.g. R 4-port)	page 33
RIE	Reactive-ion etching	page 142
SC	Strongly confined (waveguides or waveguide modes)	page 17
SCC	Series-coupled-cavity (resonant filters [38, 49])	page 39
SEBL	Scanning electron beam lithography	page 123
SOI	Silicon-on-insulator (wafer)	page 95
STE	Single-TE-mode (referring to waveguide)	page 100
STM	Single-TM-mode (referring to waveguide)	page 100
TE	Transverse-electric (mode), referring to horizontal, in-chip-plane polarization	page 23
TM	Transverse-magnetic (mode), referring to vertical, out-of-chip-plane E-field polarization	page 23
UBI	Universally balanced interferometer	page 183
UPC	Unitary phase condition	page 40

Abbreviation	Description	Definition
ZDBI	Zero differential-phase-shift bypass interferometer	page 229

List of Figures

List of Tables